# GLOBAL TRENDS IN SATELLITE-DERIVED FINE PARTICULATE MATTER
# &
# DEVELOPMENTS TO REACTIVE NITROGEN IN A GLOBAL CHEMICAL TRANSPORT MODEL

by

Brian Boys

Submitted in partial fulfillment of the
requirements for the degree of
Doctor of Philosophy

at

Dalhousie University
Halifax, Nova Scotia
August 2022

© Copyright by Brian Boys, 2022

# TABLE OF CONTENTS

## List of Tables

## List of Figures

## Abstract

At present, air pollution is the leading global environmental risk factor for premature mortality. Highly respirable fine particulate matter ($PM_{2.5}$) dominates this global burden of disease, while ozone makes smaller but noticeable contributions. Nitrogen oxides ($NO_x \equiv NO + NO_2$) modulate oxidant fields and influence air quality. This thesis is composed of three research chapters which make use of, and developments to, a global atmospheric chemical transport model (CTM) for the purposes of (i) monitoring and understanding global trends in satellite-derived $PM_{2.5}$ and (ii) improving the simulation of $NO_2$ reaction on ground surfaces.

First, aerosol optical depth (AOD) retrieved from two satellite instruments, MISR and SeaWiFS, is used in conjunction with the GEOS-Chem CTM to produce a unified 15-yr global time series (1998–2012) of ground-level $PM_{2.5}$. Four regional areas with significant and spatially coherent trends are examined in detail: eastern U.S., Arabian Peninsula, South Asia, and East Asia. The linear tendency over the eastern U.S. ($-0.37 \pm 0.13$ μg $m^{-3}$ $yr^{-1}$) agrees well with that from ground-level monitors ($-0.38 \pm 0.06$ μg $m^{-3}$ $yr^{-1}$).

Next, the trace gas dry deposition parameterization from GEOS-Chem is reimplemented to run in single-point-mode to facilitate direct evaluation of isolated components against above-canopy fluxes of nitric acid ($HNO_3$), $NO_2$, and total oxidized reactive nitrogen ($NO_y$) observed by the method of eddy covariance. A low bias of -80% in simulated nocturnal $NO_2$ deposition velocity was eliminated by representing a reaction pathway for $NO_2$ heterogeneous hydrolysis on deposition surfaces, paying attention to canopy surface area effects and interferences from soil $NO_x$ emissions.

Finally, we develop a parameterization to represent the process of subgrid dry deposition of near-surface emitted $NO_x$ and implement into the GEOS-Chem CTM along with aforementioned updates to $NO_2$ dry deposition. Resulting reductions in ground-level $NO_2$ are on the order of 5–20% with commensurate reduction in regional concentrations of total nitrate ($HNO_3$ + particulate nitrate). Large increases (>100%) in simulated surface concentrations of nitrous acid (HONO)—an important precursor of the hydroxyl radical (OH)—stem from improved representation of $NO_2$ surface processes and help to alleviate a large low bias compared to aircraft observations.

## List of Abbreviations and Symbols Used

| | |
|---|---|
| $A_{mes}$ | mesophyll cell surface area |
| ABA | abscisic acid |
| ACEnet | Atlantic Computational Excellence Network |
| AERONET | Aerosol Robotic Network |
| AOD | aerosol optical depth |
| AQG | air quality guideline |
| Ar | argon |
| BAO | Boulder Atmospheric Observatory |
| BC | black carbon aerosol |
| BRAVO | Big Bend Regional Aerosol and Visibility Observational Inventory |
| BVOC | biogenic volatile organic compound |
| CAAQS | Canadian Ambient Air Quality Standards |
| CAC | Criteria Air Contaminants |
| CASTNet | Clean Air Status and Trends Network |
| CALIPSO | Cloud-Aerosol Lidar and Infrared Pathfinder Satellite Observations |
| CAPMon | Canadian Air and Precipitation Monitoring Network |
| CFC | chlorofluorocarbon |
| $CH_4$ | methane |
| CI | confidence interval |
| CMAQ | Community Multiscale Air Quality model |
| CNN | cloud condensation nuclei |
| CO | carbon monoxide |
| $CO_2$ | carbon dioxide |
| CRF | canopy reduction factor |
| CTM | chemical transport model |
| CTR | Centerville, Alabama |
| d | displacement height |
| D | molecular diffusivity |
| DJF | December-January-February |
| DLAI | deciduous leaf area index |
| DMS | dimethyl sulfide |
| $E_{pulse}$ | emission pulse |
| EC | eddy covariance |

| | |
|---|---|
| EDGAR | Emissions Database for Global Atmospheric Research |
| EMEP | European Monitoring and Evaluation Program |
| EPA | Environmental Protection Agency |
| F | mass flux |
| *f* | ratio of species mass in a 1-D column model to a single box of equal vertical extent |
| FP | Forward Processed |
| FRM | Federal Reference Method |
| GBC | grid box center |
| GC | GEOS-Chem |
| GEOS | Goddard Earth Observing System |
| GFED | Global Fire Emissions Database |
| GLS | General Least Squares |
| GMAO | Global Modeling and Assimilation Office |
| $g_s$ | stomatal conductance |
| H | Henry's Law solubility constant |
| H* | effective Henry's solubility |
| $h_c$ | canopy height |
| HAS | hydraulic activation of stomata |
| HCFC | hydrochlorofluorocarbon |
| HCHO | formaldehyde |
| HEMCO | Harvard-NASA Emission Component |
| HFEMS | Harvard Forest Environmental Monitoring Site |
| $HNO_3$ | nitric acid |
| $H_2O_2$ | hydrogen peroxide |
| $HO_2$ | hydroperoxy radical |
| HONO | nitrous acid |
| $HO_x$ | $HO_x$ chemical family ($HO_x \equiv OH + HO_2$) |
| IMPROVE | Interagency Monitoring of Protected Visual Environments |
| JJA | June-July-August |
| K | eddy diffusivity |
| k | von Karman constant |
| $K_a$ | acid dissociation constant |
| $k_d$ | canopy deposition rate constant |
| $k_{het}$ | heterogeneous rate constant |
| $k_v$ | canopy ventilation rate constant |

| | |
|---|---|
| L | Monin-Obukhov length |
| $L_{dep}$ | loss due to dry deposition mass flux |
| LAI | leaf area index |
| LST | local solar time |
| M | molecular mass |
| MAD | median absolute deviation |
| MEGAN | Model of Emissions of Gases and Aerosols from Nature |
| MERRA | Modern-Era Retrospective analysis for Research and Application |
| MISR | Multi-angle Imaging Spectroradiometer |
| MODIS | Moderate Resolution Imaging Spectroradiometer |
| M-O | Monin-Obukhov |
| $N_2$ | dinitrogen |
| $N_r$ | reactive nitrogen |
| N.A. | North America |
| NAAQS | National Ambient Air Quality Standards |
| NASA | National Aeronautics and Space Administration |
| NEI | National Emissions Inventory |
| $NH_3$ | ammonia |
| $NH_4^+$ | ammonium |
| NMB | normalized mean bias |
| NSERC | Natural Sciences and Engineering Research Council of Canada |
| $N_2O$ | nitrous oxide |
| NO | nitrogen monoxide |
| $NO_2$ | nitrogen dioxide |
| $NO_2^-$ | nitrite |
| $NO_3^-$ | nitrate |
| $NO_x$ | nitrogen oxides ($NO_x \equiv NO + NO_2$) |
| $NO_y$ | oxidized reactive nitrogen |
| $O_2$ | dioxygen |
| $O_3$ | ozone |
| OA | organic aerosol |
| OH | hydroxyl radical |
| OMI | Ozone Monitoring Instrument |
| P | pressure |
| p | p-value |
| PAI | plant area index |

| | |
|---|---|
| PAN | peroxyacetyl nitrate |
| PAR | photosynthetically active radiation |
| PARANOX | PARAmeterization of emitted NOx |
| Pb | lead |
| PBL | planetary boundary layer |
| PBAP | primary biological aerosol particle |
| $PM_{0.1}$ | ultrafine particulate matter with diameter less than 0.1 μm |
| $PM_1$ | fine particulate matter with diameter less than 1 μm |
| $PM_{2.5}$ | fine particulate matter with diameter less than 2.5 μm |
| $PM_{10}$ | particulate matter with diameter less than 10 μm |
| $pNH_4$ | particulate ammonium |
| $pNO_3$ | particulate nitrate |
| $pSO_4$ | particulate sulphate |
| $R^2$ | coefficient of determination |
| $R_a$ | aerodynamic resistance to dry deposition |
| $r_a$ or $r_{ac}$ | aerodynamic resistance of canopy to dry deposition |
| $R_b$ | quasi-laminar boundary layer resistance to dry deposition |
| $R_c$ | surface resistance to dry deposition |
| $R_{chem}$ | resistance to chemical loss |
| $R_{cut}$, $r_{leaf}$, or $r_{lu}$ | surface resistance of leaf cuticles to dry deposition |
| $R_g$ or $r_{gc}$ | surface resistance of ground/forest floor to dry deposition |
| $r_{hyd}$ | resistance to NO2 hydrolysis on ground surfaces (dry deposition) |
| $R_{lc}$, $r_{dc}$, or $r_{cl}$ | surface resistance of lower canopy elements to dry deposition |
| $R_m$ or $r_m$ | surface resistance of leaf mesophyll to dry deposition |
| $R_s$ or $r_s$ | stomatal resistance to dry deposition |
| $R_t$ | total resistance to dry deposition |
| RETRO | Reanalysis of the Tropospheric Chemical Composition inventory |
| RH | relative humidity |
| $RO_2$ | alkylperoxy radical |
| $RO_2NO_2$ | peroxynitrate |
| $RONO_2$ | alkyl nitrate |
| RSL | roughness sublayer |
| SeaWiFS | Sea-viewing Wide Field-of-view Sensor |
| SC | sampling corrected |
| SIA | secondary inorganic aerosol |
| SNA | sulfate-nitrate-ammonium |

| | |
|---|---|
| $SO_2$ | sulfur dioxide |
| SOA | secondary organic aerosol |
| SPARTAN | Surface Particulate Matter Network |
| STAI | stem and twig area index |
| STP | standard temperature and pressure |
| T | temperature |
| $t_o$ | initial time |
| $t_{end}$ | end time |
| TN | total nitrate ($TN \equiv HNO_3 + pNO_3$) |
| $u_*$ | friction velocity |
| UV | ultraviolet |
| V | diffusion volume |
| $V_{chem}$ | chemical flux divergence velocity |
| $V_d$ | deposition velocity |
| $V_{ex}$ | exchange velocity |
| $v_t$ | mean thermal speed |
| VOC | volatile organic compounds |
| VPD | vapour pressure deficit |
| WHO | World Health Organization |
| WINTER | Wintertime INvestigation of Transport, Emissions, and Reactivity |
| WRF-Chem | Weather Research and Forecasting model coupled with Chemistry |
| $z^*$ | height of residual surface layer |
| $z_o$ | roughness length |
| | |
| $\alpha$ | canopy surface area scale factor |
| $\beta$ | von Neumann stability parameter |
| $\gamma$ | uptake coefficient |
| $\zeta$ | M-O stability parameter |
| $\eta$ | ratio of surface $PM_{2.5}$ to total column AOD |
| $\kappa$ | thermal diffusivity of air (or soil $NO_x$ scale factor) |
| $\lambda$ | wavelength |
| $\sigma$ | standard deviation (or collision diameter) |
| $\tau$ | lifetime |
| $\Phi_h$ | M-O stability correction factor for sensible heat |
| $\widehat{\Phi}$ | RSL correction function for momentum, heat, or scalars |
| $\Psi_h$ | integrated M-O stability-correction factor for sensible heat |

## Acknowledgements

The list of individuals and groups that have enabled the completion of this thesis are too numerous to mention in turn—thank-you to all of you!

A deep thanks is due to my supervising professor, Dr. Randall Martin, for his patience as I grew into a new research field and for his endless support and encouragement throughout various projects, even the esoteric ones. To my long-term committee members, Drs. Jeff Pierce and Glen Lesins, for their dedication and constructive suggestions that have greatly improved the work presented herein. To my recent committee member, Dr. Rachel Chang, for her guidance and support in the completion of this thesis. To my recent co-supervisor, Dr. Manuel Helbig, for his willing and accommodating efforts during the final stages of this thesis. And last but not least, to Balagopal Pillai, administrator of the Stetson compute cluster, for his expert and tenacious technical support.

Funding for this research was provided by NSERC and Killam scholarships, as well as the ongoing financial support from Randall Martin for which I am grateful. Computational resources included the Glooscap cluster on ACENET established by Jeff Pierce, and the Stetson cluster at Dalhousie established by Randall Martin and now supported by Rachel Chang. Much of this research would not have been possible without the many publicly available datasets that were relied upon, including the AOD datasets from NASA's AERONET, MISR, and SeaWiFS teams, the U.S. EPA's extensive ground monitoring network of criteria pollutants, the datasets detailing atmosphere-biosphere exchange at Harvard Forest led by Drs. Steve Wofsy and Bill Munger, and the NSF/NCAR WINTER aircraft campaign. Thanks also goes out to the GEOS-Chem community—it's been a pleasure to work on this impactful model with all of you and to see it evolve.

I'd also like to acknowledge my office mates, fellow grad student colleagues, and Dr. Stephen Payne, for your comradery, for being sources of knowledge, willing soundboards, and welcomed distractions.

And finally, to family and wilderness, for always being there.

# Chapter 1

# Introduction

## 1.1 Atmospheric Structure and Composition

Earth's atmosphere, a complex and dynamic layer of gases with suspended condensed phase material (aerosol and cloud), is held mostly within 10 km of the surface, thinning out to the vastness of space by 100 km (Kármán line). Atmospheric pressure decreases exponentially with altitude by a factor *e* every 7–8 km due to hydrostatic balance between gravity and the vertical pressure-gradient force. The vertical temperature profile of the atmosphere delineates four distinct layers, the troposphere, stratosphere, mesosphere, and thermosphere, as depicted in Fig. 1.1. The troposphere is the layer in direct contact with the Earth's sun-warmed surface and is characterized by decreasing temperatures with height following the adiabatic lapse rate of ca.10 °C $km^{-1}$ to an altitude of 8 to 18 km (tropopause), dependent on location and season. The troposphere contains about 85% of the total mass of the atmosphere despite occupying a much smaller fraction of the total vertical extent. Solar heating and surface wind shear generate turbulent vertical motions that result in an especially well mixed tropospheric sublayer—the planetary boundary layer (PBL)—which extends to about 1–3 km above the surface during the day, shrinking around the time of sunset to nocturnal heights often < 100 m. Boundary layer turbulence has strong influence on ambient concentrations of surface-emitted species, with poor air quality often resulting from weak PBL mixing. The PBL is ventilated to the layer above, the free troposphere, on a time scale of days to a week by weather events (i.e., frontal systems or strong convection). Although the research presented in this thesis focuses on near-surface species and processes, use of satellite remote sensing, aircraft observations, global chemical transport modeling, as well as surface observations, highlights the importance of an integrated approach to understanding surface air quality.

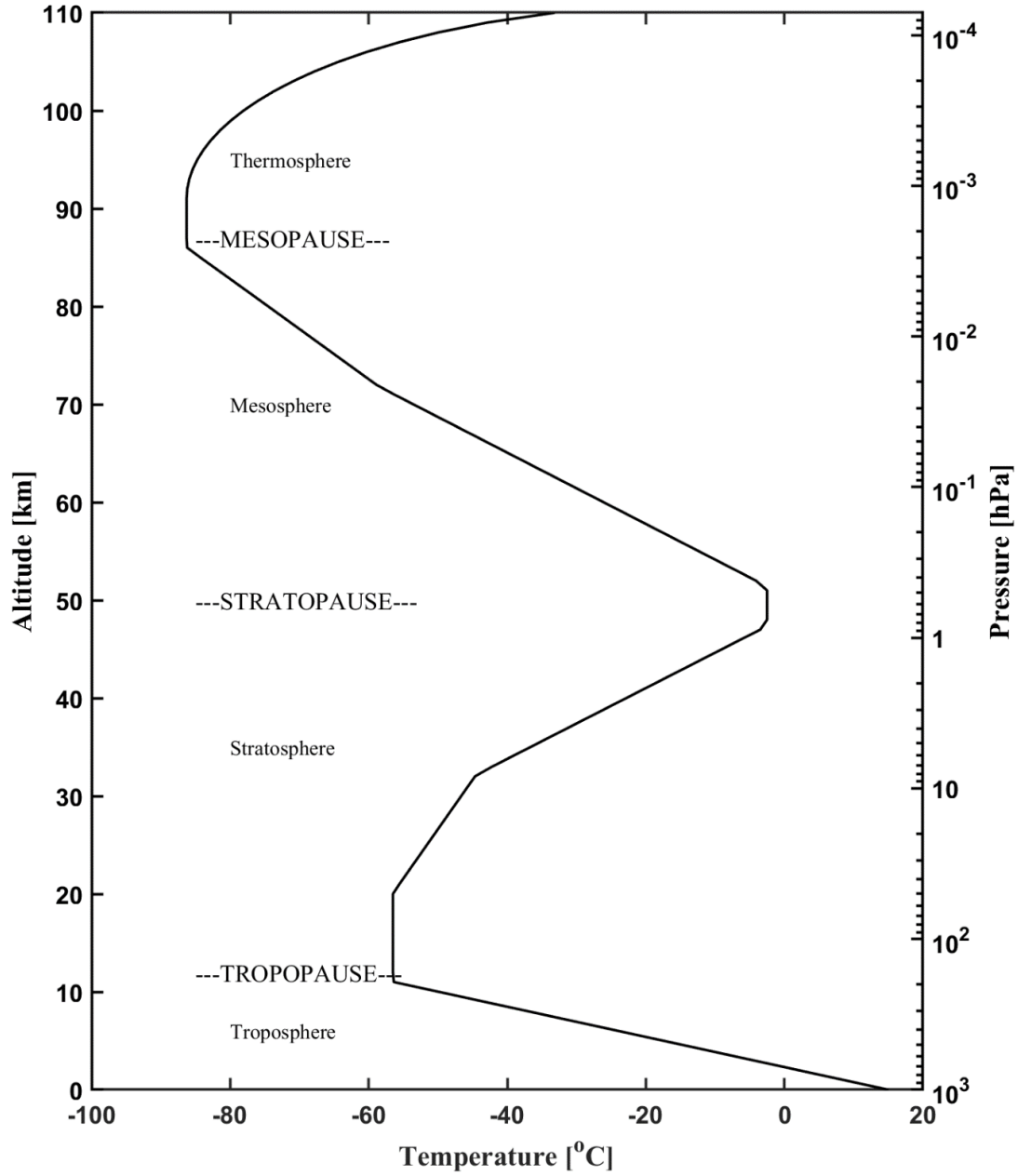


**Figure 1.1:** Vertical temperature profile of Earth's atmosphere (U.S. Standard Atmosphere, 1976).

The tropopause marks the upper limit of the troposphere and the start of the stratosphere where absorption of solar ultraviolent (UV) radiation by ozone ($O_3$) and molecular oxygen ($O_2$) causes local heating and increasing temperatures with height to the stratopause (~50 km). The positive temperature gradient throughout the stratosphere suppresses vertical motion resulting in a very stable 'stratified' layer which contains the highest concentrations of $O_3$ in the atmosphere. Above the stratopause, temperatures again decrease with height throughout the mesosphere to the mesopause (~80–90 km) at which point temperatures begin to rise throughout the thermosphere due to absorption of short-wave UV radiation by $O_2$ and molecular nitrogen ($N_2$).

Earth's atmosphere has evolved along with life and plays a vital role in supporting its habitability, i.e., through surface warming via the greenhouse effect and absorption of solar UV radiation by an elevated ozone layer. The dry atmosphere consists primarily of $N_2$ (78%), $O_2$ (21%), and noble gases (predominantly Ar, 0.93%), the abundance of which are controlled by biogeochemical processes on long (geologic) timescales. Atmospheric water vapour concentrations are highly variable, from relatively uniform stratospheric mixing ratios of less than 10 ppm (< 10 μmol $mol^{-1}$), to tropospheric values as high as 5% in hot-humid locations near the surface. Water vapour in the troposphere is driven by evapouration-precipitation cycles, and therefore location, weather, and climate. The present-day global mean lifetime (residence time) of water vapour in the atmosphere is about 8 days (Hodnebrog et al., 2019). It is the remaining trace species, comprising < 0.1% of the atmosphere, that are drivers of the greenhouse effect and tropospheric air quality—although $N_2$ and $O_2$ are involved in high-energy reactions yielding reactive trace species such as nitric oxide (NO) and $O_3$. A summary of the mixing ratios for select gasses in dry air is presented in Table 1.1.

Unwittingly at first, humankind has embarked on activities that are now affecting Earth's atmosphere, landmass, and oceans to a degree on par with geological events—no longer do Earth's systems seem as expansive as they once did. As growing populations became increasingly adept at exploiting natural resources over the past three centuries, humanity caused sufficient change to Earth's biosphere that we are now thought to be in the 'Anthropocene' epoch (Crutzen, 2002). Despite the many concerning environmental

**Table 1.1:** Mixing ratios of main gaseous species in the dry atmosphere[(a)].

| **Gaseous species** | **Chemical formula** | **Mixing ratio [mol mol$^{-1}$]** |
|---|---|---|
| Nitrogen | $N_2$ | 0.78 |
| Oxygen | $O_2$ | 0.21 |
| Argon | Ar | $9.3 \times 10^{-3}$ |
| Carbon dioxide[(b)] | $CO_2$ | $416 \times 10^{-6}$ |
| Neon | Ne | $18 \times 10^{-6}$ |
| Ozone | $O_3$ | $(0.01\text{-}10) \times 10^{-6}$ |
| Helium | He | $5.2 \times 10^{-6}$ |
| Methane[(c)] | $CH_4$ | $1.9 \times 10^{-6}$ |
| Krypton | Kr | $1.1 \times 10^{-6}$ |
| Hydrogen | $H_2$ | $500 \times 10^{-9}$ |
| Nitrous oxide[(d)] | $N_2O$ | $335 \times 10^{-9}$ |
| Carbon monoxide | CO | $(10\text{-}1000) \times 10^{-9}$ |
| Nitric acid | $HNO_3$ | $(0.01\text{-}10) \times 10^{-9}$ |
| Ammonia | $NH_3$ | $(0.01\text{-}10) \times 10^{-9}$ |
| Nitrogen dioxide | $NO_2$ | $(0.01\text{-}10) \times 10^{-9}$ |
| Formaldehyde | $CH_2O$ | $(0.01\text{-}10) \times 10^{-9}$ |
| Sulfur dioxide | $SO_2$ | $(0.01\text{-}10) \times 10^{-9}$ |

[(a)] From Chance and Martin (2017), unless otherwise indicated.
[(b)] $CO_2$ concentration in the year 2022, increasing at 2.4 ppm yr$^{-1}$ (NOAA, 2022). Preindustrial value: 280 ppm.
[(c)] $CH_4$ concentration in the year 2022, increasing at 15 ppb yr$^{-1}$ (NOAA, 2022). Preindustrial value: 800 ppb.
[(d)] $N_2O$ concentration in the year 2022, increasing at 1.2 ppb yr$^{-1}$ (NOAA, 2022). Preindustrial value: 285 ppb.

issues over this recent evolution, there have been examples of coming together to address some alarming trajectories. A global example of co-operation in this regard, and related to the atmosphere, was the 1987 Montreal protocol to end the release of long-lived chlorofluorocarbons (CFCs) responsible for catalytic depletion of stratospheric ozone. On more regional scales, the development of national clean air acts in North America and Europe have been largely successful in (i) combating concerning levels of anthropogenic

emissions that are drivers of smog pollution and acid rain, namely, sulfur dioxide ($SO_2$), carbon monoxide (CO), and nitrogen oxides ($NO_x$) (Samet, 2011; U.S. EPA, 2021) and (ii) phasing out the use of lead, a developmental neurotoxicant, in gasoline (McFarland et al., 2022). An increasingly pressing challenge facing humanity is anthropogenic global warming caused by emissions of carbon dioxide ($CO_2$), methane ($CH_4$), halogenated species, and nitrous oxide ($N_2O$) (Forster et al., 2021).

Air pollution, generally defined as trace gas or aerosol concentrations sufficient to have a negative impact on health or environment, may be of natural or anthropogenic origin and shares many sources with climate change, i.e., the burning of fossil fuels, animal husbandry, and volcanic eruption. Although anthropogenic air pollution has been associated with morbidity for many centuries (Goodhill, 1971), and much progress has been made in understanding the link between air pollution and negative health outcomes (West et al., 2016), it remains the leading global environmental risk factor for premature mortality, contributing to an estimated 6.67 million (12% of the global total) premature deaths worldwide in 2019 (Murray et al., 2020). The U.S. Clean Air Act was developed in response to severe anthropogenic air pollution mid-$20^{th}$ century and requires that the U.S. Environmental Protection Agency (EPA) set National Ambient Air Quality Standards (NAAQS) for six criteria air pollutants, namely, ground-level ozone ($O_3$), nitrogen dioxide ($NO_2$), carbon monoxide (CO), sulfur dioxide ($SO_2$), lead (Pb), and particulate matter with diameters < 10 μm ($PM_{10}$) and < 2.5 μm ($PM_{2.5}$). Similarly, Canadian Ambient Air Quality Standards (CAAQS) are set for pollutants $NO_2$, $O_3$, $SO_2$, and $PM_{2.5}$, which also have guidelines set by the World Health Organization (WHO). Table 1.2 contains current NAAQS and CAAQS standards alongside WHO air quality guidelines. Despite great improvements in air quality across the U.S. since the promulgation of the NAAQS in 1971 (Samet, 2011; U.S. EPA, 2021), ca. 97 million people (about 30% of the U.S. population) experienced levels of air pollution exceeding the NAAQS in 2020, mostly due to $O_3$ (79.2 million) and $PM_{2.5}$ (50.5 million) exceedances (U.S. EPA, 2021).

**Table 1.2:** Air quality standards for the U.S. (NAAQS) and Canada (CAAQS) alongside WHO guidelines.

| Pollutant | Averaging time | Standard | | Guideline |
|---|---|---|---|---|
| | | NAAQS[a] | CAAQS[b] | WHO[c] |
| $O_3$ | 8-hr | 70 ppb[d] | 62 ppb[d] | 100 μg $m^{-3}$ (50 ppb)[e] |
| $NO_2$ | 1-hr | 100 ppb[f] | 60 ppb[f] | n/a |
| | 24-hr | n/a | n/a | 24 μg $m^{-3}$ (13 ppb) |
| | annual | 53 ppb | 17 ppb | 10 μg $m^{-3}$ (5 ppb) |
| $SO_2$ | 1-hr | 75 ppb[g] | 70 ppb[g] | n/a |
| | 24-hr | n/a | n/a | 40 μg $m^{-3}$ (15 ppb) |
| | annual | n/a | 5 ppb | n/a |
| CO | 1-hr | 35 ppm[h] | n/a | n/a |
| | 8-hr | 9 ppm[h] | n/a | n/a |
| Pb | 3-month | 0.15 μg $m^{-3}$[i] | n/a | n/a |
| $PM_{10}$ | 24-hr | 150 μg $m^{-3}$[h] | n/a | 45 μg $m^{-3}$ |
| | annual | n/a | n/a | 15 μg $m^{-3}$ |
| $PM_{2.5}$ | 24-hr | 35 μg $m^{-3}$[j] | 27 μg $m^{-3}$[j] | 15 μg $m^{-3}$ |
| | annual | 12 μg $m^{-3}$[k] | 8.8 μg $m^{-3}$ | 5 μg $m^{-3}$ |

[a] U.S. National Ambient Air Quality Standards (NAAQS) as of 2022.
[b] Canadian Ambient Air Quality Standards (CAAQS) as of 2022.
[c] World Health Organization (WHO) air quality guidelines as of 2022.
[d] Annual 4$^{th}$ highest daily max. 8-hr concentrations, averaged over 3-yrs.
[e] 99$^{th}$ percentile of annual daily max. 8-hr concentrations, i.e., 3-4 exceedance days per year.
[f] Annual 98$^{th}$ percentile of daily max. 1-hr concentrations, averaged over 3-yrs.
[g] Annual 99$^{th}$ percentile of daily max. 1-hr concentrations, averaged over 3-yrs.
[h] Not to be exceeded more than once per year.
[i] Not to be exceeded.
[j] Annual 98$^{th}$ percentile of daily 24-hr concentrations, averaged over 3-yrs.
[k] Averaged over 3-yrs.

## 1.2 Tropospheric Chemistry

Atmospheric chemistry of the troposphere is of particular interest in efforts to understand air quality. With high concentrations of $O_2$ and $O_3$, Earth's atmosphere is an oxidizing environment. Central to tropospheric chemistry is the role of the highly reactive hydroxyl radical (OH) (Gligorovski et al., 2015; Levy, 1971; Thompson, 1992). Oxidation reactions via OH leads to the removal of many pollutants that would otherwise be inert in the troposphere, including non-radical species such as carbon monoxide (CO), hydrochlorofluorocarbons (HCFC), and some volatile organic compounds (VOC) such as methane. Furthermore, together with the hydroperoxy radical ($HO_2$) forming the steady-state $HO_x$ chemical family ($HO_x \equiv OH + HO_2$), OH is involved in both $O_3$ producing chain reactions under polluted conditions (Crutzen, 1979b) and catalytic $O_3$ consuming reactions in remote (pristine) conditions (Kley et al., 1996). Important primary sources of OH in the troposphere include: (i) photolysis of $O_3$ followed by reaction with water vapour (Levy, 1971):

$$O_3 + h\nu \longrightarrow O(^1D) + O_2 \qquad (\lambda < 320\ nm) \qquad (R1.1)$$

$$O(^1D) + H_2O \longrightarrow 2OH \qquad (R1.2)$$

(ii) photolysis of formaldehyde (HCHO) followed by reaction of $HO_2$ with NO (Meller and Moortgat, 2000):

$$HCHO + h\nu \xrightarrow{O_2} 2HO_2 + CO \qquad (\lambda < 340\ nm) \qquad (R1.3)$$

$$HO_2 + NO \longrightarrow OH + NO_2 \qquad (R1.5)$$

(iii) photolysis of nitrous acid (HONO) (Stutz et al., 2000):

$$HONO + h\nu \longrightarrow OH + NO \qquad (\lambda < 400\ nm) \qquad (R1.6)$$

Although high energy solar radiation is mostly absorbed in upper atmospheric layers, i.e., UV-C radiation (200 nm < λ < 280 nm) by $O_2$ (λ < 240 nm) and $O_3$ (λ < 320 nm), photochemical reactions continue to play an important role in the troposphere, as exemplified in reactions R1.1–6. Globally, photolysis of $O_3$ is the dominant primary source of OH in the troposphere, especially during times of intense solar radiation and high water

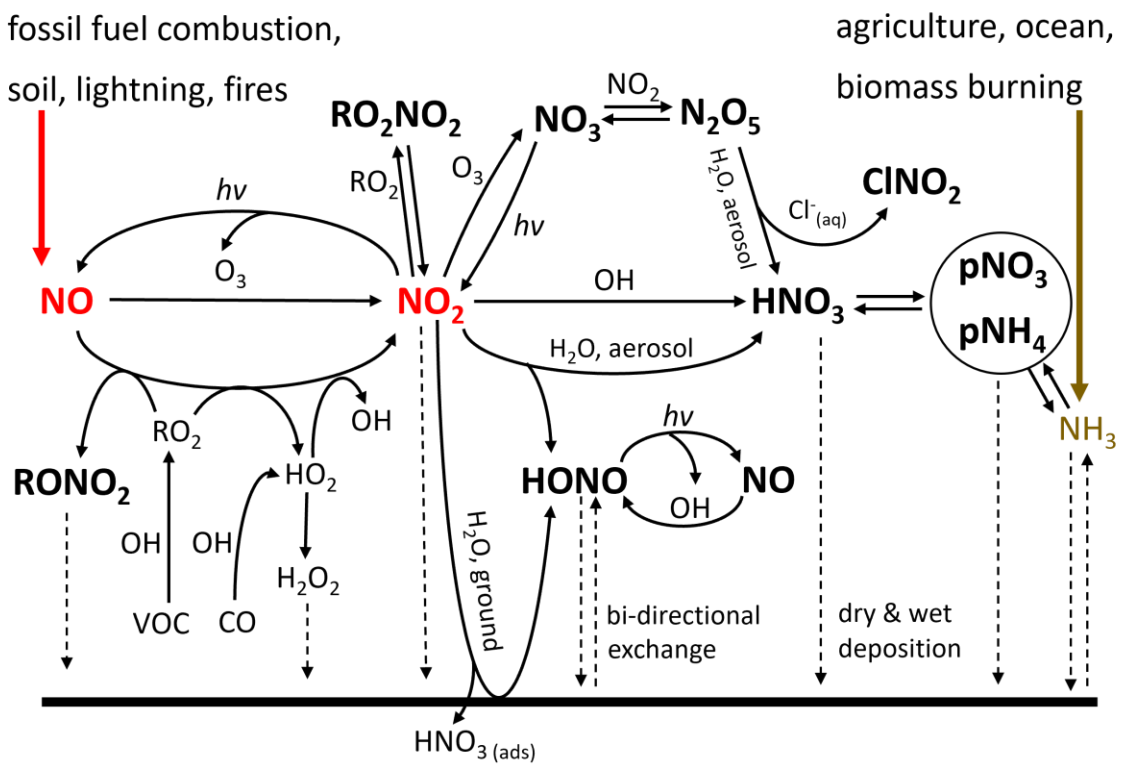


**Figure 1.2:** Tropospheric sources, sinks, and reactions of nitrogen oxides ($NO_x \equiv NO + NO_2$).

vapour concentration (i.e., summer months). However, since HONO photolyzes at longer wavelengths than $O_3$ and HCHO, reaction R1.6 plays a dominant role in primary OH production in polluted regions both shortly after sunrise and during winter months (Kim et al., 2014) when solar zenith angles are high and water vapour concentrations may be low (winter).

Once formed, OH rapidly reacts with surrounding trace species (lifetime $\tau < 1$ sec), including CO and VOCs, initiating ozone-producing photochemical chain reactions in the presence of nitrogen oxides ($NO_x \equiv NO + NO_2$) (Chameides, 1978; Crutzen, 1970), as depicted in Fig. 1.2. Although high concentrations of stratospheric $O_3$ (1–10 ppm) prevents harmful UV radiation from reaching the surface and lower concentrations in the troposphere (ppb level) provides a photolytic source of OH, elevated levels of tropospheric $O_3$ are undesirable. First, $O_3$ is a greenhouse gas, absorbing radiation at 9.6 μm which is

within the Earth's infrared atmospheric window (ca. 8 –13 μm). Current tropospheric ozone concentrations (ca. 50 ppb on average) are ca. 30–40% above preindustrial (1850 AD) levels, affecting a radiative forcing of +0.33 W $m^{-2}$ (Yeung et al., 2019). Second, ground-level $O_3$ is a toxic pollutant, adversely affecting respiratory health (Malley et al., 2017) and plant growth (Agathokleous et al., 2020). Ground-level $O_3$ has increased above preindustrial levels by 100% on average over northern midlatitudes (Yeung et al., 2019). In the vicinity of large urban centers or heavy industry, ground-level concentrations frequently exceed the WHO recommended limit of 50 ppb, and the NAAQS standard of 70 ppb in areas of the U.S. such as the Los Angeles Basin, San Joaquin Valley, industrial Midwest, and Mid-Atlantic eastern states (U.S. EPA, 2021).

### 1.2.1 *Nitrogen Oxides*

Nitrogen oxide radicals NO and $NO_2$ are important trace species in atmospheric chemistry and together form the chemical family $NO_x$ due to rapid daytime interconversion resulting from fast photochemical reactions, i.e., oxidation of NO by $O_3$ or peroxy radicals ($HO_2$ or $RO_2$), as depicted in Fig. 1.2, and photolysis of $NO_2$ leading to the (re)generation of $O_3$:

$$NO_2 + h\nu \longrightarrow O(^3P) + NO \quad (\lambda < 424\,nm) \qquad (R1.7)$$

$$O(^3P) + O_2 + M \longrightarrow O_3 + M \qquad (R1.8)$$

As depicted in Fig. 1.2, photochemical $NO_x$ cycling via $O_3$ oxidation of NO is a null cycle in terms of $O_3$ production, however, peroxy ($HO_2$ or $RO_2$) NO to $NO_2$ oxidation pathways are net $O_3$ producing. Since $NO_x$ is not consumed in $O_3$ producing $NO_x$ cycling reactions, it serves to catalyze $O_3$ production in the troposphere, such that multiple $O_3$ molecules may be produced for each $NO_x$ molecule emitted prior to eventual loss to higher oxidized forms or loss of $NO_2$ via dry deposition. Ozone-producing chain reactions catalyzed by the cycling of $NO_x$ and $HO_x$ radicals may proceed under both $NO_x$-limited and $NO_x$-saturated (also known as VOC-limited) conditions (Sillman, 1999). Tropospheric $O_3$ production is modulated by the evolution of $HO_x$, where efficient cycling occurs in transition between $NO_x$-limited and $NO_x$-saturated regimes (Jin et al., 2020; Sillman et al., 1990). In $NO_x$-saturated regimes, high emissions of $NO_x$ relative to $HO_x$ production via VOC/CO oxidation suppress OH concentrations by reaction of $NO_2$ with OH to produce $HNO_3$,

therefore reducing the oxidation capacity of the local atmosphere and leading to a build-up of primary pollutants (Martin et al., 2003b). In $NO_x$-limited regimes, low concentrations of $NO_x$ relative to $HO_x$ production results in inefficient $O_3$ producing $HO_x$ cycling, where $HO_x$ loss results from self-reaction forming peroxides, i.e., $H_2O_2$. As an aside, hydrogen peroxide ($H_2O_2$) plays an important role in the aqueous phase oxidation of $SO_2$ in cloud droplets (Seinfeld and Pandis, 2006). Decreasing (increasing) $NO_x$ emissions under $NO_x$-saturated conditions therefore leads to increased (reduced) local $O_3$ production. Outside of polluted urban centers and winter months where natural emissions of biological VOCs (i.e., isoprene and terpenes) are at a minimum, $O_3$ production is generally $NO_x$-limited and therefore highly sensitive to $NO_x$ emissions (Travis et al., 2016). Accurate representation of $NO_x$ sources and loss processes is therefore important to understanding tropospheric ozone production.

$NO_x$ is emitted to the troposphere mainly as NO and primarily through high temperature processes such as combustion and lightning, where thermolysis of $O_2$ followed by reaction of atomic oxygen with abundant $N_2$ leads to the formation of NO (Jacob, 1999). NO is also emitted from soils, along with nitrous oxide ($N_2O$)—a tropospherically inert greenhouse gas that is ozone-depleting in the stratosphere. Microbial activity in soils release NO and $N_2O$ as volatile intermediate products during the processes of: (i) nitrification—the aerobic oxidation of soil ammonium ($NH_4^+$) to nitrite ($NO_2^-$) and nitrate ($NO_3^-$) (Caranto and Lancaster, 2017) and (ii) denitrification—the anerobic reduction of nitrate and nitrite to $N_2$ (Conrad, 1996). Sources of fixed nitrogen (i.e., plant useable) to soils include symbiotic nitrogen fixing bacteria (Franche et al., 2009), organic decay, deposition, and fertilizer application. An overview of total global tropospheric $NO_x$ emissions is given in Table 1.3; all source contributions total to about 50–60 Tg N $yr^{-1}$. Fossil fuel combustion is the largest global source at around 30 Tg N $yr^{-1}$, with dominant sectoral contributions from on-road transportation (23%), energy generation (22%), shipping (20%), and industry (15%) (McDuffie et al., 2020). Non-fossil fuel sources contribute up to 50% of global $NO_x$ emissions, with large regional seasonality in soil, biomass burning, and lighting emissions. Estimates of soil $NO_x$ emission are especially difficult due to dependence on a multitude of factors such as soil type, temperature, soil nitrogen content, moisture, and dry spell length (Hudman et al., 2012). In addition, within

**Table 1.3:** Estimates of total global $NO_x$ emissions to the troposphere.

| Source | Emission [Tg N $yr^{-1}$] | Reference |
|---|---|---|
| Fossil fuel combustion[(a)] | 31.4 | McDuffie et al. (2020) |
| Aircraft | 0.7 | Seinfeld and Pandis (2006) |
| Biomass burning | 6–8 | Jaeglé et al. (2005); Lee et al. (1997) |
| Lightning | 5–8 | Miyazaki et al. (2014) |
| Soil | 4–15 | Vinken et al. (2014) |
| From stratosphere | < 0.5 | Seinfeld and Pandis (2006) |

[(a)] For the year 2017; excludes aircraft emissions.

canopy reductions of up to 70–80% have been required to reconcile measured soil emissions with above-canopy observations (Jacob and Wofsy, 1990; Lerdau et al., 2000), which has led to the implementation of deposition-based canopy reduction factors (CRF) in soil $NO_x$ parameterizations for use in atmospheric chemical transport models (Wang et al., 1998). We extend this idea of subgrid dry deposition of surface-emitted $NO_x$ in CTMs to include anthropogenic sectors such as traffic emissions (further discussed in section 1.4). Large uncertainties in ground-level $NO_x$ emissions, in particular from the transportation and soil $NO_x$ sectors, have implications for understanding ground-level $O_3$ pollution (Travis et al., 2016).

The tropospheric lifetime of $NO_x$ is relatively short (< 24-hr) and dependent on factors such as solar radiation, other trace species, and even the concentration of $NO_x$ itself. As such, $NO_x$ concentrations decrease quickly with distance from source and $NO_x$ is not transported over great distances. However, $NO_x$ can react to form longer-lived reservoir species that may be transported long distances prior to decomposing and releasing $NO_x$—the most important example being peroxyacetyl nitrate (PAN), a peroxynitrate ($RO_2NO_2$) that exists in a thermal equilibrium with $NO_2$. The predominant sink of $NO_x$ is oxidation to $HNO_3$—a highly soluble species with an affinity for surfaces; $HNO_3$ has a lifetime to deposition of a few days (weeks) in the lower (upper) troposphere (Jacob, 1999). As depicted in Fig. 1.2, three pathways exist for the formation of atmospheric $HNO_3$ from $NO_2$. The predominant daytime pathway is oxidation of $NO_2$ by OH. The predominant nocturnal pathway is oxidation of $NO_2$ by $O_3$ yielding the nitrate radical ($NO_3$), which

exists with $NO_2$ in thermochemical equilibrium with dinitrogen pentoxide ($N_2O_5$). Surface hydrolysis of $N_2O_5$ on aerosol yields $HNO_3$ (McDuffie et al., 2018b) and up to equal amounts of nitryl chloride ($ClNO_2$) on chloride-containing aerosol such as sea salt (McDuffie et al., 2018a). The third and least important $HNO_3$ formation pathway results from the heterogeneous hydrolysis of $NO_2$ on aerosol, forming $HNO_3$ and nitrous acid (HONO). Due to the relatively low $NO_2$ reactive uptake coefficient for this disproportionation reaction ($\gamma_{NO_2}10^{-7}$ to $10^{-5}$; Chapter 3) compared to $N_2O_5$ hydrolysis on aerosol ($\gamma_{N_2O_5}$~ 0.014; (McDuffie et al., 2018b)), heterogeneous hydrolysis of $NO_2$ on aerosol is not a significant $NO_x$ loss pathway (Alexander et al., 2020), unlike on ground (VandenBoer et al., 2013) and indoor surfaces (Spicer et al., 1993) which have a much greater effective surface area than does boundary layer aerosol. Atmospheric models that neglect $NO_2$ hydrolysis on ground surfaces underestimate near-surface HONO concentrations—an important primary source of OH, especially in early morning and winter months. This thesis implements this pathway into the GEOS-Chem CTM in chapters 3 and 4.

Significant emissions of ammonia ($NH_3$), ~50 Tg N $yr^{-1}$ globally (McDuffie et al., 2020), promote the uptake of $HNO_3$ to aerosol, increasing particulate nitrate ($pNO_3$) loads, especially under low temperatures in regions with high $NH_3$ emissions. This contribution to secondary inorganic aerosol (SIA) has important health and environmental implications (discussed further in sect. 1.2.2). Agricultural sources, i.e., animal husbandry and fertilizer application, dominate global $NH_3$ emissions (~60%), with oceans (~15%) and biomass burning (~10%) being other notable sources (Behera et al., 2013). In the Arctic, $NH_3$ emitted from seabird colonies can be locally significant (Croft et al., 2016).

### 1.2.2 *Aerosol*

Suspended particles in the atmosphere, or aerosol, exist across a broad range of sizes and compositions, having impacts on photo and heterogeneous chemistry (Martin et al., 2003a), air quality (discussed below), and climate (discussed below). Size plays an important role in aerosol processes, including in the aforementioned effects. Size-wise, aerosols may be classified by four modes: nucleation mode (< 10 nm in diameter), Aitken mode (~10 nm to ~100 nm), accumulation mode (~0.1 μm to ~2.5 μm), and coarse mode (> 2.5 μm)

(Seinfeld and Pandis, 2006). Atmospheric lifetimes of nucleation and larger coarse mode particles are short, on the order of minutes to hours (< 24-hr) (Feichter and Leisner, 2009). Nucleation mode particles are short-lived primarily due to coagulation with larger particles (Seinfeld and Pandis, 2006). For coarse mode particles, increasing terminal velocity with size reduces atmospheric lifetimes due to rapid dry depositional loss via gravitational settling—the settling velocity of a 100 μm (10 μm) particle is on the order of 20 cm $s^{-1}$ (0.3 cm $s^{-1}$), yielding boundary layer lifetimes on the order of tens of minutes (tens of hours) (Feichter and Leisner, 2009). Aerosol in the Aitken mode grows by both coagulation with other particles and by condensation of low volatility vapours and 'accumulates' in the accumulation mode where atmospheric lifetimes are greatest due to inefficient removal processes for this size range (Seinfeld and Pandis, 2006). Loss of accumulation mode aerosol from the atmosphere takes place primarily via wet deposition (discussed below) on time scales of days (to weeks) in the boundary layer (free troposphere) (Croft et al., 2014).

In addition to size, aerosol may be further classified based on origin, namely, directly emitted 'primary aerosol' or 'secondary aerosol' formed/grown from gas-to-particle conversion reactions, i.e., reactions of $NO_x$ and $NH_3$ that lead to the growth of particulate ammonium ($pNH_4$) nitrate ($pNO_3$) as depicted in Fig. 1.2. Nucleation mode particles are of secondary origin, resulting from complex interactions of precursor gases under specific conditions (Almeida et al., 2013). Atkin mode aerosol has both primary (i.e., combustion) and secondary (i.e., growth of nucleation mode) sources. While accumulation mode aerosol has both primary (anthropogenic and natural) and secondary (growth of Aitken aerosol) origins, coarse mode aerosol is predominantly of primary and natural origin.

Globally, natural sources dominate the atmospheric aerosol mass burden and include expansive primary sources such as seasalt aerosol from breaking waves (Jaeglé et al., 2011), lofting of wind-blown dust (Meng et al., 2021), combustion aerosol from biomass burning (Ichoku and Ellison, 2014), a diversity of primary biological aerosol particles (PBAP) from land and ocean (i.e., detritus, pollen, fungal spores, microorganisms, etc.) (Després et al., 2012), and ash from volcanic eruptions (Zhu et al., 2020). Natural sources of precursor gases for secondary aerosol include biogenic volatile organic

compounds (BVOCs) from vegetation and biomass burning VOCs leading to the formation/growth of secondary organic aerosol (SOA) (Kanakidou et al., 2005; Spracklen et al., 2011). Emissions of sulfur-containing gases such as volcanic $SO_2$ (Andres and Kasgnoc, 1998) and oceanic dimethyl sulfide (DMS) (Park et al., 2004) lead to the formation/growth of sulphate-containing aerosol ($pSO_4$). In the pristine summertime arctic, $NH_3$ emitted from seabird colonies contributes to new particle formation (nucleation events) (Croft et al., 2016), with subsequent particle growth by condensation of oxidized precursor vapours of marine origin, i.e., DMS and oceanic BVOCs (Croft et al., 2019). Natural sources of $NO_x$ also contribute to growth of secondary inorganic aerosol (SIA) via equilibrium of $HNO_3$ with $pNO_3$ in the presence of $NH_3$ (Fig. 1.2), in addition to promoting SOA growth via influence on oxidant fields (Carlton et al., 2010).

Although natural sources of aerosol dominate globally and can make leading contributions to exposure in some areas (Meng et al., 2019b), anthropogenic sources have predominant influence over air quality in most populated regions (McDuffie et al., 2021; Weagle et al., 2018). Combustion sources dominate anthropogenic sources of primary aerosol and precursor gases to secondary aerosol (McDuffie et al., 2020, 2021), although anthropogenic sources of dust (Philip et al., 2017) and agricultural emissions (Ying and Kleeman, 2006) can be locally significant. Emissions of SIA precursor gasses $SO_2$, $NH_3$, and $NO_x$ are predominately of anthropogenic origin, especially over developed regions (Park et al., 2004).

The binary classification of aerosol as primary or secondary is a simplification in some cases. Particles emitted in concentrated combustion plumes may off-gas semivolatile species as dispersion proceeds, re-condensing to particulate form as subsequent oxidation reactions produce lower volatility species (Robinson et al., 2007). Additionally, although atmospheric aerosol often exists as complex and dynamic mixtures, including within individual particles (Huang et al., 2021), it is often convenient to overlook this complexity and instead think of particles as externally mixed.

Loss of aerosol from the atmosphere occurs via wet and dry deposition. Wet deposition of aerosol involves the (i) rainout of activated CCN particles as well as in-cloud/fog scavenged particles and (ii) below-cloud washout of particles by falling

precipitation. Dry deposition of aerosol involves the adsorption of particles to ground surfaces. Wet and dry deposition processes are most efficient for Atkin/ultrafine and coarse mode particles due to Brownian diffusion and inertial effects, respectively. Except for coarse mode dust and sea salt, wet deposition dominates particulate removal globally (Croft et al., 2014; Jaeglé et al., 2011). Resulting aerosol lifetimes strongly depend on altitude, which are less than a week in the boundary layer, increasing to 2–3 weeks in the free troposphere (Croft et al., 2014). Aerosol lifetimes in the stratosphere are much longer, on the order of a year (MacMartin and Kravitz, 2019), resulting in global cooling following large stratospheric injection events.

Ambient fine particulate matter with an aerodynamic diameter less than 2.5 μm ($PM_{2.5}$) continues to be identified as the leading air pollutant type contributing to premature mortality worldwide, accounting for ca. 60% of air pollution attributable early deaths, and 7% of global total deaths, in 2019 (Murray et al., 2020)—reinforcing long-standing associations between negative health outcomes and ambient concentrations of highly respirable $PM_{2.5}$ (Dockery et al., 1993). As such, WHO air quality guidelines recommend much lower mass concentrations of $PM_{2.5}$ than other harmful pollutants such as $O_3$ and $NO_2$ (Table 1.2). Potentially even more toxic than the longer-lived accumulation mode aerosols that contribute to $PM_{2.5}$ mass are the smaller Aitken mode particles that contribute to the large number of shorter-lived ultrafine particles ($PM_{0.1}$) prevalent close to combustion sources such as roadways and cooking appliances (Schraufnagel, 2020). Aerosol is also increasingly recognized as a vector for transmission of respiratory pathogens (Ramuta et al., 2022; Wang et al., 2021). Fine aerosol generated from activities such as breathing and speaking (Coleman et al., 2021; Morawska and Buonanno, 2021) is receiving revised attention as understanding evolves to accept aerosol transmission as an important, even dominant, mode of respiratory viral transmission (Greenhalgh et al., 2021; Jimenez et al., 2021; Klompas et al., 2021; Randall et al., 2021), highlighting the need for institutional reform in the area of indoor air quality/hygiene.

Besides the health implications of ground-level particulate matter, aerosols affect climate directly by scattering incoming solar radiation leading to increased albedo (cooling effect) and by absorbing solar radiation in the case of black carbon leading to reduced

albedo (warming effect). Cooler temperatures following volcanic eruptions where emissions enter the stratosphere—resulting in long-lived stratospheric sulphate aerosol (scattering)—is an example of the aerosol direct effect (Ridley et al., 2014a; Soden et al., 2002). Aerosols also affect climate indirectly by serving as cloud condensation nuclei (CCN), thereby increasing cloud droplet number concentrations leading to brighter and longer-lived clouds (cooling effect). Taken together, aerosols have a net cooling effect on climate (Forster et al., 2021).

Aerosols are also a source of nutrients to terrestrial and marine ecosystems (Johnson et al., 2010; Mahowald et al., 2017). Unfortunately, aerosols may also be disruptive to ecosystems, such as through eutrophication via excess nutrient deposition (Brahney et al., 2015; Wolfe et al., 2001), or reduction in drought tolerance via the hydraulic activation of stomata through deposition of hygroscopic particulates to leaves (discussed further in section 1.3).

### 1.3 Dry Deposition Processes of $NO_2$

Dry deposition represents an important removal process for many trace gases, the other being wet deposition where soluble gasses are removed by in-cloud/fog rainout and below-cloud washout. The relative contributions of dry and wet deposition to net deposition are species-specific and spatiotemporally variant. For highly soluble/surface-reactive species such as $HNO_3$, dry deposition can make significant, even dominate, contributions to net deposition depending on land type and meteorology (discussed in Chapter 4). However, for other species such as accumulation mode aerosol, dry deposition makes little contribution to net deposition (as previously discussed). For a surface-reactive yet relatively insoluble species such as $NO_2$, dry deposition would be the only contributor to depositional loss (discussed in Chapter 4).

Dry deposition is an umbrella term that covers many nuanced species-specific interactions/reactions with the Earth's surface and is dependent on both the reacting atmospheric constituent and the nature of the underlying surface(s). The process of photosynthesis is an example of a specific dry deposition pathway for atmospheric $CO_2$ to

plants and phytoplankton, which is very different from the adsorption/absorption of $HNO_3$ to, or oxidative reaction of $O_3$ with, ground surfaces. For convenience and tractability, dry deposition is often parameterized in atmospheric models as a terminal sink and broadly applied across a range of species and land types using basic similarity relations such as solubility relative to $SO_2$ and oxidative potential relative to $O_3$ (Wesely, 1989; Zhang et al., 2003a). Such parameterizations of dry deposition employ a resistance model framework (Baldocchi et al., 1987), as depicted in Fig. 1.3, where the first-order rate constant to above-canopy dry deposition is represented as a deposition velocity ($V_d$) computed along the resistance pathway ($R_{total}$), i.e., $V_d = 1/R_{total}$, for a specific gas to a specific bulk surface or land type from a specified height. The resulting dry deposition flux is analogous to current, and the concentration difference between a reference height and ground surface analogous to voltage. To ensure a unidirectional (downward) dry deposition flux (F), it is assumed that concentrations at deposition surfaces are negligible such that species concentrations at dry deposition reference heights (C) may be used directly in calculating dry deposition fluxes, i.e., $F = -V_d[m\ s^{-1}]\ C[kg\ m^{-3}]$. Bulk-canopy uptake formulated through $V_d$ has contributions from many processes, including turbulent transport (aerodynamic resistance $R_a$), molecular diffusion in air (boundary layer resistance $R_b$), meteorological influence on the physical, chemical, and biological state of surfaces (i.e., stomatal resistance $R_s$), and species-specific interfacial chemistry (i.e., surface resistances $R_m$, $R_{cut}$, $R_{lc}$, and $R_g$). Formulations of the component resistances that contribute to trace gas deposition velocities are discussed in Ch 3.

Although widely used in atmospheric chemical transport models (CTMs), the simple representation of unidirectional dry deposition depicted in Fig. 1.3 does not represent bidirectional surface exchange, which has been observed for some atmospheric species under certain conditions, i.e., uptake of $NH_3$ and other semi-volatile species into dew (Wentworth et al., 2016) or dynamic adsorption of HONO to surfaces (Spicer et al., 1993; Wojtal et al., 2011). Resistance model analogs may be extended to represent bidirectional surface exchange through the introduction of a nonzero surface compensation point concentration, requiring parameterization of additional species- and surface-specific processes (Neirynck and Ceulemans, 2008; Pleim et al., 2013). In addition, representation of species-specific ground surface reactions unrelated to solubility or oxidative potential,

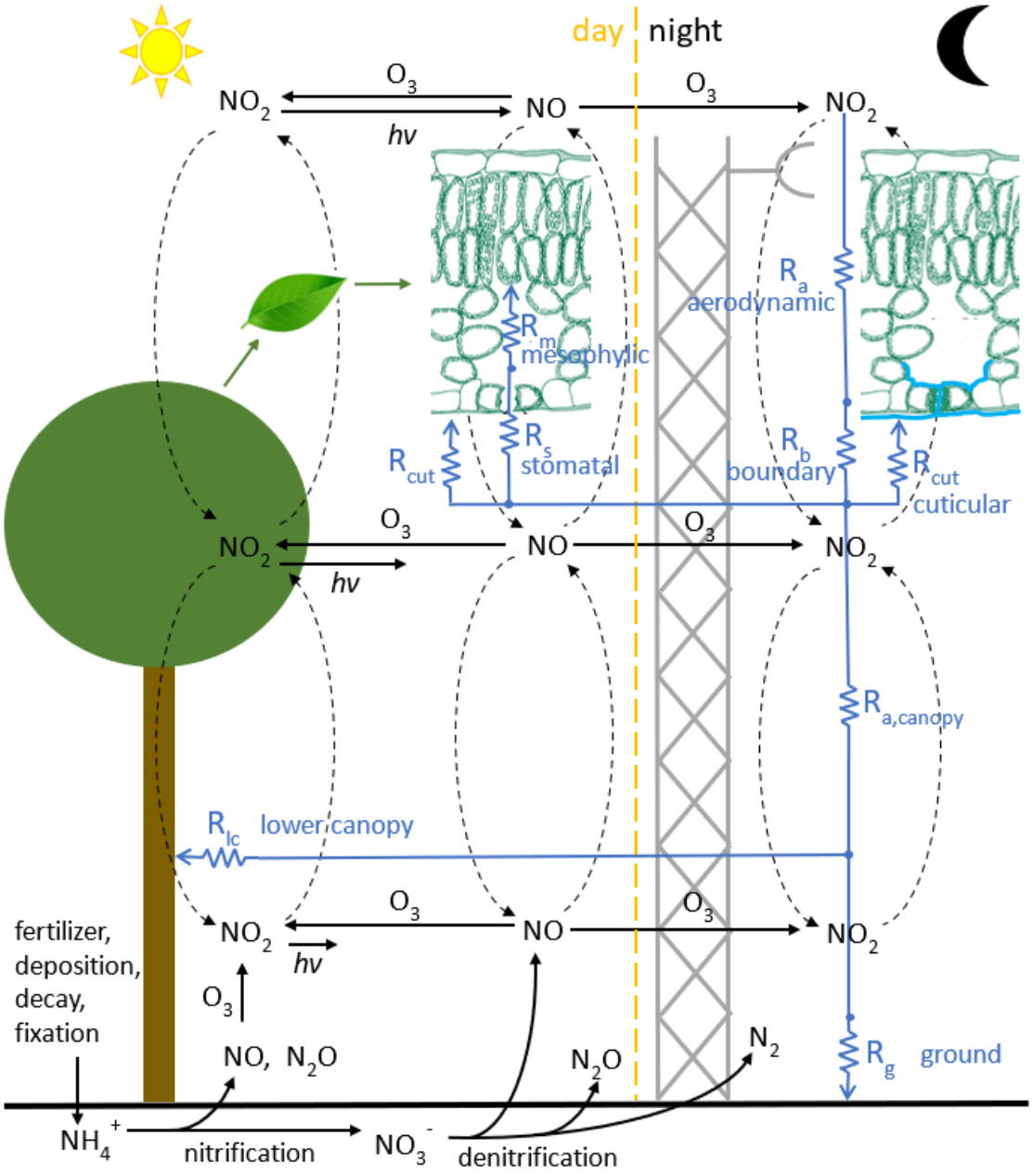


**Figure 1.3:** Dry deposition processes for $NO_2$ to a forest canopy. Depictions include: (i) day–night canopy exchange of $NO_x$, (ii) canopy level exchange measured by eddy covariance flux observations, and (iii) the resistance-in-series model framework for parameterizing dry deposition velocity. Internal leaf structure adapted from Nobel (2009).

such as the heterogeneous hydrolysis of $NO_2$ yielding adsorbed $HNO_3$ and evolved HONO (Fig. 1.2), requires updates to surface resistance ($R_c$) parameterizations in standard dry deposition schemes (the subject of Chapter 3).

The dry deposition of $NO_x$ via $NO_2$ (NO does not dry deposit), although not well understood (Seinfeld and Pandis, 2006), has been directly observed in surface-specific chamber studies to foliar (Breuninger et al., 2013; Chaparro-Suarez et al., 2011; Delaria et al., 2018; Wang et al., 2020c) and non-foliar surfaces (Grøntoft and Raychaudhuri, 2004; Hanson et al., 1989; Rondón et al., 1993), as well as through above-canopy field observations employing the eddy covariance technique (Geddes and Murphy, 2014; Horii et al., 2004; Stocker et al., 1995). Processes which have confounded interpretation of $NO_2$ uptake observations include: (i) detection interference from other gases leading to speculation of $NO_2$ compensation points below which $NO_2$ was thought to be emitted by vegetation, (ii) soil $NO_x$ emissions masking and even reversing above-canopy flux measurements, and (iii) below sensor chemical flux divergence resulting from canopy gradients in solar radiation, the latter two depicted in Fig. 1.3. Therefore, measurement and interpretation of $NO_2$ dry deposition requires highly specific $NO_2$ detection methods as well as ancillary information regarding surface emissions and below sensor chemical flux divergence.

Recent leaf-level studies of $NO_2$ uptake incorporated into a 1-D column model of a forest canopy (Delaria and Cohen, 2020) point to a significant role for canopy uptake of soil-emitted $NO_x$—up to 60%. The mechanism of this apparent dry deposition sink is still an active area of research, especially at night when leaf stomata are mostly closed (Nobel, 2009). Some branch enclosure studies have attributed non-zero water vapour flux out of leaves under dark conditions to be an indication of partially open stomata and therefore a pathway for continued stomatal uptake of depositing trace species at night (Delaria et al., 2020)—a process not currently represented in dry deposition parameterizations (Zhang et al., 2003a). However, other work attributes nocturnal non-zero water vapour flux to confounding factors such as the hydraulic activation of stomata where deposition of hygroscopic material to leaf surfaces results in thin aqueous films of concentrated solute

linking the stomatal-containing outer surfaces of leaves with the moist apolastic leaf interior (Burkhardt, 2010), as depicted in Fig. 1.3. Such a process could, in part, decouple similarity between leaf water vapour flux and stomatal dry deposition of trace species at night. Chapter 3 contributes to this active area of research.

## 1.4 Modeling Global Atmospheric Composition

Models of atmospheric chemistry are an integral component in the study of the atmosphere, developing in concert with laboratory studies and atmospheric measurements (including ground, aircraft and space-based observations) (Abbatt et al., 2014). State-of-the-science models in turn aid in the interpretation of observations of the complex atmosphere. Figure 1.4 depicts the simplest modeling framework—the zero-dimensional box model—for the representation of fundamental atmospheric processes affecting trace gas/aerosol concentrations, namely, emissions, transport (advection and turbulence), chemistry (production and loss), and deposition (wet and dry). Box models may be implemented in two frames of reference—Eulerian (fixed coordinate) or Lagrangian (moving coordinate). In a Eulerian framework, wind advects through a finite volume domain (as depicted in Fig. 1.4), whereas in a Lagrangian framework, the finite volume domain moves along with the mean wind. Box models often aid in the interpretation of observations from intensive field campaigns, where a limited spatial domain and sufficient observational constraints on model inputs enables increased focus on specific processes (McDuffie et al., 2018b, 2018a; VandenBoer et al., 2013). By the coupling of boxes, modeling utility may be extended to situations requiring higher spatial dimensions, from 1-D column models to 3-D models of the global atmosphere, albeit, at the expense of increased computational and input resources, therefore necessitating more tractable representations of fundamental processes. 1-D column models simulate the evolution of trace species concentrations along a vertical coordinate and are useful in situations where horizontal homogeneity is a reasonable approximation, such as in localized canopy studies (Ashworth et al., 2015; Bryan et al., 2012; Gao et al., 1993; Wong and Stutz, 2010) or representation of dry deposition (Delaria and Cohen, 2020) (Chapter 4 of this thesis). 3-D atmospheric chemical transport models (CTMs) simulate the spatiotemporal evolution of atmospheric trace gases and aerosols at

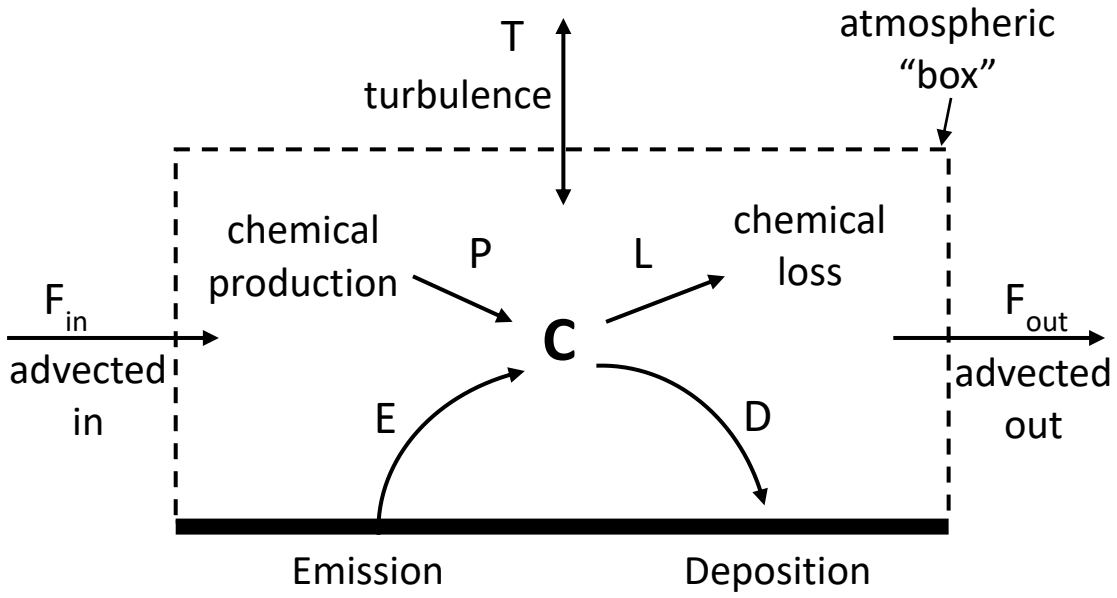


**Figure 1.4:** Atmospheric box model (zero-dimensional) depicting processes that influence the concentration *C* of a species. Adapted from Jacob (1999).

high temporal resolution and various spatial resolutions from regional to global scales using assimilated meteorology, global and regional emission inventories/schemes, and chemical and physical mechanisms reflective of atmospheric processes amenable to large scale simulation. CTMs have a wide range of applications, some examples include: aiding in the interpretation of atmospheric observations (Croft et al., 2014, 2019; Travis et al., 2016), source attribution of ambient pollutants (Weagle et al., 2018) enabling estimates of population exposure (Lee et al., 2015; McDuffie et al., 2021), simulating atmospheric deposition budgets of micronutrients to land (Geddes and Martin, 2017) and ocean (Johnson et al., 2010) ecosystems, climate impacts of short-lived radiative forcers such as aerosol (Croft et al., 2016; Ridley et al., 2014b) and ozone (Yeung et al., 2019), top-down constraints on emissions (Heald et al., 2010; Martin et al., 2003b), and use of space-based observations to improve estimated distributions of ground-level pollutants (Cooper et al., 2020; Van Donkelaar et al., 2021). The use of CTMs to estimate ground-level $PM_{2.5}$ from space-based observations of total column aerosol is discussed below in section 1.5.

Although of much different scope, the governing equations of global CTMs represent the same fundamental processes as those depicted in Fig. 1.4 for a box model.

Specifically, the local evolution in concentration $c$ of an atmospheric trace species $i$ is represented through a mass-conserving chemical continuity equation:

$$\frac{\delta c_i}{\delta t} = -\nabla \cdot (c_i \boldsymbol{V}) + S_i \quad (1.1)$$

where $-\nabla \cdot (c_i \boldsymbol{V})$ represents the transport flux divergence of species $i$ and $S_i$ the net local source; $\boldsymbol{V}$ is the 3-D wind velocity vector. The form of equation (1.1) applies to species concentrations $c_i$ when in units of mass or number density (i.e., kg $m^{-3}$ or molecules $m^{-3}$) (Brasseur and Jacob, 2017). The transport term in (1.1) has contributions from both advection and turbulence. Advection describes flow by the wind resolved at the model resolution, whereas turbulence describes flow due to both fluctuating subgrid scale winds (turbulent mixing) and larger buoyant vertical motions (convection). Although advection may be represented directly through the transport term in (1.1) using grid-resolved mean winds, turbulent transport requires parameterization (Brasseur and Jacob, 2017; Seinfeld and Pandis, 2006). The net local source term $S_i$ in (1.1) represents all the processes internal to the box in Fig. 1.4, namely, emissions, deposition (wet and dry), and chemical production and loss reactions. Given these many different processes affecting species concentrations, each with independent model formulations, CTMs represent (1.1) as a set of time-dependent, coupled partial differential equations:

$$\frac{\delta c_i}{\delta t} = \left[\frac{\delta c_i}{\delta t}\right]_{adv} + \left[\frac{\delta c_i}{\delta t}\right]_{mix} + \left[\frac{\delta c_i}{\delta t}\right]_{conv} + \left[\frac{\delta c_i}{\delta t}\right]_{wet\ dep} + \left[\frac{\delta c_i}{\delta t}\right]_{chem} + \left[\frac{\delta c_i}{\delta t}\right]_{emis} + \left[\frac{\delta c_i}{\delta t}\right]_{dry\ dep} \quad (1.2)$$

where right-hand-side terms represent, successively, rates of change of $c_i$ due to advection, turbulent (vertical) boundary layer mixing, convection, wet deposition, chemistry, emissions, and dry deposition. A commonly employed strategy for the numerical solution of the mass continuity equation in CTMs is operator splitting, where the terms of (1.2) are independently integrated over a model time step $\Delta t$ (operator duration) and the updated concentration $c_i(t+\Delta t)$ computed from the sum of component changes (Seinfeld and Pandis, 2006). The widely used GEOS-Chem CTM (www.geos-chem.org), which is used in this thesis, employs the method of operator splitting, where the terms in (1.2) are integrated independently and applied serially in the order of: advection, dry deposition, emissions,

turbulent PBL mixing, convection, chemistry, and wet deposition. An assumption of this method is that operator coupling over the integration time step is negligible, thus, modelers must optimize simulation accuracy with computational constraints (Philip et al., 2016). User-defined operator durations typically vary between 5 min to 60 min dependent on model horizontal resolution. GEOS-Chem uses separate dynamic (advection, vertical mixing, cloud convection, and wet deposition) and chemical (emissions, dry deposition, and chemistry) operator durations (time steps), where the chemical operator duration is generally twice the dynamic operator duration. To reduce computation time and facilitate use/development by a wider research community, state-of-the-science CTMs are generally run offline from the general circulation models (GCMs) that output the meteorological fields required as CTM inputs, albeit, at the expense of lack of chemical feedbacks on meteorology. Recently, however, GEOS-Chem (GC) has been coupled to the Weather Research and Forecasting (WRF) meteorological model (WRF-GC) to enable simulation of aerosol-radiation and aerosol-cloud associated feedbacks on meteorology at high resolution over regional scales (Feng et al., 2021). The standard offline version of the GEOS-Chem CTM was used throughout this thesis; further discussion of aspects of the model relating to the research presented in this thesis are included in subsequent chapters.

Due to the many non-linear processes affecting atmospheric species concentrations, all CTMs, no matter their resolution, contain parameterizations of subgrid processes that occur on scales finer than the resolution of the model. Regional to global CTMs have grid box sizes with horizontal dimensions on the order of tens to hundreds of kilometers and vertical dimensions on the order of tens to hundreds of meters. Parameterization of subgrid scale processes in CTMs may be based on (i) laboratory or field observations, or on (ii) the results of higher-resolution models that are able to resolve the subgrid scale for the process of interest; Chapter 3 updates a parameterization of $NO_2$ dry deposition using (i); Chapter 4 implements a parameterization for subgrid dry deposition of $NO_x$ into GEOS-Chem using (ii). All atmospheric models, regardless of type, require parameterization of near-surface turbulence which drives surface fluxes of momentum, heat, and mass; CTMs have many additional parameterizations across a wide range of processes, including turbulent PBL mixing, deep convection, wet and dry deposition, and emissions (Brasseur and Jacob, 2017). Biases resulting from instantaneous dilution of emissions into CTM grid boxes may

be reduced by parameterization of subgrid scale processes prior to release of processed emissions and or product(s). Such parameterizations have been developed for power plant emissions of $SO_2$ (Stevens and Pierce, 2013, 2014) and aircraft (Kraabøl et al., 2002), lighting (Cooper et al., 2014), ship (Vinken et al., 2011), and soil (Hudman et al., 2012) emissions of $NO_x$. Natural emissions of dust and seasalt aerosol have a non-linear dependence on windspeed, as such, methods must be employed to ensure grid-independence of resulting emissions at varying CTM horizontal resolutions (Meng et al., 2021). However, representing area source concentration gradients and resulting secondary pollutant concentrations, i.e., particulate nitrate, improves with CTM resolution (Zakoura and Pandis, 2018), thus welcoming strategies of targeted high-resolution simulation in global CTMs (Bindle et al., 2020; Yu et al., 2016).

### 1.5 Satellite-Derived $PM_{2.5}$

Given the significant and increasing global burden of disease attributable to ambient $PM_{2.5}$ (Health Effects Institute, 2020; Murray et al., 2020), there is great need for timely, accurate, and high-resolution awareness of $PM_{2.5}$ surface concentrations, globally, especially in populated areas. Although networks of ground-level monitors for ambient $PM_{2.5}$ have grown over recent decades, coverage in many populated regions of the world is insufficient for air quality management and exposure assessment (Martin et al., 2019). CTMs enable the simulation of ground-level pollutants (including accumulation mode aerosol that contributes to $PM_{2.5}$) globally at high temporal resolution, albeit, at relatively coarse spatial resolutions (typically hundreds to thousands of square kilometers). Remote-sensed aerosol optical depth (AOD)—a unitless measure of total-column extinction of solar radiation at a particular wavelength due to scattering and absorption by aerosol—from higher resolution satellite observations ($AOD^{sat}$) may be used to scale coincidently-sampled simulated values from a CTM ($AOD^{sim}$) to produce improved global estimates of ground-level $PM_{2.5}$ concentrations ($PM_{2.5}^{sat}$) at high resolution (van Donkelaar et al., 2006, 2010):

$$PM_{2.5}^{sat} = \frac{PM_{2.5}^{sim}}{AOD^{sim}} AOD^{sat} \tag{1.3}$$

where $PM_{2.5}^{sim}$ is ground-level accumulation mode aerosol mass concentration simulated by the CTM. It is due to the coincidence that accumulation mode aerosol both contributes to $PM_{2.5}$ mass and has significant mass extinction efficiency of solar radiation that the method of (1.3) is an effective strategy to improve estimates of ground-level $PM_{2.5}$ globally.

Satellite-derived estimates of ground-level $PM_{2.5}$ have played an important role in up-to-date air quality awareness and exposure assessment, especially in areas lacking measurement networks (Shaddick et al., 2018). Additionally, trends in satellite-derived $PM_{2.5}$ agree well with observational networks when and where available (Boys et al., 2014; van Donkelaar et al., 2015b; Meng et al., 2019a), thus providing a timely method to monitor evolution of exposure globally, as well as the response of $PM_{2.5}$ to air pollution management efforts. Current methods of estimating ground-level $PM_{2.5}$ expand on measurement-model synergy by incorporating, in addition to ground and space-based AOD measurements, *in situ* measurements of $PM_{2.5,}$ where available, for correction of satellite-derived $PM_{2.5}$ biases via geographically weighted regression (GWR) (Van Donkelaar et al., 2016). GWR predictors with which to regress observed biases are selected based on intuition, and include terms such as urban landcover, subgrid elevation difference, and aerosol composition (van Donkelaar et al., 2015a; Meng et al., 2019a), thus providing physical insight into possible sources of uncertainty for simulated $PM_{2.5}$-to-AOD relationships and directing future research efforts to improve CTM processes. A prominent predictor of bias in satellite-derived $PM_{2.5}$ is particulate nitrate (van Donkelaar et al., 2015a), which, in part, has inspired the research efforts of chapters 3 and 4 of this thesis where missing processes of $NO_2$ uptake to ground surfaces in the GEOS-Chem CTM are addressed. As depicted in Fig. 1.2, $NO_2$ is the primary source of $pNO_3$.

### 1.6 Outline and Goals of the Thesis

To a large degree, air pollution has and continues to be a consequence of anthropogenic activities. Heterogeneous change in the distribution of various air pollutants have accompanied economic, technological, and policy advances globally. As such, methods to monitor this evolution are of great interest, especially for pollutants that pose significant health risk such as fine aerosol, and satellite-derived $PM_{2.5}$ is one such method. The first

goal of this thesis was to develop a long-term and consistent time-series of satellite remote sensed AOD using satellite instruments that had well maintained radiometric stability from which to infer the corresponding satellite-derived $PM_{2.5}$ time series using a global CTM. This was the effort of Chapter 2, where a unified 15-year global time series (1998–2012) of monthly ground-level $PM_{2.5}$ at a resolution of 1˚ x 1˚ was achieved using the MISR and SeaWiFS satellite instruments and the GEOS-Chem CTM. This work was published in *Environmental Science & Technology* in 2014.

Nitrogen oxides modulate oxidant fields, influence air quality, and contribute to other reactive nitrogen species that have significant biosphere and health implications. As such, an accurate simulation of $NO_x$ processes is of great interest. Current global CTMs employ a dry deposition parameterization that allows for uptake of $NO_2$ by vegetation in daytime, but with negligible deposition occurring at night—this despite evidence of nocturnal $NO_2$ removal via heterogeneous hydrolysis on humidified ground surfaces. Motivated by laboratory studies of the heterogenous hydrolysis of $NO_2$, together with recent field studies designed to quantify the extent of this reaction on ground surfaces, in Chapter 3 we endeavor to update the parameterization of non-stomatal $NO_2$ dry deposition, mechanistically, by representing this heterogeneous reaction pathway on ground surfaces. We re-interpret an extensive dataset of eddy covariance $NO_2$ flux observations above a mixed forest canopy with the benefit of additional laboratory, field, and modeling information to explain observed $NO_2$ nocturnal deposition fluxes as driven by heterogenous hydrolysis on forest surfaces.

Combustion of fossil fuels is the dominant source of $NO_x$ to the troposphere, contributing at least half of total $NO_x$ emitted to the atmosphere (Table 1.3). Of this fraction, on-road transportation is a major source, contributing about 23% of the ca. 30 Tg N $yr^{-1}$ emitted by fossil fuels globally (McDuffie et al., 2020). Due to the many secondary reactions involving $NO_x$, parameterizations for the subgrid scale processes that occur as $NO_x$ disperses from sources such as lightning, aircraft, ship, and soil have been developed for the GEOS-Chem CTM, which has grid boxes that are hundreds to thousands of square kilometers in the horizontal and more than 100 m deep. However, despite the on-road transportation sector also being a subgrid scale emitter, especially in the absence of strong

boundary layer turbulence, these emissions of $NO_x$ are currently released into surface model grid cells directly from emission inventories. The goal of Chapter 4 was to study the effect of subgrid dry deposition of near-surface anthropogenic emissions of $NO_x$ in GEOS-Chem, in conjunction with the optimized ground surface reaction pathway from Chapter 3 which provides mechanistic utility to surface HONO production.

# Chapter 2

## Fifteen-Year Global Time Series of Satellite-Derived Fine Particulate Matter

Authors: Boys, B.L.[1], Martin, R.V.[1,2], van Donkelaar, A.[1], MacDonell, R.J.[1], Hsu, N.C.[3], Cooper, M.J.[1], Yantosca, R.M.[4], Lu, Z.[5], Streets, D.G.[5], Zhang, Q.[6], Wang, S.W.[6]

[1]Dalhousie University, Halifax, Nova Scotia, Canada

[2]Harvard-Smithsonian Center for Astrophysics, Cambridge, MA, USA

[3]NASA Goddard Space Flight Center, Greenbelt, Maryland, USA

[4]Harvard University, Cambridge, MA, USA

[5]Argonne National Laboratory, Argonne, IL, USA

[6] Center for Earth System Science, Tsinghua University, Beijing, China

Article published in Environmental Science & Technology, 48, 11109–11118, 2014.

All text, tables, figures, and presented results were contributed by the first author.

### 2.1 Abstract

Ambient fine particulate matter ($PM_{2.5}$) is a leading environmental risk factor for premature mortality. We use aerosol optical depth (AOD) retrieved from two satellite instruments, MISR and SeaWiFS, to produce a unified 15-year global time series (1998–2012) of ground-level $PM_{2.5}$ concentration at a resolution of 1˚ x 1˚. The GEOS-Chem chemical transport model (CTM) is used to relate each individual AOD retrieval to ground-level $PM_{2.5}$. Four broad areas showing significant, spatially coherent, annual trends are examined in detail: the eastern U.S. ($-0.39 \pm 0.10$ μg $m^{-3}$ $yr^{-1}$), the Arabian Peninsula ($0.81 \pm 0.21$ μg $m^{-3}$ $yr^{-1}$), South Asia ($0.93 \pm 0.22$ μg $m^{-3}$ $yr^{-1}$) and East Asia ($0.79 \pm 0.27$ μg $m^{-3}$ $yr^{-1}$). Over the period of dense *in situ* observation (1999–2012), the linear tendency for the eastern U.S. ($-0.37 \pm 0.13$ μg $m^{-3}$ $yr^{-1}$) agrees well with that from *in situ* measurements ($-0.38 \pm$

0.06 μg $m^{-3}$ $yr^{-1}$). A GEOS-Chem simulation reveals that secondary inorganic aerosols largely explain the observed $PM_{2.5}$ trend over the eastern U.S., South Asia, and East Asia, while mineral dust largely explains the observed trend over the Arabian Peninsula.

## 2.2 Introduction

Particles with an aerodynamic diameter below 2.5 μm ($PM_{2.5}$) are highly respirable and are a leading global environmental risk factor for premature mortality (Correia et al., 2013; Dockery et al., 1993; Lim et al., 2012; Pedersen et al., 2013). Recently, the World Health Organization (WHO) declared particulate matter air pollution a group 1 carcinogen to humans (IARC, 2013), adding to the known burden of disease from cardiovascular and respiratory morbidity. The WHO air quality guideline (AQG) for $PM_{2.5}$ of 10 μg $m^{-3}$ is surpassed in most industrialized regions of the world, in some areas by an order of magnitude (van Donkelaar et al., 2010). In addition to the detrimental health effects of elevated $PM_{2.5}$ concentrations, epidemiological research of 545 U.S. counties (Correia et al., 2013) and a Canadian national-level cohort (Crouse et al., 2012) failed to identify an exposure threshold where $PM_{2.5}$ reductions provided no benefit. A recent study points to prenatal morbidity at levels below the present European Union annual limit of 25 μg $m^{-3}$ (Pedersen et al., 2013). Long-term time series of spatially resolved $PM_{2.5}$ on the global scale are needed to assess health impacts and inform policy decisions.

Satellite-derived estimates of ground-level $PM_{2.5}$ have advanced in recent years due to the developments of advanced column aerosol optical depth (AOD) satellite retrievals, of global chemical transport models (CTMs) and of ground-level *in situ* observations of $PM_{2.5}$ (Engel-Cox et al., 2013). Satellite-retrieved AOD, a unitless measure of the column-integrated extinction of radiation by atmospheric particles, can be related to surface $PM_{2.5}$ by (i) use of a chemical transport model to simulate daily the $PM_{2.5}$ to AOD relationship (van Donkelaar et al., 2010; Liu et al., 2004) or (ii) statistical methods where reliable monitoring networks are used as a training data set to calibrate daily $PM_{2.5}$ to AOD relationships (Hu et al., 2014; Lee et al., 2011). The latter method can provide highly accurate $PM_{2.5}$ to AOD relationships in regions with a sufficiently dense network of ground-level measurements, while the former method can be validated where ground

measurements exist and then applied beyond the reach of globally sparse measurement networks. The surface $PM_{2.5}$ to column AOD relationship has substantial seasonal variability and daily fluctuations (Lee et al., 2011). Inter-annual variations in this relationship from changing emissions and meteorological fluctuations could complicate comparison of AOD and $PM_{2.5}$ trends such that a significant trend in AOD may not necessarily manifest as a significant trend in $PM_{2.5}$ and vice versa. Accordingly, methods to estimate spatiotemporally resolved global $PM_{2.5}$ to AOD ratios are a requirement for accurate study of the trend in satellite-derived $PM_{2.5}$.

Satellite-retrieved AOD is subject to a suite of uncertainties with contributions from sampling bias, cloud contamination, assumptions of aerosol and surface properties, and erroneous sensor calibration (Abbatt et al., 2014; Colarco et al., 2014). Radiometric stability is of particular importance to time series analysis; spurious trends in long term AOD have been inferred as a result of radiometric drift (Zhang and Reid, 2010; Zhao et al., 2008). Unfortunately, both of the Moderate Resolution Imaging Spectroradiometer (MODIS) sensors onboard NASA's Terra and Aqua satellites exhibit radiometric drift in the collection 5 product (Zhang and Reid, 2010), an issue that is addressed in the recent collection 6 product (Levy et al., 2013). The Sea-viewing Wide Field-of-view Sensor (SeaWiFS), the sole instrument on board NASA's SeaStar satellite, was designed primarily for global ocean color measurement and thus required highly accurate radiometric calibration that was maintained to an accuracy of 0.5% and temporal stability of 0.3% over its lifetime (Barnes et al., 2001; Eplee et al., 2012). The Multiangle Imaging SpectroRadiometer (MISR) onboard NASA's Terra satellite, an advanced Earth observing sensor designed primarily to retrieve tropospheric aerosol properties, is maintained to a radiometric accuracy of 3% with stability of 1% (Bruegge et al., 2007; Kahn et al., 2005). Decadal variations in satellite-retrieved AOD from SeaWiFS and MISR have been examined globally and evaluated with NASA's ground-based Aerosol Robotic Network (AERONET) of sunphotometers (Hsu et al., 2012; De Meij et al., 2012; Yoon et al., 2011; Zhang and Reid, 2010).

Globally, few regional scale $PM_{2.5}$ trends have been inferred from *in situ* measurements due to a lack of long-term monitoring networks. However, in the U.S.,

sufficient measurements have enabled detection of a 33% decrease in $PM_{2.5}$ from 2000 to 2012, with most measurement sites located in the eastern U.S. (http://www.epa.gov/airtrends/). Visibility, a widely used measure of near surface extinction by aerosol, has decreased globally over land during the past few decades, with industrializing regions such as South and East Asia experiencing the greatest declines (Wang et al., 2009). This is in contrast with improvements seen for post-industrialized Europe from the late 1980's to 2000, a result of large reductions in sulfate aerosol over this period (Berglen et al., 2007). Efforts to improve air quality have resulted in decreases in particulate matter with diameter < 10 μm ($PM_{10}$) over North America, Europe and more recently East Asia (Cheng et al., 2013a; Wang et al., 2012). However, due to the low extinction efficiency of visible radiation by these coarse particles, decreasing trends in $PM_{10}$ are not necessarily matched with improvements in visibility, especially in industrializing nations such as East Asia where the ratio of fine to coarse particles has increased (Wang et al., 2012). Regional analysis of satellite-derived $PM_{2.5}$ at 0.5˚ x 0.5˚ over the Indian subcontinent using the MISR time series from 2000 to 2010 and climatological 'surface $PM_{2.5}$ to column AOD' relationships revealed an increase of 15 to >25 μg $m^{-3}$ over the Indo-Gangetic Basin, with increases for central India in the range 5 to 15 μg $m^{-3}$ (Dey et al., 2012). Hu et al. (2014) detected a 20% decrease in $PM_{2.5}$ over 2001 to 2010 for the southeastern US, with greater reductions observed for urban and highway environments than for more remote forest areas.

In this study, we develop and interpret the first observationally-based estimate of changes in long-term global $PM_{2.5}$. Specifically, we combine satellite-derived $PM_{2.5}$ from the MISR and SeaWiFS instruments—using overpass-resolved simulated 'surface $PM_{2.5}$ to column AOD' relationships from a global CTM employing consistent assimilated meteorology—to estimate and interpret a unified, 24-hr, monthly $PM_{2.5}$ time series from January 1998 to December 2012 globally at a resolution of 1˚ x 1˚ which is amenable to time series analysis. Significant annual trends observed over four broad regions, namely: eastern U.S., Arabian Peninsula, South Asia, and East Asia, are analyzed together with simulated $PM_{2.5}$ fractional components.

## 2.3 Materials and Methods

2.3.1 *Retrieved Satellite Aerosol Optical Depth*

MISR contains nine fixed angle cameras, enabling sensitivity to angular variation in reflected sunlight originating from aerosols, clouds and surface. This allows retrieval of aerosol properties with reduced algorithmic assumptions of surface reflectance over all land types (Diner et al., 1998; Martonchik et al., 1998), including terrain with temporally varying surface features and highly reflective surfaces like deserts (Martonchik et al., 2004). AOD is retrieved from MISR at a resolution of 17.6 km x 17.6 km. The equator crossing time is 1030 hours local solar time. The 360 km across track swath results in global coverage in 9 days at the equator and 2 days near the poles. We re-gridded to daily 1˚ x 1˚ global AOD maps from 29 February 2000 to 31 Dec 2012, using daily level 2 AOD swaths at 558 nm (from the MIL2ASAE product with quality assurance flags [0 1]).

The visible to near IR spectral range of SeaWiFS allows AOD retrieval algorithms to be applied over both ocean (Sayer et al., 2012) and land (Hsu et al., 2013), yielding accuracies similar to other AOD retrieving satellites (Petrenko and Ichoku, 2013). SeaWiFS retrievals of AOD are at a resolution of 13.5 km x 13.5 km with an equator crossing time of 1200 hrs local solar time, drifting to ca. 1430 hrs by 2010. A 1502 km across track swath results in near daily coverage at the equator and daily coverage outside the tropics. We re-gridded to daily 1˚ x 1˚ global AOD maps from 01 January 1998 to mission end date December 2010, using daily level 2 AOD swaths at 550 nm (version SWDB_L2.004 with quality assurance [2 3] over ocean and [3] over land).

2.3.2 *Satellite-Derived $PM_{2.5}$*

Following van Donkelaar et al. (2010) we expressed the proportionality between ground-level $PM_{2.5}$ mass concentration and satellite-retrieved column-integrated AOD as spatially and temporally resolved correction factors [$\eta$]:

$$PM_{2.5} = \eta \times AOD \quad , \quad \eta = \frac{PM_{2.5}^{model}}{AOD^{model}} \tag{2.1}$$

where $\eta$ [µg m$^{-3}$] is the ratio of modeled $PM_{2.5}$ [µg m$^{-3}$] under reference conditions to modeled column-integrated AOD [unitless] under ambient relative humidity. We used the North American surface measurement standard of 35% relative humidity (U.S. EPA, 1997) to reference our $PM_{2.5}$ estimates. Factors which influence the value of $\eta$ include the vertical

distribution of the aerosol burden, the aerosol size distribution, aerosol composition, and relative humidity. We calculated daily global maps of $\eta$ with the 3-D global CTM, GEOS-Chem [geos-chem.org; supplemental] for the period 1 January 1998 to 31 December 2012. The relation of satellite AOD to $PM_{2.5}$ is enabled because the aerosol mass extinction efficiency for visible radiation peaks within the accumulation mode (~ 0.1 to 2.5 μm diameter particles) of the aerosol size distribution, which is the size region contributing to $PM_{2.5}$ mass.

GEOS-Chem (Bey et al., 2001; Park et al., 2004) solves for the 3-D evolution of atmospheric gases and aerosols (sulfate, nitrate, ammonium, organic and black carbon, mineral dust, and sea salt) using assimilated meteorological observations, global and regional emission inventories, and algorithms to represent the physics and chemistry of atmospheric processes, as described in the supplemental material. The CTM was driven by assimilated meteorological observations (GEOS-MERRA) at a horizontal resolution of 2˚ x 2.5˚ (lat, long) with 47 vertical levels from the surface to ca. 80 km. Modeled $PM_{2.5}$ and column AOD used in the formulation of $\eta$ were sampled at satellite overpass time (late morning for MISR and early afternoon for SeaWiFS). Daily global maps of $\eta$ at 2˚ x 2.5˚ were interpolated to 1˚ x 1˚ for application to satellite AOD values. Following (Van Donkelaar et al., 2013), for absolute satellite-derived $PM_{2.5}$ estimates, we scaled the vertical distribution of modeled aerosol extinction to match climatological monthly observations from the CALIPSO satellite lidar at 1˚ x 1˚ over 2006 – 2012. However, our analysis of time varying $PM_{2.5}$ anomalies does not employ such correction factors since CALIPSO was not operational prior to 2006.

2.3.3 *Combined Satellite-Derived $PM_{2.5}$*

A unified, monthly, satellite-derived $PM_{2.5}$ global time series at 1˚ x 1˚ from 1 January 1998 to 31 December 2012 was estimated by combining the sampling-corrected (SC), monthly SeaWiFS (1998–2010) and MISR (2000–2012) derived $PM_{2.5}$ time series. We accounted for sampling differences as:

$$SC\_MISR\_PM_{2.5,m} = \frac{GC_{PM_{2.5,m}}^{24hr}}{GC_{PM_{2.5,m}}^{MISR}} \times MISR_{PM_{2.5,m}} \quad (2.2)$$

$$SC\_SeaWiFS\_PM_{2.5,m} = \frac{GC_{PM}{}^{24hr}_{2.5,m}}{GC_{PM}{}^{SeaWiFS}_{2.5,m}} \times SeaWiFS_{2.5,m} \quad (2.3)$$

where, for month $m$, $MISR_{PM\,2.5,m}$ and $SeaWiFS_{2.5,m}$ refer to monthly satellite-derived $PM_{2.5}$ estimates from respective instruments—a threshold of at least three days per month for each 1˚ x 1˚ grid cell was required for monthly $PM_{2.5}$ averages. $GC\_PM^{24hr}_{2.5,m}$ refers to monthly mean GEOS-Chem $PM_{2.5}$ averaged over 24-hr for each day of the month. $GC\_PM^{SeaWiFS}_{2.5,m}$ and $GC\_PM^{MISR}_{2.5,m}$ refer to monthly mean GEOS-Chem $PM_{2.5}$ sampled on coincident days with each instrument during the corresponding satellite overpass period (i.e., late morning for MISR, early afternoon for SeaWiFS). Monthly modeled correction factors for incomplete sampling display distinct seasonality, as in van Donkelaar et al. (2010), especially for regions with pronounced wet and dry seasons (data not shown).

When monthly averages for each sensor exist, we calculated $PM_{2.5,m}$ as the average of monthly mean satellite-derived $PM_{2.5}$ from each instrument after accounting for their sampling differences (as shown in equations 2.2 and 2.3);

$$PM_{2.5,m} = 0.5\, SC_{MISR_{PM\,2.5,m}} + 0.5\, SC_{SeaWiFS_{PM\,2.5,m}} \quad (2.4)$$

When just one of the two satellite sensors had sufficient data to represent a monthly average, or during a pre- or post-period of operation, a virtual estimate of the sampling-corrected missing value (i.e., $SC\_MISR\_PM^{vir}_{2.5,m}$) was computed (2.5) and used in (2.4).

$$SC_{MISR_{PM}}{}^{vir}_{2.5,m} = \left(\frac{1}{8}\sum_{y=2001}^{2008} SC_{MISR_{PM}}{}^{offset}_{2.5,m(y)}\right) \times SC_{SeaWiFS_{PM\,2.5,m}} \quad (2.5)$$

where, for month $m$, $\left(\frac{1}{8}\sum_{y=2001}^{2008} SC\_MISR\_PM^{offset}_{2.5,m(y)}\right)$ is the month-specific, sampling-corrected climatological offset for MISR, and $SC\_SeaWiFS\_PM_{2.5,m}$ is the sampling-corrected estimate of SeaWiFS-derived $PM_{2.5}$. Month-specific climatological offset factors for MISR and SeaWiFS were computed using the years $y$ from 2001 to 2008, an overlap period of optimal performance for both sensors. Similar methods have been used to estimate daytime $PM_{2.5}$ over United States New England region by averaging MODIS-Terra (1030 hrs overpass) and MODIS-Aqua (1330 hrs overpass) values (Lee et al., 2011). We assessed the sensitivity of trends over the four regions examined herein to uncertainty

in offset by compiling 15 combined satellite-derived $PM_{2.5}$ time series where for each year a random offset value was drawn from a normal distribution described by mean and variance inferred between 2001–2008. The 1σ standard deviation inferred from resulting trends was found to be within 27% of corresponding trends for all four regions.

We interpreted the satellite-derived $PM_{2.5}$ time series with the GEOS-Chem model. We expressed the satellite-derived monthly $PM_{2.5}$ concentration attributable to each major chemical component (secondary inorganics ≡ sulfate + nitrate + ammonium, carbonaceous ≡ organic + black carbon, mineral dust, and sea salt) as the satellite-derived concentration scaled by the GEOS-Chem fractional concentration for each component.

2.3.4 *In Situ $PM_{2.5}$*

We evaluated the satellite-derived $PM_{2.5}$ time series anomaly with ground-based $PM_{2.5}$ measurements in the eastern U.S. (east of 90˚W) where there is a sufficiently dense, long-term federal reference method (FRM) data record from the Interagency Monitoring of Protected Visual Environments network (IMPROVE; http://vista.cira.colostate.edu/improve/) and from the Environmental Protection Agency Air Quality System (EPA AQS; http://www.epa.gov/ttn/airs/airsaqs/). U.S. FRM 24-hr gravimetric filter based *in situ* measurements ($PM_{2.5}$ – local conditions, selections from parameter code 88101), were obtained for years 1998 through 2012 (http://www.epa.gov/ttn/airs/airsaqs/detaildata/downloadaqsdata.htm). For comparison to satellite-derived $PM_{2.5}$, daily *in situ* measurements were spatially aggregated first to a daily 1˚ x 1˚ grid, followed by temporal averaging to a monthly 1˚ x 1˚ grid, followed by spatial averaging for regional analysis; an approach analogous to satellite-derived $PM_{2.5}$ since space-time averaging is not commutative for discontinuous datasets (Levy et al., 2009). We focus our evaluation on the long-term trend since that is the emphasis of this study.

2.3.5 *Estimated $PM_{2.5}$ to AOD Relationship from In Situ $PM_{2.5}$ and AERONET AOD Over the Eastern U.S.*

We evaluated the modeled $PM_{2.5}$ to AOD monthly time series with and without the use of monthly CALIPSO-based correction factors, by comparison with empirical estimates from ground-based measurements over the eastern U.S. (east of 90˚W). Monthly estimates of

the $PM_{2.5}$ to AOD relationship from January 1998 to December 2012 were compiled by aggregating daily AERONET Level 2 AOD measurements (http://aeronet.gsfc.nasa.gov/) from 1000-hrs to 1400-hrs with coincident, at 1˚ x 1˚, daily U.S. FRM 24-hr gravimetric filter-based *in situ* measurements. AERONET and $PM_{2.5}$ stations with an elevation difference of more than 100 m were excluded.

2.3.6 *Time Series Analysis*

Time series analysis was performed on data aggregated to monthly arithmetic mean values. General Least Squares (GLS) regression was performed using the basic model:

$$\boldsymbol{x} = \boldsymbol{z\beta} + \boldsymbol{e} \ , \ \boldsymbol{e} \sim N(0, \sigma^2 \boldsymbol{V}) \tag{2.6}$$

where for a time series of n months, $\boldsymbol{x}$ is a time series vector (n x 1) containing $PM_{2.5}$ values for months 1 to n; $\boldsymbol{z}$ is a design matrix (n x 2) which herein defines a linear model; $\boldsymbol{\beta}$ is a vector (2 x 1) containing the coefficients of the linear model, intercept and slope; $\boldsymbol{e}$ is an error vector (n x 1) containing the residuals not represented by the linear model, which for validity should be approximately normally distributed with zero mean, however, permitted to covary with adjacent values according to **V**—a positive definite, symmetric covariance matrix, to accommodate possible autocorrelation between adjacent months. Correlated errors between adjacent months are represented by a first order autoregressive model of $\boldsymbol{e}$, which can be expressed as:

$$e_t = \emptyset e_{t-1} + w_t \qquad t = 1, \ldots n \quad , \ \boldsymbol{w} \sim N(0, \sigma^2 \boldsymbol{I}) \tag{2.7}$$

where the residual $e_t$ for month $t$ is a fraction $\emptyset$ of the previous month's residual $e_{t-1}$ with a white noise component $w_t$, which for validity should be approximately normally distributed with zero mean, constant variance and independent. Such linear models are widely used in the analysis of environmental monthly time series data (Shumway and Stoffer, 2011; Weatherhead et al., 1998, 2002). The monthly time series was deseasonalized by subtracting the climatological monthly median prior to GLS regression. A minimum temporal coverage of 65% was applied to all 1˚ x 1˚ time series prior to spatial averaging for regional analysis to ensure annual representation of regional trends.

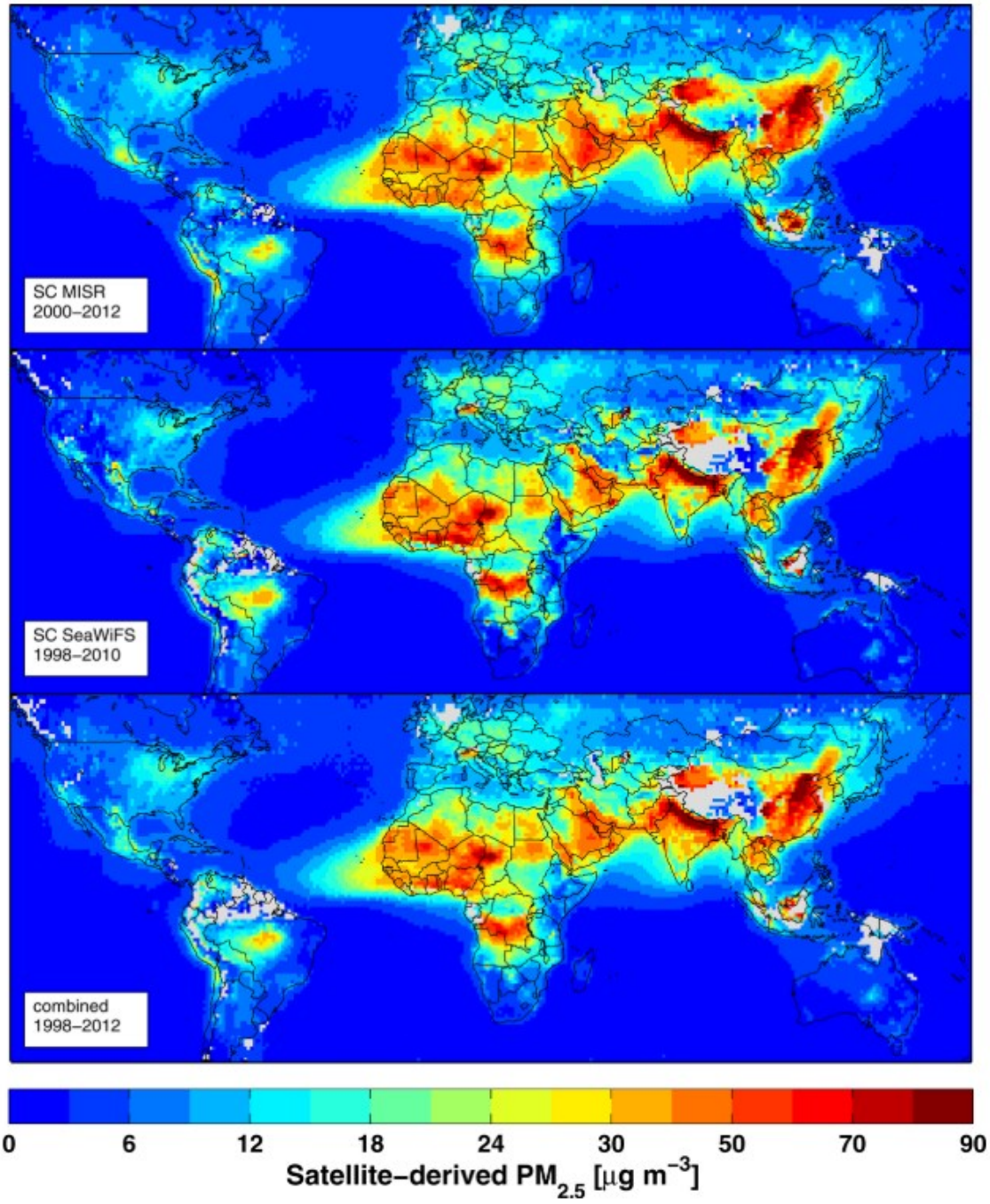


**Figure 2.1:** Satellite-derived, 24-hr, sampling-corrected $PM_{2.5}$ from MISR averaged over 2000–2012, SeaWiFS averaged over 1998–2010, and a combined MISR-SeaWiFS product averaged over 1998–2012. Grey indicates missing data.

## 2.4 Results and Discussion

### 2.4.1 *Global Trends in Satellite-Derived $PM_{2.5}$*

Figure 2.1 shows global distributions of multi-year average satellite-derived, ground-level $PM_{2.5}$ at 1˚ x 1˚. The data for sampling-corrected MISR over 2000–2012 and for sampling-corrected SeaWiFS over 1998–2010 exhibit a high degree of consistency despite having very different retrieval algorithms and slight differences in periods of observation. Both indicate broad enhancements across North Africa, the Middle East, South Asia and East Asia. Inspection of coincidently-sampled MISR- and SeaWiFS-derived climatologies reveals regions of notable difference affected by sampling, such as the biomass burning feature of South America and SeaWiFS lows over the Appalachian Mountains and Tibetan Plateau. Remaining areas of difference, namely central India and the western Arabian Peninsula, arise from differing instrument and retrieval characteristics (Petrenko and Ichoku, 2013). Figure S2.1 (top panel) depicts the percent difference between sampling corrected MISR- and sampling corrected SeaWiFS-derived $PM_{2.5}$ climatologies for overlapping years 2000–2010, which indicates the importance of accounting for climatological offsets when combing the two time series. The MISR-SeaWiFS combined product increases the number of observations and reduces instrument-specific bias through averaging to produce a more representative $PM_{2.5}$ concentration map.

Figure 2.2 shows global maps of the linear trend through satellite-derived $PM_{2.5}$ monthly mean time series. Figure S2.2 depicts the fraction of months included in the time series. Five regions exhibit spatially broad correlation between MISR- and SeaWiFS-derived trend maps: eastern U.S., Central Europe, the Arabian Peninsula, South Asia, and East Asia. The combined time series preserves these spatial tendencies. Regions of notable difference between MISR- and SeaWiFS-derived trend maps resulting from features missed by one instrument due to different periods of observation include the decreasing SeaWiFS trend over eastern Russia due to intense wildfires during summer of 1998 (Duncan et al., 2003); the increasing SeaWiFS trend over the biomass burning area of South America which exhibits a sharp decline in 2006 (Koren et al., 2007) and again after 2010; and the decreasing dust-driven SeaWiFS trend west of the Sahara. The absence of a spatially coherent trend over the remote subtropical southern ocean, as expected for this

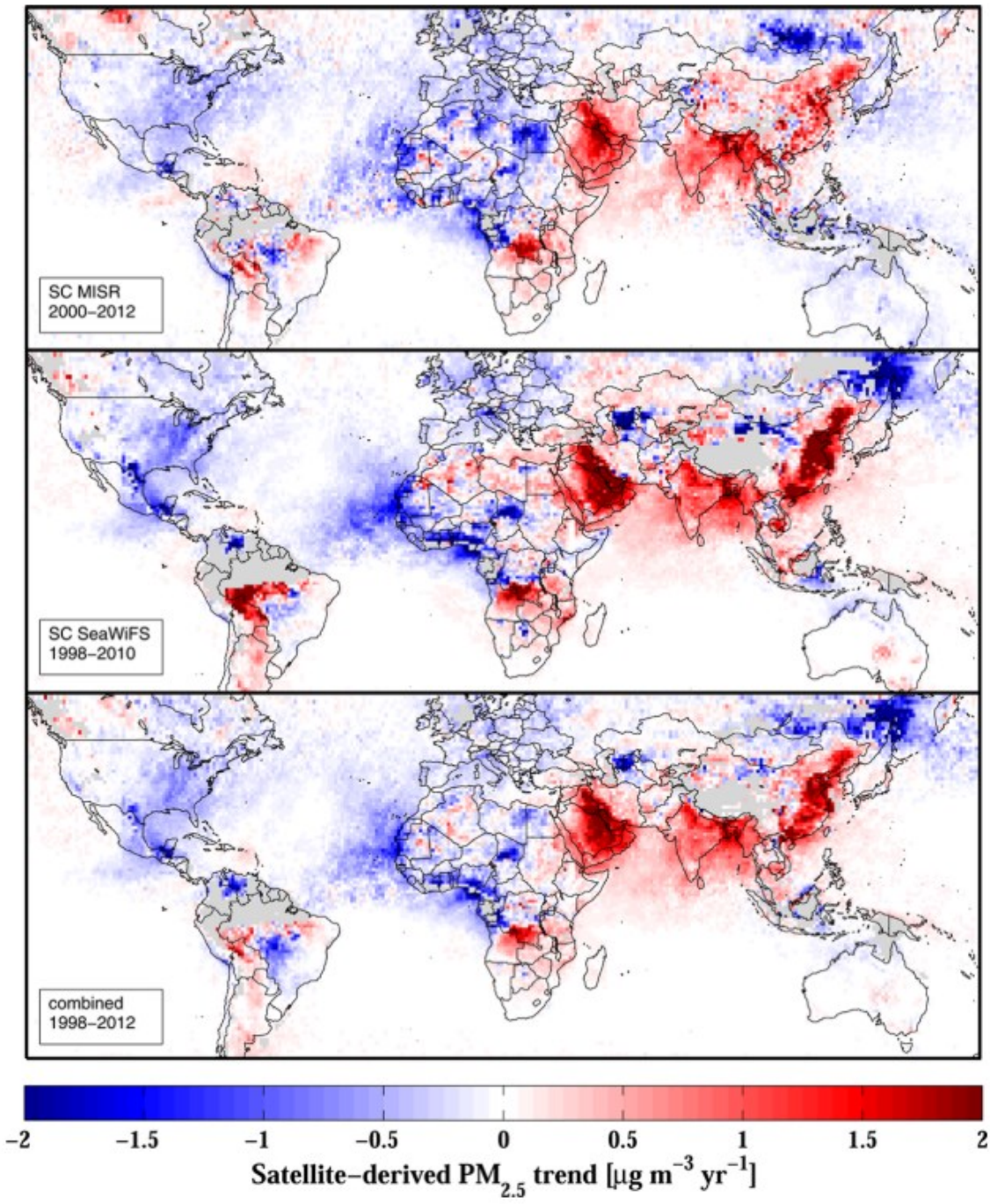


**Figure 2.2:** Slope from linear regression of satellite-derived, 24-hr, sampling-corrected, monthly $PM_{2.5}$ time series from MISR over 2000–2012, SeaWiFS over 1998–2010, and a combined MISR-SeaWiFS product over 1998–2012. Grey indicates missing data.

region, provides confidence in instrument stability (Hilboll et al., 2013). Some of these differences partially arise from remaining diurnal sampling differences and instrument-specific AOD retrieval bias as seen in trend maps created for overlapping years 2000–2010 (Figure S2.1).

Figure S2.3 shows contributions from inter-annual variations in modeled η (surface $PM_{2.5}$ to column AOD) depicted as linear tendencies. Trends in η can strengthen $PM_{2.5}$ trends compared to AOD trends in regions of changing surface emissions, such as the eastern U.S. or China as seen in the bottom panel by comparing trends in modeled η to those inferred from a simulation using constant anthropogenic emissions. Or trends in η can dampen $PM_{2.5}$ trends compared to AOD trends for regions with significant change in the vertical aerosol distribution, such as locations with a stable boundary layer downwind of strong lofted sources (i.e., Pacific Ocean west of Peru). Note that trends in surface $PM_{2.5}$ cannot be interpreted from trends in η prior to scaling such trends by AOD.

We evaluated the simulated change in η over the eastern U.S., a region with the densest collection of $PM_{2.5}$ and AERONET measurements over 1999–2012 allowing coincidently (daily) sampled monthly time series of five 1˚ x 1˚ grid cells with a minimum of 65% temporal coverage. Significant decreasing tendencies in η are found over the eastern U.S. in both empirical estimates ($-1.9\pm 0.8$ μg $m^{-3}$ $yr^{-1}$) and coincidently-sampled modeled ($-0.9 \pm 0.5$ μg $m^{-3}$ $yr^{-1}$) monthly time series over 1999–2012. This empirical trend in η emphasizes the need to account for inter-annual variation in η for satellite-derived time series of $PM_{2.5}$. Applying climatological (2006–2011) month-specific CALIPSO scale factors to adjust the simulation of η over 1999–2012 would degrade the modeled trend in η ($-0.2 \pm 0.4$ μg $m^{-3}$ $yr^{-1}$) and accordingly worsen comparisons of satellite-derived and *in situ* $PM_{2.5}$ trends over the eastern U.S.; this is likely a result of CALIPSO observations being available only in the second half of the time series.

Figure 2.3 shows the statistical significance of the combined $PM_{2.5}$ trend over land in the form of a two-sided P-value, tested against null being zero trend. Four broad regions with notable significant $PM_{2.5}$ tendencies over the 15-years of study are indicated and discussed below. Other smaller areas of significant tendency include the Po Valley of Italy (Yoon et al., 2011), and the west coast of Africa (Hsu et al., 2012). The strong negative

tendency appearing over the Aral Sea area may arise from an artifact in part of the SeaWiFS AOD time series for this region as consequence of surface assumptions over a changing bright surface; the MISR time series shows no such feature as MISR simultaneously retrieves surface reflectance along with AOD.

### 2.4.2 *Regional Trends in Satellite-Derived $PM_{2.5}$*

Figure 2.4 shows the regional monthly time series anomaly for the four areas highlighted in Figure 2.3: eastern U.S., the Arabian Peninsula, South Asia, and East Asia. Black lines indicate regional monthly anomalies from the combined $PM_{2.5}$ time series and corresponding linear fit. Colored lines depict the satellite-derived $PM_{2.5}$ trend attributable to modeled $PM_{2.5}$ components. Table 2.1 contains, for all four regions, numerical values of trends in satellite-derived $PM_{2.5}$ and in model attributed $PM_{2.5}$ components. The *in situ* $PM_{2.5}$ trend is included for the eastern U.S. Figure S2.4 depicts the four regional time series on an absolute scale with simulated $PM_{2.5}$ concentration included for comparison. Trends in Figure S2.4 are likely less accurate than in Figure 2.4 due to the use of CALIPSO measurements taken during only part of the time series. Below we discuss each region in detail.

#### 2.4.2.1 *Eastern United States*

The spatially broad and significant decreasing tendencies found in satellite-derived $PM_{2.5}$ for the eastern U.S. are well supported by a dense network of ground-based *in situ* measurements (Figure S2.5). As shown in Table 2.1, the 1998–2012 linear tendency for this region of -0.39 ± 0.10 μg $m^{-3}$ $yr^{-1}$ for the satellite-derived combined time series becomes -0.37± 0.13 μg $m^{-3}$ $yr^{-1}$ over the period of *in situ* observations (1999–2012) and is consistent with the *in situ* trend (-0.38 ± 0.06 μg $m^{-3}$ $yr^{-1}$). The *in situ* trend over the eastern U.S. was inferred from ca. 380 1˚ x 1 ˚ grid cells, yielding nearly complete spatial coverage of this region at this resolution, with an average of 1.9 *in situ* stations per cell (Figure S2.5). Excluding *in situ* stations with 'urban' designation reduces spatial coverage to ca. 260 1˚ x 1 ˚ grid cells with an average of 1.5 *in situ* stations per cell, however, affects neither trend inferred from *in situ* measurements nor combined satellite product within the bounds of 95% CI. Agreement is also observed when monthly values are aggregated from median (*in situ:* -0.34 ± 0.05 μg $m^{-3}$ $yr^{-1}$, combined satellite: -0.33 ± 0.11 μg $m^{-3}$ $yr^{-1}$) and

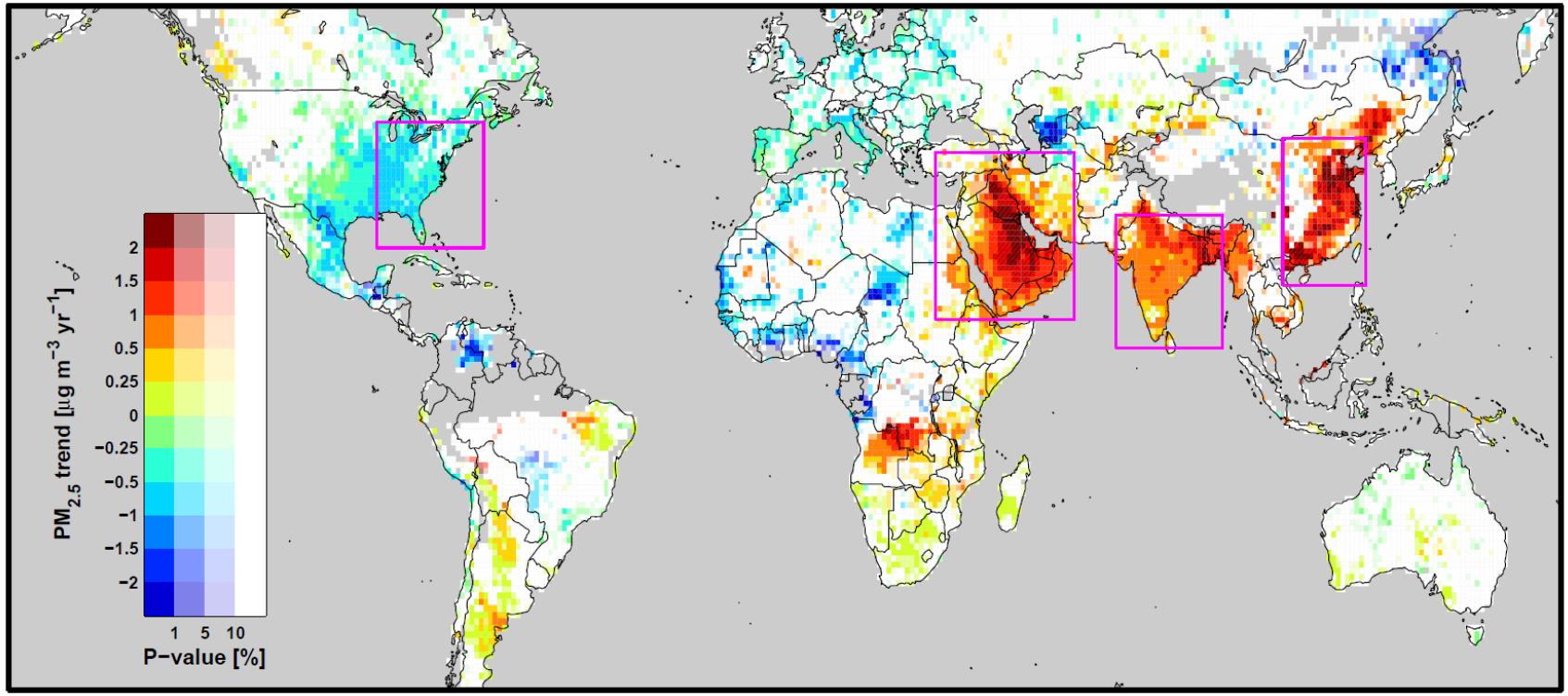


**Figure 2.3:** Statistical significance of the trend inferred from linear regression of monthly $PM_{2.5}$ time series inferred from the MISR-SeaWiFS combined product over 1998–2012. Magenta boxes indicate areas featured for regional analysis. Grey indicates water or missing data.

**Table 2.1:** Annual regional $PM_{2.5}$ trends over 1998–2012 and corresponding 95% CI [$\mu g\ m^{-3}\ yr^{-1}$] (as in Fig.2.4).

| **method** | Eastern U.S.[(a)] | Eastern U.S. | Arabian Peninsula | South Asia | East Asia |
|---|---|---|---|---|---|
| temporal coverage[(b)] | 85 | 83 | 95 | 79 | 82 |
| *in situ* | -038±0.06 | N/A | N/A | N/A | N/A |
| satellite-derived | -0.37±0.13 | -0.39±0.10 | 0.81±0.21 | 0.93±0.22 | 0.79±0.27 |
| satellite-derived[(c)] | -0.22±0.09 | -0.23±0.08 | 0.76±0.19 | 0.78±0.22 | 0.53±0.23 |
| **model attributed $PM_{2.5}$[(d)]** | | | | | |
| carbonaceous | 0.04 ±0.05 | 0 | 0.02±0.01 | 0.25±0.11 | 0.06±0.16 |
| secondary inorganic | -0.39±0.11 | -0.39±0.10 | 0.11±0.08 | 0.70±0.19 | 0.78±0.27 |
| fine mineral dust | 0 | 0 | 0.68±0.19 | -0.04±0.23 | -0.04±0.18 |

[(a)] Trends inferred over 1999–2012, a period of available *in situ* measurements.
[(b)] Average grid box temporal coverage within region after 65% threshold was applied prior to trend inference—see Figure S2.2 for global map of temporal coverage.
[(c)] Satellite-derived calculated with constant η.
[(d)] Calculated from the satellite-derived $PM_{2.5}$ time series scaled by the fractional GEOS-Chem $PM_{2.5}$ components.

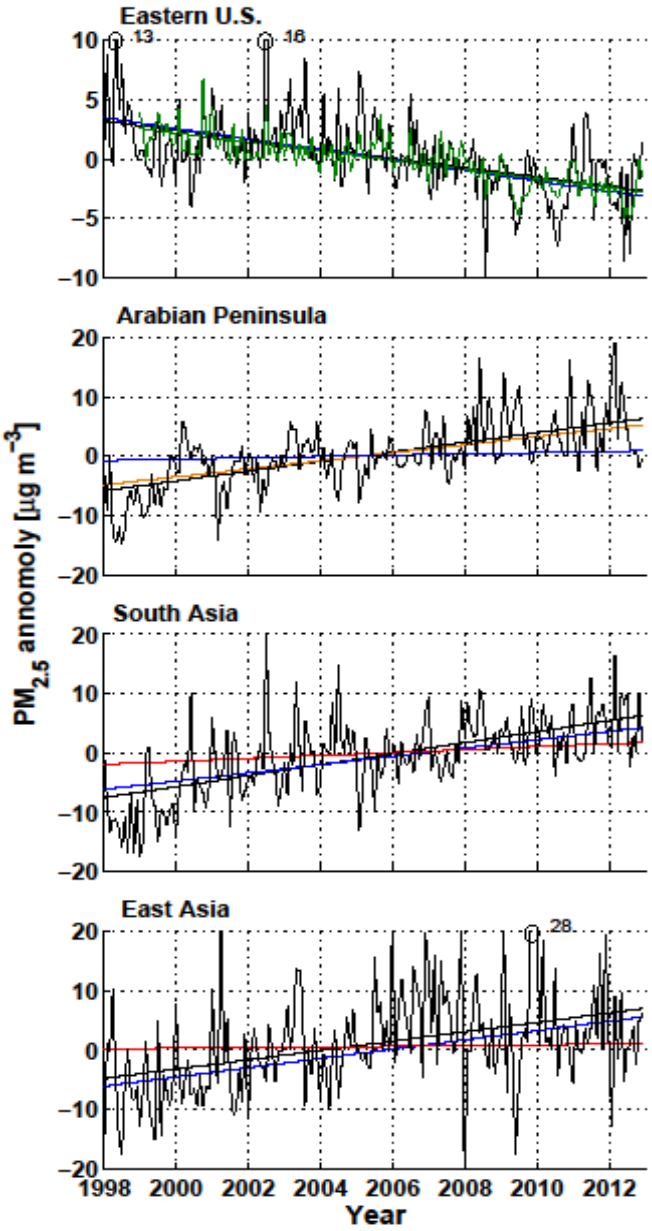


**Figure 2.4:** Regional monthly time series anomaly plots of satellite-derived $PM_{2.5}$ from a combined MISR-SeaWiFS product and the corresponding modeled species attribution. Black indicates the satellite-derived time series and corresponding GLS linear fit. Other colours indicate the satellite-derived $PM_{2.5}$ trend attributable to sulfate-nitrate-ammonium (blue), carbonaceous (red), and mineral dust (orange) aerosol as determined by the GEOS-Chem simulation. Green lines in the top panel are the *in situ* measured time series and corresponding GLS linear fit.

geometric (*in situ:* -0.33 ± 0.04 μg $m^{-3}$ $yr^{-1}$, combined satellite: -0.32 ± 0.11 μg $m^{-3}$ $yr^{-1}$) averages. The GEOS-Chem simulation attributes the trend in the eastern U.S. almost entirely to secondary inorganic aerosols (Figure 2.4), similar to the findings of (Leibensperger et al., 2012). Careful inspection of the satellite-derived $PM_{2.5}$ time series anomaly in Figure 2.4 reveals three distinct sections which mirror U.S. emissions of sulfur dioxide (http://www.epa.gov/air/airtrends/sulfur.html): [1] 1998–2002 a period of decreasing tendency, [2] 2002–2006 a period of stability, [3] 2006–2012 a period of decreasing tendency. The comparison to the *in situ* trend for this region is degraded when either η is treated as a constant (-0.22 ± 0.09 μg $m^{-3}$ $yr^{-1}$) or CALIPSO-adjusted η values are employed (-0.24 ± 0.08 μg $m^{-3}$ $yr^{-1}$). The larger uncertainty range of the satellite-derived combined time series (± 0.13 μg $m^{-3}$ $yr^{-1}$) compared to that for *in situ* observations (± 0.06 μg $m^{-3}$ $yr^{-1}$) likely arises from overestimation of simulated summer time η values over the eastern U.S.; both CALIPSO-adjusted and constant η values reduce anomalous features in the deseasonalized satellite-derived combined $PM_{2.5}$ time series (± 0.09 μg $m^{-3}$ $yr^{-1}$), however, fail to adequately account for trends in η. Comparison of satellite-derived $PM_{2.5}$ to *in situ* measurements for other areas outside of the eastern U.S. are depicted in Figure S2.5 and presented in Table S2.1. The decrease in $PM_{2.5}$ concentration over the U.S. occurring within this study period has been associated with increased life expectancy (Correia et al., 2013).

2.4.2.2 *Arabian Peninsula*

Large increases in satellite-derived $PM_{2.5}$ are apparent over the Arabian Peninsula. The regional time series anomaly has an increasing trend of 0.81 ± 0.21 μg $m^{-3}$ $yr^{-1}$. The increasing tendency occurs across all seasons, with greater increases occurring for spring and summer months of the northern hemisphere—when low relative humidity, high temperature and high wind speeds facilitate dust mobilization from arid surfaces (Shahsavani et al., 2012). Positive trends in AOD from satellite (Chin et al., 2014; Hsu et al., 2012; De Meij et al., 2012; Murphy, 2013; Zhang and Reid, 2010) and AERONET (Hsu et al., 2012; Yoon et al., 2012) over a similar time period have been reported for this region. The GEOS-Chem simulation largely attributes the observed satellite-derived $PM_{2.5}$ trend to changes in fine mineral dust. A decreasing Angstrom Exponent (a measure of

increasing aerosol size) alongside positive AOD trends for this region provides further evidence of increasing dust load (Hsu et al., 2012; Yoon et al., 2012). Decreasing trends of dust emission from neighboring African deserts, with associated tropical Atlantic outflow, have been correlated with increases in North Atlantic sea surface temperature (Chin et al., 2014; Ridley et al., 2014b) with suggestions of anthropogenic influence via a reduced indirect aerosol radiative forcing (Ridley et al., 2014b). Recent work has attributed the trends in dust emissions over the Arabian Peninsula to changes in wind speed and surface wetness (Chin et al., 2014) and associated these trends with local synoptic systems (Ganor et al., 2010). A much smaller increase in secondary inorganic and carbonaceous aerosol is also inferred from model attributed $PM_{2.5}$ over this region. This increase is partially supported by satellite observations of increased tropospheric $NO_2$ over a similar period (Hilboll et al., 2013) that might have a causal relationship with aerosol nitrate formation or likely indicates increasing anthropogenic activities that contribute to primary and secondary particulate formation.

2.4.2.3 *South Asia*

Figure 2.3 shows large increases in satellite-derived $PM_{2.5}$ over heavily populated regions of South Asia. Much of the Indo-Gangetic Basin experienced a statistically significant annual increase in $PM_{2.5}$ of more than 1 $\mu g\ m^{-3}\ yr^{-1}$. The remaining landmass of South Asia, the Indian subcontinent in particular, has on average a statistically significant annual increase in $PM_{2.5}$ of around 0.5 $\mu g\ m^{-3}\ yr^{-1}$. These spatial findings are in agreement with those reported by Dey et al. (2012) for the Indian subcontinent over 2000–2010 despite their use of constant $PM_{2.5}$ to AOD relationships—a result likely due to weak variation in South Asian $\eta$ values over this period for much of the Indian subcontinent (Figure S2.3). The annual linear tendency for the South Asian region is $0.93 \pm 0.22\ \mu g\ m^{-3}yr^{1}$. During the wet season (June–September), South Asia is influenced by strong monsoonal synoptic meteorology, during which time the Indian subcontinent can experience dust loads, especially heavy in the northern regions, from local (Thar) and neighboring (Arabian Peninsula) deserts (Dey and Di Girolamo, 2010). The anomalous spring and summer low for the years 1998 and 1999 depicted in Figure 2.4 likely result from anomalously low dust outflow from these deserts as indicated from satellite-derived $PM_{2.5}$ concentrations in dust

outflow affected regions for these two years (data not shown). From October–February, South Asia is under very different synoptic meteorology which can favor the regional buildup of anthropogenic aerosols (Dey et al., 2012; Dey and Di Girolamo, 2010, 2011). Our modeled species attribution to the observed annual South Asian trend consists of statistically significant increases in secondary inorganic and carbonaceous aerosols. Rising power sector coal consumption without flue gas desulfurization is largely responsible for the steady increases in sulfur dioxide emissions across South Asia over the last decade (Klimont et al., 2013). Emissions of carbonaceous aerosols continue to increase over South Asia, largely following residential biofuel use and energy consumption (Lu et al., 2011).

2.4.2.4 *East Asia*

For the period 1998–2012, East Asia has the highest annual average surface burden of satellite-derived $PM_{2.5}$ in the world. Erratic seasonal variation is observed in the monthly time series which displays fluctuating both summer and winter enhancements. Summer enhancements in secondary inorganics are due to favourable oxidation pathways and winter enhancements in the carbonaceous component are due to dry-stable conditions with large anthropogenic emissions (Zhang et al., 2013). An increase of $0.79 \pm 0.27$ μg $m^{-3}$ $yr^{-1}$ in $PM_{2.5}$ was observed which GEOS-Chem mostly attributes to large increases in secondary inorganic aerosols ($0.78 \pm 0.27$ μg $m^{-3}$ $yr^{-1}$). The East Asian time series steadily increases until 2007 then levels off. Xu et al (2011) describe abatement incentives in China since 2007 where installation and increased use of flue gas desulfurization systems occurred in coal fired power plants. Meanwhile, industrial sector emissions continue to increase (Klimont et al., 2013; Lu et al., 2011). As seen in Figure 2.3, local hotspots of significant increase in East Asia appear south of Beijing and throughout inland floodplains to the Pearl River Delta, which match well the temporally resolved emission distributions of primary and secondary anthropogenic particulate sources throughout this region (Hilboll et al., 2013; Lu et al., 2011). Recent studies examining the long-term trend in manually estimated atmospheric visibility, which is non-linearly sensitive to $PM_{2.5}$ as well as meteorological conditions such as relative humidity, offer a qualitative proxy to the trend in surface $PM_{2.5}$ (Cheng et al., 2013b). Several long-term visibility studies over various regions in China exhibit the ‘levelling off’ feature observed in Figure 2.4 for East Asia, where degrading

annual average visibility stabilizes or begins to improve after 2006 (Chen and Xie, 2013; Cheng et al., 2013b; Deng et al., 2012; Zhao et al., 2011).

## 2.5 Conclusions

Overall, the 15-year unified MISR- and SeaWiFS-derived global $PM_{2.5}$ monthly time series is consistent with the corresponding linear tendency observed from *in situ* observations over the eastern U.S. and with current understanding elsewhere. Time-varying '$PM_{2.5}$ to AOD' relationships were necessary to reproduce the trend in *in situ* observations. An emerging global surface particulate matter network (SPARTAN, http://www.spartan-network.org/) collocated with AERONET sites will offer further information to understand '$PM_{2.5}$ to AOD' relationships over a variety of regions (Snider et al., 2015). Our effort developed the time series of $PM_{2.5}$ anomalies over 1998–2012; van Donkelaar et al. (2015b) extend this work by combining these anomalies with other existing absolute satellite-derived $PM_{2.5}$ estimates from two datasets spanning the first (van Donkelaar et al., 2010) and second (Van Donkelaar et al., 2013) half of the 1998–2012 study period for comparison with World Health Organization air quality guidelines. Future effort would benefit from the improved spatiotemporal coverage resulting from incorporation of both MODIS-Terra and –Aqua AOD sensors from the radiometric stabilized collection 6 dataset.

## 2.6 Acknowledgements

Funding for this work was provided by NSERC Canada and by an Izaak Walton Killiam Memorial Scholarship for B. L. Boys. Computational facilities are partially provided by ACEnet, the regional high performance computing consortium for universities in Atlantic Canada. We thank the AERONET, MISR, SeaWiFS, CALIPSO, IMPROVE, and AQS science teams for making their data publicly available, as well as Michael Dowd for helpful discussions relating to time series analysis and five anonymous reviewers for their helpful comments on this manuscript.

## 2.7 Supplemental Material

Contained in the supplemental material for this chapter is a detailed description of the GEOS-Chem chemical transport model and how it was used in this study. In addition, five supplemental figures and one table are included.

### 2.7.1 *GEOS-Chem Chemical Transport Model*

The GEOS-Chem global 3-D chemical transport model (version 9-01-03; http://geos-chem.org) was used to calculate the spatiotemporally resolved relationship between ground-level $PM_{2.5}$ and satellite retrieved column aerosol optical depth (AOD) at satellite overpass and to estimate the bias in the satellite measurements due to incomplete sampling. We calculate modeled $PM_{2.5}$ as the sum of the individual aerosol components less than 2.5 μm at a relative humidity of 35% to conform with U.S. EPA measurement practices.

GEOS-Chem solves for the 3-D evolution of the coupled aerosol-oxidant system using: [1] assimilated meteorological observations; [2] global and regional emission inventories; [3] current understanding of the physics and chemistry of atmospheric processes. The CTM was operated at a horizontal resolution of 2˚ x 2.5˚ (lat, long) with 47 vertical levels from the surface to ca. 80 km. We simulated from 1 January 1998 to 1 January 2014 with dynamic (transport and convection) and chemical (chemical processes and emissions) time steps of 15 min and 60 min, respectively. We use an instantaneous vertical mixing scheme within the unstable boundary layer to which we impose a minimum mixed layer depth (Heald et al., 2012). One month model 'spin-up', which is more than double the global mean e-folding lifetime of tropospheric aerosols (Croft et al., 2014), was used to eliminate the effects of initial conditions.

[1] Assimilated meteorology

We use Modern-Era Retrospective Analysis for Research and Applications (MERRA) meteorological fields from NASA's Global Modeling and Assimilation Office (GMAO). MERRA is a consistent, long term reanalysis of satellite era observations using the Goddard Earth Observing System (GEOS) data assimilation version 5 framework (Rienecker et al., 2011).

[2] Emission inventories

Global anthropogenic emissions are taken from the Emissions Database for Global Atmospheric Research (EDGAR) inventory (Olivier et al., 2005) with regional overwrites over Canada (CAC; http://www.ec.gc.ca/pdb/cac/), Europe (EMEP; http://www.emep.int/), United States (EPA-NEI; http://www.epa.gov/ttnchie1/trends/ ), Mexico (BRAVO; (Kuhns et al., 2005)) South East Asia (STREETS; (Zhang et al., 2009b)), China and India (Lu et al., 2011). When required, anthropogenic emissions were scaled past base years using energy statistics (Donkelaar et al., 2008) and $NO_x$ emission trends inferred from the OMI satellite instrument (Lamsal et al., 2011). Non-anthropogenic emissions include biomass burning emissions (GFED-3; (Mu et al., 2011)), biogenic volatile organic compounds (Barkley et al., 2011), soil $NO_x$ (Yienger and Levy, 1995), lightning $NO_x$ (Murray et al., 2012), and volcanic $SO_2$ emissions (Fisher et al., 2011).

[3] Mechanisms

GEOS-Chem contains a detailed simulation of $HO_x$-$NO_x$-VOC-$O_3$-aerosol chemistry. Numerous updates have been implemented since the initial description in Bey et al. (2001). Updates of particular relevance to this work are those concerning the aerosol mass simulation, which include: secondary inorganic aerosol formation ($NH_4^+$, $SO_4^-$, $NO_3^-$ ) (Park et al., 2004), sea salt aerosol (Jaeglé et al., 2011), mineral dust (Fairlie et al., 2007; Zender, 2003) and carbonaceous aerosol (Henze et al., 2008; Liao et al., 2007; Park et al., 2003; Wang et al., 2011a). The simulation of aerosol-gas interactions takes place via heterogeneous chemistry (Evans and Jacob, 2005; Jacob, 2000) and aerosol effects of photolysis frequencies (Martin et al., 2003a). Wet and dry deposition is described in Bey et al. (2001) and Liu et al. (2001), with updates by Wang et al. (2011).

2.7.2 *Evaluation of GEOS-Chem*

The GEOS-Chem aerosol simulation has been extensively evaluated versus (i) surface *in situ* measurements (Fairlie et al., 2007; Fu et al., 2012; Heald et al., 2012; Jaeglé et al., 2011; Leibensperger et al., 2012; Park et al., 2003, 2004, 2006; Pye et al., 2009a; Zhang et al., 2012a), (ii) vertical profiles from aircraft measurement platforms (Donkelaar et al., 2008; Drury et al., 2010; Heald et al., 2011), and (iii) vertical profiles of extinction from

CALIPSO satellite observations (Van Donkelaar et al., 2013; Ford and Heald, 2012). Recent work by Philip et al. (2014) examines global chemical composition of GEOS-Chem simulated ground-level $PM_{2.5}$, its apportionment to satellite AOD, and comparison to speciated *in situ* observations.

Figure S2.4 shows the GEOS-Chem monthly $PM_{2.5}$ time series on an absolute scale together with available *in situ* observations and combined satellite-derived $PM_{2.5}$ time series. Over the eastern U.S. and East Asia, the GEOS-Chem simulation captures well the features and absolute concentrations of CALIPSO-adjusted satellite-derived $PM_{2.5}$. Over the eastern U.S., *insitu* $PM_{2.5}$ observations are well represented by both simulated and CALIPSO-adjusted satellite-derived $PM_{2.5}$. Over the Arabian Peninsula, GEOS-Chem captures well the features of the satellite-derived time series, albeit with an increasing low bias as seasonal $PM_{2.5}$ concentrations rise in the latter half of the time series. As described in Ridley et al. (2013), low biases in simulated mineral dust emissions exist when high-resolution surface wind fields are averaged to large grid box mean values since wind-driven mineral dust emissions are a nonlinear function of surface wind speed. Over South Asia, GEOS-Chem partially captures the large seasonal fluctuation observed in the satellite-derived time series, albeit, is biased low by a large degree, however, displays a linear tendency consistent with satellite-derived time series. There is large uncertainty in South Asian carbonaceous particulate emissions as it is difficult to characterize and quantify the many small scale emissions over populated regions; the low bias in simulated South Asian $PM_{2.5}$ depicted in Figure S2.4 may benefit from higher primary carbonaceous emissions of more than a factor of two (Fu et al., 2012).

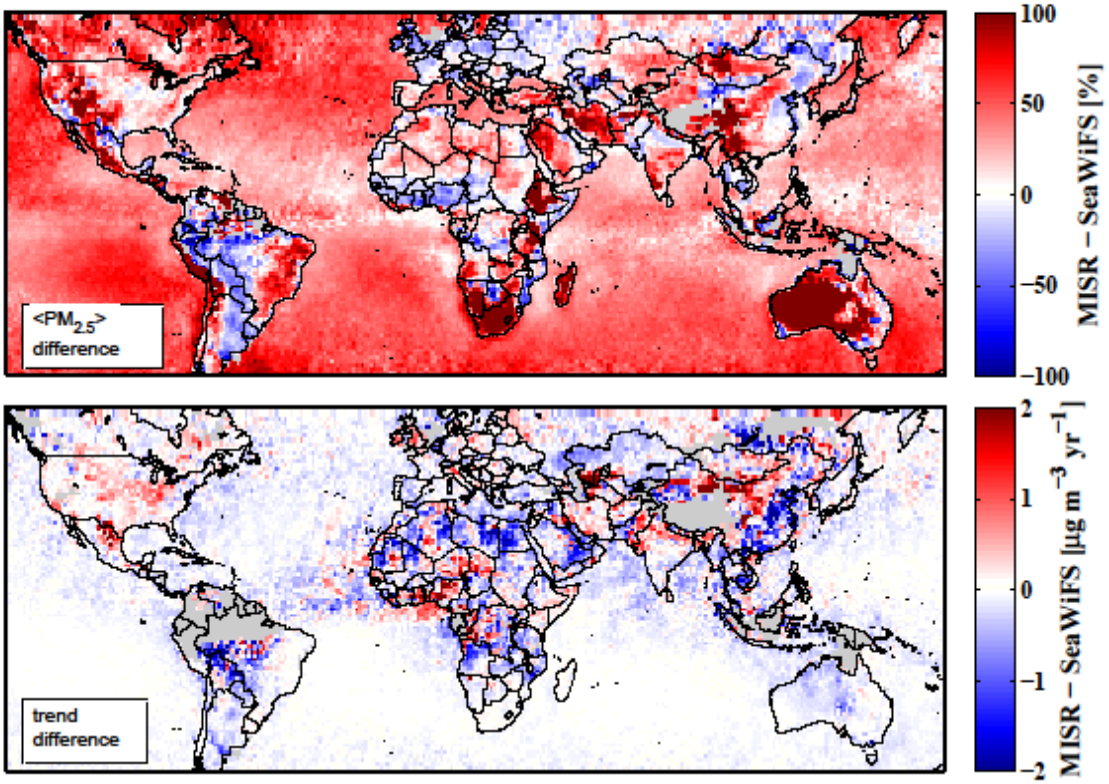


**Figure S2.1:** Difference between sampling-corrected MISR and SeaWiFS derived: (top) climatological $PM_{2.5}$ averaged over overlapping years 2000–2010 and (bottom) slope from linear regression of monthly $PM_{2.5}$ time series over 2000–2010.

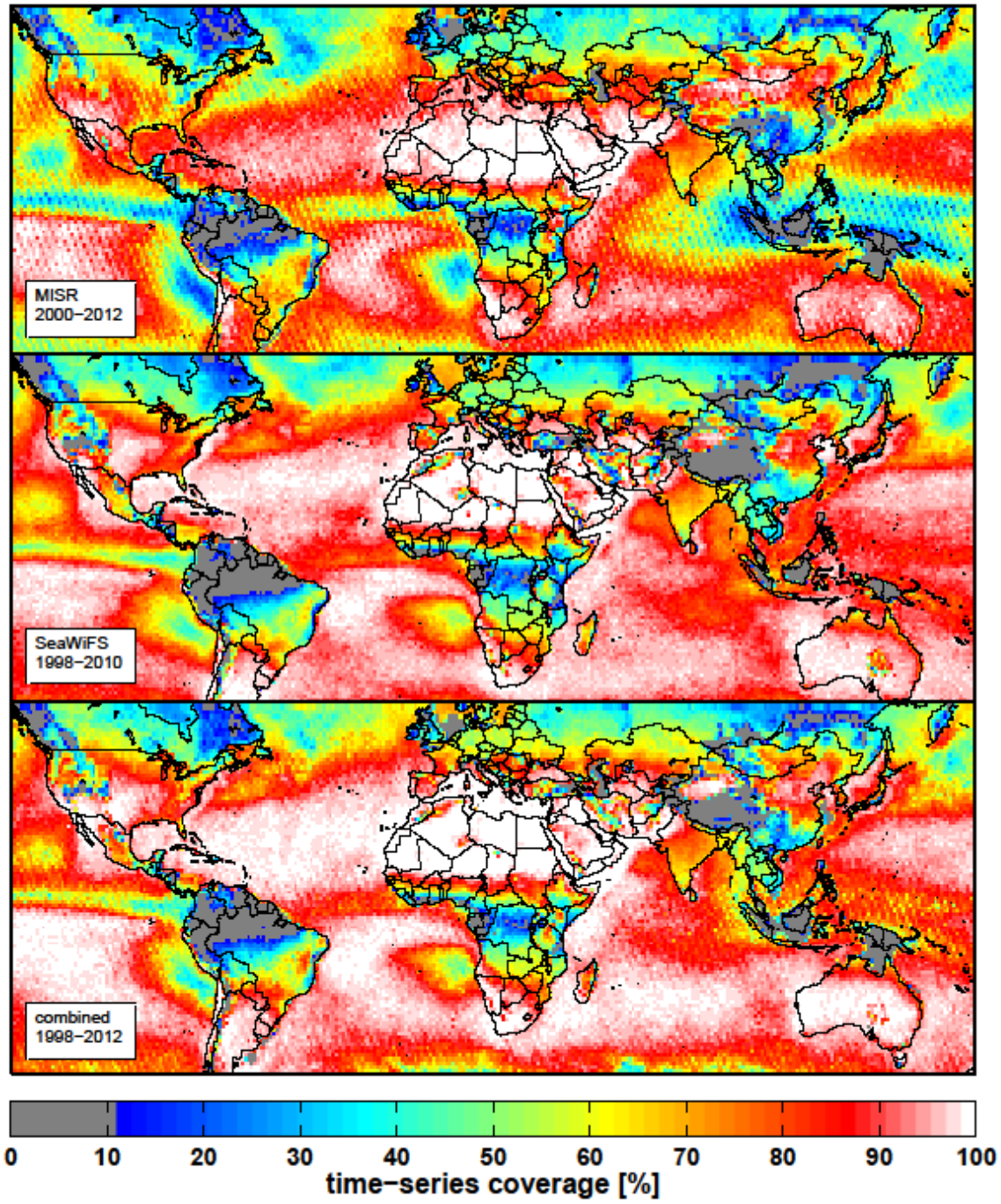


**Figure S2.2:** Percentage of months included in satellite-derived $PM_{2.5}$ time series from MISR, SeaWiFS, and a combined MISR-SeaWiFS product.

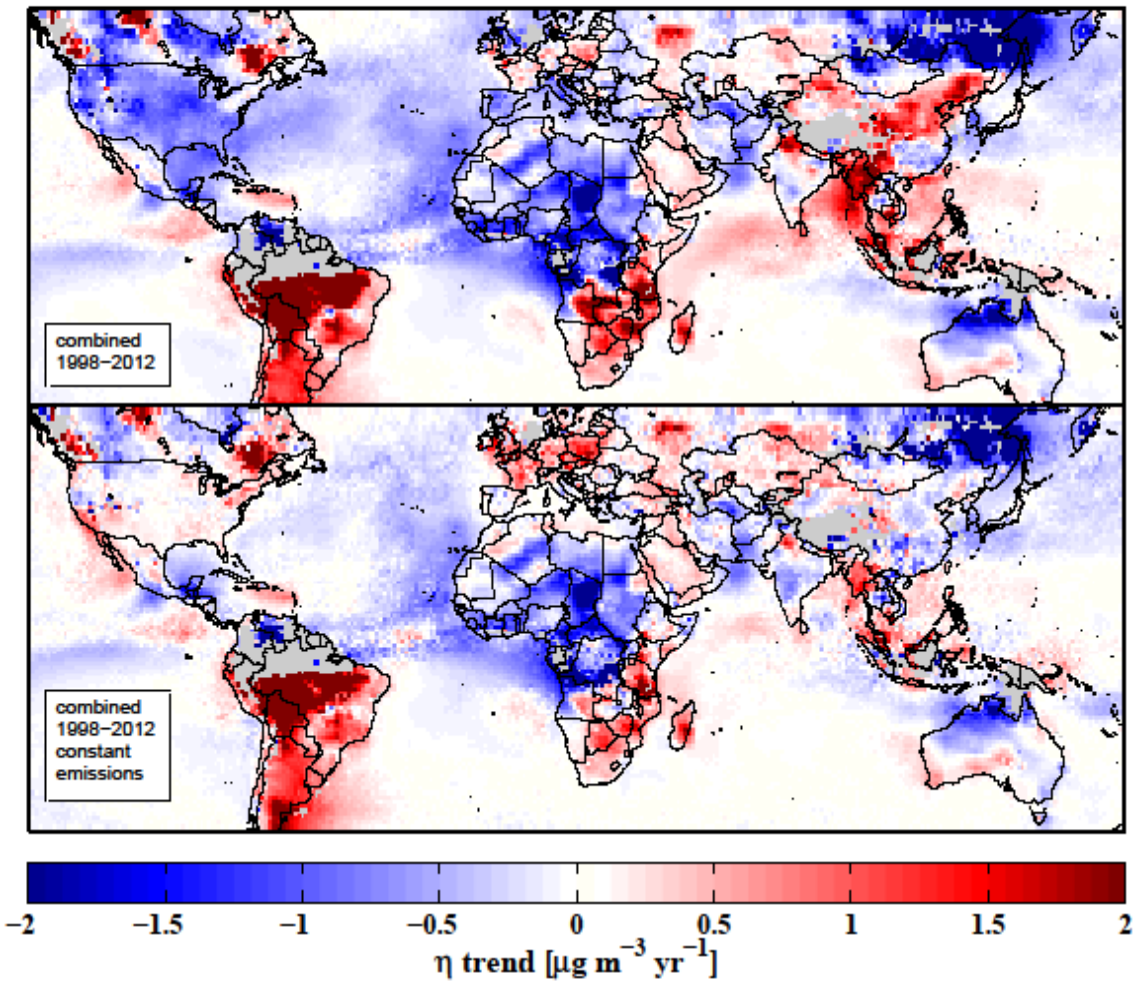


**Figure S2.3:** Slope from linear regression of modeled η ('$PM_{2.5}$ / column AOD') time series coincidently sampled with a combined MISR-SeaWiFS $PM_{2.5}$ monthly time series over 1998–2012. Grey indicates missing data. Trends through a corresponding modeled time series with anthropogenic emissions held constant at 2005 values is shown in bottom panel.

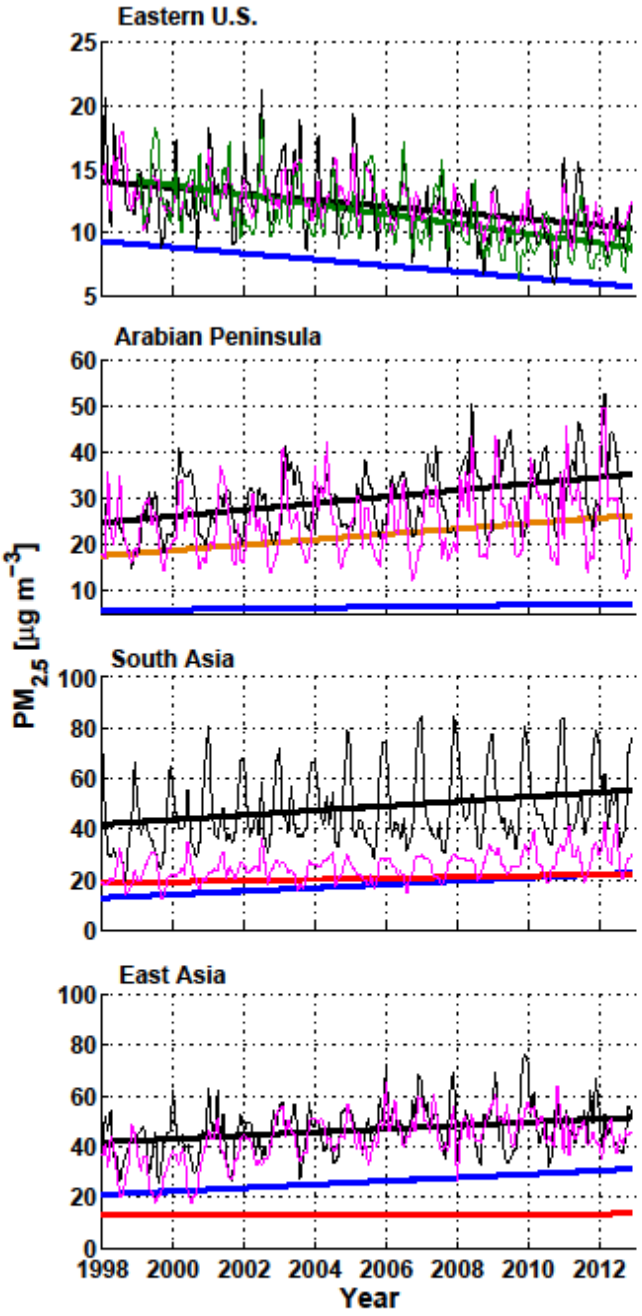


**Figure S2.4:** Regional time series plots of CALIPSO-adjusted, satellite-derived $PM_{2.5}$ from a combined MISR-SeaWiFS product, the corresponding modeled species attribution of the observed satellite trend, and the corresponding simulated $PM_{2.5}$ time series. Black indicates the satellite-derived time series and corresponding GLS linear fit. Magenta indicates the GEOS-Chem time series. Other colours indicate the satellite-derived $PM_{2.5}$ trend attributable to sulfate-nitrate-ammonium (blue), carbonaceous (red), and mineral dust (orange) aerosols as determined by the GEOS-Chem simulation. Green lines in the top panel are the *in situ* measured time series and corresponding GLS linear fit.

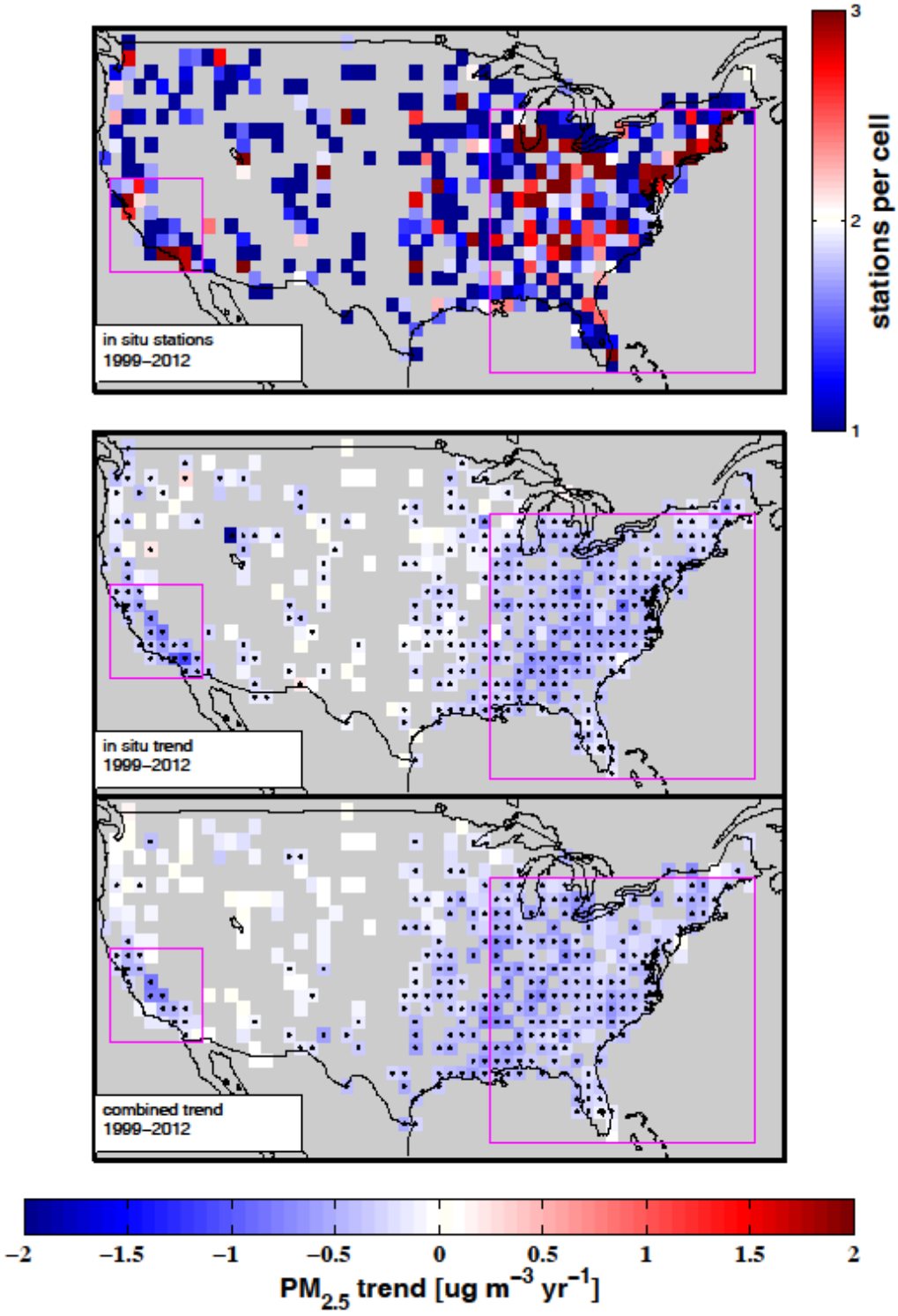


**Figure S2.5:** U.S. *in situ* FRM $PM_{2.5}$ measurement density (top). Slope from linear regression of monthly $PM_{2.5}$ time series at 1˚ x 1˚, aggregated from: U.S. *in situ* FRM $PM_{2.5}$ measurements (middle) and combined satellite-derived $PM_{2.5}$ (bottom). Grey indicates missing data or water. Black dots indicate statistically significant trends ($p < 0.05$).

**Table S2.1**: Annual U.S. $PM_{2.5}$ trends over 1999–2012 and corresponding 95% CI [μg $m^{-3}$ $yr^{-1}$] for regions depicted in Figure S2.5. Reported are annual deseasonalized linear trends inferred from monthly time series aggregated from the arithmetic mean, median, and geometric mean of 24-hr daily values.

| | | **Eastern U.S.** | | **California** | | **Remainder of U.S.** | |
|---|---|---|---|---|---|---|---|
| | | all sites | urban excld. | all sites | urban excld. | all sites | urban excld. |
| **Regional grid box sum:** | | 384 | 261 | 55 | 34 | 267 | 179 |
| **Average number of stations per grid box:** | | 1.94 | 1.53 | 1.89 | 1.51 | 1.48 | 1.29 |
| Arithmetic mean | *in situ* | -0.38±0.06 | -038±0.06 | -0.48±0.12 | -0.41±0.11 | -0.12±0.04 | -0.11±0.04 |
| | satellite-derived | -0.37±0.13 | -0.37±0.14 | -0.32±0.18 | -0.33±0.19 | -0.15±0.08 | -0.15±0.09 |
| Median | *in situ* | -0.34±0.05 | -0.34±0.05 | -0.43±0.10 | -0.37±0.09 | -0.11±0.04 | -0.09±0.03 |
| | satellite-derived | -0.33±0.11 | -0.35±0.10 | -0.24±0.14 | -0.24±0.14 | -0.10±0.06 | -0.11±0.07 |
| Geometric mean | *in situ* | -0.33±0.04 | -0.32±0.04 | -0.41±0.10 | -0.36±0.09 | -0.11±0.03 | -0.09±0.03 |
| | satellite-derived | -0.32±0.11 | -0.33±0.10 | -0.24±0.15 | -0.24±0.15 | -0.11±0.06 | -0.12±0.07 |

# Chapter 3

# Evaluation and Updates to the Oxidized Reactive Nitrogen Trace Gas Dry Deposition Parameterization from the GEOS-Chem Chemical Transport Model

## 3.1 Abstract

Dry deposition is a major loss pathway of reactive nitrogen species from the atmospheric boundary layer. Represented in chemical transport models (CTMs) as a first-order process, the rate of dry deposition is parameterized through a resistance-in-series method where component resistances representing turbulent transport ($R_a$), molecular diffusion ($R_b$), and surface uptake ($R_c$) are considered in series and expressed via the deposition velocity ($V_d$). We evaluate isolated components of the parameterization of $V_d$ in the GEOS-Chem CTM by extracting the dry deposition algorithm and reimplementing to run in single-point-mode. $R_a$ and $R_b$ components are evaluated by comparing to recently published eddy covariance inferred daytime $V_d$ of rapidly depositing species over a mixed temperate forest (Talladega National forest) for June, 2013. Modifications to $R_a$ include the evaluation of site-specific roughness length, reference height, and the influence of the roughness sublayer. Implementation of a more accurate parameterization of molecular diffusivities in air results in a large (ca. 100%) increase in $R_b$, a much-improved daytime simulation of $V_d$ for rapidly depositing species such as $HNO_3$ (NMB reduced from 47% to 4%), and significant reductions to daytime $V_d$ for $NO_2$ (-13%) and PAN (-32%) due to the influence of molecular diffusivity on stomatal uptake. Resistances to surface uptake ($R_c$) in GEOS-Chem follow a modified version of the 'big-leaf' parameterization. We evaluate the non-stomatal branch of $R_c(NO_2)$ by comparing to eddy covariance inferred nocturnal $V_d(NO_2)$ over Harvard Forest (temperate) from April–November 2000. We eliminate a low bias of ca. -80% in simulated nocturnal $V_d(NO_2)$ by representing $NO_2$ heterogeneous hydrolysis on deposition surfaces, paying attention to chemical flux divergence, soil $NO_x$ emissions, as well as canopy surface area effects. $NO_2$ ground surface hydrolysis restores peak daytime simulated $V_d\ (NO_2)$ to base GEOS-Chem value (ca. 0.8 cm $s^{-1}$). Bottom-up estimates of

nocturnal $V_d(NO_2)$ for Harvard Forest are computed from surface-specific $NO_2$ uptake coefficients to foliar, bark, and forest floor surfaces, providing an independent method of interpretation of top-down observations. Finally, we evaluate the updated oxidized reactive nitrogen dry deposition parameterization for GEOS-Chem by comparing to eddy covariance inferred $V_d(NO_y)$ over Harvard Forest from June–November 2000. Simulated values were estimated as the sum of component deposition velocities for $NO_y$ species $HNO_3$, PAN, and $NO_2$, weighted by measured concentration fractions. A small nocturnal bias remains in simulated $V_d(NO_y)$ due to the compensating effects of reduced molecular diffusivity (decreasing $V_d(HNO_3)$) and $NO_2$ heterogenous hydrolysis (increases $V_d(NO_2)$). A greater change in the daytime bias of simulated $V_d(NO_y)$, from 10% to -18%, is driven by large reductions in daytime $V_d(HNO_3)$ resulting from increased $R_b(HNO_3)$. Additionally, representing $NO_2$ hydrolysis on the ground surface through GEOS-Chem's dry deposition parameterization provides mechanistic utility to current understanding of dominant atmospheric production of HONO.

**Keywords:** dry deposition, deposition velocity, $NO_2$, HONO, $HNO_3$, $NO_y$, reactive nitrogen oxide, eddy covariance, GEOS-Chem, chemical transport model, $NO_2$ heterogeneous hydrolysis, roughness sublayer, molecular diffusion

## 3.2 Introduction

Atmospheric oxidized reactive nitrogen species ($NO_y$) together with reactive nitrogen ($N_r \equiv NO_y$ + reduced nitrogen species), are a central component of atmospheric chemistry, contributing to nitrogen loading of natural ecosystems (Clark et al., 2018) and influencing air quality (Fields, 2004), including modulation of the oxidative capacity of the local atmosphere by nitrogen oxides ($NO_x \equiv NO + NO_2$) (Crutzen, 1979a). Therefore, accurate knowledge of sources and sinks of $N_r$ is vital in understanding and modeling atmospheric chemistry, including the sensitivity of air quality to changes in anthropogenic emissions. Dry deposition of $N_r$ from the atmospheric boundary layer is an important removal process, typically contributing between 1/3 to 2/3 of total (wet + dry) deposition (Flechard et al., 2011; Hanson & Linderg, 1991; Munger et al., 1998; Sparks et al., 2008; Walker et al., 2020).

The atmosphere-surface exchange of $N_r$ may be measured directly via micrometeorological techniques (Businger, 1985; Walker et al., 2020) or under more controlled conditions via enclosure techniques (Breuninger et al., 2012; Hanson and Linderg, 1991). Direct measurements of above-canopy air-surface exchange of $N_r$ are technically complex and resource intensive, resulting in a scarcity of flux observations across representative land types and seasons (Walker et al., 2020). Therefore, studies of above-canopy dry deposition tend to be intensive in nature and are typically designed to characterize exchange processes rather than to monitor long-term deposition patterns. Dry deposition budgets thus fall to the realm of inferential methods, where deposition fluxes $F_x$ are inferred from parameterizations of above-canopy deposition velocity $V_d$—a first-order rate constant for heterogenous surface reaction/uptake for a specific gas to a specific bulk surface/land type from a specified height:

$$F_x = -V_d\,[x] \tag{3.1}$$

By convention, downward fluxes toward the surface are negative values represented by positive deposition velocities. $N_r$ component concentrations $[x]$ from which dry deposition budgets may be inferred have been obtained from: (i) surface networks such U.S. CASTNET (Clarke et al., 1997) and Canadian CAPMoN (Zhang et al., 2009), (ii) chemical transport models (CTMs) (Dennis et al., 2013; Zhang et al., 2012; Zhang et al., 2018), and (iii) satellite observations (Geddes & Martin, 2017; Kharol et al., 2018; Nowlan et al., 2014).

Deposition velocity represents a bulk quantity with contributions from complex processes including turbulent and molecular diffusion in air, meteorological influence on the physical, chemical, and biological state of surfaces, and species-specific interfacial chemistry. The most common parameterization of $V_d$ in large-scale CTMs considers the deposition pathway as a series of three resistances (Baldocchi et al., 1987; Wesely and Hicks, 1977):

$$V_d = \frac{1}{R_a(z) + R_b(x) + R_c(x)} \tag{3.2}$$

where for bulk canopy $V_d$ above a projected ground area, $R_a(z)$ is the aerodynamic resistance to turbulent transport from a specified height $z$ to the deposition surface and is common for all species, $R_b(x)$ is the species-specific quasi-laminar boundary layer resistance to transport through the thin nonturbulent layer in direct contact with surfaces, and $R_c(x)$ is the bulk canopy surface resistance for a specific land type. Expressions for $R_a$ and $R_b$ can be obtained from micrometeorological flux-gradient relationships (Garratt, 1992) and vary as a function of surface roughness, wind speed, diabatic stability, and molecular diffusivity in air. For highly soluble species such as $HNO_3$ and $H_2O_2$, contributions from $R_c$ are nominally small with resulting deposition varying between $R_a$ and $R_b$ limited depending on the state of turbulence (Nguyen et al., 2015). For species with low aqueous solubility or limited interfacial reactivity, $R_c$ is the limiting term, except under very stable conditions (Toyota et al., 2016). Given the complexity and variability of canopy types and species-specific surface reactivities, $R_c$ is difficult to treat theoretically, with parameterizations relying heavily on empirical formulations.

The most common parameterization of $R_c$ used by large scale atmospheric models, including the widely utilized WRF-Chem and GEOS-Chem CTMs, is the Wesely 1989 algorithm (Wesely, 1989), or modifications thereof (Hardacre et al., 2015). In this scheme, the bulk canopy is treated as a single uniform surface or 'big leaf" with stomatal and various non-stomatal deposition pathways acting in parallel. Furthermore, trace gas specific component surface resistances are calculated following basic similarity relations, including solubility relative to $SO_2$ and oxidative potential relative to $O_3$. Zhang et al. (2003) present a parameterization of $R_c(x)$ for use in air quality models, including at the global scale, employing similarity arguments to $SO_2$ and $O_3$ as done by Wesely et al. (1989), however, having several updates to the Wesely 1989 scheme. These updates include: online computation of within canopy aerodynamic resistance, influence of leaf water vapour pressure deficit and water stress on stomatal resistance, and updated parameterizations of non-stomatal surface resistances for $O_3$ (Zhang et al., 2002) and $SO_2$ (Zhang et al., 2003). Zhang et al. (2003) note that application of the algorithm to compounds for which little to no deposition flux observations exist will continue to be a source of significant uncertainty and call for efforts to study species-specific fluxes across representative land types and seasons.

Bulk-canopy surface resistances deviating from similarity to $SO_2$ and $O_3$ have been observed for PAN (Shepson et al., 1992; Sun et al., 2016; Turnipseed et al., 2006), $NO_2$ (Eugster & Hesterberg, 1996; Horii, 2002; Stella et al., 2013), and many other species (Nguyen et al., 2015). Wu et al. (2012) compare observed $V_{d(PAN)}$ over a coniferous forest to deposition velocities parameterized according to both the Wesely 1989 (WRF-Chem) and Zhang 2003 (NOAH) schemes and find underestimates greater than a factor of 2, motivating effort to fit non-stomatal $R_{c(PAN)}$ directly from above-canopy flux observations. Flechard et al. (2011) compare dry deposition fluxes of reactive nitrogen species $NH_3$, $NO_2$, $HNO_3$, HONO, particulate ammonium ($pNH_4$) and nitrate ($pNO_3$) across an inferential network of 55 sites throughout Europe using four existing dry deposition routines and note differences between models (up to a factor of 2-3) are often greater than differences between sites, calling for more long-term direct $N_r$ flux measurements with which to validate dry deposition algorithms.

Of the various techniques for determining canopy-scale air-surface exchange of trace gases, the eddy covariance (EC) technique is the most direct approach (Businger, 1985; Dabberdt et al., 1993; Walker et al., 2020), but requires stringent measurement methods, including fast-response chemical sensors (>1 Hz) (Baldocchi et al., 1988; Wesely and Hicks, 2000). Normalizing eddy covariance flux ($F_x = \overline{w'x'}$) by mean concentration over an equivalent averaging period—typically 30 min (Businger, 1985; Geddes & Murphy, 2014; Horii et al., 2004; Min et al., 2014; Munger et al., 1996)—results in an ecosystem-scale exchange velocity $V_{ex}$, as in 3.1, however, with the distinction that $V_{ex}$ may take on both positive (upward) and negative (downward) values whereas $V_d$ is assumed to be downward (positive) only. Eddy covariance flux measurements of $N_r$ species, e.g. $NO_2$, $NH_3$, and $NO_y$, represent the net result of a multitude of within canopy processes, including homogeneous and heterogeneous chemistry, emission, and deposition—complicating efforts to understand individual processes in the absence of ancillary information (Delany et al., 1986; Fowler et al., 2009; Geddes & Murphy, 2014; Min et al., 2014). Biogenic soil emissions of NO from microbial (de)nitrification reactions and subsequent within-canopy oxidation to $NO_2$ may diminish, even reverse, downward above-canopy deposition fluxes of $NO_2$ if the strength of local soil NO emission is sufficient to compete with, or overwhelm, deposition fluxes which have first-order dependence on above-canopy $NO_2$

concentration (Fowler et al., 1998; Neirynck et al., 2007; Stocker et al., 1993; Walton et al., 1997; Weseley & Hicks, 2000).

Aiding in the interpretation of above-canopy flux observations, chamber methods enable species-specific observations of $N_r$ uptake to both foliar (Chaparro-Suarez et al., 2011; Delaria, 2020; Hanson et al., 1989; Wang et al., 2020c) and non-foliar (Grøntoft and Raychaudhuri, 2004; Hanson et al., 1989; Spicer et al., 1989) surfaces. Conducted in either the field or lab, chamber studies can provide 'object-level' uptake observations under controlled conditions from which 'canopy-level' uptake may be estimated by application of appropriate surface area indices, i.e., leaf area index (LAI) (Delaria and Cohen, 2020; Rondón et al., 1993).

A main result of Horii et al. (2004) in their analysis of an extensive eddy covariance flux dataset of $NO_2$ over a Northeastern U.S. mixed forest (Harvard Forest) from April–November 2000 was that a persistent deposition process was active at night, yielding $NO_2$ deposition velocities on average of ca. 0.2 cm $s^{-1}$, with values up to 0.5 cm $s^{-1}$ noted under high $NO_2$ loads of ca. 30 ppb. This observation is contrary to the widely used Wesely 1989 parameterization which does not allow significant surface uptake at night when leaf stomata are assumed closed or during vegetatively dormant seasons. Geddes et al. (2014) monitored eddy covariance fluxes of NO, $NO_2$, and $NO_y$ above midlatitude (ca. 45° N) summertime mixed hardwood forests in Ontario (Canada) and Michigan (U.S.), finding on average diurnal $NO_x$ fluxes indistinguishable from zero for these relatively low $NO_y$ environments (< 2 ppb on average). However, infrequent nocturnal events with high $NO_x/NO_y$ ratios and large downward $NO_y$ fluxes could be interpreted as yielding $V_d(NO_2)$ similar to the average values of Horii et al. (2004). Geddes et al. (2014) are careful to note that above canopy fluxes of $NO_x$ are influenced not only by deposition processes, but also by within canopy emissions and chemistry, resulting in above-canopy fluxes of $NO_x$ that are confounded by a combination of counteracting mechanisms which render flux observations difficult to interpret. Horii et al. (2004) considered below sensor chemical flux divergence of $NO_2$ due to formation and subsequent hydrolysis of $N_2O_5$, showing that a maximum rate of loss is insufficient to account for observed downward nocturnal $NO_2$ flux and propose a non-stomatal hydrolysis pathway for uptake of $NO_2$ on ground and

canopy surfaces—a reaction which has been suspected in the field to be of atmospheric relevance for some time (Harrison & Kitto, 1994; Harrison et al., 1996).

The hydrolysis of $NO_2$ on hydrated surfaces (R3.1) is a well-known heterogenous reaction yielding adsorbed $HNO_3$ and evolved nitrous acid (HONO).

$$2\,NO_{2\,(g)} + H_2O_{(ads)} \xrightarrow{surface} HONO_{(g)} + HNO_{3\,(ads)} \qquad (R3.1)$$

Despite the stoichiometry of reaction R3.1, first-order kinetics in $NO_2$ have generally been observed, with a rate having dependence on surface area density (as expected for collision-limited heterogeneous catalysis), surface water content, and other surface chemical properties (Finlayson-Pitts, 2009; Finlayson-Pitts et al., 2003; Lammel, 1999; Spataro and Ianniello, 2014). In addition to hydrated ground and aerosol surfaces, reaction R3.1 has been implicated on the sea surface (Wojtal et al., 2011; Yang et al., 2021; Zha et al., 2014), on snow and ice surfaces (Beine et al., 2001; Kim and Kang, 2010), as well as on indoor surfaces (Collins et al., 2018; Febo and Perrino, 1991; Spicer et al., 1993). Spicer et al. (1993) and Collins et al. (2018) both found an indoor lifetime of $NO_2$ to reactive loss (HONO producing) on residential interior surfaces on the order of one hour in well mixed air—lower than typical ambient $NO_2$ chemical lifetimes on the order of hours in regional (Kenagy et al., 2018; Shah et al., 2020) and urban (Laughner and Cohen, 2019) outflows, and remote forest environments (Browne and Cohen, 2012). Reaction R3.1 may be an especially important surface removal process during summertime nights or winter months when $NO_2$ is longer lived with lifetimes on the order of 10 h to more than a day (Browne and Cohen, 2012; Kenagy et al., 2018; Martin et al., 2003b). Reaction R3.1 has also been implicated in the uptake of $NO_2$ through leaf stomata, where it may be an important contributor to $NO_2$ deposition within the moist and high surface area substomatal cavities (apoplast) of leaves (Ammann et al., 1995).

Although the mechanism for heterogenous hydrolysis of $NO_2$, likely involving disproportionation of $N_2O_4$ as a surface intermediate (Finlayson-Pitts et al., 2003), is still an active area of research (Bang et al., 2015; Finlayson-Pitts, 2009; Murdachaew et al., 2012; Spataro and Ianniello, 2014), uptake coefficients for $NO_2$ ($\gamma_{NO_2}$) to various surfaces have been measured. Laboratory determined values of $\gamma_{NO_2}$ are generally in the range of

$10^{-7}$ to $10^{-5}$ for humidified and aqueous surfaces of various composition (Ammann et al., 2005; Bröske et al., 2003; Kleffmann et al., 1998; Kurtenbach et al., 2001), however, values > $10^{-5}$ (Mertes and Wahner, 1995; Msibi et al., 1993) and < $10^{-8}$ (Ammann et al., 2013) to bulk liquid water have been reported. Studies finding slow uptake of $NO_2$ to bulk water understand the process as driven by low solubility and slow aqueous phase second-order hydrolysis (Cheung et al., 2000; Lee and Schwartz, 1981; Schwartz and Lee, 1995), while studies finding uptake above that which can be accounted for by these solution-phase processes suggest heterogeneous first-order hydrolysis at the air-water interface (Bambauer et al., 1994; Finlayson-Pitts et al., 2003; Mertes and Wahner, 1995; Novakov, 1995). Recent efforts to understand the orders of magnitude variation in laboratory determined $\gamma_{NO_2}$ to aqueous surfaces have employed electrospray ionization (ESI) mass spectrometry (MS) to monitor online $NO_3^-$ formation from the reaction of $NO_{2(g)}$ injected into the ESI source region with aqueous electrosprays containing various concentrations of atmospherically relevant solutes, finding large enhancements in inferred $\gamma_{NO_2}$ of up to a factor of $10^4$ to solutions containing halide salts NaX (X = Cl, Br, I) (Colussi and Enami, 2019; Kinugawa et al., 2011; Yabushita et al., 2009). It was proposed that interfacial anions ($Cl^-$, $Br^-$, $I^-$) stabilize $NO_2$ at the air-water interface, facilitating reaction R3.1. To this end, it was noted that (Bambauer et al., 1994) report enhanced uptake of $NO_2$ to aqueous droplets containing ca. 3mM NaCl, however, (Msibi et al., 1993) report a value of $\gamma_{NO_2}$ to deionized water of 8.7 x $10^{-5}$—much greater than can be accounted for by dissolution followed by second-order hydrolysis, i.e., $\gamma_{NO_2}$~ 6 x $10^{-9}$ (Ammann et al., 2013). Due to the unique complexity of the ESI process, further work is required before application of these results is made to atmospherically relevant interfacial surfaces (Gallo et al., 2019b, 2019a; Rovelli et al., 2020). Additionally, the presence of reducing solutes such as ascorbic acid (Msibi et al., 1993) and phenolic humic acid precursor molecules (Ammann et al., 2005) has been shown to significantly enhance $NO_2$ surface uptake via one-electron reduction reactions yielding nitrate/HONO, and may also contribute to $NO_2$ deposition within the interior of leaves (Farvardin et al., 2020).

For use in models of atmospheric chemistry, field measured $\gamma_{NO_2}$ have provided some constraint on the large variation in laboratory determined values. Kurtenbach et al.

(2001) studied heterogeneous HONO formation in a road traffic tunnel in Wuppertal, Germany, and found $\gamma_{NO_2}$ of ca. $10^{-6}$ measured on a sample of tunnel wall residue to be in good agreement with first order heterogeneous formation rates of HONO from the tunnel experiments. Vandenboer et al. (2013) report high resolution vertical profiles (10 m resolution to 250 m agl; <10 min/profile) of various trace species including HONO and $NO_2$ at the former Boulder Atmospheric Observatory (BAO) in Colorado, U.S.A., during late winter, 2011. The BAO site was situated in an agricultural region 32 km northeast of Boulder and was decommissioned in 2018 (Wolfe, 2018). Vandenboer et al. (2013) derive ground uptake coefficients for $NO_2$ ($\gamma_{NO_2,\ ground}$) by assuming the column integrated rate of change of HONO during the first half of the night (1800–2400 hrs) when HONO was increasing from very low daytime concentrations (mid-day photolysis lifetime of HONO < 15 min) was due to R3.1 occurring on ground surfaces, and found $\gamma_{NO_2,\ ground}$ to vary between 2 x $10^{-6}$ and 1.6 x $10^{-5}$ as a function of RH for the specific wintertime land type in the vicinity of the BAO site (grassland and tilled fields). Ren et al. (2020) monitor $NO_2$ and HONO concentrations at high temporal resolution at a meadow location (grass height ca. 30 cm, LAI ca. 6) in Melpitz, Germany, and similarly compute $NO_2$ uptake coefficients due to R3.1 during early evening when HONO is accumulating in the nocturnal boundary layer, finding $\gamma_{NO_2}$ = 2.3 ± 1.9 x $10^{-6}$. Collins et al. (2018) find $\gamma_{NO_2}$= (1–2.3) x $10^{-6}$ from $NO_2$ decay, presumably via reaction R3.1, following indoor (residential) perturbation experiments probing the gas-surface equilibrium control over HONO concentrations for which surfaces have developed sufficient reservoirs of HONO/nitrite via heterogeneous reaction of $NO_2$ and by deposition of HONO emitted during operation of a gas stove.

Despite the evidence for reaction R3.1 proceeding on outdoor and indoor surfaces, regional and global CTMs have yet to, to our knowledge, update dry deposition parameterizations of $NO_2$ to include this effect, thus potentially underestimating $V_d(NO_2)$ at night and throughout vegetatively senescent periods when stomatal uptake would be at a minimum and/or absent. In this study, we extract the trace gas dry deposition parameterization from a widely used global CTM (GEOS-Chem) and re-implement to run in single point mode to facilitate evaluation of an updated parameterization that includes the effect of reaction R3.1 on $V_d(NO_2)$ and $V_d(NO_y)$. We compare to observations of

$V_d(NO_2)$ and $V_d(NO_y)$ from an extensive publicly available dataset of $NO_2$ and $NO_y$ eddy covariance flux and speciated $NO_y$ concentration measurements over Harvard Forest, Massachusetts, U.S. (Munger and Wofsy, 2019), paying attention to soil $NO_x$ emission and canopy surface area effects. Prior to updating $R_c(NO_2)$, we evaluate the parameterization of $R_a$ and $R_b$ by comparing to recently published daytime deposition velocities of rapidly depositing species inferred over a Southern U.S. deciduous forest by the method of eddy covariance (Nguyen et al., 2015), and comment on the effects that site-specific roughness length, reference height, and the roughness sublayer have on daytime $R_a$, and the effects of molecular diffusivity on $R_b$.

## 3.3 Reference Model and Field Measurements

### 3.3.1 Dry Deposition Parameterization of Trace Gases in the GEOS-Chem CTM

To facilitate site-specific comparisons to measured deposition velocities, we extract the trace gas dry deposition source code and input parameters from GEOS-Chem v10-01 (www.geos-chem.org) and re-implement into MATLAB to run in single-point mode. We implement the option to use on-site meteorology and phenological characterizations (e.g. LAI, canopy height, and land type classification). Silva et al. (2017) note the importance of correct specification of deposition land type when comparing simulated $V_d(O_3)$ from GEOS-Chem to site-specific observations. The dry deposition flux of trace gases in GEOS-Chem proceeds in grid cells in contact with the ground surface following the inferential technique according to 3.1, with species-specific deposition velocities $V_d(x)$ computed following the standard resistance-in-series approach (3.2).

Aerodynamic resistance ($R_a$) for the turbulent transport of scalars within surface grid boxes is defined by analogy to Ohm's law, where the near surface gradient in horizontal wind (i.e., 'potential difference') is parameterized following the classic logarithmic wind law modified for diabatic stability according to Monin-Obukhov (M-O) similarity theory. $R_a$ [s $m^{-1}$] is formulated to represent the resistance to vertical transport from a reference height $z$ (i.e., grid box center which is ca. 60 m agl) down to the roughness length $z_o$ of the surface—the height above the zero-plane displacement $d$ where the

logarithmic wind profile extrapolates to zero (Garratt, 1992; Kaimal and Finnigan, 1994; Toyota et al., 2016; Wesely and Hicks, 1977):

$$R_a(z) = \frac{1}{ku_*}\left[\ln\left(\frac{z-d}{z_o}\right) - \Psi_h\left(\frac{z-d}{L}\right) + \Psi_h\left(\frac{z_o}{L}\right)\right] \quad (3.3)$$

where $k$ is the von Karman constant (0.4 in this study), $u_*$ the friction velocity—a surface layer velocity scale which characterizes the surface momentum flux (i.e., 'current'), $\Psi_h$ an integrated M-O stability-correction factor for sensible heat (supplemental material, section 3.6.1, equations 3.S3 & 3.S7) which is an empirical function of the dimensionless ratio $(z-d)\,/\,L$ where $L$ is the Monin-Obukhov length (Monin and Obukhov, 1954). Both $z_o$ and $d$ are fit parameters to the logarithmic wind profile under neutral stability (Monin and Obukhov, 1954) which depend on the nature of the rough surface (i.e., canopy height $h_c$ and object spacing) and have commonly found empirical values of $z_o \sim 1/10\ h_c$ and $d \sim 2/3\ h_c$ for many naturally vegetated surfaces (Garratt, 1992; Oke, 1987). At heights well above the surface ($z > 10h_c$), $d$ may be ignored (Garratt, 1992), as is done in GEOS-Chem since dry deposition is referenced from surface grid box centers. Equation 3.3 applies equally to all trace gas and aerosol species and assumes equivalency in the turbulent transfer of momentum and scalers, under neutral conditions, from $z$ to $z_o$. It is noted that $R_a$ according to 3.3 assumes a 'no-slip' boundary condition, that is, $u(z_o) = 0$ m s$^{-1}$, the implications of which are discussed in section 3.4.1.

Across the distance $z_o$, molecular diffusion becomes an important factor governing near-surface trace gas flux. The species-specific quasi-laminar boundary layer resistance $R_b$ accounts for the transfer of gases from $z_o$ to the deposition surface, and is estimated using the semi-empirical formulation of Wesely and Hicks, 1977:

$$R_b(x) = \frac{2}{ku_*}\left(\frac{\kappa}{D_x}\right)^{2/3} \quad (3.4)$$

where $\kappa$ is the thermal diffusivity of air, and $D_x$ the molecular diffusivity of the depositing trace gas $x$. Developments to the parameterization of $D_x$ used in GEOS-Chem are discussed in section 3.4.2.

The resistance to surface uptake of trace gases ($R_c$) in GEOS-Chem is parameterized according to a modified 'big leaf' algorithm based on the Wesely 1989 scheme, as is currently the case for the majority of global CTMs (Hardacre et al., 2015). The bulk canopy surface resistance has parallel contributions from (1) upper canopy leaf interiors via stomatal $r_s$ and mesophyll $r_m$ resistances, (2) upper canopy leaf cuticles $r_{lu}$, (3) lower canopy elements $r_{dc} + r_{cl}$, and (4) ground surface elements $r_{ac} + r_{gc}$:

$$R_c(x) = \left[1/(r_s + r_m) + 1/r_{lu} + 1/(r_{dc} + r_{cl}) + 1/\left(r_{ac} + r_{gc}\right)\right]^{-1} \quad (3.5)$$

The Wesely 1989 algorithm was originally developed over the U.S. and southern Canada for use on 11 land types, with component resistances varying across 5 seasonal categories (summer, autumn, late autumn, winter, spring). Application to a variety of trace gases was made possible by $r_s$ dependence on molecular diffusivity, and $r_m, r_{lu}$, $r_{cl}$, and $r_{gc}$ dependence on (i) aqueous solubility at neutral pH via effective Henry's solubility ($H^*$) and (ii) oxidative capacity via an estimated reactivity factor ($f_o$) categorized as unreactive ($f_o$ = 0), slightly reactive ($f_o$ = 0.1), or as reactive as $O_3$ ($f_o$ = 1). Categorized $f_o$ values are based on electron activities and rate-of-reaction with aqueous S(IV) compounds (Wesely, 1989). In-canopy aerodynamic resistance to turbulent transport to the lower canopy and ground surface is represented by land-type dependent fixed values $r_{dc}$ and $r_{ac}$, respectively. Implementation of the Wesely 1989 algorithm into GEOS-Chem included modifications for application to the global scale (Wang et al., 1998). Detailed descriptions of these modifications have been included in recent work evaluating the dry deposition of $O_3$ in GEOS-Chem (Silva and Heald, 2018; Wong et al., 2019) and can be found online at http://wiki.seas.harvard.edu/geos-chem/index.php/Dry_deposition, last accessed 22 July, 2020. Briefly, seasonality is represented via $r_s$ and $r_{lu}$ dependence on leaf area index (LAI) (Gao and Wesely, 1995); $r_s$ being computed following a multiplicative algorithm where land-type dependent maximum stomatal conductances ($g_s$ = $1/r_s$) to water vapour are modified by response functions for solar radiation and temperature, with trace gas specificity obtained by scaling resulting $g_s$ by the ratio of molecular diffusivities $D_x/D_{H_2O}$. Deposition land-types include snow/ice, deciduous forest, coniferous forest, agricultural land, shrub/grassland, desert, wetland, urban, and water according to Wesely et al. 1989, with rainforest (Jacob and Wofsy, 1990) and tundra (Jacob et al., 1992a) added as

additional land types. Meteorological inputs required in the parameterization of $V_d$ are provided from assimilated meteorological fields from NASA's Global Modeling and Assimilation Office (GMAO). Daily LAI values are interpolated from a gridded MODIS-derived monthly LAI product (Myneni et al., 2002). Following the recommendations of Shah et al. (2018), we limit the cold temperature exponential increase in the non-stomatal components of $R_c$ to a factor of 2, and impose a nominally small $R_c(HNO_3)$ = 1 s $m^{-1}$.

### 3.3.2 Eddy Covariance Flux Measurements & Site Descriptions

We evaluate parameterized species-specific deposition velocities computed using the extracted trace gas dry deposition scheme from GEOS-Chem against eddy covariance inferred deposition velocities over two mixed deciduous forests in the eastern United States. First, deposition velocities of species found to dry deposit with minimal surface resistance, namely, $H_2O_2$, hydroxy methylhydroperoxide (HMHP), and $HNO_3$, were inferred over Talladega National Forest for optimal days in June 2013 (Nguyen et al., 2015). Second, at the Harvard Forest Environmental Monitoring Site (HFEMS), a long-term hourly dataset of eddy covariance flux observations of $NO_2$ and $NO_y$, supported with ancillary measurements including $NO_y$ component concentrations, meteorological, and phenological variables enabled an in-depth evaluation of parameterized $V_d(NO_2)$ and $V_d(NO_y)$.

#### *3.3.2.1. Talladega National Forest: $H_2O_2$, HMHP, & $HNO_3$*

Nguyen et al. (2015) present a novel dataset containing eddy covariance inferred deposition velocities of 16 trace gases, including species which were found to deposit with negligible surface resistance: $H_2O_2$, hydroxy methylhydroperoxide (HMHP), and $HNO_3$. Evaluation of the resistance-in-series pathway of parameterized $V_d(x)$ from GEOS-Chem neglecting the complexities of a surface resistance $R_c$ scheme is therefore possible by comparing to observed deposition velocities of $H_2O_2$, HMHP, and $HNO_3$. Observations were taken at the Centreville (CTR) Southeastern Aerosol Research and Characterization Study (SEARCH) site (32.90289 N, 87.24968 W) near Brant, Alabama, U.S. in June, 2013. The CTR site is situated in a grassy clearing in the Talladega National Forest with large forest fetch to the N, W, and E. The mixed forest consists of coniferous and deciduous tree species, with a mean canopy height of ca. 10 m and LAI of 4.7 $m^2$ $m^{-2}$. Eddy covariance flux observations

were measured at 22 m agl from a walk-up tower, with sonic anemometer (8 Hz) and inlet to the time-of-flight (TOF) chemical ionization mass spectrometer (CIMS) (10 Hz) facing North so as to capture eddies originating over forest fetch. Included in the analysis of Nguyen et al. (2015) are daytime (10–15 LST) mean deposition velocities, averaged across five ideal days in June 2013 (6$^{th}$, 15$^{th}$, 20$^{th}$, 23$^{rd}$, and 27$^{th}$) where winds had exclusively forest fetch. To compare with the reported daytime deposition velocities of $H_2O_2$ (5.2 ± 1.1 cm s$^{-1}$), HMHP (4.1 ± 1.1 cm s$^{-1}$), and $HNO_3$ (3.8 ± 1.3 cm s$^{-1}$), we average $R_a$ and $R_b$ components of the offline dry deposition algorithm, applied at the location of the CTR site, between 10–15 LST on the same days. Meteorological inputs required to drive the $R_a$ and $R_b$ components of the algorithm at the CTR site ($u_*$, $T$, $P$, and sensible heat flux) were obtained from NASA GMAO's Godard Earth Observing System (GEOS) Forward Processed (FP) assimilated meteorological fields at hourly, 0.25° x 0.3125° resolution for North America, which Nguyen et al. (2015) note are in excellent agreement to values measured at the CTR site during the measurement period.

*3.3.2.2. Harvard Forest: $NO_2$, & $NO_y$*

The Harvard Forest Environmental Monitoring Site (HFEMS) is located in central Massachusetts, U.S. (42.54 N, 72.18 W; 340 m ASL) and situated in a mature mixed deciduous forest with a summertime deciduous leaf area index (DLAI) of ca. 3.4, summertime LAI of ca. 4.3, and stem and twig area index (STAI) of ca. 0.9 (Fig. S3.1 in supplemental material). Canopy height is ca. 20 m. Local pollution sources include a secondary paved road 1.5 km to the west, a highway ca. 5 km to the north, and a small town more than 10 km to the northwest. Due to prevailing westerly winds, emissions from Boston (100 km to the east) rarely influence the site. Cool, dry and unpolluted air from the northwest, and warm, moist, anthropogenically influenced air from the southwest are the predominant influences at this site (Horii et al., 2005).

Munger et al. (1996) describe the methodology of long-term total nitrogen oxide ($NO_y$) concentration measurements for eddy covariance flux computation, as well as other details of the HFEMS. Briefly, $NO_y$ concentrations at 8 Hz were made by reducing $NO_y$ to NO on a well aged hot gold catalyst with $H_2$, followed by detection of chemiluminescence from titration of resulting NO with $O_3$. The reducing catalyst was positioned close to the

inlet at a height of 29 m on the 30 m walk-up tower. Additional long-term trace gas measurements from this tower include the vertical profiles of NO and $NO_2$ measured with a $NO_x$ photolysis-chemiluminescence instrument (Munger et al., 1996). Concentration measurements of PAN by capillary-column gas chromatograph with electron capture detection was added to the 30 m walk-up tower in April 2000 (Horii et al., 2005). To an auxiliary 23 m scaffolding tower located ca. 100 m to the southeast of the main tower, a Tunable Diode Laser Absorption Spectrometer (TDLAS) was configured to measure eddy covariance fluxes (1 Hz) of $NO_2$ and concentrations of $HNO_3$ from April through November 2000 (Horii et al., 2004). Due to inlet wall interactions of $HNO_3$ with a characteristic time constant of ca. 10 min, high frequency concentration information required for eddy covariance flux computation was not possible. However, it was found that the hourly mean concentration was not compromised, as the fluorinated silane-coated fused silica quartz inlet walls were not a permanent sink of $HNO_3$, which was near completely transmitted to the measurement cell after sufficient equilibrium time (Horii et al., 2005). Although the measurement height of $NO_y$, NO, $NO_2$, and PAN on the main tower (29 m) did not match that of $HNO_3$ and $NO_2$ on the auxiliary tower (22 m), Horri et al. (2005) found the measurement heights of the two towers to be in the same flux regime by congruence of heat fluxes and noted as well the coherence in coincident trace gas data on the hourly timescale.

Trace gas data from the HFEMS used in this study, specifically hourly eddy covariance fluxes of $NO_y$ and $NO_2$, and hourly concentrations of $NO_y$, NO, $NO_2$, PAN, and $HNO_3$ are publicly available at http://atmos.seas.harvard.edu/lab/data/nigec-data.html, last accessed 22 July, 2020. Eddy covariance fluxes of $NO_y$ and $NO_2$ reported in the HFEMS dataset have been corrected by the ratio of observed heat flux to a mathematically smoothed heat flux analogous to the observed instrument response functions for $NO_y$ and $NO_2$, which estimates flux lost due to instrumental smoothing of high-frequency fluctuations—typically less than 20% (Horii et al., 2005; Munger et al., 1996). Exchange velocities ($V_{ex}$) are computed herein by normalizing reported hourly $NO_y$ and $NO_2$ eddy covariance fluxes by respective ambient hourly concentrations. Equating $V_{ex}$ to $V_d$ assumes that the observed flux is due to surface deposition only. Deviations from these assumptions, including surface emission of $NO_x$, chemical flux divergence of $NO_2$, and a potential non-zero

canopy accumulation rate of $NO_y$, are discussed in later sections. Eddy covariance fluxes have reduced error under conditions where turbulence is well developed (Baldocchi, 2003; Cherin et al., 2015; Goulden et al., 1996; Nguyen et al., 2015). Turbulent threshold $u_*$ values in the rage 0.15 – 0.35 m $s^{-1}$ (median 0.23 m $s^{-1}$) have been found to be representative of multiple sites across many years (Cherin et al., 2015). Herein, periods of low surface layer turbulence ($u_* < 0.2$ m $s^{-1}$) have been omitted from analysis (Altimir et al., 2006; Wu et al., 2011), resulting in ca. 25% of observed hourly nocturnal $V_d(NO_2)$ and 18% of observed hourly $V_d(NO_y)$ being removed from the HFEMS dataset. Outliers in the remaining hourly $V_d(NO_2)$ and $V_d(NO_y)$ timeseries were identified via the method of median absolute deviation (MAD) (Leys et al., 2013), where hourly values outside of the median ± 3x MAD were removed from calculations of subsequent mean values, resulting in ca. 20% of observed hourly nocturnal $V_d(NO_2)$ and 10% of observed hourly $V_d(NO_y)$ being removed from the $u_*$-filtered HFEMS dataset. Overall, 60% of the nocturnal $V_d(NO_2)$ and 74% of the $V_d(NO_y)$ hourly timeseries were retained for analysis after application of turbulence and outlier filters.

Figure S3.2 (supplemental material) depicts comparisons of hourly observations of $u_*$, sensible heat flux, downward shortwave radiation, *T*, *P*, and *RH* made over Harvard Forest to coincident values from NASA GMAO's Modern-Era Retrospective analysis for Research and Applications version 2 (MERRA-2) assimilated meteorological fields (Gelaro et al., 2017), available at hourly, 0.5° x 0.625˚ resolution from 1980 to the present day. Excellent agreement (normalized mean bias NMB < 1% and $R^2 > 0.93$) is noted for *T*, and *P*. *RH* and $u_*$ have small biases of -6% and 5%, respectively, albeit with lower $R^2$, 0.60 and 0.69, respectively. Sensible heat flux and downward shortwave radiation are each biased high by 16%, with $R^2$ of 0.68 and 0.87, respectively. Meteorological input variables required in the parameterization of $V_d$ were taken from the HFEMS data archive, specifically, *P*, *T*, *RH*, $u_*$, and sensible heat flux (Munger and Wofsy, 2020b) and incoming solar radiation (Fitzjarrald and Sakai, 2009) were available at hourly temporal resolution for the study period. Required meteorological variables not available from the HFEMS data archive (cloud fraction) where taken from MERRA-2 assimilated meteorological fields. Canopy specific inputs to the parameterization of $V_d$ include $z_o$, *d*, LAI, and deposition land-type. Land-type was set to deciduous with values for $z_o$ and *d* being

estimated as $1/10^{th}$ and $2/3^{rd}$ of canopy height ($h_c$), respectively, which are values representative of many vegetative surfaces including crops and forests (Garratt, 1992; Oke, 1987). We estimate daily LAI values from a fit to daily Plant Area Index measurements from the HFEMS, April–December, 1998–2015 (Munger and Wofsy, 2020a), corrected for the reported STAI of 0.9 $m^2$ $m^{-2}$ noted at the HFEMS (Horii et al., 2004) (Fig. S3.1).

### 3.4 Model Updates, Results & Discussion

Table 3.1 presents modifications made to the offline base dry deposition parameterization from GEOS-Chem. Parameterization P1 is equivalent to the current dry deposition scheme in GEOS-Chem, which references deposition from grid box centers (GBC) of the lowest model level, ca. 60 m. Modifications to P1 include changes to: (1) the height in which dry deposition is referenced (P2), (2) formulations to the parameterization of aerodynamic resistance $R_a$ (P3–P4), (3) parameterization of molecular diffusivity $D$ (P5), (4) formulation of non-stomatal $R_c(NO_2)$ to reflect heterogeneous hydrolysis on deposition surfaces (P6-7), and (5) implementation of published non-stomatal $R_c(PAN)$ to reflect above-canopy uptake over a forest (P8). We evaluate parameterizations P1–P5 by comparing to the deposition velocities of rapidly depositing species measured over Talladega National Forest by Nguyen et al. (2015) (Table 3.2), where it was noted that above-canopy deposition velocities for $H_2O_2$, HMHP, and $HNO_3$ corresponded to computed theoretical maximums (i.e., surface resistances are negligible) thus enabling direct comparison to the isolated component of the deposition pathway consisting of resistances $R_a$ and $R_b$, as discussed in sections 3.4.1, and 3.4.2, respectively. Parameterizations P6–P7 involve modifications to the representation of $R_c(NO_2)$ by introducing a pathway for loss due to heterogeneous hydrolysis on ground surfaces (reaction R3.1), evaluated by comparison to both above-canopy nocturnal $V_d(NO_2)$ observed at the HFEMS (sections 3.4.1–3) and bottom-up estimates of nocturnal $V_d(NO_2)$ for Harvard Forest from literature values of surface-specific deposition velocities $V_d^{surf}(NO_2)$ (section 3.4.3.5). Parameterization P8 replaces the non-stomatal component of the upper canopy $R_c$ term ($r_{lu}$ from equation 3.5) for PAN with a species-specific empirical fit following Turnipseed et al. (2006), as discussed in section 3.4.4. Finally, the

**Table 3.1:** Modifications to the offline dry deposition parameterization tested in this study. Parameterization P1 is equivalent to the current trace gas dry deposition scheme in GEOS-Chem (GC). Modifications to P1 include changes to: reference height $z_{ref}$ (P2), formulations of aerodynamic resistance $R_a$ (P3–4), molecular diffusivity $D$ (P5), and non-stomatal surface resistances ($R_c$) of $NO_2$ (P6–7) and PAN (P8).

| Param. | $z_{ref}$[(a)] | Aerodynamic Res. $R_a$ | Diffusivity $D$ | non-stomatal $R_c(NO_2)$ | non-stomatal $R_c(PAN)$ |
|---|---|---|---|---|---|
| P1 | $z_{GBC}$ | base GC (E3) | base GC (Chapman-Enskog theory with constant mfp[(b)]) | base GC (modified Wesely 1989) | base GC (modified Wesely 1989) |
| P2 | $z_{TNF}$ or $z_{HFEMS}$ | | | | |
| P3 | | RSL, $u(z_o) > 0$ m s$^{-1}$ | | | |
| P4 | | RSL, $u(z_o) = 0$ m s$^{-1}$ | | | |
| P5 | | RSL, $u(z_o) > 0$ m s$^{-1}$ (AE10) | measured & Fuller's method (E6 & E7) | | |
| P6 | | | | $r_{hyd}$ with α = 1 (E12) | |
| P7 | | | | $r_{hyd}$ with α = 2 (E12) | |
| P8 | | | | | Empirical[(c)] |

[(a)] Dry deposition reference height: $z_{GBC}$ ~ 60 m agl, $z_{TNF}$ = 20 m; $z_{HFEMS}$ = 29 m.
[(b)] Mean Free Path (mfp) held constant across depositing trace gases.
[(c)] Empirical fit of non-stomatal deposition (Turnipseed et. al., 2006) modified for LAI.

parameterization of $V_d(NO_y)$ is evaluated against observations from the HFEMS, considering $NO_y$ components $NO_2$, NO, $HNO_3$, and PAN (section 3.4.4).

### 3.4.1 Updates to the Parameterization of Aerodynamic Resistance: $R_a$

As shown in Table 3.2, parameterization P1 overestimates daytime mean deposition velocities computed at the CTR site for $H_2O_2$ (+15%), HMHP (+41%), and $HNO_3$ (+52%). Nguyen et al. (2015) found excellent agreement between hourly GEOS-FP assimilated meteorology (used herein for computation of $V_d$ in Table 3.2) and measured $u_*$, and sensible and latent fluxes at this site, however, GEOS-FP meteorology (0.25° x 0.3125°) reports $z_o$ = 2.2 m for June, 2013 at this location—much larger than would be expected given the local 10 m canopy height. Prescribing $z_o = 0.1\ h_c$—in accordance with conventionally used values for natural vegetation and in agreement with an updated land-use module developed for GEOS-Chem (Geddes et al., 2016)—results in a 35% increase in $R_a$ and notable reductions in $V_d$ high biases (P1b, Table 3.2). Despite a measurement height of 22 m, P1b purposefully computes $R_a$ from a reference height of 60 m while neglecting to include a displacement height $d$, following the computation of $R_a$ in GEOS-Chem. Neglecting $d$ increases P1b daytime $R_a(60\ m)$ by ~1%, and $R_a(20\ m)$ by ~ 9%. Although the greatest sensitivity of $R_a$ to $z$ occurs in proximity to $z_o$, as depicted in Fig. S3.3 in the supplemental

**Table 3.2:** Effects of updates to aerodynamic resistance $R_a$, and quasi-laminar sublayer resistance $R_b$ on the daytime (10–15 LT) dry deposition velocity $V_d$ of rapidly depositing species (nominally small $R_c$) over Talladega National forest (temperate, deciduous). Complete parameterization descriptions are given in Table 3.1. Cumulative modifications to base parameterization P1 are highlighted. Mean quantities are averaged across the five daytime periods in June 2013 that Nguyen et al. (2015) use in their analysis of eddy covariance inferred deposition velocities. Shown are mean quantities ± standard deviations about the hourly timeseries.

| **Parameterization**[a] | | **$H_2O_2$** | | | **HMHP** | | | **$HNO_3$** | | |
|---|---|---|---|---|---|---|---|---|---|---|
| | $R_a$ | $R_b$ | $V_d$ | **NMB**[b] | $R_b$ | $V_d$ | **NMB**[c] | $R_b$ | $V_d$ | **NMB**[d] |
| | [s/m] | [s/m] | [cm/s] | [%] | [s/m] | [cm/s] | [%] | [s/m] | [cm/s] | [%] |
| P1. (base sim.) | 9.5±2.7 | 7.1±2.1 | 6.0±1.2 | 15 | 7.7±2.9 | 5.8±1.1 | 41 | 7.6±2.9 | 5.8±1.1 | 52 |
| P1b. ($z_o = 0.1h_c$)[e] | 12.8±3.4 | \| | 5.0±1.0 | -3 | \| | 4.9±1.0 | 19 | \| | 4.9±1.0 | 29 |
| P2. ($z_{ref}$ = 20 m - d) | 9.7±2.5 | \| | 5.9±1.3 | 14 | \| | 5.8±1.2 | 40 | \| | 5.8±1.2 | 51 |
| P3. (RSL, $u(z_o)$>0) | 10.2±2.6 | \| | 5.8±1.2 | 11 | \| | 5.6±1.2 | 36 | \| | 5.6±1.2 | 47 |
| P4. (RSL, $u(z_o)$=0) | 5.3±1.4 | \| | 7.9±1.7 | 52 | \| | 7.6±1.7 | 85 | \| | 7.6±1.7 | 100 |
| P5. (*D* update) | \| | 12.9±4.9 | 4.4±1.0 | -15 | 14.9±5.7 | 4.1±1.0 | -1 | 15.7±6.0 | 4.0±0.9 | 4 |

[a] Refer to Table 3.1 for simulation descriptions. Note: $R_c$ set to 1 s $m^{-1}$ following minimum allowed in GEOS-Chem (section 3.3.1).
[b] To measured (eddy covariance) daytime (10–15 LST) $V_d(H_2O_2)$ = 5.2 ± 1.1 cm/s (Nguyen, 2015).
[c] To measured (eddy covariance) daytime (10–15 LST) $V_d(HMHP)$ = 4.1 ± 1.1 cm/s (Nguyen, 2015).
[d] To measured (eddy covariance) daytime (10–15 LST) $V_d(HNO_3)$ = 3.8 ± 1.3 cm/s (Nguyen, 2015).
[e] $z_o$ set to 10% of canopy height ($h_c$) for P1b–P9.

material (section 3.6), the difference between $R_a$ computed from an above canopy measurement height vs. typical heights from which global CTMs reference dry deposition can be significant (Figs. S3.3 & S3.4). Referencing $R_a$ from the CTR measurement height (22 m) results in a 42% decrease in $R_a$ under neutral conditions (Fig. S3.3), and 23% decrease under daytime (10-15 LST) conditions (Table 3.2, P1b vs P2). However, due to the significant contributions of $R_b$ to deposition velocities of rapidly depositing species (section 3.4.2), referencing $R_a$ from GEOS-Chem grid-box-center instead of measurement height, as is commonly done in studies comparing CTM $V_d$ to measured/inferred values (Clifton et al., 2017; Nguyen et al., 2015; Nowlan et al., 2014; Silva and Heald, 2018), results in a moderate (8%) decrease in $V_d$ for the species of Table 3.2 (P5, data not shown).

Considering that the CTR and HFEMS measurement heights, ca. 2 $h_c$ and 1.5 $h_c$, respectively, are at the upper limits of the roughness sublayer (RSL)—a region where turbulent mixing in the wake of roughness elements is enhanced above that predicted by M-O similarity theory by a factor of 2 to 3 (see section 3.6.2 in supplemental material for discussion of RSL)—$R_a$ computed according to M-O similarity theory (equation 3.3) may be in slight underestimate due to non-zero horizontal windspeeds at $z_o$ resulting from enhanced downward mixing of momentum. In an effort to quantify this effect, parameterization P3 computes $R_a$ corrected for RSL mixing and $u(z_o) > 0$ following equation 3.S10 (in supplemental material), resulting in a small (5%) increase in $R_a$ at the CTR measurement height under the daytime conditions of Table 3.2, and even smaller changes to $V_d$ given the influence of $R_b$ (section 3.4.2). The depth of the RSL, $z^*$, was estimated following Physick and Garratt (1995); for neutral and unstable conditions ($L^{-1} \leq 0$ ) $z_N^* = 50 z_o$; for very stable conditions ($z_N^* / L > 0.2$ ), $z^* = 0.37 z_N^*$; for moderately stable conditions ( $0 < z_N^* / L < 0.2$), $z^*$ is linearly interpolated between neutral and stable values. Given the lower relative measurement height at the HFEMS (~1.5$h_c$), P3 $R_a$ results in increases over P2 $R_a$ by 30% (10$^{th}$ percentile), 20% (50$^{th}$ percentile) and 18% (90$^{th}$ percentile), as depicted in Fig. S3.4. Slight reductions in $V_d(HNO_3)$ over Harvard Forest are depicted in Fig. 3.5 and discussed in section 3.4.4. Parameterization P4 in Table 3.2 shows the effect of incorrectly neglecting the non-zero wind at $z_o$ in the RSL correction of $R_a$ for use in $V_d$ calculations, which results in a reduction of $R_a$ of ca. 50%, and significant increases to the high bias of deposition velocities. As shown herein and in agreement with

previous work (Simpson et al., 1998), it may be appropriate to neglect the effects of the RSL on depositing species referenced at a height of at least 1.5–2 $h_c$, however, studies which endeavour to understand bidirectional exchange, or the dispersion of near surface emissions, should consider the effect of asymmetrical $R_a$ that the RSL imposes, as depicted in Figs. S3.3 & S3.4.

### 3.4.2 Update to the Parameterization of Molecular Diffusivities

A main result of Nguyen et al. (2015) was the illustration of the importance of molecular diffusion in atmosphere-surface exchange of rapidly depositing compounds, where it was shown that maximum daytime mean deposition velocities scale with the inverse square root of molecular mass ($M^{-1/2}$), as do gas-phase diffusion coefficients (Poling and Prausnitz, 2004). Two diffusion-limited regimes were noted: (i) diffusion to canopy surfaces when $R_c$ was negligible, and (ii) diffusion through leaf stomata for species where is $r_s$ the dominant term in $R_c$ (3.5); the species presented in Table 3.2, $H_2O_2$, HMHP, and $HNO_3$ were found to follow the former diffusion limited regime. As seen in Table 3.2, P3 high biases remain in the RSL updated parameterization. Given the dependence of maximum deposition velocity, $V_{d,max} = (R_a + R_b)^{-1}$, on molecular diffusivity through influence on $R_b$ (Meyers et al., 1989), we evaluate the parameterization of molecular diffusion coefficients in GEOS-Chem against available measurements made in air or $N_2$ near STP of atmospherically relevant species. Measured diffusion coefficients of 23 inorganic (Langenberg et al., 2020; Massman, 1998; Tang et al., 2014), and 17 organic (Gu et al., 2018; Tang et al., 2015) species are compared to in Fig. 3.1. Diffusion coefficients ($D$) measured near STP were corrected to STP using (Langenberg et al., 2020):

$$D = D_o \left(\frac{P_o}{P}\right)\left(\frac{T}{T_o}\right)^b \tag{3.6}$$

where we set the temperature power dependence $b$ = 1.75 following Fuller's method, a semi-empirical technique for the estimation of binary gas-phase diffusion coefficients (Fuller et al., 1966), discussed below. As seen in Fig. 3.1, a large high bias exists in the parameterized diffusion coefficients from the dry deposition module of GEOS-Chem, which employs the Chapman-Enskog theory for binary diffusivity (Seinfeld, 1986). The bias results from the use of a constant collision diameter $\sigma$ = 2.7 Å for all species with air,

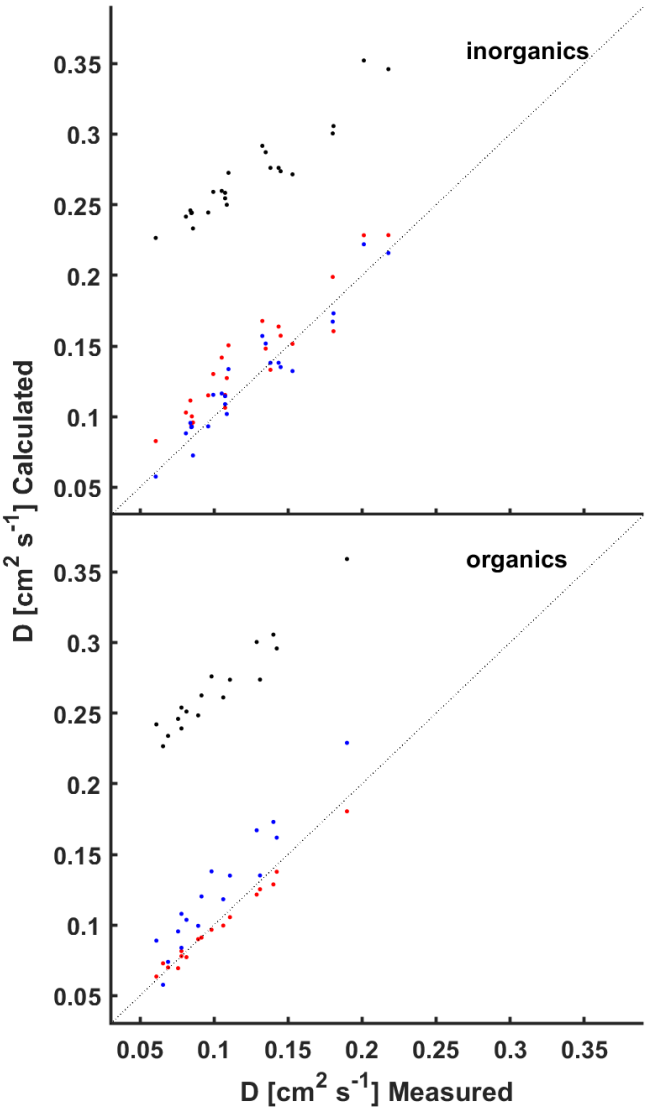


**Figure 3.1:** Measurements of gaseous diffusion coefficients of atmospherically relevant molecules in air or $N_2$ at STP are compared to calculated values. Diffusivities calculated following the method used in GEOS-Chem (**black**) are compared to those calculated following Fuller's method (**red**) and Graham's Law referenced from $D(CO_2)$ (**blue**). Measured and computed (Fuller's method) values are listed in Table S3.1.

which is an underestimate for atmospherically relevant molecules, i.e., $\sigma$ for $O_3$ with air is 3.793 Å (Massman, 1998; Poling and Prausnitz, 2004). The collision diameter $\sigma$ is a pairwise characteristic length scale of the Lennard-Jones intermolecular force, which is not

readily available for many atmospheric trace species (Tang et al., 2014). Several semi-empirical methods have been proposed for the estimation of $D$ in low pressure binary systems (Poling and Prausnitz, 2004). Fuller et al. (1966) developed a simple and generalized semi-empirical correlation equation for the estimation of binary gas-phase diffusion coefficients using additive atomic diffusion volumes $V_i$ for each species $\sum_A V_i$ and $\sum_B V_i$. The diffusion coefficient $D$ [cm$^2$ s$^{-1}$] for trace gas $A$ in bath gas $B$ is given by

$$D = \frac{10^{-3}\, T^{1.75} \left(1/M_A + 1/M_B\right)^{1/2}}{P\, [\, (\sum_A V_i)^{1/3} + (\sum_B V_i)^{1/3}\, ]^2} \tag{3.7}$$

where $P$ is the pressure [atm], $T$ is the temperature [K], and $M$ is the molecular mass [g mol$^{-1}$]. Atomic, and in some cases molecular, diffusion volumes were obtained from regression analysis of 153 binary systems across 340 T-P states and are summarized in Poling et al. (2004), Tang et al. (2014), and Tang et al. (2015). As seen in Fig. 3.1, diffusion coefficients computed using Fuller's method result in a much-improved comparison to measurements, with better agreement to organic species ($R^2$ = 0.99, and NMB = -3%) than to inorganics ($R^2$ = 0.88, and NMB = 13%), consistent with the findings of Tang et al. (2014 & 2015) from an evaluation of a comprehensive diffusivity dataset of atmospherically relevant reactive trace gases for which Tang et al. have made publicly available.

Figure 3.1 also depicts molecular diffusion coefficients approximated by Graham's law of effusion, i.e., $D_{1k} = D_{2k}\sqrt{M_2/M_1}$ (Mason and Evans, 1969), where (continuum) diffusion coefficients $D$ are approximated by Knudsen diffusion coefficients $D_k$— an oversimplification of 3.7, albeit, a strategy used in the atmospheric science community nonetheless (Nguyen et al., 2015; Weber and Renenberg, 1996; Wesely, 1989). Resulting diffusion coefficients scaled from measured $D_{CO_2}$ correlate well with measured values ($R^2$ = 0.91), with NMB to inorganic and organic species of 3% and 20%, respectively. In a review of molecular diffusivities of atmospherically relevant molecules, Massman et al. (1998) note misapplication of Graham's law to molecular diffusivities can lead to errors of up to 23%. Referencing Graham's law from measured $D_{H_2O_2}$, as done in Nguyen et al. (2015), degrades comparison to inorganic diffusivities (NMB ~ -14%), improves

comparison to organics (NMB < 2%), and has no effect on correlation ($R^2$ = 0.91) (data not shown). Sensitivity of Graham's law to choice of reference species is not surprising given the deviation of the $\sqrt{M_2/M_1}$ dependence from the functional form of 3.7. Measured and parameterized (Fuller's method) diffusion coefficients presented in Fig. 3.1 are tabulated in Table S3.1 in the supplemental material. We do not differentiate between diffusivity measurements carried out in air or $N_2$ in Fig. 3.1 or Table S3.1 as differences are expected to be small, i.e., a 2% difference in $D_{O_3}$ at STP in air vs $N_2$ according to Fuller's method, and we assume an air bath gas for all diffusion coefficients computed via Fuller's method.

Parameterization P5 in Table 3.2 computes $R_b$ according to 3.4, using measured diffusion coefficients when available (i.e., $HNO_3$ and $H_2O_2$ from Table S3.1), adjusted to ambient T-P according to 3.6, and diffusion coefficients according to Fuller's method (3.7) in the absence of measured values. Eliminating the high bias in parameterization of molecular diffusivities resulted in a near doubling of $R_b$ for the species in Table 3.2, yielding a much-improved comparison to the daytime deposition velocities of HMHP (NMB -1%) and $HNO_3$ (NMB 4%). The increase in $R_b$ for $H_2O_2$ results in a low bias of -15%, but well within the large relative uncertainty for $R_b$ due to variations in canopy structures (Massman, 1994; Sievering et al., 2001).

As previously mentioned, molecular diffusivity is involved in the parameterization of $R_c$ via influence on stomatal resistance $r_s$, which is scaled by the ratio $D_{H_2O}/D_x$ in dry deposition parameterizations commonly used in chemical transport models (Wesely, 1989; Zhang et al., 2003a). Effects of updated molecular diffusivity on the parameterization of $R_c$ in GEOS-Chem is significant for molecules which dry deposit under stomatal control, i.e., limited aqueous solubility or surface reactivity (discussed in section 3.4.4 and depicted in Figs. 3.4 & S3.9).

As noted by Nguyen et al. (2015), the practice of setting $V_d$ for rapidly depositing species equal to $V_{d(HNO_3)}$ neglects species-specific diffusion limitations, which can be important under turbulent conditions when $R_a$ is at a minimum. For example, $R_b$ for isoprene nitrate is estimated to be 23% higher than for $HNO_3$, translating to a -12% bias in

$V_d$ under the median mid-day conditions at the HFEMS ($R_a(60\ m)$ = 8.6 s $m^{-1}$, $R_b(HNO_3)$ = 12 s $m^{-1}$, Fig. S3.9).

### 3.4.3 Updates to the Parameterization of Resistance to Surface Uptake for $NO_2$: $R_c(NO_2)$

*3.4.3.1. Eddy Covariance Inferred $V_d(NO_2)$ over the HFEMS*

We restrict our analysis of eddy covariance inferred $V_d(NO_2)$ over the HFEMS to nighttime (20:00 to 04:00 LST), when above canopy $NO_2$ : $NO_x$ ~ 1 and photochemical flux divergence of the NO-$NO_2$-$O_3$ triad due to the presence of a vertical gradient in irradiance through the forest canopy (Gao et al., 1993) is absent. Nocturnal above-canopy hourly eddy covariance fluxes of $NO_2$ over Harvard Forest are predominantly (ca. 70%) downward, especially at higher ambient $NO_2$ concentrations (Fig. S3.5). Nocturnal mean (median) ± 1σ $NO_2$ fluxes from April through November 2000 are -0.8 (-0.3) ± 2 ppb cm $s^{-1}$. These downward ($p < 0.01$) above-canopy aggregate fluxes of $NO_2$ are comparable in magnitude to counteracting peak summertime nocturnal soil NO emissions, estimated by Munger et al. (1996) through a mass-balance approach to be ca. 0.9 μmole $m^{-2}$ $h^{-1}$ (3.5 ng N $m^{-2}$ $s^{-1}$, or 0.62 ppb cm $s^{-1}$) at the HFEMS. Munger et al. (1996) note nocturnal NO elevated near the forest floor by 50 ppt on average and Horii et al. (2004) show decreasing within-canopy nocturnal NO profiles with above-canopy concentrations and fluxes indistinguishable from zero despite net downward fluxes of $NO_2$. This presumably due to titration of soil-emitted NO by $O_3$ on a timescale (minutes) much shorter than in-canopy vertical mixing, followed by nocturnal canopy loss processes for $NO_2$. Studies have noted the importance of knowledge of local soil NO emissions and within-canopy processes involving $NO_x$ when interpreting above-canopy $NO_2$ fluxes (Delaria and Cohen, 2020; Eugster and Hesterberg, 1996; Flechard et al., 2011; Min et al., 2014). Using measured soil NO emissions from a Ponderosa Pine plantation 75 km from Sacramento, California, Min et al. (2014) calculate an $NO_2$ flux resulting from the reaction of soil NO with $O_3$ to be 3.5 times greater than the observed above-canopy eddy covariance $NO_2$ flux, indicating in-canopy $NO_2$ loss processes which authors mostly attribute to daytime organic nitrate production. Eugster et al. (1996) in their analysis of eddy covariance flux observations of $NO_2$ over a managed grassland in central Switzerland (Hesterberg et al., 1996) found that accounting for

counteracting fluxes of soil-emitted NO, oxidized to $NO_2$ below the height of the sensor (ca. 2.7 – 3.6 ng N $m^{-2}$ $s^{-1}$), resulted in an increase in inferred nocturnal $V_{d(NO_2)}$ by up to a factor of 2. Sensitivity tests showed a 50% change in estimated soil NO emission resulted in a change in inferred $V_{d(NO_2)}$ on the order of 25% (Eugster and Hesterberg, 1996).

In an effort to isolate the contribution that dry deposition makes to nocturnal above-canopy eddy covariance fluxes ($F_{EC}$) of $NO_2$, we infer $V_{d(NO_2)}$ following 3.8 to account for the effects of: (i) nocturnal chemical flux divergence ($V_{chem}$) and (ii) counteracting soil NO emissions assumed to rapidly titrate with $O_3$ and ventilate the canopy as $NO_2$ ($F_{soil}$). The resulting $V_{d(NO_2)}$ is a best estimate of the nocturnal dry deposition pathway with which to evaluate parameterizations:

$$V_d + V_{chem} = -V_{ex} = -\frac{(F_{EC} - F_{soil})}{[NO_2]} \quad (3.8)$$

where $V_{ex}$ is the eddy covariance observed $NO_2$ exchange velocity which does not assume predominant deposition and therefore has sign convention analogous to $F_{EC}$; $V_{chem}$ represents an estimate of below sensor nocturnal chemical loss of $NO_2$ via formation and loss of $N_2O_5$, limited by the rate of oxidation of $NO_2$ with $O_3$ (Browne and Cohen, 2012; Jacob, 2000). We use an estimate of the maximum rate of nocturnal chemical loss of $NO_2$ proposed by Horii et al. (2002) in their analysis of the data used herein, $V_{chem} \sim 0.05$ cm $s^{-1}$, which translates to a below sensor (< 29 m) nocturnal chemical lifetime of $NO_2$ to oxidation by $O_3$ of ca. 16 h at this site.

Within-canopy $NO_x$ loss processes removing up to 70–80% of soil-emitted NO in mature forest ecosystems have been required to reconcile measured soil NO emissions with above-canopy $NO_x$ observations (Jacob and Wofsy, 1990; Lerdau et al., 2000; Min et al., 2014). Emitted from soils as NO and deposited within canopies as $NO_2$, deposition-based parameterizations of soil $NO_x$ canopy reduction factors (CRF) for use in large-scale CTMs yield global mean reductions in above-canopy soil $NO_x$ fluxes from ca. 20% (Wang et al., 1998) to 50% (Yienger and Levy, 1995). We estimate hourly soil NO fluxes ventilated from the canopy as $NO_2$ ($F_{soil}$) by:

$$F_{soil}(hr) = F_{NO,max}\, \kappa\, [1 - CRF(hr)] \quad (3.9)$$

where $F_{NO,max}$ is the reported summertime peak nocturnal soil NO emission flux at the HFEMS (0.6 ppb cm $s^{-1}$), and $\kappa$ is a month-specific scale factor obtained by normalizing simulated monthly mean nocturnal soil NO emission output at the location of the HFEMS from a high resolution (0.25˚ x 0.3125˚) GEOS-Chem simulation by the peak monthly mean simulated emission (July at the location of HFEMS) (Fig. S3.6). Soil NO in GEOS-Chem follows the Berkeley-Dalhousie Soil $NO_x$ Parameterization (Hudman et al., 2012), where 60% of dry and wet deposited reactive nitrogen contributes to an available soil nitrogen reservoir which decays with an e-folding lifetime of 6 months. We parameterize $CRF$ at hourly resolution following the method used in GEOS-Chem, as implemented by Wang et al. (1998):

$$CRF = \frac{k_d}{k_v + k_d} \tag{3.10}$$

where $k_v$ [m $s^{-1}$] is the canopy air exchange/ventilation coefficient (Martens et al., 2004; Trumbore et al., 1990) and $k_d$ [m $s^{-1}$] the deposition coefficient for $NO_2$ in canopy air. $k_v$ is an empirical function of land-type, surface wind speed, and LAI and is tuned to yield canopy air residence times for soil-emitted inert tracers in the Amazon Rainforest of 1 h during daytime and 5 h at night (Jacob and Wofsy, 1990). Nocturnal canopy air residence times on the order of 2 to 10 h for the Amazon Rainforest have been estimated from in-canopy measurements of soil-emitted $^{222}$Rn (Martens et al., 2004; Trumbore et al., 1990). Application of $k_v$ to additional land types in GEOS-Chem follows:

$$k_v = k_v^{RF} \sqrt{\frac{u^2}{9} \frac{7}{LAI}} \frac{\gamma^{RF}}{\gamma} \tag{3.11}$$

where $u$ is the wind speed 10 m above the displacement height, $k_v^{RF}$ is the gas exchange coefficient tuned for the Amazon Rainforest ($LAI$ = 7, $u$ = 3 m $s^{-1}$) with daytime and nighttime values of 1x$10^{-2}$ m $s^{-1}$ and 2x$10^{-3}$ m $s^{-1}$, respectively, and $\gamma$ a nondimensional extinction coefficient for in-canopy wind speed with a value of 4 for both Rain Forest and temperate forest ecosystems (Wang et al., 1998). The deposition coefficient $k_d$ in GEOS-Chem is taken as $R_c(NO_2)^{-1}$. Hudman et al. (2012) show this representation of the CRF in GEOS-Chem results in a 16% global reduction in above-canopy $NO_x$ emission. Herein we

compute the CRF following 3.10 and 3.11 using site specific meteorology and canopy parameters. We set $k_d = [(R_c(NO_2)^{-1} + R_{chem}(NO_2 \rightarrow N_2O_5)^{-1}]$, where in addition to canopy uptake as described through $R_c(NO_2)$, we include an estimate of the minimum canopy resistance to nocturnal chemical loss of $NO_2$, $R_{chem}(NO_2 \rightarrow N_2O_5) = V_{chem}^{-1} \sim$ 2000 s $m^{-1}$. We note that $k_d$ following this approach assumes that soil NO is oxidized to $NO_2$ by $O_3$ on a much shorter timescale (minutes) than nocturnal vertical mixing of ground-level air parcels—a reasonable assumption given that: (i) nocturnal in-canopy $O_3$ concentrations on the order of 10 to 25 ppb are much greater than NO concentrations at this site (Horii et al., 2004; Munger et al., 1996) and (ii) air-parcel residence times for stable evening/nighttime conditions are on the order of tens of minutes to hours in the lower canopy of mature forests (Bannister et al., 2022; Martens et al., 2004; Trumbore et al., 1990). Recent observations of daytime air-parcel residence times in mature forest canopies are on the order of tens of seconds to a few minutes (Bannister et al., 2022; Martens et al., 2004)—much less than 1 h to which daytime $k_v^{RF}$ in 3.11 is tuned. Although beyond the scope of this work, updating the parameterization of $k_v$ in GEOS-Chem to yield more realistic daytime canopy air residence times, i.e., (Gerken et al., 2017), seems warranted. Reductions in simulated daytime canopy air residence times would result in commensurate reductions to CRF following 3.10 due to reduced time for deposition of $NO_2$ prior to canopy ventilation, however, incorporation of canopy $NO_x$ chemistry into CRF parameterization could partially offset these reductions (Delaria and Cohen, 2020; Min et al., 2014). Given the nocturnal focus of this study, we proceed herein using the CRF parameterization from GEOS-Chem, modified to include nocturnal chemical loss of $NO_2$ in addition to deposition, as previously discussed.

*3.4.3.2. Evaluation of Parameterized $V_d(NO_2)$*

Figure 3.2 depicts monthly nocturnal $V_d(NO_2)$ measured over the HFEMS from April–November 2000 alongside coincidently-sampled simulated values from parameterizations P5–7. Table 3.3 presents measured and simulated values of $V_d(NO_2)$ aggregated across all months, as well as associated canopy reduction factors (CRF) used to adjust measured $V_d(NO_2)$ for soil-emitted NO. As previously mentioned, observed hourly $V_d(NO_2)$ were subjected to an outlier filter (Fig. S3.5) prior to computation of mean values, whereas

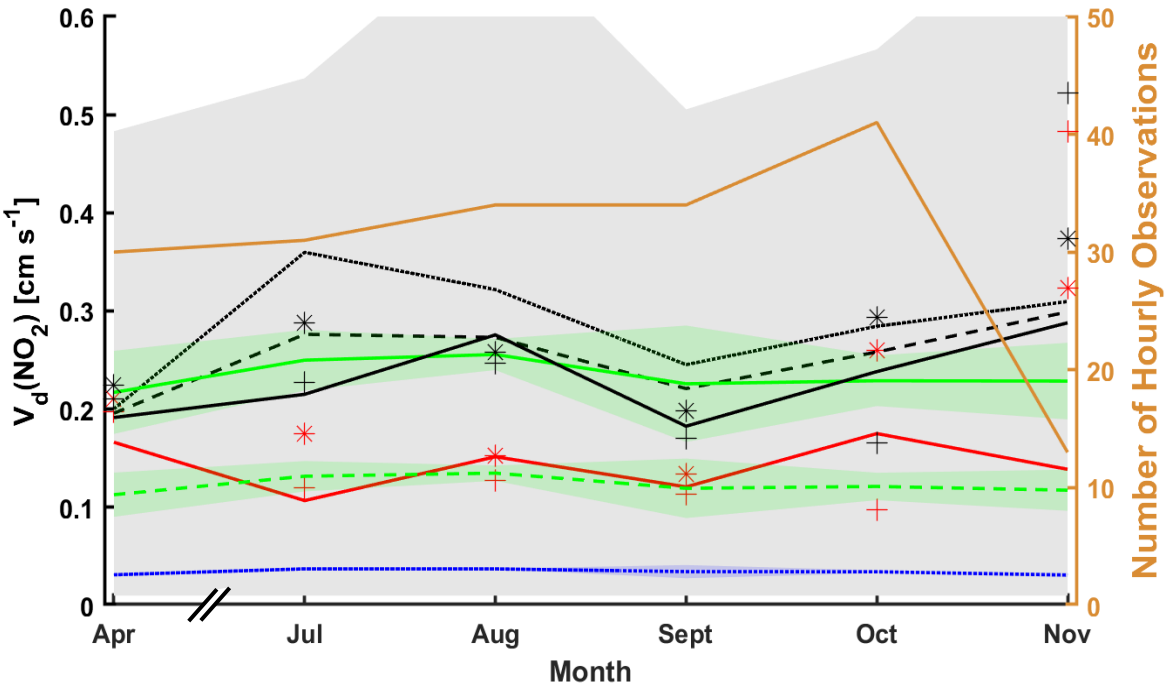


**Figure 3.2:** Monthly nocturnal (20:00–04:00 LST) $NO_2$ deposition velocities $V_d(NO_2)$ over Harvard Forest. Measured values (un)corrected for soil NO are shown in (**red) black** for mean (—), median (+), and the ratio of 'monthly mean $NO_2$ flux–to–monthly mean $NO_2$ concentration' (∗). Coincidently sampled (hourly) simulated monthly mean $V_d(NO_2)$ is depicted for parameterizations P5 (**blue**), P6 (**green dashed)** and P7 (**green solid)** which have $r_{hyd}$ (E17) α values of 0, 1, and 2, respectively. Measured monthly mean $V_d(NO_2)$ corrected for soil NO emission use simulated soil NO canopy reduction factors (E16, Fig. A6) computed with $R_c(NO_2)$ (E16) from parameterizations P5 (**black dotted**), P6 (**black dashed**), and P7 (**black solid**). Standard deviation about simulated monthly mean values, as well as measured mean values corrected for soil NO emission using CRF P7, are depicted as shaded areas. Also depicted are the number of hourly observations contributing to mean quantities (**orange**). Insufficient data prevented analysis for May and June (Fig. S3.8).

median and 'monthly mean flux–to–monthly mean concentration' ratios ( $\bar{F}/\overline{[NO_2]}$ ) were not, and instead computed directly from $u^*$ filtered (> 0.2 m $s^{-1}$) hourly data as the latter two statistics are less influenced by outliers than arithmetic means. Aggregate values of $\bar{F}/\overline{[NO_2]}$ in Fig. 3.2 and Table 3.3 are in the same units as $V_d(NO_2)$ [cm $s^{-1}$] and include corrections for $F_{soil}$ and $V_{chem}$ as do mean and median quantities computed from hourly values following 3.8. Assuming first order dependence of dry

**Table 3.3:** Nocturnal (20:00–04:00 LST) $NO_2$ deposition velocities over Harvard Forest aggregated from April – November 2000. Measured values, with and without soil NO corrections estimated using canopy reduction factors (CRF) corresponding to parameterizations P5, P6, and P7 are shown along with coincidently sampled (hourly) simulated values.

| | | $V_d(NO_2)$ [cm $s^{-1}$] | | |
|---|---|---|---|---|
| | **CRF** | 230 hourly obs. ($u_* > 0.2$ m $s^{-1}$) | | |
| | [%] | mean[(a)] | median | $\bar{F}/\overline{[NO_2]}$ |
| **Measured** | | | | |
| no soil NO | N/A | 0.15 ± 0.34 (185) | 0.13 | 0.21 |
| soil NO, CRF(P5) | 31 | 0.28 ± 0.35 (181) | 0.25 | 0.30 |
| soil NO, CRF(P6) | 47 | 0.25 ± 0.34 (181) | 0.22 | 0.28 |
| soil NO, CRF(P7) | 59 | 0.23 ± 0.35 (183) | 0.21 | 0.26 |
| **Parameterization** | | | | |
| P5 (*D* update) | N/A | 0.04 ± <0.01 | 0.04 | - |
| P6 (α = 1) | N/A | 0.12 ± 0.02 | 0.13 | - |
| P7 (α = 2) | N/A | 0.24 ± 0.04 | 0.24 | - |

[(a)] measured $V_{ex}(NO_2)$ were subjected to an outlier filter (Fig. S3.5) prior to computing mean $V_d(NO_2)$; remaining number of hourly observations are included adjacent corresponding mean values.

deposition for $NO_2$, computing values of $\bar{F}/\overline{[NO_2]}$ over long averaging times is a strategy to reduce the influence of random variability in deposition velocity estimates, especially under low $NO_2$ conditions as depicted in Fig. S3.5. Although below and in subsequent sections we report biases between simulated and measured $V_d(NO_2)$ using mean values, median and $\bar{F}/\overline{[NO_2]}$ values of $V_d(NO_2)$ are included for comparison in some depictions. We begin discussion of eddy-covariance inferred (measured) bulk canopy $V_d(NO_2)$ below, followed by discussion of the bias in simulated values stemming from the widely used Wesely 1989 parameterization of surface resistances. In subsequent section 3.4.3.3 we discuss mechanistic updates to the parameterization of $NO_2$ surface resistance (i.e., P5 & P7) developed to remedy large biases in nocturnal $V_d(NO_2)$ computed following Wesely 1989 (i.e., P5).

Measured $V_d(NO_2)$ uncorrected for the influence of soil-emitted NO (i.e., $F_{soil} = 0$) show monthly mean values in the range of 0.1 – 0.2 cm $s^{-1}$, with maximums in $V_d(NO_2)$ occurring in spring and fall months, possibly an artifact from neglecting soil NO influence

on measured $NO_2$ fluxes. For cooler months, soil NO emissions are a much smaller fraction of the peak summertime value (Fig. S3.6)—April (25%), October (50%), and November (25%). Although variability in measured nocturnal $V_d(NO_2)$ is large with standard deviations greater than mean values, corrections for above-canopy soil $NO_x$ emission results in a significant ($p < 0.03$) increase in measured nocturnal $V_d(NO_2)$ yielding monthly mean values in the approximate range of 0.2 – 0.3 cm $s^{-1}$ with potential seasonality being less apparent. Large variability in eddy covariance observed $NO_2$ flux and resulting deposition velocities have been noted in other studies (Eugster and Hesterberg, 1996; Farmer et al., 2006; Geddes and Murphy, 2014), wherein authors restrict analysis to temporally averaged values in order to reduce the effects of variability in these complex ecosystem-scale observations (Baldocchi, 2003). There are many contributions to variance in eddy covariance observations that dry deposition parameterizations would not be expected to capture, including intermittent turbulence, advection of air masses resulting in symmetrical canopy breathing fluxes, and instrumentation noise (Delany et al., 1986; Munger et al., 1996; Stella et al., 2012). Herein, we restrict analysis to aggregate values of at least one month, as simple resistance-in-series parameterizations of dry deposition employing 'big leaf' representations of $R_c$ are designed for computational expediency, general applicability over a wide range of compounds and land-types, and to reflect average estimates over weeks to months and therefore lack the necessary complexity to capture the full range of short-term variability in deposition velocities at specific sites (Wesely, 1989). Our objective is to address potential long-term biases in the parameterization of non-stomatal $V_d(NO_2)$ in GEOS-Chem, noted to be significant by Horii et al. (2002) in their initial presentation of this dataset.

Parameterization P5, which computes $R_c(NO_2)$ following the Wesely 1989 representation in GEOS-Chem, yields simulated nocturnal $V_d(NO_2)$ biased low by nearly 4x compared to observed nocturnal mean $V_d(NO_2)$ uncorrected for soil-emitted NO, increasing to a 7x low bias after correction for soil-emitted NO with a nocturnal CRF of 31% (Table 3.3). This underestimate is driven by a large nocturnal $R_c(NO_2)$ of ca. 2,700 s $m^{-1}$ in parameterization P5 (Fig. S3.8), and has been noted in previous studies comparing $NO_2$ dry deposition simulated by the Wesely 1989 parameterization to eddy covariance flux observations over forest (Horii, 2002) and grassland (Eugster and Hesterberg, 1996)

ecosystems. In particular, Eugster et al. (1996) infer a nocturnal non-stomatal $R_c(NO_2)$ median value of 700 s $m^{-1}$ (range 500 – 950 s $m^{-1}$) over a managed grassland in central Switzerland—a surface resistance on the order of 4x lower than predicted by0 the Wesely 1989 algorithm.

*3.4.3.3 Representation of $NO_2$ Hydrolysis on Deposition Surfaces*

Hori et al. (2004) note that observed nocturnal dry deposition of $NO_2$ may result from a surface hydrolysis reaction following R3.1. We replace the non-stomatal components of the bulk surface resistance scheme (3.5) for $NO_2$ in the base parameterization (P5) with a dry deposition pathway representing $NO_2$ hydrolysis on ground surfaces $r_{hyd}$ [s $m^{-1}$], formulated from the rate of molecular collisions with ground surfaces (Cano-Ruiz et al., 1993):

$$r_{hyd} = \frac{4}{\gamma_{g,NO_2}\,\overline{v_t}\,\alpha} \tag{3.12}$$

where $\gamma_{g,NO_2}$ is a ground uptake coefficient for $NO_2$ resulting from heterogeneous hydrolysis on deposition surfaces (R3.1), $\overline{v_t}$ the mean thermal speed of $NO_2$, and $\alpha$ a dimensionless scale factor introduced herein to facilitate application of 3.12 across land-types of varying surface area densities. Lammel et al. (1996) recommend reaction R3.1 be parameterized in atmospheric chemistry models using field-derived uptake coefficients, as realistic conditions (i.e., surface area density) are difficult to reproduce in the lab. We employ the field-derived ground uptake coefficient $\gamma_{g,NO_2}$ from VandenBoer et al. (2013), determined from resulting HONO emitted into the nocturnal boundary layer over a wintertime agricultural region in Colorado, U.S.A. (former BAO site). Consistent with the heterogenous hydrolysis of $NO_2$ requiring adsorbed water to proceed, VandenBoer el al. (2013) parameterize $\gamma_{g,NO_2}$ as a function of RH [%] according to 3.13 to capture the factor of 2 variability in $\gamma_{g,NO_2}$ on either side of their best fit value (8 x $10^{-6}$):

$$\gamma_{g,NO_2} = \frac{RH}{50}\,8\,x\,10^{-6} \tag{3.13}$$

Parameterization P6 computes $r_{hyd}$ with $\alpha$ = 1, resulting in a simulated nocturnal mean $V_d(NO_2)$ of 0.12 ± 0.02 cm $s^{-1}$, a threefold increase over P5 and satisfactory agreement

with observed mean $V_d(NO_2)$ uncorrected for soil-emitted NO, however, underestimating soil NO corrected observations by ca. 50% (Table 3.3). The larger nocturnal mean CRF of 47% for parameterization P6 is due to reduced nocturnal $R_c(NO_2)$ (median value ca. 750 s $m^{-1}$ for P6), resulting in a small (11%) decrease in observed mean $V_d(NO_2)$ from parameterization P5. Increasing the rate of non-stomatal uptake of $NO_2$ by computing $r_{hyd}$ with $\alpha = 2$ resulted in an unbiased simulation of nocturnal mean $V_d(NO_2)$ of 0.24 ± 0.04 cm $s^{-1}$ compared to observed mean $V_d(NO_2)$ of 0.23 ± 0.35 cm $s^{-1}$ after correction for soil-emitted NO with nocturnal mean CRF of 59% (Table 3.3). Although parameterization P7 results in satisfactory simulation of nocturnal $V_d(NO_2)$ at the HFEMS when averaged across all months (April–November), intra- and inter-month variability in observed $V_d(NO_2)$ is not captured in simulated values, as seen in Fig. 3.2. Physical justification for the scale factor value $\alpha = 2$ necessary to match simulated with observed nocturnal mean $V_d(NO_2)$ could stem from a larger surface area available for $NO_2$ heterogeneous hydrolysis in a mature forest environment compared to the U.S. Midwest wintertime agricultural region over which VandenBoer et al. (2013) derived $\gamma_{g,NO_2}$. Heterogeneous reactions not limited by transport or diffusion to reaction surfaces are governed by a collision-limited rate which scales linearly with the surface area–to–volume ratio of the reaction vessel or environment (Jacob, 2000). Heterogeneous hydrolysis of $NO_2$ may proceed on any surface accommodating adsorbed water, including foliar surfaces, bark, or elements of the forest floor (i.e., rock, soil, and debris). Despite the hydrophobic nature of many foliar surfaces, thin aqueous films have been observed on coniferous needles (Altimir et al., 2006; Burkhardt and Gerchau, 1994) and stomata-bearing surfaces of deciduous leaves (Burkhardt et al., 1999) at ambient humidities well below saturation. In addition to radiative cooling, elevated humidity within the thin laminar boundary layer surrounding leaves may result from stomatal transpiration (Burkhardt and Hunsche, 2013) or the hydraulic activation of stomata (HAS) where liquid water is drawn from sub-stomatal cavities along stomatal walls to hygroscopic material on the leaf surface (sect. 3.4.3.4) (Burkhardt, 2010). Surface area indices [$m^2$ $m^{-2}$] for various components of the HFEMS have been estimated (Fig. S3.1), including for stems and twigs (STAI = 0.9), coniferous needles (CAI = 0.8), and deciduous leaves (DLAI = 3.4 summertime maximum). Assuming round stems and twigs (Sörgel et al., 2011) and oblate coniferous needles (Oren et al., 1986;

Riederer et al., 1988), the total wintertime canopy surface area is estimated as πSTAI + 2.7CAI ~ 5 $m^2$ $m^{-2}$. We estimate the summertime canopy surface area to be ca. 12 $m^2$ $m^{-2}$ accounting for both sides of deciduous leaves or ca. 9 $m^2$ $m^{-2}$ neglecting the non-stomatous adaxial (top) surface of deciduous leaves, in agreement with typical macroscopic surface area indices for temperate and boreal forest canopies of 12 $m^2$ $m^{-2}$ (range 5 – 14 $m^2$ $m^{-2}$) (Lammel, 1999). The surface area of the forest floor, including debris, would also be much larger than the planar ground area, and that of tree bark larger than the simple geometric surface area (see section 3.4.3.5, Table S3.2).

The lack of seasonality in observed nocturnal $V_d(NO_2)$ depicted in Fig. 3.2 may reflect an interseasonal buffering of available surface area for reaction of above canopy $NO_2$ due to increased air-parcel mixing throughout the lower canopy in the absence of deciduous leaves (see section 3.4.3.5). We did not attempt to parameterize non-stomatal deposition of $NO_2$ to upper and lower canopy elements separately in our top-down optimization of $R_c(NO_2)$, as is currently the approach in the Wesely 1989 and Zhang 2003 dry deposition schemes. Due to the lack of discernible seasonal variability in observed nocturnal $V_d(NO_2)$, observations were insufficient to justify additional variables. We acknowledge that the nocturnal canopy environment to which we optimize simulated $V_d(NO_2)$ is under reduced turbulent mixing compared to daytime when the forest would experience enhanced vertical exchange (Bannister et al., 2022; Sörgel et al., 2011; Thomas and Foken, 2007). Although daytime surface area available to above-canopy deposition is therefore likely greater than at night, nighttime sensitivity of $V_d(NO_2)$ to $\alpha$ is much greater than during the day when stomata are open and foliar uptake of $NO_2$ a more substantial pathway to deposition than non-stomatal uptake (Figs. 3.5 & S3.8). Increasing $\alpha$ from 1 to 2 results in a 73% increase in $V_d(NO_2)$ at night but only a 13% increase during the day (Fig. 3.5).

The canopy compensation point for $NO_2$ is the ambient above-canopy concentration at which point consumption (i.e., dry deposition) and production (i.e., soil emission) are in balance (Duyzer et al., 1995). Studies of above-canopy $NO_2$ exchange have observed aggregate fluxes to be upward (Min et al., 2014; Vaughan et al., 2016), downward (Coe and Gallagher, 1992; Horii et al., 2004; Walton et al., 1997), and not

significantly different from zero (Geddes and Murphy, 2014)—highlighting the importance of knowledge of below-canopy $NO_x$ emission and subsequent uptake and reaction in the interpretation of above-canopy fluxes. Although foliar compensation points for $NO_2$—a concentration below which vegetation was proposed to become a net source of $NO_2$—have been observed in the past via leaf-level chamber measurements to be generally < 2 ppb (Geßler et al., 2002; Sparks et al., 2001; Weber and Renenberg, 1996), recent chamber studies employing highly specific $NO_2$ detection methods have failed to observe such foliar emission (Breuninger et al., 2013; Chaparro-Suarez et al., 2011; Delaria et al., 2020, 2018; Wang et al., 2020c). Although these chamber studies generally observe first-order uptake of $NO_2$ under controlled conditions, constant $V_{d(NO_2)}$ inferred from linear regression of eddy covariance fluxes of $NO_2$ vs. concentration is not expected due to variability in turbulence and surface conditions affecting uptake (i.e., surface wetness, stomatal aperture, and surface area). By restricting analysis to nocturnal conditions when RH is generally high (Fig. S3.2, Table S3.3), stomata assumed closed, and turbulence well established ($u^* > 0.2$ m $s^{-1}$), we find monthly aggregate $V_{d(NO_2)}$ relatively constant in the range 0.2 – 0.3 cm $s^{-1}$ across April – November, with expected large variability on finer timescales (i.e., $\sigma$ = 0.35 cm $s^{-1}$ across the hourly dataset). Linear regression of hourly nocturnal $NO_2$ flux vs ambient $NO_2$ concentration (Fig. S3.5) yields $V_{ex(NO_2)}$ of -0.40 cm $s^{-1}$ ($p < 0.01$) over the entire $NO_2$ concentration range (up to ca. 30 ppb), and -0.26 cm $s^{-1}$ ($p < 0.01$) when the four outlying hourly observations around 30 ppb $NO_2$ are excluded—consistent with the findings of Horri et al. (2004) in their initial presentation of this data. Inferred $V_{d(NO_2)}$ = 0.21 cm $s^{-1}$ is obtained from $V_{ex(NO_2)}$ = -0.26 cm $s^{-1}$ after subtraction of $V_{chem}$ = 0.05 cm $s^{-1}$—similar to aggregate values presented in Table 3.3. The y-axis intercept of 0.11 ppb cm $s^{-1}$, although not significant ($p > 0.1$), is in line with the mean (April–November) above-canopy $NO_2$ flux of 0.13 ppb cm $s^{-1}$ resulting from estimates of soil NO emission with an average canopy reduction factor of 59% (Table 3.3, Fig. S3.6). A CRF of ca. 70% is obtained from the ratio of y-axis intercept (0.11 ppb cm $s^{-1}$, Fig. S3.5) to seasonal mean below-canopy soil NO flux (0.39 ppb cm $s^{-1}$). An $NO_2$ canopy compensation point for Harvard Forest is approximated by the x-axis intercept of ca. 0.4 ppb (Fig. S3.5).

By replacing the non-stomatal pathways of $NO_2$ deposition from the Wesely 1989 algorithm with $r_{hyd}$ according to 3.12, we assume that non-stomatal deposition of $NO_2$ is

due entirely to heterogeneous hydrolysis (R3.1). The once assumed mechanism of $NO_2$ uptake to the interior of leaves was thought to involve second-order aqueous phase hydrolysis of dissolved $NO_2$ yielding nitrite and nitrate within the moist leaf interior (apoplastic space) (Park and Lee, 1988). Ramge et al. (1993) note that second-order hydrolysis of aqueous $NO_2$ is too slow to explain observed rates of foliar uptake, proposing instead an additional pathway involving $NO_2$ scavenging by antioxidants, namely ascorbate. (Teklemariam and Sparks, 2006) found foliar uptake of $NO_2$ correlated with leaf ascorbate concentrations, although variation in plant ascorbate was induced in part by growth under variable light conditions which is known to influence leaf mesophyll cell density and therefore apoplastic surface area available for reaction (Nobel et al., 1975). Ammann et al. (1995) propose that first-order heterogenous hydrolysis of $NO_2$ (R3.1) be considered as a possible mechanism contributing to foliar uptake given the large apoplastic surface area within the interior of leaves—a factor of 10-50 greater than the corresponding LAI (Nobel et al., 1975). Zhang et al. (2003) neglect solubility contributions to $NO_2$ uptake in their dry deposition scheme, relying entirely on similarity to $O_3$ reactivity. The Wesely 1989 dry deposition scheme assigns $NO_2$ to the 'slightly reactive' category, intended for substances with limited biological reactivity but still requiring very small leaf mesophyll resistances so as to deposit under stomatal control. This classification of the Wesely scheme does not result in significant non-stomatal deposition, yielding a non-stomatal $R_c(NO_2)$ of ca. 2,700 s $m^{-1}$ at the HFEMS—much above inferred values, as previously discussed. Adding $r_{hyd}$ in parallel to the Wesely 1989 non-stomatal deposition pathway, instead of in replacement of, results in a slight increase in simulated mean $V_d(NO_2)$ over the HFEMS for parameterization P7 of ca. 10%—still supporting P7 with $\alpha > 1$, but possibly not as large as $\alpha = 2$. Variability in observed $V_d(NO_2)$ and uncertainties in the assumption of a non-stomatal $R_c(NO_2)$ pathway following similarity to $SO_2$ and $O_3$ uptake make more precise recommendations difficult.

Given the dependence of $r_{hyd}$ on surface area, land-type specific $\alpha$ values evaluated across seasons would be desirable to improve confidence for use in global CTMs. As previously mentioned, Eugster et al. (1996) infer a nocturnal non-stomatal $R_c(NO_2)$ median value of 700 s $m^{-1}$ (range 500 – 950 s $m^{-1}$) over a managed grassland in central Switzerland from soil NO corrected eddy covariance observations—similar to the median value of 750

s $m^{-1}$ simulated herein over the HFEMS (Fig. S3.9) following 3.12 with $\alpha = 1$. Pilegaard et al. (1998) report nocturnal $R_c(NO_2)$ of 771 ± 111 s $m^{-1}$ inferred from eddy covariance observations over a harvested wheat field (with re-growth) in southern Germany during mid-September. Although soil $NO_x$ contributions to above-canopy $NO_2$ flux were not considered in the analysis, given the high nocturnal $NO_2$ concentrations of 10 -30 ppbv at this location, soil $NO_x$ most likely had a reduced relative effect on resulting $V_d(NO_2)$ compared to the large influence noted by Eugster et al. (1996) where nocturnal $NO_2$ < 10 ppbv for periods when soil $NO_x$ emission would occur (T > 5 °C). Coe et al. (1992) use eddy covariance to estimate a non-stomatal $R_c(NO_2)$ of 548 s $m^{-1}$ over a Heather moorland located in southern Netherlands. Plake et al. (2015) find a maximum median nocturnal bulk $R_c(NO_2)$ over a natural grassland site in Mainz, Germany (August–September 2011) of 560 s $m^{-1}$ via the dynamic chamber approach, attributing all flux of $NO_2$ to deposition as soil NO emissions for this nutrient poor site were below detection limits of the chamber. The nocturnal $R_c(NO_2)$ values reported by Coe et al. (1992) and Plake et al. (2015) are intermediate between $r_{hyd}$ values computed using α = 1 & 2. Assigning α = 1 for low roughness vegetative land-types appears reasonable, but may yield slight underestimates in nocturnal aggregate $R_c(NO_2)$ under some conditions.

Reaction R3.1 has been observed to proceed efficiently on ice surfaces, even at low temperatures (<170 k) (Bang et al., 2015; Kim and Kang, 2010). Stocker et al. (1995) observe via eddy correlation nocturnal deposition of $NO_2$ to a snow-covered grassland in northern Colorado and report a median resistance to surface uptake of 740 s $m^{-1}$—similar to $r_{hyd}$ of 725 s $m^{-1}$ following 3.12 with α = 1, mean thermal speed ($\bar{v}_t$) computed at 260 K, and $\gamma_{g,NO_2}$ following 3.13 at 100% RH for snow covered ground. If $NO_2$ deposition persists into winter months at levels observed for late fall (Fig. 3.2), this represents a significant depositional sink for wintertime $NO_2$ not currently represented in CTMs when both the lifetime and near surface concentrations of $NO_x$ are at a maximum.

*3.4.3.4 Assumption of Nocturnal Stomatal Closure*

Many estimates of non-stomatal dry deposition for various atmospheric trace gases have been made from nighttime data under the assumption that stomata are closed and therefore nocturnal stomatal conductance negligible—an assumption also made herein. Stomatal

pores exist in leaves to optimize plant water-use-efficiency—the number of molecules of $H_2O$ transpired per molecule of $CO_2$ fixed via photosynthesis. Stomatal aperture is under guard cell regulation in response to environmental conditions such as solar radiation, guard cell $CO_2$ concentration, soil moisture, water vapor pressure deficit (VPD), and temperature (Costa et al., 2015; Nobel, 2009). Fully open stomata occupy ca. 0.2% – 2% of leaf surface area, with a density of ca. 50 to 300 stomata per $mm^2$ on the stomata containing surfaces of leaves of temperate terrestrial plants, making available a moist interior leaf surface area to photosynthetic mesophyll cells that is in the range of 10–50 times larger than the projected leaf area (LAI) (Nobel, 2009; Nobel et al., 1975).

Stomatal aperture is interdependent on several factors and has proven difficult to generalize. Despite longstanding uncertainty regarding nocturnal stomatal behavior (Caird et al., 2007; Costa et al., 2015; Dawson et al., 2007), it is generally assumed that at night in response to elevated guard cell $CO_2$ concentrations due to cellular respiration and the absence of photosynthetically active radiation (PAR), the stomata of C3 and C4 plants are nearly closed (Nobel, 2009), therefore shunting trace gas exchange. In both the widely used Wesely 1989 and Zhang 2003 dry deposition schemes, stomata are assumed to be closed at night and therefore all nocturnal deposition parameterized through non-stomatal pathways. This despite studies on a number of plant species that have noted up to 75% of species exhibit nocturnal transpiration above that expected from cuticular water loss when stomata are fully closed (Caird et al., 2007; Snyder et al., 2003). Although branch enclosure (chamber) studies consistently find stomatal control dominates daytime foliar uptake of $NO_2$, uncertainty remains regarding the importance of non-stomatal pathways at night. Some studies note negligible non-stomatal contributions to $NO_2$ deposition, attributing observed nocturnal/dark uptake to partially open stomata (Chaparro-Suarez et al., 2011; Delaria et al., 2020; Gebler et al., 2000; Rondón et al., 1993; Sparks et al., 2001), while others find non-stomatal contributions to be non-negligible (Geßler et al., 2002; Hanson et al., 1989; Thoene et al., 1996; Wang et al., 2020c; Weber and Renenberg, 1996). This amalgam of contradicting results warrants further consideration.

Both canopy-scale and leaf-level observations of trace gas uptake attempt to separate stomatal from non-stomatal pathways. A simple approach is to assign

nocturnal/dark uptake as entirely non-stomatal, dependent on the assumption of stomatal closure. Chamber studies may induce stimuli known to reduce stomatal aperture, such as water stress, elevated $CO_2$, and the plant hormone abscisic acid (ABA) (Chaparro-Suarez et al., 2011; Costa et al., 2015; Delaria et al., 2020). Trace gas specific stomatal conductance ($g_{sx}$) may also be deduced by scaling stomatal conductance to water vapor ($g_s$)—inferred in chamber studies by normalizing measured water vapor flux by leaf VPD (Delaria et al., 2020; Thoene et al., 1996; Wang et al., 2020c), and in canopy-scale studies by inversion of the Penman-Monteith equation using above-canopy water vapor flux (Lamaud et al., 2009)—by the ratio of diffusivities $D_x/D_{H_2O}$ in air. Estimates of stomatal conductance enable separation of non-stomatal from stomatal uptake, including estimates of mesophilic resistance to the leaf interior, by non-linear fits to plots of $V_d(x)$ vs $g_{sx}$ (Delaria et al., 2020). However, this method assumes that the measured evaporative flux is due entirely to gaseous diffusion of water vapor through stomatal pores, without contribution from other sources including evaporation from soil or moisture that may be present on canopy elements as a result of precipitation, dew, or elevated humidity. Significant scatter and elevated values in inferred stomatal conductance have been noted at the canopy scale for RH > 60% and for a period of time (days) following rainfall, motivating effort to fit relations of $g_s$ to $CO_2$ assimilation flux (which assume nocturnal stomatal closure) on ideal days for application across all conditions of canopy moisture (Lamaud et al., 2009; Plake et al., 2015; Stella et al., 2013).

Mounting evidence exists for the presence of thin aqueous films on foliar surfaces at ambient humidities well below saturation, resulting from the deliquescence of deposited hygroscopic material in the high humidity laminar boundary layer of transpiring leaves (Burkhardt et al., 1999, 2001a; Burkhardt and Gerchau, 1994; Burkhardt and Hunsche, 2013; Grantz et al., 2018). Concentrated solutions of deliquesced material have sufficiently low surface tension to spread over hydrophobic leaf cuticles and penetrate stomatal pores as thin liquid films (< 100 nm thick), connecting to apoplastic liquid water within the leaf interior—a process known as ‘hydraulic activation of stomata’ (HAS) (Burkhardt, 2010). An osmotic gradient in water potential drives water movement through hydraulically activated stomata to the leaf exterior where evaporation occurs uncoupled from stomatal

aperture—a process known as 'wicking'. This additional pathway for water efflux escapes stomatal regulation, therefore reducing plant water-use-efficiency and drought tolerance. Significant increases in minimum cuticular conductance to water on the order of 23% - 30% have been noted across both coniferous and deciduous tree species for foliage exposed to ambient air (ionic aerosol concentration of 4.9 μg $m^{-3}$) compared to filtered air (ionic aerosol concentration of 0.67 μg $m^{-3}$), with leaf cuticle loads of ionic mass of 1.66 μg $cm^{-2}$ and 9.01 μg $cm^{-2}$ after 1 and 2 yr of exposure, respectively (Burkhardt et al., 2018); it was noted that this ambient ionic aerosol concentration, consisting mostly of nitrate, was about half of that implicated in causing widespread forest decline over northeastern Bavaria during the late 1980's. Similar experiments conducted on shorter lived faba beans (*Vicia faba*) across multiple seasons noted significant increases in both minimum cuticular conductance (16% average, 80% max. for July) and nocturnal stomatal conductance (ca. 40%) to water (Grantz et al., 2018). Foliar exposure studies to elevated concentrations of hygroscopic aerosol have found large increases in nocturnal stomatal conductance (80–90%) when stomatal aperture was at a minimum, decreasing to less than 30% for: (i) fully open stomata when water vapor dominates transpiration (Burkhardt et al., 2001b) and (ii) 7 h post exposure presumably due to stomatal uptake of dissolved ions through thin aqueous films (Motai et al., 2018). The latter indicating that wicking of water via HAS requires continuous deposition of hygroscopic material to leaf cuticles in order to maintain a sufficient osmotic gradient. Cuticle loads of hygroscopic material of up to 50 μg $cm^{-2}$ in these exposure studies were in the range found on urban trees (Burkhardt, 2010).

Considering the evidence for a liquid phase water loss pathway via HAS on plants exposed to modest levels of hygroscopic aerosol, overprediction of stomatal conductance inferred from water vapor flux or sap flow measurements may exist in studies conducted near urban environments—especially under dark conditions when stomatal aperture is at a minimum and wicking from HAS is a larger relative fraction of total foliar water loss. Chamber studies may be particularly susceptible to this overprediction given the mechanically mixed conditions often used to minimize diffusive boundary layer resistances (Burkhardt et al., 2001b; Pariyar et al., 2013). This confounds partitioning of non-stomatal and stomatal deposition pathways, especially at night, from scaled estimates of stomatal conductance to water vapor. Additionally, nocturnal ambient RH is often elevated at

locations with lush vegetation, as it is during summer at the HFEMS (RH ~ 90%, Table S3.3), when growth of aqueous films have been observed to occlude stomatal pores (Grantz et al., 2018). Heterogeneous hydrolysis of $NO_2$ would be expected to proceed on foliar as well as other surfaces under these conditions. Thoene et al. (1996) monitor $NO_2$ uptake to Norway Spruce (*Picea abies*) using a branch enclosure and note positive correlation of $NO_2$ uptake to daytime RH between 5% to 60% that cannot be explained by changes in stomatal conductance, proposing thin water films forming on needle surfaces as a plausible explanation. Nocturnal uptake of $NO_2$ to urban-influenced vegetated surfaces through a mechanism involving HONO production has been implicated in the field on several occasions (Harrison and Kitto, 1994; Ren et al., 2020; Stutz et al., 2002), including the RH dependence of this $NO_2$ reactive uptake (Stutz et al., 2004; VandenBoer et al., 2013).

We compare the efficiency of $NO_2$ uptake to both non-foliar and foliar surfaces by compiling $NO_2$ uptake coefficients $\gamma_{NO_2}$ inferred from literature values of surface-specific (leaf-level) deposition velocities $V_d^{surf}$ (Table S3.2). All surface-specific $NO_2$ deposition velocities were obtained from chamber studies with the exception of uptake to snow which was inferred from the eddy covariance method. Values of leaf-level $V_d^{surf}$ for both deciduous and coniferous species were averaged across periods of minimum stomatal conductance resulting from the absence of PAR or the influence of ABA, and are interpreted herein for the purpose of computing resulting $\gamma_{NO_2}$ as non-stomatal. Surface areas used in flux normalization are reported when available and care must be taken when comparing surface-specific $V_d^{surf}$ and $\gamma_{NO_2}$ as various surface area indices are used (i.e., planar, geometric, LAI, and total leaf area). Indeed, some studies report $V_d^{surf}$ to coniferous species normalized to total leaf area (Breuninger et al., 2013; Hanson et al., 1989) as stomata are distributed across the whole needle surface (amphistomatic), while others normalize to projected LAI as is routinely done for deciduous leaves which generally have stomata on the lower (abaxial) leaf surface; failing to recognize this difference would result in a misrepresentation of $V_d^{surf}$ by a factor of ca. 2.7 for coniferous species (Riederer et al., 1988).

Inferred values of $\gamma_{NO_2}$ in Table S3.2 fall within the range of values expected for uptake due to $NO_2$ heterogenous hydrolysis, generally $10^{-6}$ to $10^{-5}$, supporting the

possibility that R3.1 is the predominant mechanism driving uptake to both the non-foliar and dark/ABA influenced foliar surfaces presented. Three features stand out in the tabulated values of $V_d^{surf}$ and $\gamma_{NO_2}$ presented in Table S3.2. First, an apparent dependence on surface moisture. Teflon, a hydrophobic and inert material, exhibits negligible uptake (albeit at an unknown RH), while large RH dependence is seen for uptake to tree bark, wood board, and wool carpet. The RH dependence of uptake to bark and wool is similar to the factor of two increase in $\gamma_{g,NO_2}$ between RH 50% – 100% (3.13), while for foliar surfaces which have more accurately quantified surface areas, normalized uptake was not observed to exceed that of a planar surface of distilled water (discussed further below). Secondly, surface area available for heterogeneous reaction has direct influence on resulting material-specific uptake, as expected for a collision-limited heterogeneous process such as R3.1. Surfaces with complex and undetermined microscopic surface areas (i.e., bark, wool carpet, forest floors, and snow) exhibit much higher $V_d^{surf}$ and resulting $\gamma_{NO_2}$— a factor of 3 to 30 larger than to surfaces normalized by accurate predictions of available surface area (i.e., bulk water and foliar). This increased uptake to convoluted surfaces could be an indirect measure of the total microscopic surface area available for reaction, thus highlighting the utility of using field-derived uptake coefficients in parameterizing dry deposition models. Thirdly, an interesting feature stands out between $NO_2$ uptake to coniferous vs. deciduous leaves when stomatal aperture is at a minimum. Normalized by LAI, $V_d^{surf}$ and inferred $\gamma_{NO_2}$ to coniferous species are on average 2.7x larger than to deciduous species, a factor equal to the ratio of 'total needle surface area to projected LAI' (Riederer et al., 1988). Since coniferous needles have stomata distributed across the entire leaf surface, whereas most deciduous trees have stomata located on the lower (abaxial) leaf surface and a thicker hydrophobic wax cuticle on the upper (adaxial) leaf surface, the 2.7-fold larger uptake to LAI normalized coniferous species may reflect the absence of thin water films on the adaxial surface of deciduous leaves. These inferences are consistent with the work of Summer et al. (2004) where similar rates of $NO_2$ heterogeneous hydrolysis across a variety of hydrophilic and hydrophobic surfaces were understood in the context of available surface areas supporting thin water films.

Surface area also plays an important role in trace gas uptake within the interior of leaves. Nobel et al. (1975) found that a 4-fold increase in $CO_2$ uptake per unit LAI between shade and sun leaves of the deciduous species 'Creeping Charlie' (*Plectranthus parviflorus*) can be explained by the corresponding increase in mesophyll cell surface area per unit LAI ($A^{mes}$/LAI), and that internal leaf resistance to $CO_2$ per unit area of mesophyll cells remained constant. To our knowledge, no such analysis has been conducted for foliar uptake of $NO_2$. Delaria et al. (2020) provide estimates of mesophilic resistance ($r_m$) of $NO_2$ to six coniferous and four deciduous tree species native to California, with values of $r_m$ ranging between 20 s $m^{-1}$ to 130 s $m^{-1}$ (median: 48 s $m^{-1}$, mean: 57 s $m^{-1}$) per unit LAI, which at the forest canopy scale would represent a small (< 5%) and modest (ca. 15%) fraction of bulk canopy $R_c(NO_2)$ for nighttime and daytime conditions at Harvard Forest, respectively, during summer (Fig. S3.8 & Table S3.3). Nonetheless, using the $A^{mes}$/LAI value of 50 corresponding to deciduous sun leaves from Nobel et al. (1975) and the $NO_2$ uptake coefficient to distilled water of 2.3 x $10^{-6}$ (Table S3.2), an estimate of $r_m$ due to uptake on moist intercellular leaf surfaces is ca. 100 s $m^{-1}$. This suggests, on average, an additional pathway for $NO_2$ uptake to leaf interiors with a resistance on the order of 100 s $m^{-1}$ is acting in parallel to reaction R3.1, such as $NO_2$ scavenging by apoplastic antioxidants (Farvardin et al., 2020; Msibi et al., 1993; Ramge et al., 1993; Teklemariam and Sparks, 2006). However, the assumption that the ratio $A^{mes}$/LAI = 50 is representative and constant across the species examined by Delaria et al. (2020) is a generalized approximation and further work is required to understand the mechanisms driving intra- and interspecies variability in $r_m$. Future leaf-level study into the mechanism of foliar $NO_2$ uptake would benefit from consideration of $A^{mes}$/LAI as well as apoplastic antioxidant concentrations.

*3.4.3.5 Bottom-up Estimates of Nocturnal $V_d(NO_2)$ at the HFEMS*

Surface-specific $NO_2$ uptake coefficients ($\gamma_{NO_2}$) to both foliar and non-foliar forest elements (Table S3.2) facilitate bottom-up estimates of nocturnal bulk canopy $R_c(NO_2)$ and resulting $V_d(NO_2)$ to forest environments when corresponding surface area scale factors (i.e., DLAI, CLAI, and STAI) and meteorological data (i.e., wind speed, friction velocity, temperature, and RH) are available. Bottom-up estimates of nocturnal $R_c(NO_2)$ for Harvard

Forest were computed as parallel contributions of uptake to leaves, bark, and the forest floor:

$$R_c(NO_2) = \left[1/r_{leaf} + 1/r_{bark} + 1/\left(r_a + r_{floor}\right)\right]^{-1} \quad (3.14)$$

where in-canopy aerodynamic resistance $r_a$ was computed according to Zhang et al. (2003) as a prescribed land-type specific value with LAI and friction velocity ($u*$) dependence (see Table S3.3). $NO_2$ uptake to snow is ca. 1/3 that of the forest floor (Table S3.2) and we make the assumption that the forest floor is snow covered in winter months (DJFM) when ambient temperature is below 0°C. Fig. 3.3 depicts monthly estimates of nocturnal component resistances ($r_c$) and resulting bottom-up bulk-canopy $R_c(NO_2)$ following 3.14 and $V_d(NO_2)$ following 3.2. Also depicted are monthly estimates of top-down $R_c(NO_2)$ from $r_{hyd}$ following 3.12 and resulting $V_d(NO_2)$ following 3.2. Due to the compensating seasonal contributions of $r_{leaf}$ and $r_{floor}$ to total $NO_2$ deposition, bottom-up nocturnal $V_d(NO_2)$ shows little seasonality and is in the range of eddy covariance inferred $V_d(NO_2)$ (ca. 0.2–0.3 cm $s^{-1}$) observed from spring through fall. Bottom-up and top-down estimates of $V_d(NO_2)$ agree to within 17% over the twelve month period when top-down $V_d(NO_2)$ is computed using $\alpha = 2$, diverging to 83% difference using $\alpha = 1$. Computing $NO_2$ uptake to bark using the lower (dry) uptake coefficient of $\gamma_{NO_2}^{bark} = 5.0 \times 10^{-6}$ from Table S3.2 results in bark/twig surfaces contributing about half of total nocturnal canopy dry deposition of $NO_2$. Although this chamber-measured uptake coefficient to bark is in line with additional observations of uptake to coarse wood board for RH > 50% (Table S3.2), uncertainty exists in the applicability of this single value of $\gamma_{NO_2}^{bark}$ to all stem and twig surfaces of the canopy—specifically, RH-dependence and microscopic surface area variation are absent. A sensitivity test involving a 50% reduction in $\gamma_{NO_2}^{bark}$ to $2.5 \times 10^{-6}$ increases $r_c^{bark}$ to 1.5–1.6 x $10^3$ s $m^{-1}$, reducing canopy uptake to bark surfaces from 47% to 31% over all seasons (data not shown). Resulting bottom-up $V_d(NO_2)$ (seasonal mean of 0.22 cm $s^{-1}$) is still within the range of eddy covariance inferred values (Fig. 3.2) and in better agreement with top-down estimates.

These simple estimates of bottom-up bulk canopy $V_d(NO_2)$ provide a useful sanity check on eddy covariance inferred values and are a starting point for a mechanistic

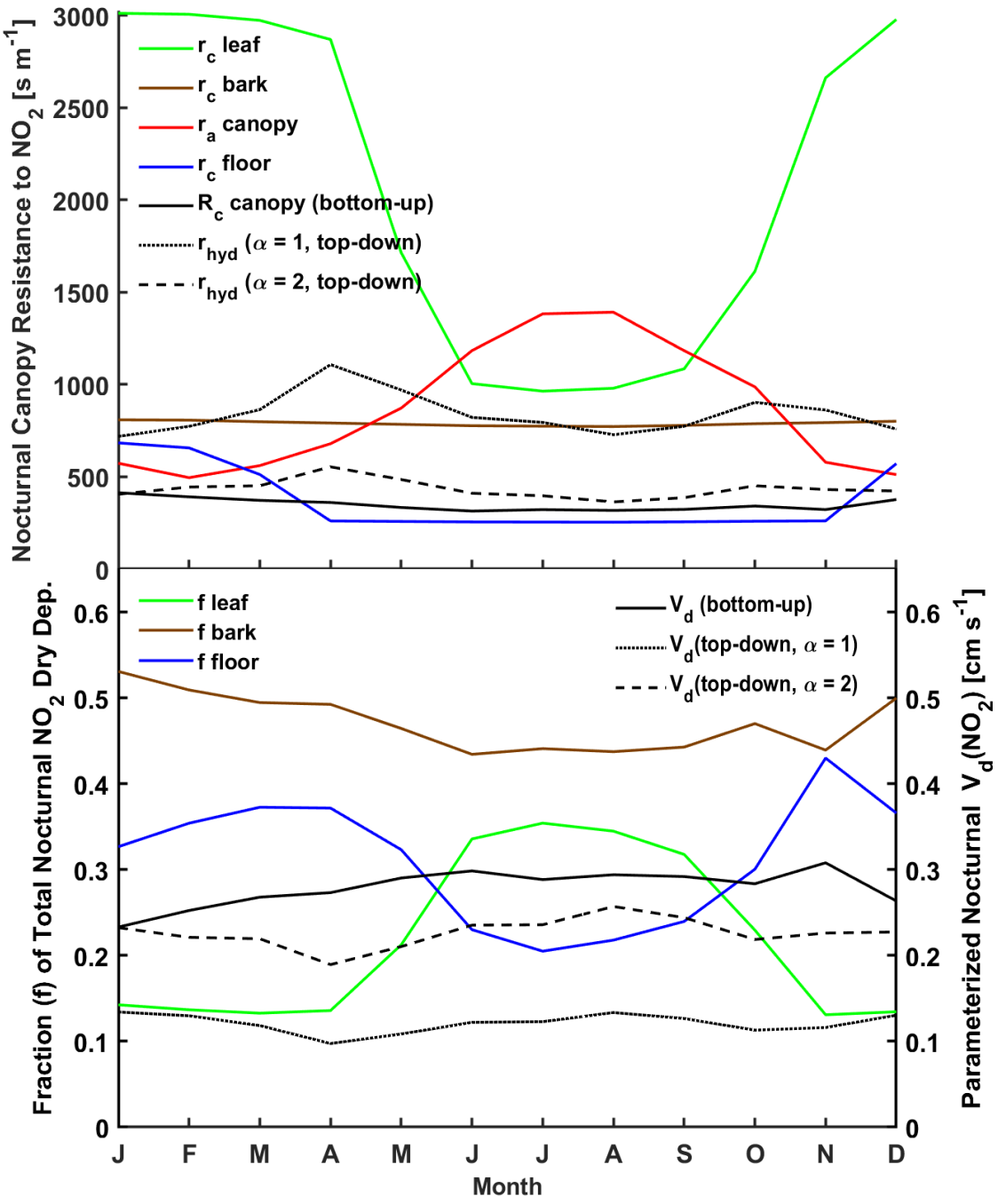


**Figure 3.3: (TOP)** Component canopy resistances $r_c$ for nocturnal $NO_2$ uptake to leaves, bark, and the forest floor at Harvard Forest, and resulting 'bottom-up' bulk-canopy $R_c$. Also included are 'top-down' optimized bulk canopy resistances $r_{hyd}$. **(BOTTOM)** Resulting 'bottom-up' and 'top-down' canopy-scale deposition velocities $V_d(NO_2)$, including fractional contributions of leaf, bark, and forest floor surfaces to total canopy $NO_2$ uptake. Monthly values of resistances, deposition velocities, and meteorological inputs are included in Table S3.3.

explanation of the lack of seasonality in inferred nocturnal $V_d(NO_2)$, namely, from a buffering of available forest surface area for uptake of above-canopy $NO_2$ across seasons.

*3.4.3.6 HONO Emission from $NO_2$ Dry Deposition*

Given the evidence for heterogeneous reaction of $NO_2$ on ground surfaces being the dominant source of near-surface nocturnal HONO outside of proximity to primary emissions (Ren et al., 2020; VandenBoer et al., 2013; Wong et al., 2011), recent implementation of R3.1 into CTMs was motivated by efforts to address widespread underestimates in simulated HONO mixing ratios. CTMs with representation of this mechanism include the Community Multiscale Air Quality (CMAQ) model (Czader et al., 2012; Gonçalves et al., 2012; Sarwar et al., 2008; Zhang et al., 2012b) and Weather Research and Forecasting model coupled with Chemistry (WRF-Chem) (Li et al., 2010; Zhang et al., 2016). To date, these implementations have followed a collision-limited heterogeneous rate constant $k_{het}$ for ground surface $NO_2$ uptake:

$$k_{het} = \frac{\gamma_{NO_2}\,\overline{v_t}}{4}\left(\frac{S_g}{V}\right) \tag{3.15}$$

where $k_{het}$ [$s^{-1}$] describes the first-order loss of $NO_2$ from the CTM's lowest level. Following R3.1, the rate of production of HONO would require $k_{het}$ to be scaled by a factor of ½. $S_g/V$ is the surface area density of ground surface elements within the lowest model level. In lab studies, S/V ratios may be computed from the geometry of well mixed reaction vessels; in the field, $S_g/V$ ratios are land-type specific and dependent on atmospheric stability. Models often parameterize $S_g/V$ for foliar surfaces as 2LAI/H, where H is the height of the lowest model level (ca. 17 m for CMAQ and 30 m for WRF-Chem) and both sides of deciduous leaves are assumed to support aqueous films sufficient for R3.1 to proceed. As discussed in section 3.4.3.4, the upper (adaxial) surface of deciduous leaves may not support sufficient water at humidities below saturation. The accurate determination of complex microscopic surface area of natural (and indoor) surfaces, together with dynamic turbulence conditions, renders $S_g/V$ a difficult parameter to pin-down.

Implementing reaction R3.1 on the ground surface via 3.15 neglects aerodynamic ($R_a$) and diffusive ($R_b$) transport terms, a reasonable assumption if $R_a + R_b << R_c$. Nocturnal median $R_c(NO_2)$ updated herein over Harvard Forest was found to be ca. 370 s m$^{-1}$ for $\alpha$ = 2—much greater than either the nocturnal median $R_a(29\ m)$ of 22 s m$^{-1}$ or $R_b(NO_2)$ of 18 s m$^{-1}$ (Fig. S3.8). Continuing to reference $R_a$ from the 29 m reference height at the HFEMS, ca. 9% of $R_a(29m)$ > 100 s m$^{-1}$ and 4% of $R_a(29m)$ > 400 s m$^{-1}$ across hourly observations from June–November 2000 (Fig. S3.4); neglecting $R_a$ under these conditions yields overestimates in resulting $V_d(NO_2)$ of 30% and 100%, respectively. Referencing $R_a$ from the center of GEOS-Chem's lowest model level (ca. 60 m) results in 14% of $R_a(60\ m)$ > 100 s m$^{-1}$ and 6% of $R_a(60\ m)$ > 400 s m$^{-1}$. Considering the large range of $R_a$ in global CTMs due to variability in surface roughness conditions and diabatic stabilities, with frequent occurrences of $R_a$ > 1000 s m$^{-1}$ under very stable nocturnal conditions (Toyota et al., 2016), implementation of R3.1 into global CTMs favours the approach developed herein where ground surface hydrolysis of $NO_2$ is treated in the context of a resistance-in-series dry deposition parameterization. Study of reactive uptake of gasses to indoor surfaces has found a transport-limited rate (i.e., $R_c$ may be neglected) when $\gamma$ > ~ 3x10$^{-4}$ for typical indoor turbulence conditions, and a collision-limited rate (i.e., $R_a + R_b$ may be neglected) when $\gamma$ < ~ 5x10$^{-7}$ (Cano-Ruiz et al., 1993)—the $\gamma_{g,NO_2}$ values for R3.1 are intermediate between these regimes, thus supporting the inclusion of both transport and surface uptake resistances.

Although the focus of this work is on the effect that R3.1 has on $V_d(NO_2)$, there is much interest in an accurate HONO simulation given that the nocturnal build-up of HONO, both in near-surface air and on deposition surfaces, results in an early morning burst of OH and NO radicals as HONO photolyzes (Finlayson-Pitts, 2009; Ren et al., 2020), initiating photochemistry prior to other $HO_x$ precursors (Platt et al., 1980). The effect of updates to $V_d(NO_2)$ via R3.1 on the HONO simulation in GEOS-Chem is the subject of Chapter 4 of this thesis.

### 3.4.4 Evaluation of Parameterized $V_d(NO_y)$

The utility of the HFEMS for evaluating parameterizations of atmosphere-surface exchange stems from the extensive datasets of meteorological, phenological, and trace gas

observations spanning many months to years at high temporal (hourly) resolution. Of particular interest for the evaluation of simulated $V_d(NO_y)$ is the period from June–November 2000, when hourly observations of above-canopy $HNO_3$ concentration—a significant contributor to $NO_y$ dry deposition at this location (Horii et al., 2005)—was added to the suit of long-term measurements which include hourly concentrations of total $NO_y$ and component species NO, $NO_2$, and PAN alongside hourly measurements of eddy covariance $NO_y$ flux (Fig. S3.7). Fig. 3.4 (top) shows a smoothed diel climatology of total $NO_y$, NO, $NO_2$, $HNO_3$ and PAN, averaged across June–November 2000–2002. Also depicted is inferred $NO_y$ calculated from the sum of aforementioned component species. Fig. 3.4 (middle) depicts species-specific fractional contributions to measured $NO_y$. On average, $NO_y$ inferred from the sum of measured component species is 77% of measured $NO_y$, with component species contributing 48% ($NO_2$), 16% ($HNO_3$), 8% (PAN), and 4% (NO) to measured $NO_y$. As discussed in Horii et al., (2005), the HFEMS is influenced by two predominant airmasses: (i) northwesterly flow which brings cool, dry, and less polluted air with an $NO_y$ concentration budget that is mostly closed by $NO_x$, $HNO_3$, and PAN, and (ii) southwesterly flow consisting of warmer, humid, and significantly more polluted air wherein up to 50% of the $NO_y$ budget remains unaccounted for, although the rank of measured contributions remains in the order $NO_2$ > $HNO_3$ > PAN > NO. The flux budget analysis of Horii et al., (2005) in their initial presentation of this dataset supported the presence of an unidentified rapidly depositing $NO_y$ species in southwesterly flows, corroborating estimates that alkyl nitrates resulting from oxidation of biogenic isoprene and monoterpenes in the presence of $NO_x$ could contribute up to 25% of summertime $NO_y$ deposition at the HFEMS (Munger et al., 1998).

To compare to $V_d(NO_y)$ inferred from measured fluxes, we compute simulated deposition velocities $V_{d,sim}(NO_y)$ from a linear combination of parameterized component deposition velocities $V_d(x_i)$ weighed by species-specific concentration fractions (Michou et al., 2005; Wu et al., 2011):

$$V_{d,sim}(NO_y) = \frac{\sum_i [x_i]\, V_d(x_i)}{\sum_i [x_i]} \tag{3.16}$$

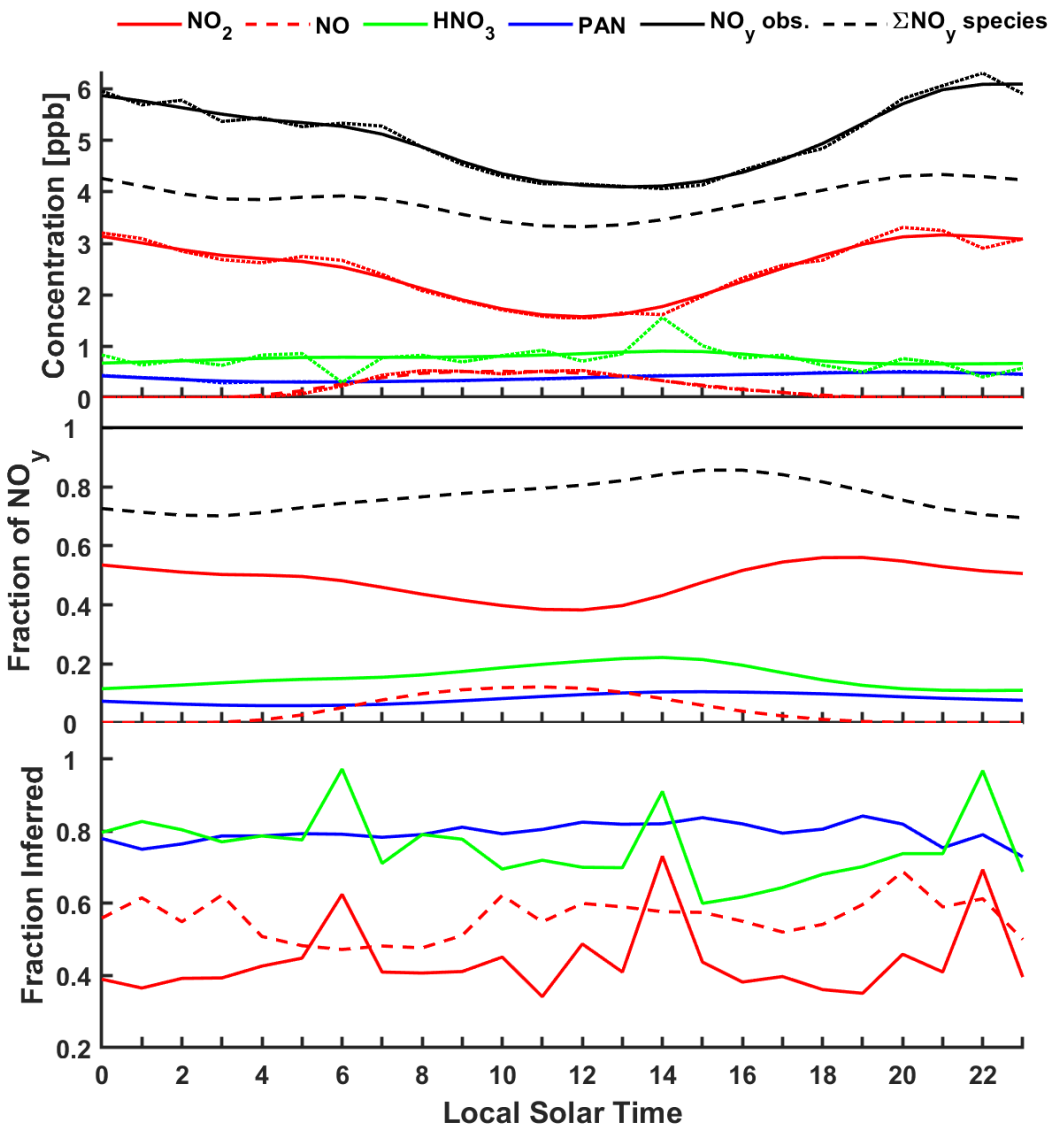


**Figure 3.4: (TOP)** Diel climatology of observed $NO_y$ and component species $NO_2$, $HNO_3$, PAN, and NO measured at Harvard Forest, MA, U.S., between June–November 2000–2002. Solid lines depict a smoothing spline fit to hourly mean concentrations (dotted). Also shown is the sum of smoothed $NO_y$ component species concentrations. **(MIDDLE)** Fractional contributions of $NO_y$ component species to measured $NO_y$ computed from ratios of smoothed diel mean concentrations (top panel). Shown are individual $NO_y$ species fractions (colored, as above), and sum of species fractions (dashed, black). **(BOTTOM)** Fraction of hourly component $NO_y$ species concentrations (colored, as above) that are inferred (equation 3.17) as a gap-filling strategy in the calculated $V_d(NO_y)$ hourly time series (equation 3.16) spanning June–November 2000.

However, due to the large number of coincident hourly observations required for the comparison, only 19 coincident hourly values exist across the entire data set consisting of over 2000 hourly measurements of $V_d(NO_y)$ from June–November 2000. For this reason, a gap-filling method is employed to estimate date (d) and hour (h) specific missing $NO_y$ component concentrations $[x_i]_{d,h}^{infer}$ of $NO_2$, NO, $HNO_3$, and PAN from measured $NO_y$:

$$[x_i]_{d,h}^{infer} = \left(\frac{\overline{[x_i]}_h^{meas}}{\overline{[NO_y]}_h^{meas}}\right)_{clim} [NO_y]_{d,h}^{meas} \quad (3.17)$$

where the diel climatology of component fractions $\overline{[x_i]}_h^{meas}/\overline{[NO_y]}_h^{meas}$, depicted in Fig. 3.4, are computed over June–November 2000–2002 and subjected to a smoothing spline fit. This method of gap-filling was employed by Wu et al., (2005) in their application of this dataset to evaluate simulated $NO_y$ deposition velocities from the WRF-Chem and NOAH-GEM dry deposition modules—a difference being that herein we compute component fractions as the ratio of smoothed means rather than the mean of ratios to reduce the effect of outliers (data not shown). The fraction of inferred species-specific hourly concentrations for the study period is depicted in Fig. 3.4. A high fraction of inferred values for PAN results from the absence of hourly observations for August–November 2000, thus relying on years 2001–2002 to inform the climatology for use in 3.17 (Fig. S3.7). $HNO_3$ is also inferred to a large degree; although hourly concentrations were measured fairly consistently from June–November 2000, monthly coverage was only about 20% (Fig. S3.7).

Figure 3.5 depicts simulated diel mean deposition velocities for $HNO_3$, PAN, and $NO_2$ over Harvard Forest, aggregated from hourly values computed using observed meteorological (Fig. S3.2) and phenological (LAI) (Fig. S3.1) inputs. Simulated component resistances $R_a$, $R_b$, and $R_c$ for $HNO_3$, $NO_2$, and PAN are depicted in Fig. S3.8. Shown for $V_d(HNO_3)$ include parameterizations P2 (base GEOS-Chem with $R_a(29m)$), P3 (RSL corrections to $R_a(29m)$ assuming $u(z_o)$>0 m/s), and P5 (improved calculation of molecular diffusivity). The small increase in daytime $R_a$ of ca. 15% due to the incorporation of the effects of the RSL according to equation 3.S10 in the supplemental material results in a small (ca. 7%), yet significant ($p<0.05$) decrease in daytime $V_d(HNO_3)$—a slightly

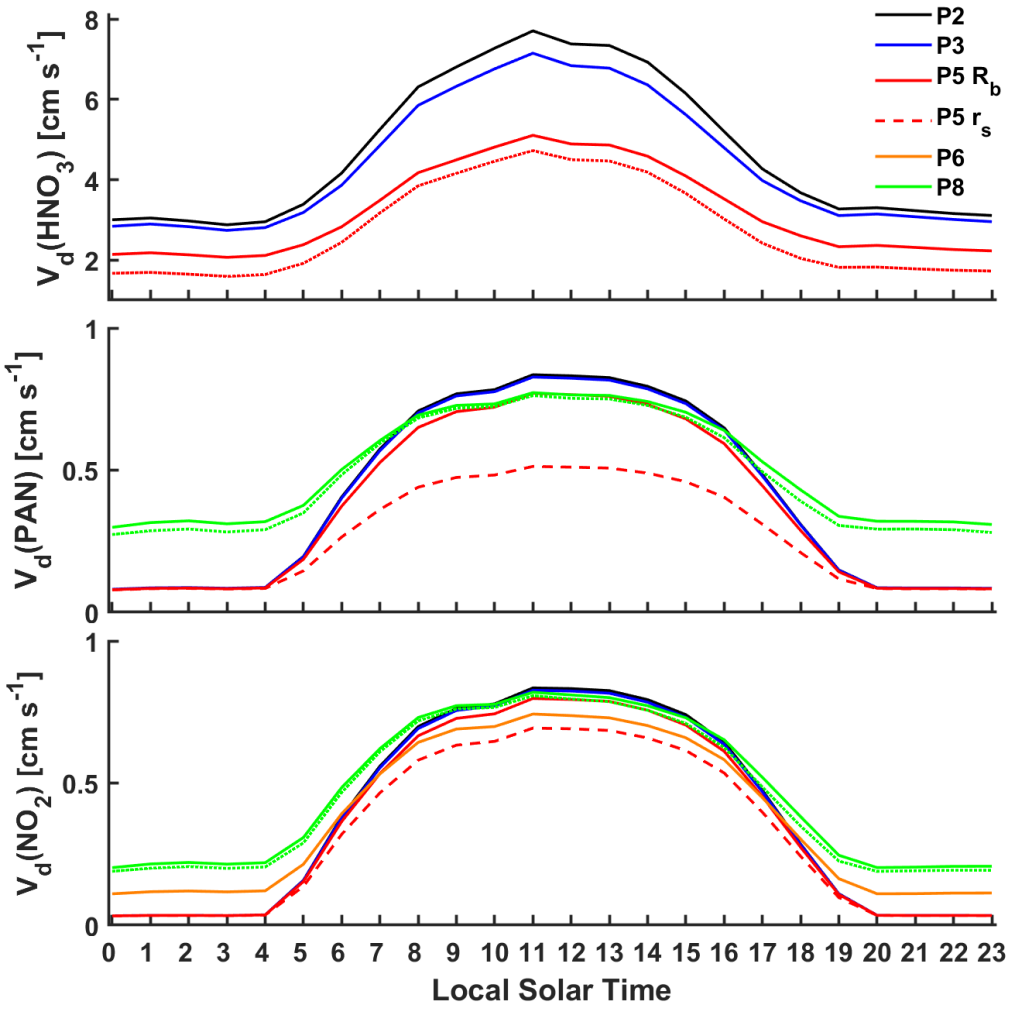


**Figure 3.5:** Simulated diel mean deposition velocities for $HNO_3$, PAN, and $NO_2$ over Harvard Forest (June–November 2000). Diel mean values are from a continuous hourly dataset computed with observed meteorological and phenological (e.g. LAI, $z_o$) inputs. Depicted parameterizations from Table 3.1 include: P2, P3, P5's effect on quasi-laminar sublayer resistance $R_b$ and resistance to stomatal uptake $r_s$, and P8's effect on $V_d(NO_2)$ and $V_d(PAN)$. **Dotted lines** depict P8 $V_d$ referenced from the center of GEOS-Chem's lowest grid box (~60 m agl) instead of measurement height (29 m). Changes in component resistances $R_a$, $R_b$, and $R_c$ are shown in Fig. S3.8.

greater change than observed over Talladega National Forest (section 3.4.1, Table 3.2) where the higher relative measurement height (2 $h_c$ vs 1.5 $h_c$ at HFEMS) would reduce the effects of the RSL on $R_a$. P3 has a reduced effect on nocturnal $V_d(HNO_3)$ resulting from the lower depth of influence of the RSL under stable conditions. Due to the low aqueous solubility of $NO_2$ and PAN, $R_c$ is the dominant term in the resistance pathway for these species (Fig. S3.8) outside of very stable nocturnal conditions (Fig. S3.4); accordingly, RSL corrections to $R_a$ have negligible influence on resulting deposition velocities for these species. Large reductions in simulated $V_d(HNO_3)$ are seen for P5, where the use of accurate molecular diffusivities results in a significant increase to $R_b(HNO_3)$ of ca. 95%. Increases in $R_b(NO_2)$ and $R_b(PAN)$ of ca. 60% and 110%, respectively, result in insignificant reductions to $V_d(NO_2)$ across all times of day and small reductions in daytime $V_d(PAN)$ of 7% due to the dominant contributions of $R_c$ for these species (Fig. S3.8). In addition, due to the dependence of trace gas specific stomatal conductance on the ratio of molecular diffusivities $D_x/D_{H_2O}$, further reductions are seen in daytime mean $V_d$ of up to 13% and 32% for $NO_2$ and PAN, respectively. At night when stomates are assumed to be closed ($r_s > 10^4$ s m$^{-1}$), non-stomatal branches of $R_c$ become limiting, reducing the effects of updates to molecular diffusivity for species of low aqueous solubility. Included in Fig. 3.5 for simulated $V_d(NO_2)$ is the effect of replacing the non-stomatal branch of $R_c$ with $r_{hyd}$ according to 3.12, resulting in large increases in nocturnal $V_d(NO_2)$ from a negligibly small value of 0.04 cm s$^{-1}$ in the P5 parameterization. The relative increase in daytime $V_d(NO_2)$ is much less (24% for $\alpha = 2$) due to competing stomatal uptake, however, enough to restore peak daytime $V_d(NO_2)$ to P2-base levels. The reduced diurnal variability in simulated $V_d(NO_2)$ for parameterization P8, ca. 4-fold compared to 20-fold for P2, is consistent with diurnal cycles in $V_d(NO_2)$ inferred from canopy-scale observations where daytime values are on the order of 2–7x larger than at night (Eugster and Hesterberg, 1996; Hanson and Linderg, 1991; Plake et al., 2015; Rondón et al., 1993; Stella et al., 2013; Walton et al., 1997). Greater diurnal variation is seen in leaf-level uptake, with daytime deposition velocities ca. 10-fold larger on average than in the absence of photosynthetically active radiation (Delaria et al., 2020, 2018).

Turnipseed et al. (2006) present eddy covariance flux observations of PAN over a coniferous forest ecosystem, noting significant nocturnal non-stomatal uptake increasing

when surfaces are wet, and that the assumption of negligible non-stomatal loss in the Wesely 1989 parameterization appears to be in contradiction to a growing body of evidence suggesting nighttime deposition of PAN. We therefore implement the recommended empirical updates developed by Turnipseed et al. (2006) into parameterization P8, which include replacing the non-stomatal resistance to cuticular deposition ($r_{lu}$ in 3.5) with 250 s $m^{-1}$ to dry surfaces and 125 s $m^{-1}$ to wet surfaces, scaled by the ratio $LAI_{HFEMS}$ / 3.5, where 3.5 $m^2$ $m^{-2}$ was the LAI at the study site. Turnipseed et al. (2006) define the surface as wet during and immediately following precipitation events, or when ambient RH > 96%; herein, we define the canopy as wet when RH > 96%. It is noted that this empirical update is not mechanistically based, nor is it clear as to the general applicability to other land types. As is often the case in parameterizations of dry deposition, further study across many land-types and seasons is warranted. The update to non-stomatal uptake of PAN reduces median nocturnal $R_c(PAN)$ from ca. 1000 s $m^{-1}$ to 200 s $m^{-1}$ (Fig. S3.8), resulting in an increase to $V_d(PAN)$ of ca. 2.5x at night, and 60% during the day (Fig. 3.5). As is the case with $NO_2$, recent chamber studies of foliar uptake of PAN both question (Place et al., 2020) and support (Sun et al., 2016) the role of non-stomatal deposition, rendering dry deposition of PAN an active area of research.

Stomatal conductance in GEOS-Chem, and other large scale CTMs, is dependent on land type, temperature, and solar radiation. Long-term ozone-meteorology correlations (Kavassalis and Murphy, 2017) and recent leaf-level $NO_2$ uptake observations (Delaria et al., 2020) have highlighted the importance of representing water vapor pressure deficit and soil moisture, respectfully, in parameterizations of stomatal conductance in dry deposition algorithms. Recent model intercomparison studies examining the influence of these hydrometeorological variables on stomatal conductance, deposition velocities, and surface trace gas concentrations (Delaria and Cohen, 2020; Wong et al., 2019) corroborate calls to include response functions for these variables in parameterizations of stomatal conductance, as is done in the generalized bulk surface resistance scheme of Zhang 2003. We have not included these recommendations herein, but note the 20–30% reduction in July mean daytime $V_d(O_3)$ over the Northeastern U.S. depicted in Wong et al., (2019) resulting from the implementation of the Zhang 2003 surface resistance scheme into GEOS-Chem.

As previously discussed in section 3.4.1, studies comparing CTM-simulated deposition velocities to measurement-inferred values often reference $R_a$ from CTM grid-box-center instead of measurement height (Clifton et al., 2017; Nguyen et al., 2015; Nowlan et al., 2014; Silva and Heald, 2018). Increases in $R_a$ when referenced from the center of GEOS-Chem's lowest level (ca. 60 m) instead of the 29 m measurement height over Harvard Forest results in moderate, although significant ($p<0.05$), reductions in simulated $V_d(HNO_3)$ of 10% (daytime) to 20% (nighttime), as depicted in Fig. 3.5. However, these moderate increases in $R_a$ are insufficient to cause significant change to either $V_d(PAN)$ or $V_d(NO_2)$ which deposit under $R_c$ control.

Observations of hourly above-canopy $NO_y$ fluxes at the HFEMS are mostly downward (>99%, Fig. S3.9), regardless of adjustment for soil-emitted NO. Figure 3.6 depicts eddy covariance inferred diel mean $V_d(NO_y)$ alongside simulated (3.16) values for parameterizations P2, P5, and P8. Inferred $V_d(NO_y)$ was calculated from observed $V_{ex}(NO_y)$ (Fig. S3.9) adjusted for estimates of soil-emitted NO ventilating the canopy as $NO_2$, analogous to $V_d(NO_2)$ in 3.8. As seen in Fig. 3.6, soil-NO corrections to observed $V_{ex}(NO_y)$ result in small increases to inferred $V_d(NO_y)$—ca. 9% for parameterizations P2 and P5 reducing to ca. 4% for P8 due to a simulated increase in the canopy reduction factor (3.10, Fig. S3.6) from updates to non-stomatal $NO_2$ uptake. By far the largest contributor to simulated $V_d(NO_y)$ is $HNO_3$, contributing over 75% to 24-hr $NO_y$ flux for parameterization P2 (Table 3.4). Despite significant nocturnal mean $NO_2$ concentrations of over 3 ppb (Fig. 3.4), $NO_2$ makes near-negligible contributions to nocturnal $V_d(NO_y)$ in parameterizations P2 and P5. Updates to the parameterization of molecular diffusivity (P5) results in large reductions in simulated $V_d(NO_y)$ and resulting 24-hr depositional flux (26% reduction, Table 3.4) due to large reductions in $V_d(HNO_3)$, exposing a morning peak in inferred $V_d(NO_y)$ which simulated values fail to capture. By monitoring the rate of change of vertically-integrated in-canopy concentration profiles, Munger et al. (1996) showed that canopy storage contributions to above-canopy $NO_x$ and $O_3$ fluxes were small at Harvard Forest, however, as noted by Horii et al. (2005), $NO_y$ fluxes measured at the HFEMS did not include a storage term as canopy vertical profiles of $NO_y$ were not available. Geddes et al. (2014) measured eddy covariance fluxes of $NO_y$, NO, and $NO_2$ above two midlatitude mixed hardwood forests and noted problematic interpretation of $NO_y$ fluxes between the

**Table 3.4:** Inferred mean fluxes of $NO_y$ and measured component species over Harvard Forest.

| **Parameterization** | **Flux [ngN $m^{-2}$ $s^{-1}$]**[(a)] | | | |
|---|---|---|---|---|
| | $HNO_3$ | $NO_2$ | PAN | $NO_y$[(b)] |
| P2 | 19 ± 24 | 4.4 ± 7.1 | 1.1 ± 1.4 | 25 ± 30 |
| P3, $R_a$ update | 18 ± 22 | 4.3 ± 7.0 | 1.1 ± 1.5 | 23 ± 29 |
| P5, $D$ update | 13 ± 16 | 3.7 ± 5.9 | 0.7 ± 0.9 | 17 ± 21 |
| P7, $R_c(NO_2)$, α = 2 | 13 ± 16 | 5.8 ± 7.4 | 0.7 ± 0.9 | 19 ± 22 |
| P8, $R_c(PAN)$ | 13 ± 16 | 5.8 ± 7.4 | 1.3 ± 1.4 | 20 ± 23 |

[(a)] 24 hr mean (± σ) fluxes inferred from the product of simulated $V_d(x)$ and gap-filled measured concentrations over June – November 2000.
[(b)] inferred $NO_y$ flux from the sum of inferred component $HNO_3$, $NO_2$, and PAN.

hours 07:30 – 11:00 LST due to suspected canopy storage contributions. Due to the absence of in-canopy $NO_y$ measurements from which to evaluate canopy storage, Geddes et al. (2014) considered observations of above-canopy $NO_y$ flux unrepresentative of the depositional flux over this timeframe and excluded observations during these hours from analysis. The anomalous morning peak in eddy covariance inferred $V_d(NO_y)$ depicted in Fig. 3.6 could, in part, be due to canopy storage contributions at Harvard Forest. It is also possible that the morning low bias in simulated $V_d(NO_y)$ results from heavy reliance on the climatological diel profile of $HNO_3$ (Fig. 3.4) due to the paucity of hourly $HNO_3$ observations (Fig. S3.7). It is conceivable that mixing down of rapidly depositing $NO_y$ species (i.e., $HNO_3$ or organic nitrates) as growth of the morning boundary layer erodes the residual layer above could induce a downward spike in above-canopy $NO_y$ flux. Future analysis of this measurement-model discrepancy would benefit from in-canopy vertical profiles of $NO_y$ and component species at hourly resolution. Updates to non-stomatal deposition of $NO_2$ and PAN in parameterization P8 result in noticeable increases in simulated $V_d(NO_y)$ and an 18% increase in inferred 24-hr $NO_y$ flux due to large increases in inferred dry deposition of $NO_2$ (56%) and PAN (85%) (Table 3.4).

Also depicted in Fig. 3.6 is the effect on eddy covariance inferred $V_d(NO_y)$ from a maximum estimate of emitted HONO due to the heterogeneous hydrolysis of $NO_2$ (R3.1) on deposition surfaces. Assuming complete HONO emission to the gas phase, and subsequent ventilation from the canopy, results in a 4% increase in eddy covariance inferred $V_d(NO_y)$. Uncertainties exist around the nature of the dynamic equilibrium that

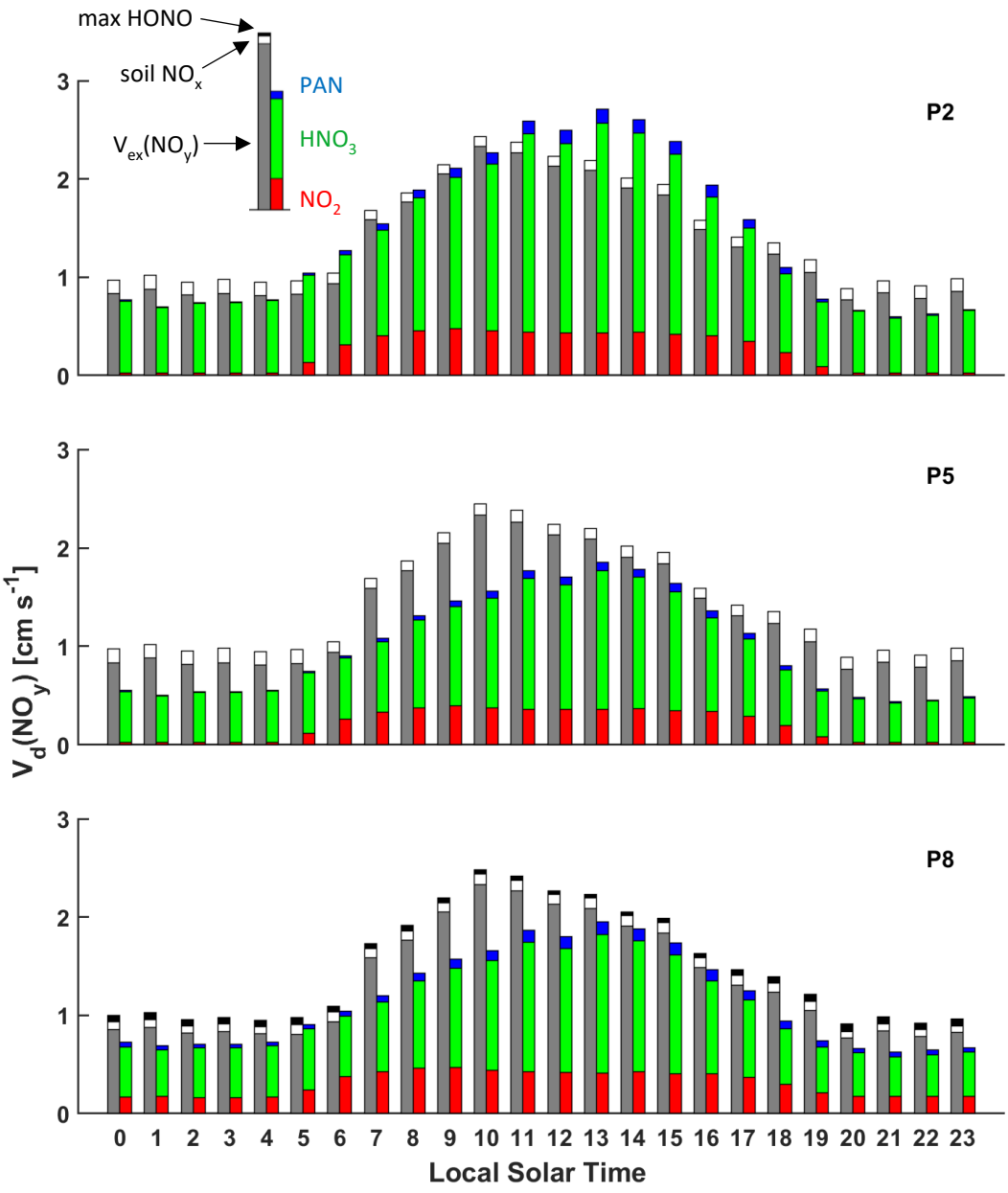


**Figure 3.6:** Diel $NO_y$ deposition velocity $V_d(NO_y)$ climatology over Harvard Forest (June–November 2000). Observed mean $V_{ex}(NO_y)$ (**grey**) is depicted with estimated contributions to $V_d(NO_y)$ from soil $NO_x$ (**white**) and HONO (**black**) emission. Simulated $V_d(NO_y)$ are depicted as the sum of contributing $NO_y$ components: $NO_2$ (**red**), $HNO_3$ (**green**), and PAN (**blue**) for three simulation types: **(Top)** base (P2), **(Middle)** updated $R_a$ and diffusivity $D$ (P5), and **(Bottom)** updated $R_c(NO_2)$ and $R_c(PAN)$ (P8).

establishes between evolved and adsorbed HONO (Collins et al., 2018; Harrison et al., 1996; Lee, 2012; Spicer et al., 1993; Wojtal et al., 2011) and implications of a nocturnal reservoir of deposited HONO as a daytime source of HONO to the atmospheric surface layer (He et al., 2006; Ren et al., 2020; VandenBoer et al., 2014, 2015). Lee et al. (2012) monitor near continuous above-canopy $NO_2$ and HONO concentrations and eddy covariance fluxes at the HFEMS during 2011 and find nocturnal enhancements in HONO concomitant with $NO_2$, especially at elevated concentrations. Neither upward nor downward fluxes of HONO were observed, suggestive of establishment of dynamic equilibrium between HONO emission and deposition at the HFEMS where perturbation fluxes are below detection limits. Measurements of HONO and $NO_2$ fluxes over grassland and sugar beet surfaces have highlighted the bi-directional nature of HONO exchange—HONO emission was found to dominate the bi-directional flux under elevated $NO_2$ concentrations (ca. >10 ppb for the land-types studied) while deposition was noted to be dominant at lower ambient $NO_2$ concentrations (Harrison et al., 1996; Harrison and Kitto, 1994). The diel flux behaviour of HONO is likely multifactorial, depending on land-type, meteorology, and trace gas and particulate concentrations (Pusede et al., 2015a; VandenBoer et al., 2015). The absence of significant fluxes of HONO at the HFEMS noted by Lee et al. (2012), despite observed downward nocturnal fluxes of $NO_2$ and nocturnal enhancement of HONO, does not exclude $NO_2$ heterogeneous hydrolysis as a precursor for HONO, rather, indicates the importance of deposition and re-emission processes from canopy surfaces which may dominate HONO behaviour at rural forest sites (Ren et al., 2011, 2020; Sörgel et al., 2011; Zhou et al., 2002) in the absence of strong pulses of ambient $NO_2$ perturbing the dynamic equilibrium between adsorbed and gas phase HONO—as is routinely observed in laboratory studies (Finlayson-Pitts et al., 2003; Spicer et al., 1993).

Figure 3.7 compares inferred diel mean $V_d(NO_y)$ with simulated values according to parameterization P8 which includes all updates discussed herein (Table 3.1). Inferred $V_d(NO_y)$ was corrected for soil-emitted NO but not for potential HONO emission given the findings of Lee et al. (2012). Also depicted for inferred $V_d(NO_y)$ are diel medians and ratios of 'mean flux–to–mean concentration' ($-\overline{F_{NO_y}} \,/\, \overline{[NO_y]}$). As with our analysis of $V_d(NO_2)$, we restrict our comparison to aggregate values of $V_d(NO_y)$ in order to reduce the effects of

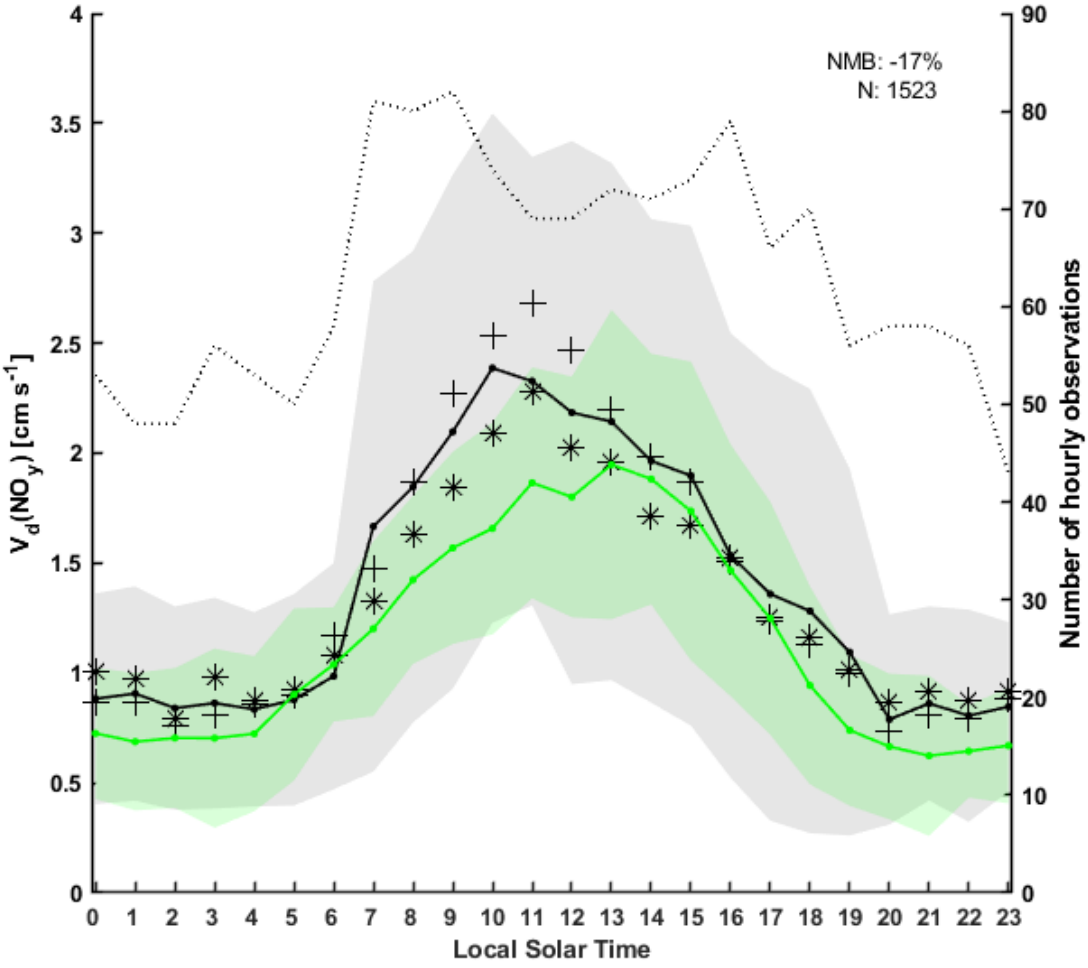


**Figure 3.7:** Diel $NO_y$ deposition velocity $V_d(NO_y)$ climatology over Harvard Forest (June–November 2000). Measured $V_d(NO_y)$ is depicted in **black** as mean (—), median (+), and ratio of 'mean $NO_y$ flux–to–mean $NO_y$ concentration' (*****). Simulated mean $V_d(NO_y)$ (coincidently sampled with hourly obs.) is shown in **green** for an optimized simulation (Table 3.1, P8). Standard deviations about corresponding mean values are depicted as shaded areas. Also depicted are the number of hourly values contributing to mean quantities (**black dotted),** and an inset quantifying normalized mean bias (NMB) between measured and simulated mean $V_d(NO_y)$ with the number of contributing hourly observations tabulated (N).

random variability as is commonly done in comparison of eddy covariance inferred exchange velocities with parameterized values (Clifton et al., 2017; Eugster and Hesterberg, 1996; Turnipseed et al., 2006). By randomly sampling a cumulative number of

days over $10^4$ iterations, we find that $R^2$ and NMB between eddy covariance inferred and simulated $V_d(NO_y)$ stabilize after ca. 30 days of observation (Fig. S3.10), converging to 0.9, and -17%, respectively, after the 110 days of observation available for this dataset between June–November 2000. The large number of days required for stabilization of model-measurement comparison could result from the high fraction of inferred concentrations of $HNO_3$ (Fig. 3.4)—the main contributor to $V_d(NO_y)$—along with the incomplete closure of the $NO_y$ budget. As seen from Fig. 3.7, a moderate underestimate of 17% exists in simulated $V_d(NO_y)$, with a slightly higher daytime bias (-18%) than at night (-10%). Excluding the period from 07:00–11:00 reduces the daytime bias in simulated $V_d(NO_y)$ to -12%, and 24-hr bias to -13%. As previously mentioned, the $NO_y$ concentration budget at the HFEMS is closed to 77% on average from observations of $NO_x$, $HNO_3$, and PAN. Horii et al. (2005) provide evidence of a rapidly depositing unidentified $NO_y$ species at this site, especially under southwesterly flow, and speculate the unidentified $NO_y$ species as organic nitrates.

## 3.5 Conclusions

Extraction of the trace gas dry deposition algorithm from GEOS-Chem and implementation to run offline in single point mode enabled detailed evaluation of various branches of the algorithm against eddy covariance inferred deposition velocities over two North American forest ecosystems. Observations of deposition velocities for species that deposit under dynamical control (i.e., nominally small $R_c$) facilitated the identification of a large high bias in the parameterization of molecular diffusivity in GEOS-Chem, which after correction resulted in improved representation of simulated $V_d(NO_y)$ to an extensive dataset spanning many months. Site-specific roughness length and reference height were found to be an important constraint on $R_a$ for rapidly depositing species, whereas corrections for the influence of the roughness sublayer (RSL) were found to be minor at the measurement heights involved, and negligible at the dry deposition reference height used in GEOS-Chem.

A large low bias in simulated nocturnal $V_d(NO_2)$ was addressed by representing $NO_2$ heterogeneous hydrolysis in the calculation of non-stomatal surface resistance. A

literature review of surface-specific deposition velocities to both non-foliar and nocturnal foliar surfaces highlight the importance of considering microscopic surface area for heterogeneous reaction, and enabled estimates of bottom-up $V_d(NO_2)$ for Harvard Forest which agree well with parameterized values optimized from eddy covariance inferred values. Consideration of soil $NO_x$ emission on eddy covariance inferred $V_d(NO_2)$ was found to be important.

We persist with the assumption that nocturnal uptake of $NO_2$ follows non-stomatal pathways, as is currently the case in dry deposition schemes widely used in atmospheric CTMs. Meanwhile, the nocturnal behavior of stomata remains an active area of research. Confounding processes such as the hydraulic activation of stomata (HAS) complicate the inference of stomatal conductance to trace gases from observations of water vapor flux, especially in the dark in well mixed chambers. It would be helpful for future enclosure studies of $NO_2$ uptake to consider the effects of disproportion of $NO_2$ on foliar surfaces, as well as potential biases in estimates of stomatal conductance resulting from possible HAS.

We recommend the implementation of a mechanistic non-stomatal surface resistance scheme for $NO_2$ in atmospheric CTMs. We present two approaches that result in general agreement for a mature mixed-deciduous forest ecosystem. The simplest approach being to represent non-stomatal resistance to $NO_2$ uptake as $r_{hyd}$ with $\alpha = 2$ for high surface area land-types such as urban and forest, and $\alpha = 1$ for remaining land types. Long-term field studies quantifying atmosphere-surface exchange across a variety of land-types and seasons would facilitate further development of species-specific dry deposition pathways.

## 3.6 Supplemental Material

### 3.6.1 Aerodynamic Resistance ($R_a$) in the Surface Layer

Turbulent vertical transport of scalars within the atmospheric surface layer, often described as the lowest 10% of the planetary boundary layer where fluxes of momentum, heat, and mass are assumed to be constant with height, is an important process governing surface-atmosphere exchange. Aerodynamic resistance ($R_a$) to turbulent transport, most commonly

parameterized in CTMs following 3.3, can take on a large range of values depending on the state of surface layer turbulence. Cumulative distributions of hourly values computed over Harvard Forest (June–November 2000) using MERRA-2 assimilated meteorology are depicted in Fig. S3.4 for two reference heights, 29 m and 60 m, along with $R_a$ inferred from measured horizontal wind and friction velocity ($u*$) at 29 m, $R_a(29m) = u(29m)\ u*^{-2}$, assuming a no-slip boundary condition, i.e., $u(z_o) = 0$ m s$^{-1}$. Computed from the center of the lowest level in GEOS-Chem, P1 $R_a(60\ m)$ ranges from ~6 s m$^{-1}$ (5$^{th}$ percentile) to ~400 s m$^{-1}$ (95$^{th}$ percentile) with 50$^{th}$ percentile $R_a(60m)$ ~18 s m$^{-1}$. Thus, $R_a$ has variable influence to total resistance represented through $V_d$, ranging from minor under well mixed conditions for species with significant $R_c$, i.e., $O_3$ (Massman, 1994), HCN (Nguyen et al., 2015), and $NO_2$ (herein), to significant for species with negligible $R_c$ under typical diabatic conditions, to dominant under conditions of very high stability and intermittent turbulence (Toyota et al., 2016).

An equivalent formulation of $R_a$ to that of 3.3 may be expressed as a vertical integration of eddy diffusivity $K_c$ (Garratt, 1992):

$$R_a = \int_{z_o}^{z-d} \frac{1}{K_c(z)}\, dz \qquad (3.S1)$$

$K_c$ is the eddy diffusivity for scalar quantities which is commonly represented as the product of characteristic surface layer scaling parameters *friction velocity* $u*$ and height $z$ above the *displacement length* $d$ (Kaimal and Finnigan, 1994), corrected for non-neutral conditions via an empirically determined, dimensionless, flux-gradient relation for sensible heat $\phi_h$ commonly used interchangeably for scalar quantities:

$$K_c = \frac{u_* k(z-d)}{\phi_h(\zeta)} \qquad (3.S2)$$

where $k$ = 0.4 is the von Karman constant, $\phi_h$ is a function of the dimensionless M-O stability parameter $\zeta = (z - d) / L$, where L is the M-O length (Monin and Obukhov, 1954). Dimensionless flux-gradient relations used to compute surface layer $R_a$ in GEOS-Chem have the following functional ($\phi_h$) and integral ($\Psi_h$) forms:

Unstable conditions ($\zeta < 0$) (Garratt, 1992; Holtslag et al., 1990)

$$\phi_h = (1 - 15\,\zeta)^{-1/2} \tag{3.S3}$$

$$\Psi_h = 2\ln\left[\frac{1 + \phi_h^{-1}}{2}\right] \tag{3.S4}$$

Stable conditions ($0 < \zeta \leq 1$) (Dyer, 1974)

$$\phi_h = 1 + 5\zeta \tag{3.S5}$$

Stable conditions ( $1 < \zeta$ ) (Holtslag et al., 1990)

$$\phi_h = 5 + \zeta \tag{3.S6}$$

Stable conditions ($0 < \zeta$ ) (Holtslag and Bruin, 1988)

$$\Psi_h = -\left[a\zeta + b\left(\zeta - \frac{c}{d}\right)e^{-d\,\zeta} + \frac{bc}{d}\right] \tag{3.S7}$$

where $a$ = 0.7, $b$ = 0.75, $c$ = 5, and $d$ = 0.35.

### 3.6.2 Roughness Sublayer (RSL)

Within a distance of 2–3x the canopy height ($h_c$) above the surface, the so called roughness sublayer (RSL), turbulent eddy structure is significantly different from that of the remaining surface layer above (Finnigan et al., 2009; Raupach et al., 1996). Turbulent flows in the wake of roughness elements are dominated by structures of a larger length scale than predicted by 3.S2 where turbulent eddies are parameterized to scale on a distance $z$ above $d$ (Finnigan, 2000). Near the canopy top, $K_c$ is enhanced over that predicted by M-O similarity theory by a factor of 2 to 3 (Cellier and Brunet, 1992; Raupach et al., 1996), reaching agreement by ca. $2h_c$ (Simpson et al., 1998). To avoid underestimating turbulent transport of momentum, heat, and mass, models that employ gradient transport theory (K-theory) may scale eddy diffusivities within the RSL to values above those predicted by M-O similarity theory (Bryan et al., 2012; Mölder et al., 1999; Neirynck and Ceulemans, 2008; Sellers et al., 1986; Stroud et al., 2005). RSL functions $\widehat{\phi_x}$ designed as perturbations to the dimensionless universal M-O functions $\phi_x(\zeta)$ can be applied in multiplicative form yielding modified M-O stability functions $\Phi_x$:

$$\Phi_x = \phi_x(\zeta)\,\widehat{\phi_x} \tag{3.S8}$$

where *x* refers to either momentum, heat, or scalar quantities. Several RSL functional forms have been proposed of varying complexity, all of which contain an additional RSL length scale, i.e., $z^*$ in 3.S9. Computing mean wind and scalar profiles requires integral forms of corresponding non-dimensional M-O stability functions (Panofsky, 1963), and some RSL modified M-O stability functions have analytical solutions to integral forms (Arnqvist and Bergström, 2015; de Ridder, 2010), while others require numerical integration (Cellier and Brunet, 1992; Garratt, 1980; Harman and Finnigan, 2007; Mölder et al., 1999; Wenzel et al., 1997). Physick and Garratt, (1995) implement a simple RSL lower boundary correction into a mesoscale model using the RSL function:

$$\widehat{\phi_M} = \widehat{\phi_h} = 0.5 \exp\left[0.7\,\frac{(z-d)}{(z^*-d)}\right] \qquad (3.S9)$$

where the RSL correction is treated the same for both momentum $\widehat{\phi_M}$ and sensible heat $\widehat{\phi_h}$ and is independent of buoyancy. Turbulent mixing within the upper canopy at *d* is enhanced by ca. 2-fold, with $\widehat{\phi_M}$ and $\widehat{\phi_h}$ decaying to unity at the top of the RSL $z^*$. It is noted that the additional mixing in the wake of roughness elements within the RSL reduces vertical gradients from those of M-O adjusted logarithmic values extrapolated from above the RSL; as such, the flux-gradient wind profile adjusted for stability and RSL effects can no longer be integrated assuming $u(z_o) = 0$ for $z < z^*$. An updated formulation of $R_a$ which accounts for RSL effects and $u(z_o) > 0$ can be expressed as (Physick and Garratt, 1995):

$$R_a(z < z^*) = \frac{1}{ku_*}\left[\ln\left(\frac{z-d}{z_o}\right) - \Psi_h\left(\frac{z-d}{L}\right) + \Psi_h\left(\frac{z_o}{L}\right) + \int_z^{z^*} \phi_h\left(1-\widehat{\phi_h}\right)z^{-1}dz\right] \qquad (3.S10)$$

At the top of the RSL where $z = z^*$ and $\widehat{\phi_h} \sim 1$, $R_a$ from 3.3 & 3.S10 become equivalent. Above the RSL ($z > z^*$) M-O similarity theory applies, and $R_a$ follows 3.3.

Figure S3.3 depicts the effects of enhanced RSL mixing on $K_c$ and $R_a$ as a function of reference height *z* above the displacement height *d* for a rough surface ($z_o$ = 1 m) under neutral stability conditions ($L^{-1} \sim 0$) and light winds ($u_*$ = 0.2 m s$^{-1}$). $K_c$ and $K_c^{-1}$ calculated using the RSL modified M-O stability function $\Phi_x$ from 3.S8 are shown in Fig. S3.3a & b, respectively (red trace), and are compared to values from M-O similarity theory which

neglects RSL effects (green trace). The largest relative difference in RSL corrected $K_c$ occurs at $z_o$, where the effect of 3.S9 is largest. Shown in Fig. S3.3c is $R_a(z)$ computed following M-O similarity theory (3.3, green trace) alongside $R_a(z)$ according to 3.S10 (blue trace); the integral in 3.S10 was evaluated numerically via Simpson's method. Enhanced RSL mixing results in a weaker above-canopy vertical gradient in $R_a$, while allowing $u(z-_o)$>0 in 3.S10 results in a large displacement of $R_a(z_o)$ as there is now aerodynamic resistance required to extinguish the non-zero wind at this height. $R_a$ following 3.3 and 3.S10 asymptotically converge to equivalency by $z = z^*$, with good and excellent agreement by $z = 2h_c$ (10%) and $z = 3h_c$ (3%), respectively, under these neutral test conditions. Reduced gradients in $R_a$ with height results from growth of turbulent eddies ($K_c$) according to mixing length $z - d$. As previously noted, $R_a$ computed from integration of $K_c^{-1}$ (3.S2) where $K_c$ is corrected for buoyancy following $\phi_h$ is equivalent to $R_a$ computed following 3.3, both being depicted in Fig. S3.3c (green trace). Integration of $K_c^{-1}$ where $K_c$ is corrected for buoyancy and RSL effects following the modified M-O stability correction $\widehat{\phi_h}$ is not equivalent to RSL $R_a$ computed following 3.S10, as seen in Fig. S3.3c (red trace)—the former assumes $u(z_o) = 0$, and the later $u(z_o)>0$. The vertical gradients of these two methods are identical, however, $R_a$ corrected for the RSL following 3.S10 is shifted by $R_a(z_o)$.

It is noted that RSL corrected $R_a$ has directional asymmetry, where aerodynamic resistance to upward transport of surface emissions (red trace in Figs. S3.3 & S3.4) is significantly less than aerodynamic resistance to dry deposition (blue trace in Figs. S3.3 & S3.4). This directional asymmetry is intuitive, as resistance to upward mixing of surface emissions would not be impeded, but enhanced, by non-zero wind at $z_o$, whereas dry deposition of uniformly mixed trace species from aloft require contact with surface elements for removal. It is also noted that many efforts to simulate bidirectional surface exchange of atmospheric trace species employ $R_a$ following standard M-O similarity theory according to 3.3 for both emission and deposition pathways, thus failing to account for directional asymmetry in resulting fluxes (Haghighi and Or, 2015; Karamchandani et al., 2015; Nemitz et al., 2000; Su et al., 2011; Wen et al., 2014; Wentworth et al., 2014). To prevent the underestimation of upward sensible and latent heat fluxes, Sellers et al. (1986) in their formulation of a Simple Biosphere Model (SiB) for use in General Circulation Models (GCMs) impose an aerodynamic resistance to emission from an integration of a

RSL modified $K_h$, which would be similar to that presented in Fig. S3.3c (red trace). In Chapter 4 of this thesis, directional asymmetry of $R_a$ is implemented into a simple model of subgrid dry deposition of near-surface emitted $NO_x$.

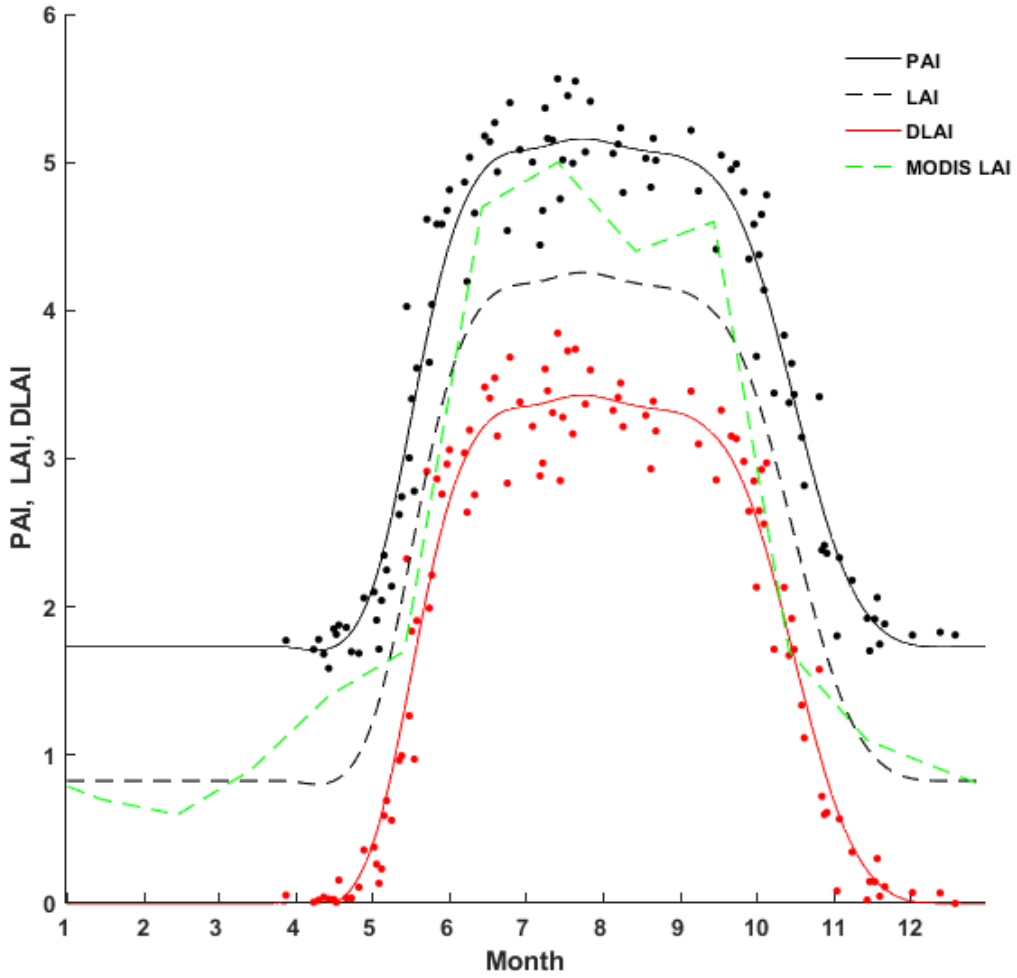


**Figure S3.1:** Observed plant area index (**PAI**) and deciduous leaf area index (**DLAI**) at Harvard Forest. Leaf area index (**LAI**) includes both deciduous and coniferous foliage and is computed herein as a spline-fit to observed PAI corrected for reported stem and twig area index (STAI, 0.9). Also depicted is **MODIS LAI** for the corresponding 0.25° x 0.25° grid cell for the year 2005, as is used in GEOS-Chem for simulation years prior to 2005. Measurements of PAI and DLAI were obtained from the Harvard Forest Data Archive (Munger and Wofsy, 2020a). STAI = 0.9 was reported by Horii et al. (2005).

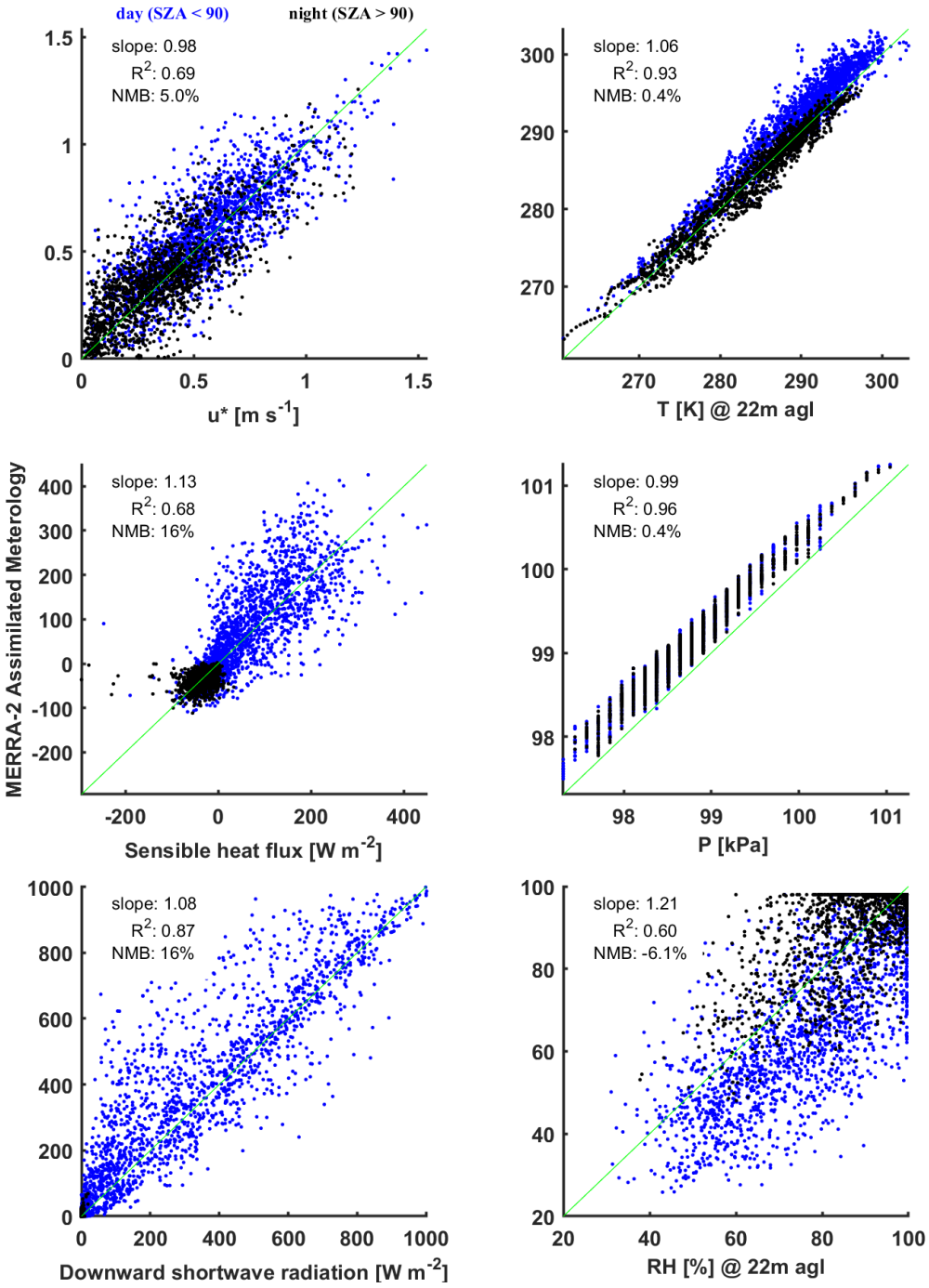


**Figure S3.2:** Comparisons of hourly observations of $u_*$, sensible heat flux, downward shortwave radiation, *T*, *P*, and *RH*, made over Harvard Forest to coincident values from GEOS assimilated meteorological fields (MERRA2 @ 0.5 º x 0.625 º). Striations in comparison of pressure result from measured values reported on 133 Pa intervals.

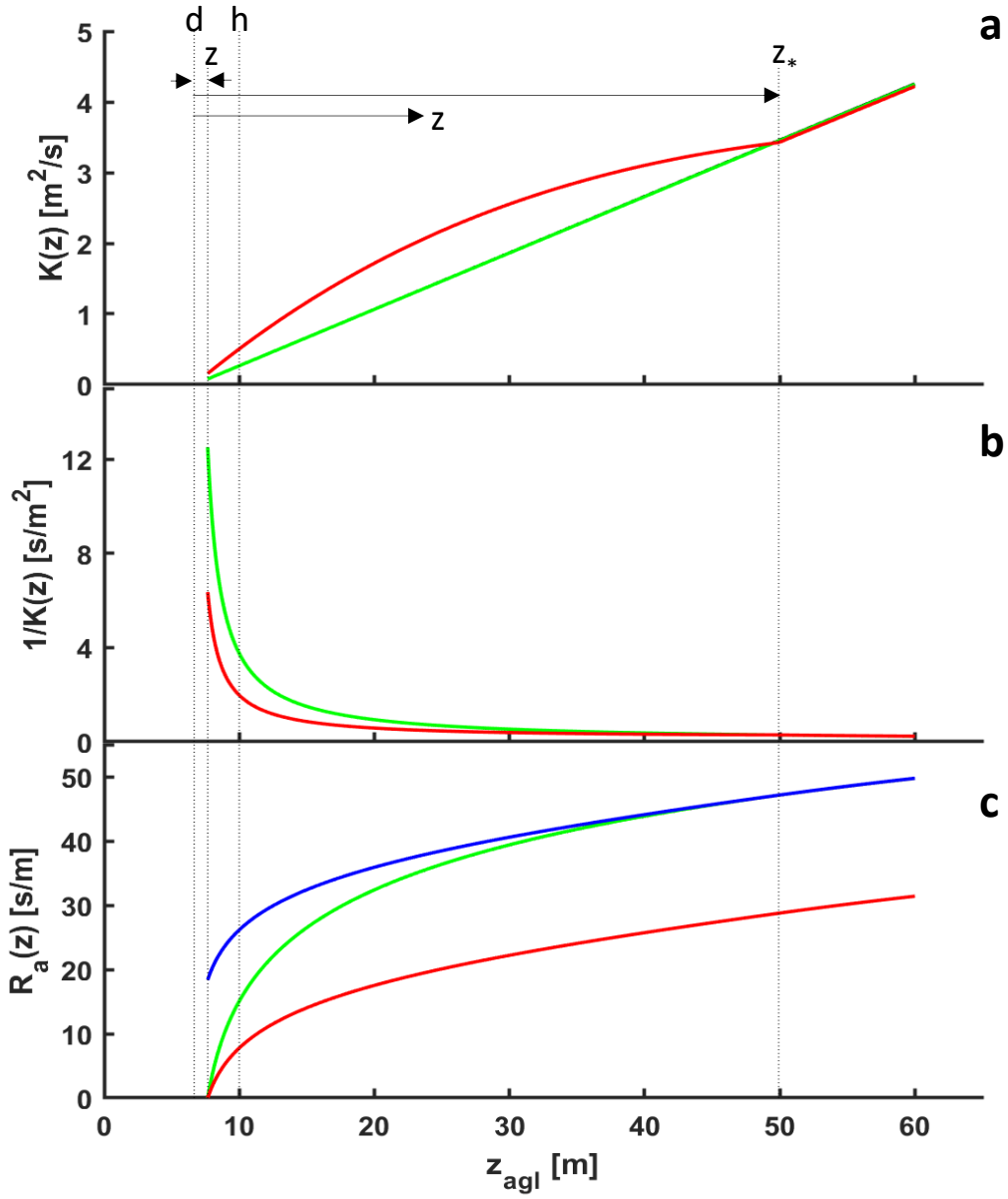


**Figure S3.3: (a)** Turbulent eddy diffusivity *K(z)* above a rough surface ($z_o$ = 1 m) computed via standard Monin-Obukhov similarity theory according to equation 3.S2 (green) and using a perturbed Monin-Obukhov form (3.S8) to account for enhanced mixing within the roughness sublayer (red). **(b)** $K(z)^{-1}$ depicts the integrand of corresponding aerodynamic resistance calculations (3.S1). **(c)** Aerodynamic resistance $R_a(z)$ computed from $K(z)^{-1}$ (3.S1) with stability correction functions according to M-O similarity theory (green) and a roughness-sublayer perturbed from (3.S8) (red), both of which assume zero wind at the roughness length $z_o$. $R_a(z)$ which accounts for both enhanced roughness sublayer mixing and non-zero wind at $z_o$ is depicted in blue according to 3.S10. Note: (1) calculations of $K(z)$ and $R_a(z)$ commence from $z_o$ and are dependent on the altitude $z$ above the displacement height $d = 2/3h_c$ of the surface. Roughness elements are of height $h_c$ above ground level (agl), yielding a roughness sublayer height $z^*$ above $d$; (2) meteorological conditions are taken as light winds ($u_* = 0.2$ m/s) and a neutrally stable atmosphere ($L^{-1} \sim 0$ m$^{-1}$ ).

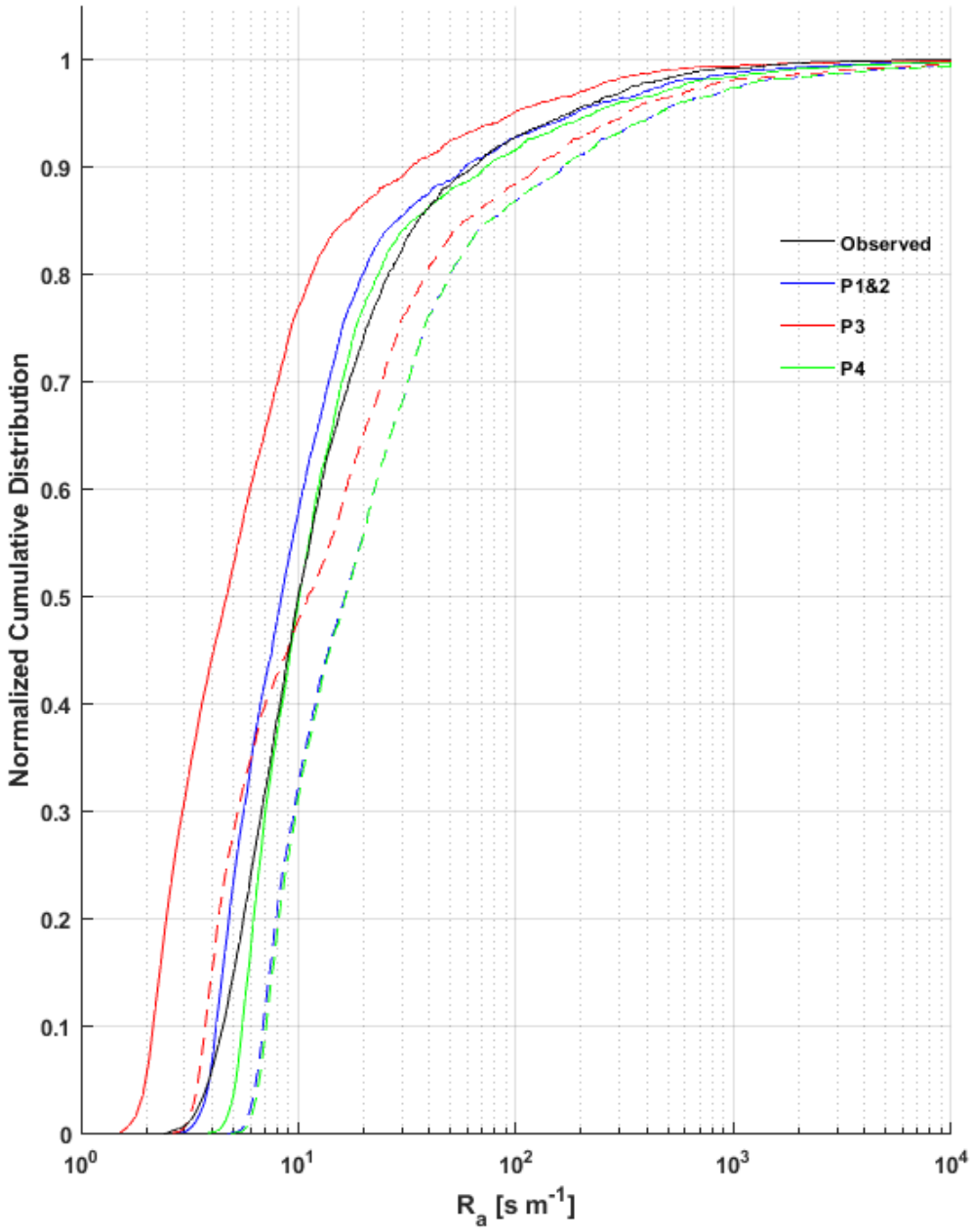


**Figure S3.4:** Cumulative distributions of hourly aerodynamic resistance $R_a$ over Harvard Forest from June – November 2000. Observed $R_a(29\ m) = u(29\ m)/u_*^2$, is compared to coincidently-sampled (hourly) simulated values P1&2, P3, and P4 integrated from both the measurement height at Harvard Forest, 29 m (**solid lines**) and the approximate midpoint of GEOS-Chem's 1st level, ca. 60 m (**dashed lines**).

**Table S3.1:** Species specific comparison of parameterized diffusivities (Fuller's method) to referenced measured values in air or $N_2$. Diffusivities are reported at 273 K and 101325 Pa following equation 3.6**.**

| Species | Fuller's Method | Measured | | Ref.[a] |
|---|---|---|---|---|
| | $D_o$ ($cm^2\ s^{-1}$) | $D_o$ ($cm^2\ s^{-1}$) | | |
| **inorganics** | | | | |
| $HNO_3$ | 0.130 | 0.099 | ± 0.008 | 1 |
| $NO_3$ | 0.142 | 0.105 | ± 0.053 | 1 |
| HONO | 0.151 | 0.110 | ± 0.03 | 1 |
| $NH_3$ | 0.228 | 0.201 | ± 0.011 | 1 |
| $SO_2$ | 0.115 | 0.107 | ± 0.015 | 1 |
| $H_2SO_4$ | 0.094 | 0.085 | ± 0.011 | 1 |
| $H_2O_2$ | 0.168 | 0.133 | ± 0.04 | 1 |
| HOBr | 0.115 | 0.096 | ± 0.01 | 1 |
| HBr | 0.127 | 0.109 | ± 0.033 | 1 |
| HCl | 0.148 | 0.135 | ± 0.008 | 1 |
| $Cl_2$ | 0.106 | 0.107 | ± 0.011 | 1 |
| $I_2$ | 0.083 | 0.061 | ± 0.015 | 1 |
| $Br_2$ | 0.096 | 0.086 | ± 0.007 | 1 |
| $NO_2$ | 0.157 | 0.145 | ± 0.001 | 2 |
| $N_2O_4$ | 0.111 | 0.084 | ± 0.004 | 2 |
| $N_2O_5$ | 0.103 | 0.081 | ± 0.005 | 2 |
| $ClONO_2$ | 0.100 | 0.085 | ± 0.001 | 2 |
| $O_3$ | 0.152 | 0.153 | ± 0.001 | 2 |
| $H_2O$ | 0.229 | 0.218 | | 3 |
| $CO_2$ | 0.133 | 0.138 | | 3 |
| $N_2O$ | 0.164 | 0.144 | | 3 |
| CO | 0.161 | 0.181 | | 3 |
| NO | 0.199 | 0.180 | | 3 |
| **organics** | | | | |
| methane | 0.181 | 0.190 | ± 0.006 | 4 |
| ethane | 0.122 | 0.129 | ± 0.006 | 4 |
| propane | 0.097 | 0.098 | ± 0.006 | 4 |
| ethylene | 0.129 | 0.140 | ± 0.006 | 4 |
| benzene | 0.077 | 0.081 | ± 0.003 | 4 |
| toluene | 0.069 | 0.076 | ± 0.005 | 4 |
| xylene | 0.064 | 0.061 | ± 0.006 | 4 |
| methanol | 0.138 | 0.142 | ± 0.012 | 4 |
| ethanol | 0.106 | 0.111 | ± 0.008 | 4 |
| acetone | 0.091 | 0.092 | ± 0.006 | 4 |

| | | | | |
|---|---|---|---|---|
| methyl ethyl ketone | 0.082 | 0.078 | ± 0.002 | 4 |
| formic acid | 0.125 | 0.131 | ± 0.005 | 4 |
| acetic acid | 0.100 | 0.106 | ± 0.006 | 4 |
| peroxyacetyl nitrate | 0.080 | - | | - |
| Hydroxymethyl hydroperoxide | 0.107 | | | |
| $CCl_4$ | 0.070 | 0.069 | ± 0.003 | 5 |
| $CH_2Cl_2$ | 0.090 | 0.089 | ± 0.005 | 5 |
| $CHCl_3$ | 0.078 | 0.078 | ± 0.003 | 5 |
| $CHBr_3$ | 0.073 | 0.066 | ± 0.001 | 5 |

[(a)] References for measured diffusion coeficients:
(1) Tang et al. (2014)
(2) Langenberg et al. (2020)
(3) Massman et al. (1998)
(4) Tang et al. (2015)
(5) Gu et al. (2018)

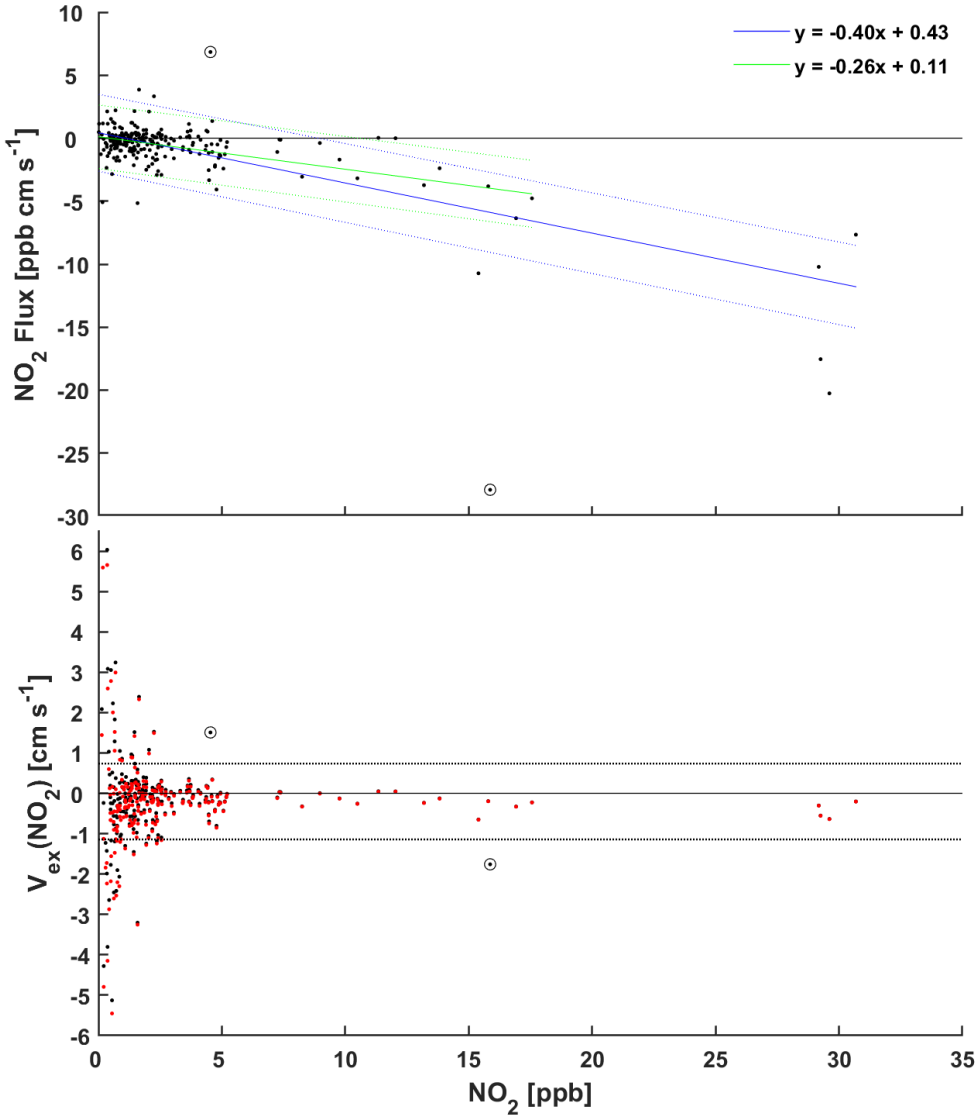


**Figure S3.5:** Nocturnal (20–4 LST) hourly eddy covariance $NO_2$ flux (**TOP**) and resulting hourly exchange velocities $V_{ex}(NO_2)$ (**BOTTOM**) as a function of $NO_2$ concentration. These publicly available measurements (Horii, 2004) were taken over an established mixed deciduous forest (Harvard Forest, MA, USA) from April–November 2000. Estimated above-canopy soil $NO_x$ flux was subtracted from measured hourly $NO_2$ fluxes in order to estimate $V_{ex}(NO_2)$ due to deposition (**red dots**, BOTTOM). Dashed lines in bottom plot depict boundaries of an outlier filter applied to hourly $V_{ex}(NO_2)$ prior to calculation of means. Data points excluded from analysis based on visual inspection are circled. Hourly observations coincident with $u_* < 0.2$ m s$^{-1}$ were excluded from analysis.

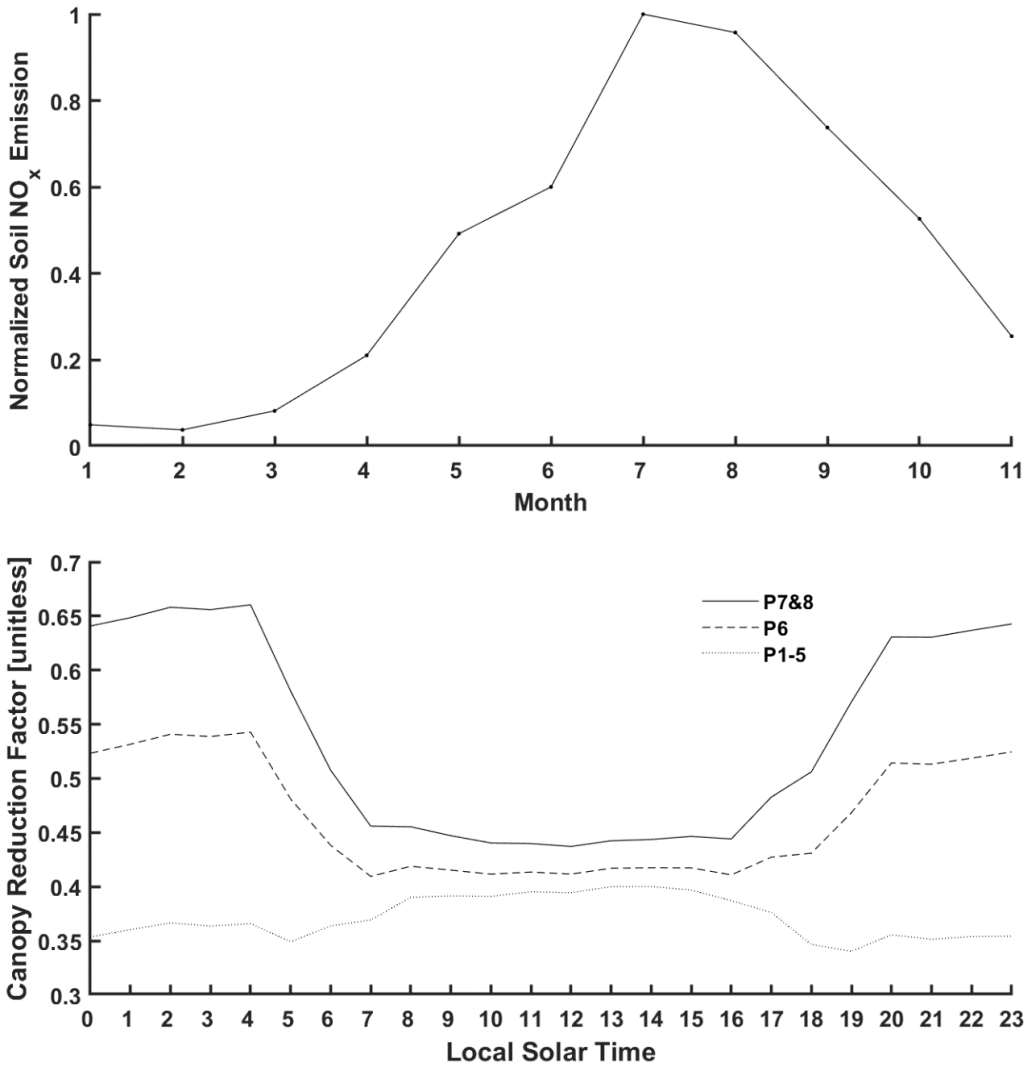


**Figure S3.6:** (**TOP**) Normalized monthly nocturnal soil NO emissions from GEOS-Chem (1/4° x 5/16°) at the location of the HFEMS for 2013. (**BOTTOM**) Diel climatology (April, July–November 2000) of the soil $NO_x$ canopy reduction factor from GEOS-Chem (3.10) shown for parameterizations P1–5, P6, and P7&8 (Table 3.1).

**Table S3.2:** Inferred $NO_2$ uptake coefficients $\gamma_{NO_2}$ to both non-foliar and foliar materials from literature values of surface deposition velocities $V_d^{surf}$. Abbreviations used: Eddy Covariance (EC), Non-Stomatal (NS), Leaf Area Index (LAI), Table (T), Figure (F).

| Material | Measurement Technique<br>method/location/condition | $V_d^{surf}$<br>[cm $s^{-1}$] | $\gamma_{NO_2}$ [(a)]<br>(unitless) | Surface Area[(b)] | T<br>[°C] | RH<br>[%] | Ref.[(i)] |
|---|---|---|---|---|---|---|---|
| **Non-Foliar Surfaces** | | | | | | | |
| teflon | chamber/ lab | ~ 0 | ~ 0 | total | 29.4 | ? | 1 |
| distilled water | chamber/ lab | 0.021 | $2.3 \times 10^{-6}$ | total (planar) | 29.4 | N/A | |
| wet bark | chamber/ lab | 0.093 | $1.0 \times 10^{-5}$ | total (geometric) | 29.4 | N/A | |
| dry bark | chamber/ lab | 0.047 | $5.0 \times 10^{-6}$ | total (geometric) | 29.4 | ? | |
| wood board (untreated, | chamber/ lab | 0.0023 | $2.5 \times 10^{-7}$ | total (geometric) | 22 | 0 | 2 |
| hard, fine) | | 0.0050 | $5.4 \times 10^{-7}$ | | | 50 | |
| | | 0.020 | $2.2 \times 10^{-6}$ | | | 90 | |
| wood board (untreated, soft, coarse) | chamber/ lab | 0.010 | $1.1 \times 10^{-6}$ | total (geometric) | 22 | 0 | 2 |
| | | 0.022 | $2.4 \times 10^{-6}$ | | | 50 | |
| | | 0.089 | $9.7 \times 10^{-6}$ | | | 90 | |
| wool carpet | chamber/ lab | 0.051 | $5.5 \times 10^{-6}$ | planar | | 0 | 2 |
| | | 0.073 | $7.9 \times 10^{-6}$ | | | 50 | |
| | | 0.13 | $1.4 \times 10^{-5}$ | | | 90 | |
| forest floor (hardwood) | chamber/ lab | 0.47 | $5.0 \times 10^{-5}$ | planar | 29.4 | ? | 1 |
| forest floor (coniferous) | chamber/ lab | 0.48 | $5.1 \times 10^{-5}$ | planar | | | |
| forest floor | chamber/ field | 0.40 | $4.3 \times 10^{-5}$ | planar | 10 to 22 | ambient | 3 |
| snow | EC/ prairie/ winter | 0.14 | $1.6 \times 10^{-5}$ | planar | -20 to 0 | N/A | 4[(c)] |
| **Foliar Surfaces** | | | | | | | |
| White pine (Pinus strobus) | chamber/field/NS | 0.043 | $4.6 \times 10^{-6}$ | LAI | 30 | 67 | 5 |
| | | 0.016 | $1.7 \times 10^{-6}$ | total leaf area[(d)] | | | |
| 10 tree species: 6 conif., 4 decid. | chamber/ lab | | | | 20 | <90 | 6[(i)] |

| | | | | | | | |
|---|---|---|---|---|---|---|---|
| Coniferous, avg. of 6 species | dark | 0.034 (0.009–0.087) | 3.7 x $10^{-6}$ | LAI | | | T2[f] |
| | | 0.013 | 1.4 x $10^{-6}$ | total leaf area[d] | | | |
| Deciduous, avg. of 4 species | dark | 0.017 (0.004–0.037) | 1.9 x $10^{-6}$ | LAI | | | T2[f] |
| | | 0.0090 | 9.8 x $10^{-7}$ | total leaf area[d,e] | | | |
| CA Oak (Quercus agrifolia) | chamber/ lab/ dark | 0.015 | 1.6 x $10^{-6}$ | LAI | 22 | 50–65 | 7 |
| | | 0.0080 | 8.7 x $10^{-7}$ | total leaf area[d,e] | | | |
| 5 tree species: 4 decid., 1 conif. | chamber/ lab | | | "leaf area" | | | 8[h] |
| avg. of 4 conif. species | abscisic acid | 0.013 (0–0.025) | 1.4 x $10^{-6}$ | | 20–25 | 50–60 | F5[g] |
| avg. of all 5 species | dark | 0.012 (0.004–0.021) | 1.3 x $10^{-6}$ | | 20 | 50 | F7[f] |
| 2 conif. species: pine & spruce | chamber/ field/ dark | 0.056 (0.03–0.08) | 6.2 x $10^{-6}$ | LAI | 10–14 | 50–70 | 3[h] |
| | | 0.021 | 2.3 x $10^{-6}$ | total leaf area[d] | | | |
| 8 tree species: 3 conif., 5 decid. | chamber/ lab | | | | 29.4 | ? | 1 |
| Coniferous, avg. of 3 species | dark (min $g_s$) | 0.015 (0.003–0.03) | 1.6 x $10^{-6}$ | total leaf area | | | F4[g] |
| Deciduous, avg. of 5 species | NS at $g_s$= 0 | 0.014 | 1.5 x $10^{-6}$ | LAI | | | T2[g] |
| | | 0.007 | 7.5 x $10^{-7}$ | total leaf area[d,e] | | | |
| Norway Spruce (Picea abies L.) | chamber/ field/ dark | 0.014 | 1.5 x $10^{-6}$ | total leaf area | 11.3±2.8 | 85.4±11.1 | 9, T2[g,h] |
| Deciduous leaves (average) | | 0.015 | 1.7 x $10^{-6}$ | LAI | | | all |
| Deciduous leaves (average) | | 0.007 | 7.5 x $10^{-7}$ | total leaf area[d] | | | all |
| Coniferous leaves (average) | | 0.015 | 1.7 x $10^{-6}$ | total leaf area[d] | | | all |

[a] Uptake coefficients for $NO_2$ inferred herein from literature values of surface deposition velocities: $\gamma_{NO_2} = 4\, v_d^{surf}\, \bar{v}_t^{-1}$, where $\bar{v}_t$ is the mean thermal speed of $NO_2$, and $v_d^{surf}$ the material-specific deposition velocity measured from well-mixed (minimal $R_a + R_b$) chamber studies, with the exception of uptake to snow which was measured via the EC method.

[b] Surface area used to normalize material-specific deposition fluxes in the computation of material-specific $v_d^{surf}$.

[c] $v_d^{surf}$ to snow was computed herein from reported EC-inferred $R_c(NO_2)$ to snow of 740 ± 210 s $m^{-1}$.

[d] Reported $v_d^{surf}$ normalized to LAI (projected leaf area) were scaled herein to reflect uptake to total leaf surface area—a factor of two for deciduous leaves and 2.7 for coniferous needles (see section 3.4.3.4).

[e] Non-stomatous adaxial (top) side of deciduous leaves may not have sufficient thin water films (Burkhardt et al., 1999) to support $NO_2$ uptake via hydrolysis.

[f] Mean value averaged herein from reported values.

[g] $v_d^{surf}$ computed herein by normalizing reported mean $NO_2$ flux by mean concentration.

[h] References which find stomatal conductance sufficient to explain observed $NO_2$ uptake.

[i] References for material-specific $v_d^{surf}(NO_2)$
(1) Hanson et al. (1989)
(2) Grøntoft et al. (2004)
(3) Rondón et al. (1993)
(4) Stocker et al. (1995)
(5) Wang et al. (2020)
(6) Delaria et al. (2020)
(7) Delaria et al. (2018)
(8) Chaparro-Suarez et al. (2011)
(9) Breuninger et al. (2013)

**Table S3.3:** Calculated monthly nocturnal above-canopy $V_d(NO_2)$ at Harvard Forest using bulk-canopy $R_c(NO_2)$ computed from: (1) bottom-up estimates of component canopy surface resistances using surface-specific $NO_2$ uptake coefficients (Table S3.2) and relevant surface area scaling; (2) $r_{hyd}$ (equation 3.12) with top-down constraints on the surface area scaling term α.

| | Jan. | Feb. | March | April | May | June | July | Aug. | Sept. | Oct. | Nov. | Dec. |
|---|---|---|---|---|---|---|---|---|---|---|---|---|
| **Canopy Conditions**[a] | | | | | | | | | | | | |
| T [°C][b] | -7.2 | -6.2 | -0.2 | 4.5 | 9.7 | 15 | 17 | 18 | 14 | 7.2 | 3.0 | -2.0 |
| RH [%][b] | 82 | 73 | 79 | 72 | 79 | 88 | 89 | 88 | 91 | 85 | 84 | 79 |
| LAI | 0.83 | 0.83 | 0.83 | 0.88 | 2.3 | 4.0 | 4.2 | 4.2 | 3.9 | 2.5 | 1.1 | 0.83 |
| $u^*$ [m $s^{-1}$][c] | 0.57 | 0.62 | 0.59 | 0.51 | 0.47 | 0.42 | 0.38 | 0.38 | 0.41 | 0.45 | 0.57 | 0.60 |
| **Aerodynamic Res.**[d] | | | | | | | | | | | | |
| $R_a$(29 m) [s $m^{-1}$] | 11.6 | 10.1 | 11.3 | 13.9 | 13.2 | 14.9 | 16.9 | 17.3 | 15.7 | 14.6 | 10.7 | 12.0 |
| **Quasi-Laminar Res.**[d] | | | | | | | | | | | | |
| $R_b$(NO2) [s $m^{-1}$] | 14.0 | 12.1 | 12.8 | 14.9 | 14.8 | 16.4 | 17.8 | 16.7 | 16.3 | 15.4 | 12.6 | 12.5 |
| **Bottom-up $V_d(NO_2)$**[e] | | | | | | | | | | | | |
| $r_c$, leaf [s $m^{-1}$] | 3010 | 3010 | 2970 | 2870 | 1710 | 1010 | 960 | 980 | 1090 | 1610 | 2660 | 2980 |
| $r_c$, bark [s $m^{-1}$] | 809 | 807 | 798 | 792 | 784 | 777 | 774 | 772 | 779 | 788 | 794 | 801 |
| $r_a$, canopy [s $m^{-1}$] | 573 | 495 | 561 | 679 | 872 | 1180 | 1380 | 1390 | 1180 | 988 | 579 | 512 |
| $r_c$, floor [s $m^{-1}$] | 684 | 657 | 513 | 261 | 258 | 256 | 255 | 254 | 256 | 259 | 261 | 571 |
| $R_c$, canopy [s $m^{-1}$] | 414 | 392 | 372 | 361 | 334 | 314 | 322 | 318 | 323 | 342 | 323 | 377 |
| $V_d$ [cm $s^{-1}$] | 0.23 | 0.25 | 0.27 | 0.27 | 0.29 | 0.3 | 0.29 | 0.29 | 0.29 | 0.28 | 0.31 | 0.26 |
| **Top-down $V_d(NO_2)$**[f] | | | | | | | | | | | | |
| $R_c = r_{hyd}$(α=1) [s $m^{-1}$] | 719 | 773 | 864 | 1108 | 970 | 822 | 795 | 728 | 774 | 903 | 862 | 759 |
| $R_c = r_{hyd}$(α=2) [s $m^{-1}$] | 406 | 445 | 452 | 554 | 485 | 411 | 397 | 364 | 387 | 452 | 431 | 423 |
| $V_d$ (α=1) [cm $s^{-1}$] | 0.13 | 0.13 | 0.12 | 0.1 | 0.11 | 0.12 | 0.12 | 0.13 | 0.13 | 0.11 | 0.12 | 0.13 |
| $V_d$ (α=2) [cm $s^{-1}$] | 0.23 | 0.22 | 0.22 | 0.19 | 0.21 | 0.24 | 0.24 | 0.26 | 0.24 | 0.22 | 0.23 | 0.23 |

[a] T, RH, and $u^*$ are nocturnal (2000 – 0400 LST) monthly medians computed from an hourly data set spanning 2000 – 2002.
[b] Temperature and RH at 15 m.
[c] Periods of low turbulence, indicated by $u_* < 0.2$ m $s^{-1}$, were excluded.

(d) Above-canopy aerodynamic resistance computed as $R_a$(29m) = $u$ (29 m)/$u_*^2$; quasi-laminar boundary layer resistance $R_b$ computed following equation 3.4.

(e) Bottom-up $V_d(NO_2)$ computed following 3.2, with $R_c = \left[1/r_{leaf} + 1/r_{bark} + 1/\left(r_a + r_{floor}\right)\right]^{-1}$. Component $r_c = 4/(\bar{v}_t\, \gamma\, \alpha)$, where uptake coefficients are averaged from Table S3.2 values: $\bar{\gamma}_{leaf}$ = 1.7 x $10^{-6}$, $\bar{\gamma}_{bark}$ = 5.0 x $10^{-6}$, $\bar{\gamma}_{floor}$ = 4.3 x $10^{-5}$, $\bar{\gamma}_{snow}$ = 1.6 x $10^{-5}$. The forest floor was assumed snow covered for months DJFM when T < 0 °C. Canopy component surface area scale factors where: $\alpha_{leaf} = [1\ (RH < 95\%)\ \text{or}\ 2\ (\text{RH} > 95\%)]DLAI + 2.7CAI$, where CAI = 0.83, and DLAI = LAI – CAI are the projected areas of coniferous needles and deciduous leaves; $\alpha_{bark} = \pi$STAI, where STAI = 0.9 is the projected area of tree branches; $\alpha_{floor}$ = 1 as $\bar{\gamma}_{floor}$ and $\bar{\gamma}_{snow}$ from Table S3.2 are reported for planar surface areas. Note, $NO_2$ hydrolysis is assumed to occur on the stomatal surfaces of leaves (lower for deciduous and total for coniferous) due to the presence of thin water films (see section 3.4.3.4). In-canopy aerodynamic resistance ($r_a$) follows Zhang et al. (2003) $r_a = R_{ac0}\ LAI^{0.25}\ u^{*-2}$, where $R_{ac0}$ are landtype specific prescribed values.

(f) Top-down $V_d(NO_2)$ computed following 3.2 and $r_{hyd}$ following 3.12. Note, snow is assumed present for months DJFM when T< 0 °C where $\bar{\gamma}_{snow}$ = 1.6 x $10^{-5}$ is used for all available surface area for $r_{hyd}$, α = 1, and ½ of available surface area for $r_{hyd}$, α = 2.

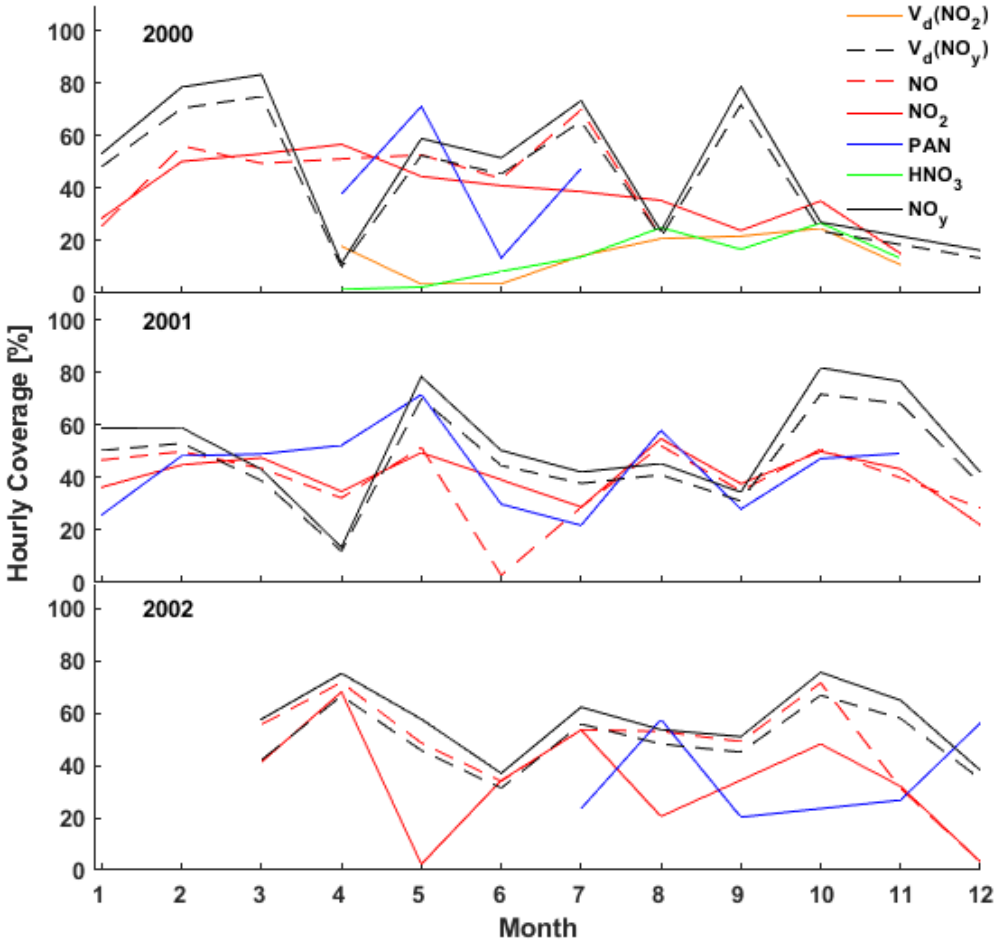


**Figure S3.7:** Hourly coverage of above-canopy trace gas and deposition velocity ($V_d$) measurements at HFEMS. Concentration measurements include $NO_2$, NO, $HNO_3$, PAN, and $NO_y$. Measurements taken during conditions of low turbulence ($u_* < 0.2$ m $s^{-1}$) where omitted from analysis.

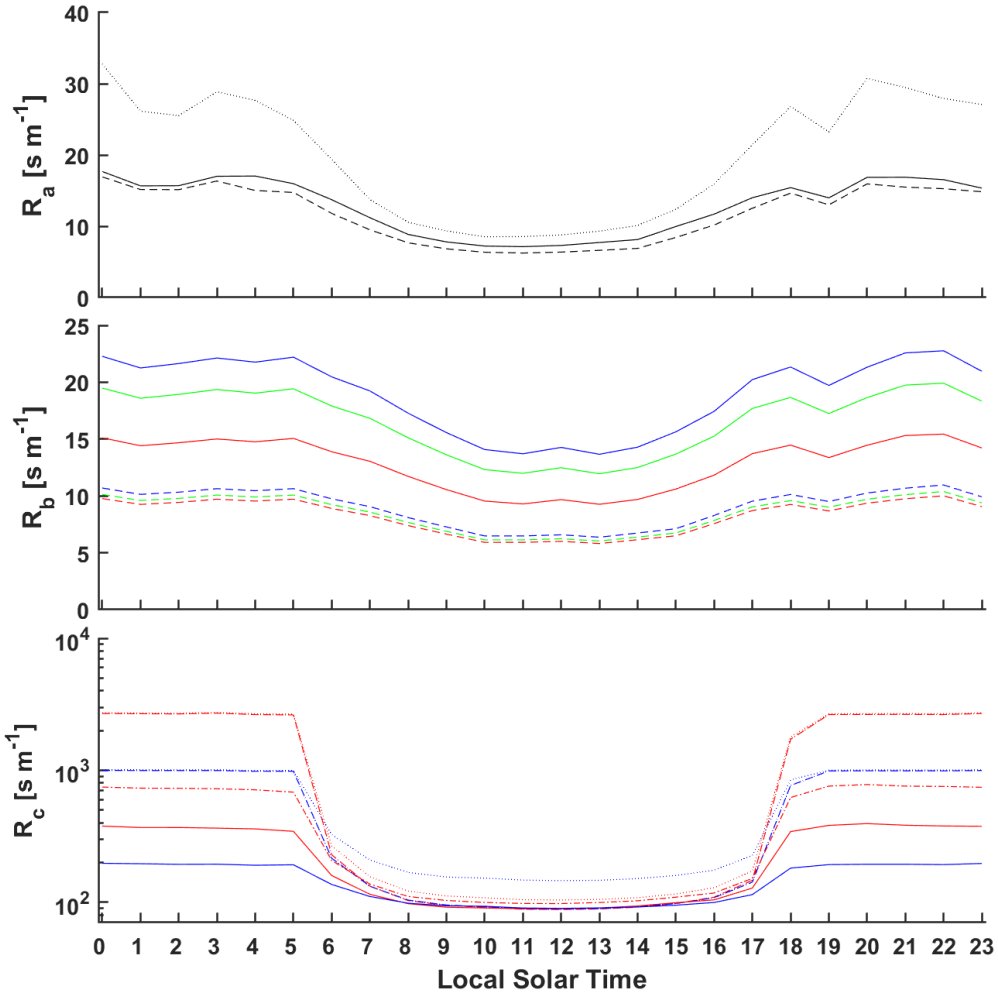


**Figure S3.8:** Median component resistances $R_a$, $R_b$, and $R_c$ of deposition velocities for $HNO_3$ (**green**), $NO_2$ (**red**), and PAN (**blue**). Aerodynamic resistance $\boldsymbol{R_a}$ is common to all species and depicted for parameterizations P2 (black, dashed) and P3 (black, solid) computed from the 29 m measurement height; P3 $R_a$(65 m) is shown as dotted. Quasi-laminar boundary layer resistance $\boldsymbol{R_b}$ is shown for all species according to parameterizations P1 (dashed) and P5 (solid). Surface layer resistances $\boldsymbol{R_c}$ are depicted for parameterizations P1(dashed), P5 (dotted), P6 (dot-dash), and P8(solid).

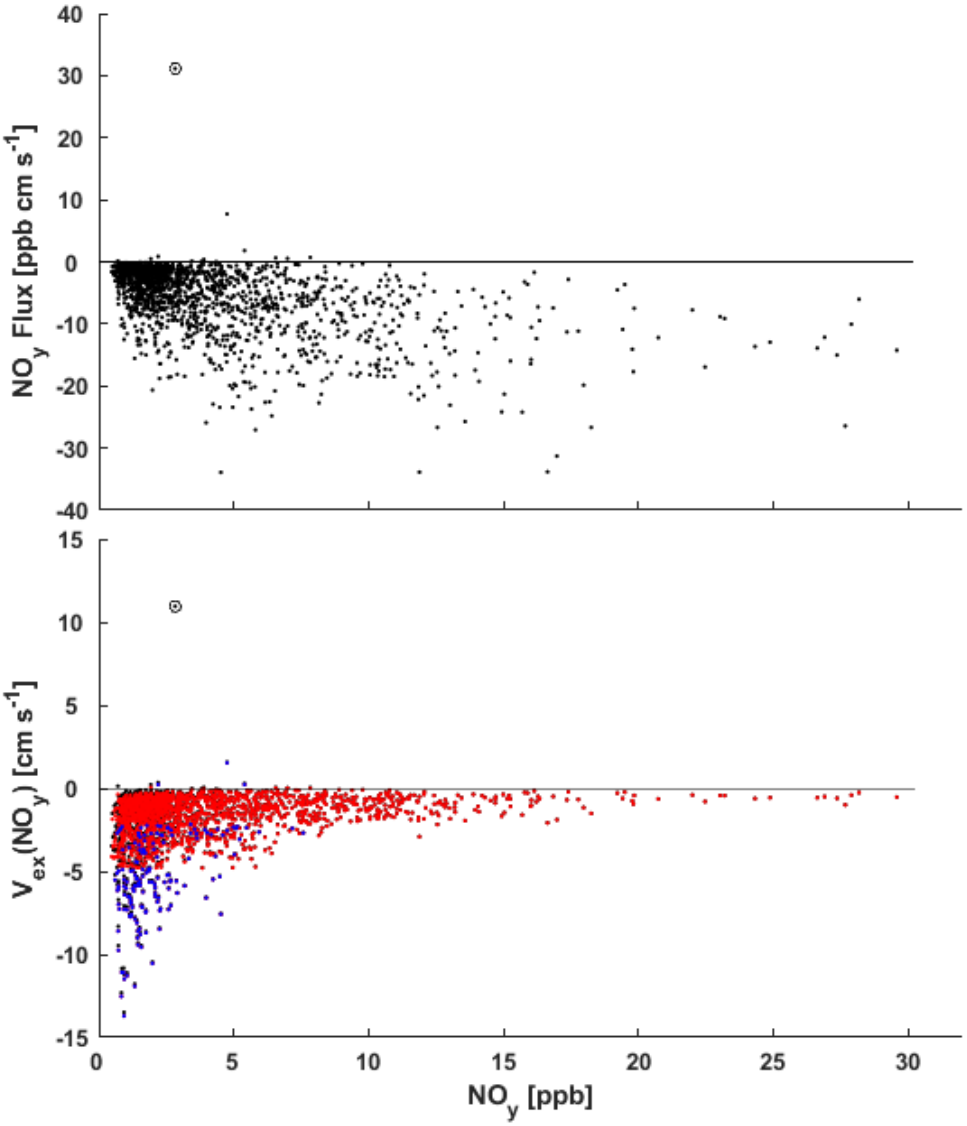


**Figure S3.9:** Hourly $NO_y$ flux (**Top**) and resulting exchange velocities $V_{ex}(NO_y)$ (**Bottom**) as a function of $NO_y$ concentration. These publicly available measurements (Horii, 2004) were made via eddy covariance over an established mixed deciduous forest (Harvard Forest, MA, U.S.) from June-November 2000. Estimated above-canopy soil $NO_x$ flux was subtracted from measured hourly $NO_y$ fluxes in order to estimate $V_{ex}(NO_y)$ due to deposition (red dots, BOTTOM). Data excluded by a nighttime and daytime $V_{ex}(NO_y)$ outlier filter are shown in blue. Data points excluded from analysis based on visual inspection are circled. Hourly observations coincident with $u_* < 0.2$ m $s^{-1}$ were excluded from analysis.

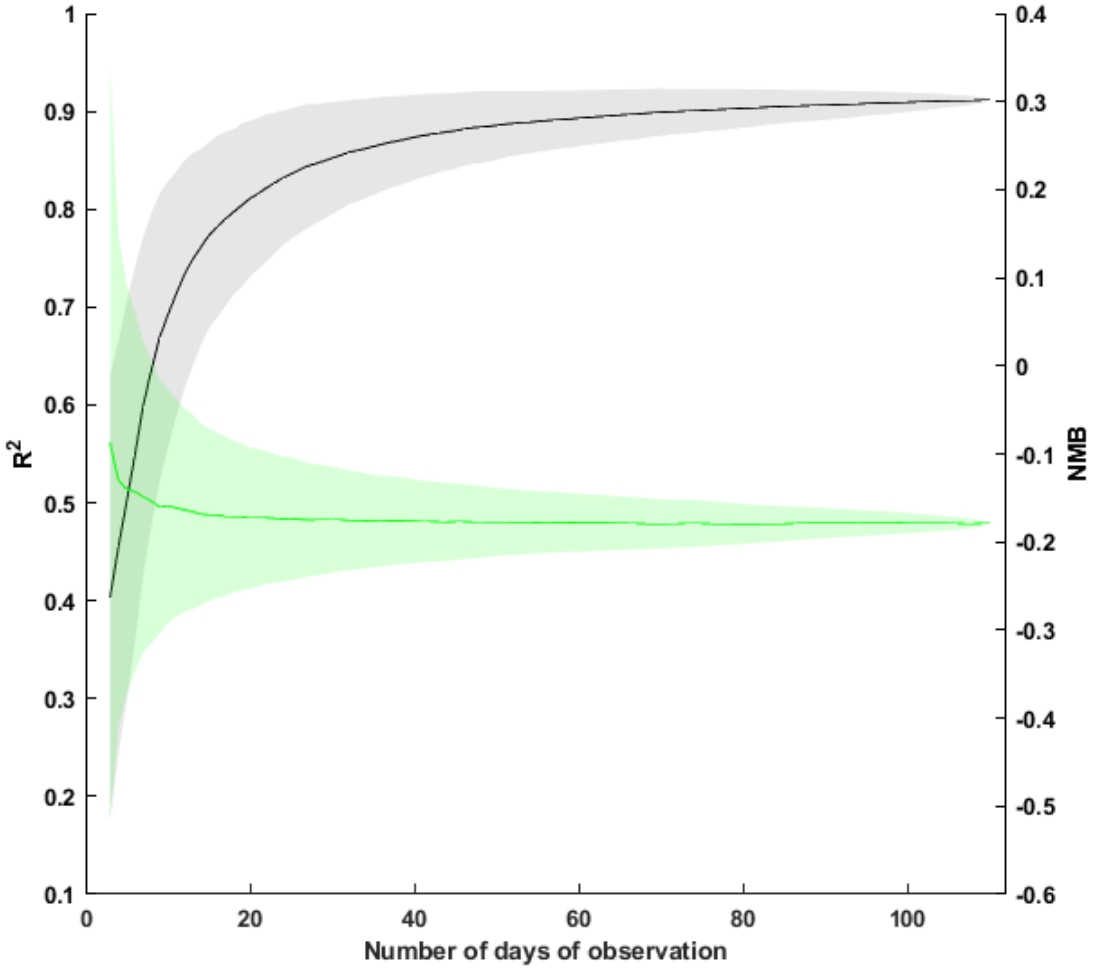


**Figure S3.10:** Coefficient of determination $R^2$ (**black**) and normalized mean bias NMB (**green**) between 24-hr average observed and parameterized (P8) $V_d(NO_y)$ as a function of the number of days contributing to the average. Standard deviations were obtained by randomly sampling the corresponding number of days over $10^4$ iterations and are depicted as shaded regions.

# Chapter 4

# Implications of Subgrid Dry Deposition of $NO_2$ with a Pathway for Ground Surface Hydrolysis and HONO Production in a Global Chemical Transport Model (GEOS-Chem)

## 4.1 Abstract

Near-surface concentrations of nitrous acid (HONO), an important photolytic source of OH, are biased low in atmospheric models that neglect formation via heterogeneous hydrolysis of $NO_2$ on ground surfaces. We implement this reaction pathway into the GEOS-Chem chemical transport model (CTM) as a dry deposition process, resulting in large (>100%) increases in near-surface HONO concentrations and improved comparison to HONO observations from the WINTER aircraft campaign over the northeastern U.S. where a significant low bias in nocturnal near-surface (<120 m) HONO of more than 60% was reduced to ca. 20%. Although improved, daytime low biases in simulated HONO persist and are discussed in the context of several other potential sources of daytime HONO not currently included in GEOS-Chem. In addition to providing mechanistic utility for a dominant nocturnal HONO source, $NO_2$ hydrolysis on ground surfaces provides a non-stomatal pathway for $NO_2$ dry deposition at locations and times when uptake would otherwise be near negligible in GEOS-Chem, such as at night and vegetatively senescent periods. A 4% increase in $NO_y$ total (wet + dry) deposition results over wintertime eastern North America, with much larger increases of up to 100% close to $NO_x$ sources for high-latitude cities.

In addition, we develop a simple method for large scale CTMs to reconcile subgrid dry deposition of near-surface emitted species that have chemical lifetimes much longer than the timescale for turbulent vertical mixing within the lowest model level. We implement our parameterization of subgrid dry deposition into GEOS-Chem via a 4-D look-up table and apply it to near-surface anthropogenic emissions of $NO_x$ and nocturnal HONO. Significant diel variation exists in resulting effective reductions of $NO_x$ emissions due to subgrid dry deposition, with nocturnal reductions of 10–20% and daytime reductions

near-negligible outside of high latitudes during winter months. An effective reduction of 4% is noted for total annual $NO_x$ emitted over eastern N.A. Large increases in $NO_y$ total deposition for urban centers, driven predominantly by subgrid dry deposition, are in the range 20–100% for summertime and a factor of 2–3 for wintertime, shifting the deposition pattern of oxidized reactive nitrogen closer to source and reducing the export of $NO_y$ out of Canada and the U.S.

Despite reductions in ground-level $NO_2$ concentrations on the order of 5–20%, with commensurate reduction in regional concentrations of total nitrate (TN = $HNO_3$ + $pNO_3$), increases in daytime TN at urban centers of up to 60% during winter correlate with large increases in HONO and OH, highlighting the important role of HONO as a photolytic source of OH during times of reduced solar radiation, and the influence on secondary chemistry.

**Keywords:** $NO_2$ heterogeneous hydrolysis; disproportionation; dry deposition; subgrid; HONO; OH; chemical transport model; GEOS-Chem

## 4.2 Introduction

A fundamental challenge models of atmospheric chemistry face is representativeness of scale—processes, many of which are non-linear, must be simulated across large domains to be tractable. As computational capability improves, so too does the resolution amenable to simulation, however, if a variable cannot be resolved at an operational resolution and this variable is involved in a non-linear process, a subgrid scale results (Ridley et al., 2013). Methods such as targeted high resolution simulation (Bindle et al., 2020; Yu et al., 2016) and parameterization of subgrid scale processes (Brasseur and Jacob, 2017; Stevens and Pierce, 2013; Vinken et al., 2011) have greatly improved the capability of global chemical transport models (CTMs), yet many subgrid processes remain unrepresented. One such underrepresentation is the dry deposition of species emitted/formed in proximity to deposition surfaces.

Near-surface emitted species are assumed to mix instantaneously within the ground-level grid boxes of atmospheric models, which for global CTMs can span over 100 m vertically. Subsequent unidirectional dry deposition typically follows a 'second-generation' type resistance-in-series model (Wesely and Hicks, 2000), where deposition is parameterized to occur from grid cells at the lowest model level to a single uniform surface ('big-leaf') according to a parameterized first-order rate constant known as the deposition velocity ($V_d$) which has contributions from turbulent transport, molecular diffusion, and surface uptake reactions. This method assumes a positive concentration gradient is maintained from the surface to the height at which deposition velocity calculations are referenced, typically the center of the lowest model level—an assumption that holds for secondary species such as $O_3$ and $SO_2$, but fails near-source for surface emitted species such as $NH_3$ and $NO_2$. Potential underestimates in the dry deposition of near-surface emitted species results from the combination of (i) the vertical extent of surface grid boxes failing to capture near-surface concentration gradients and (ii) imposition of a resistance to turbulent transport computed to grid box centers. In a Large-Eddy Simulation (LES) of turbulent dispersion with dry deposition of $NH_3$ emitted from an area source modeling a cattle feedlot in Fort Collins, Colorado, Lassman et al. (2020) find that 20% of emitted $NH_3$ dry deposits within the first 5 km downwind of the feedlot under neutral to somewhat unstable daytime summer conditions. It was noted that most deposition occurs within 3 km and very little over the next 10 km as near-surface layers become depleted of $NH_3$. Lassman et al. (2020) comment that under extremely unstable atmospheric conditions, concentrated plumes may rapidly mix away from the surface resulting in almost no near-source deposition, while under stable conditions a concentrated plume would be expected to linger along the surface. Given the high vertical resolution of their LES simulation—5 m near-surface increasing to 60 m at 1 km—these results would be a subgrid process in a global CTM such as GEOS-Chem, thus requiring parameterization.

The potential underestimate in dry deposition of near-surface emitted $NO_x$ is of particular interest given the influence that $NO_x$ has on photochemistry and the oxidizing power of the atmosphere (Crutzen, 1979a; Jacob et al., 1992b), air quality (Fields, 2004; Pusede et al., 2015b), and the eutrophication of natural ecosystems including potential for loss of biodiversity (Obbink et al., 2010; Paulot et al., 2013; Zhang et al., 2012a). Given

that $NO_x$ is predominantly a near-surface emitted species, large vertical gradients in concentration often exist, especially in proximity to urban landscapes (Dieudonné et al., 2013). A large fraction of anthropogenic $NO_x$ emission occurs near the ground surface via the combustion of fossil fuels (McDuffie et al., 2020). In the U.S., mobile sources accounted for ca. 60% of $NO_x$ emissions in the year 2002 (U.S. EPA, 2008, 2010), decreasing to ca. 40% or less in summer months for recent years (Travis et al., 2016). A large fraction of natural $NO_x$ emission occurs from the ground surface via microbial (de)nitrification reactions (Medinets et al., 2015), and within-canopy reductions of up to 70–80% have been required to reconcile measured soil emissions with above canopy observations (Jacob and Wofsy, 1990; Lerdau et al., 2000). Subsequent development of deposition-based canopy reduction factors (CRF) for use in large-scale CTMs reduce global mean above-canopy soil $NO_x$ fluxes by 20–50% (Wang et al., 1998; Yienger and Levy, 1995). Although the mechanism of this subgrid process is still an active area of research (Min et al., 2014), a recent canopy-resolving 1-D model study highlights the importance that foliar dry deposition of $NO_2$ makes to in-canopy soil $NO_x$ reductions, removing as much as 60% of soil emitted $NO_x$ prior to canopy ventilation (Delaria and Cohen, 2020). Travis et al. (2016) note that zeroing out soil $NO_x$ emissions (18% of total $NO_x$ emitted to the summertime southeast U.S.) halves the necessary reduction in anthropogenic non-powerplant surface $NO_x$ emissions (from 60% to 30%) required to reconcile GEOS-Chem simulated fields, in particular a daytime high bias in $O_3$, with a suite of aircraft- and surface-based observations over the summertime southeastern U.S. In addition to uncertainties in soil $NO_x$ emissions and subsequent canopy uptake, subgrid dry deposition of anthropogenic near-surface emitted $NO_x$ could potentially further explain a portion of this necessary reduction.

In Chapter 3, section 3.4.3, a large low bias in GEOS-Chem simulated nocturnal $V_d(NO_2)$ was eliminated by representing the heterogeneous disproportionation of $NO_2$ on wet/humidified ground surfaces—a well-known phenomenon that has been studied in the lab (Finlayson-Pitts et al., 2003; Kleffmann et al., 2003; Spicer et al., 1993) and field (Harrison et al., 1996; Harrison and Kitto, 1994; Kurtenbach et al., 2001; Ren et al., 2020; VandenBoer et al., 2013; Wojtal et al., 2011) for some time. Although the reaction mechanism is still an active area of research (Spataro and Ianniello, 2014), the

stoichiometric equation yielding adsorbed nitric acid ($HNO_3$) and evolved nitrous acid (HONO) is shown in reaction R4.1. HONO is also formed in the atmosphere by the homogeneous reaction of NO with OH (reaction R4.2), however, efficient photolysis (Kraus and Hofzumahaus, 1998) (reaction R4.3) generally results in much lower daytime concentrations than at night when near-surface HONO accumulates due to R4.1—an exception being the remote tropical marine boundary layer where, away from strong $NO_x$ sources, HONO has the opposite diel profile with peak daytime concentrations correlating to a photolytic source (Kasibhatla et al., 2018; Reed et al., 2017).

$$2\,NO_{2\,(g)} + H_2O_{(ads)} \xrightarrow{surf} HONO_{(g)} + HNO_{3\,(ads)} \qquad (R4.1)$$

$$NO_{(g)} + OH_{(g)} + M \rightarrow HONO_{(g)} + M \qquad (M = N_2, O_2) \qquad (R4.2)$$

$$HONO_{(g)} \xrightarrow{hv} OH + NO \quad (\lambda < 400\,nm) \qquad (R4.3)$$

Reactions R4.1–3 are included in GEOS-Chem, however, R4.1 is represented on aerosol surfaces only. It is generally believed that R4.1 is the predominant nocturnal source of atmospheric HONO in anthropogenically influenced regions (Kanaya et al., 2007; Li et al., 2011; Sarwar et al., 2008; Zhang et al., 2016), with ground surfaces dominating boundary layer production (Gonçalves et al., 2012; Harrison et al., 1996; Harrison and Kitto, 1994; Kleffmann et al., 2003; Laufs et al., 2017; Meng et al., 2020; Qin et al., 2009; VandenBoer et al., 2013; Vogel et al., 2003; Wong et al., 2011; Yu et al., 2009). Except under extreme haze episodes, ground surfaces typically provide 1–2 orders of magnitude more surface area for heterogeneous reaction than does typical boundary layer aerosol, thus enabling R4.1 to proceed at appreciable rates despite small $NO_2$ reactive uptake coefficients ($\gamma_{NO_2}$ < 5 x $10^{-5}$ Table S3.2 from Chapter 3). However, this is not universally true, as was recently shown by Meng et al. (2020) in their analysis of high-resolution vertical profiles of HONO and $NO_2$ over Beijing, severe haze episodes ($PM_1$ ~100–200 μg $m^{-3}$) can provide sufficient aerosol surface area (ca. 30% of that of the ground surface) that aerosol surfaces may dominate nocturnal HONO production aloft in the residual layer.

Given the importance of the hydroxyl radical (OH) as an oxidant in the atmosphere (Gligorovski et al., 2015; Levy, 1971; Thompson, 1992), there is much interest in an

accurate HONO simulation due to reaction R4.3 as a direct source of OH. Owing to its nocturnal accumulation and efficient photolysis, HONO is a dominant early morning source of OH in polluted environments at a time when other sources, such as the photolysis of $O_3$ and formaldehyde (HCHO), are small (Alicke et al., 2003; Platt et al., 2002; Winer and Biermann, 1994). Additionally, the photolysis of HONO can make significant contributions to near-surface daytime OH, contributing to as much as half of primary OH production over a 24-hr period (Finlayson-Pitts, 2009; Gligorovski et al., 2015), and has been found to dominate daytime production under polluted wintertime conditions (Elshorbany et al., 2010; Kim et al., 2014; Ren et al., 2006; Villena et al., 2011), as well as being an important contributor to OH in the polluted marine boundary layer (Cui et al., 2019; Wen et al., 2019). As a result, HONO has been implicated in photochemical smog events (Tan et al., 2019; Zhang et al., 2019), as well as in wintertime high $O_3$ episodes (Rappenglück et al., 2014).

In addition to emission via R4.1, surface uptake of HONO has been identified as a key process in governing boundary layer concentrations. HONO is a photolabile weak acid ($pK_a$ = 3.3 at 25 °C) with limited undissociated solubility (Henry's solubility $H_{HONO}$ = 49 M atm$^{-1}$ vs $H_{HNO_3}$ = 2.1 x 10$^5$ M atm$^{-1}$ (Sander, 2015)), resulting in a diel pattern of surface-dependent dynamic equilibria that establish between deposition and re-emission. Nocturnal evolution of near-surface concentrations typically follow a pattern of evening build-up to a pseudo-steady-state characterized by concomitant emission (R4.1) and dry deposition (Stutz et al., 2004). Accordingly, field studies endeavoring to measure ground uptake coefficients for both $NO_2$ and HONO have exploited this typical diel pattern by attributing early evening build-up of HONO to R4.1 and late evening approach to pseudo-steady-state to dry deposition, noting possible re-emission the following day due to dew evaporation (He et al., 2006; Ren et al., 2020) or reactive displacement (VandenBoer et al., 2015). Wentworth et al. (2016) quantify the role of dew as a nocturnal reservoir and morning source of $NH_3$ at a remote summertime grassland, noting that other atmospheric trace gases with effective Henry's solubilities $H^* > 10^5$ M atm$^{-1}$ ($H^*_{HONO}$ = 2.6 x 10$^5$ M atm$^{-1}$ at pH 7 (Park and Lee, 1988)) might also be influenced by dew formation and evaporation in a similar manner—an assertion which (Ren et al., 2020) corroborates for HONO over a rural summertime grassland. Other studies have highlighted the gas-surface dynamic

equilibrium that establishes from a surface reservoir of HONO/nitrite, resulting in periods of apparent zero order formation (Wojtal et al., 2011), or re-emission buffering changes in concentration from rapid air mass exchange (Collins et al., 2018; Febo and Perrino, 1991; Spicer et al., 1993; Wainman et al., 2001; Wang et al., 2020a, 2020b).

Currently, GEOS-Chem represents bidirectional exchange, i.e., for $NH_3$, as independent emissions and deposition processes. In an effort to address the bidirectional nature of the dynamic equilibrium that HONO establishes with surfaces, Karamchandani et al. (2015) developed a process-based surface model framework for the heterogeneous formation of HONO in the Comprehensive Air quality Model with extensions (CAMx) CTM, where processes including (de)sorption, leaching into soils and penetration into vegetation, surface chemistry, and re-emission into air were simulated from a reservoir of deposited species ($NO_2$, $HNO_3$, and HONO). Surface model parameters were refined by comparing sensitivity simulations to measurements of $NO_2$, $HNO_3$, and HONO made during the Study of Houston Atmospheric Radical Precursors (SHARP) campaign, April–May 2009, where authors acknowledge uncertainties in model parameters, but note the useful scaffold from which to build on as future measurement data becomes available and understanding evolves. A point of interest is that Karamchandani et al. (2015) use the unmodified CAMx dry deposition parameterization of Wesely et al. (1989), which does not take into account the increased uptake of $NO_2$ from reaction R4.1 occurring on ground surfaces. Reaction R4.1 has the potential to significantly increase the dry depositional sink of $NO_2$ at night and during vegetatively senescent periods (Chapter 3, section 3.4.3.3). Furthermore, box model analysis of urban areas have parameterized ground surface HONO emission by assuming $NO_2$ surface uptake is driven entirely by reaction R4.1 with resulting HONO emitted at a 50% yield using values for $V_d(NO_2)$ from either the Wesely 1989 deposition model (Aumont et al., 2003) or assuming a constant value for $V_d(NO_2)$ of 0.1 cm $s^{-1}$ (Kanaya et al., 2007). Both box model studies include simultaneous dry deposition of HONO according to Wesely et al. (1989) and find that urban HONO resulting from this parameterization makes significant contributions to daytime OH in winter, and morning OH in summer.

Many atmospheric chemical transport models, including the widely utilized GEOS-Chem and WRF-Chem CTMs, have yet to represent (to our knowledge) some key HONO pathways, including (i) updates to dry deposition parameterizations to include the effects of R4.1 on ground surfaces, and (ii) HONO as a species that is dry deposited and possibly re-emitted from surface reservoirs. In an effort to address widespread underestimates in simulated HONO concentrations, some CTMs, including CMAQ (Czader et al., 2012; Gonçalves et al., 2012; Sarwar et al., 2008; Zhang et al., 2012b) and WRF-Chem (Li et al., 2010; Zhang et al., 2016), have implemented reaction R4.1 on ground surfaces via a collision-limited heterogeneous rate constant $k_{het}$ describing first-order loss of $NO_2$ to ground surfaces from the lowest model level:

$$k_{het} = \frac{\gamma_{NO_2}\,\overline{v_t}}{4}\left(\frac{S_g}{V}\right) \tag{4.1}$$

where $\gamma_{NO_2}$ is the reactive uptake coefficient (reaction probability) for $NO_2$ resulting from heterogeneous hydrolysis, $\overline{v_t}$ is the mean molecular (thermal) speed of $NO_2$ in air, and $S_g/V$ the surface area density of the ground surface within the lowest model level. Following the stoichiometry of R4.1, the rate of HONO production from heterogeneous hydrolysis of $NO_2$ would require $k_{het}$ to be scaled by a factor of ½. Implementing reaction R4.1 on the ground surface via 4.1 neglects aerodynamic transport and diffusive terms, a reasonable assumption for heterogeneous reactions with small enough uptake coefficients ($\gamma <$ ~ 5 x $10^{-7}$) where very slow surface reaction is rate controlling (Cano-Ruiz et al., 1993). However, $NO_2$ ground uptake coefficients are generally in the range 2 x $10^{-6} < \gamma_{NO_2} <$ 5 x $10^{-5}$ (Chapter 3, equation 3.13, and Table S3.2), thus supporting the inclusion of both transport and surface-uptake resistances such as through a standard resistance-in-series parameterization of dry deposition (Chapter 3, section 3.4.3.6 for further discussion). Additionally, including R4.1 in a parameterization of dry deposition provides mechanistic utility to HONO emission via subgrid dry deposition of near-surface emitted $NO_x$—a main component of this study.

This Chapter implements into the GEOS-Chem CTM recommended updates to trace gas dry deposition from Chapter 3, including (i) an updated calculation of molecular diffusivities to address high biases and (ii) reaction R4.1 on ground surfaces to address a

low bias in nocturnal $V_d(NO_2)$ as well as to provide mechanistic utility to near-surface HONO production. HONO wet and dry deposition are also implemented. In addition to the updates recommended from Chapter 3, this chapter develops and implements into GEOS-Chem a simple method to reconcile subgrid dry deposition of near-surface emitted species that have chemical lifetimes (i.e., hours for $NO_x$) much longer than the timescale for turbulent vertical mixing within the lowest model level (i.e., minutes during daytime to ca. 1 h at night). We apply our method of subgrid dry deposition to near-surface anthropogenic emissions of $NO_x$ and nocturnal HONO. Results are discussed in the context of a high resolution nested North American simulation for the year 2013. In addition, relevant updates are evaluated against HONO observations from the WINTER aircraft campaign which took place over the Northeastern U.S. from February to March 2015.

### 4.3 GEOS-Chem

The GEOS-Chem 3-D chemical transport model (Bey et al., 2001) version 10.01 (http://geos-chem.org) was used for this study. GEOS-Chem is driven by assimilated meteorological fields produced by the Global Modeling and Assimilation Office (GMAO) at NASA (http://gmao.gsfc.nasa.gov). We use GEOS-FP assimilated meteorology (Lucchesi, 2013) at the native horizontal resolution of 1/4° x 5/16° and temporal resolution of 3-hr for 3-D fields and 1-hr for 2-D fields. For our study area of the U.S. and Canada, we run a nested configuration of GEOS-Chem over North America and adjacent oceans (130–60°W, 9.75–60°N) at native resolution (1/4° x 5/16°), with user-defined dynamic (advection, vertical mixing, cloud convection, and wet deposition) and chemical (emissions, dry deposition, and chemistry) time steps of 5 min and 10 min, respectively. Dynamic boundary conditions to the nested simulations were archived from global simulations at a horizontal resolution of 2° x 2.5° following six months of model spin-up to reduce the effects of initial conditions. The GEOS-Chem simulations have 47 vertical levels from the surface to 0.1 hPa (ca.80 km), including ca. 35 levels within the troposphere and 8 levels below 1 km where vertical grid resolution increases from ca. 120 m to 150 m. We analyze simulated output from 1 December 2012 to 31 November 2013, and periods between 1 February to 15 March 2015 coincident in time and space with the WINTER

aircraft campaign over the northeast U.S., as discussed below in section 4.5.2. Nested simulations commence 14 days prior to the start date of data analysis.

### 4.3.1. General Description of Base Simulation

GEOS-Chem includes a detailed simulation of $HO_x$-$NO_x$-VOC-$O_3$-$BrO_x$-aerosol chemistry (Fisher et al., 2016; Mao et al., 2010, 2013a; Travis et al., 2016) with over 550 reactions and transporting 66 tracers in the standard tropospheric chemistry scheme, which was selected for use herein. A variety of externally mixed aerosol species including the sulfate-nitrate-ammonium complex (SNA), hydrophobic and hydrophilic organic aerosol (OA), black carbon (BC), dust, and sea salt are represented (Kim et al., 2015). The simulation of aerosol-gas interaction takes place via heterogeneous chemistry (Evans and Jacob, 2005; Jacob, 2000; Mao et al., 2013b), thermodynamic partitioning of the SNA complex according to the ISORROPIA II equilibrium model (Fountoukis and Nenes, 2007; Pye et al., 2009b) and aerosol effects on photolysis frequencies (Martin et al., 2003a). The vertical mixing of tracers between model levels within the planetary boundary layer (PBL) follows a K-theory parameterization with nonlocal mixing under unstable conditions as formulated by Holtslag and Boville (1993) and implemented by Lin and McElroy (2010). The wet deposition scheme includes both rainout (in-cloud) and washout (below-cloud) scavenging of aerosol and soluble gases by precipitation, and is described in Liu et al. (2001) and Amos et al. (2012) for the model version used herein.

Dry deposition in GEOS-Chem is represented as an irreversible first-order loss process from surface grid boxes where the flux $F_x$ of a depositing species $x$ is proportional to the above-canopy deposition velocity $V_d$ (positive down):

$$F_x = -V_d\,[x] \tag{4.2}$$

Species-specific deposition velocities are computed following a standard resistance-in-series scheme:

$$V_d = (R_a + R_b + R_c)^{-1} \tag{4.3}$$

where $R_a$ is the aerodynamic resistance to turbulent transport from a reference height $z$ (center of surface grid boxes, ca. 60 m agl) to the roughness length ($z_o$) of the surface; $R_b$

represents resistance due to molecular diffusion across a quasi-laminar boundary layer; $R_c$ reflects the resistance to surface uptake of the impacting species. The dry deposition surface in GEOS-Chem is treated as a single uniform surface (i.e., 'big leaf') following the widely utilized Wesely 1989 algorithm (Wesely, 1989) modified for application to the global scale (Wang et al., 1998). Both foliar and non-foliar deposition pathways are represented across 11 subgrid land-types. Formulations for $R_a$, $R_b$, and $R_c$ used in GEOS-Chem are discussed in Chapter 3, section 3.3.1. Following the recommendations of (Shah et al., 2018), we limit the cold temperature exponential increase in the non-stomatal components of $R_c$ to a factor of 2, and set a nominally small $R_c(HNO_3) = 1$ s $m^{-1}$. We present several updates to dry deposition in GEOS-Chem, as discussed in section 4.4.

Anthropogenic emissions in GEOS-Chem are managed via the Harvard-NASA Emission Component (HEMCO) module which processes input emission data inventories, at any spatial and temporal resolution, for use on the user-defined grid (Keller et al., 2014). Global anthropogenic emissions of $NO_x$ and CO are taken from the Emissions Database for Global Atmospheric Research (EDGAR v4.2; http://edgar.jrc.ec.europa.eu/). Global anthropogenic VOC emissions are taken from the Reanalysis of the Tropospheric Chemical Composition inventory (RETRO; http://eccad.sedoo.fr/). Regional overwrites of anthropogenic emissions occur over Canada (CAC; http://ec.gc.ca/inrp-npri/), United States (EPA NEI 2011; http://www.epa.gov/chief), Europe (EMEP; http//emep.int/), Mexico (BRAVO; (Kuhns et al., 2005)), and Asia (MIX; (Li et al., 2015). Anthropogenic emissions of $NO_x$, $SO_2$, CO, VOCs, and $NH_3$ over the United States from the U.S. EPA's National Emissions Inventory (NEI) were scaled from the base year of 2011 to simulation years by application of species-specific scale factors calculated from the EPA's national annual trend report (U.S. Environmental Protection Agency, 2021). Shipping emissions of $NO_x$ are processed by the PARANOX module (PARAmeterization of emitted $NO_x$) which accounts for subgrid $O_3$ and $HNO_3$ production within the plume over a period of 5 h and was implemented into GEOS-Chem by Vinken et al. (2011) via look-up-tables. Year-specific biomass burning emissions (wildfires and agricultural fires) are from the Global Fire Emissions Database (GFED) v4 (Giglio et al., 2013). Biogenic VOCs from the Model of Emissions of Gases and Aerosols from Nature (MEGAN) v2.1 (Guenther et al., 2012). Soil $NO_x$ emissions, including from fertilizer application, follow the parameterization of

Hudman et al. (2012), with emissions being subjected to online canopy reduction to account for possible subgrid vegetative uptake prior to ventilation from the canopy (Wang et al., 1998). Other sources of natural emission include lightning $NO_x$ (Murray et al., 2012), volcanic $SO_2$ (Diehl et al., 2012), oceanic DMS (Johnson, 2010), sea salt aerosol (Jaeglé et al., 2011), and mineral dust (Fairlie et al., 2010; Zender, 2003).

## 4.4 Updates to GEOS-Chem

GEOS-Chem simulations evaluated herein are presented in Table 4.1 and include several serial updates to the base simulation (S1) relating primarily to the dry deposition of trace gases. Updated simulations S2-S5, discussed in detail in the following sections, include: S2 with updates to $R_a$, molecular diffusivity in air, and implementation of HONO wet and dry deposition; S3 with representation of reaction R4.1 on ground surfaces, including HONO emission and updates to $R_c(NO_2)$ and $R_c(HONO)$ using field-measured uptake coefficients; S4 and S5 which include a representation of subgrid dry deposition of anthropogenic surface-emitted $NO_x$ with (S4) or without (S5) subgrid dry deposition of surface-emitted HONO at night.

### 4.4.1 Simulation S2

#### *4.4.1.1 Updates to $R_a$ and Molecular Diffusivities in Air*

We update the parameterization of aerodynamic resistance ($R_a$) in GEOS-Chem in two ways. First, by including the displacement height $d$ correction to the height for which $R_a$ is referenced (Chapter 2, equation E3). We estimate the displacement height from the surface roughness length using the relation $d \sim 6.7z_o$ derived from conventionally used values of $z_o$ (~1/10 $h_c$) and $d$ (~2/3 $h_c$) for naturally vegetated surfaces (Garratt, 1992; Oke, 1987), where $h_c$ is the canopy height. Although $d$ may be neglected at heights > 10 $h_c$ (Garratt, 1992), we include it herein for completion as forest and built land types have $z_o > 1$ m, where the center of the lowest model level (ca. 60 m) from which $R_a$ is computed to would be < 10 $h_c$. Second, we update the Monin-Obukhov (M-O) stability-correction functions used in the computation of $R_a$ under non-neutral conditions (Chapter 2, section 5.1) to those employed in the updated surface layer formulation of the Weather Research and

**Table 4.1:** Serial modifications made to the base GEOS-Chem (GC) simulation.

<table>
<tr><th>Simulation</th><th>Aerodyn. Res.<br>$R_a$</th><th>Diffusivity<br>$D$</th><th colspan="2">Non-stomatal dry deposition<br>$NO_2$ | HONO</th><th>Wet dep.<br>HONO</th><th>Subgrid dry dep.</th></tr>
<tr><td>S1</td><td>base GC</td><td>base GC</td><td>base GC<br>(Wesely 1989)</td><td>base GC (none)</td><td>base GC (none)</td><td rowspan="2">base GC<br>(none)</td></tr>
<tr><td>S2</td><td rowspan="3">$z_{ref}$ above $d$,<br>update $\Psi_h$ [a]<br>(sect. 4.8.1)</td><td rowspan="3">Graham's<br>Law<br>(sect. 4.4.1.1)</td><td>Wesely 1989</td><td rowspan="3">update<br>surface uptake<br>(sect. 4.4.2.2)</td><td rowspan="3">implement<br>rainout & washout<br>(sect. 4.4.1.2)</td></tr>
<tr><td>S3</td><td>implement<br>$NO_2$ het. hyd.<br>(sect. 4.4.2.1)</td><td>$NO_x$ & HONO [b]</td></tr>
<tr><td>S4</td><td>$NO_x$ [c]</td></tr>
<tr><td>[d] S5.1 & 5.2[e]</td><td colspan="5"></td></tr>
</table>

[a] Reference height ($z_{ref}$) above displacement height ($d$) instead of above ground level, and updated stability correction functions.
[b] Subgrid dry deposition applied to both anthropogenic surface $NO_x$ and surface emitted HONO, as discussed in section 4.4.3.1.
[c] Subgrid dry deposition applied to anthropogenic surface $NO_x$ only.
[d] Simulation S5 has only been run for the period of the WINTER aircraft campaign (February–March 2015) .
[e] Simulation S5.1 uses $NO_2$ uptake coeficent $\gamma_{a,NO_2} = 10^{-4}$ to describe R1 on aerosol, which in S5.2 is updated to $\gamma_{a,NO_2} = 5 \times 10^{-6}$.

Forecasting (WRF) model (Fig. S4.1, equations 4.S1–5 in supplemental material), which are applicable over a greater range of diabatic stabilities (Jiménez et al., 2012).

Figure S4.2 in the supplemental material depicts annual mean and median $R_a$ from simulation S2 along with percent change from the base simulation (S1) over Canada and the U.S. Aggregate values of $R_a$ over eastern and western N.A. are included in Table S4.1 in the supplemental material. From Table S4.1, a large degree of separation between 24-hr annual mean and median $R_a$ is noted for simulation S1 over both eastern N.A. (mean: 360 ± 810 m $s^{-1}$, median: 100 m $s^{-1}$) and western N.A. (mean: 920 ± 1400 m $s^{-1}$, median: 260 m $s^{-1}$), with larger relative differences at night due to calm stable conditions. As depicted in Fig. S4.2, large reductions in mean $R_a$ on the order of 25% to 75% are noted for simulation S2 across North America, with small to negligible change in both daytime mean and 24-hr median $R_a$. These changes in $R_a$ indicate the reduced influence of a small number of outlying values at night under very stable conditions due to use of more appropriate stability correction functions (Fig. S4.1).

The influence of updates to $R_a$ on the dry deposition velocities for nitric acid $V_d(HNO_3)$ are included in Fig. 4.1 and Table S4.1. Small spatial changes in annual mean $V_d(HNO_3)$ are anti-correlated to small changes in median $R_a$, with increases in $V_d(HNO_3)$ of less than 4% over high roughness surfaces, i.e., forested regions, and reductions in $V_d(HNO_3)$ of less than 2% over low roughness surfaces, i.e., agricultural regions. Outside of a small reduction in nocturnal median $V_d(HNO_3)$ over eastern N.A. from 1.0 cm $s^{-1}$ to 0.9 cm $s^{-1}$ due to the updated stability correction function under slightly stable conditions (Fig. S4.1), no other change in annual aggregate $V_d(HNO_3)$ is seen for eastern N.A. or western N.A. (Table S4.1).

Following the identification of a large high bias in computed molecular diffusivities in GEOS-Chem, with implications for both $R_b$ and $R_c$ as discussed in Chapter 3, section 3.4.2, we update the calculation of species-specific molecular diffusion coefficients ($D_x$) according to Graham's Law, assuming that $D_x = D_{ref}\sqrt{M_{ref}/M_x}$ and using $CO_2$ as a reference gas. $D_{CO_2}$ is computed following Fuller's method (Chapter 3, section 3.4.2,

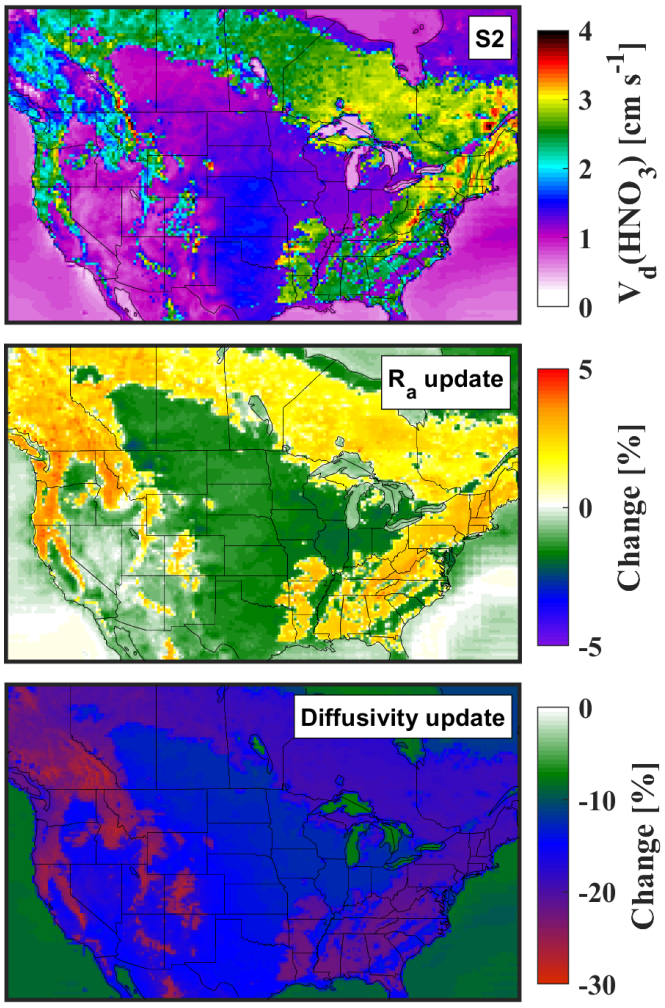


**Figure 4.1: (TOP)** Annual (2013) mean dry deposition velocities for nitric acid from simulation S2 with percent change in $V_d(HNO_3)$ resulting from serial updates to base simulation S1, including updates to **(MIDDLE)** aerodynamic resistance $R_a$, and **(BOTTOM)** molecular diffusivity $D_x$.

equation 3.7). Future work will instead use measured $D_x$, where available (Chapter 3, Table S3.1), and Fuller's method in the absence of a measured value. Resulting annual mean $R_b(HNO_3)$ from simulation S2 is included in Fig. S4.2 and Table S4.1. Large increases in $R_b(HNO_3)$ on the order of 60–100% result from reduction of a large high bias in simulated molecular diffusivity (Chapter 3, section 3.4.2). Resulting reductions in $V_d(HNO_3)$ from this diffusivity update are depicted in Fig. 4.1 and are on the order of 10–20%. Larger

reductions are noted during the day when $R_b$ is a larger fraction of total resistance than at night when $R_a$ is the dominant resistance to dry deposition of $HNO_3$ (Table S4.1).

*4.4.1.2. Implementation of Wet and Dry Deposition of HONO*

Despite longstanding recommendation that HONO wet and dry deposition be included in atmospheric chemistry models (Jacob, 2000), these removal processes have yet to be represented in widely used CTMs, including GEOS-Chem, or to our knowledge, WRF-Chem.

We add HONO to the wet deposition scheme in GEOS-Chem which includes rainout (in-cloud scavenging) and washout (below-cloud scavenging by precipitation) processes (Jacob et al., 2000). Required inputs are taken from (Park and Lee, 1988) and include the Henry's law solubility constant ($H_{HONO}$ = 49 M $atm^{-1}$ at 25 °C), acid dissociation constant ($K_a$ = 5.3 x $10^{-4}$ M at 25 °C), and enthalpy of vaporization ($\Delta H^{\circ}_{vap}$= 9.7 kcal $mol^{-1}$ = 41 kJ $mol^{-1}$) for $HONO_{(aq)}$. A pH-dependent effective Henry's solubility ($H^*$) which accounts for the equilibrium between dissolved HONO and its conjugate base nitrite may be computed:

$$H^*_{HONO} = H_{HONO}\left(1 + \frac{K_a}{[H^+]}\right) \quad (4.4)$$

GEOS-Chem assumes a pH of 4.5 for rainwater, yielding an effective Henry's solubility for HONO of 870 M $atm^{-1}$ at 25 °C. Luo et al. (2020) develop spatiotemporally varying rainwater pH for use in GEOS-Chem based on simulated cloud pH (Alexander et al., 2012), which was found to result in simulated rainwater pH on the order of 4.3 to 6.9, however, these updates were not included in the model version used herein.

We add HONO to the standard dry deposition scheme in GEOS-Chem using required input parameters $H^*$ and the reactivity factor for biological substances from (Wesely, 1989) which assumes a surface pH of 7 across all deposition land types. Fig. S4.3 in the supplemental material shows seasonal (DJF and JJA) maps of mean $V_d(HONO)$ across night and day periods from simulation S2. Appreciable solubility of HONO at neutral pH results in efficient deposition over bodies of water ($V_d(HONO)$ ~ 0.5–1.5 cm $s^{-1}$ depending on windspeed) and leaf interiors when stomata are open during the day

($V_d(HONO)$ ~ 0.5–0.8 cm $s^{-1}$ depending on LAI). At night over land $V_d(HONO)$ is reduced to < 0.3 cm $s^{-1}$ with lowest deposition velocities ( < 0.1 cm $s^{-1}$) over forested regions due to stomatal closure and prescribed in-canopy aerodynamic resistance to the lower canopy and ground surface where additional non-stomatal deposition may occur. We note that $H^*_{HONO}$ at pH 7 following 4.4 (~2.6 x $10^5$ M $atm^{-1}$) is greater than the value assigned in Wesely, (1989) (1x$10^5$ M $atm^{-1}$), however, in simulation S3 we update the calculation of resistance to surface uptake of HONO $R_c(HONO)$ over land using a field-measured uptake coefficient, as discussed in section 4.4.2.2. To bodies of water the Wesely 1989 scheme assigns a resistance to surface uptake of 0 s $m^{-1}$ to all dry depositing trace gases, however, the minimum surface resistance in GEOS-Chem is limited to 1 s $m^{-1}$ to avoid unrealistically large deposition velocities of highly soluble species (i.e., $HNO_3$) under turbulent conditions. The surface resistance to $SO_2$, $H_2O_2$, and HONO over water in GEOS-Chem is currently set to 2 s $m^{-1}$, and species with very low aqueous solubility such as $NO_2$ are assumed to have negligible uptake (very high surface resistance) to water, as seen in Fig. 4.2 and discussed in section 4.4.2.1.

### 4.4.2 Simulation S3

#### *4.4.2.1. Updating $NO_2$ Dry Deposition to Include Ground Surface Hydrolysis Yielding Evolved HONO*

In Chapter 3, section 3.4.3.2, a large low bias in simulated nocturnal mean $V_d(NO_2)$ from the GEOS-Chem dry deposition parameterization was eliminated by representing a non-stomatal dry deposition pathway due to heterogeneous hydrolysis of $NO_2$:

$$r_{hyd} = \frac{4}{\gamma_{g,NO_2}\,\overline{v_t}\,\alpha} \tag{4.5}$$

where $r_{hyd}$ [s $m^{-1}$] is the resistance to bulk surface uptake of $NO_2$ due to reaction R4.1; $\gamma_{g,NO_2}$ is a field-derived, RH-dependent, ground uptake coefficient for R4.1 (8x$10^{-6}$ x RH[%] / 50) (VandenBoer et al., 2013); $\overline{v_t}$ [m $s^{-1}$] is the mean thermal speed of $NO_2$; $\alpha$ is a dimensionless scale factor to relate $NO_2$ uptake to land types of different surface area density than the wintertime tilled soil/grasslands that surround the site where $\gamma_{g,NO_2}$ was derived (BAO tower, Colorado, U.S., February–March 2011). We add $r_{hyd}$ according to

4.5 in parallel to the existing bulk surface resistance scheme for $NO_2$ dry deposition in GEOS-Chem, with $\alpha$ values according to recommendations from Chapter 3: $\alpha = 2$ for high roughness land types (deciduous, coniferous, rainforests, and urban) and $\alpha = 1$ for all remaining land types, including snow covered ground. Surface grid-box-center RH values are used to compute $\gamma_{g,NO_2}$, except over water, ice and snow where RH is set to 100% resulting in $\gamma_{g,NO_2} = 1.6 \times 10^{-5}$, which is in agreement with observed uptake over snow ($\gamma_{snow,NO_2} = 1.6 \times 10^{-5}$, Ch. 3, Table S3.2). In anthropogenically-influenced marine boundary layers, nocturnal $NO_2$-to-HONO conversion rates—estimated via the rate of increase in the HONO/$NO_2$ ratio shortly after sunset when ambient HONO is accumulating—have been observed to vary between $6 \times 10^{-3}$ to $6 \times 10^{-2}$ $h^{-1}$, with campaign means ranging from $1.2 \times 10^{-2}$ to $4.5 \times 10^{-2}$ $h^{-1}$ (Cui et al., 2019; Wen et al., 2019; Yang et al., 2021; Zha et al., 2014), and attributed to heterogenous conversion of $NO_2$ at the air-sea interface. Assuming a nocturnal marine boundary layer height of ca. 100 m (Brown et al., 2004), representative aerodynamic ($R_a$) and quasi-laminar boundary layer ($R_{b(NO_2)}$) resistances of 100 s $m^{-1}$ and 30 s $m^{-1}$, respectively (Fig. S4.2), and nocturnal HONO production following the stoichiometry of reaction R4.1, setting $\gamma_{sea,NO_2} = 1.6 \times 10^{-5}$ results in an estimated $NO_2$–to–HONO conversion rate of $2.4 \times 10^{-2}$ $h^{-1}$—within the range of campaign average marine conversion rates. Using a literature-maximum uptake value to water of $\gamma_{NO_2} = 8.7 \times 10^{-5}$, which was reported by Msibi et al. (1993) for uptake of $NO_2$ to deionized water, results in a nocturnal marine $NO_2$–to–HONO conversion rate of $9.3 \times 10^{-1}$ $h^{-1}$—more than a factor of two larger than the maximum campaign mean value of $4.5 \times 10^{-2}$ $h^{-1}$ (Yang et al., 2021). Using the uptake value for $NO_2$ to distilled water listed in Chapter 3, Table S3.2 ($\gamma_{NO_2} = 2.3 \times 10^{-6}$) results in a conversion rate of $3.7 \times 10^{-3}$ $h^{-1}$—more than a factor of three smaller than the minimum campaign mean value of $1.2 \times 10^{-2}$ $h^{-1}$ (Cui et al., 2019). The reactive uptake of $NO_2$ to salt water is an active area of research (Colussi and Enami, 2019; Rovelli et al., 2020), with marine-based field studies noting a positive temperature dependence for ambient $NO_2$–to–HONO conversion rates (Wen et al., 2019), possibly due to an equilibrium solvation process for HONO governed by the temperature dependent Henry's Law coefficient (Wojtal et al., 2011).

Figure 4.2 shows seasonal (DJF and JJA) mean $V_d(NO_2)$ for night and day periods from base GEOS-Chem simulation S1 alongside values from updated simulation S3. As previously mentioned, negligible dry deposition of $NO_2$ to snow, ice, and water occur in the base simulation, where uptake of $NO_2$ is under stomatal control with maximum deposition velocities approaching 1 cm $s^{-1}$ over daytime forested areas with high leaf area index (LAI). At night when stomata are assumed closed, S1 $V_d(NO_2)$ over vegetated land-types is at a minimum (< 0.06 cm $s^{-1}$), with forest environments having slightly lower values than low roughness land-types such as agricultural and grassland due to larger prescribed in-canopy aerodynamic resistance and larger prescribed resistance to the ground surface for forest environments (Wesely, 1989). Significant increases in nocturnal $V_d(NO_2)$ across all land types and water is seen in simulation S3, with nocturnal $V_d(NO_2)$ over forested regions in the range 0.20-0.25 cm $s^{-1}$, in agreement with eddy covariance inferred values over Harvard Forest (Chapter 3, section 3.4.3.3). Simulated $V_d(NO_2)$ over snow and nocturnal agricultural/grassland land-types are in the range 0.1 – 0.15 cm $s^{-1}$, which are in better agreement with values inferred from measurements over these land types (Coe and Gallagher, 1992; Eugster and Hesterberg, 1996; Pilegaard et al., 1998; Plake et al., 2015; Stocker et al., 1995). Interestingly, daytime $V_d(NO_2)$ over vegetated land in S3 is not enhanced, but slightly reduced, over S1 despite $r_{hyd}$ being added in parallel to the existing resistance pathway—a result of increased stomatal resistance due to elimination of the low bias in molecular diffusivity.

In addition to representing a missing dry deposition pathway for $NO_2$, reaction R4.1 implemented via $r_{hyd}$ provides mechanistic utility to HONO emission, linking $NO_2$ dry deposition to ground surface HONO emission. In accordance with the stoichiometry of reaction R4.1, we release half the molar quantity of $NO_2$ deposited along the $r_{hyd}$ pathway as HONO into surface grid boxes and assume the remaining half is dry deposited as $HNO_3$.

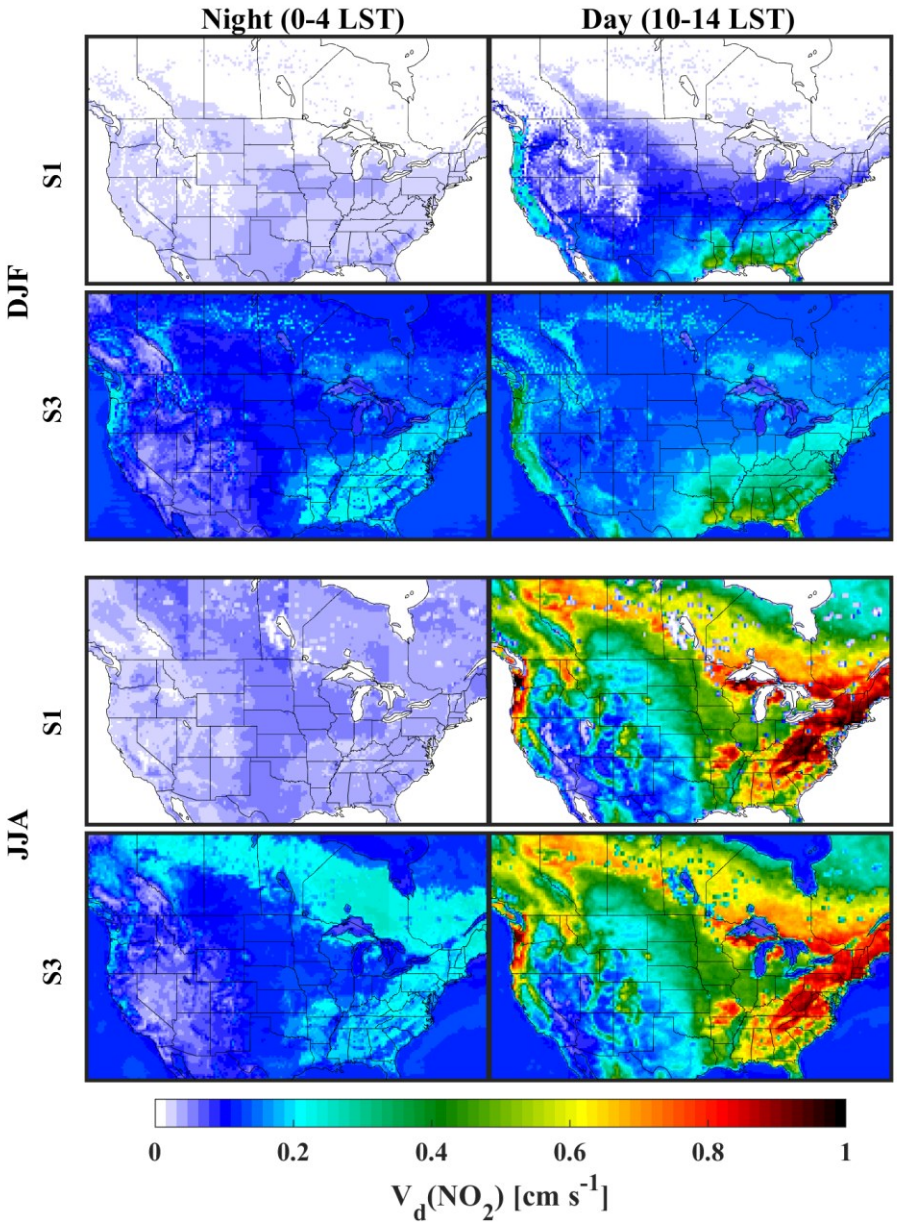


**Figure 4.2:** Dry deposition velocities for $NO_2$ from base simulation S1 and updated simulation S3. Depicted are winter (DJF) and summer (JJA) means for night and day periods.

*4.4.2.2 Updates to HONO Dry Deposition*

We update the calculation of $V_d(HONO)$ in simulation S3 by setting the bulk surface resistance $R_c(HONO)$ as the minimum between values computed from both the (i) modified Wesely 1989 parameterization (simulation S2) and (ii) equation 4.5 using the best-fit field-derived ground uptake coefficient for HONO of $\gamma_{g,HONO}$ = 8.7 x $10^{-5}$ from (VandenBoer et al., 2013). From vertical profiles of HONO integrated across the depth of the nocturnal boundary layer (NBL) at a rural wintertime grassland/tilled earth site in Boulder, CO, Vandenboer et al. (2013) infer $\gamma_{g,HONO}$ (range: 2 x $10^{-5}$ to 2 x $10^{-4}$) over the second half of the night after HONO concentrations have increased from daytime minimums, assuming integrated NBL HONO is a function of ground surface production via R4.1 and simultaneous first-order dry deposition—a model which has been used to understand nocturnal HONO evolution at both urban (Stutz et al., 2004) and summertime rural grassland (Ren et al., 2020) sites. This uptake coefficient ($\gamma_{g,HONO}$ = 8.7 x $10^{-5}$) is within the range reported by a recent laboratory study quantifying HONO uptake to agricultural soil (Indiana, U.S.) under atmospherically relevant conditions, finding $\gamma_{g,HONO}$ ranging from 2.5 x $10^{-4}$ at 0% RH to 1.1 x $10^{-5}$ at 80% RH (Donaldson et al., 2014).

Large increases in $V_d(HONO)$ over land, with no change over water, in simulation S3 indicates that $R_c(HONO)$ computed following equation 4.5 using $\gamma_{g,HONO}$ is lower (greater) over land (water) than in simulation S2 (Fig. S4.3). Largest S3 increases in $V_d(HONO)$ (>4x) are noted for nighttime and winter months over forested regions, while smaller increases on the order of 50–100% are seen for low roughness land types and summertime forests during the day. A final point of difference between S2 and S3 $V_d(HONO)$ is that values for forested regions are greater than for smoother land-types across all seasons and times of day in simulation S3—a pattern only observed during daytime summer months in simulation S2. Simulated S3 values of $V_d(HONO)$ are within the range reported by (Harrison and Kitto, 1994) of 0.2–1.7 cm $s^{-1}$ measured by the gradient technique over a U.K. grassland when $NO_2$ concentrations were low and HONO fluxes downward.

**4.4.3 Simulations S4 & S5.1**

*4.4.3.1 Subgrid Dry Deposition of $NO_x$*

Due to the vertical extent of ground-level grid boxes in global CTMs such as GEOS-Chem (ca. 120 m), dry deposition of near-surface emitted (or formed) species with appreciable surface interaction could be underestimated, especially under conditions of weak mixing. In an effort to understand and correct for this subgrid effect, we develop an offline 1-D column model from which we track dry depositional loss of an otherwise inert (assumed) near-surface emitted (or formed) tracer as it undergoes vertical mixing to 120 m. The evolution in concentration from a near-surface pulse of emission into an empty 1-D column ca. 120 m deep is modeled using a continuity equation in Eulerian form:

$$\frac{\partial c}{\partial t} = E_{pulse} + \left[\frac{\partial c}{\partial t}\right]_{turb} + L_{dep} \tag{4.6}$$

where right-hand-side terms represent successively the contributions from an initial near-surface emission pulse $E_{pusle}$, turbulent mixing, and dry deposition $L_{dep}$.

The initial ($t_o$) concentration profile resulting from $E_{pulse}$ is assumed to take the sigmoid profile shape depicted in Fig. S4.4, where normalized concentrations are nearly constant from the surface to ca. 2 m, falling to ca. 10% at 4 m and diminishing to near zero by 5 m. At $t_o$, 90% of the emitted mass is below 3 m. This arbitrary emission profile is intended to represent that from the passage of a typical motor vehicle, and is consistent with the vertical extent of above roadway mixing zones (2.5–3.5 m) from which traffic emissions are simulated to emanate in near-road dispersion models (Held et al., 2003; Wang et al., 2011b).

Turbulent mixing in 4.6 is parameterized following the classic 1-D turbulent diffusion equation in analogy to Fick's law of molecular diffusion, which assumes turbulent flux is proportional to the local mean concentration gradient (K-theory):

$$\left[\frac{\partial c}{\partial t}\right]_{turb} = \frac{\partial}{\partial z}\left[K\frac{\partial c}{\partial z}\right] \tag{4.7}$$

where $K$ is the turbulent (eddy) diffusion coefficient for scalar quantities. We use the classic surface layer parameterization of $K$ following Monin-Obukhov (M-O) similarity theory (Monin and Obukhov, 1954), modified to account for the enhanced turbulent mixing within

the roughness sublayer (RSL) which extends to approximately 2–3 canopy heights ($h_c$) above the surface:

$$K = \frac{u_* k(z-d)}{\phi_h \widehat{\phi_x}} \tag{4.8}$$

where $u_*$ is the friction velocity characterizing surface momentum flux, $z$ the height above the displacement height $d$, $k$ the von Karman constant (0.4), and $\phi_h$ a dimensionless M-O stability correction factor for sensible heat assumed to apply equally to chemical mixing ratios. Empirically determined functions of $\phi_h$ for use under stable and unstable conditions are depicted in Fig. S4.1 and presented in the supplemental material (equations 4.S1 & 4.S4). $\widehat{\phi_x}$ is an empirically determined RSL correction which increases values of $K$ by a factor of two above that predicted from the standard M-O parameterization near the canopy top (i.e., $\widehat{\phi_x} \sim 0.5$ at $h_c$), decaying to unity at the top of the RSL (ca. 2–3 $h_c$). We use the formulation of $\widehat{\phi_x}$ from (Physick and Garratt, 1995) (equation 3.S9 in Chapter 3, section 3.6.2). RSL correction applied to flux-gradient calculations of turbulent transport was noted to be an important component in the parameterization of upward sensible and latent heat fluxes in the Simple Biosphere Model (SiB) (Sellers et al., 1986) used in the GEOS General Circulation Model (GCM) from which meteorological fields driving GEOS-Chem are produced.

Dry depositional loss ($L_{dep}$) from the 1-D column model described by 4.6 is parameterized following the standard resistance-in-series approach (equations 4.2 & 4.3) from the lowest finite volume grid cell (grid structure described below). Resistances used in the calculation of deposition velocities are identical to those used in the updated GEOS-Chem simulation S3, with the exception of aerodynamic resistance $R_a$, where instead a formulation is used which accounts for the non-zero $R_a$ value at the roughness length $z_o$ due to RSL effects (equation 3.S10 from Chapter 3, section 3.6.2). All $NO_x$ from $E_{pulse}$ is treated as NO which does not dry deposit (i.e., $V_d(NO_x, t_o) = 0$ cm $s^{-1}$) and is assumed to oxidize to $NO_2$ with a fixed e-folding time of 60 s corresponding to an $O_3$ concentration of ca. 40 ppb (an assumption discussed below).

Equation 4.6 is discretized over a finite volume staggered vertical grid and solved numerically by employing operator splitting and using an explicit forward-in-time,

centered-in-space (FTCS) Euler's method to advance turbulent mixing. Due to the nature of turbulent mixing in reducing mean concentration gradients, numerical solutions to 4.7 using an explicit FTCS method results in stable solutions so long as integration time steps are sufficiently small to prevent turbulent diffusion across a grid cell (i.e., $\Delta t < \Delta z^2/2K$ ) (Brasseur and Jacob, 2017). To ensure stability and accuracy, time steps were kept small enough to maintain the von Neumann stability parameter β in the range $0 \leq \beta \leq ¼$ (Press, 1992).

$$\beta = K\frac{\Delta t}{\Delta z^2} \tag{4.9}$$

A vertical grid to ca. 120 m is defined from input of $z_o$, where we set the depth of the first level as 10 $z_o$—the approximate height of the roughness elements. Subsequent levels are 1.2x the depth of the level below, resulting in greater resolution over low roughness surfaces. Eddy diffusivities are computed at level edges while mean concentration gradients are computed from grid-box-centers. Reflective upper and lower boundary conditions are used when advancing turbulent mixing (4.7). Four input variables are required to advance solutions of 4.6: (1) friction velocity $u_*$, (2) M-O length $L$, (3) the sum of quasi-laminar and bulk surface resistances $R_b$ + $R_c$, and (4) roughness length $z_o$. The meteorological fields used to drive GEOS-Chem are a source of $u_*$, $L$, and $z_o$ at hourly resolution. Simulated values of $R_b$ and $R_c$ are available from the dry deposition module of GEOS-Chem at a temporal resolution equal to the emission time step.

Figure 4.3 depicts a nighttime and daytime realization of our 1-D column model for subgrid dry deposition of near-surface $NO_x$ using median values of input variables over Calgary, AB from 15 July 2013. Column-resolved and column-integrated time series are shown. Included in the column-integrated time series are mass evolutions from a single GEOS-Chem size surface grid box according to the dry deposition scheme from GEOS-Chem simulations S3 & S4. At $t_o$, all emissions are contained within the lowest level of the 1-D column model, which is of greater depth ($z\_top(L=1) = 10z_o$) than the vertical extent of $E_{pulse}$ (< 5 m, Fig. S4.4) for this location. Initially, dry depositional loss ($L_{dep}$) is negligible as $NO_x$ from $E_{pulse}$ consists entirely of NO. However, as NO oxidizes to $NO_2$ with an assumed e-folding time of 60 s, total-column $NO_x$ loss due to dry deposition begins

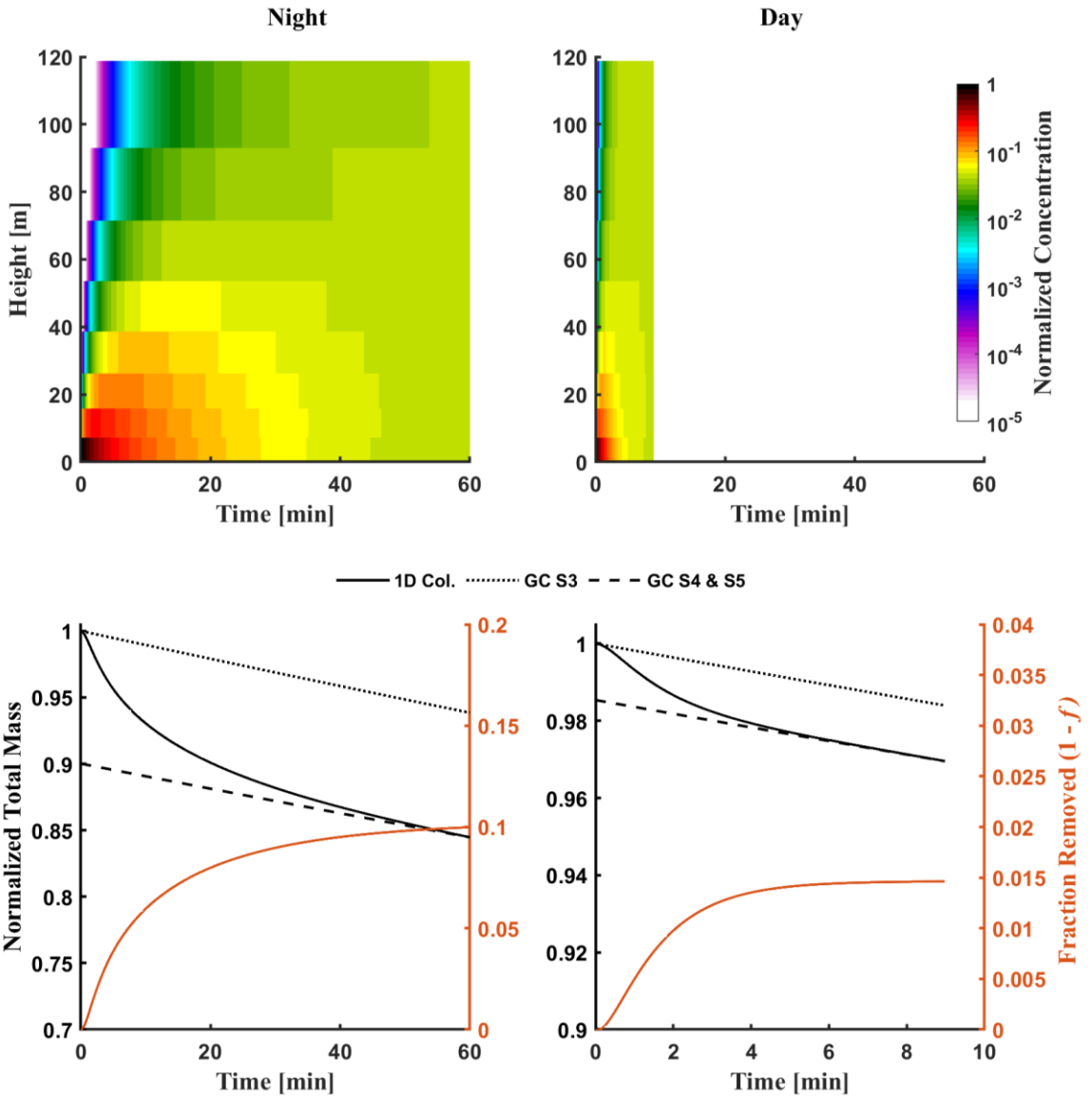


**Figure 4.3: (TOP)** Normalized concentration time series from nighttime and daytime realizations of the 1-D column model used for estimating subgrid dry deposition of near-surface emitted $NO_x$ in GEOS-Chem. **(BOTTOM)** Corresponding normalized total column mass in the 1-D column model and single boxes (120 m in depth) using equivalent dry deposition parameterizations from GEOS-Chem (GC) simulations S3, S4, and S5. Conditions are for Calgary, AB on 15 July 2013, with median nighttime (daytime) input values: $u^* = 0.3$ (0.6) m $s^{-1}$, $L^{-1} = 0.01$ (-0.008) $m^{-1}$, $R_b(NO_2) = 22$ (11) s $m^{-1}$, $R_c(NO_2) = 360$ (240) s $m^{-1}$, and $z_o = 0.6$ (0.6) m. Also depicted are time series of the fraction $(1 - f)$ of near surface $NO_x$ emissions removed due to subgrid dry deposition.

to exceed that from a single grid box of depth 120 m, i.e., GEOS-Chem simulation S3 (GC S3). As vertical mixing proceeds and surface levels become depleted, deposition from the high resolution 1-D column model (1D Col) slows, eventually approaching that from the single GEOS-Chem size grid box. This happens much sooner under daytime conditions due to increased turbulence under diabatically unstable conditions. The underestimate in dry deposition of near-surface $NO_x$ emissions resulting from instantaneous dilution into surface grid boxes in GEOS-Chem may be estimated by the ratio ($f$) of column-integrated mass to mass remaining in a single box of equal vertical extent at the time of plume resolution ($t_{end}$):

$$f = \frac{m(t_{end})^{1D\ Col}}{m(t_{end})^{GC\ S3}} \tag{4.10}$$

The fraction of surface emission removed due to subgrid dry deposition ($1 - f$) is included as a time series in Fig. 4.3. As mixing proceeds, the effect of subgrid dry deposition diminishes, ending with the 1-D column model containing ca. 90% of the $NO_x$ remaining in a single GEOS-Chem size box after 1 h under nighttime conditions, and > 98% under daytime conditions when the plume resolves in under 10 minutes We define plume resolution at the time $t_{end}$ when a positive concentration gradient from the surface to grid-box-center is achieved, consistent with the assumption of a resistance-in-series model of dry deposition (Wesely and Hicks, 2000). We set a maximum time for $t_{end}$ of 60 minutes, the resolution of the 2-D meteorological fields. For the nighttime example depicted in Fig. 4.3, removing the 60-minute time limit results in a $t_{end}$ of 75 minutes and a < 2% increase in $f$.

Scaling $E_{pulse}$ by a factor $f$ prior to release into a GEOS-Chem size grid box results in agreement with the 1-D column model at the time of plume resolution and is a strategy to account for subgrid dry deposition in GEOS-Chem simulations S4 & S5. The result of such a strategy is depicted in Fig. 4.3 as:

$$m(t)^{GC\ S4} = fE_{pulse}e^{-kt} \tag{4.11}$$

where $k$ is the first order dry deposition rate constant from a GEOS-Chem size grid box, i.e., $k[s^{-1}] = V_d^{GC\ S3}/z_{top}^{GC}(1)$ with $z_{top}^{GC}(1)$ ~ 120 m. Given the first-order dependence of

both dry deposition and the parameterization of turbulent mixing used in 4.6, our formulation of $f$ is independent of the absolute value of $E_{pulse}$.

We implement our parameterization of subgrid dry deposition of anthropogenic near-surface (non-stack) emissions of $NO_x$ into GEOS-Chem via a 4-D look-up-table containing $f$ along dimensions of $u*$, $L^{-1}$, $R_b + R_c$, and $z_o$. Figure 4.4 depicts the fraction of $E_{pulse}$ removed due to subgrid dry deposition, i.e., $(1 - f)$, along each dimension of the look-up-table using values for the remaining three dimensions from $10^4$ random selections of coincident input values over eastern N.A. (east of 100°W) on 15 July 2013. Highlighted in green are traces along each discretized dimension through median input values (red dots) of the remaining three dimensions. Input dimensions are discretized over a greater range of values than is observed in histograms of $u*$, $L^{-1}$, $R_b(NO_2) + R_c(NO_2)$, and $z_o$ (Fig. S4.5). Large increases in the fraction of surface $NO_x$ removed occur as surface layer turbulence decreases, as seen along dimensions of $u*$ and $L^{-1}$. An exponential response is noted in the $u*$ dimension, with 1-$f$ increasing sharply with decreasing $u*$ until very low values of $u*$ (< 0.01 m $s^{-1}$) when 1-$f$ decreases due to very high aerodynamic resistances under stagnant conditions. A sigmoidal response in 1-$f$ is seen along the dimension $L^{-1}$, with greatest sensitivity near neutral conditions ($L^{-1}$ = 0 $m^{-1}$). Sensitivity to surface resistances $R_b + R_c$ increases substantially as resistances drop below ca. $10^3$ s $m^{-1}$. Sensitivity to surface roughness $z_o$ is reduced under conditions of high turbulence when 1-$f$ is low (<5%). Under low turbulence conditions (i.e., small $u*$ and $L^{-1} > 0$), sensitivity to $z_o$ increases, with $1 - f$ decreasing for $z_o$ > ca. 0.4 m. This is the point at which nearly all $E_{pulse}$ is contained within the first level of the 1-D column model (Fig. S4.4), where further increasing the vertical extent of the first level with increasing $z_o$ would enhance turbulent mixing out of this level (4.8) but alter deposition little—an example of subgrid effects within our simple 1-D column model. Over low roughness surfaces ($z_o$ < ca. 0.1 m), reductions in 1-$f$, which become more apparent for values seen under low turbulence conditions, i.e., 1-$f$ > ca. 0.2, can be explained by a shallow first model layer (< 1 m) containing a small fraction of $E_{pulse}$ (Fig. S4.4) and slow downward mixing of overlying $NO_x$. The slight zig-zag behavior along the $z_o$ dimension is a result of variability in the height of the 1-D column, which is set from the integer number of levels not exceeding a total depth of 120 m. Maximum effect occurs as $z_0$ approaches 2 m, when a 4-layer column to ca. 120 m switches to a 3-layer

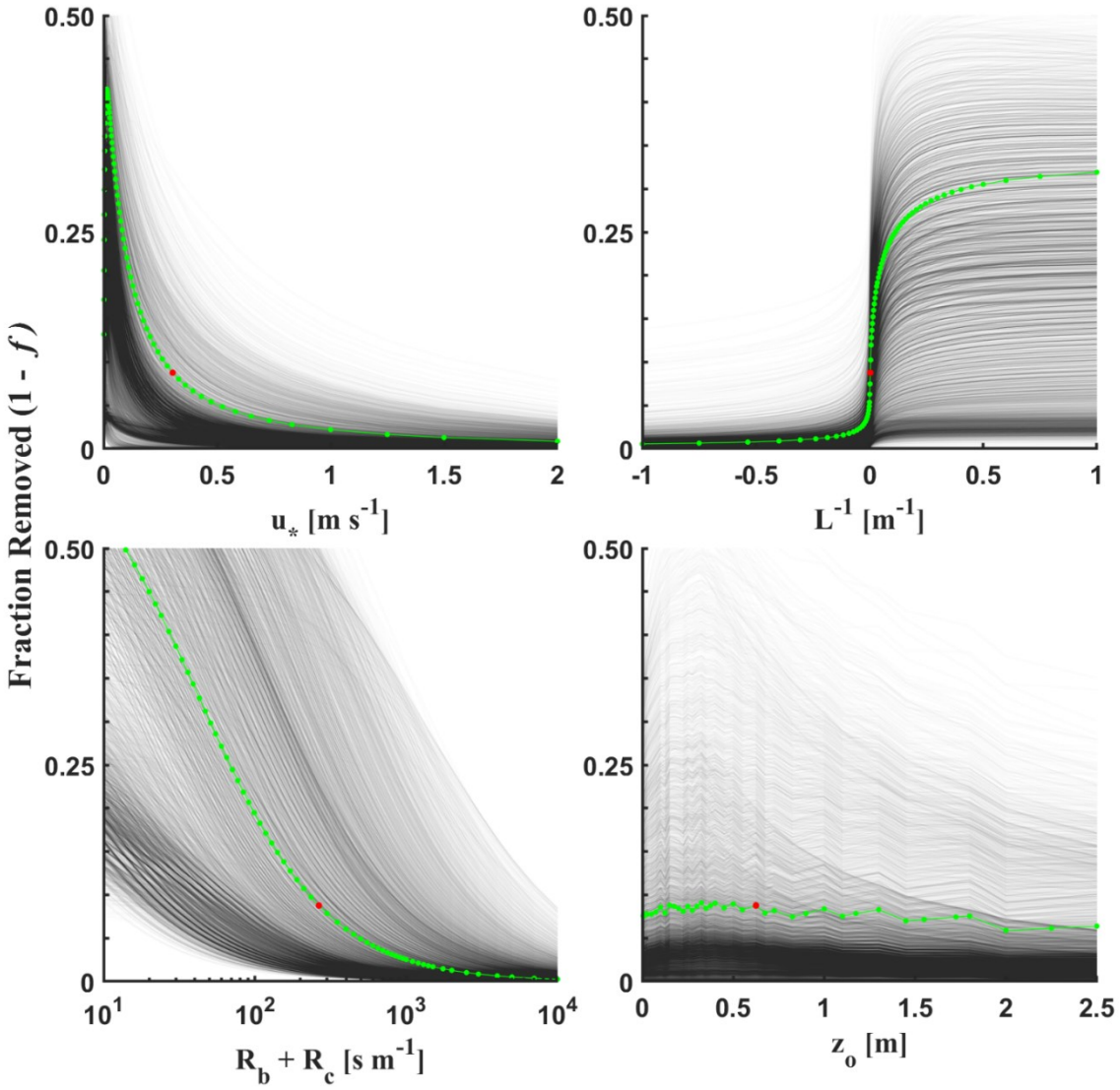


**Figure 4.4:** Look-up-table values of $f$ depicted as the fraction of near surface $NO_x$ emissions removed, i.e., $(1 - f)$, along input dimensions required for the parameterization: friction velocity $u_*$, inverse M-O length $L^{-1}$, dry deposition resistances $R_b(NO_2) + R_c(NO_2)$ and roughness length $z_o$. Thin black lines depict slices through each dimension using values for the remaining three dimensions from $10^4$ random selections of coincident input values over eastern North America (east of 100°W) on 15 July 2013. Highlighted in **green** are traces along each discretized dimension through median input values (**red dots**) of remaining three dimensions.

column to ca. 80 m—future work will address this effect by allowing thickness variability in the top level. Our simple column model suggests subgrid dry deposition could be an important consideration in large scale CTMs under conditions of low turbulence for species with surface resistances below ca. $10^3$ s $m^{-1}$.

Our parameterization of subgrid dry deposition of near-surface anthropogenic (non-stack) $NO_x$ emissions is implemented into GEOS-Chem simulations S4 & S5. We retrieve look-up-table $f$ values for $NO_x$ along the $R_b + R_c$ dimension by computing surface resistance for $NO_x$ assuming negligible uptake of NO (i.e., $R_c(NO) = \infty$):

$$R_c(NO_x) = \frac{[NO_x]}{[NO_2]} R_c(NO_2) \tag{4.12}$$

Thus, only the $NO_2$ that evolves from the initial pulse of NO ($E_{pulse}$) at an assumed e-folding time of 1 minute on approach to the $NO_2$ / $NO_x$ ratio simulated online is subjected to subgrid dry deposition. In their near-road dispersion model of $NO_x$, Valencia et al. (2018) assume a $NO_2$ / $NO_x$ ratio of 0.2 at the source, which was within the range typical of road traffic emissions of 0.1 to 0.25. However, the U.S. EPA NEI 2011 emission inventory, used in GEOS-Chem simulations herein, contains both NO and $NO_2$ emission data for which we implement a single look-up-table of $f$ which treats all emitted $NO_x$ as NO. Implementing separate NO and $NO_2$ specific look-up-tables for subgrid dry deposition will be the subject of future work. We do not apply $f$ values to soil $NO_x$ emissions as GEOS-Chem already contains a parameterization for the subgrid dry deposition of soil $NO_x$ via an online canopy reduction factor (CRF) (equation 3.10 in Chapter 3), however, future work will include updating the calculation of CRF in GEOS-Chem to include reaction R4.1 which will increase CRF values, especially at night (Chapter 3, Fig. S3.6).

As previously mentioned, the NO to $NO_2$ oxidation lifetime used herein for anthropogenic surface emissions subjected to subgrid dry deposition assumes a constant $O_3$ concentration of ca. 40 ppb (Fig. S4.6)—a reasonable assumption under well-mixed daytime conditions at most locations, however, an overestimate at night when near-surface $O_3$ is reduced from daytime highs (Fig. S4.7). Future work will include adding simulated surface $O_3$ as a fifth dimension to look-up-table values of $f$ to control the rate of surface emitted NO oxidation, as well as including mass-balance of $O_3$ loss resulting from

oxidation of NO in the subgrid dry deposition scheme. In the meantime, we proceed herein with a 4-D look-up-table employing a simplistic exponential decay approach for NO to $NO_2$ oxidation (Cole and Summerhays, 1979), noting that sensitivity of *f* to $O_3$ is small for $O_3$ concentrations > ca. 20 ppb, albeit, increasing sharply below ca. 10 ppb (Fig. S4.6). Although large reductions in anthropogenic $NO_x$ emissions across North America over the past two decades (McDuffie et al., 2020) have resulted in reduced $O_3$ titration near-source in $NO_x$-saturated $O_3$-production regimes such as roadside (Ontario Ministry of the Environment and Climate Change, 2016) and urban centers (Jin et al., 2020; Mitchell et al., 2021; Simon et al., 2015), we caution that the simple model of subgrid dry deposition of $NO_x$ presented herein does not resolve subgrid $O_3$ titration—conditions that would therefore be expected to overestimate subgrid dry deposition of $NO_x$ in simulations S4 and S5. With higher CTM horizontal resolutions enabled via nested model domains and more recently through user-defined stretched-grids in cubed-sphere CTM formulation (Bindle et al., 2020), urban-scale titration events will become increasingly resolved. Nocturnal mixing in the urban environment has additional complexities that are not yet represented in GEOS-Chem, including parameterization of the excess sensible heat flux resulting from storage in urban surfaces (Halios and Barlow, 2018), which Travis et al. (2022) attribute as the explanation for the low bias in GEOS-Chem simulated nighttime $O_3$ in a recent campaign in Seoul, South Korea (May–June 2016). Additionally, greater uptake of oxidation catalysts in the vehicle fleet is resulting in increased $NO_2$ / $NO_x$ emission ratios, leading to on-road values on the order of 30% (Jenkin et al., 2008; Richmond-Bryant et al., 2017). We find the $NO_2$ / $NO_x$ ratio in on-road emissions from the U.S. EPA NEI 2011 inventory is on average 9%, with maximum local values up to 17% (data not shown). The limitations of simulation S4 with respect to urban ozone titration events is discussed further in section 4.6.4.

Implementation of look-up-table values of *f* into GEOS-Chem simulation S4 results in seasonally and diurnally varying maps of 1-*f* (Fig. S4.8). Daytime values are generally < 4% and much smaller than nocturnal values (5–25%) which show greater dependence on surface roughness, as previously discussed. Largest diel variations are seen over the high deserts of the western U.S., followed by summertime agricultural regions. Seasonality in daytime values (JJA < 4%, DJF < 2%) results from reduced $R_c(NO_2)$ during summer

months due to stomatal uptake of $NO_2$ (data not shown). Seasonality in nocturnal values is most apparent over agricultural regions with midwest and eastern areas showing JJA highs > 15% and the California valley showing DJF highs >20%. Seasonality is also noted for Canadian boreal forest regions (SON lows < 5%). These seasonalities reflect changes in $R_a$ more so than seasonal changes in either $R_c(NO_2)$ or $z_o$ (Fig. S4.9), as expected from the dimensional sensitivities of 1-$f$ depicted in Fig. 4.4.

In addition to subgrid dry deposition of near-surface anthropogenic $NO_x$ emissions, simulation S4 also includes subgrid dry deposition of surface emitted HONO, including that resulting from $NO_2$ uptake along the $r_{hyd}$ pathway (i.e., reaction R4.1 via equation 4.5), where half of the reaction yield is re-emitted as HONO and the remaining half irreversibly dry deposited as $HNO_3$. A HONO-specific look-up-table is used, where the simulation of $f_{HONO}$ values differs in two ways from that of $f_{NOx}$. First, there is no time delay to onset of dry deposition as it is assumed that emitted HONO may be simultaneously dry deposited. Second, HONO is assumed to be emitted from the roughness elements which provide the surfaces for reaction R4.1 to proceed, therefore no emission profile is used. Our implementation of subgrid dry deposition of HONO into GEOS-Chem differs from that of $NO_x$ in that subgrid dry deposition of HONO is permitted only at night (solar zenith angle > 90°). During the day, efficient photolysis precludes the assumption of HONO as an inert tracer—an assumption in the formulation of our 1-D column model (4.6) used in the calculation of both $f_{NOx}$ and $f_{HONO}$. The lifetime of $NO_2$ to heterogeneous hydrolysis via reaction R4.1 has been reported to be on the order of one hour in well-mixed indoor air (Collins et al., 2018; Spicer et al., 1993)—lower than typical ambient daytime chemical lifetimes which are in the range of 1–6 h for low- to mid-latitude urban plumes (Beirle et al., 2011; Laughner and Cohen, 2019), and 11 +/- 5 h for remote continental conditions (Romer et al., 2016). During winter months and summer nights, $NO_x$ is longer lived with ambient chemical lifetimes on the order of 10 h to more than a day (Browne and Cohen, 2012; Kenagy et al., 2018; Martin et al., 2003b). The timescale for turbulent vertical mixing of near-surface emissions within surface grid boxes of GEOS-Chem is much shorter than these ambient chemical lifetimes, on average by more than a factor of 10. The $50^{th}$ and $95^{th}$ percentiles of day (night) mixing times over Canada and U.S. are 12 minutes (50 minutes), and 19 minutes (59 minutes), respectively (data not shown). Therefore, treatment of $NO_x$

as a chemically inert tracer (save for dry deposition) over the timescale of turbulent vertical mixing within surface grid boxes of GEOS-Chem appears to be a reasonable approximation.

### 4.4.4 Simulation S5.2

#### *4.4.4.1 Heterogeneous Hydrolysis of $NO_2$ on Aerosol*

Laboratory determined values of $NO_2$ reactive uptake ($\gamma_{NO_2}$) to humidified or aqueous surfaces of various composition are generally in the range of $10^{-7}$ to $10^{-5}$ (Ammann et al., 2005; Bröske et al., 2003; Kleffmann et al., 1998; Kurtenbach et al., 2001), however, values $> 10^{-5}$ (Mertes and Wahner, 1995; Msibi et al., 1993) and $< 10^{-8}$ (Ammann et al., 2013) to bulk liquid water have been reported. Formation of HONO from heterogenous reaction of $NO_2$ is suggested to follow the stoichiometry of reaction R4.1 on most humidified surfaces, however, surfaces containing reducing solutes such as ascorbic acid (Msibi et al., 1993) and phenolic humic acid precursors (Ammann et al., 2005) have been shown to enhance $NO_2$ uptake and result in larger HONO yields. Photoenhanced reduction of $NO_2$ on certain dust aerosol (Ndour et al., 2008), organic aerosol (Bröske et al., 2003; Monge et al., 2010) and humic surfaces (George et al., 2005; Msibi et al., 1993; Stemmler et al., 2006) has been shown to produce HONO at greater than 50% yield. While an active area of research, processes such as photobleaching result in unrecoverable loss of photochemical activity, making the persistence of this process difficult to constrain (Ye et al., 2017). It is noted that the heterogeneous hydrolysis of $NO_2$ on humidified/wet inert surfaces (R4.1) is not photoenhanced (Laufs and Kleffmann, 2016; Ramazan et al., 2004). Photolysis of nitrate or surface absorbed $HNO_3$ is a possible renoxification pathway yielding $NO_2$ as the primary photolysis product; subsequent surface-dependent HONO formation may proceed from secondary surface reactions of $NO_2$, including heterogeneous hydrolysis (R4.1) (Laufs and Kleffmann, 2016) and/or photosensitized reduction via surface adsorbed organics (Ye et al., 2016). Efforts to correct daytime underestimates in simulated near-surface HONO include scaling $\gamma_{NO_2}$ by normalized factors of solar radiation (Zhang et al., 2016) or $NO_2$ photolysis frequencies (Liu et al., 2019; Wong et al., 2013), resulting in maximum daytime values of $\gamma_{NO_2}$ in the range $5 \times 10^{-5}$ to $10^{-3}$ in corresponding atmospheric models.

Several updates to the representation of heterogenous hydrolysis of $NO_2$ in GEOS-Chem have been made subsequent to version 10-01 employed herein. As previously mentioned, reaction R4.1 is represented in the base simulation on aerosol surfaces only, with a reactive uptake coefficient (reaction probability) $\gamma_{NO_2}^{aerosol}$ = $10^{-4}$ and yielding equimolar amounts of HONO and $HNO_3$. This $NO_2$ uptake coefficient is ca. 2x larger than the maximum daytime value, and 100x larger than the nocturnal value, used in WRF-Chem (Zhang et al., 2016). Holmes et al. (2019) develop and implement into GEOS-Chem a method for simulating heterogeneous cloud chemistry from entrainment-limited uptake, and include reaction R4.1 on liquid clouds using $\gamma_{NO_2}^{cloud,liq}$ = $10^{-8}$ which assumes $NO_2$ uptake is due to aqueous solubility and slow solution-phase second-order hydrolysis (Ammann et al., 2013; Cheung et al., 2000), not first-order heterogeneous hydrolysis which has been observed to proceed up to a factor of 40–100x faster on wet borosilicate glassware in the lab (Finlayson-Pitts et al., 2003). Holmes et al. (2019) also implement aerosol-dependent $\gamma_{NO_2}^{aerosol}$ into GEOS-Chem, using recommended values from recent literature; values include $10^{-4}$ for soot and sea salt at RH ≥ 70%, $10^{-6}$ for organic aerosol, 5 x $10^{-6}$ for secondary inorganic aerosol (SIA; sulfate, nitrate, and ammonium), and $10^{-8}$ for dust and sea salt at RH < 40%. Photoenhanced uptake to absorbing dust and organic aerosol was not considered, nor was loss of soot reactivity. These updated values of $\gamma_{NO_2}^{aerosol}$ are now standard in GEOS-Chem subsequent to version 12.6.0. Alexander et al. (2020) find that these updated values of $\gamma_{NO_2}^{aerosol}$ render heterogeneous hydrolysis of $NO_2$ on aerosol of negligible importance for global nitrate production (<1%) compared to it being the third most important nitrate formation pathway (12%) in a simulation with $\gamma_{NO_2}^{aerosol}$ = $10^{-4}$. Furthermore, Alexander et al. (2020) note the significant role that heterogeneous hydrolysis of $NO_2$ on aerosol surfaces has on governing HONO concentrations in simulations with $\gamma_{NO_2}^{aerosol}$ = $10^{-4}$, noting reductions in simulated HONO below 1 km of up to 100% both from using $\gamma_{NO_2}^{aerosol}$ values from Holmes et al. (2019) and in a sensitivity simulation where $\gamma_{NO_2}^{aerosol}$ was set to a constant value of $10^{-7}$. To address a low bias in GEOS-Chem simulated (v10-01) HONO over the northeastern U.S. during winter, Jaeglé et al. (2018) keep $\gamma_{NO_2}^{aerosol}$ = $10^{-4}$ and increase the molar yield of HONO to unity, thus assuming HONO is the sole product of reaction R4.1 on aerosol. Jaeglé et al. (2018) find this modification sufficient to

eliminate the factor of 2 low bias in simulated nocturnal HONO concentraions below 1 km compared to observations from the WINTER aircraft campaign (discussed below in section 4.5.2).

In simulation S5.2 we set $\gamma_{NO_2}^{aerosol}$ = 5 x $10^{-6}$ on all aerosol types—a reduction by a factor of 40 and the value recently used by: (i) (Meng et al., 2020) to estimate the HONO production rate on aerosol during a field study which measured high-resolution vertical profiles of nocturnal HONO and $NO_2$ over Beijing, China and (ii) Holmes et al. (2019) in GEOS-Chem for sulfate-nitrate-ammonium aerosol.

## 4.5 Measurements for Model Evaluation

### 4.5.1 Surface Ozone

Ground-level ozone measurements across the U.S. for the year 2013 were obtained from the Environmental Protection Agency's (EPA) Air Quality System (AQS) internet database (US Environmental Protection Agency (EPA), 2016). Hourly observations were spatially averaged to the GEOS-Chem grid (1/4° x 5/16°) for coincident comparison to simulated values. For species that dry deposit and lack strong surface emission sources, i.e., secondary pollutants such as $HNO_3$ and $O_3$, more representative comparison to surface observations may be achieved in large scale CTMs through the resistance-in-series model of dry deposition. Implicit subgrid vertical gradients within the lowest model level may be inferred from explicit model concentrations and deposition velocities (Travis and Jacob, 2019; Zhang et al., 2012a):

$$C(z_s) = [1 - R_a(z_1, z_s)\, V_d(z_1)]\, C(z_1) \tag{4.13}$$

where $z_1$ refers to the center height of the lowest model level (ca. 60 m in GEOS-Chem), $z_s$ an arbitrary height below $z_1$ but above $z_o + d$, and $C(z_s)$ the implicit concentration at this height. Subgrid vertical gradients in concentration depend on both atmospheric stability and resistance to surface uptake. To compare to surface ozone observations, we infer simulated surface ozone at 10 m following 4.13; future work will likely use implicit simulated $O_3$ at 2 m in the parameterization of subgrid $NO_x$ dry deposition. Largest subgrid

vertical gradients in simulated ozone result under stable conditions, whereas negligible gradients exist during turbulent daytime conditions (Fig. S4.7).

### 4.5.2 WINTER Aircraft Campaign

A suite of aircraft observations from the Wintertime INvestigation of Transport, Emissions, and Reactivity (WINTER) campaign, which consisted of 13 flights each of ca. 8 h duration over the Northeast U.S. between 3 February–13 March 2015 from the National Science Foundation (NSF)/National Center for Atmospheric research (NCAR) C-130 aircraft platform, are publicly available (https://www.eol.ucar.edu/field_projects/winter). As depicted in Fig. S4.11, flights took place over and downwind major pollution regions, including the Ohio River Valley and Eastern Seaboard, with an approximately equal amount of day/night flight time which predominately sampled the planetary boundary layer—ca. 70% (40%) of flight time was within 1 km (500 m) of the surface.

For evaluation of the updates to GEOS-Chem presented herein, we coincidently sample (at 1-minute intervals) model concentrations with observations from the WINTER dataset presented by Jaeglé et al. (2018; personal communication, 30 June 2021), including concentrations of HONO, $NO_x$, $HNO_3$, and particulate nitrate ($pNO_3$). Following the recommendations of Jaeglé et al. (2018), we exclude intervals where either $NO_x$ or $SO_2$ concentrations are greater than 10 ppb in order to avoid subgrid scale plumes not resolved by GEOS-Chem; this filter eliminates ca. 3% of the observations averaged on 1-minute intervals.

## 4.6 Results and Discussion

### 4.6.1 Effective Reduction in Anthropogenic Surface $NO_x$ Emission Due to Subgrid Dry Deposition

Figure 4.5 depicts seasonal maps of total PBL $NO_x$ emission (over land) in GEOS-Chem alongside the fraction corresponding to anthropogenic near-surface sources. Also depicted are effective reductions in both anthropogenic near-surface and total PBL emissions resulting from subgrid dry deposition of anthropogenic near-surface $NO_x$. We use the term

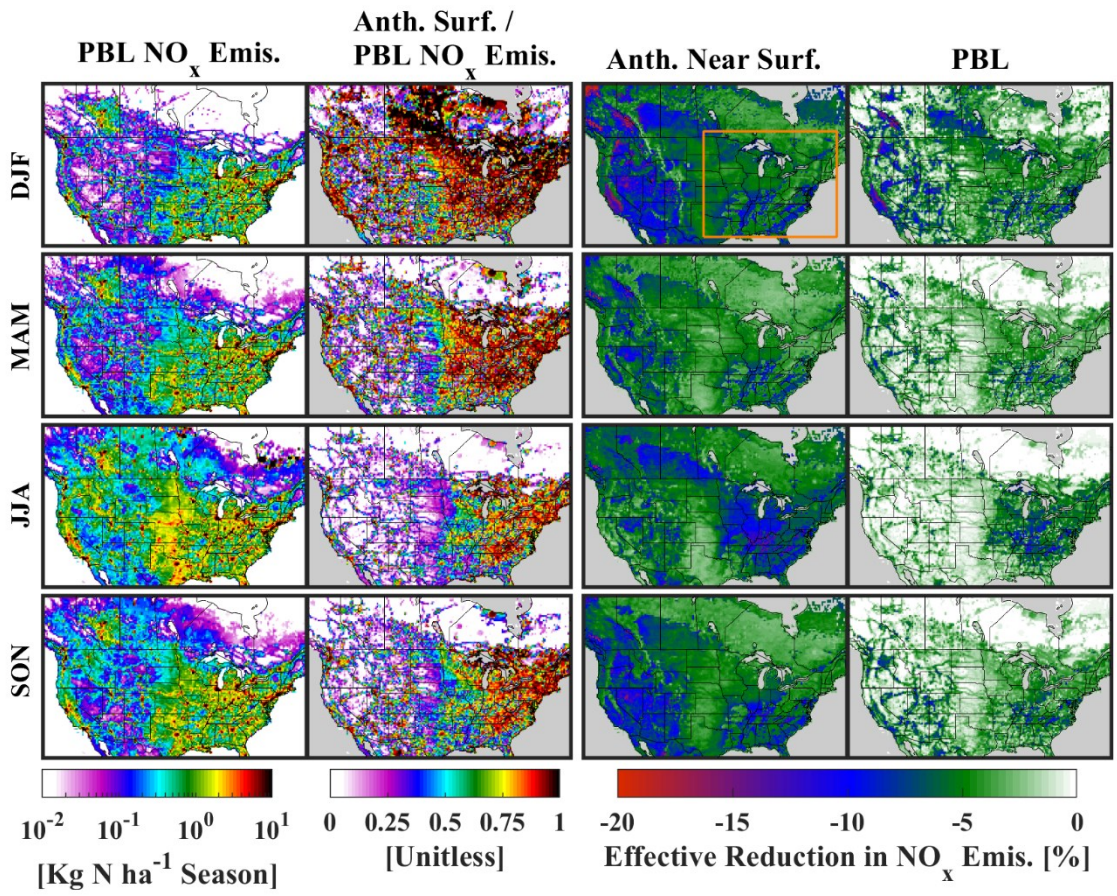


**Figure 4.5:** Seasonal total PBL $NO_x$ emission (over land) in GEOS-Chem (far left) adjacent the fraction corresponding to anthropogenic near-surface (non-stack) sources (center left). Effective reductions in seasonal total $NO_x$ emissions for both anthropogenic near-surface (center right) and total PBL sources (far right) due to subgrid dry deposition are shown for simulation S4. Area of eastern N.A. highlighted in orange is discussed throughout.

'effective reduction' to highlight that this does not indicate a bias in the emission inventory, rather, the fraction of near-surface emitted $NO_x$ that dry deposits prior to plume resolution within the first model level. Urban emissions are primarily (>90%) anthropogenic and surface based, with little seasonality (see also Fig. S4.10 depicting diel $NO_x$ emission for select urban locations as well as regionally across eastern N.A). Regionally, anthropogenic near-surface emissions comprise a smaller but nonetheless substantial fraction of total emissions—for the region of eastern N.A. highlighted in Fig. 4.5, 76% (59%) of total PBL $NO_x$ emissions are from anthropogenic near-surface sources during winter (summer)

(Table 4.2). Total PBL $NO_x$ emissions over eastern N.A. peak during summer months due to soil $NO_x$ contributions, resulting in reductions in the ratio of 'anthropogenic near-surface–to–total emissions' outside of urban areas. Summertime anthropogenic near-surface emissions are ca. 5% higher over eastern N.A. compared to wintertime, whereas total PBL emissions are 37% higher (Table 4.2). Implementation of our parameterization of subgrid dry deposition into GEOS-Chem yields a pattern of anthropogenic near-surface $NO_x$ emission reductions similar to the pattern of $(1 - f)$ depicted in Fig. S4.8. Effective reductions in 24-hr mean anthropogenic near-surface emissions range from 3–15%, with seasonality patterning $R_a$ (Fig. S4.9, section 4.4.3). Accordingly, significant diel variation in effective reductions of $NO_x$ emission occurs (Fig. S4.10), with nocturnal reductions in the range 10–20% and daytime reductions near-negligible outside of high latitudes during winter months.

Recent studies evaluating GEOS-Chem against a suite of summertime aircraft-based measurements over N.A. have concluded that the EPA's NEI 2011 emission inventory may be biased high for oxidized nitrogen (Seltzer et al., 2015; Travis et al., 2016). In particular, Travis et al. (2016) endeavored to understand the summertime high $O_3$ bias in GEOS-Chem over the southeastern U.S. (evident in Fig. S4.7), where part of their analysis focused on uncertainties in $NO_x$ emission sectors. It was found that $NO_x$ emissions from non-powerplant anthropogenic surface sources, the sectors with the greatest uncertainty, had to be reduced by 60% in order to reconcile GEOS-Chem simulated fields with a suite of aircraft-based observations of $O_3$, $NO_x$ and oxidation products, satellite observations of $NO_2$, and surface network observations of nitrate wet deposition. The representation of subgrid dry deposition of $NO_x$ presented herein can only explain an 8% effective reduction in such emissions over the summertime southeastern U.S. Travis et al. (2016) note that zeroing out soil $NO_x$ emissions (18% of total $NO_x$ emitted to southeast U.S.) reduces the necessary reduction in anthropogenic non-powerplant surface emissions from 60% to 30%. Canopy reduction of soil-emitted NO has been identified as a key process in reconciling measured soil emissions with above canopy observations (Jacob and Wofsy, 1990; Lerdau et al., 2000), with recent interest in more detailed understanding of the role of $NO_2$ dry deposition in this process (Delaria and Cohen, 2020). The calculation of the soil $NO_x$ canopy reduction factor (CRF) in GEOS-Chem takes place outside of the

**Table 4.2:** Total over land emission and deposition budgets for the area of eastern North America highlighted in Fig. 4.5.

| GEOS-Chem | Emission [Gg N] | | | Deposition [Gg N] | | | | | | | |
|---|---|---|---|---|---|---|---|---|---|---|---|
| Simulation | $NO_x$ | $NO_x$ | HONO | $NO_2$ | HONO | HONO | $HNO_3$ | $HNO_3$ | $NO_y$ | $NO_y$ | $NO_y$ |
| | Anth. Surf.[a] | PBL Tot. | PBL Tot. | Dry (SG[c]) | Dry (SG) | Wet | Dry | Wet | Dry (SG) | Wet | Total |
| **year** | | | | | | | | | | | |
| S1 (base) | 1890 | 2790 | 14.2 | 159(0) | 0(0) | 0 | 1030 | 632 | 1420(0) | 992 | 2410 |
| S2 | 1890 | 2790 | 14.2 | 140(0) | 7.61(0) | 5.28 | 959 | 679 | 1310(0) | 1060 | 2370 |
| S3 | 1890 | 2790 | 110 | 212(0) | 41.5(0) | 7.89 | 926 | 659 | 1380(0) | 1030 | 2410 |
| S4 | 1770[b] | 2670[b] | 107[b] | 279(78.7) | 70.8(32.9) | 7.54 | 888 | 639 | 1430(112) | 1000 | 2430 |
| **DJF** | | | | | | | | | | | |
| S1 (base) | 461 | 603 | 3.17 | 27.5(0) | 0(0) | 0 | 145 | 145 | 228(0) | 218 | 446 |
| S2 | 461 | 603 | 3.17 | 25.5(0) | 3.4(0) | 2.16 | 135 | 152 | 217(0) | 229 | 446 |
| S3 | 461 | 603 | 38.2 | 54.7(0) | 17.7(0) | 3.19 | 124 | 143 | 247(0) | 218 | 465 |
| S4 | 432[b] | 574[b] | 35.4[b] | 68.4(17.3) | 27.3(11.5) | 2.97 | 116 | 137 | 261(28.8) | 209 | 471 |
| **JJA** | | | | | | | | | | | |
| S1 (base) | 483 | 825 | 3.86 | 54.3(0) | 0(0) | 0 | 410 | 226 | 526(0) | 321 | 846 |
| S2 | 483 | 824 | 3.86 | 46.2(0) | 1.26(0) | 0.764 | 380 | 245 | 479(0) | 346 | 824 |
| S3 | 483 | 824 | 20.3 | 56.3(0) | 5.58(0) | 1.1 | 373 | 242 | 485(0) | 342 | 827 |
| S4 | 449[b] | 791[b] | 21.4[b] | 79(25.6) | 11.6(6.32) | 1.11 | 359 | 237 | 499(31.9) | 335 | 834 |

[a] Anthropogenic near-surface (non-stack) $NO_x$ emissions into the lowest model level.
[b] Anthropogenic near-surface emissions of $NO_x$ and HONO are subject to subgrid (SG) dry deposition in simulation S4, resulting in an *effective* reduction in the emissions released into the lowest model level, not a true reduction in the bottom-up emission inventory.
[c] Contribution of subgrid (SG) dry deposition to total amount.

dry deposition module where updates to $NO_2$ dry deposition presented herein (Table 4.1) are implemented. As a result, only the base simulation S1 uses equivalent parameterizations of $R_c(NO_2)$ for both the CRF and $V_d(NO_2)$—future work will endeavor to use updated $R_c(NO_2)$ in the calculation of soil $NO_x$ CRF in GEOS-Chem. The simple parameterization of canopy reduction of soil-emitted NO in GEOS-Chem—represented as oxidation to $NO_2$ with subsequent canopy uptake (Chapter 3, section 3.4.3.1)—yields a global reduction in above-canopy soil $NO_x$ emission of 16% (Hudman et al., 2012). Preliminary analysis shows the summertime 24-hr mean CRF used in GEOS-Chem increasing from ca. 40% to 60% for a mature eastern U.S. forest (Harvard Forest) upon updating $R_c(NO_2)$ according to simulation S3 (data not shown). It will be interesting to discover the degree of summertime soil $NO_x$ reductions that result, which would further alleviate a portion of the necessary reductions in anthropogenic summertime $NO_x$ emissions from the EPA's NEI 2011 inventory upon implementation into GEOS-Chem. Jaeglé et al. (2018) found that emissions from the EPA's NEI 2011 inventory implemented in GEOS-Chem resulted in an updated simulation of $NO_y$ in good agreement (to within 10% on average) with the WINTER aircraft observations over wintertime Northeast U.S.—a period when soil $NO_x$ emissions would be at a minimum. We find that subgrid dry deposition reduces effective total PBL $NO_x$ emission into GEOS-Chem by ca. 5% for wintertime eastern N.A. (Table 4.2).

### 4.6.2 Evaluation of simulated HONO vertical profiles with the WINTER aircraft campaign

Figure 4.6 shows vertical mean profiles of daytime and nocturnal $NO_x$ and HONO from the WINTER aircraft campaign together with coincidently-sampled values from base and updated simulations. Steep vertical gradients observed below 1 km indicate predominant surface sources for $NO_x$ and HONO, consistent with the $NO_x$ emission inventory (i.e., Fig. 4.5) and current understanding of HONO formation being a predominantly ground surface based mechanism in anthropogenically influenced regions (Zhang et al., 2016). All simulations generally well represent the observed $NO_x$ vertical profile, however, the base simulation S1 underestimates daytime and nocturnal mean HONO by more than a factor

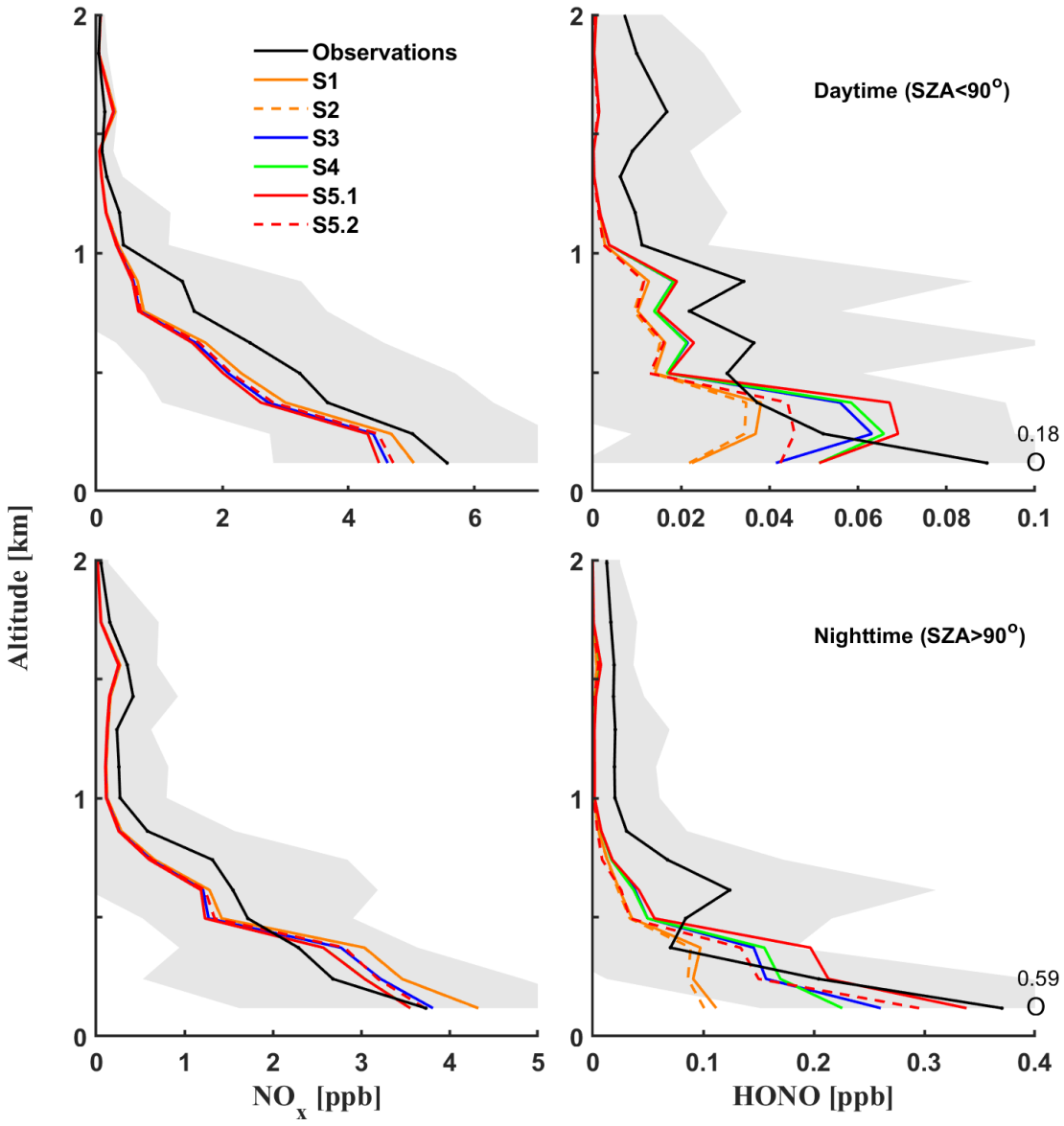


**Figure 4.6:** Vertical profiles of daytime and nocturnal mean $NO_x$ and HONO observed during the WINTER aircraft campaign (black line with grey shade indicating standard deviation) and simulated mean profiles coincidently sampled from base (S1) and updated (S2–S5) GEOS-Chem simulations. Flight #9 which took place offshore during nocturnal morning hours of 23 February 2015 has been removed from analysis (see Fig. S4.12 and text for discussion).

of 2, both near-surface (<120 m) and below 1 km. This despite an overly large $NO_2$ uptake coefficient for reaction R4.1 to all aerosol types ($\gamma_{NO_2}^{aerosol} = 10^{-4}$) as well as the absence of HONO wet and dry deposition pathways (Table 4.1). Jaeglé et al. (2018) address the underestimate in GEOS-Chem simulated HONO by increasing the molar yield of HONO from reaction R4.1 on aerosol from 50% to 100%, which had the effect of nearly doubling mean HONO below 1 km.

Campaign minimums in ambient HONO and $HNO_3$ concentrations have been observed during rainfall events (Li et al., 2012). As previously mentioned, HONO is not subject to wet or dry deposition in base GEOS-Chem simulation S1. Implementing standard wet and dry deposition of HONO in simulation S2 resulted in a <10% reduction in campaign mean HONO below 1 km. A larger reduction of 20% occurred for the nocturnal flight commencing February 22$^{nd}$, where the airmass sampled 100–400 km offshore (compare Figs. S4.11 & S4.12) experienced rain events as it was being advected away from land according to backward trajectory calculations performed using the HYSPLIT model (Stein et al., 2015) with North American Mesoscale (NAM) Forecast System meteorology at 12 km resolution (data not shown). Despite observed nocturnal mean $NO_x$ concentrations on the order of 2 ppb below ca. 400 m for the 22/23 February flight, nocturnal mean HONO was below the detection limit (data not shown). As depicted in Fig. S4.11, sampling altitudes for this offshore flight corresponded to the model's second (125–250 m) and third levels (250–375 m). Elevated HONO concentrations have been observed in polluted nocturnal marine boundary layers, where heterogeneous formation was understood to take place at the air-sea interface via $NO_2$ hydrolysis (Cui et al., 2019; Wen et al., 2019; Yang et al., 2021; Zha et al., 2014) and resulting HONO concentrations possibly buffered by surface reservoirs of adsorbed species (Wojtal et al., 2011). Therefore, elevated HONO concentrations would be expected closer to the ocean surface in the presence of elevated $NO_x$, however, offshore nocturnal flights below 100 m—the typical height of a nocturnal marine boundary layer (Brown et al., 2004)—were not conducted during the WINTER campaign. Given the large relative extent of the low altitude offshore flight tracks during the nocturnal morning hours of 23 February 2015 (Fig. S4.11), inclusion results in a local minimum in campaign mean nocturnal HONO at model levels 2–3 that is overestimated in all simulations (Fig. S4.13). Coincidently-sampled simulated

$NO_x$ and HONO concentrations for this offshore nocturnal flight are on the order of 2–3 ppb and 0.15–0.35 ppb, respectively (data not shown). Although implementation of HONO wet and dry deposition into the model in simulation S2 does result in a >25% reduction in simulated HONO between 125–375 m for the 22/23 February flight track—larger than the <10% reduction at these levels depicted in Fig. 4.6—the large high bias persists in simulation S2 (Fig. S4.13). Removing this offshore flight track from analysis results in the mean vertical profiles depicted in Fig. 4.6, which shows a steady decrease in nocturnal HONO from the surface to ca. 400 m. Although investigation into the bias of this particular nocturnal flight track is beyond the scope of this work, a possible contribution may be a low bias in wet deposition in the version of GEOS-Chem used herein. Luo et al. (2019) propose updates to the wet deposition scheme in GEOS-Chem, including spatiotemporally varying in-cloud condensation water and empirical washout rates for $HNO_3$ and aerosol. These updates were shown to greatly reduce high biases in simulated $HNO_3$ and ammonium nitrate aerosol concentrations (Luo et al., 2019), and have been included in recent model studies (McDuffie et al., 2021; Travis et al., 2022). Luo et al. (2020) propose further updates to wet deposition in GEOS-Chem, including replacing the model's constant rainwater pH of 4.5 used in the calculation of $H^*$ (4.4) with spatiotemporally varying values based on simulated cloud water pH.

As seen in Fig. 4.6, representing ground surface production of HONO via heterogeneous hydrolysis of $NO_2$ through dry deposition in simulation S3, which also includes updated surface resistance to dry deposition of HONO over land (Fig. S4.3), resulted in large increases in mean HONO below 1 km of 64% (day) and 93% (night) above simulation S2 values. Larger increases are seen in near-surface HONO for both day (90%) and night (160%), with corresponding reductions in $NO_x$ of 8% and 11%, respectfully. Implementing subgrid dry deposition of $NO_x$—which emits HONO as part of the mechanism—and nocturnal subgrid dry deposition of HONO in simulation S4 has a small effect on HONO concentrations below 1 km—a <10% change from simulation S3 values. Moderate effects are noted for near-surface (< 120 m) HONO—a 13% nighttime decrease and 24% daytime increase relative to simulation S3. Although subgrid dry deposition of $NO_x$ has minimal effect on regional HONO concentrations over the domain of the

WINTER campaign, significant increases noted at urban locations will be discussed in section 4.6.4 (Figs. 4.8 & 4.9).

Bidirectional surface exchange is represented in GEOS-Chem through independent emission and dry deposition processes. A notable exception is the soil $NO_x$ parameterization, where 60% of total deposited reactive nitrogen contributes to a soil reservoir with a lifetime of 6 months (Hudman et al., 2012). Gas-surface dynamic equilibriums are a subgrid feature in a large scale CTM, especially at night due to steep near-surface vertical gradients. Our inclusion of surface emitted nocturnal HONO as a species subjected to subgrid dry deposition in simulation S4 was an initial estimate at representing bidirectional exchange. Although near-surface HONO is much increased above the base simulation, better capturing the near-surface maximum in the observations, underestimates on the order of 40% remain in near-surface HONO for simulation S4 for both day and night, although only the nocturnal bias is statistically significant ($p < 0.05$). Eliminating subgrid dry deposition of HONO in simulation S5.1 improves near-surface nocturnal comparison in Fig. 4.6, albeit, with an unrealistically high $NO_2$ uptake to aerosol ($\gamma_{NO_2}^{aerosol} = 10^{-4}$), as in simulations S1–S4. Updating $\gamma_{NO_2}^{aerosol}$ to 5 x $10^{-6}$ in simulation S5.2 results in a 25–30% reduction in mean HONO below 1 km and an absolute (relative) reduction in near-surface HONO of ca. 0.01 ppb (18%) for daytime and 0.04 ppb (12%) for nighttime. Consistent with observations, simulation S5.2 displays a steep vertical gradient in nocturnal HONO below 500 m, with a near-surface mean concentration (0.30 ± 0.18 ppb) slightly less than (ca. 20%), although not significantly different from ($p > 0.1$), the observed mean (0.37 ± 0.22 ppb). Direct emissions of HONO in simulations herein are from the NEI 2011 anthropogenic emissions inventory, which employs a widely used $HONO/NO_x$ ratio of 0.8% for traffic emissions (Aumont et al., 2003; Czader et al., 2012; Kurtenbach et al., 2001). Recent modeling studies of (sub)urban environments have examined the effect of doubling the $HONO/NO_x$ traffic emission ratio to 1.6%, finding insignificant (< 2%) (Zhang et al., 2016) to modest (10–36%) (Czader et al., 2015) increases in simulated near-surface HONO. When compared to diel measured HONO, these large changes in the traffic emission ratio had little influence on improving simulated values outside of morning rush hours (Czader et al., 2015). Considering the order of magnitude increase in simulated HONO emission over wintertime eastern N.A. by

representing $NO_2$ heterogeneous hydrolysis on ground surfaces in simulation S3 (Table 4.2), it is unlikely that updates to the HONO/$NO_x$ traffic emission ratio in GEOS-Chem would yield significant change in simulated HONO—consistent with the findings of Zhang et al. (2016) that R4.1 on ground surfaces is the predominant source of nocturnal HONO in a polluted region.

A local maximum at ca. 600 m exists in the observed nocturnal HONO vertical profile depicted in Fig. 4.6. Absent in all simulations, this local maximum drives a low bias of 33% in mean HONO below 1 km in simulation S5.2. Strengthening the filter for subgrid scale plumes in the WINTER dataset by reducing the maximum allowed $NO_x$ concentration on 1-minute intervals from 10 ppb to 5 ppb has little effect on the local maximum in coincidently-sampled HONO, nor does an additional filter requiring coincidently-sampled CO be less than one standard deviation above the campaign mean value (150 ± 23 ppb, < 1 km) (data not shown). Two flight tracks contribute to the local maximum aloft in observed nocturnal HONO—(i) a nighttime costal flight on 20 February 2015 between Norfolk VA and New York City, and (ii) an inland flight on the evening of 24 February 2015 between VA and southern PA (data not shown). Removing these flight tracks from analysis (Fig. S4.14) eliminates the local maximum aloft, resulting in a continuous decrease in nocturnal HONO from the surface to 1 km (Fig. S4.15)—a gradient best captured in simulation S5.2 which has a NMB below 1 km of 19% and a near-surface concentration (0.30 ± 0.18 ppb) slightly greater than, although not significantly different from ($p > 0.1$), the observed mean (0.23 ± 0.20 ppb). It is expected that representing surface $O_3$ concentration in the parameterization of subgrid dry deposition of NO in future work will result in further reductions in simulated nocturnal HONO. Although the flight tracks responsible for the nocturnal local maximum had only a short duration during daytime, their removal from the dataset resulted in the elimination of local maxima in daytime HONO between 0.5 – 1 km, resulting in a continuous decrease in HONO with height from the surface to 1 km (Fig. S4.15).

Daytime HONO is biased low in all simulations, with simulation S5.2 biased low near-surface by more than a factor of two, and below 1 km by more than 30%. Low biases persist above the PBL (> 1 km) as well. Daytime low biases in simulated HONO are well

documented phenomenon in atmospheric models, with numerous potential sources being studied in this active area of research. Sources of HONO in addition to those represented herein (i.e., direct anthropogenic emission, reaction R4.1 on ground and aerosol surfaces, and reaction R4.2) include: (i) photolysis of nitrate or surface adsorbed $HNO_3$ (Rappenglück et al., 2014), (ii) photosensitized reduction of $NO_2$ via surface adsorbed organics (Villena et al., 2011), (iii) release of nocturnally deposited HONO from evaporating dew (Ren et al., 2020; Wentworth et al., 2016), and (iv) emission from soils due to reactive displacement via deposition of strong acids (VandenBoer et al., 2015), acid-base equilibria of soil water (Su et al., 2011), or (de)nitrifying microbial processes (Oswald et al., 2013). Figure S4.16 in the appendix depicts both measured and simulated vertical mean profiles of $HNO_3$, $pNO_3$, and total nitrate ($TN \equiv HNO_3 + pNO_3$) from the WINTER campaign. In comparing Figs. 4.6 & S4.16, low biases in simulated daytime HONO above the PBL correlate with high biases in TN, consistent with the findings of Ye et al. (2018) that photolysis of particulate nitrate could be a major source of HONO in low-$NO_x$ air masses, and an obvious direction for future work. Kasibhatla et al. (2018) implement nitrate photolysis on sea-salt aerosol in GEOS-Chem, where it was shown to be a required process enabling model reproduction of observed diel HONO profiles in the remote (low-$NO_x$) marine boundary layer. Nitrate photolysis is now a tunable feature (off by default) in GEOS-Chem v12.6.0, facilitating development of this potentially important renoxification pathway involving HONO.

The large high biases in simulated $HNO_3$ and $pNO_3$ depicted in Fig. S4.16 are well documented for GEOS-Chem versions up to and including v12 (Heald et al., 2012; Jaeglé et al., 2018; Luo et al., 2019; Zhang et al., 2012a), as well as in other CTMs to varying degrees (Colette et al., 2011; Simon et al., 2012; Zakoura and Pandis, 2018). Although an unbiased simulation of $HNO_3$ and $pNO_3$ is beyond the scope of this work, it is instructive to mention the several recent literature recommendations relating to these long-standing biases. Shah et al. (2018) implement temperature-dependent livestock emissions of $NH_3$ which resulted in a factor of 2 reduction from this sector over the period of the WINTER campaign, as well as updating the dry deposition of $HNO_3$ by limiting $R_c(HNO_3)$ to 1 s $m^{-1}$ (an update included herein and now standard in GEOS-Chem v12.6.0). In addition to these updates, Jaeglé et al. (2018) test several modifications to heterogeneous uptake

coefficients to aerosol for reactions yielding $HNO_3$, including $\gamma_{NO_2}^{aerosol}$ (emit all as HONO), $\gamma_{NO_3}^{aerosol}$ (reduce 10x), and $\gamma_{N_2O_5}^{aerosol}$ (several updates resulting in 2x reduction over the domain of the WINTER campaign). Recently, McDuffie et al. (2021) implement into GEOS-Chem v12.1.0 several literature recommendations to address high biases in simulated aerosol nitrate, including an updated parameterization of $\gamma_{N_2O_5}^{aerosol}$ (McDuffie et al., 2018b, 2018a) which is now standard in GEOS-Chem v12.6.0, an updated wet deposition scheme following Luo et al. (2019, 2020), and the aforementioned update to $R_c(HNO_3)$.

Although we expect simulation S5.2 with an updated 5-D look-up-table containing an ozone dimension for subgrid dry deposition of $NO_x$ to yield the best nocturnal comparison to vertical mean profiles of HONO from the WINTER aircraft campaign, currently, S5.2 has been run only for the duration of the WINTER campaign (February–March 2015) and with a 4-D look-up-table which assumes a constant $O_3$ concentration of ca. 40 ppb for the purpose of subgrid dry deposition of $NO_x$, as previously discussed. In the meantime, we proceed herein with seasonal analysis of simulations up to S4, which as of present are complete. We note that nocturnal near-surface concentrations of HONO in simulations S3 and S4 are only slightly below those of S5.2 due to the very high $\gamma_{NO_2}^{aerosol}$ used in S3 and S4, and that concentrations in S5.2 are expected to decrease with a 5-D look-up-table, albeit, to a presently undetermined extent.

### 4.6.3. Changes in Simulated $NO_y$ Deposition

Figure 4.7 (top) depicts simulated (S4) spatial distributions of summer (JJA) and wintertime (DJF) total (wet + dry) deposition of oxidized nitrogen ($NO_y$) over the U.S. and Canada alongside serial change resulting from sequential updates to simulations S2 through S4. Due to the short lifetime of $NO_x$ to oxidation to more rapidly depositing $NO_y$ species, deposition patterns of $NO_y$ share a smoothed resemblance with $NO_x$ emissions (Fig. 4.5). Seasonal maximums in deposition occur over regions and locations of elevated anthropogenic activity, including along the West Coast and eastern N.A., with anthropogenically influenced $NO_y$ deposition continuing off the east coast for at least several hundred kilometers. Elevated summertime $NO_y$ deposition across the U.S. Midwest

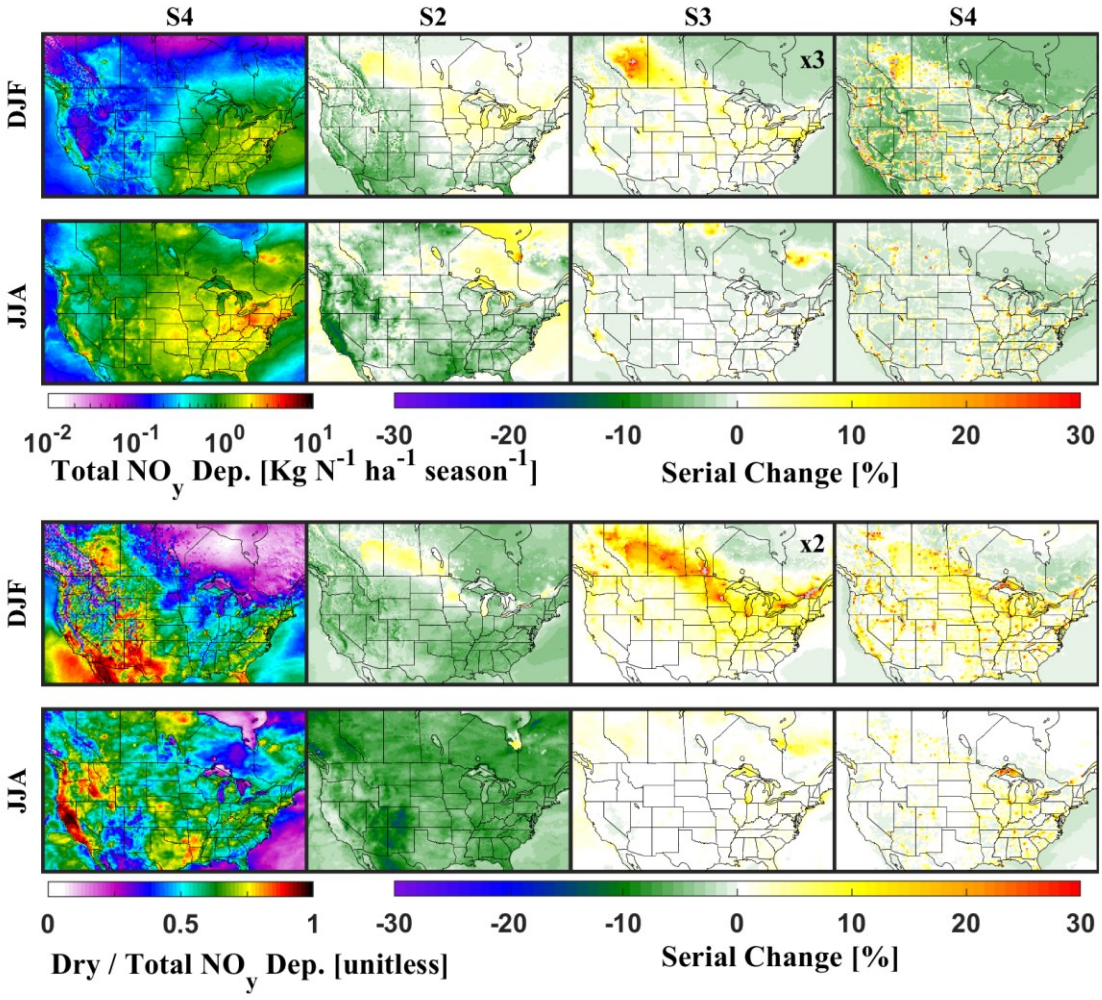


**Figure 4.7: (TOP)** Total (wet + dry) deposition of reactive nitrogen oxides ($NO_y$) for summer (JJA) and winter (DJF) seasons for the year 2013 from GEOS-Chem simulation S4 (top left) adjacent serial percent changes for indicated simulations, i.e., for S2: 100x(S2-S1)/S1, and for S4: 100x(S4-S3)/S3. **(BOTTOM)** Dry / Total $NO_y$ deposition ratios for simulation S4 adjacent serial percent changes for indicated simulations. Note, interpretation of percent change in DJF total deposition and the ratio dry/total deposition for simulation S3 requires application of indicated multiplicative factors. Grey indicates off-scale.

and northern Canada reflect soil and forest fire sources of $NO_x$. The seasonality in $NO_y$ deposition (JJA 128% higher than DJF for area depicted) is greater than the seasonality in $NO_x$ emissions (JJA 88% higher than DJF for area depicted) due to shorter $NO_x$ lifetimes in summer months resulting from higher concentrations of photochemical oxidants such as $O_3$ (Fig. 4.9 & Fig. S4.7) and OH (Fig. 4.9), as discussed below in section 4.6.4. Simulated (S4) annual mean total deposition flux of $NO_y$ over eastern N.A. of ca. 5 kg N $ha^{-1}$ $yr^{-1}$ for the year 2013 is ca. 50% of the value from earlier GEOS-Chem studies, including from Zhang et al. (2012a) for the years 2006–2008 and Geddes and Martin (2017) for the years 1996–2014, however, consistent with the large reductions in North American $NO_x$ emissions over the past two decades (McDuffie et al., 2020). Geddes and Martin (2017) employ inverse modeling of satellite $NO_2$ columns to produce top-down $NO_x$ emission estimates for a global study of long-term $NO_y$ deposition, finding reductions over eastern N.A. of up to 60% over the 18-year time series, with values across the polluted Ohio River valley falling to 6 kg N $ha^{-1}$ $yr^{-1}$ by 2014. We find annual mean $NO_y$ deposition over the northeast U.S. (35°–50°N, 65°–90°W) to be 6.0 kg N $ha^{-1}$ $yr^{-1}$ in base simulation S1, increasing slightly to 6.2 kg N $ha^{-1}$ $yr^{-1}$ for simulation S4. Critical loads of reactive nitrogen are in the range 5–35 kg N $ha^{-1}$ $yr^{-1}$ for various freshwater and terrestrial ecosystems, dependent on ecosystem type, management history, and soil conditions (World Health Organization, 2000). We find deposition of $NO_y$ alone exceeds 5 kg N $ha^{-1}$ $yr^{-1}$ across 14% of the land region of North America depicted, with small variation between simulations (< 2%) at this percentile; over eastern N.A., minimum exceedance increases to 47%, with variation between simulations < 5% (data not shown).

Over the land area of North America depicted in Fig. 4.7, wet and dry deposition of $NO_y$ is in balance, with dry deposition making slightly larger contributions to total deposition (56–60%); the contribution over eastern N.A is similar (55–60%, Table 4.2). As seen in the bottom left panels of Fig. 4.7, seasonal variation in the ratio of 'dry / total $NO_y$ deposition' exists on smaller scales, with some areas alternating between dry and wet dominated. The balance between wet and dry deposition of $NO_y$ over a large area buffers regional change in total deposition from simulation updates affecting dry deposition. Figures S4.17 and S4.18 in the supplemental material depict seasonal dry and wet deposition patterns, respectfully, alongside serial change resulting from sequential updates

to simulations S2 through S4 where modulating effects on total $NO_y$ deposition are apparent. Simulation S2 includes updates to aerodynamic resistance $R_a$, molecular diffusivity in air, and inclusion of HONO as a species that is both dry and wet deposited (Table 4.1). The predominant effect of simulation S2 updates on $NO_y$ deposition is the increase in quasi-boundary layer resistance $R_b$, which slows the dry deposition of rapidly depositing species such as $HNO_3$ (Fig. 4.1 & Table 4.2). The diffusivity update in S2 also results in small increases in surface resistance $R_c$ for species that deposit under stomatal control during daytime, i.e., $NO_2$ (Fig. 4.2 & Table 4.2). Reductions in $NO_y$ dry deposition of 5–15% across much of the U.S. and Canada (Fig. S4.17), including an 8% reduction over eastern N.A. (Table 4.2), are countered by nearly equivalent increases in $NO_y$ wet deposition (Fig. S4.18), including a 7% increase over eastern N.A. (Table 4.2), resulting in the muted change to total $NO_y$ deposition depicted for S2 where reductions over eastern N.A. are less than 2% (Table 4.2). The small wintertime (DJF) increase in the ratio 'dry / total NOy deposition' over the Canadian prairies and extending into Minnesota is due to HONO dry deposition which was absent in the base simulation S1 (data not shown).

Implementation of $NO_2$ heterogenous hydrolysis on ground surfaces (R4.1) in simulation S3 resulted in large increases in wintertime dry deposition of $NO_y$ over anthropogenically influenced regions of Canada and northeast U.S. Dry deposition of $NO_2$ over wintertime eastern N.A. is more than a factor of two greater than in simulation S2, affecting a 14% (4%) increase in $NO_y$ dry (total) deposition (Table 4.2), with similar change over the U.S. and Canada (data not shown). Much larger increases in $NO_y$ total deposition on the order of 100% are seen over southern Alberta, where $NO_2$ would otherwise have near-negligible deposition (Fig. 4.2). Due to dominant stomatal uptake of $NO_2$ during summer months, the parallel pathway for heterogeneous hydrolysis on ground surface elements in simulation S3 results in a much smaller summertime increase in $NO_2$ deposition—23% JJA increase across eastern N.A. Very small increases in summertime $NO_y$ dry deposition in simulation S3 are nearly countered by corresponding decreases in wet deposition, resulting in negligible change in total deposition outside of heavily polluted urban locations such as Los Angeles (L.A.) and areas with forest fire activity.

Subgrid dry deposition of $NO_x$ and HONO in simulation S4 increases total $NO_y$ deposition above S3 values over areas with large anthropogenic emissions of near-surface $NO_x$, such as major highways and urban locations. As with simulation S3, greatest relative change occurs during winter months when stomatal uptake is at a minimum due to senescent foliage and temperatures below 5°C when stomatal resistance is parameterized to increase sharply (Wesely, 1989). Local increase in $NO_y$ deposition in cities and along highways induces reductions over adjacent regions. Averaged across the U.S. and Canada, or eastern N.A., relative change is low throughout the seasons (< 2%) due to the compensating decrease in wet deposition. Over cities, however, a much greater response is observed.

Figure 4.8 depicts diel profiles of January and July mean dry deposition flux for $NO_2$ and both dry and total deposition flux for $NO_y$ over select urban centers including: L.A., Seattle, Calgary, and Chicago, as well as regional profiles for eastern N.A. Also included are diel profiles of the ratio '$NO_y$ total deposition / PBL $NO_x$ emission', which quantifies the net export of oxidized reactive nitrogen from the respective area assuming effective mass balance between $NO_x$ and $NO_y$, i.e., that all primary emissions of $NO_y$ originate as $NO_x$. Cities are large net exporters of $NO_y$, taking up on average only a small fraction relative to the $NO_x$ they emit—less than 5% in simulation S2 for January and between 7–26% for July. A large increase in urban 24-hr $NO_y$ total deposition in simulation S4 is driven by enhanced deposition spanning early evening until shortly after sunrise—consistent with the period of maximum subgrid dry deposition of $NO_x$ and resulting HONO. For July, increases in $NO_y$ total deposition of 23% (Seattle) to 100% (Calgary) are noted; for January, the result is more extreme, with simulated increases by a factor of 2–3 for L.A., Seattle, and Chicago, and a factor of 16 for Calgary over a 24-hr period. Simulated change in urban uptake of $NO_y$ is driven predominantly by subgrid dry deposition (simulation S4), however, notable increases exist at some locations for simulation S3, i.e., wintertime Seattle and Chicago, and summertime L.A. The simulated net export of $NO_y$ from cities is notably reduced in simulation S4, with $NO_y$ uptake of up to 15% of local $NO_x$ emitted into the PBL for January, and up to 33% for July. Integrated over larger areas, such as eastern N.A., $NO_y$ uptake is a much greater fraction of regional $NO_x$ emissions, to the point of becoming $NO_y$ neutral, and even a net sink for summer months (Fig. 4.8 and Table

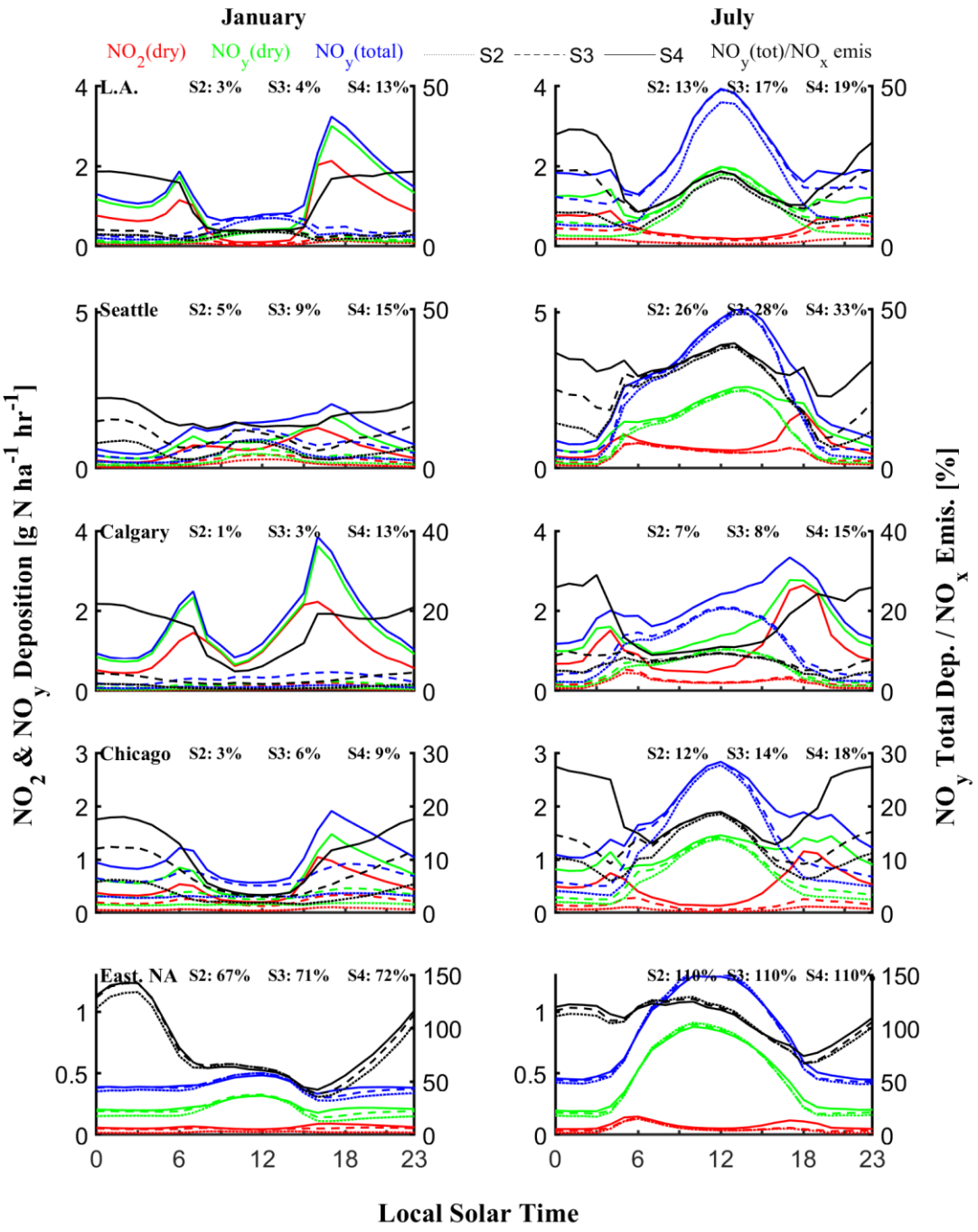


**Figure 4.8:** Monthly mean diel profiles of dry deposition flux for $NO_2$ and both dry and total (wet + dry) deposition flux for $NO_y$ over select urban centers and eastern North America are depicted for three updated simulations: S2, S3, and S4. Diel ratios of '$NO_y$ total deposition / PBL $NO_x$ emitted' are depicted in black and plotted as a percentage along with 24-hr monthly mean values included as insets. PBL $NO_x$ emissions from simulation S2 are used in all ratios depicted.

4.2) when the oxidation lifetime of $NO_2$ to rapidly depositing $HNO_3$ is reduced due to elevated OH (section 4.6.4). Over the land region of the U.S. and Canada depicted in Fig. 4.7, wintertime (DJF) export of $NO_y$ decreases from 29% in simulation S2, to 26% (S3), to 21% (S4); summertime (JJA) export of $NO_y$ is much lower, and decreases from 7% (S2), to 6% (S3), to 2% (S4) (data not shown).

As previously discussed, through increasing surface uptake of $NO_2$ to all land-types via reaction R4.1 (simulation S3) and by representing subgrid uptake of anthropogenically emitted near-surface $NO_x$ that dry deposits prior to turbulent resolution within the lowest model level (simulation S4), $NO_2$ dry deposition close to source is enhanced. Nowlan et al. (2014) present a global high resolution (0.1° x 0.1°) dataset of $NO_2$ inferential dry deposition fluxes using satellite $NO_2$ columns to scale GEOS-Chem simulated surface concentrations, where model deposition velocities were calculated at high resolution using LAI and land-use maps at 0.1° x 0.1°. Globally, it was found that $NO_2$ dry deposition was 3% of $NO_x$ emitted. Over Canada and the U.S., we find that $NO_2$ dry deposition is ca. 5% of total $NO_x$ emitted in simulation S2, increasing to 7% for S3 and 9% for S4 (data not shown); similar results are noted over eastern N.A. (Table 4.2). In an inferential study of global $NO_2$ dry deposition using satellite-based measurements of $NO_2$ and GEOS-Chem simulated deposition velocities, Nowlan et al. (2014) found that $NO_2$ dry deposition makes significant, even dominant, contributions to total $NO_y$ dry deposition proximal to urban centers due to deposition to vegetated surfaces outside of largely non-vegetated downtown cores. Nowlan et al. (2014) found that dry deposition of $NO_2$ over a selection of urban areas contributed on average 9–36%, and as much as 85%, of total $NO_y$ dry deposition. Averaged across the four urban centers depicted in Fig. 4.8, we find $NO_2$ contributions to 24-hr mean $NO_y$ dry deposition increasing from 38% (S2) to 51% (S3) to 60% (S4), with hourly contributions approaching 100% shortly before sunset and shortly after sunrise when subgrid dry deposition of $NO_2$ is still high (Fig. S4.10) and resulting HONO not yet subject to nocturnal subgrid dry deposition as SZA < 90°. Updates to $NO_2$ dry deposition in simulations S3 and S4 add to the findings of Nowlan et al. (2014) that $NO_2$ is a significant contributor to $NO_y$ dry deposition over urban areas.

### 4.6.4 Effects of Updates on Simulated Surface Concentrations

Figure 4.9 depicts spatial distributions of simulated (S4) surface concentrations of 24-hr $NO_2$, HONO, and total nitrate (TN ≡ $HNO_3$ + $pNO_3$), and daytime $O_3$ and OH for January and July adjacent percent change (absolute change for HONO) between simulations S2 and S4. Annual mean surface concentrations of aforementioned species (save OH) adjacent serial change resulting from sequential updates to simulations S2 through S4 are depicted in Fig. S4.19 in the supplemental material. Diel profiles of simulated (S2, S3, and S4) mean surface concentrations for January and July over select urban centers (L.A., Seattle, Calgary, and Chicago) and eastern N.A. are depicted for HONO and OH in Fig. 4.10, and for $NO_x$, NO, TN, and particulate sulfate ($pSO_4$) in Fig. S4.20. Hourly percent change in $NO_x$, HONO, OH, $O_3$, and TN surface concentrations between simulation S2 and simulations S3 and S4 over aforementioned locations are depicted in Fig. 4.11.

Due to the relatively short lifetime of $NO_x$ of less than a day, spatial patterns of $NO_2$ surface concentration mirror $NO_x$ emission sources, with seasonality over developed regions resulting from longer wintertime lifetimes and reduced boundary layer depths. Large reductions in wintertime $NO_2$ concentration over remote locations such as northern Canada result from updating $R_c(NO_2)$ in simulation S3 to include a hydrolysis pathway on ground surfaces—a period when deposition would otherwise be near-negligible (Fig. 4.2). Over metropolitan areas, subgrid deposition of $NO_x$ (simulation S4) is the dominant contributor to reductions in surface concentrations for both winter and summer (Figs. 4.11 & S4.20), whereas over regional areas of anthropogenic influence, updates to simulations S3 and S4 make similar contributions, i.e., -12% and -19% change in 24-hr surface $NO_2$ over eastern N.A. from simulation S2 to simulations S3 and S4, respectively. Although reductions in $NO_2$ concentrations are attributed to reduced lifetimes to dry deposition, urban concentrations will also be influenced by reduced lifetime to gas-phase oxidation due to both $NO_x$ reductions in a $NO_x$-saturated chemical regime (Laughner and Cohen, 2019) and large wintertime increases in urban OH due to HONO photolysis, as discussed below.

The strong photolytic sink of HONO (reaction R4.3) and the heterogeneous hydrolysis of $NO_2$ (reaction R4.1) as a dominant nocturnal source of HONO results in distinct spatiotemporal patterns and diel cycles in near-surface HONO concentrations for

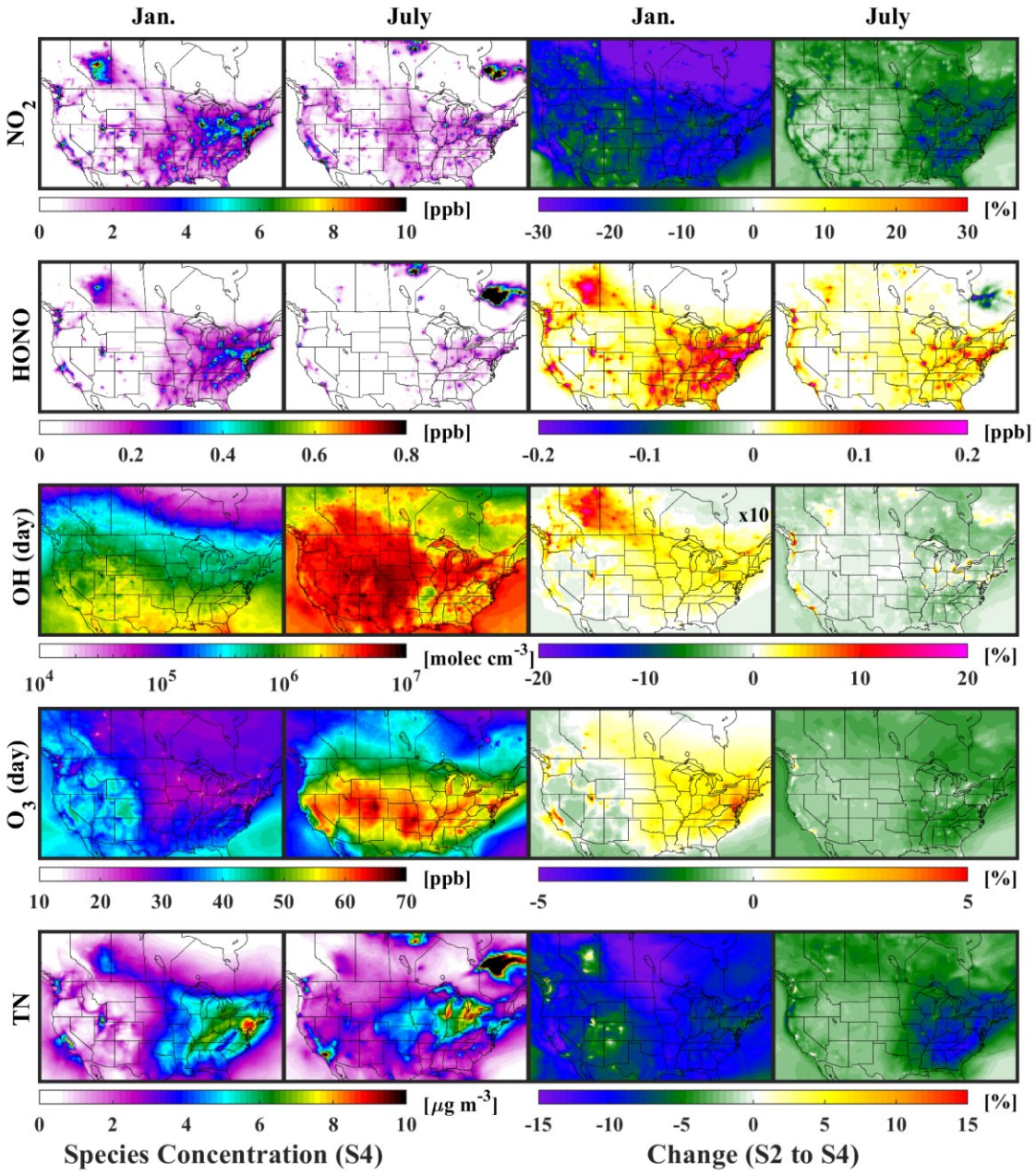


**Figure 4.9:** Monthly mean surface concentrations of 24-hr $NO_2$, HONO, and total nitrate ($TN \equiv HNO_3 + pNO_3$), and daytime $O_3$ and OH from simulation S4 adjacent percent change between simulations S2 and S4, i.e., 100x(S4-S2)/S2. Daytime averages are conducted over 6–16 LST for Jan. and 4–18 LST for July. Note, absolute change (S4-S2) is depicted for HONO. Note, interpretation of percent change in January OH concentrations require application of indicated multiplicative factor.

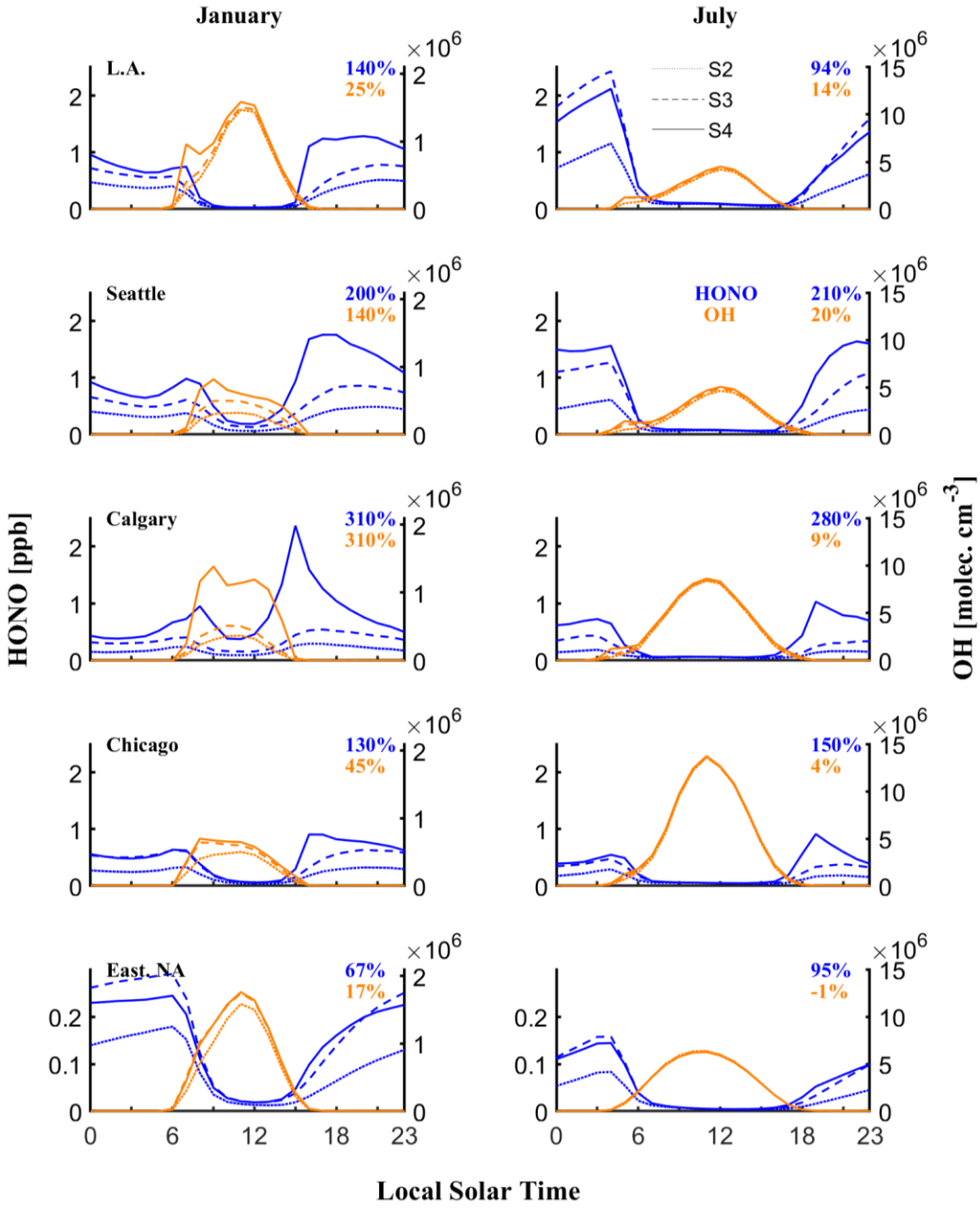


**Figure 4.10:** Monthly mean diel profiles of ground-level HONO (blue) and OH (orange) for select urban centers and eastern N.A. (over land) are depicted for three updated simulations: S2, S3, and S4. Percent change in HONO (24-hr) and OH (daytime) between simulations S2 and S4, i.e., 100x(S4-S2)/S2, are shown as insets. Daytime averages conducted over 6–16 LST for Jan. and 4–18 LST for July.

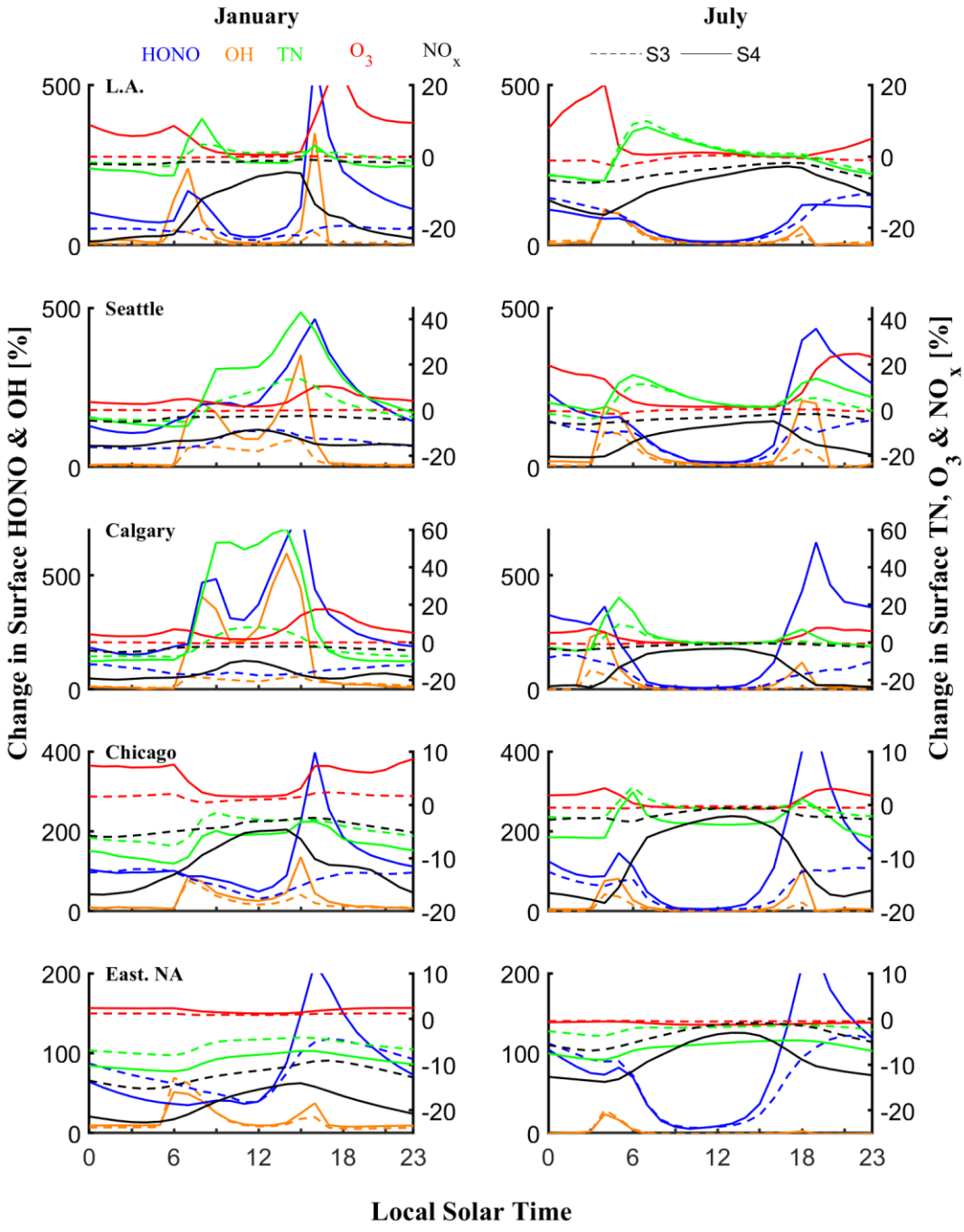


**Figure 4.11:** Percent change in HONO, OH, total nitrate (TN ≡ $HNO_3$ + $pNO_3$), $O_3$, and $NO_x$ surface concentrations between simulation S2 and simulations S3 and S4 for select urban centers and eastern N.A.

moderate to high $NO_x$ environments. As depicted in Fig. 4.9, spatiotemporal patterns of near-surface 24-hr HONO resemble those of $NO_2$, namely wintertime maximums increasing with proximity to $NO_x$ sources. As depicted in Fig. 4.10, over urban centers and the eastern U.S., HONO exhibits a clear diel cycle with daytime minimums and increasing concentrations shortly before sunset. Nocturnal behavior is varied, with examples of a leveling off on approach to an apparent pseudo steady state (PSS) where HONO production via reaction R4.1 becomes balanced by dry deposition loss once near-surface concentrations build (Stutz et al., 2004). In other instances, HONO concentrations continue to build throughout the night, reaching a maximum concentration around sunrise—a diel cycle that has been observed in the summertime Pearl River Delta region of China where campaign average HONO reached a maximum concentration of 1.5 ppb ($HONO/NO_2$ ratio of ca. 9%) around sunrise (Li et al., 2012).

Representing reaction R4.1 on ground surfaces in simulation S3 resulted in a nearly 7-fold increase in annual HONO emission over eastern N.A. (11-fold DJF, 4-fold JJA, Table 4.2) and is the predominant mechanism contributing to the large regional nocturnal increases in surface HONO seen in Figs. 4.9–11 and S4.19. Regionally, subgrid dry deposition of $NO_x$ and HONO in simulation S4 has little effect (< 10%) on HONO emission over eastern N.A. As depicted in Figs. 4.10 and S4.19, moderate to large increases in nocturnal urban HONO due to subgrid dry deposition of $NO_x$ is compensated regionally by reductions in HONO outside of metropolitan areas. Subgrid dry deposition of HONO constitutes about half of the dry deposition flux of HONO over eastern N.A. in simulation S4 (Table 4.2). Moderate to large peaks in early morning/evening HONO emerge in simulation S4 for some urban centers (Figs. 4.10–11)—the product of elevated $NO_x$ emissions persisting through periods of diabatic stability when subgrid dry deposition has greatest effect (Fig. S4.10). For the urban centers included in Fig. 4.10, monthly mean nocturnal concentrations of HONO are in the range of 0.5–2 ppb for simulation S4, yielding $HONO/NO_2$ ratios on the order of 5–10% (Fig. S4.21). The $HONO/NO_2$ ratio, as well as $NO_2$ normalized HONO production rates, are commonly reported indices used to indicate the extent/efficiency of heterogenous $NO_2$ conversion to HONO assuming reaction R4.1 is first order in $NO_2$. Primary emission of HONO from fuel combustion is often characterized by a $HONO/NO_x$ emission ratio of 0.8% (Kurtenbach et al., 2001; Meng et al., 2020)—

much lower than typical nocturnal HONO/$NO_2$ ratios observed in the field, indicating that ambient HONO is mostly formed through secondary reaction, although interpretation may be confounded by other processes such as reactions involving $NO_2$ (i.e., $N_2O_5$ formation) (VandenBoer et al., 2013) and bidirectional surface exchange of HONO (Spicer et al., 1993; Wojtal et al., 2011). Nonetheless, nocturnal HONO/$NO_2$ ratios for developed environments are generally in the range of 2–13% (Lammel and Cape, 1996), and often correlated with humidity up to a RH of ca. 70–90% (Li et al., 2012; Meng et al., 2020; Qin et al., 2009; Stutz et al., 2004; Yu et al., 2009). Less frequently, larger urban nocturnal HONO/$NO_2$ ratios have been observed. Yu et al. (2009) report campaign-mean values (January–February 2003, Kathmandu, Nepal, 5–15°C, RH > 60%) increasing from ca. 5% at sunset to ca. 15% early morning, with a maximum ratio of 30%. Qin et al. (2009) report campaign-mean values (July 2006, Guanggzhou City, South China, > 25°C, RH > 50%) increasing from ca. 7% at sunset to ca. 18% before sunrise, with a maximum ratio of 37%. From the WINTER data presented in Fig. 4.6, we find a nocturnal mean value of HONO/$NO_2$ of ca. 7% below 1 km, increasing to 10% near-surface (<120 m)—similar to the nocturnal mean value of HONO/$NO_2$ over northeastern (eastern) N.A. for January of 10% (9%) in both simulations S3 and S4 (Fig. S4.21). Simulated mean values of near-surface nocturnal HONO/$NO_2$ coincidently-sampled with WINTER data presented in Fig. 4.6 increase from 2.6% in base simulation S1 to: 6.9% (S3), 6.4% (S4), 9.6% (S5.1), and 8% (S5.2). From the WINTER data presented in Fig. S4.15, where flights contributing to an unresolved local maximum in nocturnal HONO at ca. 650 m have been removed, we find a nocturnal mean value of HONO/$NO_2$ of 4.0% below 1 km, increasing to 6.0% near-surface (<120 m). Coincidently-sampled simulated near-surface values increase from 2.9% in base simulation S1 to: 5.0% (S3), 5.7% (S4), 9.2% (S5.1), and 7.1% (S5.2).

Large seasonality in photochemically produced oxidants $O_3$ and OH is readily apparent in Fig. 4.9, with daytime concentrations over eastern N.A. larger by a factor of 2 and 5, respectively, for July over January. Due to increased solar radiation and water vapour concentrations, the rates of many photochemical processes are elevated in summer months (Kleinman, 1991), as is also reflected in the wintertime meridional gradient in OH over North America seen in Fig. 4.9. Outside of metropolitan areas, a seasonal transition from $NO_x$-limited to $NO_x$-saturated $O_3$ production occurs in September over the eastern

U.S. due to large reductions in emission of biological volatile organic compounds (BVOVs) such as isoprene (Jacob et al., 1995). Wintertime spatial distributions reflect a pattern of low $O_3$ in areas with reduced photochemical production of $HO_x$ (reduced solar radiation and humidity), decreasing with elevated $NO_x$ concentrations due to further $NO_x$-driven reductions in $HO_x$, i.e., $HNO_3$ formation. Widespread reductions in anthropogenic emissions of $NO_x$ across North America over the past two decades have resulted in a well-documented heterogeneous pattern of change in ground-level $O_3$ which reflects the spatiotemporal variation in $O_3$ production regimes, and includes: (i) increasing $O_3$ at night, in urban centers, and winter months due to reduced $O_3$ titration and (ii) decreasing daytime $O_3$ during summer months outside of urban centers (Jin et al., 2020; Simon et al., 2015). The small (< 5%) changes in daytime surface $O_3$ over the U.S. and Canada between simulations S2 and S4 depicted in Fig. 4.9 fit this qualitative description of $NO_x$ reductions in spatiotemporally varying chemical regimes. Travis et al. (2016) address a high summertime bias in GEOS-Chem simulated $O_3$ over the southeast U.S. by reducing anthropogenic surface $NO_x$ emissions by a factor of 2, affecting a much larger reduction in daytime surface $O_3$ than seen in simulation S4. Furthermore, the small summertime reductions in surface $O_3$ across eastern N.A. of less than 2% between simulations S2 and S4 are more than countered by increases in surface $O_3$ between simulations S1 and S2 (Fig. S4.19). Increased resistance to stomatal uptake in simulation S2 due to correction of a low bias in the calculation of molecular diffusivity reduces daytime $V_d(O_3)$, affecting a 4% increase in daytime surface $O_3$ over summertime eastern N.A. As seen in Fig. 4.11, much larger increases in morning, evening, and nocturnal surface $O_3$ on the order of 10%–20% occur in urban areas and correlate to reductions in simulated surface $NO_x$ concentrations, presumably due to reduced titration (Yan et al., 2018), thus highlighting the importance of future work which will include simulated surface $O_3$ concentrations in estimates of subgrid dry deposition of surface emitted $NO_x$. The introduction of additional sources of HONO (and therefore OH) in simulations S3 and S4 would also be expected to contribute to $O_3$ increase, especially in wintertime conditions (Aumont et al., 2003).

Simulated peak daytime OH concentrations depicted in Figs. 4.9–10 are mostly within the range observed at various large cities, including 3–10 x $10^6$ molecules $cm^{-3}$ for summer campaigns and 1–2 x $10^6$ molecules $cm^{-3}$ for winter campaigns (Kanaya et al.,

2007). Kim et al. (2014) report measured noontime (11 A.M.–1 P.M. LST) mean OH concentrations of 2.7 x $10^6$ molecules $cm^{-3}$ at the former BAO site (ca. 33 km north of Denver) for late February 2011, noting HONO photolysis as the dominant early morning net OH source and a significant daytime net source (second to $O_3$ photolysis). We find noontime (11 A.M.–1 P.M. LST) mean OH for January at this high elevation urban-influenced location of ca. 2.7 x $10^{-6}$ molecules $cm^{-3}$ for simulation S4, an 11% increase over simulation S2. Relative contributions of updates in simulations S3 and S4 to diel profiles of surface OH are reflected in Figs. 4.10–11. Over eastern N.A., simulation S3 is responsible for the notable increase in regional wintertime OH for morning hours, where effects peak shortly after sunrise and decay by noon. For summer, regional change in OH is negligible in simulations S3 and S4 despite large enhancements in nocturnal HONO. Relative contributions at urban locations are variable, with early morning peaks and daytime winter peak OH concentrations being affected predominantly, or comparably, by updates to either simulation. Although sharpest change in early morning/evening HONO and OH is noted for simulation S4 (Fig. 4.11), restraint is warranted in interpretation until surface $O_3$ is included in the parameterization of subgrid dry deposition of $NO_x$, as previously discussed.

Increases in simulated daytime OH depicted in Fig. 4.9 follow enhanced production of HONO for situations where $O_3$ photolysis is not the overwhelming source, such as for locations and times of low solar radiation and $O_3$ concentration. Slight reductions in daytime mean surface OH otherwise occur between simulations S2 and S4 concomitant to small reductions in surface $O_3$. Regional enhancements in daytime OH over wintertime northeast U.S. are on the order of 25%, with larger increases at urban centers, i.e., 45% for Chicago in January, decreasing to 4% in July (Fig. 4.10). Much larger increases in daytime winter OH are seen at higher latitudes, such as the industrial region of Alberta, with regional increases of over 100% and localized increase over 200% at urban and industrial centers such as Calgary (310% increase in Fig. 4.10), Edmonton, and the oil sands. At other urban locations depicted in Fig. 4.10, increases in daytime winter OH vary between 25% to 140%, and are accompanied by early morning spikes characteristic of photolysis of nocturnally accumulated HONO in moderate to high $NO_x$ environments (Aumont et al., 2003; Kanaya et al., 2007; Kim et al., 2014; Winer and Biermann, 1994). For July, when

peak daytime OH levels are larger than for January by a factor of 3 to 6, increases in daytime mean OH between simulations S2 and S4 are much lower, on the order of 4% to 20%. Despite this lower daytime summer change in OH, photolysis of nocturnally accumulated HONO remains the dominant early morning source of urban OH (Figs. 4.10–11) when production from other sources, i.e., photolysis of $O_3$ and formaldehyde, is low (Alicke et al., 2003; Winer and Biermann, 1994). The spatiotemporal patterns of change in daytime OH depicted in Figs. 4.9–11 corroborate the findings of Aumont et al. (2003) where it was found that the effect of additional sources of HONO (direct emission and heterogeneous production via $NO_2$ hydrolysis on aerosol and ground surfaces) caused box model simulated OH concentrations of typical northern midlatitude (45°N) urban and polluted rural atmospheres to increase from summer to winter, and from background to polluted conditions. Specifically, Aumont et al. (2003) show that these additional HONO sources have significant impact on early morning summertime OH concentrations, and major impacts persisting throughout the day during wintertime. Additionally, Aumont et al. (2003) note the nonlinear effect that additional sources of HONO have on OH production, finding that for wintertime urban conditions indirect production of OH resulting from additional HONO is about as large as direct production from HONO photolysis. To this effect, Jenkin et al. (2008) highlight the importance that photolysis of HONO has on secondary oxidant production, and the resulting influence on $NO_2$ oxidation, finding that under $NO_x$-saturated (-limited) conditions, a single HONO photolysis event leads to more (less) than one $NO_2$ to $HNO_3$ oxidation event.

Despite the widespread reductions in surface $NO_2$ concentrations depicted in Fig. 4.9, with generally corresponding reductions in TN, three developed areas stand out with increasing wintertime TN, namely, Calgary/Edmonton, Vancouver/Seattle, and Salt Lake City—all of which show substantial increase in daytime winter HONO and OH. As seen in Figs. 4.11 & S4.20, particularly large daytime increases in OH and TN are seen in simulation S4 for Seattle and Calgary, corroborating the findings of Aumont et al. (2003) that wintertime urban HONO can have a large impact on secondary chemistry at northern midlatitude locations. These daytime enhancements in TN are sufficient to counter nocturnal reductions (-3% for Seattle and -10% for Calgary), yielding the 24-hr increases seen in Fig. 4.9 at these locations (7% for Seattle and 10% for Calgary). Wintertime

nocturnal reductions in TN due to reduced $NO_x$ concentrations are seen across all urban and regional areas depicted in Fig. 4.11 for simulations S3 and S4 despite varying degrees of reduced nocturnal $O_3$ titration in simulation S4. The small increase in nocturnal TN for summertime Seattle (3%), despite reductions in surface $NO_x$, may be due to reduced nocturnal $O_3$ titration in simulation S4, an artifact of the assumption of a constant $O_3$ concentration of ca. 40 ppb for the purpose of NO to $NO_2$ conversion in subgrid dry deposition applied to $NO_x$ emissions. It is hypothesized that a more realistic treatment of NO to $NO_2$ oxidation of surface emissions, including resulting mass balance of simulated $O_3$, would buffer the large morning/evening spikes in HONO and OH depicted for simulation S4 in Figs. 4.10–11, however, the summertime early morning spikes in OH and TN seen at all urban and regional locations due to the enhanced nocturnal build-up of HONO would be expected to persist to an appreciable degree, as demonstrated in simulation S3 which has negligible effect on surface $O_3$ concentrations.

The notable reduction in wintertime TN of 10–15% throughout the Canadian prairies and northern U.S. Midwest depicted in Fig. 4.9 is a partial explanation of the high bias in previous satellite-derived $PM_{2.5}$ noted by van Donkelaar et al. (2015a) for this region, where particulate nitrate was found to be the dominant contributor to a predicted bias. Representing a pathway for wintertime $NO_2$ dry deposition via heterogeneous hydrolysis on ground surfaces in simulation S3 results in a wintertime reduction in TN for this region on the order of 5–10%, with further reductions from simulation S4 < 5% (data not shown). The July reduction in TN over eastern N.A. of ca. 6%, with local reductions across the southeast U.S. of more than 10% (Fig. 4.9), is due primarily to updates in simulation S4, and concomitant with reductions in surface $NO_x$ concentrations. As with $O_3$, notable increase in TN in simulation S2 (Fig. S4.19) results from updates to the calculation of molecular diffusivity, which unlike for $O_3$ has predominant effect on $V_d(HNO_3)$ via increased $R_b(HNO_3)$ as opposed to resistance to stomatal uptake, as $HNO_3$ has a nominally small resistance to surface uptake, i.e., $R_c(HNO_3) = 1$ cm $s^{-1}$. Due to $V_d(pNO_3) << V_d(HNO_3)$, largest seasonal enhancements in TN for simulation S2 (> 20%) occur over summertime forested regions (data not shown), when warmer temperatures favor $HNO_3$ partitioning, i.e., larger $HNO_3$ / TN ratios, and $R_b(HNO_3)$ contributes a larger fraction of total resistance due to reduced $R_a$ over high roughness surfaces such as forests

(Fig. S4.2). The small decrease in surface HONO concentrations of 5–10%, and even smaller reductions in surface $NO_2$ (<3%), depicted in Fig. S4.19 for simulation S2 result from the inclusion of wet and dry deposition of HONO in addition to updates to molecular diffusivity. The small feedback on $NO_2$ results from HONO formation pathways in the base simulation, i.e., reactions R4.1 (on aerosol) and R4.2.

As previously mentioned, wintertime surface OH over the northeastern U.S. (35°–45°N, 65°–90° W) is increased by ca. 25% in simulation S4 over simulation S2, predominantly due to updates in simulation S3, as depicted in Figs. 4.10 & S4.19. This significant increase in OH due to inclusion of additional sources of HONO is similar to the 20% increase in OH noted by Jaeglé et al. (2018) over this wintertime region resulting from a 5-fold increase in formaldehyde (HCHO) emissions required to improve GEOS-Chem simulated HCHO with both aircraft (WINTER campaign) and surface observations. In a detailed GEOS-Chem analysis of wintertime oxidation pathways influencing secondary inorganic aerosol (SIA) formation over the northeast U.S., Shah et al. (2018) note a weak response in SIA concentrations (< 4%) to the factor of 5 increase in HCHO emissions from Jaeglé et al. (2018). Shah et al. (2018) attributes the low sensitivities in wintertime SIA components ($pSO_4$ and $pNO_3$) with primary sources of $HO_x$ to the various pathways contributing to $SO_2$ and $NO_2$ oxidation, noting that only 35% (36%) of $pSO_4$ ($HNO_3$) formation occurs via direct OH oxidation of $SO_2$ ($NO_2$). We find that the additional HONO sources included in simulations S3 and S4 increase $pSO_4$ concentrations over S2 values for the wintertime northeast U.S. by ca. 5% and 6%, respectively, with negligible change for summertime when $pSO_4$ concentrations are more than a factor of 2 larger (Fig. S4.20) and change in regional OH is small.

## 4.7 Conclusions

Several serial updates pertaining mostly to trace gas dry deposition were implemented into the GOES-Chem CTM. Results were discussed in the context of a high resolution nested North American simulation for the year 2013, and relevant updates evaluated against HONO observations from the WINTER aircraft campaign which took place over the

northeastern U.S. from February to mid-March 2015. Implemented updates recommended from Chapter 3 of this thesis include:

1. Correction of a high bias in the calculation of molecular diffusivity (simulation S2), which decreased deposition velocities for species that: (i) dry deposit with negligible surface resistance, i.e., $HNO_3$ where a 10–20% decrease in annual mean $V_d(HNO_3)$ affecting a 5–15% increase in surface TN concentrations were observed and (ii) those that deposit under stomatal control, i.e., $NO_2$ and $O_3$, where annual mean surface $O_3$ increased by up to 4%.

2. Addressing a low bias in nocturnal $V_d(NO_2)$ by representing $NO_2$ heterogenous hydrolysis (reaction R4.1) on ground surfaces in simulation S3, providing a non-stomatal pathway for $NO_2$ uptake when deposition would otherwise be near-negligible, i.e., at night and during vegetatively senescent periods. Resulting increases in $NO_2$ dry deposition drive a 4% increase in total (wet + dry) $NO_y$ deposition over wintertime eastern North America (< 1% for summer), with increases of up to 100% over wintertime Alberta. Importantly, the heterogeneous hydrolysis of $NO_2$—a disproportionation reaction yielding adsorbed $HNO_3$ and evolved HONO—represented as a dry deposition process, provides mechanistic utility to nocturnal HONO formation and resulted in large increases in near-surface HONO of over 100%, making important contributions to reducing a low bias to observations from the WINTER aircraft campaign.

In addition to the updates recommended from Chapter 3, this chapter develops and implements into GEOS-Chem a simple method to reconcile subgrid dry deposition of near-surface emitted species that have chemical lifetimes much greater than the timescale for turbulent vertical mixing within the lowest model—ca. 12 minutes during the day and < 1 hour at night. We apply our method of subgrid dry deposition to near-surface anthropogenic emissions of $NO_x$ and nocturnal HONO in simulation S4, however, note that species with surface resistances below ca. $10^3$ s $m^{-1}$ should also be considered for subgrid dry deposition in large scale CTMs. Effective reductions in 24-hr mean anthropogenic near-surface emissions of NOx range from 3–15%, with seasonality patterning aerodynamic resistance ($R_a$). Accordingly, significant diel variation exists in effective reductions of $NO_x$ emission, with nocturnal reductions in the range of 10–20% and daytime

reductions near-negligible outside of high latitudes during winter months. The effective reduction over summertime southeastern U.S. of 8% is much lower than the 60% reduction required by Travis et al. (2016) to reconcile GEOS-Chem simulated fields with a suite of aircraft- and surface-based observations. Future work will include updating the calculation of the canopy reduction factor (CRF) used for soil $NO_x$ emission in GEOS-Chem to include reaction R4.1 on canopy surfaces, which is expected to further alleviate the proposed high summertime bias for surface $NO_x$ emissions in the EPA's NEI 2011 inventory.

Large increases in $NO_y$ total deposition at urban centers, driven predominantly by subgrid dry deposition, are on the order of 23–100% for summertime and a factor of 2–3 for wintertime. The regional export of $NO_y$ out of the U.S. and Canada is reduced from 29% (S1) to 21% (S4) for winter, and from 7% (S1) to 2% (S4) for summer, with total annual $NO_2$ dry deposition increasing from 5% of $NO_x$ emitted in simulation S2, to 7% (S3), to 9% (S4). Contributions of $NO_2$ to 24-hr $NO_y$ dry deposition over urban centers increase from 38% (S2), to 51% (S3), to 60% (S4).

The effect of updates in simulations S3 and S4 on daytime $O_3$ is small (< 5% decrease), and largely countered by updates in simulation S2 (< 4% increase). Increases in nocturnal urban $O_3$ on the order of 10–20% in simulation S4 highlight the importance of future work to include simulated surface $O_3$ concentrations as an input parameter modulating the NO to $NO_2$ reaction time in the formulation of subgrid dry deposition of near-surface NO emissions.

Increased production of HONO in simulation S3 has a significant effect on wintertime surface OH concentrations, when reduced solar radiation and humidity limits OH production via $O_3$ photolysis. Large regional increases in daytime winter OH on the order of 25–100% are seen in simulation S3, with larger increases at northern midlatitude urban centers in simulation S4. Summertime increases in OH are more subdued owing to higher baseline concentrations, however, a characteristic early morning spike in OH due to nocturnal accumulation of HONO is an increasing feature in simulations S3 and S4. Notable secondary effects of increased wintertime OH include larger daytime TN concentrations at northern midlatitude urban centers of up to 60% despite reductions in $NO_x$ concentrations, and a small increase in wintertime $pSO_4$ of 6% over the Northeast U.S.

Regional reductions in wintertime TN on the order of 10–15% throughout the Canadian prairies and northern U.S. Midwest is a partial explanation of the high bias in previous satellite-derived $PM_{2.5}$ estimates noted by van Donkelaar et al. (2015a) for this region where particulate nitrate was found to be the dominant contributor to a predicted bias.

A large low bias in simulated daytime HONO remains in both the PBL and free troposphere. Several daytime sources of HONO are yet to be developed in GEOS-Chem, including $HNO_3$/nitrate photolysis, photoenhanced heterogeneous $NO_2$ reduction, and daytime release of nocturnally deposited HONO. Given the significance of atmospheric HONO as a near-surface source of OH, especially during periods of low solar radiation when production from other photolytic sources is reduced, future developments to GEOS-Chem in this area are recommended.

## 4.8 Supplemental Material

### 4.8.1 Monin-Obukhov (M-O) Stability-Correction/Universal Functions

Dimensionless flux-gradient relations $\phi(\zeta)$, also known as Monin-Obukhov (M-O) stability-correction/universal functions, are empirically determined functions of the dimensionless M-O stability parameter $\zeta = (z - d) / L$ where L is the M-O length (Monin and Obukhov, 1954) and therefore application constrained to the stability range over which observations were made. We update functional ($\phi_h$) and integral ($\Psi_h$) forms of the M-O flux-gradient relations for sensible heat used in the calculations of aerodynamic resistance and turbulent eddy diffusivity to those employed in the recent surface layer formulation of the Weather Research and Forecasting (WRF) model (Jiménez et al., 2012). Functional forms were selected based on applicability across a wide stability range, from the convective limit ($\zeta \to -\infty$), through neutral conditions ($\zeta \to 0$), to very stable conditions ($\zeta > 10$) where $\phi_h(\zeta)$ approaches a constant value of ca. 7 (Fig. s4.1). Updated functional forms for $\phi_h(\zeta)$ and $\Psi_h(\zeta)$, listed below for convenience, are described in Jiménez et al. (2012) which use the formulation by Grachev et al. (2000) for unstable conditions, and Cheng and Brutsaert (2005) for stable conditions. M-O universal functions used in the base

simulation S1 (equations 3.S3–7 in Chapter 3, section 3.6.1) are plotted alongside updated functions in Fig. S4.1.

**Unstable conditions ($\zeta < 0$)**

$$\phi_h = (1 - 34\zeta)^{-1/3} \tag{4.S1}$$

$$\Psi_h = \frac{\Psi_{K,h}(\zeta) + \zeta^2 \Psi_{C,h}(\zeta)}{1 + \zeta^2} \tag{4.S2}$$

where $\Psi_{K,h}(\zeta)$ is an integrated Kansas-type function (Paulson, 1970) from the base simulation (Chapter 3, equation 3.S4) which is weighted in 4.S2 towards near-neutral conditions, and $\Psi_{C,h}(\zeta)$ weighted towards convective conditions and taking the form

$$\Psi_{C,h} = \frac{3}{2} ln\left(\frac{y^2 + y + 1}{3}\right) - \sqrt{3}\, arctan\left(\frac{2y + 1}{\sqrt{3}}\right) + \frac{\pi}{3} \tag{4.S3}$$

where $y = (1 - 34\zeta)^{1/3}$

**Stable conditions ($\zeta > 0$)**

$$\phi_h = 1 + c\left(\frac{\zeta + \zeta^d(1 + \zeta^d)^{\frac{1-d}{d}}}{\zeta + (1 + \zeta^d)^{\frac{1}{d}}}\right) \tag{4.S4}$$

$$\Psi_h = -c\, ln\left\{\zeta + [1 + \zeta^d]^{\frac{1}{d}}\right\} \tag{4.S5}$$

where c = 5.3, and d = 1.1.

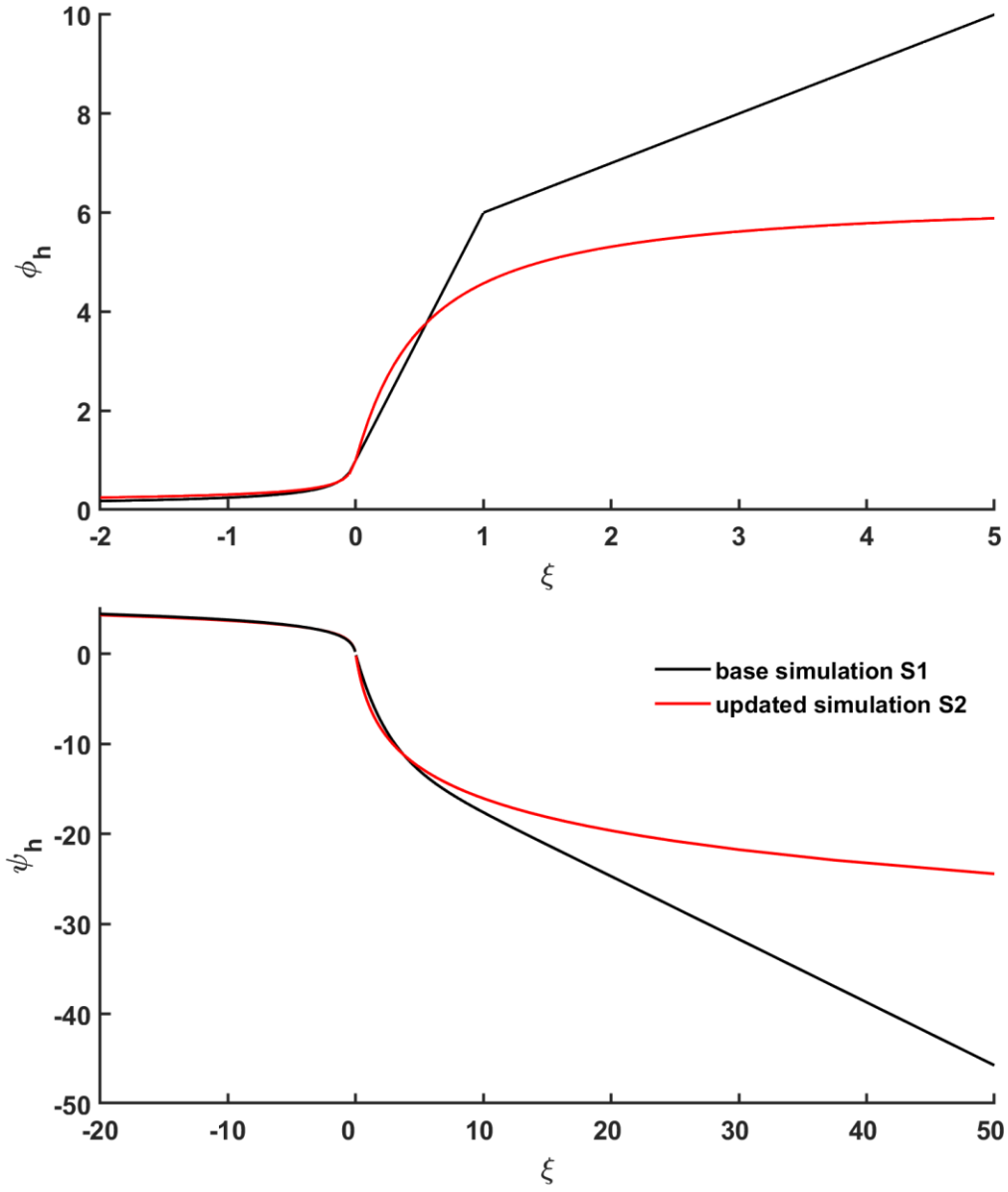


**Figure S4.1.** Dimensionless flux-gradient relations for sensible heat ($\phi_h$) and resulting integrated stability-correction functions ($\Psi_h$) which are a function of the dimensionless M-O stability parameter $\xi = (z - d) / L$. Depicted are functions following base GOES-Chem (Chapter 3, section 3.6, equations 3.S3–7), and an updated simulation S2 with functions used in WRF-Chem (equations 4.S1–5).

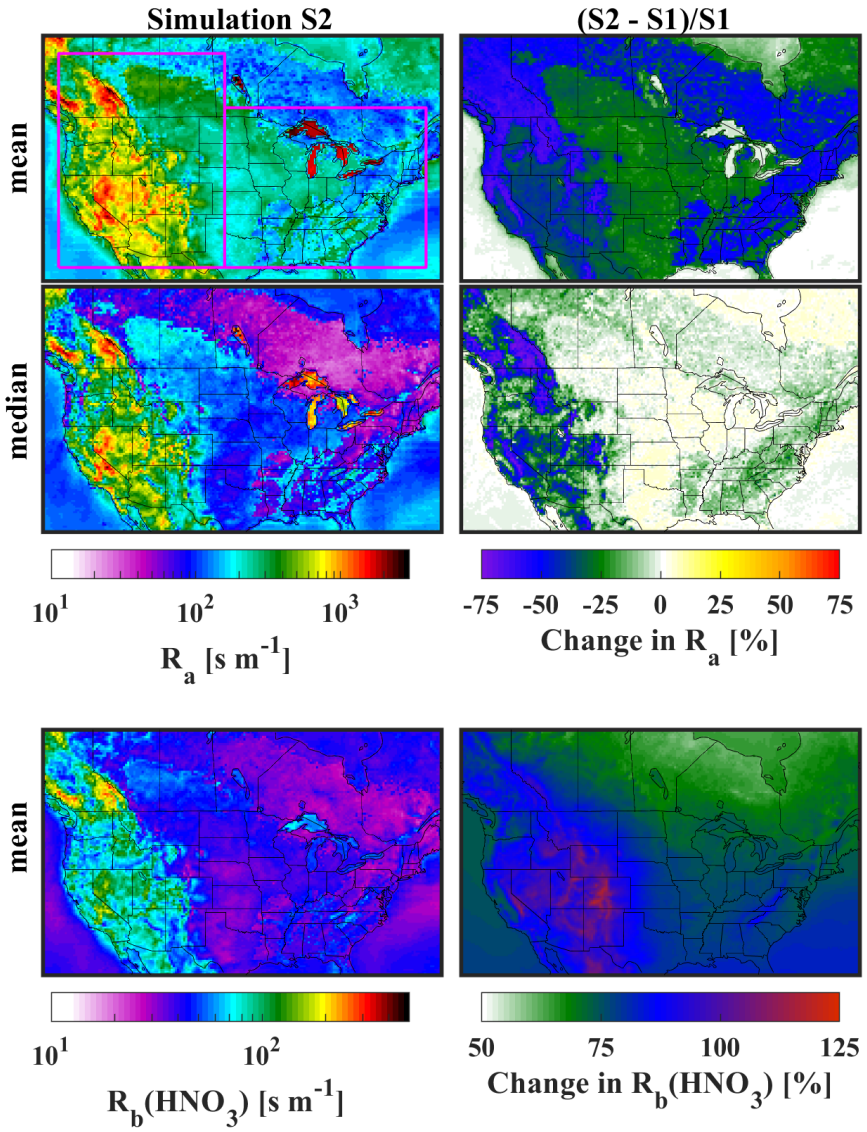


**Figure S4.2.** Annual (2013) mean and median aerodynamic resistance $R_a$ and mean laminar boundary layer resistance $R_b(HNO_3)$ for simulation S2 adjacent corresponding percent change from base simulations S1. Regions of eastern N.A. and western N.A. over which values are aggregated in Table S4.1 are indicated.

**Table S4.1:** Aerodynamic resistance $R_a$, nitric acid boundary layer resistance $R_b(HNO_3)$, and resulting deposition velocities $V_d(HNO_3)$ aggregated over the regions of eastern North America (ENA) and western North America (WNA) depicted in Fig. S4.2 from base simulation S1 and updated simulation S2 which includes serial updates to $R_a$ and molecular diffusivity $D_x$. Shown are annual (2013) means ± standard deviations alongside median values () for day (10–14 LST), night (0–4 LST), and 24-hr periods.

| GC Sim. | $R_a$ [s m$^{-1}$] | | | $R_b(HNO_3)$ [s m$^{-1}$] | | | $V_d(HNO_3)$ [cm s$^{-1}$] | | |
|---|---|---|---|---|---|---|---|---|---|
| | Day | Night | 24-hr | Day | Night | 24-hr | Day | Night | 24-hr |
| **ENA** | | | | | | | | | |
| S1 | 110±730 (25) | 500±1500 (92) | 360±810 (100) | 12±14 (9) | 28±50 (15) | 22±23 (15) | 3.5±2.2 (3.0) | 1.4±1.4 (1.0) | 2.1±1.4 (1.8) |
| S2($R_a$) | 110±720 (24) | 340±950 (95) | 260±640 (100) | " | " | " | 3.5±2.3 (3.0) | 1.4±1.4 (0.9) | 2.1±1.4 (1.7) |
| S2($D_x$) | " | " | " | 21±25 (16) | 50±88 (27) | 39±40 (27) | 2.8±1.7 (2.5) | 1.2±1.1 (0.9) | 1.8±1.1 (1.5) |
| **WNA** | | | | | | | | | |
| S1 | 76±430 (28) | 1600±2800 (270) | 920±1400 (260) | 13±21 (9) | 56±97 (27) | 37±46 (23) | 3.1±2.1 (2.6) | 0.8±1.1 (0.4) | 1.7±1.2 (1.3) |
| S2($R_a$) | 62±250 (29) | 860±1500 (260) | 510±710 (230) | " | " | " | 3.2±2.2 (2.6) | 0.8±1.1 (0.4) | 1.7±1.2 (1.3) |
| S2($D_x$) | " | " | " | 25±39 (18) | 100±180 (49) | 70±84 (44) | 2.5±1.6 (2.1) | 0.7±0.9 (0.4) | 1.4±0.9 (1.1) |

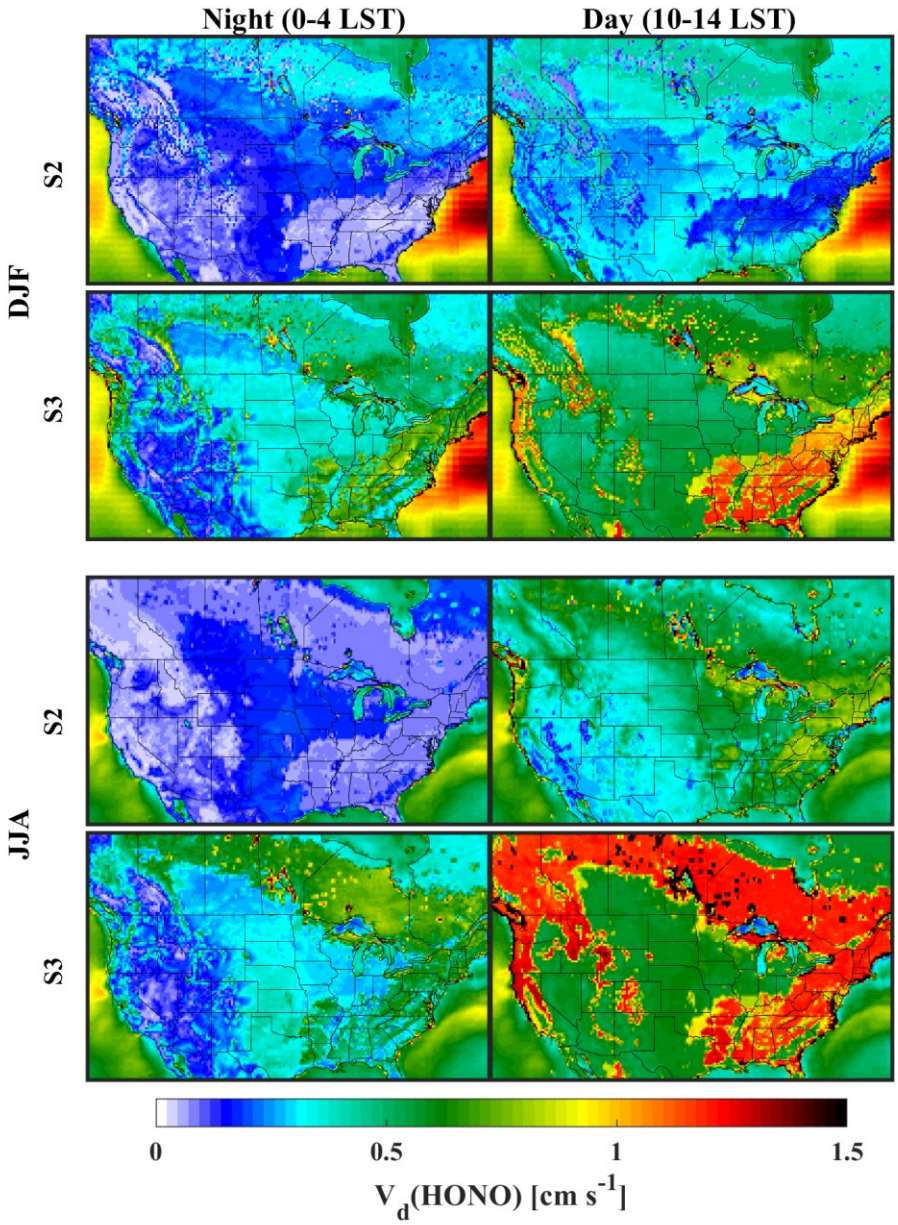


**Figure S4.3.** Dry deposition velocities for nitrous acid (HONO) from updated simulations S2 and S3. Depicted are winter (DJF) and summer (JJA) means for night and day periods.

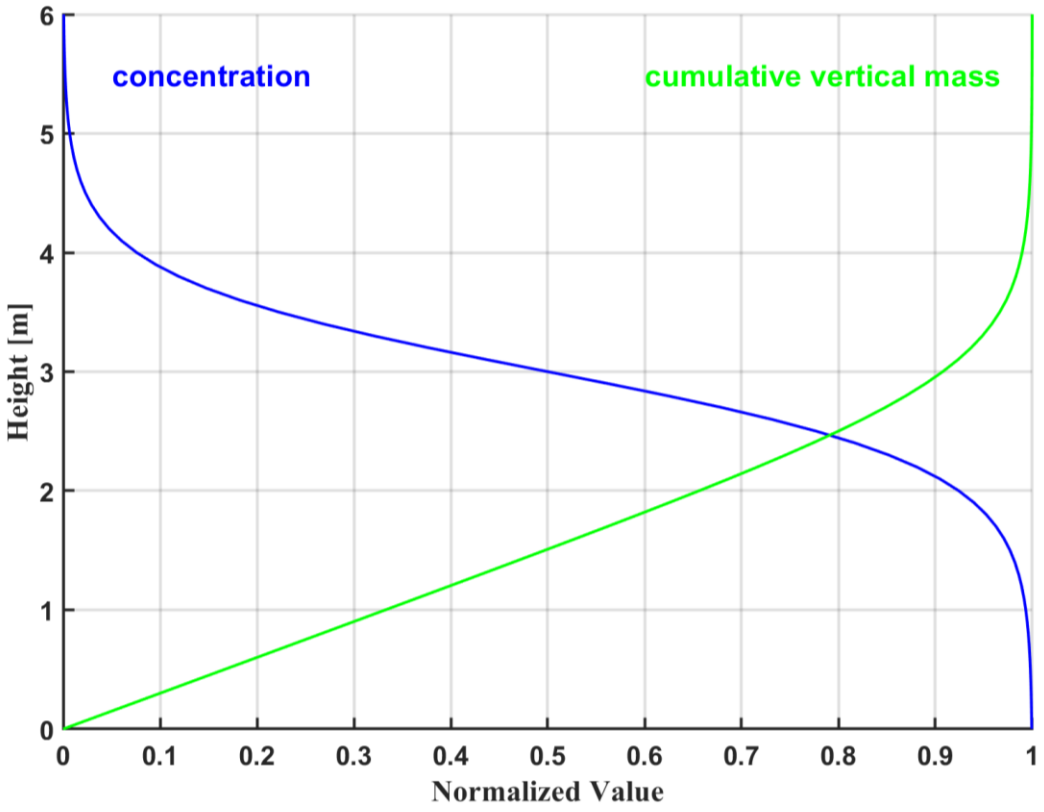


**Figure S4.4:** Arbitrary emission profile ($E_{pulse}$) designed to emulate the passage of a typical motor vehicle. $E_{pulse}$ at $t_o$ is discretized onto a finite volume vertical grid and evolved according to equation 4.6 through turbulent diffusion with a reflective top boundary condition at 120 m and dry deposition lower boundary condition (section 4.4.3.1).

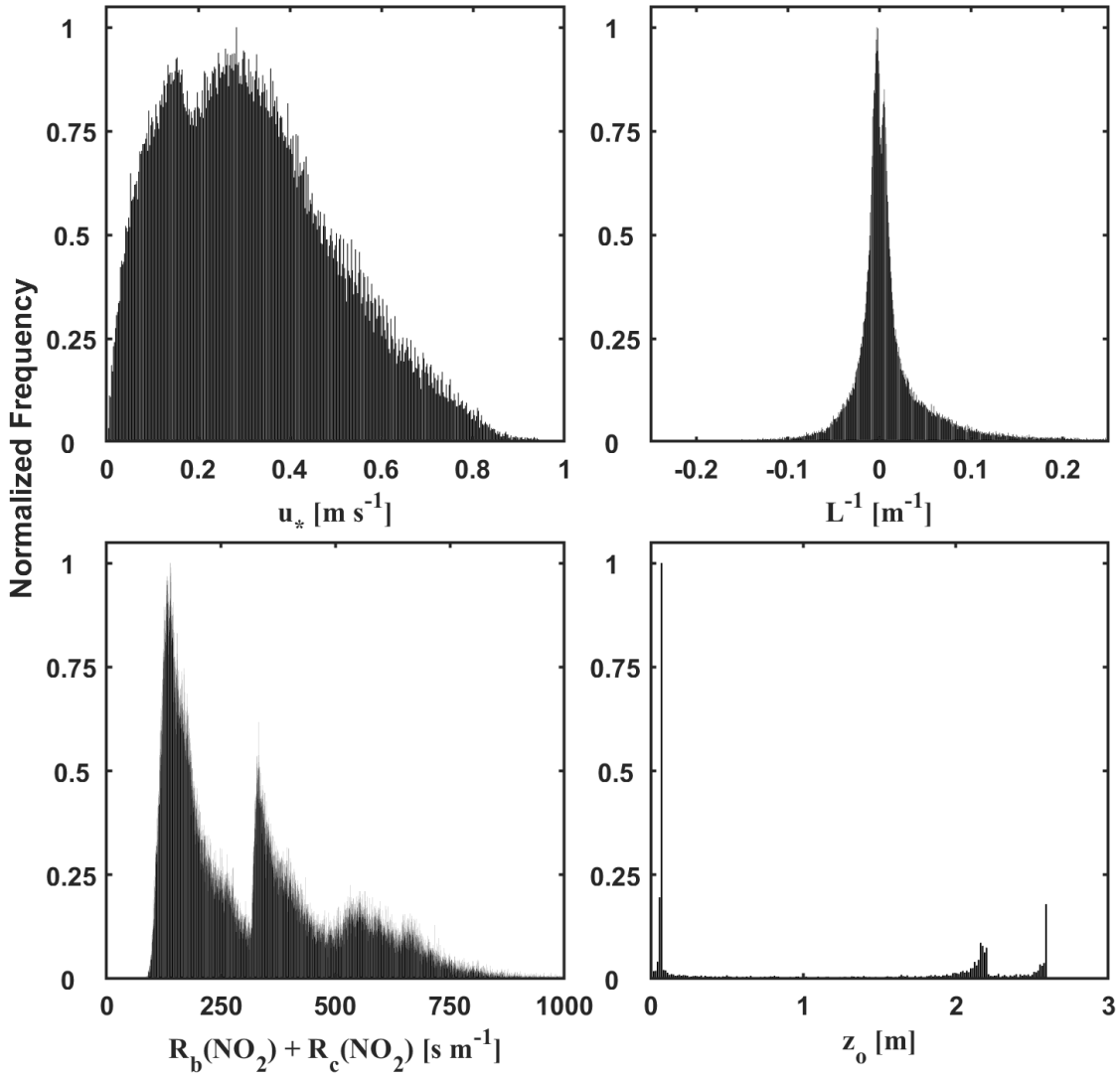


**Figure S4.5.** Histograms of input variables required for the parameterization of subgrid dry deposition of near surface $NO_x$ emissions in GEOS-Chem. Hourly values of *friction velocity* $u_*$, *inverse M-O length* $L^{-1}$, *and roughness length* $z_o$ over eastern North America (east of 100°W) are from GEOS-FP meteorological fields at horizontal resolution of 1/4° x 5/16°. Hourly values of $R_b(NO_2)$ and $R_c(NO_2)$ are output from the corresponding nested GEOS-Chem simulation S4. Hourly values are for 15 July 2013.

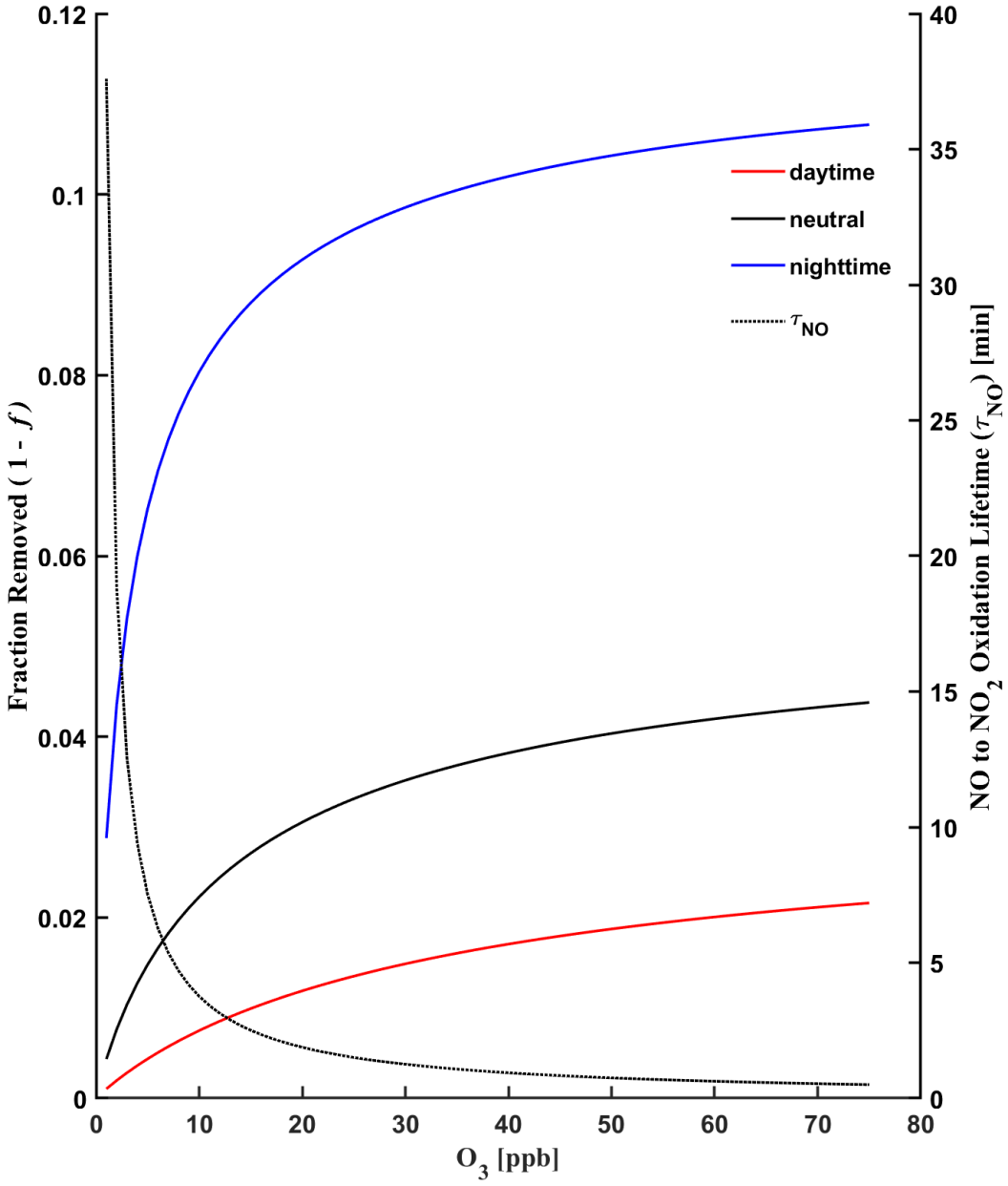


**Figure S4.6:** Sensitivity of subgrid dry deposition of surface emitted NO ($1 - f$) to $O_3$ concentrations under daytime ($u_* = 0.6$ m s$^{-1}$, $L^{-1} = -8.0 \times 10^{-3}$, $R_b + R_c = 250$ s m$^{-1}$), neutral ($u_* = 0.4$ m s$^{-1}$, $L^{-1} = 0$, $R_b + R_c = 300$ s m$^{-1}$), and nighttime ($u_* = 0.4$ m s$^{-1}$, $L^{-1} = 1.1 \times 10^{-2}$, $R_b + R_c = 380$ s m$^{-1}$) meteorological conditions over a moderately rough surface ($z_o = 0.6$ m). Also depicted are lifetimes of NO oxidation by $O_3$ ($\tau_{NO}$).

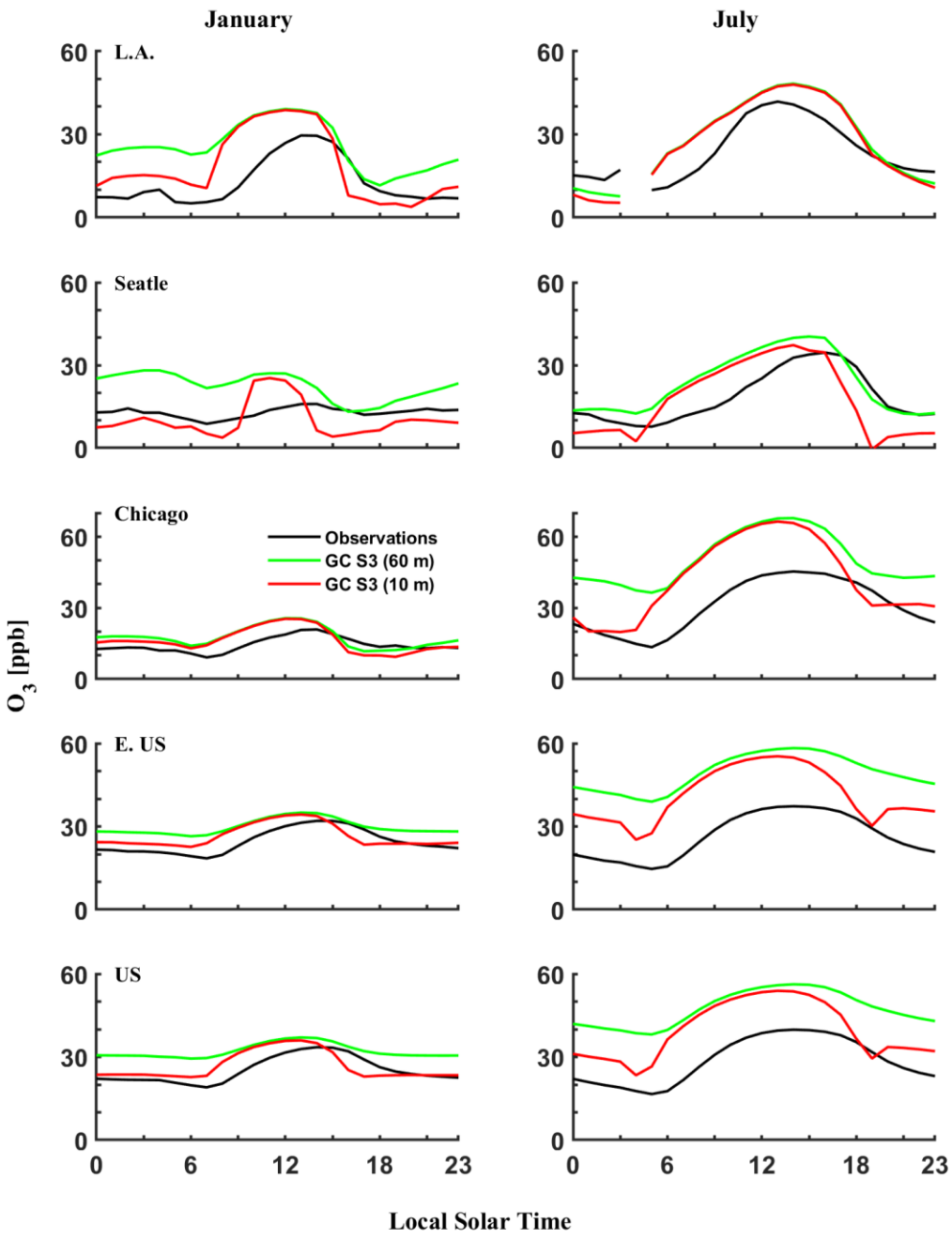


**Figure S4.7:** Observed and simulated (GC S3) surface $O_3$ at various urban locations and across the eastern and contiguous U.S. for January and July 2013. Simulated values coincidently sampled with observations are shown for the lowest model level centered at ca. 60 m and an implicit model concentration at the subgrid height of 10 m inferred from the resister-in-series parameterization of dry deposition (section 4.5.1).

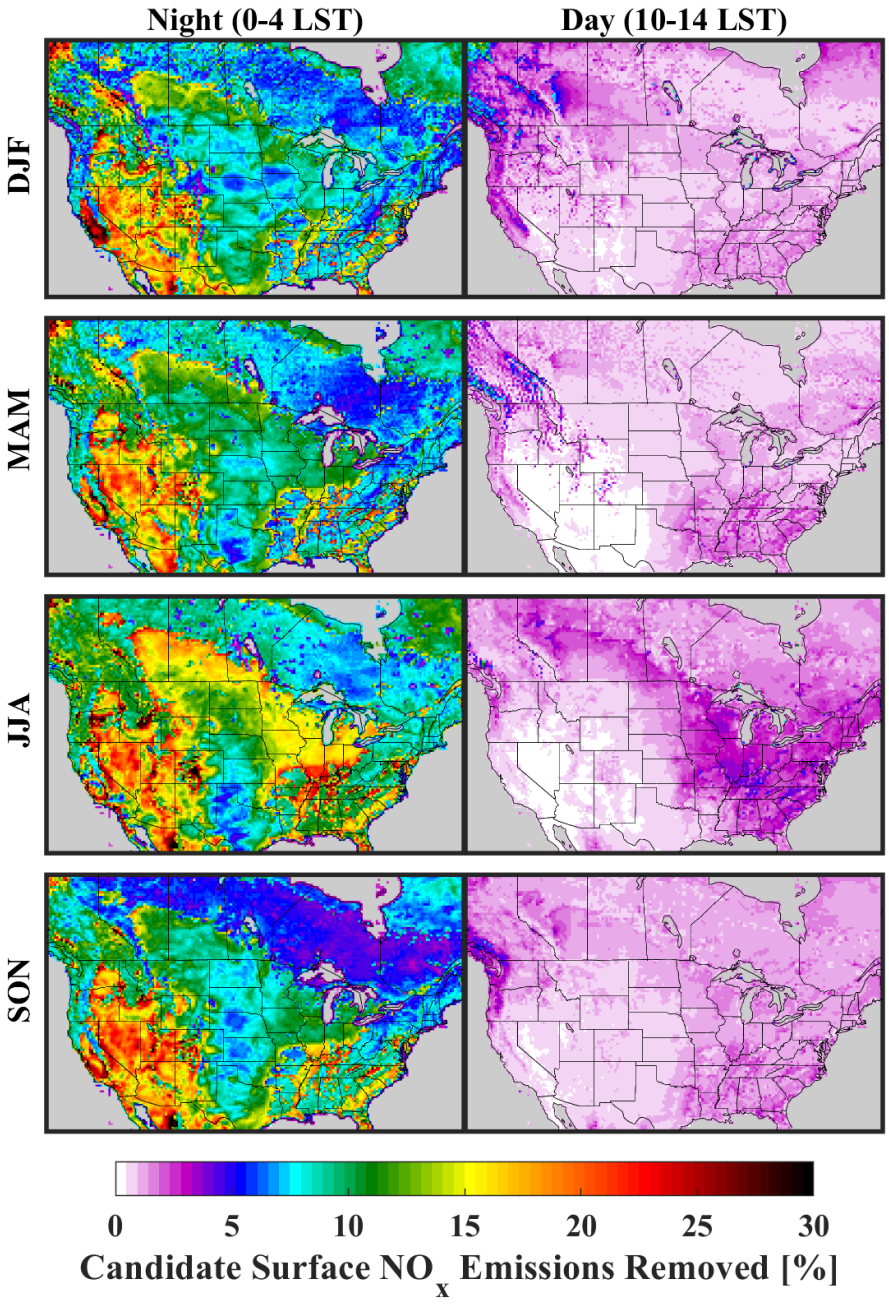


**Figure S4.8:** Candidate surface $NO_x$ emissions removed (anthropogenic, non-stack), depicted as $(1 - f) \times 100$, from implementation of our paramaterization of subgrid dry deposition via look-up-table values of $f$ into GEOS-Chem simulation S4. Shown are nighttime and daytime seasonal means for the year 2013. Note, 'candidate' assumes emissiosns are diurnally and seasonally constant.

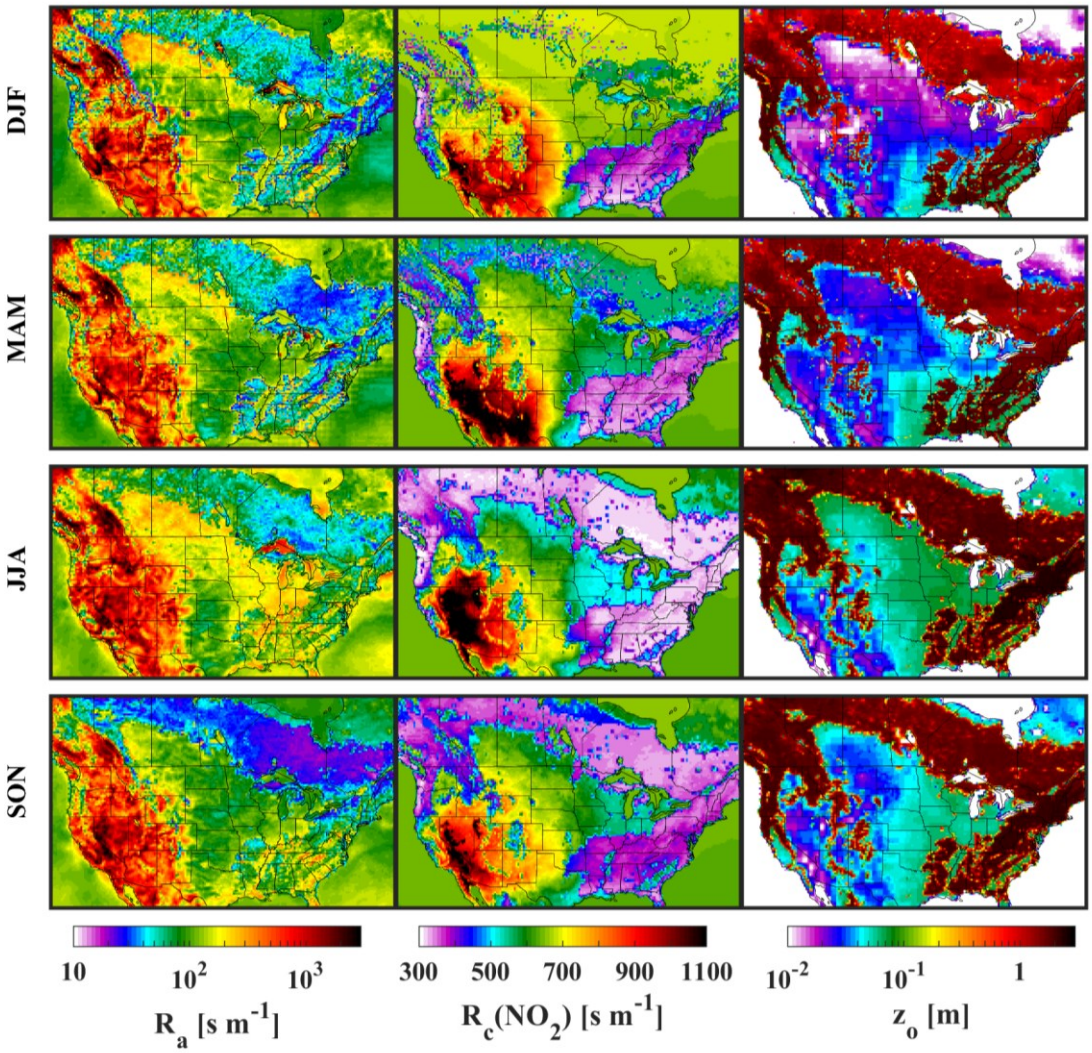


**Figure S4.9:** Nocturnal (0–4 LST) seasonal mean *aerodynamic resistance* $R_a$, bulk *surface resistance* to $NO_2$ uptake $R_c(NO_2)$, and *roughness length* $z_o$ from GEOS-Chem simulation S4.

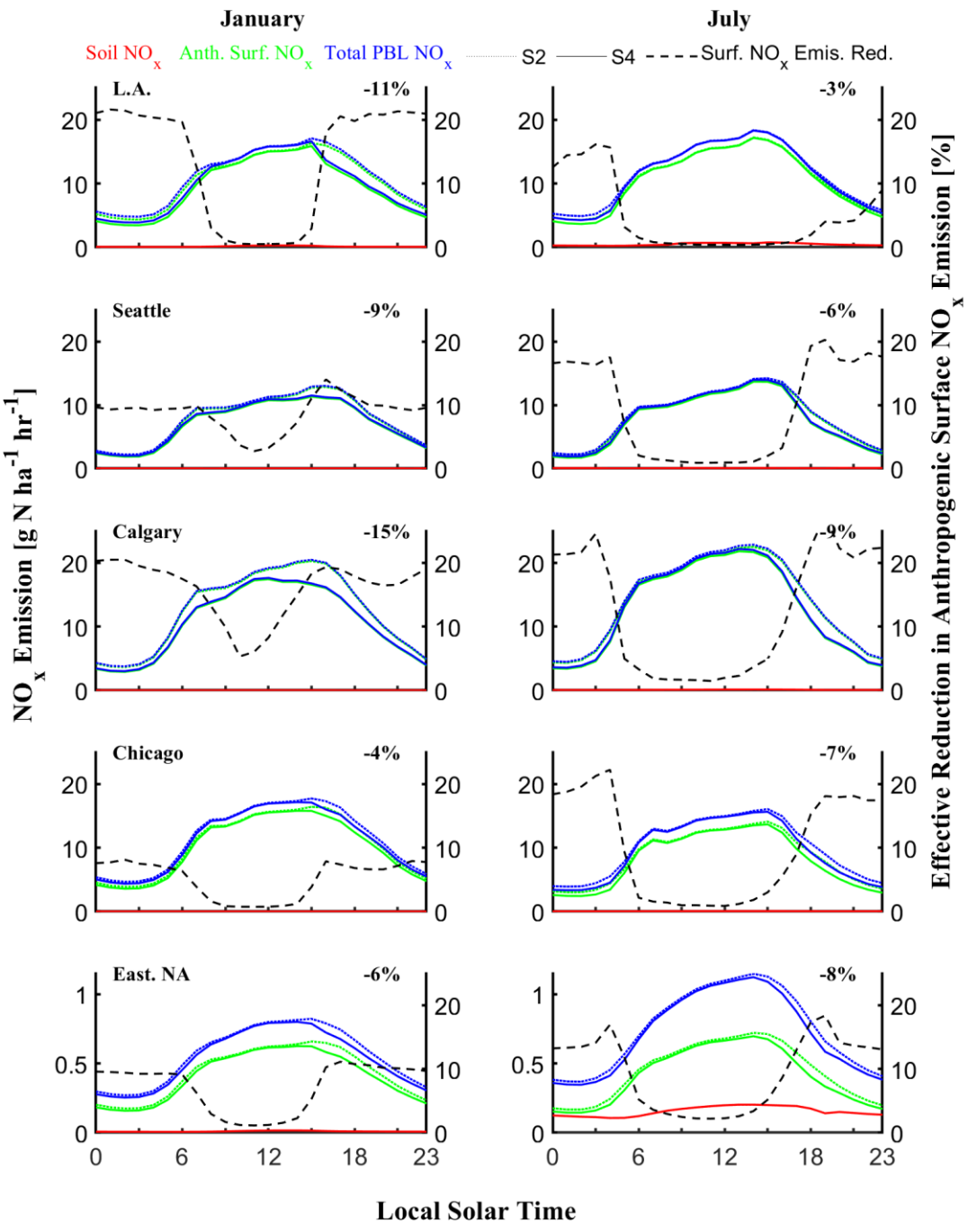


**Figure S4.10**: Diel profiles of monthly mean $NO_x$ emissions at select urban centers, and regionally across Eastern N.A. (over land), including soil $NO_x$, non-stack anthropogenic surface emissions (i.e., transportation, residential), and total $NO_x$ emitted into the PBL from natural (soil & fire) and all anthropogenic sources. Also depicted are hourly effective reductions in anthropogenic surface $NO_x$ emissions resulting from subgrid dry deposition (S4), with percent change in 24-hr anthropogenic surface emission for each location/region included as an inset.

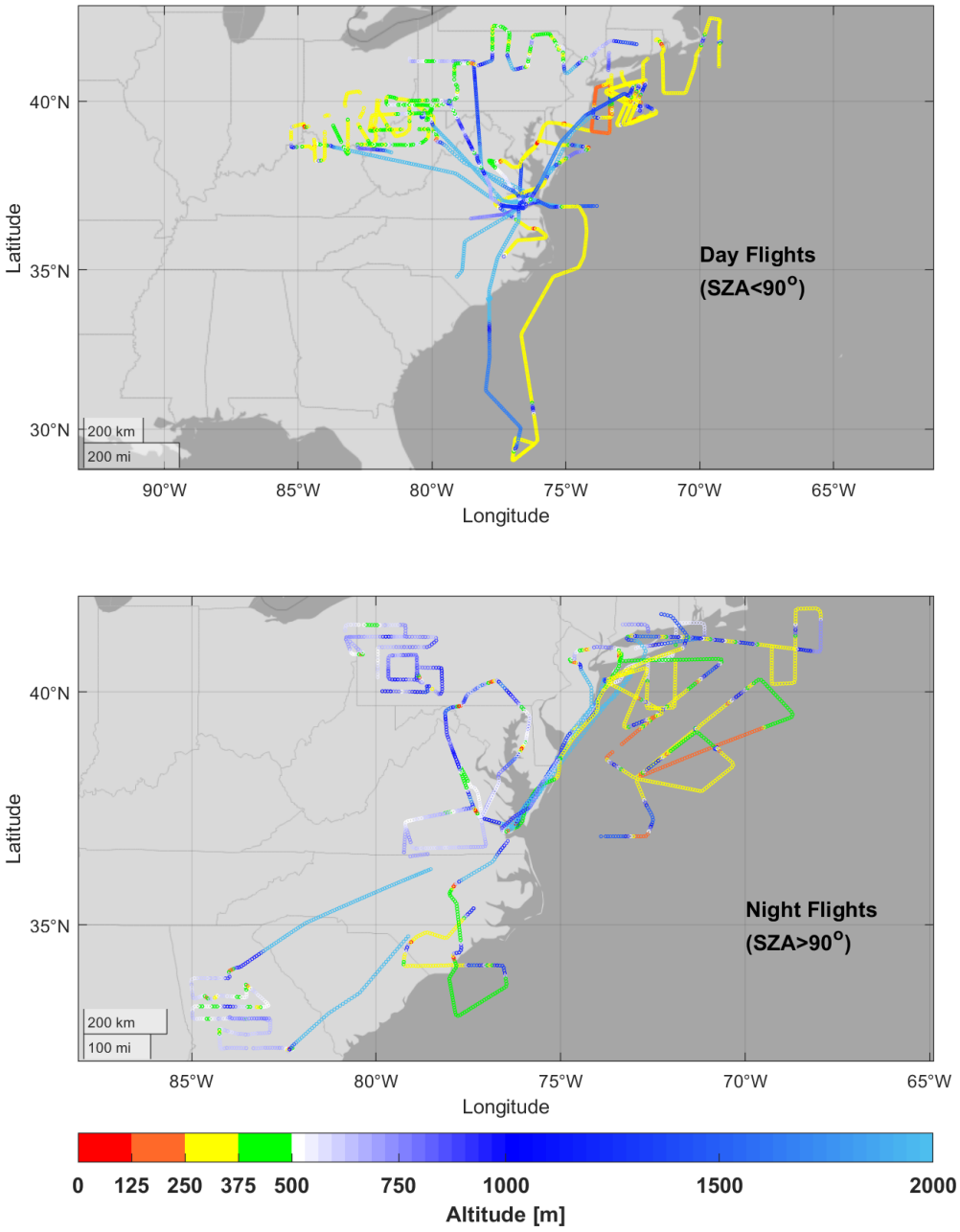


**Figure S4.11:** Altitude (above surface) of observations from the WINTER aircraft campain which consisted of 13 flgihts between 3 February–13 March 2015. Colorbar to 500 m is an approximate depiction of the lowest four GEOS-Chem levels. A maximum altitude of 2 km was set in the colorbar despite flight tracks occuring above this altitude. Campaign mean profiles of daytime and nocturnal $NO_x$ and HONO are depicted in Fig. S4.13.

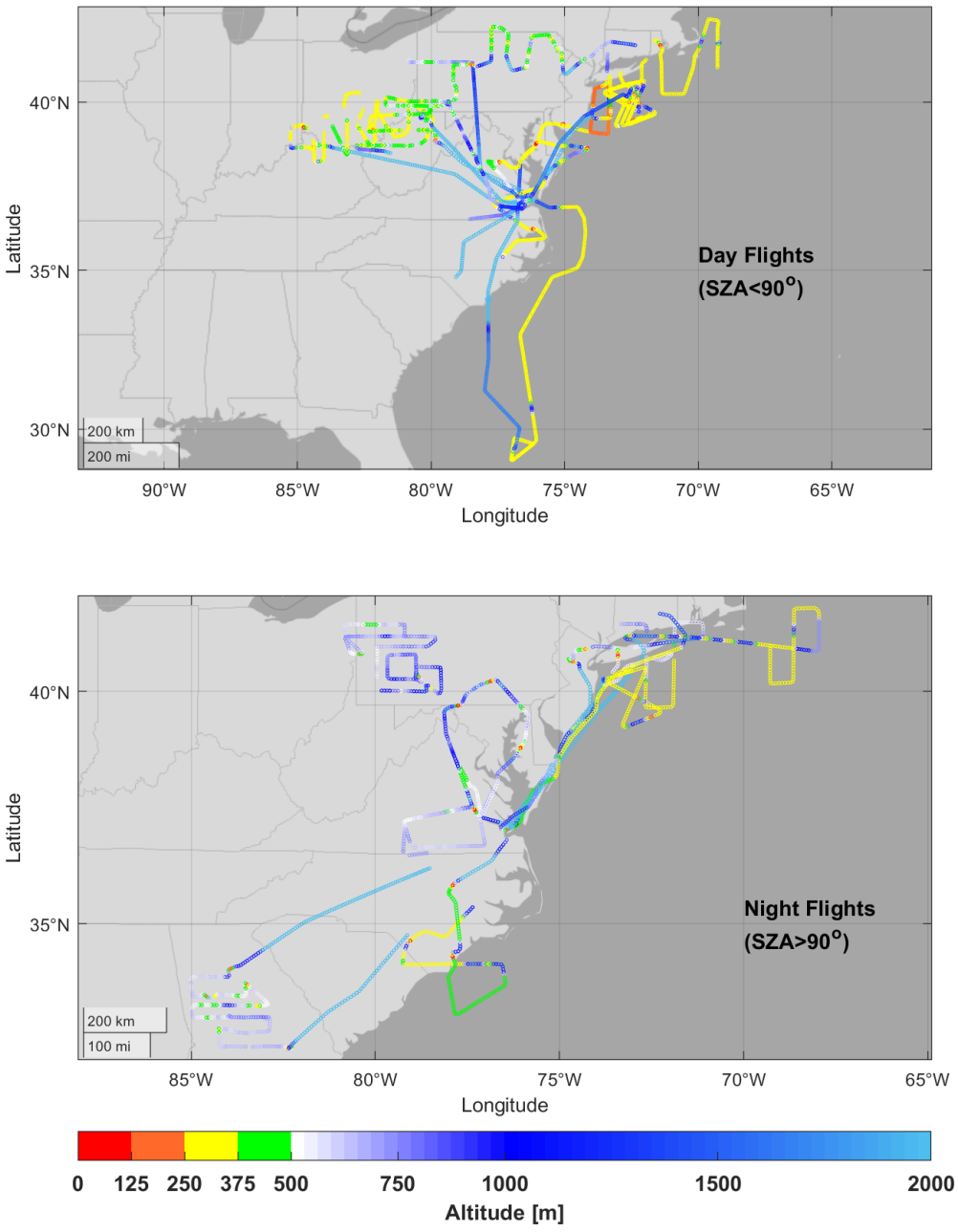


**Figure S4.12:** As Fig. S4.11, however, with flight track #9 (offshore, nocturnal, 22/23 February 2015) removed. Campaign mean profiles of daytime and nocturnal $NO_x$ and HONO are depicted in Fig. 4.6.

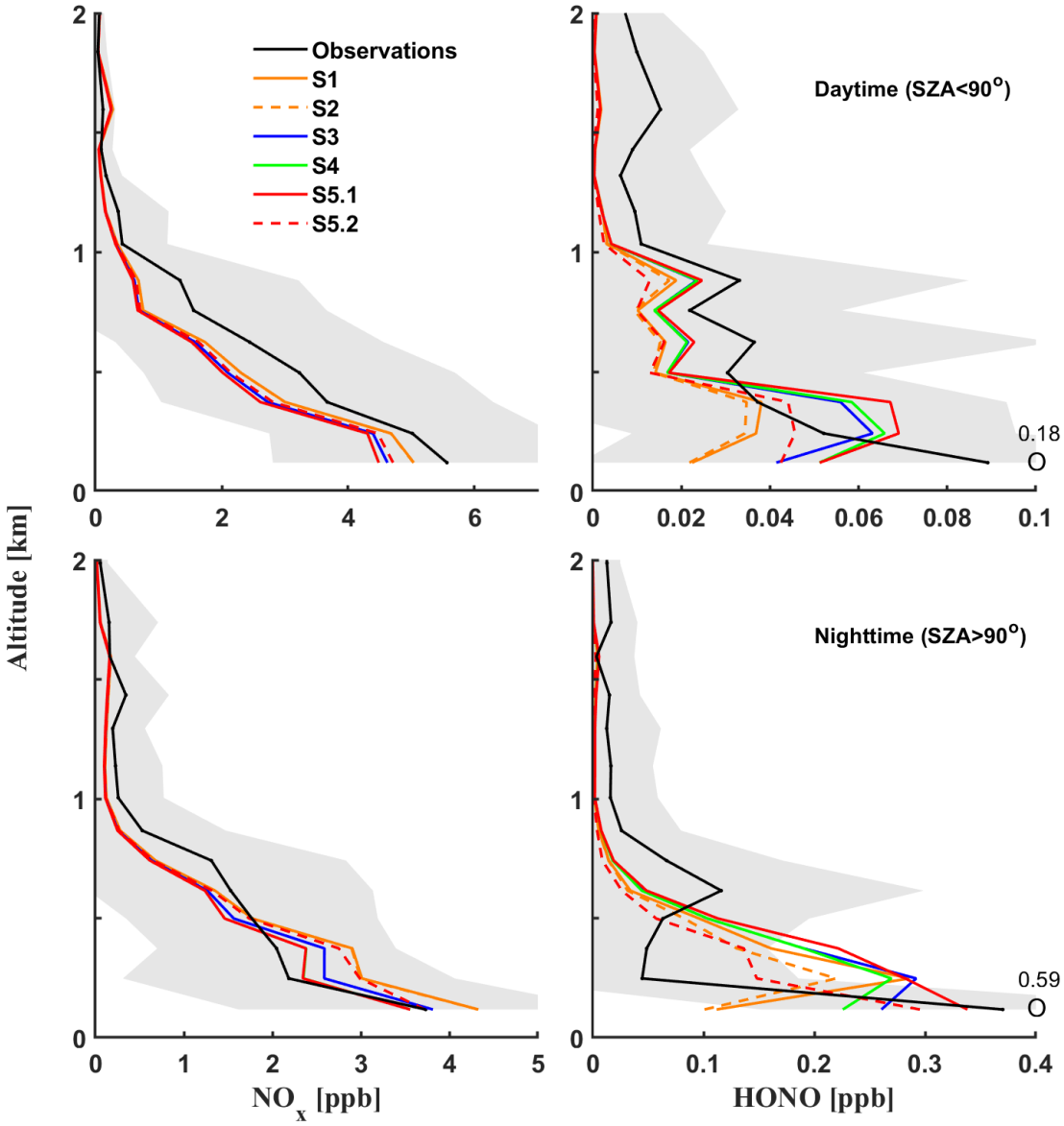


**Figure S4.13:** Vertical profiles of daytime and nocturnal mean $NO_x$ and HONO observed during the WINTER aircraft campaign (black line with grey shade indicating standard deviation) and simulated mean profiles coincidently sampled from base (S1) and updated (S2–S5) GEOS-Chem simulations.

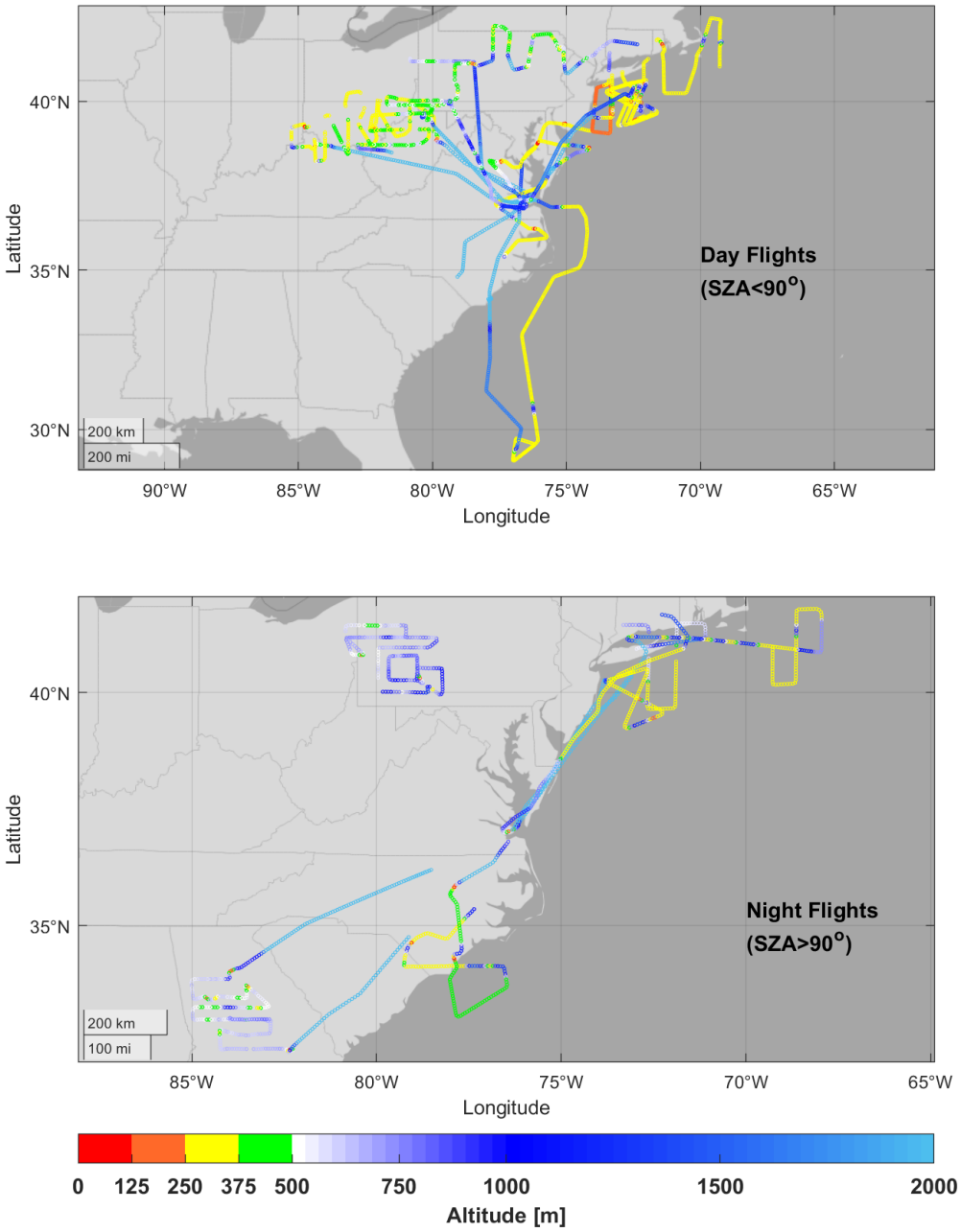


**Figure S4.14:** As Figure S4.11, however, with flight track numbers 8 (costal, nocturnal, 20 February 2015), 9 (offshore, nocturnal, 22/23 February 2015), and 10 (inland, nocturnal, 24 February 2015) removed. Resulting campaign mean profiles of daytime and nocturnal $NO_x$ and HONO are depicted in Fig. S4.15.

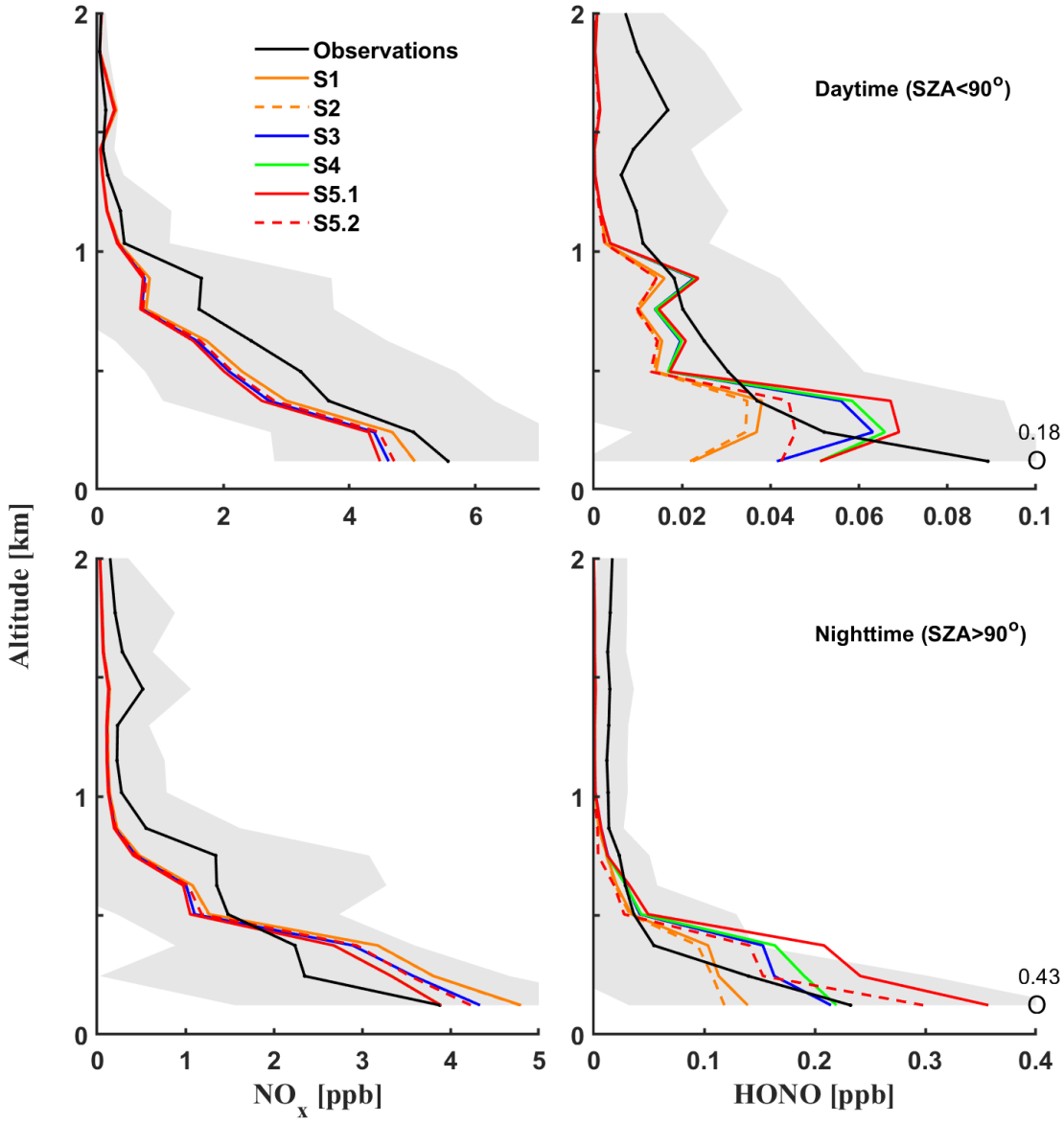


**Figure S4.15:** Vertical profiles of daytime and nocturnal mean $NO_x$ and HONO observed during the WINTER aircraft campaign (black line with grey shade indicating standard deviation) and simulated mean profiles coincidently sampled from base (S1) and updated (S2–S5) GEOS-Chem simulations. Flight numbers 8, 9, and 10 have been removed from analysis (see Fig. S4.14).

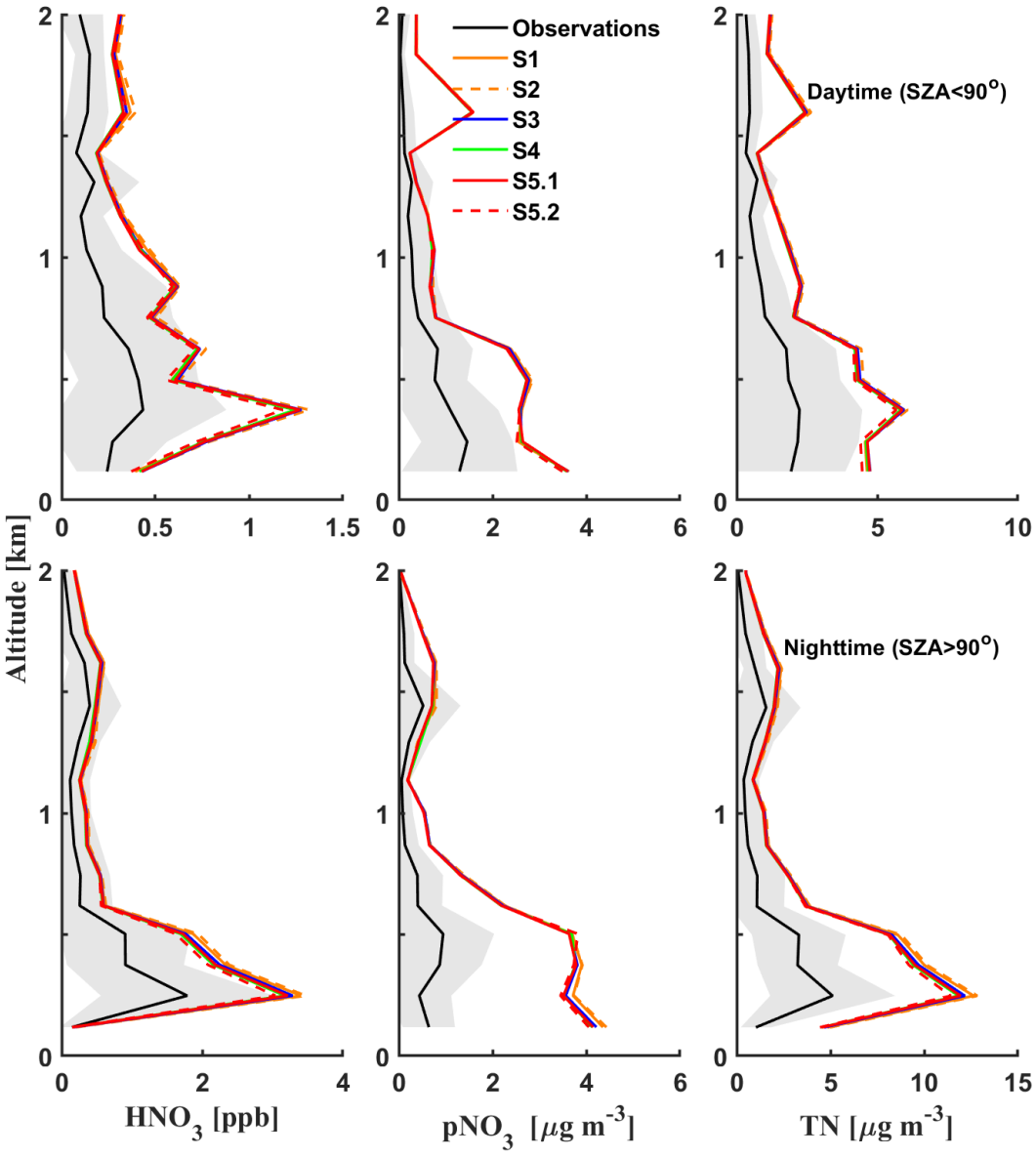


**Figure S4.16:** Vertical profiles of daytime and nocturnal mean $HNO_3$ and $pNO_3$ observed during the WINTER aircraft campaign (black line with grey shade indicating standard deviation) and simulated mean profiles coincidently sampled from base (S1) and updated (S2–S5) GEOS-Chem simulations. Also depicted is resulting total nitrate (TN ≡ $HNO_3$ + $pNO_3$).

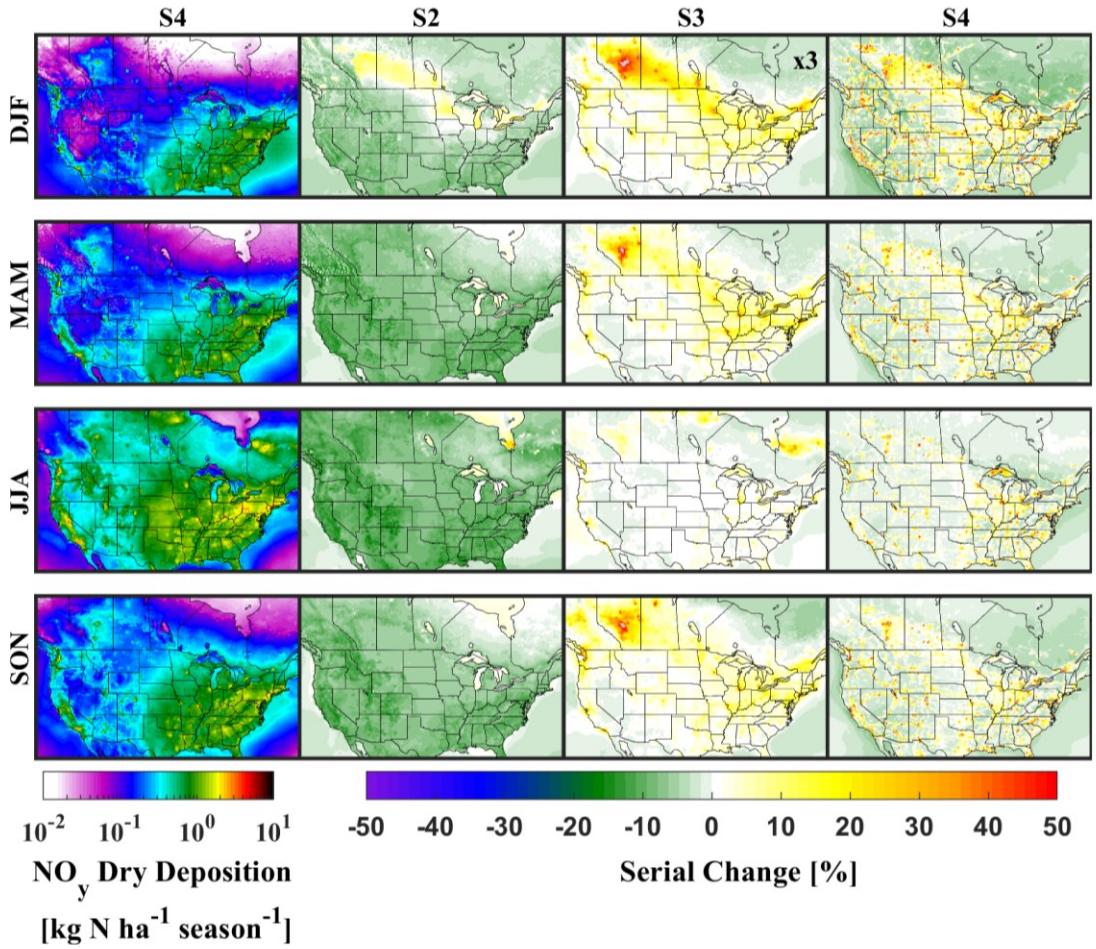


**Figure S4.17:** Seasonal dry deposition of reactive nitrogen oxides ($NO_y$) for the year 2013 from GEOS-Chem simulation S4 (left most column) adjacent serial percent changes for indicated simulations, i.e., for S2: 100x(S2-S1)/S1, and for S4: 100x(S4-S3)/S3. Note, interpretation of percent change in DJF dry deposition for simulation S3 requires application of indicated multiplicative factor. Grey indicates off-scale.

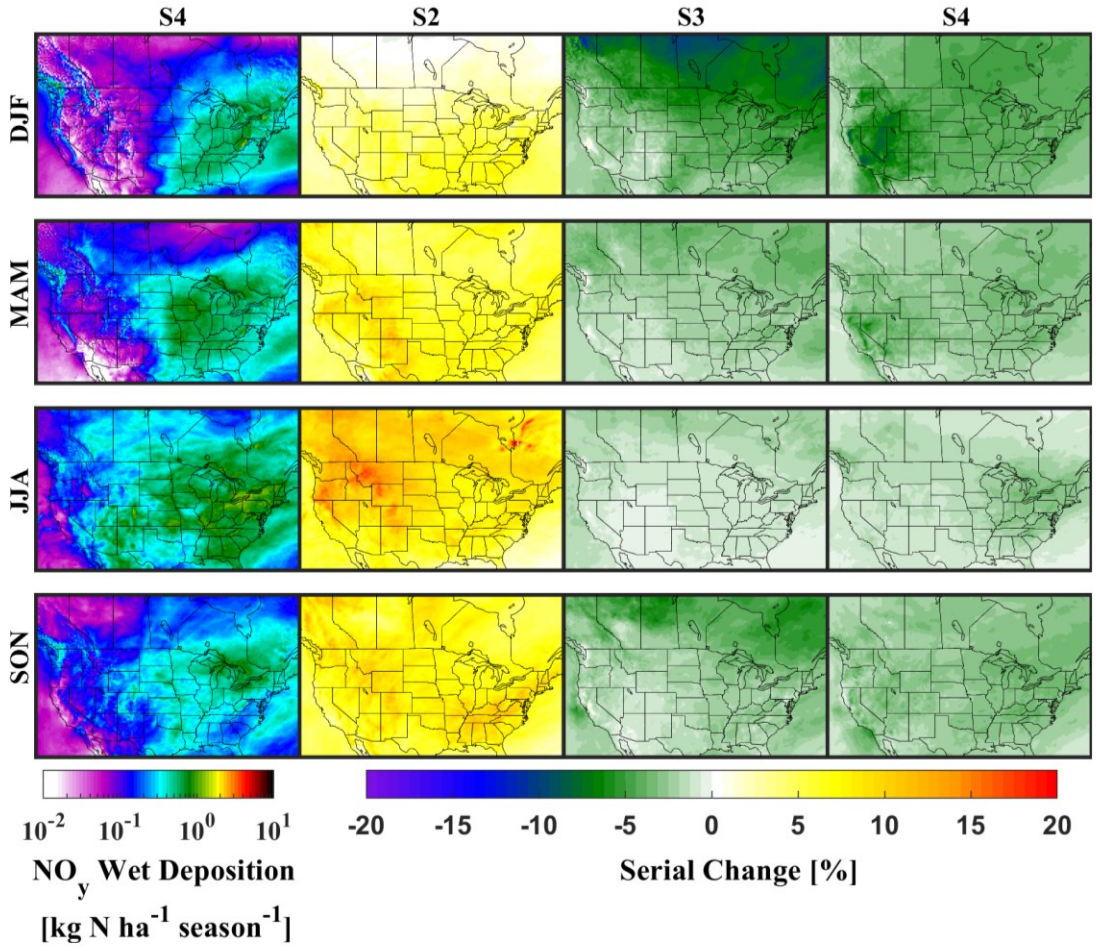


**Figure S4.18:** Seasonal wet deposition of reactive nitrogen oxides ($NO_y$) for the year 2013 from GEOS-Chem simulation S4 (left most column) adjacent serial percent changes for indicated simulations, i.e., for S2: 100x(S2-S1)/S1, and for S4: 100x(S4-S3)/S3. Grey indicates off-scale.

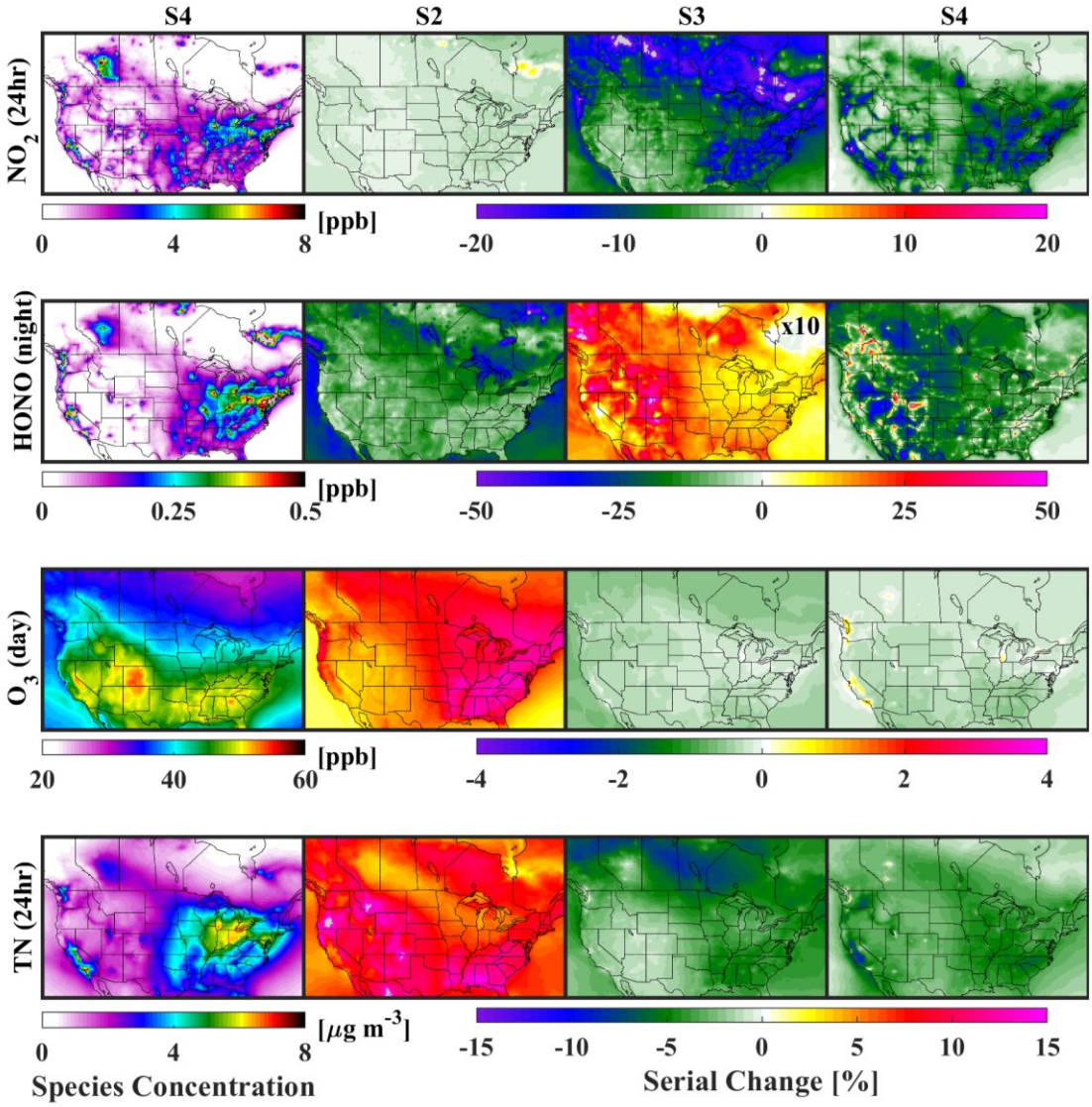


**Figure S4.19:** Annual mean surface concentrations of $NO_2$, HONO, $O_3$, and total nitrate (TN ≡ $HNO_3$ + $pNO_3^-$) from simulation S4 (left most column) adjacent serial percent change for indicated simulations, i.e., for S2: 100x(S2-S1)/S1, and for S4: 100x(S4-S3)/S3. Note, interpretation of percent change in nocturnal HONO concentrations for simulation S3 requires application of indicated multiplicative factor. Grey indicates off-scale.

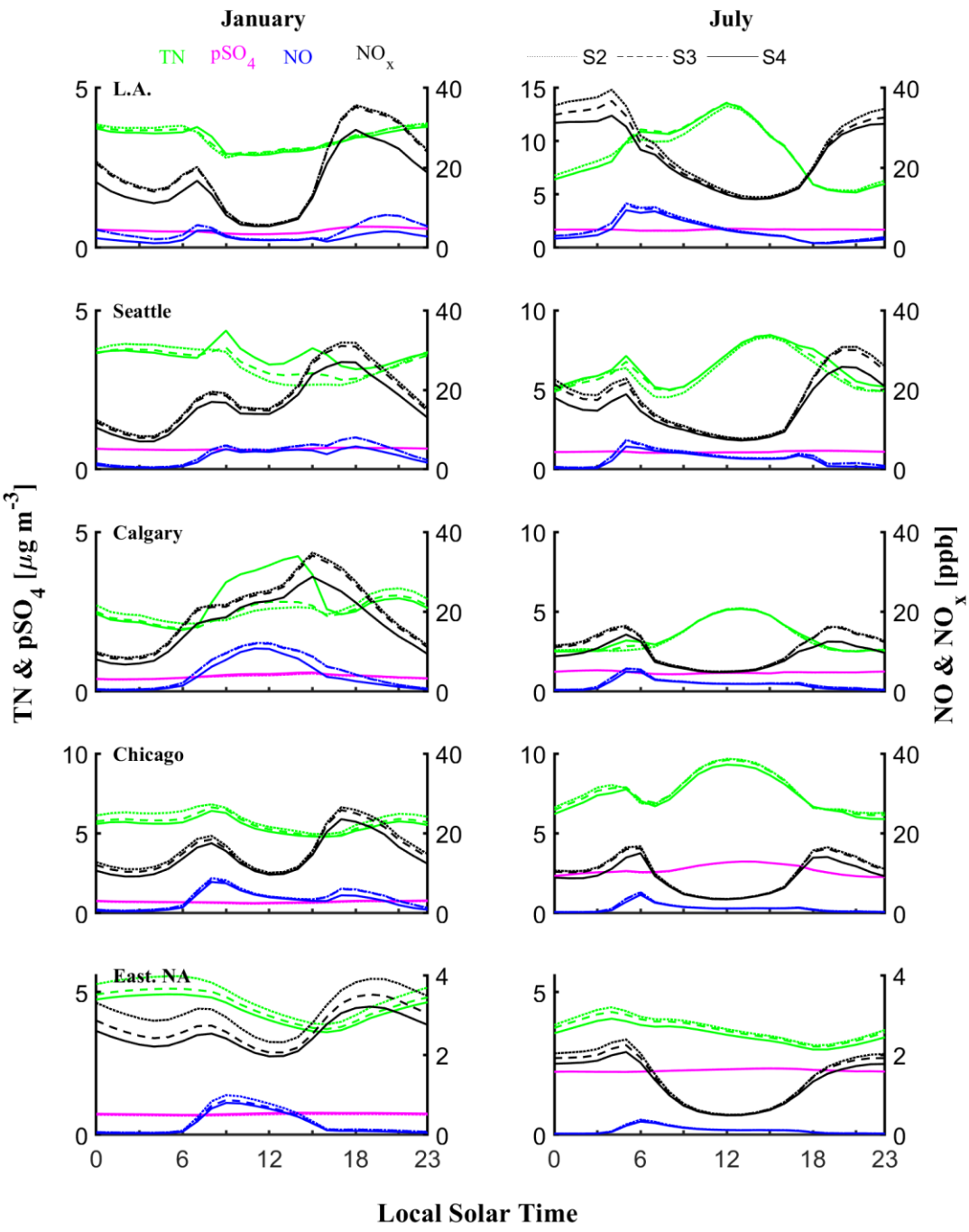


**Figure S4.20:** Monthly mean diel profiles of ground-level total nitrate (TN ≡ $HNO_3$ + $pNO_3^-$), particulate sulfate ($pSO_4$), NO, and $NO_x$ for select urban centers and eastern N.A. (over land) are depicted for three updated simulations: S2, S3, and S4.

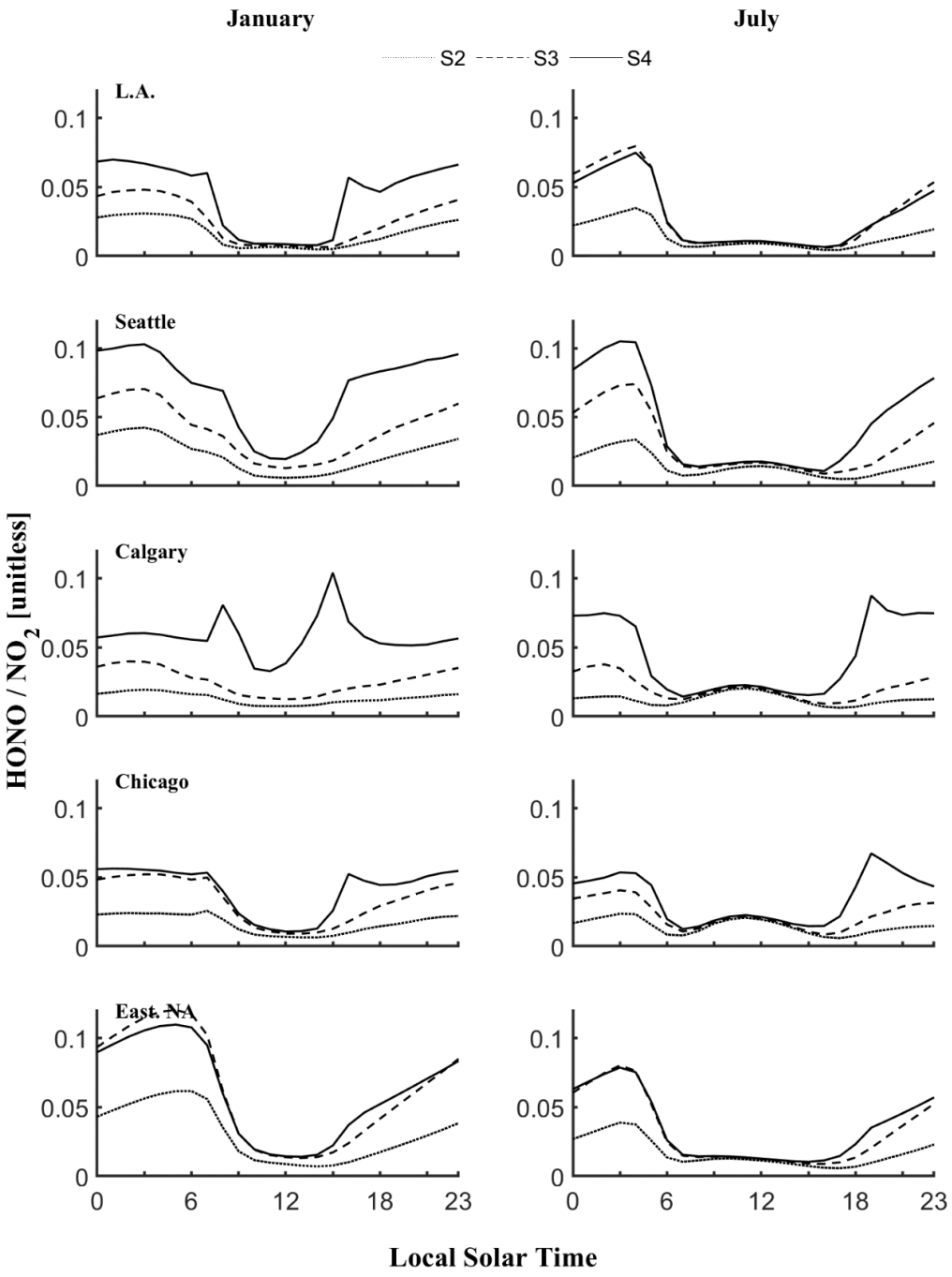


**Figure S4.21:** Monthly mean diel profiles of $HONO/NO_2$ ratios for select urban centers and eastern N.A. (over land) are depicted for three updated simulations: S2, S3, and S4.

# Chapter 5

# Conclusion

## 5.1 Summary

Aerosols and nitrogen oxides are short lived atmospheric trace species that are involved in a wide variety of atmospheric processes with important implications for climate and air quality (Szopa et al., 2021). Aerosols have been shown to have a net cooling effect on climate (Forster et al., 2021), be a source of nutrients to land and marine ecosystems (Johnson et al., 2010; Mahowald et al., 2017), influence heterogeneous and photochemistry (Jacob, 2000; Martin et al., 2003a), and be detrimental to health (Murray et al., 2020). Nitrogen oxides influence climate and air quality by modulating oxidant fields, contributing to tropospheric $O_3$ production, and ultimately being a source of nitrate aerosol. Therefore, the ability to monitor aerosol and $NO_x$ distributions globally, as well as accurately simulate atmospheric processes involving these species, is important for climate and air quality related research. This thesis presented three research chapters which made use of, and developments to, a global atmospheric chemical transport model (GEOS-Chem) for the purposes of (i) monitoring and understanding global trends in satellite-derived $PM_{2.5}$ and (ii) improved simulation of $NO_2$ reaction on ground surfaces.

In Chapter 2, we develop and interpret the first observationally-based estimate of changes in long-term global $PM_{2.5}$. Specifically, we combine satellite-derived $PM_{2.5}$ from the MISR and SeaWiFS instruments—using overpass-resolved simulated 'surface $PM_{2.5}$ to column AOD' relationships from the GEOS-Chem global CTM employing consistent assimilated meteorology—to estimate and interpret a unified, 24-hr, monthly $PM_{2.5}$ time series from January 1998 to December 2012 globally at a resolution of 1˚ x 1˚. Four broad areas showing significant, spatially coherent, annual trends are examined in detail: eastern U.S. ($-0.39 \pm 0.10$ μg $m^{-3}$ $yr^{-1}$), Arabian Peninsula ($0.81 \pm 0.21$ μg $m^{-3}$ $yr^{-1}$), South Asia ($0.93 \pm 0.22$ μg $m^{-3}$ $yr^{-1}$) and East Asia ($0.79 \pm 0.27$ μg $m^{-3}$ $yr^{-1}$). Over the period of dense

*in situ* observation (1999 – 2012), the linear tendency for the eastern U.S. (-0.37 ± 0.13 μg $m^{-3}$ $yr^{-1}$) agrees well with that from *in situ* measurements (-0.38 ± 0.06 μg $m^{-3}$ $yr^{-1}$); time-varying '$PM_{2.5}$ to AOD' relationships were necessary to reproduce the trend in *in situ* observations. A GEOS-Chem simulation reveals that secondary inorganic aerosols largely explain the observed $PM_{2.5}$ trend over the eastern U.S., South Asia, and East Asia, while mineral dust largely explains the observed trend over the Arabian Peninsula. The methods of this work were used by van Donkelaar et al. (2015b) to analyze trends in population-weighted $PM_{2.5}$ exposure, globally, from 1998 through 2012.

In Chapter 3, the trace gas dry deposition algorithm from GEOS-Chem was extracted and reimplemented to run offline in single point mode to enable detailed evaluation of various branches of the algorithm against eddy covariance inferred deposition velocities over two North American forest ecosystems. Two large biases in separate parts of the algorithm were discovered and addressed with mechanistic updates. First, correction of a large low bias in the parameterization of molecular diffusion coefficients resulted in large (~100%) increases in quasi-boundary layer surface resistances ($R_b$), yielding much improved simulation of deposition velocities of rapidly depositing species such as $HNO_3$. Second, a low bias of -80% in simulated nocturnal $NO_2$ deposition velocity was eliminated by representing a reaction pathway for $NO_2$ heterogeneous hydrolysis on deposition surfaces. Consideration of soil $NO_x$ emission and canopy surface area effects were found to be important when comparing simulated with eddy covariance inferred $V_d(NO_2)$. Bottom-up estimates of nocturnal $V_d(NO_2)$ for Harvard Forest computed from surface-specific $NO_2$ uptake coefficients to foliar, bark, and forest floor surfaces provide an independent method of interpretation of top-down observations. Finally, it is noted that representing $NO_2$ hydrolysis on the ground surface through a CTM's dry deposition parameterization provides mechanistic utility to current understanding of dominant atmospheric production of HONO.

Chapter 4 evaluates the effects of recommended Chapter 3 updates to GEOS-Chem's trace gas dry deposition parameterization on a high-resolution simulation over North America. In addition to these aforementioned updates, I develop and implement into GEOS-Chem a parameterization to represent the process of subgrid dry deposition of near-

surface anthropogenic emissions of $NO_x$. Resulting reductions in ground-level $NO_2$ are on the order of 5–20% with commensurate reduction in regional concentrations of total nitrate ($HNO_3$ + particulate nitrate). Large increases (>100%) in simulated surface concentrations of nitrous acid (HONO)—an important precursor of the hydroxyl radical (OH)—stem from improved representation of $NO_2$ surface processes and help to alleviate a large low bias compared to aircraft observations.

## 5.2 Future Work

Trend analysis of satellite-derived $PM_{2.5}$ requires long-term radiometric stability of satellite sensors as well as long-term consistency of the meteorological products and emissions inventories required as inputs to the global CTM. Since the publication of Chapter 2, progress has been made in including radiometrically stabilized MODIS satellite instruments in addition to MISR and SeaWiFS satellite instruments for satellite-derived $PM_{2.5}$ trend analysis (Hammer et al., 2020). In addition, recent progress has been made in development of a globally consistent, long-term anthropogenic emissions inventory for use in CTMs (McDuffie et al., 2020), which will be of benefit to future trend studies involving global CTMs.

Dry deposition schemes currently used in state-of-the-science CTMs rely heavily on similarity arguments to extend surface uptake parameterizations optimized from observations of $SO_2$ and $O_3$ deposition to many other trace gasses (Wesely, 1989; Zhang et al., 2003a). Although aqueous solubility and oxidation potential broadly cover air-surface interactions for many species, this is not generally applicable to all atmospheric trace gasses known to dry deposit, as was exemplified for the case of $NO_2$ in Chapter 3. Long-term field studies quantifying atmosphere-surface exchange across a variety of land-types and seasons would facilitate further development of species-specific dry deposition pathways.

Updates to $NO_2$ dry deposition implemented into GEOS-Chem in Chapter 4 add to the findings of Nowlan et al. (2014) that $NO_2$ is a significant contributor to $NO_y$ dry deposition in urban areas. It would be interesting future work to reapply the methods of Nowlan et al. (2014), namely, inferential $NO_2$ dry deposition flux estimates using satellite-

derived surface $NO_2$ concentrations and GEOS-Chem simulated deposition velocities, while including updates to $NO_2$ dry deposition presented herein and satellite-derived $NO_2$ following Cooper et al. (2020) where ground level $NO_2$ concentrations are inferred globally at unprecedented spatial resolution (3.5 km x 7 km) from the TROPOMI satellite instrument.

As mentioned in Chapter 4, a large low bias in simulated daytime HONO remains in both the PBL and free troposphere. Several daytime sources of HONO are yet to be developed in GEOS-Chem, including $HNO_3$/nitrate photolysis, photoenhanced heterogeneous $NO_2$ reduction, and daytime release of nocturnally deposited HONO. Given the significance of atmospheric HONO as a near-surface source of OH, especially during periods of low solar radiation when production from other photolytic sources is reduced, future developments to GEOS-Chem in this area are recommended.

Also mentioned in Chapter 4 are several 'future works', including (i) updating the calculation of the canopy reduction factor (CRF) used for soil $NO_x$ emission in GEOS-Chem to include the effects of $NO_2$ hydrolysis (reaction R4.1) on canopy surfaces, which is expected to further alleviate the proposed high summertime bias for surface $NO_x$ emissions in the EPA's NEI 2011 inventory (Travis et al., 2016); (ii) instead of computing molecular diffusion coefficients according to Graham's Law, measured diffusion coefficients will be used, where available (Chapter 3, Table S3.1), and values simulated via Fuller's method in the absence of a measured value; (iii) adding simulated surface $O_3$ as a fifth dimension to look-up-table values of $f$—the fraction of near-surface emitted $NO_x$ lost to subgrid dry deposition—to control the rate of surface emitted NO to $NO_2$ oxidation, as well as including mass-balance of $O_3$ loss resulting from oxidation of NO in the subgrid dry deposition scheme.

# Bibliography

Abbatt, J., George, C., Melamed, M., Monks, P., Pandis, S. and Rudich, Y.: Nes Directions: Fundamentals of atmospheric chemistry: keeping a three-legged stool balanced, Atmosperic Environ., 84, 390–391, 2014.

Agathokleous, E., Feng, Z., Oksanen, E., Sicard, P., Wang, Q., Saitanis, C. J., Araminiene, V., Blande, J. D., Hayes, F., Calatayud, V., Domingos, M., Veresoglou, S. D., Peñuelas, J., Wardle, D. A., de Marco, A., Li, Z., Harmens, H., Yuan, X., Vitale, M. and Paoletti, E.: Ozone affects plant, insect, and soil microbial communities: A threat to terrestrial ecosystems and biodiversity, Sci. Adv., 6(33), 1–18, doi:10.1126/sciadv.abc1176, 2020.

Alexander, B., Allman, D. J., Amos, H. M., Fairlie, T. D., Dachs, J., Hegg, D. A. and Sletten, R. S.: Isotopic constraints on the formation pathways of sulfate aerosol in the marine boundary layer of the subtropical northeast Atlantic Ocean, J. Geophys. Res. Atmos., 117(6), 1–17, doi:10.1029/2011JD016773, 2012.

Alexander, B., Sherwen, T., Holmes, C. D., Fisher, J. A., Chen, Q. and Evans, M. J.: Global inorganic nitrate production mechanisms : comparison of a global model with nitrate isotope observations, Atmos. Chem. Phys., 20, 3859–3877, doi:10.5194/acp-20-3859-2020, 2020.

Alicke, B., Geyer, A., Hofzumahaus, A., Holland, F., Konrad, S., Pätz, H. W., Schäfer, J., Stutz, J., Volz-Thomas, A. and Platt, U.: OH formation by HONO photolysis during the BERLIOZ experiment, J. Geophys. Res. Atmos., 108(4), doi:10.1029/2001jd000579, 2003.

Almeida, J., Schobesberger, S., Kürten, A., Ortega, I. K., Kupiainen-Määttä, O., Praplan, A. P., Adamov, A., Amorim, A., Bianchi, F., Breitenlechner, M., David, A., Dommen, J., Donahue, N. M., Downard, A., Dunne, E., Duplissy, J., Ehrhart, S., Flagan, R. C., Franchin, A., Guida, R., Hakala, J., Hansel, A., Heinritzi, M., Henschel, H., Jokinen, T., Junninen, H., Kajos, M., Kangasluoma, J., Keskinen, H., Kupc, A., Kurtén, T., Kvashin, A. N., Laaksonen, A., Lehtipalo, K., Leiminger, M., Leppä, J., Loukonen, V., Makhmutov, V., Mathot, S., McGrath, M. J., Nieminen, T., Olenius, T., Onnela, A., Petäjä, T., Riccobono, F., Riipinen, I., Rissanen, M., Rondo, L., Ruuskanen, T., Santos, F. D., Sarnela, N., Schallhart, S., Schnitzhofer, R., Seinfeld, J. H., Simon, M., Sipilä, M., Stozhkov, Y., Stratmann, F., Tomé, A., Tröstl, J., Tsagkogeorgas, G., Vaattovaara, P., Viisanen, Y., Virtanen, A., Vrtala, A., Wagner, P. E., Weingartner, E., Wex, H., Williamson, C., Wimmer, D., Ye, P., Yli-Juuti, T., Carslaw, K. S., Kulmala, M., Curtius, J., Baltensperger, U., Worsnop, D. R., Vehkamäki, H. and Kirkby, J.: Molecular understanding of sulphuric acid-amine particle nucleation in the atmosphere, Nature, 502(7471), 359–363, doi:10.1038/nature12663, 2013.

Altimir, N., Kolari, P., Tuovinen, J.-P., Vesala, T., Bäck, J., Suni, T., Kulmala, M. and Hari, P.: Foliage surface ozone deposition: a role for surface moisture?, Biogeosciences, 3(2), 209–228, doi:10.5194/bg-3-209-2006, 2006.

Ammann, M., Stalder, M., Suter, M., Brunold, C., Baltensperger, U., Jost, D. T., Türler, A. and Gäggeler, H. W.: Tracing uptake and assimilation of NO2 in spruce needles with 13N, J. Exp. Bot., 46(11), 1685–1691, doi:10.1093/jxb/46.11.1685, 1995.

Ammann, M., Rössler, E., Strekowskit, R. and George, C.: Nitrogen dioxide multiphase chemistry: Uptake kinetics on aqueous solutions containing phenolic compounds, Phys. Chem. Chem. Phys., 7(12), 2513–2518, doi:10.1039/b501808k, 2005.

Ammann, M., Cox, R. A., Crowley, J. N., Jenkin, M. E., Mellouki, A., Rossi, M. J., Troe, J. and Wallington, T. J.: Evaluated kinetic and photochemical data for atmospheric chemistry: Volume VI - Heterogeneous reactions with liquid substrates, Atmos. Chem. Phys., 13(16), 8045–8228, doi:10.5194/acp-13-8045-2013, 2013.

Amos, H. M., Jacob, D. J., Holmes, C. D., Fisher, J. A., Wang, Q., Yantosca, R. M., Corbitt, E. S., Galarneau, E., Rutter, A. P., Gustin, M. S., Steffen, A., Schauer, J. J., Graydon, J. A., St Louis, V. L., Talbot, R. W., Edgerton, E. S., Zhang, Y. and Sunderland, E. M.: Gas-particle partitioning of atmospheric Hg(II) and its effect on global mercury deposition, Atmos. Chem. Phys., 12(1), 591–603, doi:10.5194/acp-12-591-2012, 2012.

Andres, R. J. and Kasgnoc, A. D.: A time-averaged inventory of subaerial volcanic sulfur emissions, J. Geophys. Res. Atmos., 103(D19), 25251–25261, doi:10.1029/98JD02091, 1998.

Arnqvist, J. and Bergström, H.: Flux-profile relation with roughness sublayer correction, Q. J. R. Meteorol. Soc., 141(689), 1191–1197, doi:10.1002/qj.2426, 2015.

Ashworth, K., Chung, S. H., Griffin, R. J., Chen, J., Forkel, R., Bryan, A. M. and Steiner, A. L.: FORest Canopy Atmosphere Transfer (FORCAsT) 1.0: A 1-D model of biosphere-atmosphere chemical exchange, Geosci. Model Dev., 8(11), 3765–3784, doi:10.5194/gmd-8-3765-2015, 2015.

Aumont, B., Chervier, F. and Laval, S.: Contribution of HONO sources to the NOx/HOx/O3 chemistry in the polluted boundary layer, Atmos. Environ., 37(4), 487–498, doi:10.1016/S1352-2310(02)00920-2, 2003.

Baldocchi, D. D.: Assessing the eddy covariance technique for evaluating carbon dioxide exchange rates of ecosystems: Past, present and future, Glob. Chang. Biol., 9(4), 479–492, doi:10.1046/j.1365-2486.2003.00629.x, 2003.

Baldocchi, D. D., Hicks, B. B. and Camara, P.: A canopy stomatal resistance model for gaseous deposition to vegetated surfaces, Atmos. Environ., 21(1), 91–101, doi:10.1016/0004-6981(87)90274-5, 1987.

Baldocchi, D. D., Hincks, B. B. and Meyers, T. P.: Measuring Biosphere-Atmosphere Exchanges of Biologically Related Gases with Micrometeorological Methods, Ecology, 69(5), 1331–1340, doi:10.2307/1941631, 1988.

Bambauer, A., Brantner, B., Paige, M. and Novakov, T.: Laboratory Study of NO2 Reaction With Dispersed and Bulk Liquid Water, Atmosperic Environ., 28(20), 3225–3232, 1994.

Bang, J., Lee, D. H., Kim, S. K. and Kang, H.: Reaction of Nitrogen Dioxide with Ice Surface at Low Temperature (>170 K), J. Phys. Chem. C, 119(38), 22016–22024, doi:10.1021/acs.jpcc.5b05497, 2015.

Bannister, E. J., Jesson, M., Harper, N. J., Hart, K. M., Curioni, G. and Mackenzie, A. R.: Air-parcel residence times in a mature forest : observational evidence from a free-air CO 2 enrichment experiment, Atmos. Chem. Phys. Discuss., (May), 1–27, 2022.

Barkley, M. P., Palmer, P. I., Ganzeveld, L., Arneth, A., Hagberg, D., Karl, T., Guenther, A., Paulot, F., Wennberg, P. O., Mao, J., Kurosu, T. P., Chance, K., Müller, J. F., Smedt, I. De, Roozendael, M. Van, Chen, D., Wang, Y. and Yantosca, R. M.: Can a " state of the art " chemistry transport model simulate Amazonian tropospheric chemistry ?, J. Geophys. Res., 116, D16302, doi:10.1029/2011JD015893, 2011.

Barnes, R. A., Eplee, R. E., Schmidt, G. M., Patt, F. S. and McClain, C. R.: Calibration of SeaWiFS I Direct techniques, Appl. Opt., 40(36), 6682, doi:10.1364/ao.40.006682, 2001.

Behera, S. N., Sharma, M., Aneja, V. P. and Balasubramanian, R.: Ammonia in the atmosphere: A review on emission sources, atmospheric chemistry and deposition on terrestrial bodies, Environ. Sci. Pollut. Res., 20(11), 8092–8131, doi:10.1007/s11356-013-2051-9, 2013.

Beine, H. J., Honrath, R. E., Fuentes, J. D., Shepson, P. B. and Bottenheim, J. W.: Snowpack Photochemical Production of HONO: a Major Source of OH in the Arctic Boundary Layer in Springtime, Geophys. Res. Lett., 28(21), 4087–4090, 2001.

Beirle, S., Boersma, K. F., Platt, U., Lawrence, M. G. and Wagner, T.: Megacity Emissions and Lifetimes of Nitrogen Oxides Probed from Space, Science (80-. )., 333(6050), 1737–1739, doi:10.1126/science.1207824, 2011.

Berglen, T. F., Myhre, G., Isaksen, I. S. A., Vestreng, V. and Smith, S. J.: Sulphate trends in Europe: Are we able to model the recent observed decrease?, Tellus, Ser. B Chem. Phys. Meteorol., 59(4), 773–786, doi:10.1111/j.1600-0889.2007.00289.x, 2007.

Bey, I., Jacob, D. J., Yantosca, R. M., Logan, J. A., Field, B. D., Fiore, A. M., Li, Q.-B., Liu, H.-Y., Mickley, L. J. and Schultz, M. G.: Global Modeling of Tropospheric Chemistry with Assimilated Meteorology: Model Description and Evaluation, J. Geophys. Res., 106, 73–95, doi:10.1029/2001JD000807, 2001.

Bindle, L., Martin, R., Cooper, M., Lundgren, E., Eastham, S., Auer, B., Clune, T., Weng, H., Lin, J., Murray, L., Meng, J., Keller, C., Pawson, S. and Jacob, D.: Grid-Stretching Capability for the GEOS-Chem 13.0.0 Atmospheric Chemistry Model, Geosci. Model Dev. Discuss., (December), 1–21, doi:10.5194/gmd-2020-398, 2020.

Boys, B. L., Martin, R. V., Van Donkelaar, A., MacDonell, R. J., Hsu, N. C., Cooper, M. J., Yantosca, R. M., Lu, Z., Streets, D. G., Zhang, Q. and Wang, S. W.: Fifteen-year global time series of satellite-derived fine particulate matter, Environ. Sci. Technol., 48(19), 11109–11118, doi:10.1021/es502113p, 2014.

Brahney, J., Ballantyne, A. P., Kociolek, P., Leavitt, P. R., Farmer, G. L. and Neff, J. C.: Ecological changes in two contrasting lakes associated with human activity and dust transport in western Wyoming, Limnol. Oceanogr., 60(2), 678–695, doi:10.1002/lno.10050, 2015.

Brasseur, G. P. and Jacob, D. J.: Modeling of Atmospheric Chemistry, Cabridge University Press., 2017.

Breuninger, C., Oswald, R., Kesselmeier, J. and Meixner, F. X.: The dynamic chamber method: Trace gas exchange fluxes (NO, NO 2, O 3) between plants and the atmosphere in the laboratory and in the field, Atmos. Meas. Tech., 5(5), 955–989, doi:10.5194/amt-5-955-2012, 2012.

Breuninger, C., Meixner, F. X. and Kesselmeier, J.: Field investigations of nitrogen dioxide (NO2) exchange between plants and the atmosphere, Atmos. Chem. Phys., 13(2), 773–790, doi:10.5194/acp-13-773-2013, 2013.

Bröske, R., Kleffmann, J. and Wiesen, P.: Heterogeneous conversion of NO2 on secondary organic aerosol surfaces: A possible source of nitrous acid (HONO) in the atmosphere?, Atmos. Chem. Phys., 3(3), 469–474, doi:10.5194/acp-3-469-2003, 2003.

Brown, S. S., Dibb, J. E., Stark, H., Aldener, M., Vozella, M., Whitlow, S., Williams, E. J., Lerner, B. M., Jakoubek, R., Middlebrook, A. M., DeGouw, J. A., Warneke, C., Goldan, P. D., Kuster, W. C., Angevine, W. M., Sueper, D. T., Quinn, P. K., Bates, T. S., Meagher, J. F., Fehsenfeld, F. C. and Ravishankara, A. R.: Nighttime removal of NOx in the summer marine boundary layer, Geophys. Res. Lett., 31(7), 2–6, doi:10.1029/2004GL019412, 2004.

Browne, E. C. and Cohen, R. C.: Effects of biogenic nitrate chemistry on the NOx lifetime in remote continental regions, Atmos. Chem. Phys., 12(24), 11917–11932, doi:10.5194/acp-12-11917-2012, 2012.

Bruegge, C. J., Diner, D. J., Kahn, R. A., Chrien, N., Helmlinger, M. C., Gaitley, B. J. and Abdou, W. A.: The MISR radiometric calibration process, Remote Sens. Environ., 107(1–2), 2–11, doi:10.1016/j.rse.2006.07.024, 2007.

Bryan, A. M., Bertman, S. B., Carroll, M. A., Dusanter, S., Edwards, G. D., Forkel, R., Griffith, S., Guenther, A. B., Hansen, R. F., Helmig, D., Jobson, B. T., Keutsch, F. N., Lefer, B. L., Pressley, S. N., Shepson, P. B., Stevens, P. S. and Steiner, A. L.: In-canopy gas-phase chemistry during CABINEX 2009: Sensitivity of a 1-D canopy model to vertical mixing and isoprene chemistry, Atmos. Chem. Phys., 12(18), 8829–8849, doi:10.5194/acp-12-8829-2012, 2012.

Burkhardt, J.: Hygroscopic particles on leaves: nutrients or desiccants?, Ecol. Monogr., 80(3), 369–399, 2010.

Burkhardt, J. and Gerchau, J.: Thin Water Films on Coniferous Needles, Atmosperic Environ., 28(12), 2001–2017, 1994.

Burkhardt, J. and Hunsche, M.: " Breath figures " on leaf surfaces — formation and effects of microscopic leaf wetness, Front. Plant Sci., 4(October), 1–9, doi:10.3389/fpls.2013.00422, 2013.

Burkhardt, J., Kaiser, H., Goldbach, H. and Kappen, L.: Measurements of electrical leaf surface conductance reveal recondensation of transpired water vapour on leaf surfaces, Plant, Cell Environ., 22(2), 189–196, doi:10.1046/j.1365-3040.1999.00387.x, 1999.

Burkhardt, J., Koch, K. and Kaiser, H.: Deliquescence of Deposited Atmospheric Particles on Leaf Surfaces, Air-Surface Exch. Gases Part., 1, 313–321, doi:10.1007/978-94-010-9026-1_31, 2001a.

Burkhardt, J., Kaiser, H., Kappen, L. and Goldbach, H. E.: The possible role of aerosols on stomatal conductivity for water vapour, Basic Appl. Ecol., 364, 351–364, 2001b.

Burkhardt, J., Zinsmeister, D., Grantz, D. A., Vidic, S. and Sutton, M. A.: Camouflaged as degraded wax : hygroscopic aerosols contribute to leaf desiccation , tree mortality , and forest decline Camouflaged as degraded wax : hygroscopic aerosols contribute to leaf desiccation , tree mortality , and forest decline, Environ. Res. Lett., 13(8), 085001, 2018.

Businger, J. A.: Evaluation of the Accuracy with Which Dry Deposition Can Be Measured with Current Micrometeorological Techniques, J. Clim. Appl. Meteorol., 25, 1100–1124, 1985.

Caird, M. A., Richards, J. H. and Donovan, L. A.: Nighttime Stomatal Conductance and Transpiration, Plant Physiol., 143, 4–10, doi:10.1104/pp.106.092940, 2007.

Cano-Ruiz, J. A., Kong, D., Balas, R. B. and Nazaroff, W. W.: Removal of Reactive Gases at Indoor Surfaces: Combining Mass Transport and Surface Kinetics, Atmosperic Environ., 27(13), 2039–2050, 1993.

Caranto, J. D. and Lancaster, K. M.: Nitric oxide is an obligate bacterial nitrification intermediate produced by hydroxylamine oxidoreductase, Proc. Natl. Acad. Sci. U. S. A., 114(31), 8217–8222, doi:10.1073/pnas.1704504114, 2017.

Carlton, A. G., Pinder, R. W., Bhave, P. V. and Pouliot, G. A.: To what extent can biogenic SOA be controlled?, Environ. Sci. Technol., 44(9), 3376–3380, doi:10.1021/es903506b, 2010.

Cellier, P. and Brunet, Y.: Flux-gradient relationships above tall plant canopies, Agric. For. Meteorol., 58, 93–117, 1992.

Chameides, W. L.: THE PHOTOCHEMICAL ROLE OF TROPOSPHERIC NITROGEN OXIDES, Geophys. Res. Lett., 5(1), 17–20, 1978.

Chaparro-Suarez, I. G., Meixner, F. X. and Kesselmeier, J.: Nitrogen dioxide (NO2) uptake by vegetation controlled by atmospheric concentrations and plant stomatal aperture, Atmos. Environ., 45(32), 5742–5750, doi:10.1016/j.atmosenv.2011.07.021, 2011.

Chen, Y. and Xie, S. dong: Long-term trends and characteristics of visibility in two megacities in southwest China: Chengdu and Chongqing, J. Air Waste Manag. Assoc., 63(9), 1058–1069, doi:10.1080/10962247.2013.791348, 2013.

Cheng, Y. and Brutsaert, W.: Flux-profile relationships for wind speed and temperature in the stable atmospheric boundary layer, Boundary-Layer Meteorol., 114(3), 519–538, doi:10.1007/s10546-004-1425-4, 2005.

Cheng, Z., Jiang, J., Fajardo, O., Wang, S. and Hao, J.: Characteristics and health impacts of particulate matter pollution in China (2001-2011), Atmos. Environ., 65, 186–194, doi:10.1016/j.atmosenv.2012.10.022, 2013a.

Cheng, Z., Wang, S., Jiang, J., Fu, Q., Chen, C., Xu, B., Yu, J., Fu, X. and Hao, J.: Long-term trend of haze pollution and impact of particulate matter in the Yangtze River Delta, China, Environ. Pollut., 182, 101–110, doi:10.1016/j.envpol.2013.06.043, 2013b.

Cherin, N., Roustan, Y., Musson-Genon, L. and Seigneur, C.: Modelling atmospheric dry deposition in urban areas using an urban canopy approach, Geosci. Model Dev., 8(3), 893–910, doi:10.5194/gmd-8-893-2015, 2015.

Cheung, J. L., Li, Y. Q., Boniface, J., Shi, Q., Davidovits, P., Worsnop, D. R., Jayne, J. T. and Kolb, C. E.: Heterogeneous Interactions of NO2 with Aqueous Surfaces, J. Phys. Chem. A, 104(12), 2655–2662, doi:10.1021/jp992929f, 2000.

Chin, M., Diehl, T., Tan, Q., Prospero, J. M., Kahn, R. A., Remer, L. A., Yu, H., Sayer, A. M., Bian, H., Geogdzhayev, I. V., Holben, B. N., Howell, S. G., Huebert, B. J., Hsu, N. C., Kim, D., Kucsera, T. L., Levy, R. C., Mishchenko, M. I., Pan, X., Quinn, P. K., Schuster, G. L., Streets, D. G., Strode, S. A. and Torres, O.: Multi-decadal aerosol variations from 1980 to 2009: A perspective from observations and a global model, Atmos. Chem. Phys., 14(7), 3657–3690, doi:10.5194/acp-14-3657-2014, 2014.

Clark, C. M., Phelan, J., Doraiswamy, P., Buckley, J., Cajka, J. C., Dennis, R. L., Lynch, J., Nolte, C. G. and Spero, T. L.: Atmospheric deposition and exceedances of critical loads from 1800−2025 for the conterminous United States, Ecol. Appl., 28(4), 978–1002, doi:10.1002/eap.1703, 2018.

Clarke, J. F., Edgerton, E. S. and Martin, B. E.: Dry deposition calculations for the clean air status and trends network, Atmos. Environ., 31(21), 3667–3678, doi:10.1016/S1352-2310(97)00141-6, 1997.

Clifton, O. E., Fiore, A. M., Munger, J. W., Malyshev, S., Horowitz, L. W., Shevliakova, E., Paulot, F., Murray, L. T. and Griffin, K. L.: Interannual variability in ozone removal by a temperate deciduous forest, Geophys. Res. Lett., 44(1), 542–552, doi:10.1002/2016GL070923, 2017.

Coe, H. and Gallagher, M. W.: Measurements of dry deposition of NO2 to a Dutch heathland using the eddy-correlation technique, Q. J. R. Meteorol. Soc., 118, 767–786, 1992.

Colarco, P. R., Kahn, R. A., Remer, L. A. and Levy, R. C.: Impact of satellite viewing-swath width on global and regional aerosol optical thickness statistics and trends, Atmos. Meas. Tech., 7(7), 2313–2335, doi:10.5194/amt-7-2313-2014, 2014.

Cole, H. S. and Summerhays, J. E.: cole_1979_JAPCA_NO2_NOx_disperson_model_OLM.pdf, J. Air Pollut. Control Assoc., 29(8), 812–817, 1979.

Coleman, K. K., Tay, D., Tan, K., Ong, S., Son, T., Koh, M., Nasir, H., Mak, T., Chu, J., Milton, D., Chow, V., Tambyah, P., Chen, M. and Tham, K.: Viral Load of SARS-CoV-2 in Respiratory Aerosols Emitted by COVID-19 Patients while Breathing, Talking, and Singing, Clin. Infect. Dis., 1–31, 2021.

Colette, A., Granier, C., Hodnebrog, Jakobs, H., Maurizi, A., Nyiri, A., Bessagnet, B., D'Angiola, A., D'Isidoro, M., Gauss, M., Meleux, F., Memmesheimer, M., Mieville, A., Roüil, L., Russo, F., Solberg, S., Stordal, F. and Tampieri, F.: Air quality trends in Europe over the past decade: A first multi-model assessment, Atmos. Chem. Phys., 11(22), 11657–11678, doi:10.5194/acp-11-11657-2011, 2011.

Collins, D. B., Hems, R. F., Zhou, S., Wang, C., Grignon, E., Alavy, M., Siegel, A. and Abbatt, J. P. D.: Evidence for Gas − Surface Equilibrium Control of Indoor Nitrous Acid, Environ. Sci. Technol., 52, 12419–12427, doi:10.1021/acs.est.8b04512, 2018.

Colussi, A. J. and Enami, S.: Detecting intermediates and products of fast heterogeneous reactions on liquid surfaces via online mass spectrometry, Atmosphere (Basel)., 10(2), doi:10.3390/atmos10020047, 2019.

Conrad, R.: Soil Microorganisms as Controller of Atmospheric Trace Gases (H2, CO, CH4, OCS, N2O, and NO), Microbiol. Rev., 60(4), 609–640, 1996.

Cooper, M., Martin, R. V, Wespes, C., Coheur, P., Clerbaux, C. and Murray, L. T.: Tropospheric nitric acid columns from the IASI satellite instrument interpreted with a chemical transport model: Implications for parameterizations of nitric oxide production by lightning, J. Geogr. Res. Atmos., 119, 68–79, doi:10.1002/2014JD021907.Received, 2014.

Cooper, M. J., Martin, R. V., McLinden, C. A. and Brook, J. R.: Inferring ground-level nitrogen dioxide concentrations at fine spatial resolution applied to the TROPOMI satellite instrument, Environ. Res. Lett., 15(10), doi:10.1088/1748-9326/aba3a5, 2020.

Correia, A. W., Arden Pope, C., Dockery, D. W., Wang, Y., Ezzati, M. and Dominici, F.: Effect of air pollution control on life expectancy in the United States: An analysis of 545 U.S. Counties for the period from 2000 to 2007, Epidemiology, 24(1), 23–31, doi:10.1097/EDE.0b013e3182770237, 2013.

Costa, J. M., Monnet, F., Jannaud, D., Leonhardt, N., Ksas, B., Reiter, I. M., Pantin, F. and Genty, B.: OPEN ALL NIGHT LONG : The Dark Side of Stomatal Control 1, Plant Physiol., 167, 289–294, doi:10.1104/pp.114.253369, 2015.

Croft, B., Pierce, J. R. and Martin, R. V.: Interpreting aerosol lifetimes using the GEOS-Chem model and constraints from radionuclide measurements, Atmos. Chem. Phys., 14(8), 4313–4325, doi:10.5194/acp-14-4313-2014, 2014.

Croft, B., Wentworth, G. R., Martin, R. V., Leaitch, W. R., Murphy, J. G., Murphy, B. N., Kodros, J. K., Abbatt, J. P. D. and Pierce, J. R.: Contribution of Arctic seabird-colony ammonia to atmospheric particles and cloud-albedo radiative effect, Nat. Commun., 7, 1–10, doi:10.1038/ncomms13444, 2016.

Croft, B., Martin, R. V., Richard Leaitch, W., Burkart, J., Chang, R. Y. W., Collins, D. B., Hayes, P. L., Hodshire, A. L., Huang, L., Kodros, J. K., Moravek, A., Mungall, E. L., Murphy, J. G., Sharma, S., Tremblay, S., Wentworth, G. R., D Willis, M., Abbatt, J. P. D. and Pierce, J. R.: Arctic marine secondary organic aerosol contributes significantly to summertime particle size distributions in the Canadian Arctic Archipelago, Atmos. Chem. Phys., 19(5), 2787–2812, doi:10.5194/acp-19-2787-2019, 2019.

Crouse, D. L., Peters, P. A., van Donkelaar, A., Goldberg, M. S., Villeneuve, P. J., Brion, O., Khan, S., Atari, D. O., Jerrett, M., Pope, C. A., Brauer, M., Brook, J. R., Martin, R. V., Stieb, D. and Burnett, R. T.: Risk of nonaccidental and cardiovascular mortality in relation to long-term exposure to low concentrations of fine particulate matter: A canadian national-level cohort study, Environ. Health Perspect., 120(5), 708–714, doi:10.1289/ehp.1104049, 2012.

Crutzen, P. J.: The influence of nitrogen oxides on the atmospheric ozone content, Q. J. R. Meteorol. Soc., 96(408), 320–325, 1970.

Crutzen, P. J.: THE ROLE OF NO AND N02 IN THE CHEMISTRY OF THE TROPOSPHERE AND STRATOSPHERE, Ann. Rev. Earth Planet. Sci., 7, 443–72, 1979a.

Crutzen, P. J.: The Role of NO and NO2 in the Chemistry of the Troposphere and Stratosphere, Ann. Rev. Earth Planet. Sci., 7, 443–72, 1979b.

Crutzen, P. J.: Geology of mankind - Crutzen - Nature, Nature, 415(January), 2002, 2002.

Cui, L., Li, R., Fu, H., Li, Q., Zhang, L., George, C. and Chen, J.: Formation features of nitrous acid in the offshore area of the East China Sea, Sci. Total Environ., 682, 138–150, doi:10.1016/j.scitotenv.2019.05.004, 2019.

Czader, B. H., Rappenglück, B., Percell, P., Byun, D. W., Ngan, F. and Kim, S.: Modeling nitrous acid and its impact on ozone and hydroxyl radical during the Texas Air Quality Study 2006, Atmos. Chem. Phys., 12(15), 6939–6951, doi:10.5194/acp-12-6939-2012, 2012.

Czader, B. H., Choi, Y., Li, X., Alvarez, S. and Lefer, B.: Impact of updated traffic emissions on HONO mixing ratios simulated for urban site in Houston , Texas, Atmos. Chem. Phys., 15, 1253–1263, doi:10.5194/acp-15-1253-2015, 2015.

Dabberdt, W. F., Lenschow, D. H., Horst, T. W., Zimmerman, P. R., Oncley, S. P. and Delany, A. C.: Atmosphere-Surface Exchange Measurements, Science (80-. )., 260, 1472–1481, 1993.

Darwin, F.: Observations on Stomata, Philos. Trans. R. Soc. B Biol. Sci., 190, 531–621, 1898.

Dawson, T. E., Burgess, S. S. O., Tu, K. P., Oliveira, R. S., Santiago, L. S., Fisher, J. B., Simonin, K. A. and Ambrose, R.: Nighttime transpiration in woody plants from contrasting ecosystems, Tree Physiol., 27, 561–575, 2007.

Delany, A. C., Fitzjarrald, D. R., Lenschow, D. H., Pearson, R., Wendel, G. J. and Woodrufl, B.: Direct measurements of nitrogen oxides and ozone fluxes over grassland, J. Atmos. Chem., 4(4), 429–444, doi:10.1007/BF00053844, 1986.

Delaria, E., Place, B., Liu, A. and Cohen, R.: Laboratory measurements of stomatal NO2 deposition to native California trees and the role of forests in the NOx cycle, Atmos. Chem. Phys., 20(2), 14023–14041, doi:10.5194/acp-2020-240, 2020.

Delaria, E. R.: The rates and processes affecting the deposition of NOx to vegetation at leaf-level and canopy-level scales: impacts on NOx lifetimes and budgets in the troposphere, University of California, Berkeley. [online] Available from: https://escholarship.org/uc/item/98384265, 2020.

Delaria, E. R. and Cohen, R. C.: A model-based analysis of foliar NOx deposition, Atmos. Chem. Phys., 20, 2123–2141, doi:10.5194/acp-20-2123-2020, 2020.

Delaria, E. R., Vieira, M., Cremieux, J. and Cohen, R. C.: Measurements of NO and NO2 exchange between the atmosphere and Quercus agrifolia, Atmos. Chem. Phys., 18(19), 14161–14173, doi:10.5194/acp-18-14161-2018, 2018.

Deng, J., Du, K., Wang, K., Yuan, C. S. and Zhao, J.: Long-term atmospheric visibility trend in Southeast China, 1973-2010, Atmos. Environ., 59, 11–21, doi:10.1016/j.atmosenv.2012.05.023, 2012.

Dennis, R. L., Schwede, D. B., Bash, J. O., Pleim, J. E., Walker, J. T. and Foley, K. M.: Sensitivity of continental united states atmospheric budgets of oxidized and reduced nitrogen to dry deposition parametrizations, Philos. Trans. R. Soc. B Biol. Sci., 368(1621), doi:10.1098/rstb.2013.0124, 2013.

Després, V. R., Alex Huffman, J., Burrows, S. M., Hoose, C., Safatov, A. S., Buryak, G., Fröhlich-Nowoisky, J., Elbert, W., Andreae, M. O., Pöschl, U. and Jaenicke, R.: Primary biological aerosol particles in the atmosphere: A review, Tellus, Ser. B Chem. Phys. Meteorol., 64(1), doi:10.3402/tellusb.v64i0.15598, 2012.

Dey, S. and Di Girolamo, L.: A climatology of aerosol optical and microphysical properties over the Indian subcontinent from 9 years (2000-2008) of Multiangle Imaging Spectroradiometer (MISR) data, J. Geophys. Res. Atmos., 115(15), 1–22, doi:10.1029/2009JD013395, 2010.

Dey, S. and Di Girolamo, L.: A decade of change in aerosol properties over the Indian subcontinent, Geophys. Res. Lett., 38(14), 1–5, doi:10.1029/2011GL048153, 2011.

Dey, S., Di Girolamo, L., van Donkelaar, A., Tripathi, S. N., Gupta, T. and Mohan, M.: Variability of outdoor fine particulate (PM 2.5) concentration in the Indian Subcontinent: A remote sensing approach, Remote Sens. Environ., 127, 153–161, doi:10.1016/j.rse.2012.08.021, 2012.

Diehl, T., Heil, A., Chin, M., Pan, X., Streets, D., Schultz, M. and Kinne, S.: Anthropogenic, biomass burning, and volcanic emissions of black carbon, organic carbon, and SO2 from 1980 to 2010 for hindcast model experiments, Atmos. Chem. Phys. Discuss., 12, 24895–24954, doi:10.5194/acpd-12-24895-2012, 2012.

Dieudonné, E., Ravetta, F., Pelon, J., Goutail, F. and Pommereau, J. P.: Linking NO2 surface concentration and integrated content in the urban developed atmospheric boundary layer, Geophys. Res. Lett., 40(6), 1247–1251, doi:10.1002/grl.50242, 2013.

Diner, D. J., Beckert, J. C., Reilly, T. H., Bruegge, C. J., Conel, J. E., Kahn, R. A., Martonchik, J. V., Ackerman, T. P., Davies, R., Gerstl, S. A. W., Gordon, H. R., Muller, J. P., Myneni, R. B., Sellers, P. J., Pinty, B. and Verstraete, M. M.: Multi-angle imaging spectroradiometer (MISR) instrument description and experiment overview, IEEE Trans. Geosci. Remote Sens., 36(4), 1072–1087, doi:10.1109/36.700992, 1998.

Dockery, D. W., Pope, C., Xu, X., Spengler, J. D. and et al.: An Assiciation Between Air Pollution and Mortality in Six U.S. Cities, N. Engl. J. Med., 329(24), 1753–1759, 1993.

Donaldson, M. A., Berke, A. E. and Raff, J. D.: Uptake of gas phase nitrous acid onto boundary layer soil surfaces, Environ. Sci. Technol., 48(1), 375–383, doi:10.1021/es404156a, 2014.

van Donkelaar, A., Martin, R. V. and Park, R. J.: Estimating ground-level PM2.5 using aerosol optical depth determined from satellite remote sensing, J. Geophys. Res. Atmos., 111(21), 1–10, doi:10.1029/2005JD006996, 2006.

van Donkelaar, A., Martin, R. V., Brauer, M., Kahn, R., Levy, R., Verduzco, C. and Villeneuve, P. J.: Global estimates of ambient fine particulate matter concentrations from satellite-based aerosol optical depth: Development and application, Environ. Health Perspect., 118(6), 847–855, doi:10.1289/ehp.0901623, 2010.

van Donkelaar, A., Martin, R. V, Spurr, R. J. D. and Burnett, R. T.: High-Resolution Satellite-Derived PM 2.5 from Optimal Estimation and Geographically Weighted Regression over North America, Environ. Sci. Technol., 49, 10482–10491, doi:10.1021/acs.est.5b02076, 2015a.

van Donkelaar, A., Martin, R. V, Brauer, M. and Boys, B. L.: Use of Satellite Observations for Long-Term Exposure Assessment of Global Concentrations of Fine Particulate Matter, Environ. Health Perspect., 123(2), 135–143, 2015b.

van Donkelaar, A., Martin, R. V, Leaitch, W. R., Macdonald, A. M., Walker, T. W., Streets, D. G. and Zhang, Q.: Analysis of aircraft and satellite measurements from the Intercontinental Chemical Transport Experiment (INTEX-B) to quantify long-range transport of East Asian sulfur to Canada, Atmos. Chem. Phys., 8, 2999–3014, 2008.

van Donkelaar, A., Martin, R. V., Spurr, R. J. D., Drury, E., Remer, L. A., Levy, R. C. and Wang, J.: Optimal estimation for global ground-level fine particulate matter concentrations, J. Geophys. Res. Atmos., 118(11), 5621–5636, doi:10.1002/jgrd.50479, 2013.

van Donkelaar, A., Martin, R. V., Brauer, M., Hsu, N. C., Kahn, R. A., Levy, R. C., Lyapustin, A., Sayer, A. M. and Winker, D. M.: Global Estimates of Fine Particulate Matter using a Combined Geophysical-Statistical Method with Information from Satellites, Models, and Monitors, Environ. Sci. Technol., 50(7), 3762–3772, doi:10.1021/acs.est.5b05833, 2016.

van Donkelaar, A., Hammer, M. S., Bindle, L., Brauer, M., Brook, J. R., Garay, M. J., Hsu, N. C., Kalashnikova, O. V., Kahn, R. A., Lee, C., Levy, R. C., Lyapustin, A., Sayer, A. M. and Martin, R. V.: Monthly Global Estimates of Fine Particulate Matter and Their Uncertainty, Environ. Sci. Technol., 55(22), 15287–15300, doi:10.1021/acs.est.1c05309, 2021.

Drury, E., Jacob, D. J., Spurr, R. J. D., Wang, J., Shinozuka, Y., Anderson, B. E., Clarke, A. D., Dibb, J., Mcnaughton, C. and Weber, R.: Synthesis of satellite ( MODIS ), aircraft ( ICARTT ), and surface ( IMPROVE , EPA - AQS , AERONET ) aerosol observations over eastern North America to improve MODIS aerosol retrievals and constrain surface aerosol concentrations and sources, J. Geogr. Res., 115, D14204, doi:10.1029/2009JD012629, 2010.

Duncan, B. N., Martin, R. V, Staudt, A. C., Yevich, R. and Logan, J. A.: Interannual and seasonal variability of biomass burning emissions constrained by satellite observations, J. Geophys. Res., 108, doi:10.1029/2002JD002378, 2003.

Duyzer, J. ., Weststrate, H. and Walton, S.: Exchange of Ozone and Nitrogen Oxides Between the Atmosphere and Coniferous Forest, Water. Air. Soil Pollut., 85, 2065–2070, 1995.

Dyer, A. J.: A Review of Flux-Profile Relationships, Boundary-Layer Meteorol., 7, 363–372, 1974.

Elshorbany, Y. F., Kleffmann, J., Kurtenbach, R., Lissi, E., Rubio, M., Villena, G., Gramsch, E., Rickard, A. R., Pilling, M. J. and Wiesen, P.: Seasonal dependence of the oxidation capacity of the city of Santiago de Chile, Atmos. Environ., 44(40), 5383–5394, doi:10.1016/j.atmosenv.2009.08.036, 2010.

Engel-Cox, J., Kim Oanh, N. T., van Donkelaar, A., Martin, R. V. and Zell, E.: Toward the next generation of air quality monitoring: Particulate Matter, Atmos. Environ., 80, 584–590, doi:10.1016/j.atmosenv.2013.08.016, 2013.

Eplee, R. E., Meister, G., Patt, F. S., Barnes, R. A., Bailey, S. W., Franz, B. A. and McClain, C. R.: On-orbit calibration of SeaWiFS, Appl. Opt., 51(36), 8702–8730, doi:10.1364/AO.51.008702, 2012.

Eugster, W. and Hesterberg, R.: Transfer resistances of NO2 determined from eddy correlation flux measurements over a litter meadow at a rural site on the Swiss plateau, Atmos. Environ., 30(8), 1247–1254, doi:10.1016/1352-2310(95)00418-1, 1996.

Evans, M. J. and Jacob, D. J.: Impact of new laboratory studies of N2O5 hydrolysis on global model budgets of tropospheric nitrogen oxides, ozone, and OH, Geophys. Res. Lett., 32(9), 1–4, doi:10.1029/2005GL022469, 2005.

Fairlie, T. D., Jacob, D. J. and Park, R. J.: The impact of transpacific transport of mineral dust in the United States, Atmosperic Environ., 41, 1251–1266, doi:10.1016/j.atmosenv.2006.09.048, 2007.

Fairlie, T. D., Jacob, D. J., Dibb, J. E., Alexander, B., Avery, M. A., Van Donkelaar, A. and Zhang, L.: Impact of mineral dust on nitrate, sulfate, and ozone in transpacific Asian pollution plumes, Atmos. Chem. Phys., 10(8), 3999–4012, doi:10.5194/acp-10-3999-2010, 2010.

Farmer, D. K., Wooldridge, P. J. and Cohen, R. C.: Application of thermal-dissociation laser induced fluorescence (TD-LIF) to measurement of HNO3, ∑alkyl nitrates, ∑peroxy nitrates, and NO2 fluxes using eddy covariance, Atmos. Chem. Phys., 6(11), 3471–3486, doi:10.5194/acp-6-3471-2006, 2006.

Farvardin, A., Isabel, A., Llorens, E., Garc, P., Scalschi, L. and Vicedo, B.: The Apoplast : A Key Player in Plant Survival same, Antioxidants, 6(604), doi:10.3390/antiox9070604, 2020.

Febo, A. and Perrino, C.: Prediction and Experimental Evidence for High Air Concentration of Nitrous Acid in Indoor Evnivronments, Atmosperic Environ., 25, 1055–1061, 1991.

Feichter, J. and Leisner, T.: Climate engineering: A critical review of approaches to modify the global energy balance, Eur. Phys. J. Spec. Top., 176(1), 81–92, doi:10.1140/epjst/e2009-01149-8, 2009.

Feng, X., Lin, H., Fu, T. M., Sulprizio, M. P., Zhuang, J., Jacob, D. J., Tian, H., Ma, Y., Zhang, L., Wang, X., Chen, Q. and Han, Z.: WRF-GC (v2.0): Online two-way coupling of WRF (v3.9.1.1) and GEOS-Chem (v12.7.2) for modeling regional atmospheric chemistry-meteorology interactions, Geosci. Model Dev., 14(6), 3741–3768, doi:10.5194/gmd-14-3741-2021, 2021.

Fields, S.: Global Nitrogen: Cycling out of Control, Environ. Health Perspect., 112(10), 556–563, 2004.

Finlayson-Pitts, B. J.: Reactions at surfaces in the atmosphere: integration of experiments andtheory as necessary (but not necessarily sufficient) for predicting thephysical chemistry of aerosols, Phys. Chem. Chem. Phys., 11(36), 7759, doi:10.1039/b916865f, 2009.

Finlayson-Pitts, B. J., Wingen, L. M., Sumner, A. L., Syomin, D. and Ramazan, K. A.: The heterogeneous hydrolysis of NO2 in laboratory systems and in outdoor and indoor atmospheres: An integrated mechanism, Phys. Chem. Chem. Phys., 5(2), 223–242, doi:10.1039/B208564J, 2003.

Finnigan, J.: Turbulence in plant canopies, Annu. Rev. Fluid Mech., 35, 519–571, doi:10.2480/agrmet.20.1, 2000.

Finnigan, J. J., Shaw, R. H. and Patton, E. G.: Turbulence structure above a vegetation canopy, J. Fluid Mech., 637(May), 387–424, doi:10.1017/S0022112009990589, 2009.

Fisher, J. A., Jacob, D. J., Wang, Q., Bahreini, R., Carouge, C. C., Cubison, M. J., Dibb, J. E., Diehl, T., Jimenez, J. L., Leibensperger, E. M., Lu, Z., Meinders, M. B. J., Pye, H. O. T., Quinn, P. K., Sharma, S., Streets, D. G., Donkelaar, A. Van and Yantosca, R. M.: Sources , distribution , and acidity of sulfate e ammonium aerosol in the Arctic in winter e spring, Atmos. Environ., 45(39), 7301–7318, doi:10.1016/j.atmosenv.2011.08.030, 2011.

Fisher, J. A., Jacob, D. J., Travis, K. R., Kim, P. S., Marais, E. A., Miller, C. C., Yu, K., Zhu, L., Yantosca, R. M., Sulprizio, M. P., Mao, J., Wennberg, P. O., Crounse, J. D., Teng, A. P., Nguyen, T. B., Clair, J. M. S., Cohen, R. C., Romer, P., Nault, B. A., Wooldridge, P. J., Jimenez, J. L., Campuzano-Jost, P., Day, D. A., Hu, W., Shepson, P. B., Xiong, F., Blake, D. R., Goldstein, A. H., Misztal, P. K., Hanisco, T. F., Wolfe, G. M., Ryerson, T. B., Wisthaler, A. and Mikoviny, T.: Organic nitrate chemistry and its implications for nitrogen budgets in an isoprene- and monoterpene-rich atmosphere: Constraints from aircraft (SEAC4RS) and ground-based (SOAS) observations in the Southeast US, Atmos. Chem. Phys., 16(9), 5969–5991, doi:10.5194/acp-16-5969-2016, 2016.

Fitzjarrald, D. and Sakai, R.: Radiation Measurements at Harvard Forest EMS Tower 1991-2007, , Harvard Forest Data Archive: HF102, 2009.

Flechard, C. R., Nemitz, E., Smith, R. I., Fowler, D., Vermeulen, A. T., Bleeker, A., Erisman, J. W., Simpson, D., Zhang, L., Tang, Y. S. and Sutton, M. A.: Dry deposition of reactive nitrogen to European ecosystems: A comparison of inferential models across the NitroEurope network, Atmos. Chem. Phys., 11(6), 2703–2728, doi:10.5194/acp-11-2703-2011, 2011.

Ford, B. and Heald, C. L.: An A-train and model perspective on the vertical distribution of aerosols and CO in the Northern Hemisphere, J. Geogr. Res., 117, D06211, doi:10.1029/2011JD016977, 2012.

Forster, P., Storelvmo, T., Armour, K., Collins, W., Dufresne, J. L., Frame, D., Lunt, D. J., Mauritsen, T., Palmer, M. D., Watanabe, M., Wild, M. and Zhang, H.: The Earth's Energy Budget, Climate Feedbacks, and Climate Sensitivity. In Climate Change 2021: The Physical Science Basis. Contribution of Working Group I to the Sixth Assessment Report of the Intergovernmental Panel on Climate Change., 2021.

Fountoukis, C. and Nenes, A.: ISORROPIA II: a computationally efficient thermodynamic equilibrium model for K+–Ca2+–Mg2+–NH4+–Na+–SO42−–NO3−–Cl−–H2O aerosols, Atmos. Chem. Phys., 7(17), 4639–4659, doi:10.5194/acp-7-4639-2007, 2007.

Fowler, D., Flechard, C., Skiba, U., Coyle, M. and Cape, J. N.: The atmospheric budget of oxidized nitrogen and its role in ozone formation and deposition, New Phytol., 139(1), 11–23, doi:10.1046/j.1469-8137.1998.00167.x, 1998.

Fowler, D., Pilegaard, K., Sutton, M. A., Ambus, P., Raivonen, M., Duyzer, J., Simpson, D., Fagerli, H., Fuzzi, S., Schjoerring, J. K., Granier, C., Neftel, A., Isaksen, I. S. A., Laj, P., Maione, M., Monks, P. S., Burkhardt, J., Daemmgen, U., Neirynck, J., Personne, E., Wichink-Kruit, R., Butterbach-Bahl, K., Flechard, C., Tuovinen, J. P., Coyle, M., Gerosa, G., Loubet, B., Altimir, N., Gruenhage, L., Ammann, C., Cieslik, S., Paoletti, E., Mikkelsen, T. N., Ro-Poulsen, H., Cellier, P., Cape, J. N., Horváth, L., Loreto, F., Niinemets, Ü., Palmer, P. I., Rinne, J., Misztal, P., Nemitz, E., Nilsson, D., Pryor, S., Gallagher, M. W., Vesala, T., Skiba, U., Brüggemann, N., Zechmeister-Boltenstern, S., Williams, J., O'Dowd, C., Facchini, M. C., de Leeuw, G., Flossman, A., Chaumerliac, N. and Erisman, J. W.: Atmospheric composition change: Ecosystems-Atmosphere interactions, Atmos. Environ., 43(33), 5193–5267, doi:10.1016/j.atmosenv.2009.07.068, 2009.

Franche, C., Lindström, K. and Elmerich, C.: Nitrogen-fixing bacteria associated with leguminous and non-leguminous plants, Plant Soil, 321(1–2), 35–59, doi:10.1007/s11104-008-9833-8, 2009.

Fu, T., Cao, J. J., Zhang, X. Y., Lee, S. C., Zhang, Q., Han, Y. M., Qu, W. J., Han, Z., Zhang, R. and Wang, Y. X.: Carbonaceous aerosols in China: top-down constraints on primary sources and estimation of secondary contribution, Atmos. Chem. Phys., 12, 2725–2746, doi:10.5194/acp-12-2725-2012, 2012.

Fuller, E. N., Schettler, P. D. and Giddings, J. C.: A new method for prediction of binary gas-phase diffusion coefficients, Ind. Eng. Chem., 58(5), 18–27, doi:10.1021/ie50677a007, 1966.

Gallo, A., Farinha, A. S. F., Emwas, A. H., Santana, A., Nielsen, R. J., Goddard, W. A. and Mishra, H.: Reply to the ‘Comment on “The chemical reactions in electrosprays of water do not always correspond to those at the pristine air–water interface”’ by A. J. Colussi and S. Enami, Chem. Sci., 2019, 10, DOI: 10.1039/c9sc00991d, Chem. Sci., 10, 8256–8261, doi:10.1039/c9sc00991d, 2019a.

Gallo, A., Farinha, A. S. F., Dinis, M., Emwas, A. H., Santana, A., Nielsen, R. J., Goddard, W. A. and Mishra, H.: The chemical reactions in electrosprays of water do not always correspond to those at the pristine air-water interface, Chem. Sci., 10(9), 2566–2577, doi:10.1039/c8sc05538f, 2019b.

Ganor, E., Osetinsky, I., Stupp, A. and Alpert, P.: Increasing trend of African dust, over 49 years, in the eastern Mediterranean, J. Geophys. Res. Atmos., 115(7), 1–7, doi:10.1029/2009JD012500, 2010.

Gao, W. and Wesely, M. L.: Modeling Gaseous Dry Deposition Over Regional Scales with Satellite Observations--I. Model Development, Atmosperic Environ., 29(6), 727–737, 1995.

Gao, W., Wesely, M. L. and Doskey, P. V.: Numerical modeling of the turbulent diffusion and chemistry of NOx, O3, isoprene, and other reactive trace gases in and above a forest canopy, J. Geophys. Res., 98(D10), doi:10.1029/93jd01862, 1993.

Garratt, J. R.: Surface influence on vertical profiles in the atmospheric near-surface layer, Q. J. R. Meteorol. Soc., 96, 211–255, 1980.

Garratt, J. R.: The atmospheric boundary layer, edited by J. . Houghton, M. J. Rycroft, and A. J. Dessler, Cambridge University Press., 1992.

Gebler, A., Rienks, M. and Rennenberg, H.: NH3 and NO2 fluxes between beech trees and the atmosphere - Correlation with climatic and physiological parameters, New Phytol., 147(3), 539–560, doi:10.1046/j.1469-8137.2000.00712.x, 2000.

Geddes, J. A. and Martin, R. V.: Global deposition of total reactive nitrogen oxides from 1996 to 2014 constrained with satellite observations of NO2 columns, Atmos. Chem. Phys., 17(16), 10071–10091, doi:10.5194/acp-17-10071-2017, 2017.

Geddes, J. A. and Murphy, J. G.: Observations of reactive nitrogen oxide fluxes by eddy covariance above two midlatitude North American mixed hardwood forests, Atmos. Chem. Phys., 14(6), 2939–2957, doi:10.5194/acp-14-2939-2014, 2014.

Geddes, J. A., Heald, C. L., Silva, S. J. and Martin, R. V.: Land cover change impacts on atmospheric chemistry: Simulating projected large-scale tree mortality in the United States, Atmos. Chem. Phys., 16(4), 2323–2340, doi:10.5194/acp-16-2323-2016, 2016.

Gelaro, R., McCarty, W., Suárez, M. J., Todling, R., Molod, A., Takacs, L., Randles, C. A., Darmenov, A., Bosilovich, M. G., Reichle, R., Wargan, K., Coy, L., Cullather, R., Draper, C., Akella, S., Buchard, V., Conaty, A., da Silva, A. M., Gu, W., Kim, G. K., Koster, R., Lucchesi, R., Merkova, D., Nielsen, J. E., Partyka, G., Pawson, S., Putman, W., Rienecker, M., Schubert, S. D., Sienkiewicz, M. and Zhao, B.: The modern-era retrospective analysis for research and applications, version 2 (MERRA-2), J. Clim., 30(14), 5419–5454, doi:10.1175/JCLI-D-16-0758.1, 2017.

George, C., Strekowski, R. S., Kleffmann, J., Stemmler, K. and Ammann, M.: Photoenhanced uptake of gaseous NO2 on solid organic compounds: A photochemical source of HONO?, Faraday Discuss., 130(2), 195–210, doi:10.1039/b417888m, 2005.

Gerken, T., Chamecki, M. and Fuentes, J. D.: Air-Parcel Residence Times Within Forest Canopies, Bound. Layer Meteorol., 165, 29–54, 2017.

Geßler, A., Rienks, M., Rennenberg, H. and Geßler, A.: Stomatal uptake and cuticular adsorption contribute to dry deposition of NH 3 and NO 2 to needles of adult spruce ( Picea abies ) trees, New Phytol., 156, 179–194, 2002.

Giglio, L., Randerson, J. T. and Van Der Werf, G. R.: Analysis of daily, monthly, and annual burned area using the fourth-generation global fire emissions database (GFED4), J. Geophys. Res. Biogeosciences, 118(1), 317–328, doi:10.1002/jgrg.20042, 2013.

Gligorovski, S., Strekowski, R., Barbati, S. and Vione, D.: Environmental Implications of Hydroxyl Radicals (•OH), Chem. Rev., 115(24), 13051–13092, doi:10.1021/cr500310b, 2015.

Gonçalves, M., Dabdub, D., Chang, W. L., Jorba, O. and Baldasano, J. M.: Impact of HONO sources on the performance of mesoscale air quality models, Atmos. Environ., 54(2), 168–176, doi:10.1016/j.atmosenv.2012.02.079, 2012.

Goodhill, V.: Maimonides--modern medical relevance, Trans Am Acad Ophthalmol Otolaryngol, 75(3), 463, 1971.

Goulden, M. L., Munger, J. W., Fan, S. M., Daube, B. C. and Wofsy, S. C.: Measurements of carbon sequestration by long-term eddy covariance: Methods and a critical evaluation of accuracy, Glob. Chang. Biol., 2(3), 169–182, doi:10.1111/j.1365-2486.1996.tb00070.x, 1996.

Grachev, A. A., Fairall, C. W. and Bradley, E. F.: Convective profile constants revisited, Boundary-Layer Meteorol., 94(3), 495–515, doi:10.1023/A:1002452529672, 2000.

Grantz, D. A., Zinsmeister, D. and Burkhardt, J.: Ambient aerosol increases minimum leaf conductance and alters the aperture – flux relationship as stomata respond to vapor pressure deficit ( VPD ), New Phytol., 219, 275–286, doi:10.1111/nph.15102, 2018.

Greenhalgh, T., Jimenez, J. L., Prather, K. A., Tufekci, Z., Fisman, D. and Schooley, R.: Ten scientific reasons in support of airborne transmission of SARS-CoV-2, Lancet, 397(10285), 1603–1605, doi:10.1016/S0140-6736(21)00869-2, 2021.

Grøntoft, T. and Raychaudhuri, M. R.: Compilation of tables of surface deposition velocities for O3, NO2 and SO2 to a range of indoor surfaces, Atmos. Environ., 38(4), 533–544, doi:10.1016/j.atmosenv.2003.10.010, 2004.

Gu, W., Cheng, P. and Tang, M.: Compilation and evaluation of gas phase diffusion coefficients of halogenated organic compounds, R. Soc. Open Sci., 5(7), doi:10.1098/rsos.171936, 2018.

Guenther, A. B., Jiang, X., Heald, C. L., Sakulyanontvittaya, T., Duhl, T., Emmons, L. K. and Wang, X.: The model of emissions of gases and aerosols from nature version 2.1 (MEGAN2.1): An extended and updated framework for modeling biogenic emissions, Geosci. Model Dev., 5(6), 1471–1492, doi:10.5194/gmd-5-1471-2012, 2012.

Haghighi, E. and Or, D.: Linking evaporative fluxes from bare soil across surface viscous sublayer with the Monin-Obukhov atmospheric flux-profile estimates, J. Hydrol., 525, 684–693, doi:10.1016/j.jhydrol.2015.04.019, 2015.

Halios, C. H. and Barlow, J. F.: Observations of the Morning Development of the Urban Boundary Layer Over London, UK, Taken During the ACTUAL Project, Boundary-Layer Meteorol., 166(3), 395–422, doi:10.1007/s10546-017-0300-z, 2018.

Hammer, M. S., Van Donkelaar, A., Li, C., Lyapustin, A., Sayer, A. M., Hsu, N. C., Levy, R. C., Garay, M. J., Kalashnikova, O. V., Kahn, R. A., Brauer, M., Apte, J. S., Henze, D. K., Zhang, L., Zhang, Q., Ford, B., Pierce, J. R. and Martin, R. V.: Global Estimates and Long-Term Trends of Fine Particulate Matter Concentrations (1998-2018), Environ. Sci. Technol., 54(13), 7879–7890, doi:10.1021/acs.est.0c01764, 2020.

Hanson, P. J. and Linderg, S. E.: Dry Deposition of Reactive Nitrogen Compounds: A Review of Leaf, Canopy AND Non-Foliar Measurements, Atmos. Eniviron., 25A, 1615–1634, 1991.

Hanson, P. J., Rott, K., Taylor, G. E., Gunderson, C. A., Lindberg, S. E. and Ross-Todd, B. M.: NO2 Deposition to Elements Representative of a Forest Landscape, Atmos. Environ., 23, 1783–1794, 1989.

Hardacre, C., Wild, O. and Emberson, L.: An evaluation of ozone dry deposition in global scale chemistry climate models, Atmos. Chem. Phys., 15(11), 6419–6436, doi:10.5194/acp-15-6419-2015, 2015.

Harman, I. N. and Finnigan, J. J.: A simple unified theory for flow in the canopy and roughness sublayer, Boundary-Layer Meteorol., 123(2), 339–363, doi:10.1007/s10546-006-9145-6, 2007.

Harrison, R. M. and Kitto, A. N.: Evidence for a surface source of atmospheric nitrous acid, Atmos. Eniviron., 28A, 1089–1094, 1994.

Harrison, R. M., Peak, J. D. and Collins, G. M.: Tropospheric cycle of nitrous acid, , 101(2), 1996.

He, Y., Zhou, X., Hou, J., Gao, H. and Bertman, S. B.: Importance of dew in controlling the air-surface exchange of HONO in rural forested environments, Geophys. Res. Lett., 33(2), 2–5, doi:10.1029/2005GL024348, 2006.

Heald, C. L., Ridley, D. A., Kreidenweis, S. M. and Drury, E. E.: Satellite observations cap the atmospheric organic aerosol budget, Geophys. Res. Lett., 37(24), 1–5, doi:10.1029/2010GL045095, 2010.

Heald, C. L., Coe, H., Jimenez, J. L., Weber, R. J., Bahreini, R., Middlebrook, A. M., Russell, L. M., Jolleys, M., Fu, T. M., Allan, J. D., Bower, K. N., Capes, G., Crosier, J., Morgan, W. T., Robinson, N. H., Williams, P. I., Cubison, M. J., Decarlo, P. F. and Dunlea, E. J.: Exploring the vertical profile of atmospheric organic aerosol: Comparing 17 aircraft field campaigns with a global model, Atmos. Chem. Phys., 11(24), 12676–12696, doi:10.5194/acp-11-12673-2011, 2011.

Heald, C. L., Collett, J. L., Lee, T., Benedict, K. B., Schwandner, F. M., Li, Y., Clarisse, L., Hurtmans, D. R., Van Damme, M., Clerbaux, C., Coheur, P. F., Philip, S., Martin, R. V. and Pye, H. O. T.: Atmospheric ammonia and particulate inorganic nitrogen over the United States, Atmos. Chem. Phys., 12(21), 10295–10312, doi:10.5194/acp-12-10295-2012, 2012.

Health Effects Institute: State of Global Air 2020. Special Report., Boston, MA. [online] Available from: https://www.stateofglobalair.org/resources, 2020.

Held, T., Chang, D. P. Y. and Niemeier, D. A.: UCD 2001: An improved model to simulate pollutant dispersion from roadways, Atmos. Environ., 37(38), 5325–5336, doi:10.1016/j.atmosenv.2003.09.015, 2003.

Henze, D. K., Seinfeld, J. H., Ng, N. L., Kroll, J. H., Fu, T., Jacob, D. J. and Heald, C. L.: and Physics Global modeling of secondary organic aerosol formation from aromatic hydrocarbons : high- vs . low-yield pathways, Atmos. Chem. Phys., 8, 2405–2421, 2008.

Hesterberg, R., Blatter, F. M., Rosset, M., Neftel, A., Eugster, W. and Wanner, H.: Deppsotion of Nitrogen-Containing Compounds to an Extensively Managed Grassland in Central Switzerland, Environ. Pollut., 91(1), 21–34, 1996.

Hilboll, A., Richter, A. and Burrows, J. P.: Long-term changes of tropospheric NO2 over megacities derived from multiple satellite instruments, Atmos. Chem. Phys., 13(8), 4145–4169, doi:10.5194/acp-13-4145-2013, 2013.

Hodnebrog, O., Myhre, G., Samset, B. H., Alterskjær, K., Andrews, T., Boucher, O., Faluvegi, G., Fläschner, D., M Forster, P., Kasoar, M., Kirkeväg, A., Lamarque, J. F., Olivié, D., B Richardson, T., Shawki, D., Shindell, D., P Shine, K., Stier, P., Takemura, T., Voulgarakis, A. and Watson-Parris, D.: Water vapour adjustments and responses differ between climate drivers, Atmos. Chem. Phys., 19(20), 12887–12899, doi:10.5194/acp-19-12887-2019, 2019.

Holmes, C. D., Bertram, T. H., Confer, K. L., Graham, K. A., Ronan, A. C., Wirks, C. K. and Shah, V.: The Role of Clouds in the Tropospheric NOx Cycle: A New Modeling Approach for Cloud Chemistry and Its Global Implications, Geophys. Res. Lett., 46(9), 4980–4990, doi:10.1029/2019GL081990, 2019.

Holtslag, A. A. M. and Boville, B. A.: Local Versus Nonlocal Boundary-Layer Diffusion in a Global Climate Model, J. Clim., 6, 1825–1841, 1993.

Holtslag, A. A. M. and Bruin, H. A. R.: Applied Modeling of the Nighttime Surface Energy Balance over Land, J. Appl. Meteorol., 27, 689–703, 1988.

Holtslag, A. A. M., De Bruijn, E. I. F. and Pan, H. L.: A High Resolution Air Mass Transformation Model for Short-Range Weather Forecasting, Mon. Weather Rev., 118, 1561–1575, 1990.

Horii, C. V.: Tropospheric reactive nitrogen speciation, deposition, and chemistry at Harvard Foreset, Harvard University., 2002.

Horii, C. V., Munger, J. W., Wofsy, S. C., Zahniser, M., Nelson, D. and McManus, J. B.: Fluxes of nitrogen oxides over a temperate deciduous forest, J. Geophys. Res. D Atmos., 109(8), doi:10.1029/2003JD004326, 2004.

Horii, C. V., Munger, J. W., Wofsy, S. C., Zahniser, M., Nelson, D. and Mcmanus, J. B.: Atmospheric reactive nitrogen concentration and flux budgets at a Northeastern U . S . forest site, Agric. For. Meteorol., 133, 210–225, doi:10.1016/j.agrformet.2006.03.005, 2005.

Hsu, N. C., Gautam, R., Sayer, A. M., Bettenhausen, C., Li, C., Jeong, M. J., Tsay, S. C. and Holben, B. N.: Global and regional trends of aerosol optical depth over land and ocean using SeaWiFS measurements from 1997 to 2010, Atmos. Chem. Phys., 12(17), 8037–8053, doi:10.5194/acp-12-8037-2012, 2012.

Hsu, N. C., Jeong, M. J., Bettenhausen, C., Sayer, A. M., Hansell, R., Seftor, C. S., Huang, J. and Tsay, S. C.: Enhanced Deep Blue aerosol retrieval algorithm: The second generation, J. Geophys. Res. Atmos., 118(16), 9296–9315, doi:10.1002/jgrd.50712, 2013.

Hu, X., Waller, L. A., Lyapustin, A., Wang, Y. and Liu, Y.: 10-year spatial and temporal trends of PM2.5 concentrations in the southeastern US estimated using high-resolution satellite data, Atmos. Chem. Phys., 14(12), 6301–6314, doi:10.5194/acp-14-6301-2014, 2014.

Huang, Y., Mahrt, F., Xu, S., Shiraiwa, M., Zuend, A. and Bertram, A. K.: Coexistence of three liquid phases in individual atmospheric aerosol particles, Proc. Natl. Acad. Sci. U. S. A., 118(16), doi:10.1073/pnas.2102512118, 2021.

Hudman, R. C., Moore, N. E., Mebust, A. K., Martin, R. V., Russell, A. R., Valin, L. C. and Cohen, R. C.: Steps towards a mechanistic model of global soil nitric oxide emissions: Implementation and space based-constraints, Atmos. Chem. Phys., 12(16), 7779–7795, doi:10.5194/acp-12-7779-2012, 2012.

IARC: Outdoor Air Pollution a Leading Environmental Cause of Cancer Deaths., 2013.

Ichoku, C. and Ellison, L.: Global top-down smoke-aerosol emissions estimation using satellite fire radiative power measurements, Atmos. Chem. Phys., 14(13), 6643–6667, doi:10.5194/acp-14-6643-2014, 2014.

Jacob, D.: Introduction to Atmospheric Chemistry, Princeton University Press, Princeton, New Jersey., 1999.

Jacob, D. J.: Heterogeneous chemistry and tropospheric ozone, Atmos. Environ., 34(12–14), 2131–2159, doi:10.1016/S1352-2310(99)00462-8, 2000.

Jacob, D. J. and Wofsy, S. C.: Budgets of reactive nitrogen, hydrocarbons, and ozone over the Amazon forest during the wet season, J. Geophys. Res., 95(D10), doi:10.1029/jd095id10p16737, 1990.

Jacob, D. J., Fan, S., Wofsy, S. C., Spiro, P. A., Bakwin, P. S., Fitzjarrald, D. R. and Moore, K. E.: Deposition of Ozone to Tundra, J. Geophys. Res., 97, 473–479, 1992a.

Jacob, D. J., Wofsy, S. C., Bakwin, P. S. and et al.: Summertime Photochemistry of the Troposphere at High Northern Latitudes, J. Geophys. R, 97(15), 16421–16431, 1992b.

Jacob, D. J., Liu, H. and Yantosca, R. M.: Harvard wet deposition scheme for GMI. [online] Available from: http://acmg.seas.harvard.edu/geos/wiki_docs/deposition/wetdep.jacob_etal_2000.pdf, 2000.

Jacob, J., Horowitz, W., William, J., Heikes, G., Dickerson, R., Artz, S. and Keene, W. C.: Conditions for ozone production over the easte United States in September oxides, J. Geogr. Res., 100, 9315–9324, 1995.

Jaeglé, L., Quinn, P. K., Bates, T. S., Alexander, B. and Lin, J. T.: Global distribution of sea salt aerosols: New constraints from in situ and remote sensing observations, Atmos. Chem. Phys., 11(7), 3137–3157, doi:10.5194/acp-11-3137-2011, 2011.

Jaeglé, L., Shah, V., Thornton, J. A., Lopez-hil, F. D., Lee, B. H. and Mcduf, E. E.: Nitrogen Oxides Emissions , Chemistry , Deposition , and Export Over the Northeast United States During the WINTER Aircraft Campaign, J. Geogr. Res. Atmos., 123, 12368–12393, doi:10.1029/2018JD029133, 2018.

Jenkin, M. E., Utembe, S. R. and Derwent, R. G.: Modelling the impact of elevated primary NO2 and HONO emissions on regional scale oxidant formation in the UK, Atmos. Environ., 42(2), 323–336, doi:10.1016/j.atmosenv.2007.09.021, 2008.

Jimenez, J. L., Marr, L. C., Randall, K., Ewing, E. T., Tufekci, Z., Greenhalgh, T., Hegarty, O., Dancer, S. J., Bluyssen, P. M., Buonanno, G., Loomans, M., Yao, M., Wargocki, P., Melikov, A. K., Prather, K. A., Tellier, R., Tang, J., Li, Y., Morawska, L. and Fisman, D.: Echoes Through Time: The Historical Origins of the Droplet Dogma and its Role in the Misidentification of Airborne Respiratory Infection Transmission, Submitt. Prepr., doi:10.2139/ssrn.3904176, 2021.

Jiménez, P. A., Dudhia, J., González-Rouco, J. F., Navarro, J., Montávez, J. P. and García-Bustamante, E.: A revised scheme for the WRF surface layer formulation, Mon. Weather Rev., 140(3), 898–918, doi:10.1175/MWR-D-11-00056.1, 2012.

Jin, X., Jin, X., Fiore, A., Fiore, A., Boersma, K. F., Boersma, K. F., Smedt, I. De and Valin, L.: Inferring Changes in Summertime Surface Ozone-NOx-VOC Chemistry over U.S. Urban Areas from Two Decades of Satellite and Ground-Based Observations, Environ. Sci. Technol., 54(11), 6518–6529, doi:10.1021/acs.est.9b07785, 2020.

Johnson, M. S., Meskhidze, N., Solmon, F., Gassó, S., Chuang, P. Y., Gaiero, D. M., Yantosca, R. M., Wu, S., Wang, Y. and Carouge, C.: Modeling dust and soluble iron deposition to the South Atlantic Ocean, J. Geophys. Res. Atmos., 115(15), 1–13, doi:10.1029/2009JD013311, 2010.

Johnson, M. T.: A numerical scheme to calculate temperature and salinity dependent air-water transfer velocities for any gas, Ocean Sci., 6(4), 913–932, doi:10.5194/os-6-913-2010, 2010.

Kahn, R., Li, W. H., Martonchik, J. V., Bruegge, C. J., Diner, D. J., Gaitley, B. J., Abdou, W., Dubovik, O., Holben, B., Smirnov, A., Jin, Z. and Clark, D.: MISR calibration and implications for low-light-level aerosol retrieval over dark water, J. Atmos. Sci., 62(4), 1032–1052, doi:10.1175/JAS3390.1, 2005.

Kaimal, J. C. and Finnigan, J. .: Atmospheric Boundary Layer Flows, Their Structure and Measurement, Oxford University Press., 1994.

Kanakidou, M., Seinfeld, J. H., Pandis, S. N., Barnes, I., Dentener, F. J., Facchini, M. C., Van Dingenen, R., Ervens, B., Nenes, A., Nielsen, C. J., Swietlicki, E., Putaud, J. P., Balkanski, Y., Fuzzi, S., Horth, J., Moortgat, G. K., Winterhalter, R., Myhre, C. E. L., Tsigaridis, K., Vignati, E., Stephanou, E. G. and Wilson, J.: Organic aerosol and global climate modelling: a review, Atmos. Chem. Phys., 5(4), 1053–1123, doi:10.5194/acp-5-1053-2005, 2005.

Kanaya, Y., Cao, R., Akimoto, H., Fukuda, M., Komazaki, Y., Yokouchi, Y., Koike, M., Tanimoto, H., Takegawa, N. and Kondo, Y.: Urban photochemistry in central Tokyo: 1. Observed and modeled OH and HO2 radical concentrations during the winter and summer of 2004, J. Geophys. Res. Atmos., 112(21), doi:10.1029/2007JD008670, 2007.

Karamchandani, P., Emery, C., Yarwood, G., Lefer, B., Stutz, J., Couzo, E. and Vizuete, W.: Implementation and refinement of a surface model for heterogeneous HONO formation in a 3-D chemical transport model, Atmos. Environ., 112, 356–368, doi:10.1016/j.atmosenv.2015.01.046, 2015.

Kasibhatla, P., Sherwen, T., Evans, M. J., Carpenter, L. J., Reed, C., Alexander, B., Chen, Q., Sulprizio, M. P., Lee, J. D., Read, K. A., Bloss, W., Crilley, L. R., Keene, W. C., Pszenny, A. A. P. and Hodzic, A.: Global impact of nitrate photolysis in sea-salt aerosol on NOx, OH, and O3 in the marine boundary layer, Atmos. Chem. Phys., 18(15), 11185–11203, doi:10.5194/acp-18-11185-2018, 2018.

Kavassalis, S. C. and Murphy, J. G.: Understanding ozone-meteorology correlations: A role for dry deposition, Geophys. Res. Lett., 44(6), 2922–2931, doi:10.1002/2016GL071791, 2017.

Keller, C. A., Long, M. S., Yantosca, R. M., Da Silva, A. M., Pawson, S. and Jacob, D. J.: HEMCO v1.0: A versatile, ESMF-compliant component for calculating emissions in atmospheric models, Geosci. Model Dev., 7(4), 1409–1417, doi:10.5194/gmd-7-1409-2014, 2014.

Kenagy, H. S., Sparks, T. L., Ebben, C. J., Wooldrige, P. J., Lopez-Hilfiker, F. D., Lee, B. H., Thornton, J. A., McDuffie, E. E., Fibiger, D. L., Brown, S. S., Montzka, D. D., Weinheimer, A. J., Schroder, J. C., Campuzano-Jost, P., Day, D. A., Jimenez, J. L., Dibb, J. E., Campos, T., Shah, V., Jaeglé, L. and Cohen, R. C.: NOx Lifetime and NOy Partitioning During WINTER, J. Geophys. Res. Atmos., 123(17), 9813–9827, doi:10.1029/2018JD028736, 2018.

Kharol, S. K., Shephard, M. W., McLinden, C. A., Zhang, L., Sioris, C. E., O'Brien, J. M., Vet, R., Cady-Pereira, K. E., Hare, E., Siemons, J. and Krotkov, N. A.: Dry Deposition of Reactive Nitrogen From Satellite Observations of Ammonia and Nitrogen Dioxide Over North America, Geophys. Res. Lett., 45(2), 1157–1166, doi:10.1002/2017GL075832, 2018.

Kim, P. S., Jacob, D. J., Fisher, J. A., Travis, K., Yu, K., Zhu, L., Yantosca, R. M., Sulprizio, M. P., Jimenez, J. L., Campuzano-Jost, P., Froyd, K. D., Liao, J., Hair, J. W., Fenn, M. A., Butler, C. F., Wagner, N. L., Gordon, T. D., Welti, A., Wennberg, P. O., Crounse, J. D., St. Clair, J. M., Teng, A. P., Millet, D. B., Schwarz, J. P., Markovic, M. Z. and Perring, A. E.: Sources, seasonality, and trends of southeast US aerosol: An integrated analysis of surface, aircraft, and satellite observations with the GEOS-Chem chemical transport model, Atmos. Chem. Phys., 15(18), 10411–10433, doi:10.5194/acp-15-10411-2015, 2015.

Kim, S., Vandenboer, T. C., Young, C. J., Riedel, T. P., Thornton, J. A. and et al.: The primary and recycling sources of OH during the NACHTT-2011 campaign: HONO as an important OH primary source in the wintertime Saewung, J. Geophys. Res., 3(3), 180–198, doi:10.1002/2013JD021040.Received, 2014.

Kim, S. K. and Kang, H.: Efficient conversion of nitrogen dioxide into nitrous acid on ice surfaces, J. Phys. Chem. Lett., 1(20), 3085–3089, doi:10.1021/jz1011669, 2010.

Kinugawa, T., Enami, S., Yabushita, A., Kawasaki, M., Hoffmann, M. R. and Colussi, A. J.: Conversion of gaseous nitrogen dioxide to nitrate and nitrite on aqueous surfactants, Phys. Chem. Chem. Phys., 13(11), 5144–5149, doi:10.1039/c0cp01497d, 2011.

Kleffmann, J., Becker, K. H. and Wiesen, P.: Investigation of the heterogeneous NO2 conversion on perchloric acid surfaces, J. Chem. Soc. - Faraday Trans., 94(21), 3289–3292, doi:10.1039/a805440a, 1998.

Kleffmann, J., Kurtenbach, R., Lörzer, J., Wiesen, P., Kalthoff, N., Vogel, B. and Vogel, H.: Measured and simulated vertical profiles of nitrous acid - Part I: Field measurements, Atmos. Environ., 37(21), 2949–2955, doi:10.1016/S1352-2310(03)00242-5, 2003.

Kleinman, L. I.: Seasonal dependence of boundary layer peroxide concentration: the low and high NOx regimes, J. Geophys. Res., 96(D11), 721–733, doi:10.1029/91jd02040, 1991.

Kley, D., Grutzen, P. J., Smit, H. G. J., Vömel, H., Oltmans, S. J., Grassl, H. and Ramanathan, V.: Observations of near-zero ozone concentrations over the convective Pacific: Effects on air chemistry, Science (80-. )., 274(5285), 230–233, doi:10.1126/science.274.5285.230, 1996.

Klimont, Z., Smith, S. J. and Cofala, J.: The last decade of global anthropogenic sulfur dioxide: 2000-2011 emissions, Environ. Res. Lett., 8(1), doi:10.1088/1748-9326/8/1/014003, 2013.

Klompas, M., Milton, D. K., Rhee, C. and Baker, M.: Current Insights Into Respiratory Virus Transmission and Potential Implications for Infection Control Programs, Ann. Intern. Med., doi:10.7326/M21-2780, 2021.

Koren, I., Remer, L. A. and Longo, K.: Reversal of trend of biomass burning in the Amazon, Geophys. Res. Lett., 34(20), 2–5, doi:10.1029/2007GL031530, 2007.

Kraabøl, A. G., Berntsen, T. K., Sundet, J. K. and Stordal, F.: Impacts of NOx emissions from subsonic aircraft in a global three-dimensional chemistry transport model including plume processes, J. Geophys. Res. Atmos., 107(22), doi:10.1029/2001JD001019, 2002.

Kraus, A. and Hofzumahaus, A.: Field Measurements of Atmospheric Photolysis Frequencies for O3,NO2, HCHO, CH3CHO, H2O2, and HONO by UV Spectroradiometry A., J. Atmos. Chem., 31(2), 161–180, 1998.

Kuhns, H., Knipping, E. M. and Vukovich, J. M.: Development of a United States-Mexico emissions inventory for the Big Bend Regional Aerosol and Visibility Observational (BRAVO) Study, J. Air Waste Manage. Assoc., 55, 677–692, 2005.

Kurtenbach, R., Becker, K. H., Gomes, J. A. G., Kleffmann, J., Lörzer, J. C., Spittler, M., Wiesen, P., Ackermann, R., Geyer, A. and Platt, U.: Investigations of emissions and heterogeneous formation of HONO in a road traffic tunnel, Atmos. Environ., 35(20), 3385–3394, doi:10.1016/S1352-2310(01)00138-8, 2001.

Lamaud, E., Loubet, B., Irvine, M., Stella, P., Personne, E. and Cellier, P.: Partitioning of ozone deposition over a developed maize crop between stomatal and non-stomatal uptakes, using eddy-covariance flux measurements and modelling, Agric. For. Meteorol., 149(9), 1385–1396, doi:10.1016/j.agrformet.2009.03.017, 2009.

Lammel, G.: Formation of nitrous acid: Parameterization and comparison with observations, Hamburg, Germany., 1999.

Lammel, G. and Cape, J. N.: Nitrous acid and nitrite in the atmosphere, Chem. Soc. Rev., 25(5), 361–369, doi:10.1039/cs9962500361, 1996.

Lamsal, L. N., Martin, R. V, Padmanabhan, A., Donkelaar, A. Van, Zhang, Q., Sioris, C. E., Chance, K., Kurosu, T. P. and Newchurch, M. J.: Application of satellite observations for timely updates to global anthropogenic NOx emission inventories, Geophys. Res. Lett., 38, L05810, doi:10.1029/2010GL046476, 2011.

Langenberg, S., Carstens, T., Hupperich, D., Schweighoefer, S. and Schurath, U.: Technical note: Determination of binary gas-phase diffusion coefficients of unstable and adsorbing atmospheric trace gases at low temperature – arrested flow and twin tube method, Atmos. Chem. Phys., 20(6), 3669–3682, doi:10.5194/acp-20-3669-2020, 2020.

Lassman, W., Collett, J. L., Ham, J. M., Yalin, A. P., Shonkwiler, K. B. and Pierce, J. R.: Exploring new methods of estimating deposition using atmospheric concentration measurements: A modeling case study of ammonia downwind of a feedlot, Agric. For. Meteorol., 290(May), doi:10.1016/j.agrformet.2020.107989, 2020.

Laufs, S. and Kleffmann, J.: Investigations on HONO formation from photolysis of adsorbed HNO3 on quartz glass surfaces, Phys. Chem. Chem. Phys., 18, 9616–9625, doi:10.1039/C6CP00436A, 2016.

Laufs, S., Cazaunau, M., Stella, P., Kurtenbach, R., Cellier, P., Mellouki, A., Loubet, B. and Kleffmann, J.: Diurnal fluxes of HONO above a crop rotation, Atmos. Chem. Phys., 17(11), 6907–6923, doi:10.5194/acp-17-6907-2017, 2017.

Laughner, J. L. and Cohen, R. C.: Direct observation of changing NOx Lifetime in North American cities, Science (80-. )., 727(x), 723–727, 2019.

Lee, C. J., Martin, R. V., Henze, D. K., Brauer, M., Cohen, A. and Donkelaar, A. Van: Response of global particulate-matter-related mortality to changes in local precursor emissions, Environ. Sci. Technol., 49(7), 4335–4344, doi:10.1021/acs.est.5b00873, 2015.

Lee, H.: Development and Field-Deployment of an Absorption Spectrometer to Measure Atmospheric HONO and NO2, Harvard University., 2012.

Lee, H. J., Liu, Y., Coull, B. A., Schwartz, J. and Koutrakis, P.: A novel calibration approach of MODIS AOD data to predict PM2.5 concentrations, Atmos. Chem. Phys., 11(15), 7991–8002, doi:10.5194/acp-11-7991-2011, 2011.

Lee, Y. N. and Schwartz, S. E.: Reaction kinetics of nitrogen dioxide with liquid water at low partial pressure, J. Phys. Chem., 85(7), 840–848, doi:10.1021/j150607a022, 1981.

Leibensperger, E. M., Mickley, L. J., Jacob, D. J., Chen, W. T., Seinfeld, J. H., Nenes, A., Adams, P. J., Streets, D. G., Kumar, N. and Rind, D.: Climatic effects of 1950-2050 changes in US anthropogenic aerosols-Part 1: Aerosol trends and radiative forcing, Atmos. Chem. Phys., 12(7), 3333–3348, doi:10.5194/acp-12-3333-2012, 2012.

Lerdau, M. T., Munger, J. W. and Jacob, D. J.: The NO2 flux conundrum, Science (80-. )., 289(5488), 2291–2293, doi:10.1126/science.289.5488.2291, 2000.

Levy, H.: Normal Atmosphere : Large Radical and Formaldehyde Concentrations, Science (80-. )., 173(3992), 141–143, 1971.

Levy, R., Leptoukh, G., Kahn, R., Zubko, V., Gopalan, A. and Remer, L.: A Critical Look at Deriving Monthly Aerosol Optical Depth From Satellite Data, IEEE Trans. Geosci. Remote Sens., 47(8), 2942–2956, 2009.

Levy, R. C., Mattoo, S., Munchak, L. A., Remer, L. A., Sayer, A. M., Patadia, F. and Hsu, N. C.: The Collection 6 MODIS aerosol products over land and ocean, Atmos. Meas. Tech., 6(11), 2989–3034, doi:10.5194/amt-6-2989-2013, 2013.

Leys, C., Ley, C., Klein, O., Bernard, P. and Licata, L.: Detecting outliers: Do not use standard deviation around the mean, use absolute deviation around the median, J. Exp. Soc. Psychol., 49(4), 764–766, doi:10.1016/j.jesp.2013.03.013, 2013.

Li, G., Lei, W., Zavala, M., Volkamer, R., Dusanter, S., Stevens, P. and Molina, L. T.: Impacts of HONO sources on the photochemistry in Mexico City during the MCMA-2006/MILAGO Campaign, Atmos. Chem. Phys., 10(14), 6551–6567, doi:10.5194/acp-10-6551-2010, 2010.

Li, M., Zhang, Q., Kurokawa, J., Woo, J.-H., He, K. B., Lu, Z., Ohara, T., Song, Y., Streets, D. G., Carmichael, G. R., Cheng, Y. F., Hong, C. P., Huo, H., Jiang, X. J., Kang, S. C., Liu, F., Su, H. and Zheng, B.: MIX: a mosaic Asian anthropogenic emission inventory for the MICS-Asia and the HTAP projects, Atmos. Chem. Phys. Discuss., 15, 34813–34869, doi:10.5194/acpd-15-34813-2015, 2015.

Li, X., Brauers, T., Häseler, R., Bohn, B., Fuchs, H., Hofzumahaus, A., Holland, F., Lou, S., Lu, K. D., Rohrer, F., Hu, M., Zeng, L. M., Zhang, Y. H., Garland, R. M., Su, H., Nowak, A., Wiedensohler, A., Takegawa, N., Shao, M. and Wahner, A.: Exploring the atmospheric chemistry of nitrous acid (HONO) at a rural site in Southern China, Atmos. Chem. Phys., 12(3), 1497–1513, doi:10.5194/acp-12-1497-2012, 2012.

Li, Y., An, J., Min, M., Zhang, W., Wang, F. and Xie, P.: Impacts of HONO sources on the air quality in Beijing, Tianjin and Hebei Province of China, Atmos. Environ., 45(27), 4735–4744, doi:10.1016/j.atmosenv.2011.04.086, 2011.

Liao, H., Henze, D. K., Seinfeld, J. H., Wu, S. and Mickley, L. J.: Biogenic secondary organic aerosol over the United States : Comparison of climatological simulations with observations, J. Geogr. Res., 112, D06201, doi:10.1029/2006JD007813, 2007.

Lim, S. S., Vos, T., Flaxman, A. D., Danaei, G., Shibuya, K., Adair-Rohani, H., Almazroa, M. and et al.: A comparative risk assessment of burden of disease and injury attributable to 67 risk factors and risk factor clusters in 21 regions, 1990−2010: A systematic analysis for the Global Burden of Disease Study 2010, Lancet, 380(9859), 2224–2260, doi:10.1016/S0140-6736(12)61766-8.A, 2012.

Lin, J. T. and McElroy, M. B.: Impacts of boundary layer mixing on pollutant vertical profiles in the lower troposphere: Implications to satellite remote sensing, Atmos. Environ., 44(14), 1726–1739, doi:10.1016/j.atmosenv.2010.02.009, 2010.

Liu, H.-Y., Jacob, D. J., Bey, I. and Yantosca, R. M.: Constraints Pb-210 and Be-7 on Wet Deposition and Transport in a Global Three-Dimensional Chemical Tracer Model Driven by Assimilated Meteorological Fields, J. Geophys. Res., 106(D11), 12,109-12,12, doi:10.1029/2000JD900839, 2001.

Liu, Y., Park, R. J., Jacob, D. J., Li, Q., Kilaru, V. and Sarnat, J. A.: Mapping annual mean ground-level PM2.5 concentrations using Multiangle Imaging Spectroradiometer aerosol optical thickness over the contiguous United States, J. Geophys. Res. D Atmos., 109(22), 1–10, doi:10.1029/2004JD005025, 2004.

Liu, Y., Lu, K., Li, X., Dong, H., Tan, Z., Wang, H., Zou, Q., Wu, Y., Zeng, L., Hu, M., Min, K. E., Kecorius, S., Wiedensohler, A. and Zhang, Y.: A Comprehensive Model Test of the HONO Sources Constrained to Field Measurements at Rural North China Plain, Environ. Sci. Technol., 53(7), 3517–3525, doi:10.1021/acs.est.8b06367, 2019.

Lu, Z., Zhang, Q. and Streets, D. G.: Sulfur dioxide and primary carbonaceous aerosol emissions in China and India, 1996-2010, Atmos. Chem. Phys., 11, 9839–9864, 2011.

Lucchesi, R.: File Specification for GEOS-5 FP. GMAO Office Note No. 4(Version1.0)., 2013.

Luo, G., Yu, F. and Schwab, J.: Revised treatment of wet scavenging processes dramatically improves GEOS-Chem 12 . 0 . 0 simulations of surface nitric acid , nitrate , and ammonium over the United States, Geosci. Model Dev., 12(2012), 3439–3447, doi:10.5194/gmd-12-3439-2019, 2019.

Luo, G., Yu, F. and Moch, J. M.: Further improvement of wet process treatments in GEOS-Chem v12.6.0: Impact on global distributions of aerosols and aerosol precursors, Geosci. Model Dev., 13(6), 2879–2903, doi:10.5194/gmd-13-2879-2020, 2020.

MacMartin, D. G. and Kravitz, B.: Mission-driven research for stratospheric aerosol geoengineering, Proc. Natl. Acad. Sci. U. S. A., 116(4), 1089–1094, doi:10.1073/pnas.1811022116, 2019.

Mahowald, N. M., Scanza, R., Brahney, J., Goodale, C. L., Hess, P. G., Moore, J. K. and Neff, J.: Aerosol Deposition Impacts on Land and Ocean Carbon Cycles, Curr. Clim. Chang. Reports, 3(1), 16–31, doi:10.1007/s40641-017-0056-z, 2017.

Malley, C. S., Henze, D. K., Kuylenstierna, J. C. I., Vallack, H. W., Davila, Y., Anenberg, S. C., Turner, M. C. and Ashmore, M. R.: Updated global estimates of respiratory mortality in adults ≥ 30 years of age attributable to long-term ozone exposure, Environ. Health Perspect., 125(8), 1–9, doi:10.1289/EHP1390, 2017.

Mao, J., Jacob, D. J., Evans, M. J., Olson, J. R., Ren, X., Brune, W. H., St. Clair, J. M., Crounse, J. D., Spencer, K. M., Beaver, M. R., Wennberg, P. O., Cubison, M. J., Jimenez, J. L., Fried, A., Weibring, P., Walega, J. G., Hall, S. R., Weinheimer, A. J., Cohen, R. C.,

Chen, G., Crawford, J. H., McNaughton, C., Clarke, A. D., Jaeglé, L., Fisher, J. A., Yantosca, R. M., Le Sager, P. and Carouge, C.: Chemistry of hydrogen oxide radicals (HOx) in the Arctic troposphere in spring, Atmos. Chem. Phys., 10(13), 5823–5838, doi:10.5194/acp-10-5823-2010, 2010.

Mao, J., Paulot, F., Jacob, D. J., Cohen, R. C., Crounse, J. D., Wennberg, P. O., Keller, C. A., Hudman, R. C., Barkley, M. P. and Horowitz, L. W.: Ozone and organic nitrates over the eastern United States: Sensitivity to isoprene chemistry, J. Geophys. Res. Atmos., 118(19), 11,256-11,268, doi:10.1002/jgrd.50817, 2013a.

Mao, J., Fan, S., Jacob, D. J. and Travis, K. R.: Radical loss in the atmosphere from Cu-Fe redox coupling in aerosols, Atmos. Chem. Phys., 13(2), 509–519, doi:10.5194/acp-13-509-2013, 2013b.

Martens, C., Shay, T. J., Mendlovitz, H. P., Matross, D. M., Saleska, S. R., Wofsy, S. C. and et al.: Radon fluxes in tropical forest ecosystems of Brazilian Amazonia : night-time CO 2 net ecosystem exchange derived from radon and eddy covariance methods, Glob. Chang. Biol., 10, 618–629, doi:10.1111/j.1529-8817.2003.00764.x, 2004.

Martin, R. V., Jacob, D. J. and Yantosca, R. M.: Global and regional decreases in tropospheric oxidants from photochemical effects of aerosols, J. Geophys. Res., 108(D3), 4097, doi:10.1029/2002JD002622, 2003a.

Martin, R. V., Jacob, D. J., Chance, K., Kurosu, T. P., Palmer, P. I. and Evans, M. J.: Global inventory of nitrogen oxide emissions constrained by space-based observations of NO2 columns, J. Geophys. Res. D Atmos., 108(17), 1–12, doi:10.1029/2003jd003453, 2003b.

Martin, R. V., Brauer, M., van Donkelaar, A., Shaddick, G., Narain, U. and Dey, S.: No one knows which city has the highest concentration of fine particulate matter, Atmos. Environ., 3(October 2018), 100040, doi:10.1016/j.aeaoa.2019.100040, 2019.

Martonchik, J. V., Diner, D. J., Kahn, R. A., Ackerman, T. P., Verstraete, M. M., Pinty, B. and Gordon, H. R.: Techniques for the retrieval of aerosol properties over land and ocean using multiangle imaging, IEEE Trans. Geosci. Remote Sens., 36(4), 1212–1227, doi:10.1109/36.701027, 1998.

Martonchik, J. V., Diner, D. J., Kahn, R., Gaitley, B. and Holben, B. N.: Comparison of MISR and AERONET aerosol optical depths over desert sites, Geophys. Res. Lett., 31(16), 1–4, doi:10.1029/2004GL019807, 2004.

Mason, E. A. and Evans, R. B.: Graham's laws; Simple demonstrations of gases in motion: Part I, theory, J. Chem. Educ., 46(6), 358–364, doi:10.1021/ed046p358, 1969.

Massman, W. J.: An evaluation of the regional acid deposition model surface module for ozone uptake at three sites in the San Joaquin Valley of California, J. Geophys. Res., 99(D4), 8281–8294, doi:10.1029/93JD03267, 1994.

Massman, W. J.: A review of the molecular diffusivities of H2O, CO2, CH4, CO, O3, SO2, NH3, N2O, NO, and NO2 in air, O2 and N2 near STP, Atmos. Environ., 32(6), 1111–1127, doi:10.1016/S1352-2310(97)00391-9, 1998.

McDuffie, E. E., Fibiger, D. L., Dubé, W. P., Lopez Hilfiker, F., Lee, B. H., Jaeglé, L., Guo, H., Weber, R. J., Reeves, J. M., Weinheimer, A. J., Schroder, J. C., Campuzano-Jost, P., Jimenez, J. L., Dibb, J. E., Veres, P., Ebben, C., Sparks, T. L., Wooldridge, P. J., Cohen, R. C., Campos, T., Hall, S. R., Ullmann, K., Roberts, J. M., Thornton, J. A. and Brown, S. S.: ClNO2 Yields From Aircraft Measurements During the 2015 WINTER Campaign and Critical Evaluation of the Current Parameterization, J. Geophys. Res. Atmos., 123(22), 12,994-13,015, doi:10.1029/2018JD029358, 2018a.

McDuffie, E. E., Fibiger, D. L., Dubé, W. P., Lopez-Hilfiker, F., Lee, B. H., Thornton, J. A., Shah, V., Jaeglé, L., Guo, H., Weber, R. J., Michael Reeves, J., Weinheimer, A. J., Schroder, J. C., Campuzano-Jost, P., Jimenez, J. L., Dibb, J. E., Veres, P., Ebben, C., Sparks, T. L., Wooldridge, P. J., Cohen, R. C., Hornbrook, R. S., Apel, E. C., Campos, T., Hall, S. R., Ullmann, K. and Brown, S. S.: Heterogeneous N2O5 Uptake During Winter: Aircraft Measurements During the 2015 WINTER Campaign and Critical Evaluation of Current Parameterizations, J. Geophys. Res. Atmos., 123(8), 4345–4372, doi:10.1002/2018JD028336, 2018b.

McDuffie, E. E., Smith, S. J., O'Rourke, P., Tibrewal, K., Venkataraman, C., Marais, E. A., Zheng, B., Crippa, M., Brauer, M. and Martin, R. V.: A global anthropogenic emission inventory of atmospheric pollutants from sector- And fuel-specific sources (1970-2017): An application of the Community Emissions Data System (CEDS), Earth Syst. Sci. Data, 12(4), 3413–3442, doi:10.5194/essd-12-3413-2020, 2020.

McDuffie, E. E., Martin, R. V., Spadaro, J. V., Burnett, R., Smith, S. J., O'Rourke, P., Hammer, M. S., van Donkelaar, A., Bindle, L., Shah, V., Jaeglé, L., Luo, G., Yu, F., Adeniran, J. A., Lin, J. and Brauer, M.: Source sector and fuel contributions to ambient PM2.5 and attributable mortality across multiple spatial scales, Nat. Commun., 12(1), 1–12, doi:10.1038/s41467-021-23853-y, 2021.

McFarland, M. J., Hauer, M. E. and Reuben, A.: Half of US population exposed to adverse lead levels in early childhood., Proc. Natl. Acad. Sci. U. S. A., 119(11), e2118631119, doi:10.1073/pnas.2118631119, 2022.

Medinets, S., Skiba, U., Rennenberg, H. and Butterbach-Bahl, K.: A review of soil NO transformation: Associated processes and possible physiological significance on organisms, Soil Biol. Biochem., 80, 92–117, doi:10.1016/j.soilbio.2014.09.025, 2015.

De Meij, A., Pozzer, A. and Lelieveld, J.: Trend analysis in aerosol optical depths and pollutant emission estimates between 2000 and 2009, Atmos. Environ., 51, 75–85, doi:10.1016/j.atmosenv.2012.01.059, 2012.

Meller, R. and Moortgat, G. K.: Temperature dependence of the absorption cross sections of formaldehyde between 223 and 323 K in the wavelength range 225-375 nm, J. Geophys. Res. Atmos., 105(D6), 7089–7101, doi:10.1029/1999JD901074, 2000.

Meng, F., Qin, M., Tang, K., Duan, J., Fang, W., Liang, S., Ye, K., Xie, P., Sun, Y., Xie, C., Ye, C., Fu, P., Liu, J. and Liu, W.: High-resolution vertical distribution and sources of HONO and NO2 in the nocturnal boundary layer in urban Beijing, China, Atmos. Chem. Phys., 20(8), 5071–5092, doi:10.5194/acp-20-5071-2020, 2020.

Meng, J., Li, C., Martin, R. V., Van Donkelaar, A., Hystad, P. and Brauer, M.: Estimated Long-Term (1981-2016) Concentrations of Ambient Fine Particulate Matter across North America from Chemical Transport Modeling, Satellite Remote Sensing, and Ground-Based Measurements, Environ. Sci. Technol., 53(9), 5071–5079, doi:10.1021/acs.est.8b06875, 2019a.

Meng, J., Martin, R. V., Li, C., Van Donkelaar, A., Tzompa-Sosa, Z. A., Yue, X., Xu, J. W., Weagle, C. L. and Burnett, R. T.: Source Contributions to Ambient Fine Particulate Matter for Canada, Environ. Sci. Technol., 53(17), 10269–10278, doi:10.1021/acs.est.9b02461, 2019b.

Meng, J., Martin, R. V, Ginoux, P., Hammer, M., Sulprizio, M. P. and Ridley, D. A.: Grid-independent high-resolution dust emissions (v1.0) for chemical transport models: application to GEOS-Chem (12.5.0), Geosci. Model Dev., 14, 4249–4260, doi:10.5194/gmd-14-4249-2021, 2021.

Mertes, S. and Wahner, A.: Uptake of nitrogen dioxide and nitrous acid on aqueous surfaces, J. Phys. Chem., 99(38), 14000–14006, doi:10.1021/j100038a035, 1995.

Meyers, T. P., Huebert, B. J. and Hicks, B. B.: HNO_3 deposition to a deciduous forest, Bound. Layer Meteorol., 49(4), 395–410, 1989.

Meyers, T. P., Finkelstein, P., Clarke, J., Ellestad, T. G. and Sims, F.: A multilayer model for inferring dry deposition using standard meteorological measurements, J. Geogr. Res., 103(98), 22645–22661, 1998.

Michou, M., Laville, P., Serça, D., Fotiadi, A., Bouchou, P. and Peuch, V. H.: Measured and modeled dry deposition velocities over the ESCOMPTE area, Atmos. Res., 74(1–4), 89–116, doi:10.1016/j.atmosres.2004.04.011, 2005.

Min, K. E., Pusede, S. E., Browne, E. C., LaFranchi, B. W. and Cohen, R. C.: Eddy covariance fluxes and vertical concentration gradient measurements of NO and NO2 over a ponderosa pine ecosystem: Observational evidence for within-canopy chemical removal of NOx, Atmos. Chem. Phys., 14(11), 5495–5512, doi:10.5194/acp-14-5495-2014, 2014.

Mitchell, M., Wiacek, A. and Ashpole, I.: Surface ozone in the North American pollution outflow region of Nova Scotia: Long-term analysis of surface concentrations, precursor emissions and long-range transport influence, Atmos. Environ., 261, 118536, doi:10.1016/j.atmosenv.2021.118536, 2021.

Mölder, M., Grelle, A., Lindroth, A. and Halldin, S.: Flux-profile relationships over a boreal forest - Roughness sublayer corrections, Agric. For. Meteorol., 98–99, 645–658, doi:10.1016/S0168-1923(99)00131-8, 1999.

Monge, M. E., D'Anna, B., Mazri, L., Giroir-Fendler, A., Ammann, M., Donaldson, D. J. and George, C.: Light changes the atmospheric reactivity of soot, Proc. Natl. Acad. Sci. U. S. A., 107(15), 6605–6609, doi:10.1073/pnas.0908341107, 2010.

Monin, A. S. and Obukhov, A. M.: Basic laws of turbulent mixing in the surface layer of the atmosphere, Contrib. Geophys. Inst. Acad. Sci. USSR, 151, 163–187, 1954.

Morawska, L. and Buonanno, G.: The physics of particle formation and deposition during breathing, Nat. Rev. Phys., 3(May), 300–301, doi:10.1038/s42254-021-00307-4, 2021.

Motai, A., Yamazaki, M., Muramatsu, N., Watanabe, M. and Izuta, T.: Submicron ammonium sulfate particles deposited on leaf surfaces of a leafy vegetable ( Komatsuna , Brassica rapa L . var . perviridis ) are taken up by leaf and enhance nocturnal leaf conductance, Atmosperic Environ., 187(May), 155–162, doi:10.1016/j.atmosenv.2018.05.064, 2018.

Msibi, I. M., Shi, J. P. and Harrison, R. M.: Accommodation coefficient for trace gas uptake using deposition profile measurement in an annular reactor, J. Atmos. Chem., 17(4), 339–351, doi:10.1007/BF00696853, 1993.

Mu, M., Randerson, J. T., Werf, G. R. Van Der, Giglio, L., Kasibhatla, P., Morton, D., Collatz, G. J., Defries, R. S., Hyer, E. J., Prins, E. M., Griffith, D. W. T., Wunch, D., Toon, G. C., Sherlock, V. and Wennberg, P. O.: Daily and 3 - hourly variability in global fire emissions and consequences for atmospheric model predictions of carbon monoxide, J. Geogr. Res., 116, D24303, doi:10.1029/2011JD016245, 2011.

Munger, J. W., Wofsy, S. C., Bakwin, P. S., Fan, S., Goulden, M. L., Daube, B. C., Goldstein, A. H., Moore, K. E. and Fitzjarrald, D. R.: Atmospheric deposition of reactive nitrogen oxides and ozaone in a temperate deciduos forest and a subartic woodland 1. measurements and mechanisms, J. Geophys. Res., 101, 12639–12657, 1996.

Munger, J. W., Fan, S. M., Bakwin, P. S., Goulden, M. L., Goldstein, A. H., Colman, A. S. and Wofsy, S. C.: Regional budgets for nitrogen oxides from continental sources: variations of rates for oxidation and deposition with season and distance from source regions, J. Geophys. Res. Atmos., 103(D7), 8355–8368, doi:10.1029/98JD00168, 1998.

Munger, W. and Wofsy, S.: Concentrations and Surface Exchange of Air Pollutants at Harvard Forest EMS Tower since 1990, , Harvard Forest Data Archive: HF066, 2019.

Munger, W. and Wofsy, S.: Biomass Inventories at Harvard Forest EMS Tower since 1993, , Harvard Forest Data Archive: HF069., 2020a.

Munger, W. and Wofsy, S.: Canopy-Atmosphere Exchange of Carbon, Water and Energy at Harvard Forest EMS Tower since 1991, , Harvard Forest Data Archive: HF004, 2020b.

Murdachaew, G., Varner, M. E., Phillips, L. F., Finlayson-Pitts, B. J. and Gerber, R. B.: Nitrogen dioxide at the air-water interface: Trapping, absorption, and solvation in the bulk and at the surface, Phys. Chem. Chem. Phys., 204–212, doi:10.1039/c2cp42810e, 2012.

Murphy, D. M.: Little net clear-sky radiative forcing from recent regional redistribution of aerosols, Nat. Geosci., 6(4), 258–262, doi:10.1038/ngeo1740, 2013.

Murray, C. J. L., Aravkin, A. Y. A., Zheng, P., Abbafati, C. and et al.: Global burden of 87 risk factors in 204 countries and territories, 1990–2019: a systematic analysis for the Global Burden of Disease Study 2019, Lancet, 396(10258), 1223–1249, doi:10.1016/S0140-6736(20)30752-2, 2020.

Murray, L. T., Jacob, D. J., Logan, J. A., Hudman, R. C. and Koshak, W. J.: Optimized regional and interannual variability of lightning in a global chemical transport model constrained by LIS/OTD satellite data, J. Geophys. Res. Atmos., 117(20), 1–14, doi:10.1029/2012JD017934, 2012.

Myneni, R. B., Hoffman, S., Knyazikhin, Y., Privette, J. L., Glassy, J., Tian, Y., Wang, Y., Song, X., Zhang, Y., Smith, G. R., Lotsch, A., Friedl, M., Morisette, J. T., Votava, P., Nemani, R. R. and Running, S. W.: Global products of vegetation leaf area and fraction absorbed PAR from year one of MODIS data, Remote Sens. Environ., 83(1–2), 214–231, doi:10.1016/S0034-4257(02)00074-3, 2002.

Ndour, M., D'Anna, B., George, C., Ka, O., Balkanski, Y., Kleffmann, J., Stemmler, K. and Ammann, M.: Photoenhanced uptake of NO2 on mineral dust: Laboratory experiments and model simulations, Geophys. Res. Lett., 35(5), 1–5, doi:10.1029/2007GL032006, 2008.

Neirynck, J. and Ceulemans, R.: Bidirectional ammonia exchange above a mixed coniferous forest, Environ. Pollut., 154(3), 424–438, doi:10.1016/j.envpol.2007.11.030, 2008.

Neirynck, J., Kowalski, A. S., Carrara, A., Genouw, G., Berghmans, P. and Ceulemans, R.: Fluxes of oxidised and reduced nitrogen above a mixed coniferous, Environ. Pollut., 149(1), 31–43, doi:10.1016/j.envpol.2006.12.029, 2007.

Nemitz, E., Sutton, M. A., Schjoerring, J. K., Husted, S. and Paul Wyers, G.: Resistance modelling of ammonia exchange over oilseed rape, Agric. For. Meteorol., 105(4), 405–425, doi:10.1016/S0168-1923(00)00206-9, 2000.

Nguyen, T. B., Crounse, J. D., Teng, A. P., St. Clair, J. M., Paulot, F., Wolfe, G. M. and Wennberg, P. O.: Rapid deposition of oxidized biogenic compounds to a temperate forest, Proc. Natl. Acad. Sci., 112(5), E392–E401, doi:10.1073/pnas.1418702112, 2015.

Nobel, P. S.: Physicochemical and Environmental Plant Physiology, Fourth Edi., Elsevier., 2009.

Nobel, P. S., Zaragoza, L. J. and Smith, W. K.: Relation between Mesophyll Surface Area, Photosynthetic Rate, and Illumination Level during Development for Leaves of Plectranthus parviforus Henckel, Plant Physiol., 55, 1067–1070, 1975.

Novakov, T.: Laboratory Study of NO2 Reaction with Dispersed and Bulk Liquid Water--Author's Reply, Atmosperic Environ., 29(18), 2559–2560, 1995.

Nowlan, C. R., Martin, R. V., Philip, S., Lamsal, L. N., Krotkov, N. A., Marais, E. A., Wang, S. and Zhang, Q.: Global Dry Deposition of Nitrogen Dioxide and Sulfur Dioxide Inferred from Space-Based Measurements, Global Biogeochem. Cycles, 28, 1–19, doi:10.1002/2014GB004805.Received, 2014.

Obbink, R. B., Icks, K. H., Alloway, J. G., Pranger, T. S., Lkemade, R. A., Shmore, M. A. and Ustamante, M. B.: Global assessment of nitrogen deposition effects on terrestrial plant diversity : a synthesis, Ecol. Appl., 20(1), 30–59, 2010.

Oke, T. R.: Boundary Layer Climates, second., 1987.

Olivier, J. G. J., Aardenne, J. A. Van, Dentener, F. J., Pagliari, V., Ganzeveld, L. N., Peters, J. A. H. W., Olivier, J. G. J., Aardenne, J. A. Van, Dentener, F. J. and Pagliari, V.: Recent trends in global greenhouse gas emissions : regional trends 1970 – 2000 and spatial distributionof key sources in 2000, Environ. Sci., 2, 81–99, doi:10.1080/15693430500400345, 2005.

Ontario Ministry of the Environment and Climate Change: Air Quality in Ontario. [online] Available from: https://www.ontario.ca/document/air-quality-ontario-2016-report, 2016.

Oren, R., Matyssek, R. and Zimmermann, R.: Estimating photosynthetic rate and annual carbon gain in conifers from specific leaf weight and leaf biomass, Oecologia, 70, 187–193, 1986.

Oswald, A. R., Behrendt, T., Ermel, M., Wu, D., Su, H., Cheng, Y., Breuninger, C., Mougin, E., Delon, C., Loubet, B., Sörgel, M., Pöschl, U., Andreae, M. O., Meixner, F. X., Trebs, I., Wu, D., Su, H., Cheng, Y., Breuninger, C., Oswald, R., Wu, D., Su, H., Cheng, Y., Moravek, A., Delon, C., Delon, C., Loubet, B., Loubet, B., Poschl, U., Hoffmann, T., Hoffmann, T. and Andreae, M. O.: HONO Emissions from Soil Bacteria as a Major Source of Atmospheric Reactive Nitrogen Soil biogenic emissions, Science (80-. )., 341(6151), 1233–1235, 2013.

Panofsky, H. A.: Determination of stress from wind and temperature measurements, Q. J. R. Meteorol. Soc. Soc., 89(379), 85–97, 1963.

Pariyar, S., Eichert, T., Goldbach, H. E., Hunsche, M. and Burkhardt, J.: The exclusion of ambient aerosols changes the water relations of sunflower (Helianthus annuus) and bean (Vicia faba) plants, Environ. Exp. Bot., 88, 43–52, doi:10.1016/j.envexpbot.2011.12.031, 2013.

Park, J. Y. and Lee, Y. N.: Solubility and decomposition kinetics of nitrous acid in aqueous solution, J. Phys. Chem., 92(22), 6294–6302, doi:10.1021/j100333a025, 1988.

Park, R. J., Jacob, D. J., Chin, M. and Martin, R. V: Sources of carbonaceous aerosols over the United States and implications for natural visibility, J. Geogr. Res., 108, 4355, doi:10.1029/2002JD003190, 2003.

Park, R. J., Jacob, D. J., Field, B. D., Yantosca, R. M. and Chin, M.: Natural and transboundary pollution influences on sulfate-nitrate-ammonium aerosols in the United States: Implications for policy, J. Geophys. Res. D Atmos., 109(15), doi:10.1029/2003JD00473, 2004.

Park, R. J., Jacob, D. J., Kumar, N. and Yantosca, R. M.: Regional visibility statistics in the United States : Natural and transboundary pollution influences , and implications for the Regional Haze Rule, Atmos. Environ., 40, 5405–5423, doi:10.1016/j.atmosenv.2006.04.059, 2006.

Paulot, F., Jacob, D. J. and Henze, D. K.: Sources and processes contributing to nitrogen deposition: An adjoint model analysis applied to biodiversity hotspots worldwide, Environ. Sci. Technol., 47(7), 3226–3233, doi:10.1021/es3027727, 2013.

Paulson, C. A.: The Mathematical Representation of Wind Speed and Temperature Profiles in the Unstable Atmospheric Surface Layer, J. Appl. Meteorol., 9, 857–861, 1970.

Pedersen, M., Giorgis-Allemand, L., Bernard, C., Aguilera, I. and Al., E.: Ambient air pollution and low birthweight: a European cohort study (ESCAPE), Lancet, 695–704, doi:10.1016/s2213-2600(13)70192-, 2013.

Petrenko, M. and Ichoku, C.: Coherent uncertainty analysis of aerosol measurements from multiple satellite sensors, Atmos. Chem. Phys., 13(14), 6777–6805, doi:10.5194/acp-13-6777-2013, 2013.

Philip, S., Martin, R. V, Donkelaar, A. Van, Lo, J. W., Wang, Y., Chen, D., Zhang, L., Kasibhatla, P. S., Wang, S., Zhang, Q., Lu, Z., Streets, D. G., Bittman, S. and Macdonald, D. J.: Global Chemical Composition of Ambient Fine Particulate Matter for Exposure Assessment, Environ. Sci. Technol., 48, 13060–13068, 2014.

Philip, S., Martin, R. V. and Keller, C. A.: Sensitivity of chemistry-transport model simulations to the duration of chemical and transport operators: a case study with GEOS-Chem v10-01, Geosci. Model Dev., 9(5), 1683–1695, doi:10.5194/gmd-9-1683-2016, 2016.

Philip, S., Martin, R. V., Snider, G., Weagle, C. L., Van Donkelaar, A., Brauer, M., Henze, D. K., Klimont, Z., Venkataraman, C., Guttikunda, S. K. and Zhang, Q.: Anthropogenic fugitive, combustion and industrial dust is a significant, underrepresented fine particulate matter source in global atmospheric models, Environ. Res. Lett., 12(4), doi:10.1088/1748-9326/aa65a4, 2017.

Physick, W. L. and Garratt, J. R.: Incorporation of a High-Roughness Lower Boudnary into a Mesoscale Model for Studies of Dry Deposition over Complex Terrain, Boundary-Layer Meteorol., 74, 55–71, 1995.

Pilegaard, K., Hummelshøj, P. and Jensen, N. O.: Fluxes of ozone and nitrogen dioxide measured by eddy correlation over a harvested wheat field, Atmos. Environ., 32(7), 1167–1177, doi:10.1016/S1352-2310(97)00194-5, 1998.

Place, B. K., Delaria, E. R., Liu, A. X. and Cohen, R. C.: Leaf Stomatal Control over Acyl Peroxynitrate Dry Deposition to Trees, ACS Earth Sp. Chem., 4(11), 2162–2170, doi:10.1021/acsearthspacechem.0c00152, 2020.

Plake, D., Stella, P., Moravek, A., Mayer, J. C., Ammann, C., Held, A. and Trebs, I.: Comparison of ozone deposition measured with the dynamic chamber and the eddy covariance method, Agric. For. Meteorol., 206, 97–112, doi:10.1016/j.agrformet.2015.02.014, 2015.

Platt, U., Perner, D., Harris, G. W., Winer, A. M. and Pitts, J. N.: Observations of nitrous acid in an urban atmosphere by differential optical absorption, Nature, 285(5763), 312–314, 1980.

Platt, U., Alicke, B., Dubois, R., Geyer, A., Hofzumahaus, A., Holland, F., Martinez, M., Mihelcic, D., Klüpfel, T., Lohrmann, B., Pätz, W., Perner, D., Rohrer, F., Schäfer, J. and Stutz, J.: Free radicals and fast photochemistry during BERLIOZ, J. Atmos. Chem., 42(1), 359–394, doi:10.1023/A:1015707531660, 2002.

Pleim, J. E., Bash, J. O., Walker, J. T. and Cooter, E. J.: Development and evaluation of an ammonia bidirectional flux parameterization for air quality models, J. Geophys. Res. Atmos., 118(9), 3794–3806, doi:10.1002/jgrd.50262, 2013.

Poling, B. E. and Prausnitz, J. M.: The Properties of Gases and Liquids, 5th Edn., McGraw-Hill, New York., 2004.

Press, W. H.: Numerical recipes in FORTRAN : the art of scientific computing, 2nd ed., Cambridge England ; New York, NY, USA : Cambridge University Press., 1992.

Pusede, S. E., VandenBoer, T. C., Murphy, J. G., Markovic, M. Z., Young, C. J., Veres, P. R., Roberts, J. M., Washenfelder, R. A., Brown, S. S., Ren, X., Tsai, C., Stutz, J., Brune, W. H., Browne, E. C., Wooldridge, P. J., Graham, A. R., Weber, R., Goldstein, A. H., Dusanter, S., Griffith, S. M., Stevens, P. S., Lefer, B. L. and Cohen, R. C.: An Atmospheric Constraint on the NO2 Dependence of Daytime Near-Surface Nitrous Acid (HONO), Environ. Sci. Technol., 49(21), 12774–12781, doi:10.1021/acs.est.5b02511, 2015a.

Pusede, S. E., Steiner, A. L. and Cohen, R. C.: Temperature and Recent Trends in the Chemistry of Continental Surface Ozone, Chem. Rev., 115(10), 3898–3918, doi:10.1021/cr5006815, 2015b.

Pye, H. O. T., Liao, H., Wu, S., Mickley, L. J., Jacob, D. J. and Henze, D. K.: Effect of changes in climate and emissions on future sulfate-nitrate-ammonium aerosol levels in the United States, J. Geogr. Res., 114, D01205, doi:10.1029/2008JD010701, 2009a.

Pye, H. O. T., Liao, H., Wu, S., Mickley, L. J., Jacob, D. J., Henze, D. J. and Seinfeld, J. H.: Effect of changes in climate and emissions on future sulfate-nitrate-ammonium aerosol levels in the United States, J. Geophys. Res. Atmos., 114(1), 1–18, doi:10.1029/2008JD010701, 2009b.

Qin, M., Xie, P., Su, H., Gu, J., Peng, F., Li, S., Zeng, L., Liu, J., Liu, W. and Zhang, Y.: An observational study of the HONO-NO2 coupling at an urban site in Guangzhou City, South China, Atmos. Environ., 43(36), 5731–5742, doi:10.1016/j.atmosenv.2009.08.017, 2009.

Ramazan, K. A., Syomin, D. and Finlayson-Pitts, B. J.: The photochemical production of HONO during the heterogeneous hydrolysis of NO2, Phys. Chem. Chem. Phys., 6(14), 3836–3843, doi:10.1039/b402195a, 2004.

Ramge, P., Badeck, F. -W, PLÖCHL, M. and KOHLMAIER, G. H.: Apoplastic antioxidants as decisive elimination factors within the uptake process of nitrogen dioxide into leaf tissues, New Phytol., 125(4), 771–785, doi:10.1111/j.1469-8137.1993.tb03927.x, 1993.

Ramuta, M. D., Newman, C. M., Brakefield, S. F., Stauss, M. R., Wiseman, R. W., Kita-Yarbro, A., O'Connor, E. J., Dahal, N., Lim, A., Poulsen, K. P., Safdar, N., Marx, J. A., Accola, M. A., Rehrauer, W. M., Zimmer, J. A., Khubbar, M., Beversdorf, L. J., Boehm, E. C., Castañeda, D., Rushford, C., Gregory, D. A., Yao, J. D., Bhattacharyya, S., Johnson, M. C., Aliota, M. T., Friedrich, T. C., O'Connor, D. H. and O'Connor, S. L.: SARS-CoV-2 and other respiratory pathogens are detected in continuous air samples from congregate settings, Nat. Commun., 13(1), 4717, doi:10.1038/s41467-022-32406-w, 2022.

Randall, K., Ewing, E. T., Marr, L. C., Jimenez, J. L. and Bourouiba, L.: How did we get here: what are droplets and aerosols and how far do they go?, Interface Focus, 11, 1–17, doi:10.1098/rsfs.2021.0049, 2021.

Rappenglück, B., Ackermann, L., Alvarez, S., Golovko, J., Buhr, M., Field, R. A., Soltis, J. and Montague, D. C.: Strong wintertime ozone events in the Upper Green River basin , Wyoming, Atmos. Chem. Phys., 14, 4909–4934, doi:10.5194/acp-14-4909-2014, 2014.

Raupach, M. R., Finnigan, J. J. and Brunet, Y.: Coherent eddies and turbulence in vegetation canopies: the mixing-layer analogy, Boundary-Layer Meteorol., 78(3–4), 351–382, doi:10.1007/BF00120941, 1996.

Reed, C., Evans, M. J., Crilley, L. R., Bloss, W. J., Sherwen, T., Read, K. A., Lee, J. D. and Carpenter, L. J.: Evidence for renoxification in the tropical marine boundary layer, Atmos. Chem. Phys., 17, 4081–4092, doi:10.5194/acp-17-4081-2017, 2017.

Ren, X., Brune, W. H., Mao, J., Mitchell, M. J., Lesher, R. L., Simpas, J. B., Metcalf, A. R., Schwab, J. J., Cai, C., Li, Y., Demerjian, K. L., Felton, H. D., Boynton, G., Adams, A., Perry, J., He, Y., Zhou, X. and Hou, J.: Behavior of OH and HO2 in the winter atmosphere in New York City, Atmos. Environ., 40, 252–263, doi:10.1016/j.atmosenv.2005.11.073, 2006.

Ren, X., Sanders, J. E., Rajendran, A., Weber, R. J., Goldstein, A. H., Pusede, S. E., Browne, E. C., Min, K. E. and Cohen, R. C.: A relaxed eddy accumulation system for measuring vertical fluxes of nitrous acid, Atmos. Meas. Tech., 4(10), 2093–2103, doi:10.5194/amt-4-2093-2011, 2011.

Ren, Y., Stieger, B., Spindler, G., Grosselin, B., Mellouki, A., Tuch, T., Wiedensohler, A. and Herrmann, H.: Role of the dew water on the ground surface in HONO distribution: a case measurement in Melpitz, Atmos. Chem. Phys., 20(2), 13069–13089, doi:10.5194/acp-20-13069-2020, 2020.

Richmond-Bryant, J., Chris Owen, R., Graham, S., Snyder, M., McDow, S., Oakes, M. and Kimbrough, S.: Estimation of on-road NO2 concentrations, NO2/NOX ratios, and related roadway gradients from near-road monitoring data, Air Qual. Atmos. Heal., 10(5), 611–625, doi:10.1007/s11869-016-0455-7, 2017.

de Ridder, K.: Bulk transfer relations for the roughness sublayer, Boundary-Layer Meteorol., 134(2), 257–267, doi:10.1007/s10546-009-9450-y, 2010.

Ridley, D. A., Heald, C. L., Pierce, J. R. and Evans, M. J.: Toward resolution-independent dust emissions in global models: Impacts on the seasonal and spatial distribution of dust, Geophys. Res. Lett., 40(11), 2873–2877, doi:10.1002/grl.50409, 2013.

Ridley, D. A., Solomon, S., Barnes, J. E., Burlakov, V. D., Deshler, T., Dolgii, S. I., Herber, A. B., Nagai, T., Neely, R. R., Nevzorov, A. V., Ritter, C., Sakai, T., Santer, B. D., Sato, M., Schmidt, A., Uchino, O. and Vernier, J. P.: Total volcanic stratospheric aerosol optical depths and implications for global climate change, Geophys. Res. Lett., 41(22), 7763–7769, doi:10.1002/2014GL061541, 2014a.

Ridley, D. A., Heald, C. L. and Prospero, J. M.: What controls the recent changes in African mineral dust aerosol across the Atlantic?, Atmos. Chem. Phys., 14(11), 5735–5747, doi:10.5194/acp-14-5735-2014, 2014b.

Riederer, M., Kurbasik, K., Steinbrecher, R., Voss, A., Miinchen, T. U. and Miinchen, D.-: Surface areas, lengths and volumes of Picea abies (L.) Karst. needles: determination, biological variability and effect of environmental factors, Trees, 2, 165–172, 1988.

Rienecker, M. ., Suarez, M., Gelaro, J. and et al.: MERRA : NASA ' s Modern-Era Retrospective Analysis for Research and Applications, J. Clim., 24, 3624–3648, doi:10.1175/JCLI-D-11-00015.1, 2011.

Robinson, A. L., Donahue, N. M., Shrivastava, M. K., Weitkamp, E. A., Sage, A. M., Grieshop, A. P., Lane, T. E., Pierce, J. R. and Pandis, S. N.: Rethinking organic aerosols: Semivolatile emissions and photochemical aging, Science (80-. )., 315(5816), 1259–1262, doi:10.1126/science.1133061, 2007.

Romer, P. S., Duffey, K. C., Wooldridge, P. J., Allen, H. M., Ayres, B. R., Brown, S. S., Brune, W. H., Crounse, J. D., De Gouw, J., Draper, D. C., Feiner, P. A., Fry, J. L., Goldstein, A. H., Koss, A., Misztal, P. K., Nguyen, T. B., Olson, K., Teng, A. P., Wennberg, P. O., Wild, R. J., Zhang, L. and Cohen, R. C.: The lifetime of nitrogen oxides in an isoprene-dominated forest, Atmos. Chem. Phys., 16(12), 7623–7637, doi:10.5194/acp-16-7623-2016, 2016.

Rondón, A., Johansson, C. and Granat, L.: Dry Deposition of Nitrogen Dioxide and Ozone to Coniferous Forests, J. Geophys. Res., 98, 5159–5172, 1993.

Rovelli, G., Jacobs, M. I., Willis, M. D., Rapf, R. J., Prophet, A. M. and Wilson, K. R.: A critical analysis of electrospray techniques for the determination of accelerated rates and mechanisms of chemical reactions in droplets, Chem. Sci., 11(48), 13026–13043, doi:10.1039/d0sc04611f, 2020.

Samet, J.: The Clean Air Act and Health — A Clearer View from 2011, N. Engl. J. Med., 365, 198–201, doi:10.1056/NEJMp1103332, 2011.

Sander, R.: Compilation of Henry's law constants (version 4.0) for water as solvent, Atmos. Chem. Phys., 15(8), 4399–4981, doi:10.5194/acp-15-4399-2015, 2015.

Sarwar, G., Roselle, S. J., Mathur, R., Appel, W., Dennis, R. L. and Vogel, B.: A comparison of CMAQ HONO predictions with observations from the Northeast Oxidant and Particle Study, Atmos. Environ., 42(23), 5760–5770, doi:10.1016/j.atmosenv.2007.12.065, 2008.

Sayer, A. M., Hsu, N. C., Bettenhausen, C., Ahmad, Z., Holben, B. N., Smirnov, A., Thomas, G. E. and Zhang, J.: SeaWiFS Ocean Aerosol Retrieval (SOAR): Algorithm, validation, and comparison with other data sets, J. Geophys. Res. Atmos., 117(3), 1–17, doi:10.1029/2011JD016599, 2012.

Schraufnagel, D. E.: The health effects of ultrafine particles, Exp. Mol. Med., 52(3), 311–317, doi:10.1038/s12276-020-0403-3, 2020.

Schwartz, S. E. and Lee, Y. N.: Laboratory Study of NO2 Reaction with Dispersed and Bulk Liquid Water, Atmosperic Environ., 29(8), 2557–2559, 1995.

Seinfeld, J. H.: Atmospheric Chemistry and Physics of Air Pollution, John Wiley & Sons., 1986.

Seinfeld, J. H. and Pandis, S. N.: Atmospheric Chemistry and Physics: from air pollution to climate change, second., 2006.

Sellers, P. J., Mintz, Y. and Dalcher, A.: A Simple Biosphere Model (SiB) for Use within General Circulation Models, J. Atmos. Sci., 43, 505–531, 1986.

Seltzer, K. M., Vizuete, W. and Henderson, B. H.: Evaluation of updated nitric acid chemistry on ozone precursors and radiative effects, Atmos. Chem. Phys., 3(2), 5973–5986, doi:10.5194/acp-15-5973-2015, 2015.

Shaddick, G., Thomas, M. L., Amini, H., Broday, D., Cohen, A., Frostad, J., Green, A., Gumy, S., Liu, Y., Martin, R. V., Pruss-Ustun, A., Simpson, D., Van Donkelaar, A. and Brauer, M.: Data Integration for the Assessment of Population Exposure to Ambient Air Pollution for Global Burden of Disease Assessment, Environ. Sci. Technol., 52(16), 9069–9078, doi:10.1021/acs.est.8b02864, 2018.

Shah, V., Jaeglé, L., Thornton, J. A., Lopez-Hilfiker, F. D., Lee, B. H., Schroder, J. C., Campuzano-Jost, P., Jimenez, J. L., Guo, H., Sullivan, A. P., Weber, R. J., Green, J. R., Fiddler, M. N., Bililign, S., Campos, T. L., Stell, M., Weinheimer, A. J., Montzka, D. D. and Brown, S. S.: Chemical feedbacks weaken the wintertime response of particulate sulfate and nitrate to emissions reductions over the eastern United States, Proc. Natl.

Acad. Sci. U. S. A., 115(32), 8110–8115, doi:10.1073/pnas.1803295115, 2018.

Shah, V., J. Jacob, D., Li, K., Silvern, R., Zhai, S., Liu, M., Lin, J. and Zhang, Q.: Effect of changing NOx lifetime on the seasonality and long-term trends of satellite-observed tropospheric NO2 columns over China, Atmos. Chem. Phys., 20(3), 1483–1495, doi:10.5194/acp-20-1483-2020, 2020.

Shahsavani, A., Naddafi, K., Jafarzade Haghighifard, N., Mesdaghinia, A., Yunesian, M., Nabizadeh, R., Arahami, M., Sowlat, M. H., Yarahmadi, M., Saki, H., Alimohamadi, M., Nazmara, S., Motevalian, S. A. and Goudarzi, G.: The evaluation of PM10, PM2.5, and PM1 concentrations during the Middle Eastern Dust (MED) events in Ahvaz, Iran, from April through September 2010, J. Arid Environ., 77(1), 72–83, doi:10.1016/j.jaridenv.2011.09.007, 2012.

Shepson, P. B., Bottenheim, J. W., Hastie, D. R. and Venkatram, A.: Determination of the Relative Ozone and PAN Deposition Velocities at Night, Geophys. Res. Lett., 19(11), 1121–1124, 1992.

Shumway, R. H. and Stoffer, D. S.: Time Series Analysis and Its Applications, 3rd ed., Springer., 2011.

Sievering, H., Kelly, T., McConville, G., Seibold, C. and Turnipseed, A.: Nitric acid dry deposition to conifer forests: Niwot Ridge spruce-fir-pine study, Atmos. Environ., 35(22), 3851–3859, doi:10.1016/S1352-2310(01)00156-X, 2001.

Sillman, S.: The relation between ozone, NOx and hydrocarbons in urban and polluted rural environments, Atmosperic Environ., 33, 1821–1845, doi:10.1016/S1474-8177(02)80015-8, 1999.

Sillman, S., Logan, J. and Wofsy, S.: The Sensitivity of Ozone to Nitrogen Oxides and Hydrocarbons in Regional Ozone Episodes 1 Now at of Atmospheric , Oceanic , and Space Sciences , al ., to explore the factors that influence ozone in Michigan , al areas during stagnation periods , again foc, J. Geophsical Res., 95, 1837–1851, 1990.

Silva, S. J. and Heald, C. L.: Investigating Dry Deposition of Ozone to Vegetation, J. Geophys. Res. Atmos., 123(1), 559–573, doi:10.1002/2017JD027278, 2018.

Simon, H., Baker, K. R. and Phillips, S.: Compilation and interpretation of photochemical model performance statistics published between 2006 and 2012, Atmos. Environ., 61, 124–139, doi:10.1016/j.atmosenv.2012.07.012, 2012.

Simon, H., Reff, A., Wells, B., Xing, J. and Frank, N.: Ozone trends across the United States over a period of decreasing NOx and VOC emissions, Environ. Sci. Technol., 49(1), 186–195, doi:10.1021/es504514z, 2015.

Simpson, I. J., Thurtell, G. W., Neumann, H. H., Den Hartog, G. and Edwards, G. C.: The validity of similarity theory in the roughness sublayer above forests, Boundary-Layer Meteorol., 87(1), 69–99, doi:10.1023/A:1000809902980, 1998.

Snider, G., Weagle, C. L., Martin, R. V, Donkelaar, A. Van, Conrad, K., Cunningham, D. and Gordon, C.: SPARTAN : a global network to evaluate and enhance satellite-based estimates of ground-level particulate matter for global health, Atmos. Meas. Tech., 8, 505–521, doi:10.5194/amt-8-505-2015, 2015.

Snyder, K. A., Richards, J. H. and Donovan, L. A.: Night-time conductance in C 3 and C 4 species : do plants lose water at night ?, J. Exp. Bot., 54(383), 861–865, doi:10.1093/jxb/erg082, 2003.

Soden, B. J., Wetherald, R. T., Stenchikov, G. L. and Robock, A.: Global cooling after the eruption of Mount Pinatubo: A test of climate feedback by water vapor, Science (80-. )., 296(5568), 727–730, doi:10.1126/science.296.5568.727, 2002.

Sörgel, M., Trebs, I., Serafimovich, A., Moravek, A., Held, A. and Zetzsch, C.: Simultaneous HONO measurements in and above a forest canopy: Influence of turbulent exchange on mixing ratio differences, Atmos. Chem. Phys., 11(2), 841–855, doi:10.5194/acp-11-841-2011, 2011.

Sparks, J. P., Monson, R. K., Sparks, K. L. and Lerdau, M.: Leaf uptake of nitrogen dioxide (NO2) in a tropical wet forest: Implications for tropospheric chemistry, Oecologia, 127(2), 214–221, doi:10.1007/s004420000594, 2001.

Sparks, J. P., Walker, J., Turnipseed, A. W. and Guenther, A.: Dry nitrogen deposition estimates over a forest experiencing free air CO2 enrichment, Glob. Chang. Biol., 14(4), 768–781, doi:10.1111/j.1365-2486.2007.01526.x, 2008.

Spataro, F. and Ianniello, A.: Sources of atmospheric nitrous acid: State of the science, current research needs, and future prospects, J. Air Waste Manage. Assoc., 64(11), 1232–1250, doi:10.1080/10962247.2014.952846, 2014.

Spicer, C. W., Coutant, R. W., Ward, G. F., Joseph, D. W., Gaynor, A. J. and Billick, I. H.: Rates and Mechanisms of NO2 Removal From Indoor Air by Residential Materials, Environ. Int., 15, 643–654, 1989.

Spicer, C. W., Kenny, D. V, Ward, G. F. and Billick, I. H.: Transformations, lifetimes, and sources of NO2, HONO, and HNO3 in Indoor Environments, Air Waste, 43(11), 1479–1485, doi:10.1080/1073161X.1993.10467221, 1993.

Spracklen, D. V., Jimenez, J. L., Carslaw, K. S., Worsnop, D. R., Evans, M. J., Mann, G. W., Zhang, Q., Canagaratna, M. R., Allan, J., Coe, H., McFiggans, G., Rap, A. and Forster, P.: Aerosol mass spectrometer constraint on the global secondary organic aerosol budget, Atmos. Chem. Phys., 11(23), 12109–12136, doi:10.5194/acp-11-12109-2011, 2011.

Stein, A. F., Draxler, R. R., Rolph, G. D., Stunder, B. J. B., Cohen, M. D. and Ngan, F.: Noaa's hysplit atmospheric transport and dispersion modeling system, Bull. Am. Meteorol. Soc., 96(12), 2059–2077, doi:10.1175/BAMS-D-14-00110.1, 2015.

Stella, P., Loubet, B., Laville, P., Lamaud, E., Cazaunau, M., Laufs, S., Bernard, F., Grosselin, B., Mascher, N., Kurtenbach, R., Mellouki, A., Kleffmann, J. and Cellier, P.: Comparison of methods for the determination of NO-O 3-NO 2 fluxes and chemical interactions over a bare soil, Atmos. Meas. Tech., 5(6), 1241–1257, doi:10.5194/amt-5-1241-2012, 2012.

Stella, P., Kortner, M., Ammann, C., Foken, T., Meixner, F. X. and Trebs, I.: Measurements of nitrogen oxides and ozone fluxes by eddy covariance at a meadow: Evidence for an internal leaf resistance to NO2, Biogeosciences, 10(9), 5997–6017, doi:10.5194/bg-10-5997-2013, 2013.

Stemmler, K., Ammann, M., Donders, C., Kleffmann, J. and George, C.: Photosensitized reduction of nitrogen dioxide on humic acid as a source of nitrous acid, Nature, 440(7081), 195–198, doi:10.1038/nature04603, 2006.

Stevens, R. G. and Pierce, J. R.: A parameterization of sub-grid particle formation in sulfur-rich plumes for global- and regional-scale models, Atmos. Chem. Phys., 13(23), 12117–12133, doi:10.5194/acp-13-12117-2013, 2013.

Stevens, R. G. and Pierce, J. R.: The contribution of plume-scale nucleation to global and regional aerosol and CCN concentrations: Evaluation and sensitivity to emissions changes, Atmos. Chem. Phys., 14(24), 13661–13679, doi:10.5194/acp-14-13661-2014, 2014.

Stocker, D. W., Stedman, D. H., Zeller, K. F., Massman, W. J. and Fox, D. G.: Fluxes of Nitrogen Oxides and Ozone Measured by Eddy Correlation Over a Shrtgrass Prairie, J. Geophys. Res., 98(93), 12619–12630, 1993.

Stocker, D. W., Zeller, K. F. and Stedman, D. H.: O3 and NO2 fluxes over snow measured by eddy correlation, Atmos. Environ., 29(11), 1299–1305, doi:10.1016/1352-2310(94)00337-K, 1995.

Stroud, C., Makar, P., Karl, T., Guenther, A., Geron, C., Turnipseed, A., Nemitz, E., Baker, B., Potosnak, M. and Fuentes, J. D.: Role of canopy-scale photochemistry in modifying biogenic-atmosphere exchange of reactive terpene species : Results from the CELTIC field study, , 110, 1–14, doi:10.1029/2005JD005775, 2005.

Stutz, J., Kim, E. S., Platt, U., Bruno, P., Perrino, C. and Febo, A.: UV-visible absorption cross sections of nitrous acid, J. Geophys. Res. Atmos., 105(D11), 14585–14592, doi:10.1029/2000JD900003, 2000.

Stutz, J., Alicke, B. and Neftel, A.: Nitrous acid formation in the urban atmosphere: Gradient measurements of NO2 and HONO over grass in Milan, Italy, J. Geophys. Res. Atmos., 107(22), doi:10.1029/2001JD000390, 2002.

Stutz, J., Alicke, B., Ackerman, R., Geyer, A., Wang, S., White, A. B., Williams, E. J., Spicer, C. W. and Fast, J. D.: Relative humidity dependence of HONO chemistry in urban areas, J. Geophys. Res. D Atmos., 109(3), doi:10.1029/2003jd004135, 2004.

Su, H., Cheng, Y., Oswald, R., TBehrendt, T., Trebs, I., Meixner, F. X., Andreae, M. O., Cheng, P., Zhang, Y. and Poschl, U.: Soil Nitrite as a Source of Atmospheric HONO and PH Radicals, Science (80-. )., 333(September), 1616–1618, 2011.

Sun, S., Moravek, A., Trebs, I., Kesselmeier, J. and Sörgel, M.: Investigation of the influence of liquid surface films on O3 and PAN deposition to plant leaves coated with organic/inorganic solution, J. Geophys. Res., 121(23), 14,239-14,256, doi:10.1002/2016JD025519, 2016.

Szopa, S., Naik, V., Adhikary, P. and et al.: Short-Lived Climate Forcers. In Climate Change 2021: The Physical Science Basis. Contribution of Working Group I to the Sixth Assessment Report of the Intergovernmental Panel on Climate Change., 2021.

Tan, Z., Lu, K., Jiang, M., Su, R., Wang, H., Lou, S., Fu, Q., Zhai, C., Tan, Q., Yue, D., Chen, D., Wang, Z., Xie, S. and Zeng, L.: Daytime atmospheric oxidation capacity in four Chinese megacities during the photochemically polluted season : a case study based on box model simulation, Atmos. Chem. Phys., 19(3), 3493–3513, 2019.

Tang, M. J., Cox, R. A. and Kalberer, M.: Compilation and evaluation of gas phase diffusion coefficients of reactive trace gases in the atmosphere: Volume 1. Inorganic compounds, Atmos. Chem. Phys., 14(17), 9233–9247, doi:10.5194/acp-14-9233-2014, 2014.

Tang, M. J., Shiraiwa, M., Pöschl, U., Cox, R. A. and Kalberer, M.: Compilation and evaluation of gas phase diffusion coefficients of reactive trace gases in the atmosphere: Volume 2. Diffusivities of organic compounds, pressure-normalised mean free paths, and average Knudsen numbers for gas uptake calculations, Atmos. Chem. Phys., 15(10), 5585–5598, doi:10.5194/acp-15-5585-2015, 2015.

Teklemariam, T. A. and Sparks, J. P.: Leaf fluxes of NO and NO2 in four herbaceous plant species: The role of ascorbic acid, Atmos. Environ., 40(12), 2235–2244, doi:10.1016/j.atmosenv.2005.12.010, 2006.

Thoene, B., Rennenberg, H. and Weber, P.: Absorption of atmospheric NO2 by spruce (Picea abies) trees: II. Parameterization of NO2 fluxes by controlled dynamic chamber experiments, New Phytol., 134(2), 257–266, doi:10.1111/j.1469-8137.1996.tb04630.x, 1996.

Thomas, C. and Foken, T.: Flux contribution of coherent structures and its implications for the exchange of energy and matter in a tall spruce canopy, Boundary-Layer Meteorol., 123(2), 317–337, doi:10.1007/s10546-006-9144-7, 2007.

Thompson, A. M.: The oxidizing capacity of the Earth's atmosphere: Probable past and future changes, Science (80-. )., 256(5060), 1157–1165, doi:10.1126/science.256.5060.1157, 1992.

Toyota, K., Dastoor, A. P. and Ryzhkov, A.: Parameterization of gaseous dry deposition in atmospheric chemistry models: Sensitivity to aerodynamic resistance formulations under statically stable conditions, Atmos. Environ., 147, 409–422, doi:10.1016/j.atmosenv.2016.09.055, 2016.

Travis, K. R. and Jacob, D. J.: Systematic bias in evaluating chemical transport models with maximum daily 8 h average (MDA8) surface ozone for air quality applications: A case study with GEOS-Chem v9.02, Geosci. Model Dev., 12(8), 3641–3648, doi:10.5194/gmd-12-3641-2019, 2019.

Travis, K. R., Jacob, D. J., Fisher, J. A., Kim, P. S., Marais, E. A., Zhu, L., Yu, K., Miller, C. C., Yantosca, R. M., Sulprizio, M. P., Thompson, A. M., Wennberg, P. O., Crounse, J. D., St Clair, J. M., Cohen, R. C., Laughner, J. L., Dibb, J. E., Hall, S. R., Ullmann, K., Wolfe, G. M., Pollack, I. B., Peischl, J., Neuman, J. A. and Zhou, X.: Why do models overestimate surface ozone in the Southeast United States?, Atmos. Chem. Phys., 16(21), 13561–13577, doi:10.5194/acp-16-13561-2016, 2016.

Travis, K. R., Crawford, J. H., Chen, G., Jordan, C. E., Nault, B. A., Kim, H., Jose, L., Campuzano-jost, P., Dibb, J. E., Woo, J., Kim, Y., Zhai, S., Wang, X. and Erin, E.: Limitations in representation of physical processes prevent successful simulation of PM2.5 during KORUS-AQ, Atmos. Chem. Phys. Discuss., (January), doi:10.5194/acp-2021-946, 2022.

Trumbore, S. E., Keller, M., Wofsy, S. C. and DA Costa, J. M.: Measurements of Soil and Canopy Exchange Rates in the Amazon Rain Forest using 22Rn, J. Geophsical Res., 95, 16865–16873, 1990.

Turnipseed, A. A., Huey, L. G., Nemitz, E., Stickel, R., Higgs, J., Tanner, D. J., Slusher, D. L., Sparks, J. P., Flocke, F. and Guenther, A.: Eddy covariance fluxes of peroxyacetyl nitrates (PANs) and NOy to a coniferous forest, J. Geophys. Res. Atmos., 111(9), 1–17, doi:10.1029/2005JD006631, 2006.

U.S. Environmental Protection Agency: Air Pollutant Emissions Trends Data, [online] Available from: https://www.epa.gov/air-emissions-inventories/air-pollutant-emissions-trends-data (Accessed 12 June 2020), 2021.

U.S. EPA: Reference Method for the Determination of Fine Particulate Matter as PM2.5 in the Atmosphere. [online] Available from: https://www.govinfo.gov/app/details/CFR-2011-title40-vol2/CFR-2011-title40-vol2-part50-appL/context, 1997.

U.S. EPA: ISA for Oxides of Nitrogen-Health Criteria, Research Triangle Park, NC., 2008.

U.S. EPA: Primary National Ambient Air Quality Standards for Nitrogen Dioxide, Fed. Regist., 75(26), 1–65 [online] Available from: http://www.regulations.gov, 2010.

U.S. EPA: Our Nation's Air: Status and Trends Through 2020. [online] Available from: https://gispub.epa.gov/air/trendsreport/2021, 2021.

US Environmental Protection Agency (EPA): Air Quality System Data Mart, [online] Available from: http://www.epa.gov/ttn/airs/aqsdatamart (Accessed 18 May 2016), 2016.

Valencia, A., Venkatram, A., Heist, D., Carruthers, D. and Arunachalam, S.: Development and evaluation of the R-LINE model algorithms to account for chemical transformation in the near-road environment, Transp. Res. Part D Transp. Environ., 59(2), 464–477, doi:10.1016/j.trd.2018.01.028, 2018.

VandenBoer, T. C., Brown, S. S., Murphy, J. G., Keene, W. C., Young, C. J., Pszenny, A. A. P., Kim, S., Warneke, C., De Gouw, J. A., Maben, J. R., Wagner, N. L., Riedel, T. P., Thornton, J. A., Wolfe, D. E., Dubé, W. P., Öztürk, F., Brock, C. A., Grossberg, N., Lefer, B., Lerner, B., Middlebrook, A. M. and Roberts, J. M.: Understanding the role of the ground surface in HONO vertical structure: High resolution vertical profiles during NACHTT-11, J. Geophys. Res. Atmos., 118(17), 10155–10171, doi:10.1002/jgrd.50721, 2013.

VandenBoer, T. C., Markovic, M. Z., Sanders, J. E., Ren, X., Pusede, S. E., Browne, E. C., Cohen, R. C., Zhang, L., Thomas, J., Brune, W. H. and Murphy, J. G.: Evidence for a nitrous acid (HONO) reservoir at the ground surface in Bakersfield, CA, during CalNex 2010, J. Geophys. Res. Atmos., 119, 9093–9106, doi:10.1002/2013JD020971.Received, 2014.

VandenBoer, T. C., Young, C. J., Talukdar, R. K., Markovic, M. Z., Brown, S. S., Roberts, J. M. and Murphy, J. G.: Nocturnal loss and daytime source of nitrous acid through reactive uptake and displacement, Nat. Geosci., 8(1), 55–60, doi:10.1038/ngeo2298, 2015.

Vaughan, A. R., Lee, J. D., Misztal, P. K., Metzger, S., Shaw, M. D., Lewis, A. C., Purvis, R. M., Carslaw, D. C., Goldstein, A. H., Hewitt, C. N., Davison, B., Beevers, S. D. and Karl, T. G.: Spatially resolved flux measurements of NOX from London suggest significantly higher emissions than predicted by inventories, Faraday Discuss., 189, 455–472, doi:10.1039/c5fd00170f, 2016.

Villena, G., Wiesen, P., Cantrell, C. A., Flocke, F., Fried, A., Hall, S. R., Hornbrook, R. S., Knapp, D., Kosciuch, E., Mauldin, R. L., McGrath, J. A., Montzka, D., Richter, D., Ullmann, K., Walega, J., Weibring, P., Weinheimer, A., Staebler, R. M., Liao, J., Huey, L. G. and Kleffmann, J.: Nitrous acid (HONO) during polar spring in Barrow, Alaska: A net source of OH radicals?, J. Geophys. Res. Atmos., 116(24), 1–12, doi:10.1029/2011JD016643, 2011.

Vinken, G. C. M., Boersma, K. F., Jacob, D. J. and Meijer, E. W.: Accounting for non-linear chemistry of ship plumes in the GEOS-Chem global chemistry transport model, Atmos. Chem. Phys., 11(22), 11707–11722, doi:10.5194/acp-11-11707-2011, 2011.

Vogel, B., Vogel, H., Kleffmann, J. and Kurtenbach, R.: Measured and simulated vertical profiles of nitrous acid - Part II. Model simulations and indications for a photolytic source, Atmos. Environ., 37(21), 2957–2966, doi:10.1016/S1352-2310(03)00243-7, 2003.

Wainman, T., Weschler, C. J., Lioy, P. J. and Zhang, J.: Effects of surface type and relative humidity on the production and concentration of nitrous acid in a model indoor environment, Environ. Sci. Technol., 35(11), 2200–2206, doi:10.1021/es000879i, 2001.

Walker, J. T., Beachley, G., Zhang, L., Benedict, K. B., Sive, B. C. and Schwede, D. B.: A review of measurements of air-surface exchange of reactive nitrogen in natural ecosystems across North America, Sci. Total Environ., 698(August 2019), 133975, doi:10.1016/j.scitotenv.2019.133975, 2020.

Walton, S., Gallagher, M. W., Choularton, T. W. and Duyzert, J.: Ozone and NO2 Exchange to Fruit Orchards, Atmosperic Environ., 31(17), 2767–2776, 1997.

Wang, C., Bottorff, B., Reidy, E., Rosales, Colleen, Collins, D. and et al.: Cooking, Bleach Cleaning, and Air Conditioning Strongly Impact LEvels of HONO in a House, Environ. Sci. Technol., 54, 13488–13497, 2020a.

Wang, C., Collins, D. B., Arata, C., Goldstein, A. H., Mattila, J. M., Farmer, D. K., Ampollini, L., DeCarlo, P. F., Novoselac, A., Vance, M. E., Nazaroff, W. W. and Abbatt, J. P. D.: Surface reservoirs dominate dynamic gas-surface partitioning of many indoor air constituents, Sci. Adv., 6(8), 1–12, doi:10.1126/sciadv.aay8973, 2020b.

Wang, C. C., Prather, K. A., Sznitman, J., Jimenez, J. L. and Marr, L. C.: Airborne transmission of respiratory viruses, Science (80-. )., 373, doi:10.1097/00004669-199509000-00015, 2021.

Wang, K., Dickinson, R. E. and Liang, S.: Clear sky visibility has decreased over land globally from 1973 to 2007, Science (80-. )., 323(5920), 1468–1470, doi:10.1126/science.1167549, 2009.

Wang, K. C., Dickinson, R. E., Su, L. and Trenberth, K. E.: Contrasting trends of mass and optical properties of aerosols over the Northern Hemisphere from 1992 to 2011, Atmos. Chem. Phys., 12(19), 9387–9398, doi:10.5194/acp-12-9387-2012, 2012.

Wang, Q., Jacob, D. J., Fisher, J. A., Mao, J., Leibensperger, E. M., Carouge, C. C., Le Sager, P., Kondo, Y., Jimenez, J. L., Cubison, M. J. and Doherty, S. J.: Sources of carbonaceous aerosols and deposited black carbon in the Arctic in winter-spring: Implications for radiative forcing, Atmos. Chem. Phys., 11(23), 12453–12473, doi:10.5194/acp-11-12453-2011, 2011a.

Wang, W., Ganzeveld, L., Rossabi, S., Hueber, J. and Helmig, D.: Measurement report: Leaf-scale gas exchange of atmospheric reactive trace species (NO2, NO, O3) at a northern hardwood forest in Michigan, Atmos. Chem. Phys., 20(19), 11287–11304, doi:10.5194/acp-20-11287-2020, 2020c.

Wang, Y., Jacob, J. and Logan, A.: Global simulation of tropospheric O3-NOx-hydrocarbon chemistry: 1. Model Formulation, J. Geogr. Res., 103, 10713–10725, 1998.

Wang, Y. J., DenBleyker, A., McDonald-Buller, E., Allen, D. and Zhang, K. M.: Modeling the chemical evolution of nitrogen oxides near roadways, Atmos. Environ., 45(1), 43–52, doi:10.1016/j.atmosenv.2010.09.050, 2011b.

Weagle, C. L., Snider, G., Li, C., Van Donkelaar, A., Philip, S., Bissonnette, P., Burke, J., Jackson, J., Latimer, R., Stone, E., Abboud, I., Akoshile, C., Anh, N. X., Brook, J. R., Cohen, A., Dong, J., Gibson, M. D., Griffith, D., He, K. B., Holben, B. N., Kahn, R., Keller, C. A., Kim, J. S., Lagrosas, N., Lestari, P., Khian, Y. L., Liu, Y., Marais, E. A., Martins, J. V., Misra, A., Muliane, U., Pratiwi, R., Quel, E. J., Salam, A., Segev, L., Tripathi, S. N., Wang, C., Zhang, Q., Brauer, M., Rudich, Y. and Martin, R. V.: Global Sources of Fine Particulate Matter: Interpretation of PM2.5 Chemical Composition Observed by SPARTAN using a Global Chemical Transport Model, Environ. Sci. Technol., 52(20), 11670–11681, doi:10.1021/acs.est.8b01658, 2018.

Weatherhead, E. C., Reinsel, G. C., Tiao, G. C., Meng, X. L., Choi, D., Cheang, W. K., Keller, T., DeLuisi, J., Wuebbles, D. J., Kerr, J. B., Miller, A. J., Oltmans, S. J. and Frederick, J. E.: Factors affecting the detection of trends: Statistical considerations and applications to environmental data, J. Geophys. Res. Atmos., 103(D14), 17149–17161, doi:10.1029/98JD00995, 1998.

Weatherhead, E. C., Stevermer, A. J. and Schwartz, B. E.: Detecting environmental changes and trends, Phys. Chem. Earth, 27(6–8), 399–403, doi:10.1016/S1474-7065(02)00019-0, 2002.

Weber, P. and Renenberg, H.: Dependency of Nitrogen Dioxide Fluxes to Wheat (Triticum Aestivum L.) Leaves From NO2 Concentration, Light Intensity, Temperature, and Relative Humidity Determined From Controlled Dynamic Chamber Experiments, Atmosperic Environ., 30(17), 3001–3009, 1996.

Wen, D., Zhang, L., Lin, J. C., Vet, R. and Moran, M. D.: An evaluation of ambient ammonia concentrations over southern Ontario simulated with different dry deposition schemes within STILT-Chem v0.8, Geosci. Model Dev., 7(3), 1037–1050, doi:10.5194/gmd-7-1037-2014, 2014.

Wen, L., Chen, T., Zheng, P., Wu, L., Wang, X., Mellouki, A., Xue, L. and Wang, W.: Nitrous acid in marine boundary layer over eastern Bohai Sea, China: Characteristics, sources, and implications, Sci. Total Environ., 670, 282–291, doi:10.1016/j.scitotenv.2019.03.225, 2019.

Wentworth, G. R., Murphy, J. G., Gregoire, P. K., Cheyne, C. A. L., Tevlin, A. G. and Hems, R.: Soil-atmosphere exchange of ammonia in a non-fertilized grassland: Measured emission potentials and inferred fluxes, Biogeosciences, 11(20), 5675–5686, doi:10.5194/bg-11-5675-2014, 2014.

Wentworth, G. R., Murphy, J. G., Benedict, K. B., Bangs, E. J. and Collett, J. L.: The role of dew as a night-time reservoir and morning source for atmospheric ammonia, Atmos. Chem. Phys., 16(11), 7435–7449, doi:10.5194/acp-16-7435-2016, 2016.

Wenzel, A., Kalthoff, N. and Horlacher, V.: On the profiles of wind velocity in the roughness sublayer above a coniferous forest, Boundary-Layer Meteorol., 84(2), 219–230, doi:10.1023/A:1000444911103, 1997.

Wesely, M. L.: Parametrization of surface resistance to gaseous dry deposition in regional-scale numerical model, Atmos. Eniviron., 23(6), 1293–1304, 1989.

Wesely, M. L. and Hicks, B. B.: Some factors that affect the deposition rates of sulfur dioxide and similar gases on vegetation, J. Air Pollut. Control Assoc., 27(11), 1110–1116, doi:10.1080/00022470.1977.10470534, 1977.

Wesely, M. L. and Hicks, B. B.: A review of the current status of knowledge on dry deposition, Atmos. Eniviron., 34, 2261–2282, 2000.

West, J. J., Cohen, A., Dentener, F., Brunekreef, B., Zhu, T., Armstrong, B., Bell, M. L., Brauer, M., Carmichael, G., Costa, D. L., Dockery, D. W., Kleeman, M., Krzyzanowski, M., Künzli, N., Liousse, C., Lung, S. C. C., Martin, R. V., Pöschl, U., Pope, C. A., Roberts, J. M., Russell, A. G. and Wiedinmyer, C.: "what We Breathe Impacts Our Health: Improving Understanding of the Link between Air Pollution and Health," Environ. Sci. Technol., 50(10), 4895–4904, doi:10.1021/acs.est.5b03827, 2016.

Winer, A. M. and Biermann, H. W.: Long pathlength differential optical absorption spectroscopy (D O A S) measurements of gaseous HONO, NO2 and HCNO in the California South Coast Air Basin, Res. Chem. Intermed., 20(3–5), 423–445, doi:10.1163/156856794X00405, 1994.

Wojtal, P., Halla, J. D. and McLaren, R.: Pseudo steady states of HONO measured in the nocturnal marine boundary layer: A conceptual model for HONO formation on aqueous surfaces, Atmos. Chem. Phys., 11(7), 3243–3261, doi:10.5194/acp-11-3243-2011, 2011.

Wolfe, A. P., Baron, J. S. and Cornett, R. J.: Anthropogenic nitrogen deposition induces rapid ecological changes in alpine lakes of the Colorado Front Range (USA), J. Paleolimnol., 25(1), 1–7, doi:10.1023/A:1008129509322, 2001.

Wolfe, D. E.: Boulder Atmospheric Observatory: 1977–2016: The End of an Era and Lessons Learned, Bull. Am. Meteorol. Soc., 99(7), 1345–1358, doi:10.1175/BAMS-D-17-0054.1, 2018.

Wong, A. Y. H., Geddes, J. A., Tai, A. P. K. and Silva, S. J.: Importance of Dry Deposition Parameterization Choice in Global Simulations of Surface Ozone, Atmos. Chem. Phys. Discuss., 1–41, doi:10.5194/acp-2019-429, 2019.

Wong, K. W. and Stutz, J.: Influence of nocturnal vertical stability on daytime chemistry: A one-dimensional model study, Atmos. Environ., 44(31), 3753–3760, doi:10.1016/j.atmosenv.2010.06.057, 2010.

Wong, K. W., Lefer, B. L., Rappenglück, B. and Stutz, J.: Vertical profiles of nitrous acid in the nocturnal urban atmosphere of Houston, TX, Atmos. Chem. Phys., 11(8), 3595–3609, doi:10.5194/acp-11-3595-2011, 2011.

Wong, K. W., Tsai, C., Lefer, B., Grossberg, N. and Stutz, J.: Modeling of daytime HONO vertical gradients during SHARP 2009, Atmos. Chem. Phys., 13(7), 3587–3601, doi:10.5194/acp-13-3587-2013, 2013.

World Health Organization: Air Quality Guidelines. [online] Available from: https://www.euro.who.int/en/publications/abstracts/air-quality-guidelines-for-europe (last access: 1 September 2021), 2000.

Wu, Z., Wang, X., Chen, F., Turnipseed, A. A., Guenther, A. B., Niyogi, D., Charusombat, U., Xia, B., William Munger, J. and Alapaty, K.: Evaluating the calculated dry deposition velocities of reactive nitrogen oxides and ozone from two community models over a temperate deciduous forest, Atmos. Environ., 45(16), 2663–2674, doi:10.1016/j.atmosenv.2011.02.063, 2011.

Xu, Y.: Improvements in the Operation of SO2 Scrubbers in China's Coal Power Plants, Environ. Sci. Technol., 45(2), 380–385, 2011.

Yabushita, A., Enami, S., Sakamoto, Y., Kawasaki, M., Hoffmann, M. R. and Colussi, A. J.: Anion-catalyzed dissolution of NO2 on aqueous microdroplets, J. Phys. Chem. A, 113(17), 4844–4848, doi:10.1021/jp900685f, 2009.

Yan, Y., Lin, J. and He, C.: Ozone trends over the United States at different times of day, Atmos. Chem. Phys., 18(2), 1185–1202, doi:10.5194/acp-18-1185-2018, 2018.

Yang, J., Shen, H., Guo, M. Z., Zhao, M., Jiang, Y., Chen, T., Liu, Y., Li, H., Zhu, Y., Meng, H., Wang, W. and Xue, L.: Strong marine-derived nitrous acid (HONO) production observed in the coastal atmosphere of northern China, Atmos. Environ., 244(September 2020), 117948, doi:10.1016/j.atmosenv.2020.117948, 2021.

Ye, C., Gao, H., Zhang, N. and Zhou, X.: Photolysis of Nitric Acid and Nitrate on Natural and Artificial Surfaces, Environ. Sci. Technol., 50(7), 3530–3536, doi:10.1021/acs.est.5b05032, 2016.

Ye, C., Zhang, N., Gao, H. and Zhou, X.: Photolysis of Particulate Nitrate as a Source of HONO and NOx, Environ. Sci. Technol., 51(12), 6849–6856, doi:10.1021/acs.est.7b00387, 2017.

Ye, C., Zhou, X., Pu, D., Stutz, J., Festa, J., Spolaor, M., Tsai, C., Cantrell, C., Mauldin, R. L., Weinheimer, A., Hornbrook, R. S., Apel, E. C., Guenther, A., Kaser, L., Yuan, B., Karl, T., Haggerty, J., Hall, S., Ullmann, K., Smith, J. and Ortega, J.: Tropospheric HONO distribution and chemistry in the southeastern US, Atmos. Chem. Phys., 18(12), 9107–9120, doi:10.5194/acp-18-9107-2018, 2018.

Yeung, L. Y., Murray, L. T., Martinerie, P., Witrant, E., Hu, H., Banerjee, A., Orsi, A. and Chappellaz, J.: Isotopic constraint on the twentieth-century increase in tropospheric ozone, Naure, 570, 224–227, doi:10.1038/s41586-019-1277-1, 2019.

Yienger, J. and Levy, H.: Empirical model of global soil-biogenic NOx emissions, J. Geogr. Res., 100, 11447–11464, 1995.

Ying, Q. and Kleeman, M. J.: Source contributions to the regional distribution of secondary particulate matter in California, Atmos. Environ., 40(4), 736–752, doi:10.1016/j.atmosenv.2005.10.007, 2006.

Yoon, J., Von Hoyningen-Huene, W., Vountas, M. and Burrows, J. P.: Analysis of linear long-term trend of aerosol optical thickness derived from SeaWiFS using BAER over Europe and South China, Atmos. Chem. Phys., 11(23), 12149–12167, doi:10.5194/acp-11-12149-2011, 2011.

Yoon, J., Von Hoyningen-Huene, W., Kokhanovsky, A. A., Vountas, M. and Burrows, J. P.: Trend analysis of aerosol optical thickness and ngström exponent derived from the global AERONET spectral observations, Atmos. Meas. Tech., 5(6), 1271–1299, doi:10.5194/amt-5-1271-2012, 2012.

Yu, K., Jacob, D. J., Fisher, J. A., Kim, P. S., Marais, E. A., Miller, C. C., Travis, K. R., Zhu, L., Yantosca, R. M., Sulprizio, M. P., Cohen, R. C., Dibb, J. E., Fried, A., Mikoviny, T., Ryerson, T. B., Wennberg, P. O. and Wisthaler, A.: Sensitivity to grid resolution in the ability of a chemical transport model to simulate observed oxidant chemistry under high-isoprene conditions, Atmos. Chem. Phys., 16(7), 4369–4378, doi:10.5194/acp-16-4369-2016, 2016.

Yu, Y., Galle, B., Panday, A., Hodson, E., Prinn, R. and Wang, S.: Observations of high rates of NO2-HONO conversion in the nocturnal atmospheric boundary layer in Kathmandu, Nepal, Atmos. Chem. Phys., 9(17), 6401–6415, doi:10.5194/acp-9-6401-2009, 2009.

Zakoura, M. and Pandis, S. N.: Overprediction of aerosol nitrate by chemical transport models: The role of grid resolution, Atmos. Environ., 187(June), 390–400, doi:10.1016/j.atmosenv.2018.05.066, 2018.

Zender, C. S.: Mineral Dust Entrainment and Deposition (DEAD) model: Description and 1990s dust climatology, J. Geophys. Res., 108(D14), 82234, doi:10.1029/2002JD002775, 2003.

Zha, Q., Xue, L., Wang, T., Xu, Z., Yeung, C., Louie, P. K. K. and Luk, C. W. Y.: Large conversion rates of NO2 to HNO2 observed in air masses from the South China Sea: Evidence of strong production at sea surface?, Geophys. Res. Lett., 41(21), 7710–7715, doi:10.1002/2014GL061429, 2014.

Zhang, J. and Reid, J. S.: A decadal regional and global trend analysis of the aerosol optical depth using a data-assimilation grade over-water MODIS and Level 2 MISR aerosol products, Atmos. Chem. Phys., 10(22), 10949–10963, doi:10.5194/acp-10-10949-2010, 2010.

Zhang, J., An, J., Qu, Y., Liu, X. and Chen, Y.: Science of the Total Environment Impacts of potential HONO sources on the concentrations of oxidants and secondary organic aerosols in the Beijing-Tianjin-Hebei region of China, Sci. Total Environ., 647, 836–852, doi:10.1016/j.scitotenv.2018.08.030, 2019.

Zhang, L., Brook, J. R. and Vet, R.: On ozone dry deposition - With emphasis on non-stomatal uptake and wet canopies, Atmos. Environ., 36(30), 4787–4799, doi:10.1016/S1352-2310(02)00567-8, 2002.

Zhang, L., Brook, J. R. and Vet, R.: A revised parameterization for gaseous dry deposition in air-quality models, Atmos. Chem. Phys. Discuss., 3(2), 1777–1804, doi:10.5194/acpd-3-1777-2003, 2003a.

Zhang, L., Brook, J. R. and Vet, R.: Evaluation of a non-stomatal resistance parameterization for SO2 dry deposition, Atmos. Environ., 37(21), 2941–2947, doi:10.1016/S1352-2310(03)00268-1, 2003b.

Zhang, L., Vet, R., O'Brien, J. M., Mihele, C., Liang, Z. and Wiebe, A.: Dry deposition of individual nitrogen species at eight Canadian rural sites, J. Geophys. Res. Atmos., 114(2), 1–13, doi:10.1029/2008JD010640, 2009a.

Zhang, L., Jacob, D. J., Knipping, E. M., Kumar, N., Munger, J. W., Carouge, C. C., Van Donkelaar, A., Wang, Y. X. and Chen, D.: Nitrogen deposition to the United States: Distribution, sources, and processes, Atmos. Chem. Phys., 12(10), 4539–4554, doi:10.5194/acp-12-4539-2012, 2012a.

Zhang, L., Wang, T., Zhang, Q., Zheng, J., Xu, Z. and Lv, M.: Potential sources of nitrous acid (HONO) and their impacts on ozone: A WRF-Chem study in a polluted subtropical region, J. Geogr. Res. Atmos., 121, 3645–3662, doi:10.1038/175238c0, 2016.

Zhang, Q., Streets, D. G., Carmichael, G. R., He, K. B., Huo, H., Kannari, A., Klimont, Z., Park, I. S. and Reddy, S.: Asian emissions in 2006 for the NASA INTEX-B mission, Atmos. Chem. Phys., 9, 5131–5153, 2009b.

Zhang, R., Sarwar, G., Fung, J. C. H., Lau, A. K. H. and Zhang, Y.: Examining the impact of nitrous acid chemistry on ozone and PM over the pearl river delta region, Adv. Meteorol., 2012(x), doi:10.1155/2012/140932, 2012b.

Zhang, R., Jing, J., Tao, J., Hsu, S. C., Wang, G., Cao, J., Lee, C. S. L., Zhu, L., Chen, Z., Zhao, Y. and Shen, Z.: Chemical characterization and source apportionment of PM2.5 in Beijing: Seasonal perspective, Atmos. Chem. Phys., 13(14), 7053–7074, doi:10.5194/acp-13-7053-2013, 2013.

Zhang, Y., Mathur, R., Bash, J. O., Hogrefe, C., Xing, J. and Roselle, S. J.: Long-term trends in total inorganic nitrogen and sulfur deposition in the US from 1990 to 2010, Atmos. Chem. Phys., 18(12), 9091–9106, doi:10.5194/acp-18-9091-2018, 2018.

Zhao, P., Zhang, X., Xu, X. and Zhao, X.: Long-term visibility trends and characteristics in the region of Beijing, Tianjin, and Hebei, China, Atmos. Res., 101(3), 711–718, doi:10.1016/j.atmosres.2011.04.019, 2011.

Zhao, T. X. P., Laszlo, I., Guo, W., Heidinger, A., Cao, C., Jelenak, A., Tarpley, D. and Sullivan, J.: Study of long-term trend in aerosol optical thickness observed from operational AVHRR satellite instrument, J. Geophys. Res. Atmos., 113(7), 1–14, doi:10.1029/2007JD009061, 2008.

Zhou, X., Civerolo, K., Dai, H., Huang, G., Schwab, J. and Demerjian, K.: Summertime nitrous acid chemistry in the atmospheric boundary layer at a rural site in New York State, J. Geophys. Res. Atmos., 107(21), 1–11, doi:10.1029/2001JD001539, 2002.

Zhu, Y., Toon, O. B., Jensen, E. J., Bardeen, C. G., Mills, M. J., Tolbert, M. A., Yu, P. and Woods, S.: Persisting volcanic ash particles impact stratospheric SO2 lifetime and aerosol optical properties, Nat. Commun., 11(1), 1–11, doi:10.1038/s41467-020-18352-5, 2020.

# Appendix A

## A.1 Copyright Information

Chapter 2 of this thesis was previously published and is reprinted herein with permission from Environmental Science and Technology, 2014, 48, 19, 11109-11118. Copyright 2014 American Chemical Society. https://pubs.acs.org/doi/10.1021/es502113p